Transactions of the ASME, Journal of Heat Transfer (ISSN 0022-1481) is published monthly by The American Society of Mechanical Engineers, Three Park Avenue, New York, NY 10016. Periodicals postage paid at New York, NY and additional mailing offices. POSTMASTER: Send address changes to Transactions of the ASME, Journal of Heat Transfer, c/o THE AMERICAN SOCIETY OF MECHANICAL ENGINEERS, 22 Law Drive, Box 2300, Fairfield, NJ 07007-2300. **CHANGES OF ADDRESS** must be received at Society headquarters seven weeks before they are to be effective. Please send old label and new address.

Journal of Heat Transfer

Published Monthly by ASME

VOLUME 129 • NUMBER 9 • SEPTEMBER 2007

TECHNICAL PAPERS

(Contents continued on inside back cover)

This journal is printed on acid-free paper, which exceeds the ANSI Z39.48-1992 specification for permanence of paper and library materials. ♾™
♻ 85% recycled content, including 10% post-consumer fibers.

(Contents continued)

Journal of Heat Transfer Volume 129, Number 9 SEPTEMBER 2007

TECHNICAL BRIEFS

DISCUSSION

(Contents continued on facing page)

ERRATUM

The ASME Journal of Heat Transfer is abstracted and indexed in the following:

Applied Science and Technology Index, Chemical Abstracts, Chemical Engineering and Biotechnology Abstracts (Electronic equivalent of Process and Chemical Engineering), Civil Engineering Abstracts, Compendex (The electronic equivalent of Engineering Index), Corrosion Abstracts, Current Contents, E & P Health, Safety, and Environment, Ei EncompassLit, Engineered Materials Abstracts, Engineering Index, Enviroline (The electronic equivalent of Environment Abstracts), Environment Abstracts, Environmental Engineering Abstracts, Environmental Science and Pollution Management, Fluidex, Fuel and Energy Abstracts, Index to Scientific Reviews, INSPEC, International Building Services Abstracts, Mechanical & Transportation Engineering Abstracts, Mechanical Engineering Abstracts, METADEX (The electronic equivalent of Metals Abstracts and Alloys Index), Petroleum Abstracts, Process and Chemical Engineering, Referativnyi Zhurnal, Science Citation Index, SciSearch (The electronic equivalent of Science Citation Index), Theoretical Chemical Engineering

Anisotropic Heat Conduction Effects in Proton-Exchange Membrane Fuel Cells

Chaitanya J. Bapat
Graduate Research Assistant
e-mail: cjb282@psu.edu

Stefan T. Thynell[1]
Fellow ASME
e-mail: Thynell@psu.edu

Department of Mechanical and Nuclear Engineering,
The Pennsylvania State University,
University Park, PA 16802

The focus of this work is to study the effects of anisotropic thermal conductivity and thermal contact conductance on the overall temperature distribution inside a fuel cell. The gas-diffusion layers and membrane are expected to possess an anisotropic thermal conductivity, whereas a contact resistance is present between the current collectors and gas-diffusion layers. A two-dimensional single phase model is used to capture transport phenomena inside the cell. From the use of this model, it is predicted that the maximum temperatures inside the cell can be appreciably higher than the operating temperature of the cell. A high value of the in-plane thermal conductivity for the gas-diffusion layers was seen to be essential for achieving smaller temperature gradients. However, the maximum improvement in the heat transfer characteristics of the fuel cell brought about by increasing the in-plane thermal conductivity is limited by the presence of a finite thermal contact conductance at the diffusion layer/current collector interface. This was determined to be even more important for thin gas-diffusion layers. Anisotropic thermal conductivity of the membrane, however, did not have a significant impact on the temperature distribution. The thermal contact conductance at the diffusion layer/current collector interface strongly affected the temperature distribution inside the cell. [DOI: 10.1115/1.2712478]

Keywords: Proton-exchange membrane fuel cell (PEMFC), heat transfer, anisotropy, contact resistance

1 Introduction

Fuel cells (FCs) are electrochemical devices that convert chemical energy directly into electricity. Over the past few years, there has been an increasing amount of interest in the use of proton-exchange-membrane (PEM) fuel cells as an environmentally friendly power source. In these cells, oxygen and hydrogen combine to form water, and a part of the released energy from the reaction is directly converted to electricity. Thus the PEMFC produces no harmful emissions. It also operates at much lower temperatures than conventional internal combustion engines and is also thermodynamically more efficient. It is envisaged that these cells would start replacing internal combustion engines towards the end of the current decade. This would require the development of a large-scale hydrogen infrastructure [1,2], and a fuel cell that would be able to produce power at an adequate power density and at a good energy conversion efficiency [3]. A better understanding of the various processes affecting the operation of a PEMFC is required for its development as a viable energy conversion device for the future.

A schematic of a typical PEMFC is shown in Fig. 1. A PEMFC consists of a polymer electrolyte with catalyst layers sandwiched between two gas-diffusion layers (GDLs). Hydrogen and air are the reactant gases at anode and cathode, respectively. These gases flow through the gas channels that are usually machined into the current-collector plate. The current collector plate also provides a path for the excess heat to flow to the coolant. The gases then diffuse through the porous GDLs and react at the catalyst layer, which is a mixture of fine platinum particles supported on relatively large carbon particles with the membrane material filling the interstices between the carbon particles. The overall reactions occurring at the anode and cathode are, respectively, given by

$$2H_2 \rightarrow 4H^+ + 4e^-$$

$$O_2 + 4H^+ + 4e^- \rightarrow 2H_2O$$

The protons diffuse through the polymer electrolyte membrane, whereas the electrons are conducted through the current collector plates to an external circuit. It should be noted that one or two water molecules are also transported across the membrane with the proton [4]. Coolant water is circulated through the channels machined into the coolant plate to remove excess heat.

Many modeling efforts have been made to study the electrochemical-thermal aspects of fuel cells. The initial efforts in this field were made by Springer [5] and Bernardi and Verbrugge [6,7], who developed one-dimensional isothermal models for studying the effects of mass diffusion and species transport through the porous electrodes and membrane. The earliest attempts to model water and heat management issues in a PEM fuel cell were made by Fuller and Newman [8] and by Nguyen and White [9]. Djilali and Lu [10] developed a one-dimensional, nonisothermal model for studying the performance at different current densities. Wohr and co-workers [11,12] and Rowe and Li [13] also developed one-dimensional nonisothermal models to study the effects of various other parameters on fuel-cell operation. Dutta et al. [14] developed a three-dimensional single-phase isothermal model for studying transport processes in a fuel cell. Wang et al. [15,16] also developed a multidimensional isothermal model for simulating transport processes in a fuel cell with liquid water confined to catalyst layers. They analyzed the effects of hydrogen dilution at the anode inlet and interdigitated flow field on the performance of the fuel cell. Berning et al. [17] and Zhou and Liu [18] also developed three-dimensional nonisothermal models for studying fuel cell behavior. Ju et al. [19] developed a three-dimensional single-phase nonisothermal model and studied the effects of variation of thermal conductivity of the GDL and inlet humidity on fuel-cell operation. Sivertsen and Djilali [20]

[1]Corresponding author.

Contributed by the Heat Transfer Division of ASME for publication in the JOURNAL OF HEAT TRANSFER. Manuscript received November 14, 2005; final manuscript received July 26, 2006. Review conducted by Ranga Pitchumani.

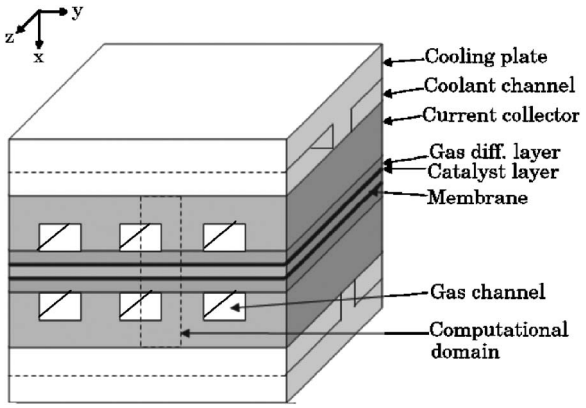

Fig. 1 Schematic of PEM fuel cell and coordinate system

also developed a nonisothermal three-dimensional model for simulating fuel cell operation and integrated it with a commercial CFD software. All these models neglected the effects of water vapor condensation on cell performance. Baschuk and Li [21] formulated a model to predict the performance of a fuel cell in the diffusion limited region of the polarization curve (high current densities). However, their model did not have an explicit two-phase model to predict the flow of different phases. Stockie [22] developed a two-dimensional model by taking into account the effects of phase and temperature change in a fuel-cell cathode. Berning and Djilali [23] developed a two-phase, multidimensional, nonisothermal model for fuel-cell simulation based on the unsaturated flow theory [24]. Wang et al. [25] developed a two-phase model for simulating transport processes in a fuel-cell cathode based on the multiphase mixture model developed by Wang and Cheng [26]. Hu et al. [27,28], Mazumder and Cole [29], and Sun et al. [30] also developed models based on the multiphase mixture model. Birgersson et al. [31] developed a two-phase, nonisothermal model for a PEMFC. Shimpalee et al. [32] implemented their two-phase model on a high performance cluster to simulate a large-scale PEMFC. Recently, Baschuk and Li [33] developed a three-dimensional formulation for modeling fuel-cell transport processes based on a two-phase, two-fluid porous media model which incorporated a spatial temperature variation. However, a complete three-dimensional implementation of this model has not yet been made.

Apart from the above models, there have been studies which concentrated on certain other specific aspects of fuel-cell operation. Nam and Kaviany [34] studied the effects of water saturation and two-layer GDL on fuel-cell operation using a one-dimensional nonisothermal model. Pasaogullari and Wang [35,36] studied the role of a microporous layer in the cathode GDL on the phase distribution. Yuan and co-workers [37] studied the variation in temperature of reactant gases in both cathode and anode gas channels. Musser and Wang [38] studied the variation of coolant temperature through the length of the cooling channel for different operating conditions of the cell. Mawardi et al. [39] studied the optimization of operating parameters of a fuel cell for obtaining the best performance. The present work is directed towards developing a better understanding of heat transfer by taking into account the effect of anisotropic thermal conductivity and contact conductance, which were not considered in previous studies with an aim to develop a more representative model for heat transfer within the fuel cell.

It is known that the GDLs and the polymer electrolyte membrane are fibrous polymer-like materials. Kurabayashi [40] noted that thin polymer films tend to show anisotropic behavior in their thermal diffusivity, as the energy transport is more efficient along the polymer chains. This has also been confirmed by many previous and new experimental results [41–43]. The ratio of conductivities in directions parallel and perpendicular to the polymer chain can also be very high. In case of GDLs and membrane, such preferential alignment of fibers and polymeric chains, respectively, can lead to anisotropic thermal conductivity. In fact, measurements of the electrical conductivity in Nafion reveal that the in-plane conductivity is about 3.5 times larger than the normal conductivity [44,45]. The thermal contact conductance at the interfaces of different layers in the fuel cell is also expected to have a significant effect on the temperature distribution inside the cell. The purpose of this paper is to bring out the effect of anisotropic thermal conductivity and thermal contact conductance on the temperature distribution within the fuel cell using a single-phase, two-dimensional model. Detailed investigation using more sophisticated models is to be considered in future publications.

2 Model Formulation

The PEMFC generates in some cases almost 50% of waste heat of the total available energy. This heat has to be effectively dissipated for stable and reliable operation of the fuel cell. The heat generated is caused by (1) kinetic loss in the catalyst layers (largely cathode), (2) Ohmic loss in the membrane and catalyst layers, and (3) reversible heat release. In the present work, a single-phase, two-dimensional model is used to assess the effects of anisotropic thermal conductivity and thermal contact resistance on the overall temperature distribution inside the cell. The complete model consists of coupled flow, species, electrochemistry, and heat transport models. The two-dimensional computational domain chosen for the present work is shown in Fig. 1.

2.1 Flow Model. The single-phase mass and momentum balance equations with appropriate source terms for the porous drag, production/consumption of reactants and the electro-osmotic drag in the membrane are solved all over the domain. The mass and momentum balances are, respectively, written as

$$\frac{\partial \varepsilon \rho}{\partial t} + \nabla \cdot (\varepsilon \rho u) = -\nabla \cdot \left(\frac{n_{\text{oe}} M_{\text{H}_2\text{O}}}{F} i \right) + S \tag{1}$$

and

$$\frac{\partial}{\partial t}(\varepsilon \rho u) + \nabla \cdot (\varepsilon \rho u u) = -\nabla(\varepsilon p) + \nabla \cdot (\varepsilon \tau) - \frac{\mu}{k_p} u \tag{2}$$

Here the first term on the right-hand side of Eq. (1) represents the source term due to the electro-osmotic drag, and the last term represents the source due to production/consumption of reactants and products. This source term is

$$S = -\frac{|\nabla \cdot i|}{2F} M_{\text{H}_2} \tag{3}$$

for the consumption of hydrogen in anode catalyst layer, whereas

$$S = -\frac{|\nabla \cdot i|}{4F} M_{\text{O}_2} \tag{4}$$

$$S = \frac{|\nabla \cdot i|}{2F} M_{\text{H}_2\text{O}} \tag{5}$$

are used to describe the consumption of oxygen and production of water, respectively, in the cathode catalyst layer. In addition, the last term in Eq. (2) represents the source term due to porous drag and is based on Darcy's law.

2.2 Species Transport Model. The flow of reacting species (hydrogen and oxygen) and water vapor is modeled by solving the species conservation equation for each of these species. The species conservation equation for species i is given by

$$\frac{\partial}{\partial t}(\varepsilon C_i) + \nabla \cdot (\varepsilon u C_i) = \nabla \cdot (\varepsilon D_i \nabla C_i) + J_i \tag{6}$$

The source terms for this equation (J_i) are the same as those given by Eqs. (3)–(5), except they are molar-based quantities.

2.3 Electrochemical Reactions. The electrochemistry is included by solving conservation of membrane phase potential over the membrane electrode assembly (MEA) with appropriate source terms in the catalyst layers for the production and consumption of protons by electrochemical reactions

$$-\nabla^2(\kappa_m \phi_m) = \nabla \cdot i \tag{7}$$

The solid phase (the platinum-carbon matrix) is assumed to be a good electrical conductor and hence the solid-phase potential is assumed to be constant in the catalyst layers.

The electrochemical reactions are modeled using the Butler-Volmer rate expressions [46], and in anode and cathode catalyst layers are, respectively, given by

$$\nabla \cdot i = j_a = i_{\text{oa}}^{\text{ref}}\left[\exp\left\{\frac{\alpha_a F}{RT}(\phi_s - \phi_m)\right\} - \exp\left\{-\frac{\alpha_c F}{RT}(\phi_s - \phi_m)\right\}\right] \times \left(\frac{C_{\text{H}_2}}{C_{\text{H}_2}^{\text{ref}}}\right)^{0.5} \tag{8a}$$

$$= j_c = i_{\text{oc}}^{\text{ref}}\left[\exp\left\{\frac{\alpha_a F}{RT}(\phi_s - \phi_m)\right\} - \exp\left\{-\frac{\alpha_c F}{RT}(\phi_s - \phi_m)\right\}\right] \times \left(\frac{C_{\text{O}_2}}{C_{\text{O}_2}^{\text{ref}}}\right) \tag{8b}$$

and elsewhere

$$\nabla \cdot i = 0 \tag{8c}$$

2.4 Heat Transport Model. The flow rates of gases inside the GDLs are expected to be extremely small due to the presence of the porous medium. Hence, heat transfer due to the flow of these gases is neglected. The heat flow is modeled using the two-dimensional heat conduction equation given by

$$\frac{\partial}{\partial t}(\rho c T) = k_{xx}\frac{\partial^2 T}{\partial x^2} + k_{yy}\frac{\partial^2 T}{\partial y^2} + q''' \tag{9}$$

where the transient term is included in the numerical scheme even though only the steady state is considered. Here, the heat source terms within the anode catalyst layer, membrane and cathode catalyst layer, are, respectively, given by

$$q''' = |j_a \eta_a| + \frac{i_m^2}{\kappa_m} \tag{10a}$$

$$q''' = \frac{i_m^2}{\kappa_m} \tag{10b}$$

$$q''' = |j_c \eta_c| + \frac{i_m^2}{\kappa_m} + \left| T\Delta S \frac{j_a}{2F} \right| - \frac{|\nabla \cdot i|}{2F} M_{\text{H}_2\text{O}} L_w \tag{10c}$$

The first term for both the anode and cathode source terms corresponds to heat generation due to kinetic loss at the catalyst reactant layer. The next term in both cases represents heat generation due to flow of ions through the membrane material. The membrane source term corresponds to heat generated due to resistance offered to the flow of protons through the membrane. The third term in case of the cathode corresponds to the heat generation due to reversible heat release. The entire reversible heat release due to the chemical reaction is assumed to occur at the cathode [19]. The last term for the cathode catalyst layer represents enthalpy change due to evaporation. The liquid water generated in the cathode is assumed to instantaneously evaporate to vapor phase. It is also assumed that water vapor can exist in a supersaturated state and behaves like an ideal gas.

2.5 Boundary Conditions

2.5.1 Flow and Species Transport. The channel pressures and concentrations of reactants and products on the anode and cathode sides are specified as boundary conditions. The experimental result used for validation of this model (see next section) is the fuel-cell polarization curve for the entire fuel cell. Hence it is desirable to use average values of pressures, reactant and product concentrations in order to validate the results. The average model parameters are calculated using an approximate analysis.

The densities of the reactant gas mixtures are calculated at exit conditions and are assumed to be constant. The temperature change of the reactant gases is neglected. The pressure variation is calculated using Bernoulli's equation with an additional term to account for the effect of wall friction. The exit concentrations are calculated using simple mass balances accounting for the production/consumption of reactants. The average quantities are taken as the arithmetic means of the inlet and outlet quantities. In spite of these simplifications, the above method of calculating the average parameters takes into account the effect of reactant flow rates, channel length, and active area, which otherwise cannot be accounted for in a two-dimensional model. It is noticed that the average values calculated above depend on the current, which is obtained from the solution of the electrochemistry model. Hence these boundary conditions are also updated during each iteration of the numerical scheme.

2.5.2 Electrochemistry. The present work studies the effect of thermal contact conductance at the GDL/current collector interface and anisotropic thermal conductivity on the temperature distribution inside the cell. It is expected that as the thermal contact conductance changes, the electrical contact resistance at that interface will also change. In the current model the electrochemical equations are solved over the MEA. Hence the effect of electrical contact resistance is taken into account in the boundary conditions. At the GDL/anode interface, they are

$$\phi_s = U_0 - V_{\text{cell}} - iAR_{\text{acontact}} - iAR_{\text{gdl}} \tag{11a}$$

$$\nabla \phi_m = 0 \tag{11b}$$

At the GDL/cathode interface, they are

$$\phi_s = iAR_{\text{ccontact}} + iAR_{\text{gdl}} \tag{12a}$$

$$\nabla \phi_m = 0 \tag{12b}$$

The corresponding heat generation terms are also added to the heat transport equation (Eq. (9)). Again the analysis presented above is simplified and more complicated issues involving the anisotropic electrical conductivity of the GDLs have not been addressed. It should also be noted that the above boundary conditions are dependent on the electric current, which comes out of the solution of the electrochemical equations. Hence, they are also updated during each iteration of the numerical scheme, as in case of the flow boundary conditions.

2.5.3 Heat Transfer Boundary Conditions. The top and bottom surfaces in the computational domain (see Fig. 2) are assumed to be insulated (symmetry boundary condition). Characteristic Re numbers for flow in the gas channels are low and in the laminar range. Hence, the heat transfer coefficients for the gas and coolant channel were calculated using

$$\text{Nu} = 2.98 \tag{13}$$

since entry lengths are relatively short compared to channel lengths. Additionally, the channel boundaries are at nearly a uniform temperature. The effect of a variable temperature along the GDL boundary on the overall heat transfer coefficient is neglected. The gas channels were assumed to have a square cross

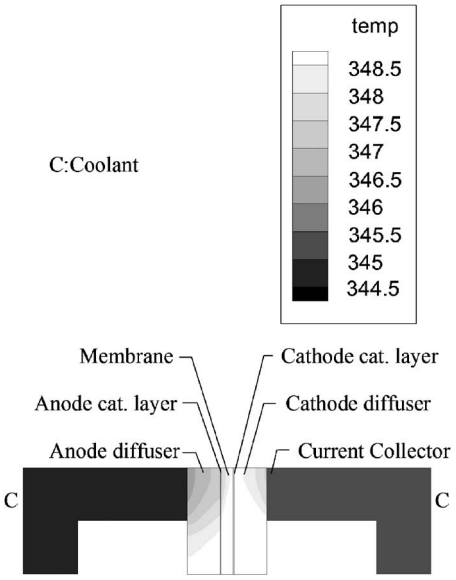

Fig. 2 Temperature distribution for base case operation

section. The gas and coolant temperatures were assumed to be at 343 K (cell operating temperature).

2.6 Property Values

2.6.1 Ionic Conductivity. The ionic conductivity of the membrane is computed from the correlation given by [5]

$$\kappa_m = (0.5139\lambda - 0.326)\exp\left[1268\left(\frac{1}{303} - \frac{1}{T}\right)\right] \tag{14}$$

where

$$\lambda = 0.043 + 17.81a - 39.85a^2 + 36.0a^3 \tag{15}$$

2.6.2 Cathode Exchange Current Density. The temperature dependence of the cathode exchange current density is evaluated from the correlation given by [47]

$$i_{oc}(T) = i_{oc}^{ref}(353\ \text{K})\exp\left[-\frac{\Delta E}{R}\left(\frac{1}{T} - \frac{1}{353.15}\right)\right] \tag{16}$$

2.6.3 GDL/Current Collector Thermal Contact Conductance. There appears to be no experimental data available in the literature for the thermal contact conductance. Mirmira et al. [48], Marotta and Fletcher [49], and Fuller and Marotta [50] have measured thermal contact conductance values for certain metal-polymer joints. The thermal contact conductance varied from 100 to 2000 $W/m^2 K$ for thicker polymers and from 1000 to 10,000 $W/m^2 K$ for thin elastomeric gaskets. Our in-house measurements of this contact conductance yielded a range from 500 to 10,000 $W/m^2 K$, depending on applied pressure [51]. Hence the thermal contact conductance was varied from 500 to 10,000 $W/m^2 K$ in the current analysis.

2.6.4 GDL/Current Collector Electrical Contact Resistance. Mishra et al. [52] measured the electrical contact resistance at this interface. The electrical contact resistance varied from 2.0 to 4.0 $m\Omega\,cm^2$ depending on the applied pressure. As the physical mechanisms controlling the thermal and electrical contact resistances are expected to be similar, a linear relationship was assumed to exist between the thermal and electrical contact resistances.

This completes the description of the numerical model. It captures the basic features of heat generation and transfer inside the PEM fuel cell. It is used to study the steady-state temperature distributions for different operating conditions. More sophisticated models involving more complicated phenomena, such as condensation, are to be considered in future work.

Table 1 Model parameters and properties [54]

Quantity	Value
Gas channel length	7.0E-2 m
Gas channel width (=depth)	10.0E-4 m
Membrane thickness	1.08 E-4 m
Gas-diffusion layer thickness	3.0E-4 m
Catalyst layer thickness	10.0E-6 m
Anode humidification temperature	343 K
Anode inlet flowrate	1200 cm^3/min
Cathode humidification temperature	343 K
Cathode inlet flow rate	2200 cm^3/min
Coolant water temperature	343 K
Gas-diffusion layer electrical resistivity	0.005 ohm-cm
Gas-diffusion layer porosity	0.4
Membrane porosity	0.4
Anode reference exchange current density	1.0E8 A/m^3
Cathode reference exchange current density	3.0E3 A/m^3
Entropy change ΔS for $H_2+\frac{1}{2}O_2 \rightarrow H_2O_{(liq.)}$	−162.4 (J/mol K)

3 Numerical Scheme

The above model thus consists of a set of two-dimensional equations for modeling species conservation, electrochemistry, fluid flow, and heat conduction inside the cell. The values of various parameters used for the model are given in Table 1.

The coupled set of equations was solved iteratively. The heat conduction equation was solved until the relative error in the overall heat balance was $<10^{-3}$, and the flow equations were solved using the SIMPLER scheme [53] until the mass source was $<10^{-8}$. The iterations were continued until convergence criteria for all the equations were simultaneously met. The computational domain was divided into a Cartesian grid of size 32×10, and grid independence was confirmed by solving the problem on a finer grid. The polarization curve was obtained using the model and the cathode reference exchange current density was used as a fitting parameter. The comparison of model results with published experimental results [54] is shown in Fig. 3, and a good agreement with the experimental data is obtained except at high current densities. The disagreement at high current densities can be explained due the fact that the model neglects two-phase effects, three-dimensional details and also the cell temperature is not maintained

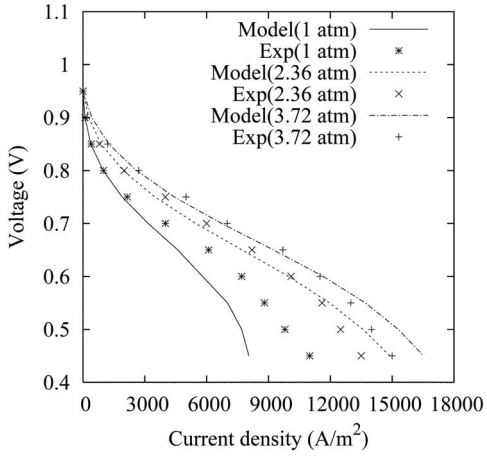

Fig. 3 Polarization curve obtained from model and compared with experimental results [54]

Table 2 Parameter values for base-case condition

Parameter	Value
Cell output voltage	0.65 V
Cell operating pressure (cathode and anode side)	2.36 atm
Height of the symmetrical section	1.0E-3 m
Channel width: Current collector width	1:1
Isotropic thermal conductivity of membrane and catalyst layers $k_{xx}=k_{yy}$	0.1 W/m K
Isotropic thermal conductivity of gas-diffusion layers $k_{xx}=k_{yy}$	1.0 W/m K
Thermal conductivity of air	0.024 W/m K
Thermal conductivity of water	0.58 W/m K
Thermal conductivity of current collector (graphite)	85.0 W/m K
Thermal contact conductance at the diffusion layer/current collector interface	3000 W/m^2 K

constant as in was done in the experiments (the coolant temperature is set equal to the cell temperature). The steady-state results obtained using this model for different operating parameter values are presented in the next section.

4 Discussion of Results

4.1 The Base Case. A parametric study is conducted to examine the effects of various input values on the temperature distribution inside the fuel cell. In order to analyze the effects of various input values, it is important to define reference values against which the variations can be compared. The operating conditions for such a base case are given in Table 2. The thermal conductivity for all the reference materials is assumed to be isotropic. The thermal conductivities of the membrane and GDLs are typical values for these materials in a dry state [55]. Any relationship between the electrical and thermal conductivities has been neglected because of the lack of experimental evidence. The current collector plate was assumed to be made of graphite (as in the experiment [54]). Other current collector plates made of materials of different thermal conductivities have not been considered in this study. The thermal contact conductance value at the current collector GDL interface is a typical value for this particular contact (see Sec. 2.6.3). As there is no experimental data currently available on the thermal contact conductance at the GDL/catalyst layer interface that contact resistance has not been considered in our model. These operating conditions are typical for a PEMFC. Analysis of this case provides important insights into the thermal behavior of the cell. The temperature distribution for this operating condition is shown in Fig. 2. It qualitatively matches the one-dimensional results obtained by Nguyen and White [9] and Rowe and Li [13].

Inspection of Fig. 2 reveals that the region in the membrane near the cathode catalyst layer develops relatively high temperatures. This region is susceptible to water loss due to evaporation. Loss of water in the membrane will result in a reduced ionic conductivity and loss of active area. Thus the maximum temperature in the membrane becomes an important output from this study. The region in contact with the current collector tends to be at a lower temperature than the rest of the MEA. Thus this region is susceptible to problems associated with condensation of water vapor. Thus the minimum temperature in the GDLs is also an important output, potentially affecting the operation of the fuel cell. It is also important to know the difference between these two temperatures. A temperature difference of even 2–3 K can result a significant difference in the saturation pressure for water. This can lead to vastly different evaporation and condensation characteristics in the vicinity of these two regions. Thus it is important to minimize the temperature gradients inside the cell.

The contact resistance at the interface between the current collector and GDL is expected to play an important role in determining these temperatures. It is also seen that since the current collector also removes excess heat from the MEA, the in-plane thermal conductivity of GDLs is also expected to play an important role in determining the temperature distribution inside the fuel cell. The following sections present the effects of changing various parameters on the temperature distribution inside the cell.

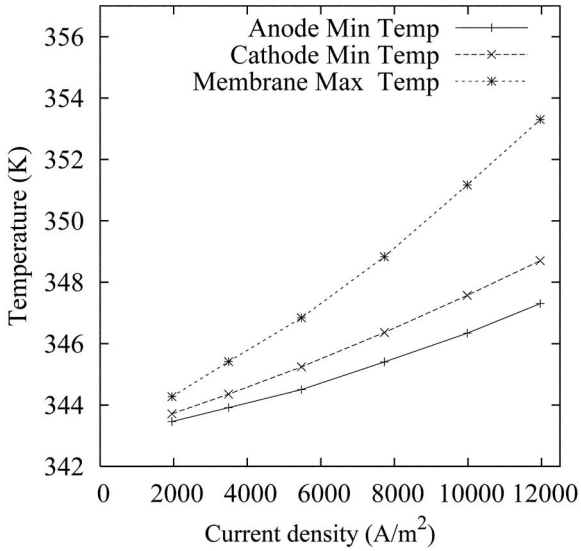

Fig. 4 Variation of membrane and GDL temperatures with current density

4.2 Effect of Current Density. As discussed previously, many works are available that have assumed the temperature to be uniform. It is important to know the conditions under which such an assumption is reasonable. As the operating current density of the fuel cell increases the cell must dissipate a larger amount of waste heat. Thus increasing current density can lead to nonuniform temperature distribution in the cell. The variation of maximum temperature in the membrane and the minimum temperatures in the GDLs is shown in Fig. 4. As expected, both the maximum and minimum temperatures in the cell increase as the current density increases. It is also seen that the difference between the two temperatures also increases with increasing current density. It should be noted that the relationship between fuel cell temperatures and current density is expected to be nonlinear. However, as the total temperature rise is only a few degrees, the nonlinearity is not reflected in the results.

It can also be observed that the difference between the two temperatures is more than 2 K beyond a current density of around 6000 A/m^2. Such a temperature difference will produce a difference in the saturation pressure of about 4–5 kPa which may be of significant concern for dry-out or flooding behavior inside the fuel cell.

4.3 Effect of Thermal Contact Conductance. It was shown in Sec. 4.1 that the thermal contact conductance at the interface between the current collector and GDL can play an important role in fuel cell operation. Figure 5 shows the temperature distributions for two values of the contact conductance. All other parameters were kept the same as that for the base case. (The geometry of Fig. 5 is same as that of Fig. 2. However, now the entire current collector plate is not shown as the temperature in the current collector plates is uniform because of their high thermal conductivity.)

It is seen that the temperatures inside the MEA increase with decreasing thermal contact conductance. A larger area or volume of the membrane is now at a high temperature. This can lead to a serious deterioration of the membrane properties, including dry-out of the membrane. However, higher temperatures in the cath-

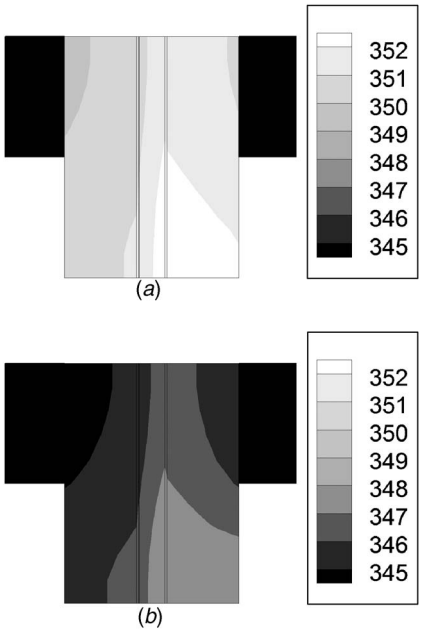

Fig. 5 Temperature distribution at two values of thermal contact conductance: (*a*) $h_{contact}=500\ W/m^2\,K$, and (*b*) $h_{contact}=10{,}000\ W/m^2\,K$

ode GDL can lead to reduced tendency for condensation, and the temperatures also tend to be more uniform throughout the MEA. Higher temperatures reduce the membrane ionic conductivity by reducing the water vapor activity and increase the cathode reaction rate. In general however, the fuel cell output characteristics are more severely affected by the change in membrane ionic conductivity than the corresponding increase in cathode reaction rate. Hence, it is desirable to have lower temperatures in the membrane and hence a high value of thermal contact conductance.

A higher value of the contact conductance also results in lower temperatures in the GDLs. This can exacerbate problems related to condensation. Therefore, a technique is needed to reduce the temperatures in the membrane without creating low temperatures in the GDLs.

4.4 Effect of Anisotropy in Thermal Conductivity of the Gas-Diffusion Layer. As mentioned previously, the heat generated in the cathode catalyst layer and the membrane must be effectively transferred to the current collector (cooling plate) via the GDLs. The GDLs are constructed from porous, fibrous materials. Their thermal conductivity is expected to be anisotropic, depending on the orientation of the fibers. One possible approach to achieve effective heat transfer is to increase the in-plane thermal conductivity of the GDL. The effect of changing the in-plane thermal conductivity on the overall temperature distribution of the cell is shown Fig. 6. The normal thermal conductivity was kept constant at the base-case value and the in-plane conductivity was varied.

It is seen that a low value of the in-plane thermal conductivity results in high temperatures in the membrane and formation of a hot spot. The average temperature in the GDLs in contact with the current collectors is lower than in the isotropic case. This leads to a higher probability of problems associated with condensation in the GDLs. Such a condition is thus highly undesirable. A higher value of the in-plane thermal conductivity, however, leads to a much more uniform temperature distribution. The maximum temperature is also lower than the situation involving a low in-plane thermal conductivity, as shown in Fig. 6. Thus, it would be highly desirable to tailor the GDLs to have a high value of in-plane thermal conductivity.

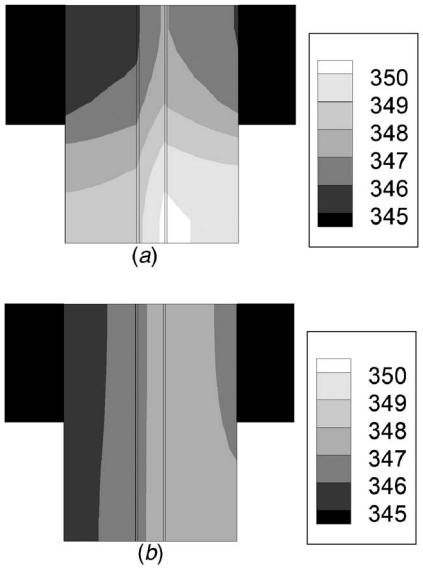

Fig. 6 Effect of anisotropy in thermal conductivity of gas-diffusion layers on temperature (*a*) $k_{yy}/k_{xx}=0.33$ and (*b*) $k_{yy}/k_{xx}=10.0$

4.5 Effect of Anisotropic Thermal Conductivity of the Membrane. Nafion is generated by copolymerization of a perfluorinated vinyl ether comonomer with tetrafluoroethylene (TFE) and made into sheets through an extrusion process. This extrusion process can cause a preferential orientation of fibers in the machine direction [44]. Hence, the thermal conductivity of the membrane can be expected to be higher in the in-plane direction. The effect of anisotropic thermal conductivity of the membrane on the temperature distribution inside the cell is shown in Fig. 7. It appears that the anisotropic membrane thermal conductivity may not have a significant impact on the temperature distribution in the cell unless the normal thermal conductivity is extremely low.

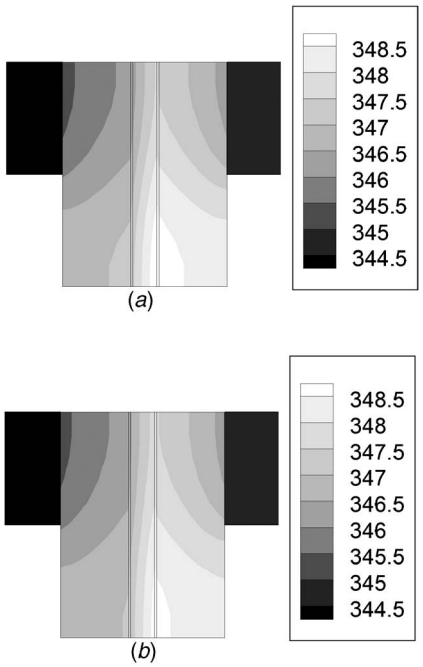

Fig. 7 Effect of anisotropy in thermal conductivity of membrane on temperature (*a*) $k_{yy}/k_{xx}=0.33$ and (*b*) $k_{yy}/k_{xx}=10.0$

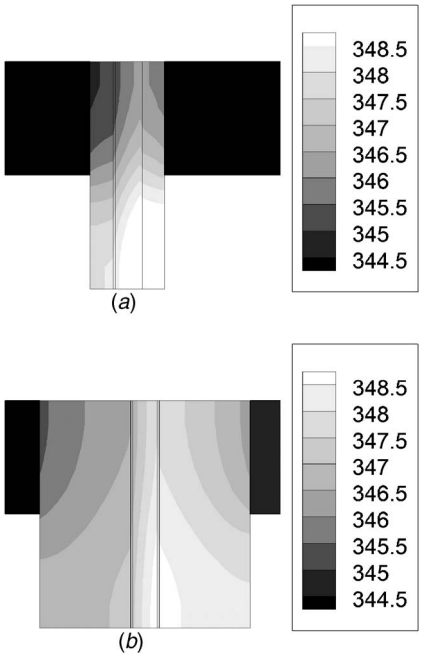

Fig. 8 Effect of GDL thickness on temperatures inside the cell (*a*) GDL thickness=100 μm and (*b*) GDL thickness=400 μm

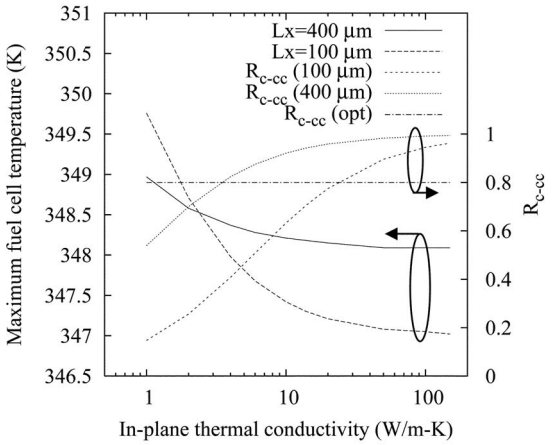

Fig. 9 Variation of maximum fuel cell temperature with increasing *y* direction thermal conductivity. (All other parameter values are at base-case condition.)

4.6 Effect of Gas-Diffusion Layer Thickness. The thickness of the GDL tends to be different depending on the manufacturer. The effect of changing thickness of the GDLs is shown in Fig. 8. The temperature distributions are shown for two extreme values of thicknesses. It can be seen that, as expected, a greater thickness leads to an increase in the area at higher temperatures in the membrane. It can also be noted that in case of a thin GDL, the complete upper half of the cell has lower temperatures than the lower half. A thin GDL, even though desirable from a mass diffusion point of view, can lead to low temperatures and cause condensation problems. The lower temperatures in this region can also cause reduced reaction rates.

In case of thin diffusion layers, it is also important to note that a possible reduction in the resistance to diffusion of the reactant gases does not compensate for the reduction in the heat transfer resistance. A thin diffusion layer in fact makes it more difficult for the reactant gases to reach the catalyst in areas where the GDL is in contact with the current collector. The resistance to diffusion of reactant gases reduces only in the region of GDL directly exposed to the gas channel. Thus in areas where the GDL is in contact with the current collector, the reactant concentration is not high for the thin GDL and does not compensate for lower temperatures. Hence, in case of thin GDLs, it is especially important to have a high value of the in-plane thermal conductivity.

It can thus be seen that thermal contact conductance at the GDL/current collector interface, in-plane GDL conductivity, and the GDL thickness are the most important factors affecting the heat transfer characteristics. These factors are subject to optimization within practical limits to achieve the most uniform temperature distribution inside the cell. The next section analyzes the limits on the optimum heat transfer performance that can be obtained by varying these parameters and the reasons for those limits.

4.7 Optimum Heat Transfer Performance and Approximate Aanalysis. The variation of maximum cell temperature with the in-plane thermal conductivity for different GDL thicknesses is shown in Fig. 9. It can be seen that the maximum temperature for the isotropic case is higher for the thinner GDL. Thus the maximum cell temperature does not reduce with thickness of the GDL as intuitively expected. It can also be seen that the net decrease in temperature obtained by increasing the in-plane thermal conductivity reduces with increasing thickness of the GDL. Thus there is a greater scope to obtain better heat transfer characteristics by increasing the in-plane thermal conductivity in case of a thin GDL. It is also seen that in both the cases the maximum temperature in the cell initially decreases and then levels off beyond a certain value of the in-plane thermal conductivity. Thus, increasing the in-plane thermal conductivity beyond this point will not lead to any substantial improvements in the heat transfer characteristics. These trends in heat transfer in the cell can be explained using the following approximate analysis.

The schematic for the approximate analysis along with the possible heat flow paths from the high temperature region is shown in the Fig. 10. The heat generated in the MEA can either be dissipated to the gas flowing in the channel, or it can be conducted to the current collector, which itself has a high thermal conductivity. The resistance to heat transfer to the gas channel and current collector are, respectively, approximately given by

$$R_{gc} = \frac{L_x}{k_{xx} L_{y1}} + \frac{1}{h_{\text{gas}} L_{y1}} \tag{17a}$$

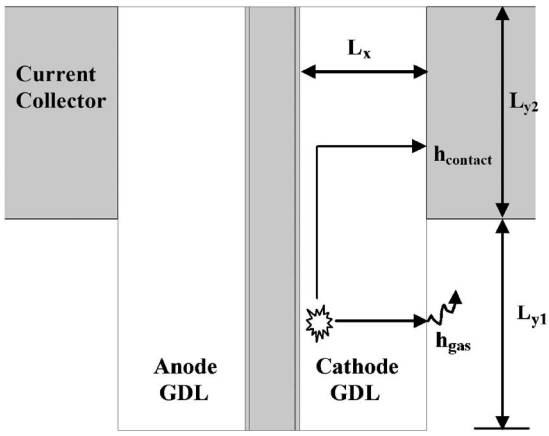

Fig. 10 A simplified view of heat transfer in a fuel cell

$$R_{cc} = \frac{L_{y1}}{k_{yy}L_x} + \frac{L_x}{k_{xx}L_{y2}} + \frac{1}{h_{\text{contact}}L_{y2}} \tag{17b}$$

The convective resistance to heat flow at the GDL/gas channel boundary is about 2–4 times larger than any other resistance in the cell (for the base-case condition parameters chosen in this analysis). Thus most of the heat flows through the current collector via its interface to the GDL. Thus heat transfer characteristics can be improved by reducing the resistance to heat flow towards the current collector. It can also be noticed from the discussion in the previous section that as the hotspot is formed near the midpoint of the gas channel, the resistance to flow in the in-plane direction is the most critical resistance determining the maximum temperature in the fuel cell. In this context, it is useful to define the following dimensionless parameter using Eq. (17*b*): the ratio of the net normal and interfacial resistance to the total resistance ($R_{c\text{-}cc}$) given by

$$R_{c-cc} = \frac{\dfrac{L_x}{k_{xx}L_{y2}} + \dfrac{1}{h_{\text{contact}}L_{y2}}}{\dfrac{L_{y1}}{k_{yy}L_x} + \dfrac{L_x}{k_{xx}L_{y2}} + \dfrac{1}{h_{\text{contact}}L_{y2}}} \tag{18}$$

The above ratio thus indicates the relative importance of the thermal contact resistance and the normal resistance for the flow of heat towards the current collector. A low value of the above ratio would indicate that the maximum temperature in the cell can be reduced by increasing the in-plane thermal conductivity.

It was shown earlier in this section that a reduction in the GDL thickness results in an increase in the maximum temperature in the cell. It can be seen from Eq. (17*b*) that a reduction in the GDL thickness decreases the normal resistance (second term in Eq. (17*b*) and increases the in-plane resistance (first term in Eq. (17*b*), which is also the larger of the two resistances ($L_{y1} > L_x$ generally). As seen earlier, the in-plane resistance is the most critical resistance determining the maximum temperature in the cell and hence the cell temperature increases. It was also observed that the maximum temperature in the cell levels off beyond a certain value of the in-plane thermal conductivity. This is because the ratio $R_{c\text{-}cc}$ reaches a limiting high value beyond which heat transfer can be improved only by increasing the thermal contact conductance. This also explains the fact that the reduction in maximum temperature for thick GDLs is lower than thin GDLs as the limiting value of $R_{c\text{-}cc}$ is reached earlier in the former case as shown in Fig. 9. Thus, in view of the numerical results presented in this work using the input values in Tables 1 and 2, the limiting condition for optimizing the heat transfer characteristics in the fuel cell is given as

$$R_{c\text{-}cc} = 0.8 \tag{19}$$

for all practical purposes (see Fig. 9). This condition can be used to determine the optimum combination of GDL thickness and in-plane thermal conductivity for minimizing temperature gradients within the cell.

5 Conclusions

The work described herein presents a parametric study on the possible effects of anisotropic thermal conductivity and contact conductance on the temperature distribution inside a fuel cell. The analysis leads to some important insights into the temperature distribution of the cell. Based on the chosen set of operating conditions, the following conclusions can be drawn from the analysis:

1. A low value of thermal contact conductance at the GDL/current collector interface can lead to high temperatures inside the fuel cell. This contact conductance is the single most important factor controlling the temperature distribution inside a fuel cell.
2. The thermal conductivity of GDLs can have a great impact on the temperature gradients inside a cell. It is desirable to have a high in-plane thermal conductivity for the GDL from the heat transfer point of view. However there exists an optimum value of the in-plane thermal conductivity beyond which no significant improvement in heat transfer characteristics can be obtained simply by increasing the thermal conductivity.
3. Thin GDLs lead to a highly nonuniform distribution of temperature. However, there is a greater scope for reducing the temperature gradients by increasing the in-plane thermal conductivity in case of thin GDLs than the thicker GDLs.
4. Anisotropic behavior of the thermal conductivity of the membrane does not have a serious impact on the cell operation.

It must be noted that the above results are based on a single-phase model, which neglects the effects of vapor condensation and associated mass transfer limitations. Moreover, the current study concentrates only on the heat transfer aspects of the fuel cell performance. A more detailed analysis with more comprehensive models concentrating on other aspects of fuel cell operation will be the subject of future publications.

Acknowledgment

Funding from the National Science Foundation (Grant No. CTS-0226095) is gratefully acknowledged. Comments and suggestions from the reviewers are much appreciated.

Nomenclature

A = area (m^2)
a = water vapor activity
C_i = species concentration (mol/m^3)
c = specific heat capacity (J/kg K)
D_h = hydraulic diameter (m)
ΔE = activation energy (J/mol)
F = Faraday's constant (C/mol)
h = heat transfer coefficient (W/m^2 K)
h_{contact} = thermal contact conductance (W/m^2 K) $h_{\text{contact}} = q''_{\text{interface}}/\Delta T_{\text{interface}}$
i = current density (A/m^2)
J_i = source term in the species concentration equation (mol/m^3 s)
j = exchange current density (A/m^3)
k = thermal conductivity (W/m K)
k_p = hydraulic permeability (m^2)
L_x = diffusion layer thickness (m)
L_{y1} = gas channel half width (m)
L_{y2} = current collector half width (m)
L_w = latent heat of vaporization of water (J/kg)
M = molecular weight (kg/mol)
Nu = Nusselt number Nu=h D_h/k_f
n_{oe} = electro-osmotic drag coefficient
p = pressure (Pa)
q''' = heat source (W/m^3)
R = electrical resistance (ohm), ideal gas constant (kJ/kg K)
R_{gc} = thermal resistance to flow to gas channel (K/W)
R_{cc} = thermal resistance to flow to current collector (K/W)
$R_{c\text{-}cc}$ = nondimensional thermal resistance
S = entropy (J/kg K), source term in continuity equation (kg/m^3 s)
T = temperature (K)
t = time (s)
U_0 = open circuit potential (V)

V_{cell} = cell output voltage (V)
u = velocity (m/s)

Greek Symbols

α = charge transfer coefficient
ε = porosity
η = overpotential (V)
κ = membrane ionic conductivity (S/m)
λ = water content of the membrane
μ = viscosity (Pa s)
ρ = density (kg/m^3)
τ = viscous stress (Pa)
ϕ = potential (V)

Subscripts

ref = reference
a = anode
c = cathode
contact = interface between two layers
gas = gas (cathode/anode channel)
gdl = gas-diffusion layer
m = membrane
oa = anode reference
oc = cathode reference
sat = saturation
s = solid
xx = normal
yy = in-plane

References

[1] Wilkins, F., 2002, "National Hydrogen Energy Roadmap," U. S. Department of Energy, **url**: http://www1.eere.energy.gov/hydrogenandfuelcells/pdfs/national_h2_roadmap.pdf

[2] Feng, W., Wang, S., Weidou, N., and Chen, C., 2004, "The Future of Hydrogen Infrastructure for Fuel Cell Vehicles in China and a Case of Application in Beijing," Int. J. Hydrogen Energy, **29**(4), pp. 355–367.

[3] Ahluwalia, R. K., Wang, X., Rousseau, A., and Kumar, R., 2004, "Fuel Economy of Hydrogen Fuel Cell Vehicles," J. Power Sources, **130**(1-2), pp. 192–201.

[4] Choi, K. H., Peck, D. H., Kim, C. S., Shin, D. R., and Lee, T. H., 2000, "Water Transport in Polymer Membranes for PEMFC," J. Power Sources, **86**(1-2), pp. 197–201.

[5] Springer, T. E., Zawodzinski, T. A., and Gottesfeld, S., 1991, "Polymer Electrolyte Fuel Cell Model," J. Electrochem. Soc., **138**(8), pp. 2334–2342.

[6] Bernardi, D. M., and Verbrugge, M. W., 1991, "Mathematical Model of a Gas Diffusion Electrode Bonded to a Polymer Electrolyte," AIChE J., **37**(8), pp. 1151–1163.

[7] Bernardi, D. M., and Verbrugge, M. W., 1992, "A Mathematical Model of Solid-Polymer-Electrolyte Fuel Cell," J. Electrochem. Soc., **139**(9), pp. 2477–2490.

[8] Fuller, T. F., and Newman, J., 1993, "Water and Thermal Management in Solid-Polymer-Electrolyte Fuel Cell," J. Electrochem. Soc., **140**(5), pp. 1218–1225.

[9] Nguyen, T. V., and White, R. E., 1993, "A Water and Heat Management Model for Proton-Exchange-Membrane Fuel Cell," J. Electrochem. Soc., **140**(8), pp. 2178–2186.

[10] Djilali, N., and Lu, D., 2002, "Influence of Heat Transfer on Gas and Water Transport in Fuel Cells," Int. J. Therm. Sci., **41**(1), pp. 29–40.

[11] Bevers, D., Wohr, M., Yasuda, K., and Oguro, K., 1997, "Simulation of a Polymer Electrolyte Fuel Cell Electrode," J. Appl. Electrochem., **27**(11), pp. 1254–1264.

[12] Wohr, M., Bolwin, K., Schnurnberger, W., Fischer, M., Neubrand, W., and Eigenberger, G., 1998, "Dynamic Modeling and Simulation of a Polymer Membrane Fuel Cell including Mass Transport Limitation," Int. J. Hydrogen Energy, **23**(3), pp. 213–218.

[13] Rowe, A., and Li, X., 2001, "Mathematical Modeling of Proton Exchange Membrane Fuel Cells," J. Power Sources, **102**(1-2), pp. 82–96.

[14] Dutta, S., Shimpalee, S., and Van Zee, J. W., 2000, "Three-Dimensional Numerical Simulation of Straight Channel PEM Fuel Cells," J. Appl. Electrochem., **30**(2), pp. 135–146.

[15] Um, S., Wang, C. Y., and Chen, K. S., 2000, "Computational Fluid Dynamics Modeling of Proton Exchange Membrane Fuel Cell," J. Electrochem. Soc., **147**(12), pp. 4485–4493.

[16] Um, S., and Wang, C. Y., 2003, "Three-Dimensional Analysis of Transport and Electrochemical Reactions in Polymer Electrolyte Fuel Cells," J. Power Sources, **125**(1), pp. 40–51.

[17] Berning, T., Lu, D. M., and Djilali, N., 2002, "Three-Dimensional Computational Analysis of Transport Phenomena in a Fuel Cell," J. Power Sources, **106**(1-2), pp. 284–294.

[18] Zhou, T., and Liu, H., 2001, "A General Three-Dimensional Model for Proton Exchange Membrane Fuel Cell," Int. J. Transp. Phenom., **3**(3), pp. 177–198.

[19] Ju, H., Meng, H., and Wang, C. Y., 2005, "A Single-Phase, Non-Isothermal Model for PEM Fuel Cell," Int. J. Heat Mass Transfer, **48**(7), pp. 1303–1315.

[20] Sivertsen, B. R., and Djilali, N., 2005, "CFD-Based Modeling of Proton Exchange Membrane Fuel Cells," J. Power Sources, **141**(1), pp. 65–78.

[21] Baschuk, J. J., and Li, X., 2000, "Modelling of Polymer Electrolyte Membrane Fuel Cells With Variable Degrees of Water Flooding," J. Power Sources, **86**(1-2), pp. 181–196.

[22] Stockie, J. B., 2002, "A Finite Volume Method for Multicomponent Gas Transport in a Porous Fuel Cell Electrode," in *Proceedings of the IMECE'02, 2002 ASME International Mechanical Engineering Congress and Exposition*, November 17-22, 2002, New Orleans, Louisiana, USA, HTD-Vol. 7, pp. 393–400.

[23] Berning, T., and Djilali, N., 2003, "A 3D, Multiphase, Multicomponent Model of the Cathode and Anode of the PEM Fuel Cell," J. Electrochem. Soc., **150**(12), pp. A1589–A1598.

[24] Wang, C. Y., and Cheng, P., 1997, "Multiphase Flow and Heat Transfer in Porous Media," Adv. Heat Transfer, **30**, pp. 93–196.

[25] Wang, Z. H., Wang, C. Y., and Chen, K. S., 2001, "Two-Phase Flow and Transport in the Air Cathode of Proton Exchange Membrane Fuel Cells," J. Power Sources, **94**(1), pp. 40–50.

[26] Wang, C. Y., and Cheng, P., 1996, "A Multiphase Mixture Model for Multiphase Multi-component Transport in Capillary Porous Media-I. Model Development," Int. J. Heat Mass Transfer, **39**(17), pp. 3607–3618.

[27] Hu, M., Gu, A., Wang, M., Zhu, X., and Yu, L., 2004, "Three Dimensional, Two-Phase Flow Mathematical Model for PEM Fuel Cell: Part I. Model Development," Energy Convers. Manage., **45**(11-12), pp. 1861–1882.

[28] Hu, M., Zhu, X., Wang, M., Gu, A., and Yu, L., 2004, "Three Dimensional, Two-Phase Flow Mathematical Model for PEM Fuel Cell: Part II. Analysis and Discussion of the Internal Transport Mechanisms," Energy Convers. Manage., **45**(11-12), pp. 1883–1916.

[29] Mazumder, S., and Cole, J. V., 2003, "Rigorous 3-D Mathematical Modeling of PEM Fuel Cells II. Model Predictions With Liquid Water Transport," J. Electrochem. Soc., **150**(11), pp. A1510–A1517.

[30] Sun, H., Liu, H., and Guo, L., 2005, "PEM Fuel Cell Performance and its Two-Phase Mass Transport," J. Power Sources, **143**(1-2), pp. 125–135.

[31] Birgersson, E., Noponen, M., and Vynnycky, M., 2005, "Analysis of a Two-Phase Non-Isothermal Model for a PEMFC," J. Electrochem. Soc., **152**(5), pp. A1021–A1034.

[32] Shimpalee, S., Greenway, S., Spuckler, D., and Van Zee, J. W., 2004, "Predicting Water and Current Distributions in a Commercial-Size PEMFC," J. Power Sources, **135**(1-2), pp. 79–87.

[33] Baschuk, J. J., and Li, X., 2004, "A General Formulation for a Mathematical PEM Fuel Cell Model," J. Power Sources, **142**(1-2), pp. 134–153.

[34] Nam, J. H., and Kaviany, M., 2003, "Effective Diffusivity and Water-Saturation Distribution in Single- and Two-layer PEMFC Diffusion Medium," Int. J. Heat Mass Transfer, **46**(24), pp. 4595–4611.

[35] Pasaogullari, U., and Wang, C. Y., 2004, "Two-Phase Transport and the Role of Microporous Layer in Polymer Electrolyte Fuel Cells," Electrochim. Acta, **49**(25), pp. 4359–4369.

[36] Pasaogullari, U., and Wang, C. Y., 2005, "Two-Phase Modeling and Flooding Prediction of Polymer Electrolyte Fuel Cells," J. Electrochem. Soc., **152**(2), pp. A380–A390.

[37] Yuan, J., Rokni, M., and Sundén, B., 2003, "A Numerical Investigation of Gas Flow and Heat Transfer in Proton Exchange Membrane Fuel Cells," Numer. Heat Transfer, Part A, **44**(3), pp. 255–280.

[38] Musser, J., and Wang, C. Y., 2000, "Heat Transfer in a Fuel Cell Engine," in *Proceedings of the NHTC'00, 34th National Heat Transfer Conference*, Pittsburgh, Pennsylvania, August 20–22, NHTC-Vol. 1, pp. 291–297.

[39] Mawardi, A., Yang, F., and Pitchumani, R., 2005, "Optimization of the Operating Parameters of a Proton Exchange Membrane Fuel Cell for Maximum Power Density," J. Fuel Cell Sci. Technol., **2**(2), pp. 121–135.

[40] Kurabayashi, K., 2001, "Anisotropic Thermal Properties of Solid Polymers," Int. J. Thermophys., **12**(1), pp. 277–288.

[41] Hansen, D., and Bernier, G. A., 1972, "Thermal Conductivity of Polyethylene: The Effects of Crystal Size, Density and Orientation on the Thermal Conductivity," Polym. Eng. Sci., **12**(3), pp. 204–208.

[42] Morelli, D. T., Heremans, J., Sakomoto, M., and Uher, C., 1986, "Anisotropic Heat Conduction in Diacetylenes," Phys. Rev. Lett., **57**(7), pp. 869–872.

[43] Kurabayashi, K., Asheghi, M., Touzelbaev, M., and Goodson, K. E., 1999, "Measurement of the Thermal Conductivity in Polyimide Films," J. Microelectromech. Syst., **8**(2), pp. 180–191.

[44] Mauritz, K. A., and Moore, R. B., 2004, "State of Understanding of Nafion," Chem. Rev. (Washington, D.C.), **104**(10), pp. 4535–4585.

[45] Gardner, C. L., and Anantaraman, A. V., 1998, "Studies on Ion-Exchange Membranes. II. Measurement of the Anisotropic Conductance of Nafion," J. Electroanal. Chem., **449**(1-2), pp. 209–214.

[46] Newman, J. S., 1973, *Electrochemical Systems*, Prentice-Hall, Englewood Cliffs, Chap. 1.

[47] Parthasarathy, A., Srinivasan, S., and Appleby, J. A., 1992, "Temperature Dependence of the Electrode Kinetics of Oxygen Reduction at Platinum/Nafion Interface—A Microelectrode Investigation," J. Electrochem. Soc., **139**(9), pp. 2530–2537.

[48] Mirmira, S. R., Marotta, E. E., and Fletcher, L. S., 1998, "Thermal Contact Conductance of Elastomeric Gaskets," J. Thermophys. Heat Transfer, **12**(3), pp. 454–456.

[49] Marotta, E. E., and Fletcher, L. S., 1996, "Thermal Contact Conductance of Selected Polymeric Materials," J. Thermophys. Heat Transfer, **10**(2), pp. 334–342.
[50] Fuller, J. J., and Marotta, E. E., 2001, "Thermal Contact Conductance of Metal/Polymer Joints: An Analytical and Experimental Investigation," J. Thermophys. Heat Transfer, **15**(2), pp. 228–238.
[51] Hollinger, A., 2006, "Contact Resistance Measurements of Gas-Diffusion Layers and Membrane for Fuel Cell Applications," Senior Honors thesis, Department of Engineering Science and Mechanics, The Pennsylvania State University, University Park, PA.
[52] Mishra, V., Yang, F., and Pitchumani, R., 2004, "Measurement and Prediction of Electrical Contact Resistance Between Gas-Diffusion layers and Bipolar Plate for Applications to PEM Fuel Cells," J. Fuel Cell Sci. Technol., **1**(1), pp. 2–9.
[53] Patankar, S. V., 1980, *Numerical Heat Transfer and Fluid Flow*, Hemisphere, Washington, D.C.
[54] Wang, L., Husar, A., Zhou, T., and Liu, H., 2003, "A Parametric Study of Fuel Cell Performances," Int. J. Hydrogen Energy, **28**(11), pp. 1263–1272.
[55] Saxena, V., and Thynell, S. T., 2007, "Thermal Conductivity Measurements of Polymer Electrolyte Membrane and Gas-diffusion Layers in PEM Fuel Cell Using Pulsed Photothermal Radiometry" (in preparation).

The Error Analysis of a Steady-State Thermal Conductivity Measurement Method With Single Constant Temperature Region

Ming-Tsung Sun[1]
Chin-Hsiang Chang[2]

Department of Mechanical Engineering,
Chang Gung University,
259 Wen-Hwa 1st Road,
Kwei-Shan, Tao-Yuan 333, Taiwan

A method for steady-state thermal conductivity measurement with single constant temperature region has been developed. To better understand the accuracy of the method a numerical model is devised and verified by experimental results. The ratios of thermal conductivity derived from the temperature distribution solutions to that given in the numerical model are obtained and shown. They can be used to correct the systematic error of measurement introduced by the one-dimensional approximation. Finally, the measurement uncertainty due to misalignment of the temperature sensors and the limitation of sensing devices is also investigated. The numerical model is suitable for estimating the range of confidence in practical measurements. [DOI: 10.1115/1.2739585]

Keywords: steady-state thermal conductivity measurment, systematic error, measurment uncertainty

1 Introduction

In the applications of the steady-state measurement of thermal conductivity, at least two constant temperature regions are believed to be essential as a heat source and a heat sink, respectively. The constant temperature region as the heat sink requires cumbersome equipment. This limits the use of steady-state measurement methods in laboratories and makes them unsuitable for in situ measurements. In other words, it is hard to apply a steady-state measurement method in a portable apparatus. Extra care has also been taken in the insulation of the apparatus when test samples have small values of thermal conductivity, such as that of the insulation materials. In this case, the destruction of the test sample is inevitable [1]. However, for the composite insulation materials consisting of vacuum layers or glass panels [2], an inverse computational method to evaluate temperature dependence of thermal conductivity [3], or materials with a nonhonogenous inner structure [4], nondestructive evaluation of the thermal conductivity is required.

In spite of the inconvenience steady-state measurement methods may bring, they are still widely used due to their reliability in measuring composite insulation materials. To fulfill the requirement of nondestructive steady-state measurement of thermal conductivity, Chuah and Sun [5] proposed a method that requires only one constant temperature region as the heat source. A detailed working principle of the method is given by Chuang [6] who devised a microcontroller to perform the automatic measuring procedures. Here, we give only a brief description and show the schematic drawing of the device in Fig. 1.

The method makes use of two electronically controlled heating devices to keep the heating cover and the heating plate at constant temperatures, T_U and T_0, respectively, on one side of the test sample. The diameter of the heating cover is D_o and that of the heating plate is D_c. The heating plate is placed inside the heating cover with a small gap, g, inbetween them to avoid direct conduction heat transfer and maintain a larger area of constant temperature. The heating cover is placed inside a stainless-steel housing. The enclosed space between two heating devices and the housing is filled with aerogel.

On the other side of the test sample, a Teflon disk is placed aligned with the heating compartment to hold five temperature sensors. The Teflon disk sizes are D_l in diameter and s in thickness. One of the five temperature sensors is located at the center of the disk and the other four equally spaced on the concentric circle of radius d. They are placed on the side of the disk next to the sample.

Making T_U and T_0 equal, a region of constant temperature can be formed on one side of a test sample. This ensures that the heating power of the heating plate will transmit upward into the test sample only. Since the heat flux moves mostly in the longitudinal direction across the thickness of the test sample, one can achieve effective one-dimensional heat transfer in the measurement. When the temperatures on both sides of the test sample become stable, the temperatures, the thickness of the material, and the heat flux are measured to evaluate the thermal conductivity of the test sample. Using this method, the thermal conductivity of a piece of polystyrene foam was measured and compared with the result using the guarded hot plate method. The relative difference is within 3% [7].

However, due to the multidimensional effect and the temperature distribution on the low-temperature side, the temperature difference used to calculate the thermal conductivity may greatly deviate from that in one-dimensional heat transfer. This situation can be worsened when the sample thickness is larger. Since the systematic variation is inevitable, it is then a good practice to estimate the systematic error of the measured thermal conductivity as a function of the relative sample thickness, H/D_o. The geometric parameter, D_c over D_o, is also considered since it contributes to the systematic error.

As for the random errors, the sources can be the uncertainties of

[1]Corresponding author. e-mail: mtsun@mail.cgu.edu.tw
[2]e-mail: changch@post.savs.ilc.edu.tw

Contributed by the Heat Transfer Division of ASME for publication in the JOURNAL OF HEAT TRANSFER. Manuscript received January 10, 2006; final manuscript received December 14, 2006. Review conducted by A. Haji-Sheikh. Paper presented at the ASME Summer Heat Transfer Conference (HT2003), Las Vegas, NV, USA, July 21–23, 2003.

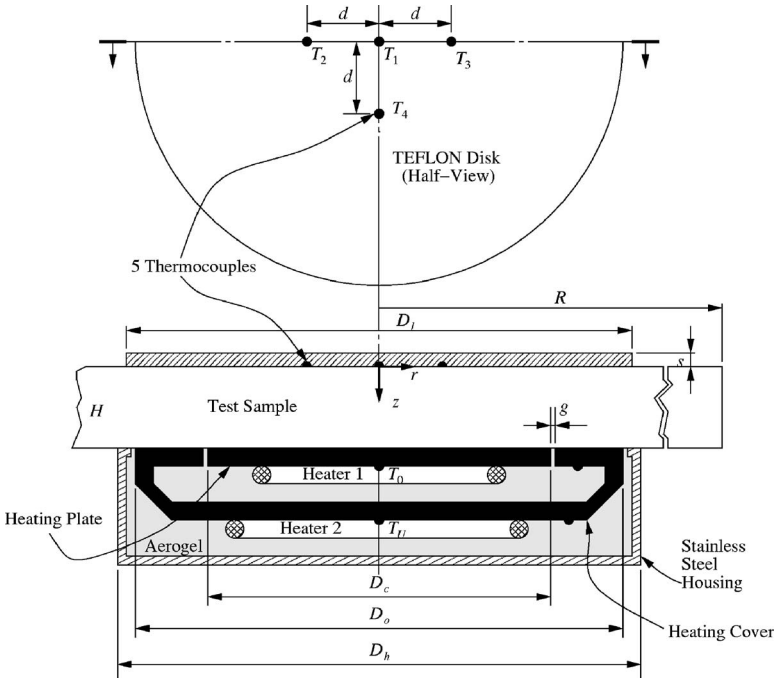

Fig. 1 The descriptive diagram of the device that measures steady-state thermal conductivity.

sensor measurement and imperfect alignment of the five temperature sensors with the heating compartment. They propagate through the formula used for thermal conductivity evaluation. Both systematic and random errors require close investigation before the measurement method can be confidently practiced.

To accomplish the analysis without dealing with the errors caused by insufficiency in the fabrication skill of the experiment apparatus, we established a theoretical model in axial symmetric cylindrical coordinates. The theoretical model is solved numerically because the boundary conditions of free convection are nonlinear and the thermal conductivities of samples are functions of temperature. For nonlinear problems such as the wall effect on hot-wire measurements [8], numerical solutions are often sought. From the model, temperature distribution in the sample can be solved. The heat flux from the heating plate is determined from the solution of temperature distribution since the temperature value is specified on the boundary of the constant temperature region.

With the heat flux and the temperature distribution, the thermal conductivity can be derived from the numerical simulation according to the formula of one-dimensional heat conduction used by the measuring method. This thermal conductivity, denoted as k_E, is different from what is specified in the numerical model, which is denoted as k_R. The ratio of k_E to k_R, the k ratio $r_k = k_E/k_R$, is an indication of measurement deviations from real situations.

By varying the affecting factors, such as H/D_o and D_c/D_o, one can derive a series of k ratios that can be used to correct the measured thermal conductivity in practical applications. Varying D_c/D_o provides information of the device's geometric effect. It will be shown in Sec. 4 that the geometric effect is smaller as D_c/D_o is smaller. However, due to the manufacturing technique it cannot be too small. It is noted that as D_c/D_o decreases, the gap, g, is maintained at a constant value as well as D_o. That is the area of the constant temperature region remains fixed while the area of the heating plate decreases. In this case, the temperature in the gap can be considered uniformly distributed and with the same value as that of the heating plate and the heating cover.

Finally, the thermal conductivity uncertainty is estimated with the analysis of the error caused by the measurement uncertainty that propagates through the formulation used in the method. In the analysis, an alternative way of determining the maximum temperature on the lower temperature side is proposed. The thermal conductivity uncertainty is expressed as a function of the misalignment of the temperature sensors with the centerline of the heating plate on the lower temperature side.

2 The Experiment

In order to verify the numerical model in this study, an experiment is first carried out. According to the measuring method the thermal conductivity, k_E, is

$$k_E(T_m) = \frac{\dot{Q}H}{A(T_0 - T_{\max})} \tag{1}$$

where $T_{\max}$ is the maximum temperature at the lower temperature side of the test sample and $T_m = (T_0 + T_{\max})/2$ is the mean temperature at which the test sample is supposed to possess k_E.

If the Teflon disk plate is aligned with the heating plate, $T_{\max} = T_1$. Since it is hard to align the two parts in real measurements, Chuah and Sun [5] proposed an approximate function of temperature distribution as follows

$$T(x,y) = c_1x^2 + c_2x + c_3y^2 + c_4y + c_5 \tag{2}$$

where c_i, $i = 1 \ldots 5$, are five coefficients to be determined with the five known locations of temperature sensors and the temperatures measured from each sensor, respectively. The maximum temperature $T_{\max}$ occurs at the location where the partial derivatives of Eq. (2) with respect to x and y are zero, i.e., $\partial T/\partial x = 0$ and $\partial T/\partial y = 0$. Substituting the coordinates solved from the set of the two equations into Eq. (2), one can obtain $T_{\max}$ as

$$T_{\max} = c_5 - \left(\frac{c_2^2}{4c_1} + \frac{c_4^2}{4c_3}\right) \tag{3}$$

However, since the geometry of the device is axisymmetric, the temperature distribution can also be described by the following function

Table 1 The readings of the sensors and the derived quantities.

T_1 (°C)	T_2 (°C)	T_3 (°C)	T_4 (°C)	T_5 (°C)	$\dot{Q}$ (W)	$T_{\max}$ (°C)	T_m (°C)
27.18	26.95	27.12	27.08	27.05	0.541	27.22	32.59

$$T(r) = -ar^2 + b = -a[(x - x_0)^2 + (y - y_0)^2] + b \tag{4}$$

The maximum temperature is supposed to occur at (x_0, y_0). Using least squares fit, one can solve for the unknown parameters a, b, and (x_0, y_0). In the solutions, b is the maximum temperature, $T_{\max}$, which can be expressed as

$$T_{\max} = T_1 - \frac{(T_2 - T_3)^2 + (T_4 - T_5)^2}{4(T_2 + T_3 + T_4 + T_5 - 4T_1)} \tag{5}$$

where T_1 is measured from the central sensor; T_2 and T_3 are measured from the sensors aligned with the center; and T_4 and T_5 are measured likewise but in the perpendicular direction. This form of temperature distribution is much simpler than Eq. (2) because there is no need to solve any coefficients.

The geometry of the experimental device has the following dimensions: D_o=218 mm, H=29 mm, D_c=185 mm, R=240 mm, D_l=200 mm, d=40 mm, and s=6 mm. The configuration of experimental device used is in the upsidedown position of that shown in Fig. 1. The constant temperature region is controlled at T_0=40 °C. The test sample we use in the experiment is a piece of expanded polystyrene type XI (EPS) thermal foam board.

Due to the quality of the heater controllers, the temperature of the heating plate can only be maintained at 37.95 °C. The ambient air temperature, T_a, is 23.35 °C. When all the readings are stable for at least 30 min, they are recorded in Table 1. $T_{\max}$ is evaluated from T_1 to T_5 using Eq. (5). Substituting the measurement data into Eq. (1), we have 0.0544 W/m K as the k_E of the test sample evaluated at T_m=32.59 °C.

3 The Numerical Model

The numerical model used in this study is based on the heat conduction equation in cylindrical coordinates. Since the device is axially symmetric, we only need to consider a two-dimensional problem. The governing equation is

$$\rho c \frac{\partial T}{\partial t} = \frac{k_r}{r}\frac{\partial}{\partial r}\left(r\frac{\partial T}{\partial r}\right) + k_z\frac{\partial^2 T}{\partial z^2} \tag{6}$$

where ρ and c are the density and heat capacity of the material under testing. To simplify the problem, we first assume that the test sample has a constant c and isotropic k, i.e., k_r=k_z. The isotropic k value of the test sample (EPS foam of ASTM designation type XI) is a function of temperature as

$$k = 0.000163 \times T + 0.04265 \tag{7}$$

where temperature T is in °C and k is in W/m K. This formula is derived by linear regression of the data provided by Thermal Foams, Inc. The thermal conductivity of the Teflon disk plate is also a function of temperature [9] as

$$k = 0.001 \times T + 0.323 \tag{8}$$

where the units are the same as those in Eq. (7).

The boundary conditions of the numerical model are summarized in Table 2 where the origin of the coordinates is at the center of the Teflon disk plate on the inner surface (as shown in Fig. 1).

One may argue that the heat transfer across the interface of two contact surfaces depends on the profile of the surfaces as in the studies of many, such as Wahid et al. [10–12]. In our model, the interfaces locate at the two sides of the test sample in contact with the heating plate and the Teflon disk plate. As a matter of fact, if the k value of the test sample is as small as in our case, the contact surface effect can be ignored. However, for large k values, dissipative jelly can be applied at the interfaces to fill the voids and minimize the contact surface effect of the interface air layer. Therefore, we ignore the effect in our model with the assumption that one should use dissipative jelly in the practical applications of the method for measuring the materials of large k value.

As mentioned before, the coefficient of free convection on each boundary is nonlinear. In this study, we use the empirical formulation of convection coefficient given by Janna [13]. For the vertical surfaces, the formulation is

$$h_{L,V} = \frac{k_f}{L} \times \left\{ 0.825 + \frac{0.387\mathrm{Ra}_{L_C}^{1/6}}{\left[1 + \left(\frac{0.492}{\mathrm{Pr}}\right)^{9/16}\right]^{8/27}} \right\}^2 \tag{9}$$

where the unit of convection coefficient is $\mathrm{W/m^2\,K}$. For the lower surfaces, the convection coefficient is

$$h_{L,H_l} = \frac{k_f}{L} \times 0.27\mathrm{Ra}_{L_C}^{1/4} \tag{10}$$

For the upper surfaces of the test sample, depending on the range of Rayleigh number the coefficient are given as

$$h_{L,H_u} = \frac{k_f}{L} \times 0.54\mathrm{Ra}_{L_C}^{1/4}, \quad 2.6 \times 10^4 < \mathrm{Ra}_{L_C} < 10^7$$

$$h_{L,H_u} = \frac{k_f}{L} \times 0.15\mathrm{Ra}_{L_C}^{1/3}, \quad 10^7 < \mathrm{Ra}_{L_C} < 3 \times 10^{10} \tag{11}$$

In Eqs. (9)–(11), k_f is the thermal conductivity of the fluid, which is air in our case; Ra_{L_C} is the Rayleigh number based on the characteristic length L_C; Pr is the Prandtl number of the air; and L is the width of the surface.

Since the measuring method is done under steady-state measurement, the time varying term on the left-hand side of Eq. (6) equals zero. The successive over relaxation (SOR) method is chosen due to its wide use in parabolic problems. The acceptance criterion of a convergent solution is that the maximum relative variation of temperature in the model is less than 10^{-9}. Asymptotic tests are done first to determine the maximum grid sizes and the minimum radius of the test sample in the numerical model.

After the temperature distribution in the numerical model is solved, the measuring process is simulated by first acquiring temperatures, T_i, at the locations of the five temperature sensors (i

Table 2 The boundary conditions of the model.

r coordinate	z coordinate	B.C. description
r=0	$-s \le z \le H$	Axial symmetric
r=R	$0 \le z \le H$	Free conv.[a] ($h_{L,V}$)
$0 < r \le D_o/2$	z=H	Isothermal (T=T_0)
$D_o/2 < r \le R$	z=H	Free conv.[b] (h_{L,H_l})
$0 < r \le D_l/2$	z=$-s$	Free conv.[c] (h_{L,H_u})
r=$D_l/2$	$-s < z \le 0$	Free conv.[a] ($h_{L,V}$)
$D_l/2 < r \le R$	z=0	Free conv.[c] (h_{L,H_u})

[a]Equation (9) on vertical walls.
[b]Equation (10) on horizontal walls facing downward.
[c]Equation (11) on horizontal walls facing upward.

$=1,2,3,4,5$) and the heat transfer rate of the heating plate, $\dot{Q}$, out of the heating plate into the test sample. $T_{\max}$ can be determined according to Eq. (5). The heat transfer rate, $\dot{Q}$, which is supposed to be the power of the heater on the heating plate, is evaluated as by

$$\dot{Q} = 2\pi \left\{ \sum_{i=1}^{m} r_i \times \Delta r_i \times k\left(\frac{T_{i,n} + T_{i,n-1}}{2}\right) \times \frac{T_{i,n} - T_{i,n-1}}{z_n - z_{n-1}} + \sum_{j=n+1}^{N} \left(r_m + \frac{\Delta r_m}{2} \right) \times \left[\Delta z_j \times k\left(\frac{T_{m,j} + T_{m+1,j}}{2}\right) \times \frac{T_{m,j} - T_{m+1,j}}{r_{m+1} - r_m} + \frac{\Delta z_N}{2} \times k\left(\frac{3T_{m,N} + T_{m,N-1} + 3T_{m+1,N} + T_{m+1,N-1}}{8}\right) \times \frac{3T_{m,N} + T_{m,N-1} - 3T_{m+1,N} - T_{m+1,N-1}}{4(r_{m+1} - r_m)} \right] \right\} \tag{12}$$

where z_N locates at the interface between the heating plate and the test sample; $r_m + \Delta r_m/2$ locates at the rim of the heating plate; and $(z_n + z_{n-1})/2$ is the surface where we integrate the heat flux in the z direction. With the resulting $\dot{Q}$ and $T_{\max}$, and the known variables in the model T_0, $A = (\pi D_c^2)/4$, and H, the k_E from the numerically simulating measurement, can be determined using Eq. (1). This k_E is then divided by $k_R = k(T_m)$ evaluated with Eq. (7) to give the k ratio for the given parameters.

To analyze the random error of the measurement, we have to consider the error from temperature measurement, temperature control, and the heating power readout that propagate to generate uncertainty in the measured thermal conductivity δk_E. The relative uncertainty of the measured thermal conductivity u_{k_E} can be expressed as

$$u_{k_E} \equiv \frac{\delta k_E}{k_E} = \left\{ \left(\frac{\delta \dot{Q}}{\dot{Q}} \right)^2 + \left(\frac{\delta T_0}{T_0 - T_{\max}} \right)^2 + \left(\frac{T_{\max}}{T_0 - T_{\max}} \frac{\delta T_{\max}}{T_{\max}} \right)^2 \right\}^{1/2} \tag{13}$$

In the equation, both the measurement error and the offset of the temperature sensors that propagate through the temperature distribution function contribute to $\delta T_{\max}/T_{\max}$. The situation of the offset temperature sensors is simulated by finding the temperature of each sensor from the numerical solution of temperature distribution on the lower temperature side of the sample with the desired offset amount.

4 Results and Discussions

In verifying the numerical model, the numerical model is built according to the setups of the experiment. Except for the constant temperature region, the temperature distribution on the contact surface between the sample and the housing is considered. The temperature in between D_o and D_h is specified with linear distribution from T_0 to T_a, which is very close to the real situation.

With the parameters specified in the experiment, the asymptotic tests for the model give the results of 36 longitudinal nodes and 241 radial nodes for the computational domain. The temperature at the monitoring location where T_1 is measured has a relative variation of less than 10^{-4} when the node numbers increase further.

The results of the simulation are listed in the first row of Table 3 in which $T_2 - T_5$ are not listed and are the same due to axial symmetric and aligned Teflon disk assumptions. Compared with the experimental results, although there is at most 3% difference for all the quantities, the calculated k_E using Eq. (1) is also 0.0544 W/m K. By this, the numerical model is verified.

In order to see the effect of convection coefficients, the convection coefficients from Eqs. (9)–(11) are multiplied with a h factor and used in the numerical model. The results are shown in the second row of Table 3 and indicate that although the convection coefficients increase by 20%, the predicted k_E varies by less than 1%. This shows that the measuring method is insensitive to the conditions of the environment. It is interesting to note from the results that the simulated T_1 and $\dot{Q}$ with the 1.2 h factor are much closer to the experimental ones. Therefore, Janna's formulation may not be able to apply directly in this case. Therefore, the 1.2 h factor is used in the following simulations for error analysis.

Table 3 The simulation results.

h factor	T_1 (°C)	$\dot{Q}$ (W)	$T_{\max}$ (°C)	T_m (°C)	k_E (W/m K)
1.0	27.68	0.524	27.68	32.82	0.0544
1.2	27.29	0.540	27.29	32.62	0.0540

To analyze the systematic error of the measuring method, the relative thickness of the test sample, H/D_o, and the relative diameter of the heating plate, D_c/D_o, are varied in the numerical model. The k ratios resulting from the numerical model are shown in Fig. 2 with solid symbols, in which the case of the experiment is indicated by an arrow.

In Fig. 2, it is expected that as the thickness of the sample and the area of the heating decrease relative to the unchanged constant temperature area, the situation of ideal one-dimensional heat conduction can be better approximated. Also, since the radial heat flux always makes the heating power of the heating plate larger than what actually penetrates the sample, it consequently introduces a larger k value. That is, the k ratios of this measurement method are always greater than unity.

However, the k ratio values do not approach unity when the relative thickness of the sample approaches zero. This is caused by the discontinuity of the thermal effusivity, which locates at the edge of the Teflon disk and is near the rim of the heating cover. As shown in Fig. 3, the discontinuity of thermal effusivity at D_l contributes to the jag of the temperature distribution. The location is near D_c, which is the outer boundary of $\dot{Q}$ considered for calculating the k value. When the sample thickness is small, $\dot{Q}$ is still overestimated since the heat flux is greater in regions not covered by the Teflon disk. To further show this, the discontinuity of the thermal effusivity is moved away from the rim of the heating plate, that is, the size of the Teflon disk is enlarged up to the size where there is no more change to the resulting k ratios. The final dimension of the disk is 400 mm in diameter with the associated ratio $D_l/D_o = 1.84$, which is twice the original size. The k ratios obtained with the new model are also shown in Fig. 2 using open symbols. The k ratios of the same D_c/D_o are smaller than before and approach unity when the relative thickness approaches zero.

Yet, the values of the k ratio are quite large. It is interesting to see the effect of the temperature distribution outside the constant temperature region. To do so, the temperatue varying boundary condition is removed and the values of the k ratio turn out to be about half of the previous results. They are shown in Fig. 4 with a different vertical scale. The effect of the rim is much more obvious in this case for both the value differences and the shape of the curves.

In addition to isotropic materials, an anisotropic material is modeled such that its thermal conductivity in the radial direction is three times that in the longitudinal direction, i.e., $k_r = 3k_z$. The resulting k ratios are so close to that of an isotropic material that they overlap in the figure and are needless to show in the paper. This result may suggest that the measurement method is insensitive to the type of material under testing, at least for any composite material whose effective thermal conductivities in two directions are related by a proportional factor only.

As for the uncertainty of the measured thermal conductivity caused by the measurement uncertainties of the temperature read-

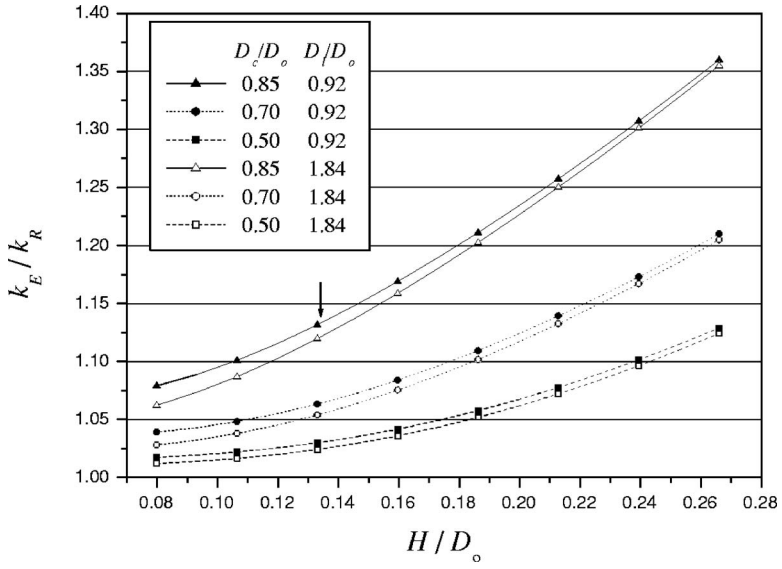

Fig. 2 The *k* ratio derived from different geometric parameters.

ings, the temperature control, the heating power reading, and the misalignment of the Teflon disk is inspected. The measurement uncertainties considered in our case are ±0.5°C (ΔT_i) for temperature measurement (considering a random error of ±0.4°C from NIST certified standard for a T-type thermocouple and a bias error of ±0.3°C), ±0.0195 W ($\Delta \dot{Q}$) (using a 10 W heater with an 8-bit resolution pulse width modulation (PWM) controller) for the power readout, ±0.5°C (ΔT_0) for constant temperature control, and d for both x_{offset} and y_{offset}.

In the analysis, both the approximate temperature distribution functions, Eqs. (2) and (4), on the lower temperature surface of a test sample are considered. Equation (13) gives us an estimation of relative uncertainty of measured k shown in Fig. 5. In the figure, the left panel is the uncertainty estimated using Eq. (3) to evaluate $T_{\max}$ while the right panel is that using Eq. (5). On the left panel, u_{k_E} varies axisymmetrically in the range from 0.08939 to 0.13795. On the right panel, u_{k_E} varies more or less axisymmetrically in the range from 0.08965 to 0.10353. Comparing the two panels, one can see that using Eq. (5) to evaluate $T_{\max}$ introduces less error than using Eq. (3) with the same amount of misalignment.

The reason for this is more mathematical than physical. Equations (3) and (5) have the same highest order (second order) of spatial coordinate, which is high enough to describe the relatively flat distribution shown in Fig. 3 for $r < d$. However, with five temperature sensors, Eq. (3) is the highest-order function one can use. It cannot tolerate the slightest measuement uncertainty since five known temperature values determine only five unknown coefficients. Nonetheless, with Eq. (5), the measurement uncertainty of each temperature is allowed since the least-squared-fit method is used to solve the four unknowns and has a degree of freedom of 1 (5−4). If a function of higher-order polynomial is used, the degree of freedom is reduced. Consequently, the approximated function tolerates less measurement uncertainty.

In order to observe the effect of measurement uncertainties on u_{k_E}, the uncertainties are varied with the use of both equations to

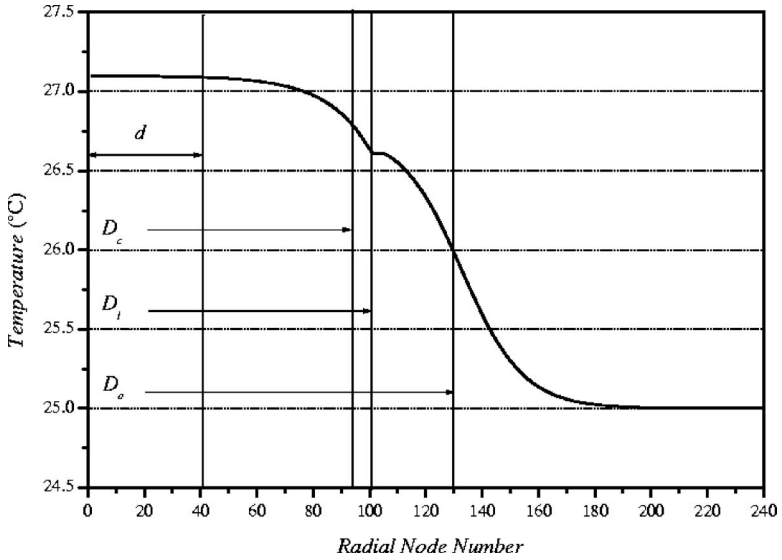

Fig. 3 The temperature distribution on the lower temperature side of a sample.

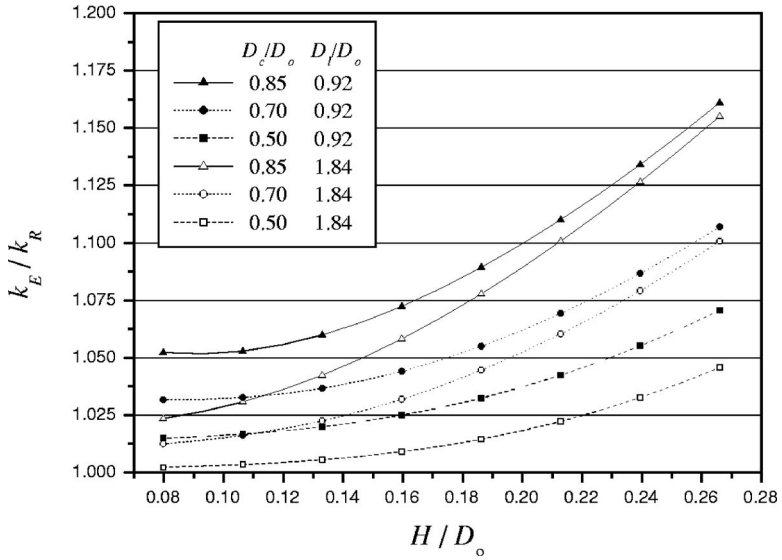

Fig. 4 The *k* ratio derived without temperature distribution outside the constant temperature region.

evaluate T_{max}. In Fig. 6, the results in Fig. 5 are repeated as Line 1 and 2 for the left and right panel, respectively, expressed as the functions of radial offset, r_{offset}. If the measurement uncertainties can be lower, such as $\Delta\dot{Q} = \pm 0.00122$ W (using a 10 W heater with a 12-bit resolution PWM controller), the measurement uncertainties ΔT_i and ΔT_0 being the same as ±0.5 °C, the values of u_{k_E} reduce significantly and are shown as Lines 3 and 4, respectively. It is noted that the tendency of variation in u_{k_E} with respect to r_{offset} is independent of the measurement uncertainties.

5 Conclusion

The numerical model for error analysis of the steady-state thermal conductivity measurement method is established. It is verified by an experiment on a piece of EPS with a prototype measurement device. This model is capable of estimating both systematic and random error of measurements. With the numerical model, systematic errors are derived as correction factors (*k* ratios) to improve measurement accuracy in practical applications.

In this study, it is found that the diameter of the Teflon disk

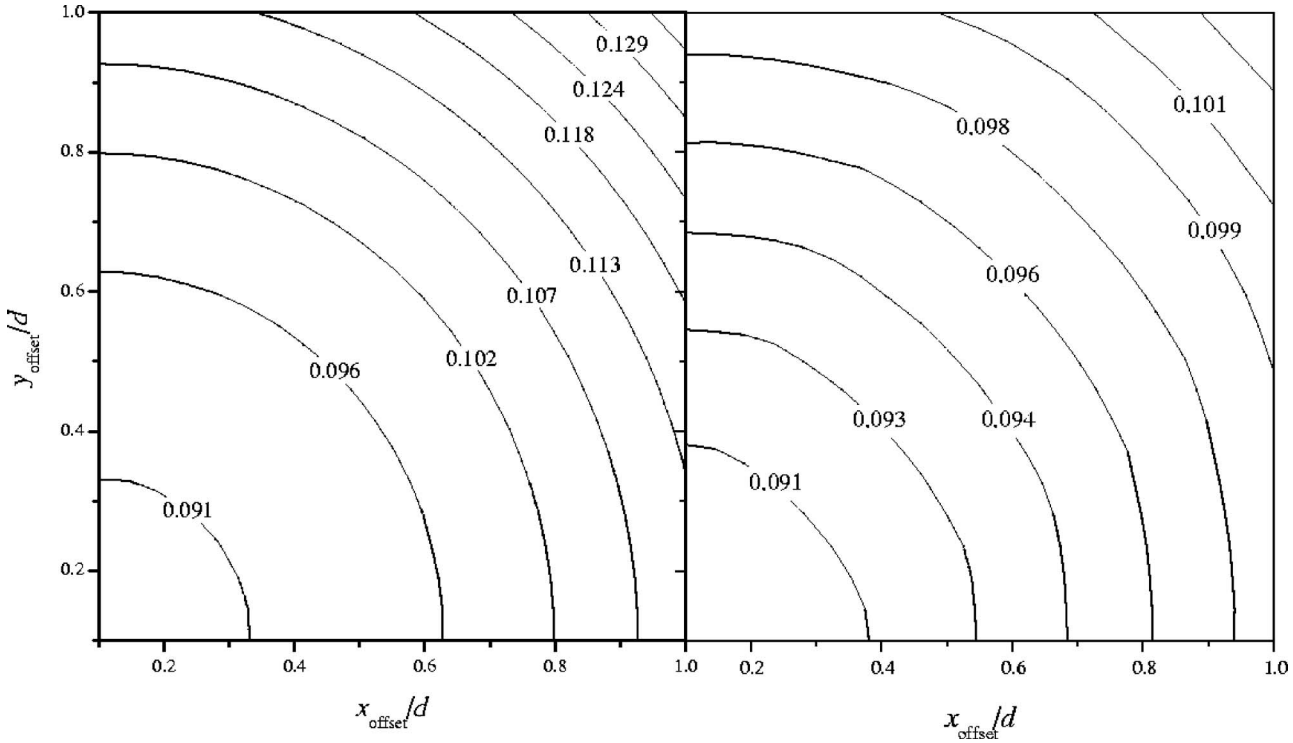

Fig. 5 The relative uncertainty of k_E caused by the uncertainties of measurement and the offset of temperature sensors embedded in the Teflon disk plate using both Eq. (2) (left panel) and Eq. (4) (right panel) to evaluate T_{max}.

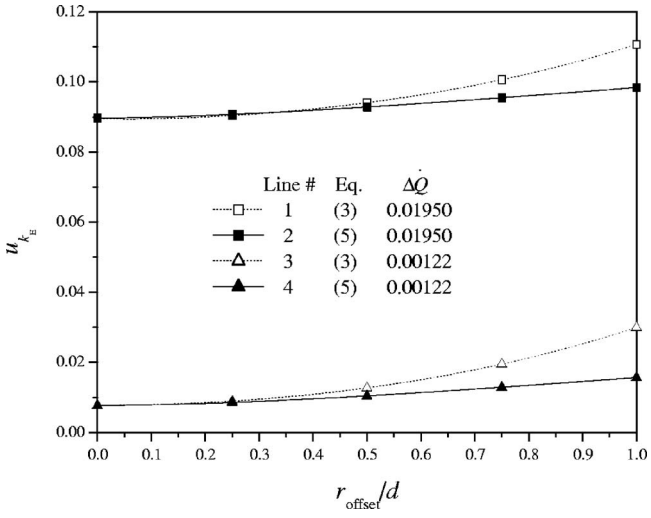

Fig. 6 The relative uncertainty of k_E caused by the uncertainties of measurement and the offset of temperature sensors in the radial direction.

plate, D_l, should be larger than two times D_o to minimize the systematic error. If one wishes to lower the systematic error further, the housing outside the constant temperature area should not contact with the test sample. It is also realized that the measurement method is insensitive to composite materials whose effective thermal conductivities in two directions are related to a proportional factor only. Furthermore, the use of approximate temperature distribution function, Eq. (4), can better describe the actual situation and keep minimal the random error introduced by the misalignment of temperature sensors. This shows that the goal of using an approximate temperature distribution function for k measurement is achieved. The random error in k measurement strongly depends on the uncertainties of the heating power, measuring temperature, and the misalignment of temperature sensors on the lower temperature side.

Referring to Fig. 4, by choosing proper geometric parameters, for example, $D_c/D_o=0.5$ and $D_l/D_o=1.84$, the systematic error can be kept under 5% within a considerable range of sample thickness, $H/D_o<0.27$. Therefore, the measurement method is considered to be an affordable method due to its simplicity.

However, for more accurate measurements, the systematic error has to be taken into account. But the systematic error also depends on the mean temperature, the ambient temperature, and the k value of the test samples. Though the systematic error can be expressed as an empirical function of geometric parameters and temperatures, it is almost impossible to make the function in a closed form due to its dependency on the unknown itself. Therefore, it is necessary to perform a large number of calculations with this numerical model and generate an equal amount of results. By using an optimization method, such as artificial neuro networks, together with the results, it is possible to seek a calibrating function for real applications of the measurement method.

Acknowledgment

This work was supported by NSC of Taiwan under Grant No. NSC-95-2119-M-182-001.

Nomenclature

a = coefficient of the alternative approximation temperature distribution function
A = area of the heating plate, m^2
b = coefficient of the alternative approximation temperature distribution function
c_i = coefficients of the original approximation temperature distribution function
d = distance of the four temperature sensors from the center, m
D_c = diameter of the heating plate, m
D_h = diameter of the housing, m
D_o = diameter of the constant temperature region, m
D_l = diameter of the Teflon plate, m
h_{L,H_l} = coefficient of free convection on a horizontal lower surface of width L, W/m^2 K
h_{L,H_u} = coefficient of free convection on a horizontal upper surface of width L, W/m^2 K
$h_{L,V}$ = coefficient of free convection on a vertical surface of width L, W/m^2 K
H = thickness of a test sample, m
k = thermal conductivity of a homogeneous material, W/m K
k_f = thermal conductivity of the ambient fluid (air), W/m K
k_r = translational thermal conductivity of a composite material, W/m K
k_z = longitudinal thermal conductivity of a composite material, W/m K
k_E = measured thermal conductivity of a test sample, W/m K
k_R = real thermal conductivity of the test sample, W/m K
L = width of a boundary surface of free convection, m
L_C = characteristic length of a free convection surface, m
Pr = Prandtl number of the air
$\dot{Q}$ = heat transfer rate of the heating plate, W
r = radial coordinate, m
r_k = k ratio
R = maximum radius of the test sample in the numerical model, m
Ra_{L_C} = Rayleigh number based on L_C
s = thickness of the Teflon disk plate, m
T_0 = temperature of the constant temperature region, °C
T_a = ambient air temperature, °C
T_c = temperature at the center of the lower temperature surface, °C
$T_{\max}$ = maximum temperature on the sample surface opposite to the constant temperature region, °C
T_m = mean temperature of T_0 and $T_{\max}$, °C
u_{k_E} = relative uncertainty of measured thermal conductivity, k_E
x_0, y_0 = location of maximum temperature relative to the center of the Teflon disk plate, m
z = longitudinal coordinate, m
Δr = radial grid size, m
Δz = longitudinal grid size, m

References

[1] Caps, R., Heinemann, U., Fricke, J., and Keller, K., 1997, "Thermal Conductivity of Polyimide Foams," Int. J. Heat Mass Transfer, **40**, pp. 269–280.
[2] Collins, R. E., Fisher-Cripps, A. C., and Tang, J. Z., 1992, "Transparent Evacuated Insulation," Sol. Energy, **49**(3), pp. 333–350.
[3] Martin, T. J., and Dulikravich, G., 2000, "Inverse Determination of Temperature-Dependent Thermal Conductivity Using Steady Surface Data on Arbitrary Objects," ASME J. Heat Transfer, **122**, pp. 450–459.
[4] Herwig, H. and Beckert, K., 2000, "Fourier Versus Non-Fourier Heat Conduction in Materials With a Nonhomogeneous Inner Structure," ASME J. Heat Transfer, **122**, pp. 363–365.
[5] Chuah, Y. K., and Sun, M. T., 1997, "Research on Insulation Testing and Vacuum Insulation Technology (2)," National Council of Science, Taiwan, Report on Supported Research Project (in Chinese), pp. 8–10.
[6] Chuang, C. C., 1998, "Application of Micro-controller on the Development of

Heat Transfer Coefficient Measurement Instrument," Master's thesis, Chang-Gung University, Taoyuan, Taiwan (in Chinese), pp. 12–14.
[7] Sun, M. T., Chang, C. H., Chuang, C. C., and Chuah, Y. K., 2002, "A Portable Apparatus with One Constant Temperature Zone for Thermal Conductivity Measurement," *Proceedings 26th Conference on Theoretical and Applied Mechanics*, Hu-Wei, Taiwan, December 20–21, pp. A049.1-2.
[8] Shi, J.-M., Breuer, M., Durst, F., and Schafer, M., 2003, "An Improved Numerical Study of the Wall Effect on Hot-Wire Measurements," ASME J. Heat Transfer, **125**, pp. 595–603.
[9] Incropera, F. P., and DeWitt, D. P., 2001, *Fundamentals of Heat and Mass Transfer*, 5th ed., Wiley, New York, pp. A14–A15.
[10] Wahid, S. M. S., Madhusudana, C. V., and Leonardi, E., 1998, "An Investigation of the Effect of Gases on Thermal Gap Conductance at Low Contact Pressure," *Proceedings of 11th International Heat Transfer Conference*, **7**, Kyongju, Korea, August 23–28, Taylor & Francis, Philadelphia, PA, pp. 95–100.
[11] Wahid, S. M. S., 2003, "Numerical Analysis of Heat Flow in Contact Heat Transfer," Int. J. Heat Mass Transfer, **46**, pp. 4751–4754.
[12] Wahid, S. M. S., and Madhusudana, C. V., 2003, "Thermal Contact Conductance: Effect of Overloading and Load Cycling," Int. J. Heat Mass Transfer, **46**, pp. 4139–4143.
[13] Janna, W. S., 1986, *Engineering Heat Transfer*, PWS Publishers, Boston, pp. 533–539.

Stochastic Heat Transfer in Fins and Transient Cooling Using Polynomial Chaos and Wick Products

A. F. Emery
e-mail: emery@u.washington.edu

D. Bardot

Department of Mechanical Engineering,
University of Washington,
Seattle, WA 98195-2600

Stochastic heat transfer problems are often solved using a perturbation approach that yields estimates of mean values and standard deviations for properties and boundary conditions that are random variables. Methods based on polynomial chaos and Wick products can be used when the randomness is a random field or white noise to describe specific realizations and to determine the statistics of the response. Polynomial chaos is best suited for problems in which the properties are strongly correlated, while the Wick product approach is most effective for variables containing white noise components. A transient lumped capacitance cooling problem and a one-dimensional fin are analyzed by both methods to demonstrate their usefulness. [DOI: 10.1115/1.2739586]

Keywords: stochastic heat transfer, uncertainty, predictions

Introduction

Most analytic solutions and many experimental analyses for heat transfer are based upon deterministic systems even though it is often recognized that thermal properties or boundary conditions may possess considerable randomness. Of course, there are some thermal systems that are well known as being stochastic in nature. The stochastic effects of weather, solar irradiation, radiation through cloud cover, upwelling radiation in oceans, heat transfer and flow in porous media, and the age-old problem of turbulence all possess a degrees of random effects that make deterministic modeling inappropriate. The fields of imaging, remote sensing, combustion, and its interaction with flow have similar problems. There is a large body of current literature about the stochastic effects in all of these areas. In heat transfer and fluid dynamics, probably the most intensely investigated area is that of turbulence. Even a cursory literature search will turn up an almost uncountable number of citations related to turbulence or its slightly simpler variation, i.e., Burger's equation, many by mathematicians who have approached the topic from the point of view of stochastic differential equations.

Yet even with the longstanding interest in the stochastic nature of problems such as these and with the benefit of a substantial body of work by civil engineers related to the stochastic nature of structures and their response to wind loads and earthquakes and by electrical engineers studying the effects of noise on signal transmission for communication and radar detection, both going back more than four decades, the heat transfer community has only recently begun to consider these effects. Part of the reason may be that in many heat transfer experiments there are so many parameters with inherent randomness that cannot be well quantified that investigators are willing to accept a considerable degree of imprecision without trying to quantify it in terms of a stochastic process. For example, maintaining a prescribed temperature at the boundary is difficult to do, surface convection coefficients are generally variable in space and time, particularly for turbulent flows, and most thermal properties are functions of temperature, e.g., conductivity and specific heat capacity, or of surface conditions; e.g., surface emissivity or nucleate boiling conditions. All of these effects introduce randomness that cannot be easily described and whose effects are hard to delineate.

Figure 1(*a*) depicts the stochastic variation in the ambient temperate observed during the transient cooling of a cylinder. The measured surface heat flux is shown in Fig. 1(*b*) and compared to that predicted from a code [1]. How much the heat flux measurements are affected by the time varying ambient air temperature versus noise in the measurements is open to question. One certainly expects that the surface heat transfer coefficient is affected by the varying air temperature and local air currents. While the question cannot be answered in its entirety, understanding how randomness affects the results can help us decide whether it is the measurement noise, the system noise, or the inherent nature of the stochastic effects that dominate.

Most studies that take randomness into account have been based on Monte Carlo (MC) simulations. Effective ways to implement MC analyses and to reduce the variability of the results (usually referred to as variance reduction) are available [2]. Unfortunately, MC studies are computationally expensive and sometimes difficult to formulate. Recently, two other approaches have been introduced that may make the analyses simpler. The first is polynomial chaos, introduced by Ghanem and Spanos [3] and effectively applied to ground water flow, heterogeneous media, and free convection [4,5]. In the second, Wick products have been applied to solve partial differential equations whose properties or boundary conditions are contaminated by white noise by Holden et al. [6] and colleagues.

The aim of this presentation is to acquaint the general heat transfer practioneer with the concepts behind these two approaches and to show how they can be applied to typical heat transfer problems. For this, we treat two problems, the transient cooling of a lumped capacity system and the cooling of a fin. The appropriate equations in non-dimensional form for a constant ambient temperature are

$$\frac{d\Theta}{d\tau} = -C\Theta \tag{1}$$

Contributed by the Heat Transfer Division of ASME for publication in the JOURNAL OF HEAT TRANSFER. Manuscript received March 22, 2006; final manuscript received September 19, 2006. Review conducted by A. Haji-Sheikh. Paper presented at the 2004 ASME Heat Transfer/Fluids Engineering Summer Conference (HT-FED2004), Charlotte, NC, July 11–15, 2004, Paper No. 56740.

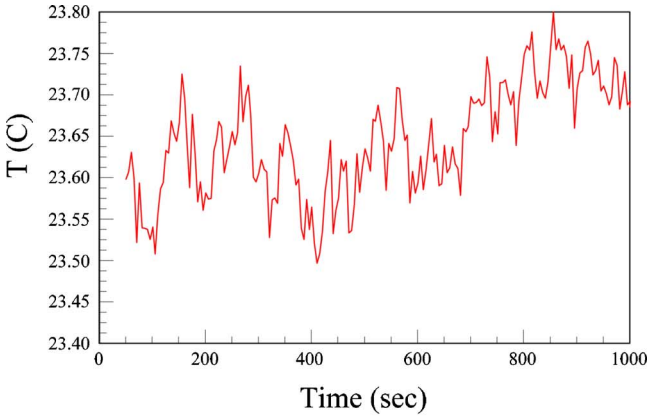

(a)

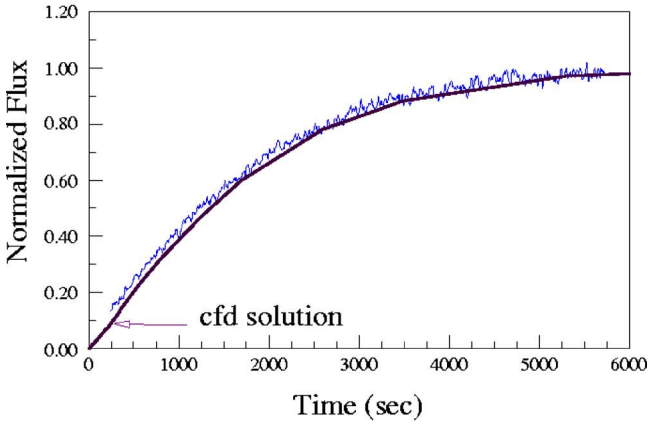

(b)

Fig. 1 (a) Measured temporal variation of ambient air temperature. (b) Measured surface heat flux, during cooling compared to predicted.

$$\frac{d^2\Phi}{d\zeta^2} = C\Phi \tag{2}$$

where

$$\Theta = \frac{T(t) - T_\infty}{T(0) - T_\infty} \quad \text{and} \quad \Phi = \frac{T(x) - T_\infty}{T(0) - T_\infty} \tag{3}$$

where τ and ζ are nondimensional quantities, $\tau = \bar{C}t$ and $\zeta = x\sqrt{\bar{C}}$, with $\bar{C}$ being the mean value of C, and C represents either $hA/\rho cV$ or hP/kA accordingly. For both cases, h is assumed to be a random quantity and we are interested in how $T(t)$ and $T(x)$ vary. Specifically, we are interested in the mean value of T and the standard deviation of T. Because Eqs. (1) and (2) contain coefficients that are random in nature, they are referred to generically as stochastic differential equations.

We need to differentiate between the terms random variables, random fields, and stochastic processes in this paper. Consider a probability space $(\Omega, \mathcal{A}, \mathcal{P})$, where Ω represents all possible events, and $\mathcal{A}$ represents the events actually occurring. There may be n sets of events actually occurring. For example, in the fin problem there may be randomness in both the heat transfer coefficient and the thermal conductivity with a specific value of h and of k constituting a single event. P represents a measure of the probability, i.e., $\mathcal{P}(\mathcal{A})$ is the probability that $\mathcal{A}$ occurred. A stochastic process, i.e., $X(x, \omega)$, is formally defined as a set of random variables or random n-vectors (if more than one event $\mathcal{A}$ occurred) where x represents a dimension of the problem, i.e., time, space, or time and space, and ω represents a specific realization, i.e. an event. For a specific value of x, say x_i, $X(x_i, \omega)$ represents a random variable or random vector in the probability space. For each fixed ω, say ω_j, $X(x, \omega_j)$ represents a real valued or n-vector valued function over the x-dimensional space.

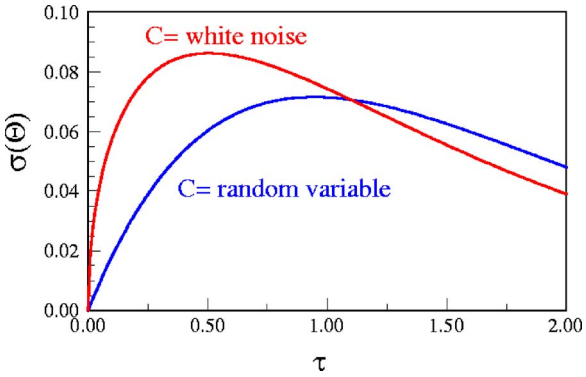

Fig. 2 Comparison of $\sigma(\Theta)$ with respect to τ for C being a random variable and a stochastic process for α=0.2

We reserve the term "random variable" for the case when the statistical character of C is constant. If its mean and standard deviation vary with τ or ζ in a fixed and deterministic manner, it is termed a "random field." If, on the other hand, $C(\tau)$ is represented as $\bar{C} + \sigma w$, where w is white noise we term it as a "Stochastic process," which will be taken to be homogeneous, i.e., of constant standard deviation and mean.

Random Variable Versus Stochastic Process

The behavior of the response is significantly different for the cases of C being a random variable or a white noise process.

For a C a random Gaussian variable with a coefficient of variation $\alpha(=\sigma(C)/\bar{C})$, the deterministic solution of Eq. (1) is

$$\Theta(\tau) = e^{-C\tau} \tag{4a}$$

Using standard equations (see the Appendix) we obtain the expected value

$$E[\Theta(\tau)] = e^{-\bar{C}\tau} e^{\frac{\alpha^2\tau^2}{2}} \tag{4b}$$

and variance

$$\sigma^2[\Theta(\tau)] = e^{-2\bar{C}\tau}(e^{2\alpha^2\tau^2} - e^{\alpha^2\tau^2}) \tag{4c}$$

If C is corrupted with white noise, i.e., $C = \bar{C}(1 + \alpha w)$, where w represents white noise, Eq. (1) is a stochastic differential equation and we cannot use Eqs. (A4) and (A5), but must follow Soong [7] to obtain

$$E[\Theta(\tau)] = e^{-\bar{C}\tau} \tag{5a}$$

$$\sigma^2[\theta(\tau)] = e^{-2\bar{C}\tau}(e^{\alpha^2\tau} - 1) \tag{5b}$$

Note the fundamental difference in the solutions. For a random variable, τ appears in conjunction with α as $\alpha^2\tau^2$, while for a white noise process, it appears as $\alpha^2\tau$. It is particularly interesting that the mean values, Eqs. (4*b*) and (5*a*) differ in form and that the mean value for the white noise process is simply the deterministic solution based upon $\bar{C}$. Figure 2 compares the standard deviation for the two different types of randomness.

Homogeneous Chaos. The basis for both polynomial chaos and the Wick product is Wiener's observation that any random quantity that possesses a finite variance can be represented by a series of Hermite polynomials in terms of a standard Gaussian random variable, that is,

Table 1 Chaos polynomials

Order i	One random variable $h_i(\xi)$	Two random variables $\Psi_i(\xi_1,\xi_2)$
Zeroth	1	1
First	ξ	ξ_1
		ξ_2
Second	ξ^2-1	ξ_1^2-1
		$\xi_1\xi_2$
		ξ_2^2-1

$$X(\tau)=\sum_{i=0}^{\infty} X_i(\tau)h_i(\xi) \tag{6a}$$

where $h_i(\xi)$ are Hermite polynomials given by

$$h_i(\xi)=-(1)^i e^{\xi^2/2}\frac{d^i}{d\xi^i}e^{-\xi^2/2} \tag{6b}$$

and ξ is of zero mean and unit standard deviation. This representation is referred to as homogeneous chaos. The $h_i(\xi)$ are orthonormal with respect to the weight function $e^{-\xi^2/2}/\sqrt{2\pi}$ over the range $-\infty\le\xi<\infty$ and the first several are shown in Column 2 of Table 1.

Note that since $h_1(\xi)=\xi$, the first two terms of the series are the standard representation of a Gaussian random variable with $X_0(t)=E(X(t))$ and $X_1=\sigma(X)$. Equation (1) for C having a white noise component is usually interpreted in the sense of an Ito equation [8,9] and has the analytical solution

$$\Theta(\tau)=e^{-\bar{C}\tau-\frac{1}{2}\alpha^2\tau+\alpha B(\tau)} \tag{7}$$

where $B(\tau)$ represents a Brownian process. From Holden et al. [6], Eq. (7) can be formally expanded as

$$\Theta(\tau)=e^{-\bar{C}\tau}\left(h_0\left(\frac{B(\tau)}{\sqrt{\tau}}\right)+(\alpha\sqrt{\tau})h_1\left(\frac{B(\tau)}{\sqrt{\tau}}\right)+\frac{1}{2!}(\alpha\sqrt{\tau})^2h_2\left(\frac{B(\tau)}{\sqrt{\tau}}\right)\cdots\right) \tag{8}$$

While most analyses assume Gaussian random variables, it is clear that other distributions may be more appropriate. In fact, from the solution (Eq. (4*a*)), we see that $\Theta(\tau)$ has a log-normal distribution and $\Theta(\tau)$ is restricted to the range $0\le\Theta<\infty$. Xiu and Karniadakis [10] noted that the representation in terms of Hermite polynomials may not be the most efficient. They point out that the Hermite polynomials are a subset of Askey polynomials and give the following table of polynomials that are appropriate for different ranges of the random variables (Table 2).

The use of the appropriate polynomials is optimal, in the sense of requiring the smallest number of terms in the expansion, and using Hermite polynomials to represent non-Gaussian processes often requires one or two more terms than the optimal expansion. The problem comes with mixing the representation. For example, if C is truly Gaussian, then it should be expanded in Hermite

Table 2 Orthogonal polynomials

Random variable	Orthogonal polynomials	Range of ξ
Gaussian	Hermite	$(-\infty,\infty)$
Gamma	Laguerre	$(0,\infty)$
Beta	Jacobi	(a,b)
Uniform	Legendre	(a,b)

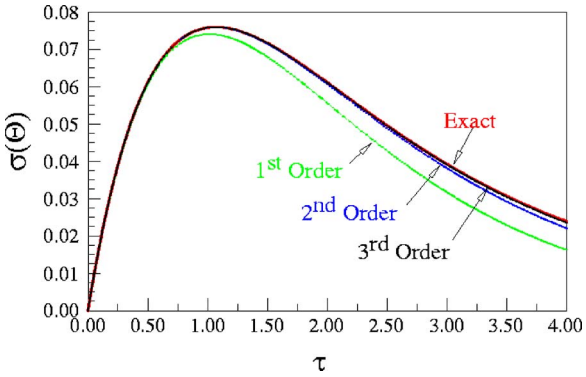

Fig. 3 Representation of $f(\Theta)$ from Eq. (1) by first- and second-order expansions (Eq. (6*a*)) for $\alpha=0.2$

polynomials, but the resulting $\Theta(\tau)$ is best approximated with Laguerre polynomials. However, the approach described above, Eq. (6*a*), which is based upon orthogonality, requires that the same polynomial be used for all expansions and since one does not know in advance which would be optimal for representing $\Theta(\tau)$, it is common to express everything in terms of Hermite polynomials. Xiu and Karniadakis [10] give the details of how to best represent random variables with differing distributions in terms of Hermite polynomials.

Positivity

The coefficient C for both Eqs. (1) and (2) must be positive. If C is taken to be a Gaussian variable, $=\bar{C}(1+\alpha\xi)$, then the coefficient of variation, α must be restricted so that $C\ge0$. Roughly speaking this means that $\alpha\le0.3$ and the analyses are limited to relatively small noise levels. Because of this other distributions are often used. A common one is the log-normal distribution $C=\exp(\xi)$. Sakamoto and Ghanem [11] give a detailed description of how to express both random variables and random fields in a series of Hermite polynomials. They note that as many as five terms, i.e., up to $h_5(\xi)$, may be needed for high accuracy. For our examples, two terms suffice, as shown in Fig. 3, for $\alpha\le0.2$. Approximately as many terms are needed as α is in tenths. As we shall see, for α higher than 0.2, one should use the Laguerre expansion to limit the number of terms needed.

Solving Stochastic Problems

Methods of solving stochastic problems generally involve two steps:

(1) representing a random field in terms of uncorrected random variables,
(2) converting all random variables into Gaussian variables.

Inasmuch as lack of correlation does not imply independence, the second step is necessary for both practical and theoretical reasons since uncorrelated Gaussian random variables are independent. The following sections on polynomial chaos and Wick products describe methods for achieving the desired conversions.

Polynomial Chaos Expansions for Random Variables

The solution of Eq. (1) is found by expressing $\Theta(\tau)$ as

$$\Theta(\tau)=\sum_{i=0}^{\infty}\Theta_i(\tau)h_i(\xi) \tag{9}$$

and substituting into Eq. (1), with C represented by Eq. (6*a*), multiplying by $h_j(\xi)$ and integrating with respect to the weight function. The coefficients $\Theta_i(\tau)$ satisfy

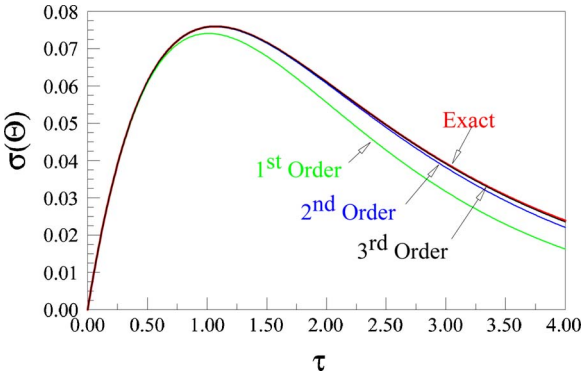

Fig. 4 Convergence of the polynomial chaos solution to the exact value for *C* being a random variable

$$\frac{d\Theta_i(\tau)}{d\tau} = -\sum_{k=0}^{N_C}\sum_{j=0}^{N_\Theta}\frac{c_{ijk}}{E(h_k^2)}C_j\Theta_k(\tau) \tag{10a}$$

where

$$E(h_k^2(\xi)) = k\,! \quad \text{and} \quad c_{ijk} = (1/\sqrt{2\pi})\int_{-\infty}^{\infty} h_i(\xi)h_j(\xi)h_k(\xi)e^{-\xi^2/2}d\xi \tag{10b}$$

In Eq. (10*a*), we have truncated the series for C and for Θ at N_C and N_Θ, respectively.

The results of this representation of $\Theta(\tau)$ in terms of the series expansion is a set of coupled equations for $\Theta_0, \Theta_1, \ldots, \Theta_{N_\Theta}$. Figure 4 compares the exact solution, i.e., Eq. (4*c*), with solutions of Eq. (9) for $N_\Theta = 1, 2$, and 3.

Even for this relatively small number of terms, the agreement is very acceptable. Unfortunately, the simultaneous equations are coupled as shown in Table 3. For Θ this is not a serious problem, but in the solution for Φ it can lead to exceptionally large matrices to invert. Keese [12] describes efficient methods for assembling and inverting these matrices.

If α is large enough to require several terms in the expansion of C, then this will require an equal number of terms in the expansion of Θ. For example, if $N_C = 5$, then one will need to solve five coupled equations for a single random variable ξ.

Multiple Random Variables—White Noise

Consider a problem in which both h and k are random variables, characterized by ξ_1 and ξ_2, respectively. That is $h = \bar{h} + \sigma(h)\xi_1$ and $k = \bar{k} + \sigma(k)\xi_2$. In determining the probability density $f(\Theta)$, we need to recognize that at any value of τ, Θ may be found in the range Θ to $\Theta + \delta\Theta$ for several different, but disparate, ranges of h and k, and the determination of $f(\Theta)$ may be challenging [13]. Ghanem and Spanos [3] have extended Wiener's concept of homogenous chaos to represent the effect of several different random variables by expanding in a series of generalized chaos polynomials in terms of standard Gaussian random variables, i.e., $\xi_1, \xi_2, \ldots, \xi_N$:

Table 3 Equations for polynomial chaos

$d\Theta_0/d\tau = -\Theta_0 - \alpha\Theta_1$
$d\Theta_1/d\tau = -\Theta_1 - \alpha\Theta_0 - 2\alpha\Theta_2$
$d\Theta_2/d\tau = -\Theta_2 - \alpha\Theta_1 - 3\alpha\Theta_3$
$d\Theta_3/d\tau = -\Theta_3 - \alpha\Theta_2 - 4\alpha\Theta_4$

$$\Theta(\tau) = \sum_{i=0}^{\infty}\Theta_i(\tau)H_i(\xi_1, \ldots, \xi_N) \tag{11}$$

where

$$H_k(\xi_1^{i_1}, \xi_2^{i_2}, \ldots, \xi_n^{i_n}) = (-1)^k e^{\xi^2/2}\frac{d^k}{d\xi_1^{i_1}\xi_2^{i_2}}e^{-\xi^2/2} \tag{12a}$$

with

$$\xi^2 = \xi_1^2 + \xi_2^2 + \cdots \xi_n^2 \tag{12b}$$

and i_j represents the number of times that ξ_j appears in H_k and $i_1 + i_2 + \cdots i_n = k$. For any given order of the generalized chaos polynomial $H_k(\xi_1^{i_1}, \xi_2^{i_2}, \ldots, \xi_n^{i_n})$ there are several unique polynomials, e.g., for H_2, we have $H_2(\xi_1, \xi_2)$, $H_2(\xi_1, \xi_3)$, $H_2(\xi_1, \xi_n)$, et seq. For each unique polynomial, there is an associated coefficient in the series (Eq. (11)). Following Ghanem and Spanos, we represent Eq. (11) in terms of these unique polynomials as a truncated series:

$$\Theta(\tau) = \sum_{i=0}^{P}\Theta_i(\tau)\Psi_i(\xi) \tag{13}$$

For two random variables ξ_1 and ξ_2, the expressions for Ψ_0, Ψ_1, and Ψ_2 are shown in column 3 of Table 1. Ghanem and Spanos termed this extension of homogeneous chaos, polynomial chaos, and the technique has been used in solving multi-random variable problems [4,5].

The total number of terms P in the series (Eq. (13)) is given by

$$P = \frac{(N_\Theta + N_\xi)!}{N_\Theta\,!\,N_\xi!} \tag{14}$$

Thus, even though the expansion (Eq. (13)) is limited to a relatively low-order polynomial Ψ_k, the number of coefficients of Θ_k that must be evaluated increases at exceptional speed. For example, using a third-order polynomial with two random variables leads to solving ten coupled equations.

Random Fields and the Karhunen-Loeve Expansion

If C is a random field, not a random variable, we can subdivide the region $0 \le \tau < \tau_{\max}$ into small increments, and assign different values of C to each subdivision when integrating with respect to τ. How to choose the value of C appropriate to the increment τ to $\tau + \delta\tau$ is an open question [14]. Common choices are the midpoint value or some spatial average over the increment. In general, midpoint, values tend to overpredict the variability in $\Theta(\tau)$ and spatial averaging under predicts the variability. Regardless of the choice, the numerical solution of Eq. (1) causes no conceptual difficulties, but it means that each solution is unique and that drawing general conclusions is not possible.

Suppose that the random field is homogeneous, i.e., its mean and standard deviation are constant with respect to τ, but that the properties are spatially correlated, i.e., that is $E(C(\tau_i), C(\tau_j)) = \Sigma_C(C_i, C_j)$. Let V be a vector of $C(\tau_i), \ldots, C(\tau_n)$ that characterizes the random field. Because the covariance matrix Σ_C is symmetric and positive definite, there is a transformation from V to Ξ for which Σ_Ξ is diagonal; i.e., the components of the new vector Ξ are uncorrelated. In the multivariate statistical literature, these new random variables are referred to as *principal components*. In the transformation $V = U\Xi$, the matrix U is formed from the eigenvectors of Σ_C. Note that while uncorrelated, the new random variables are not independent.

If instead of discrete values of C, a continuous distribution is used, then the approach described above leads to the Karhunen-Loeve expansion in terms of continuous eigenfunctions (see Ghanem and Spanos [3] for details). Inasmuch as only a few such eigenfunctions are known analytically, one generally resorts to

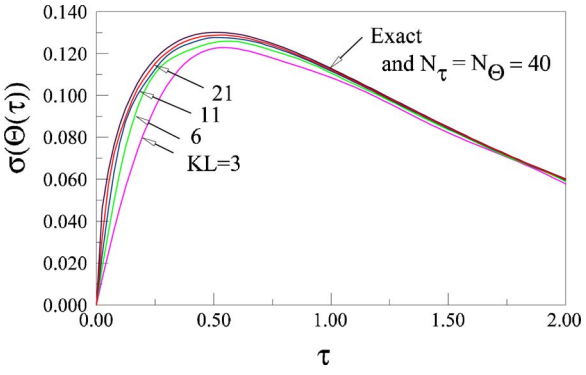

Fig. 5 Illustrating the convergence of the *K-L* approach to solving Eq. (2) for white noise

numerical evaluation, often using the finite element approach, which is then the equivalent of the discrete process described above.

If C is a Gaussian random field, then lack of correlation implies independence. The resulting random field in terms of ξ is now composed of as many independent vectors, whose components are the values of C to be associated with each increment of τ, as there are increments in τ and from the size of the expansion (Eq. (14)) the problem has become almost intractable.

The standard deviation associated with each vector equals its eigenvalue λ, and thus the combined variance of the first N vectors is

$$\sigma^2(\Xi) = \sum_{i=1}^{N} \lambda_i^2 \tag{15}$$

Frequently, and fortunately, it turns out that if the field has a reasonable degree of correlation and if the vectors Ξ are ordered in terms of the eigenvalues, with the largest eigenvalue first, the first several vectors Ξ contain most of the information and thus the number of components of Ξ needed to be considered may be small, in which case the solution becomes possible. However, because the reduced number of vectors used will not exhibit the same combined variance that the original field exhibited, it is necessary to scale them to adequately reflect the variability of the original random field [11]. By this approach, one is able to draw conclusions about the effect of types of correlation and the correlation length upon Θ and Φ.

For the case in which C is represented by white noise, Eq. (1) was solved in two ways. First, the range of τ was subdivided into N_ξ equally sized intervals and ξ_i in each interval was assumed to be an independent Gaussian random variable. Expanding $\Theta(\tau)$ using first-order Hermite polynomials,

$$\Theta(\tau) = \Theta_0(\tau) + \sum_{i=1}^{N_\xi} \Theta_i(\tau) h_1(\xi_i) \tag{16}$$

with N_ξ=40 gives the results shown in Fig. 5. The solution of the coupled equations was obtained using a fourth-order Runge-Kutta method over each of the N_τ equally sized intervals, $\Delta\tau = \tau_{\max}/N_\tau$. In this approach, good results required that integration interval, $\Delta\tau$ matched the random variable interval, $N_\xi = N_\tau$. Use of fewer values of ξ_i led to unacceptable results. If the *K-L* expansion was used, good results were obtained with a reduced number of terms as shown. In the first approach we have 41 coupled equations to solve, in the second, $KL+1$. The results based upon the one term expansion, $N_\Theta = 1$, i.e., a Gaussian expansion, are in good agreement with the exact solution and there is no need to employ higher order Hermite polynomials in the expansion for $\Theta(\tau)$, as expected from Fig. 3. However, for $C(\tau)$ given by other than Gaussian white noise, higher order expansions will generally be needed.

Stochastic White Noise Processes and Wick Products

If the correlation length is large, then only a few vectors must be considered, but if it is small, then many must be and in the limit as the field approaches white noise as many vectors as there are increments in τ must be considered as described above. If the properties constitute a random field, that is their statistics are known, then solving by using the expansion in terms of Θ_i is unrealistically expensive and one is limited to solutions that are unique to the specific random field considered.

However, if $C(\tau)$ is a mean value $\bar{C}$ modified by white noise, a different approach has been described by Holden et al. [6]. This approach is based upon the Wick product. Consider two stochastic processes, F and G, and let each be represented by an expansion in generalized chaos polynomials

$$F = \sum_i f_i H_i \quad G = \sum_j g_i H_j \tag{17a}$$

then the Wick product is defined as

$$F \diamond G = \sum_{i,j} f_i g_i H_{i+j} \tag{17b}$$

Wick products have several valuable features. They are associative, distributive, and commutative. They can be differentiated and integrated according to the usual rules of calculus. Probably most important are the relations

$$E(F \diamond G) = E(F)E(G) \quad \text{if } F \neq G \tag{18a}$$

$$F^{\diamond k} = F \diamond F^{\diamond (k-1)} \text{ with } F^{\diamond 0} = 1 \tag{18b}$$

$$E(e^{\diamond X}) = e^{E(X)} \tag{18c}$$

$$\text{if } P(F) = \sum_{n=0}^{N} a_n F, \quad P^{\diamond}(F) = \sum_{n=0}^{N} a_n F^{\diamond n} \tag{18d}$$

where $P(F)$ is a polynomial in F. Following Holden, one simply writes the original equation as

$$\frac{d\Theta(\tau)}{d\tau} = -C(\tau) \diamond \Theta(\tau) \tag{19}$$

and integrates as though it were an ordinary differential equation to obtain

$$\Theta(\tau) = \Theta_0 e^{\diamond -C\tau} \tag{20}$$

Using Eq. (18*c*), we find the expected value of $\Theta(\tau)$ to be

$$E[\Theta(\tau)] = e^{-E(C)\tau} = e^{-\bar{C}\tau} \tag{21}$$

To find the standard deviation of $\Theta(\tau)$ we cannot use Eq. (18*a*) since $F=\Theta$ and $G=\Theta$. Instead, we can show that

$$E(\Theta^2) = e^{\alpha^2\tau} E(\Theta \diamond \Theta) \tag{22a}$$

and thus

$$\sigma^2(\Theta) = e^{-2\bar{C}\tau}(e^{\alpha^2\tau} - 1) \tag{22b}$$

in agreement with Eq. (5*b*). *Note the term* $\alpha^2\tau$. If the equation is not non-dimensionalized, the units of this product are clearly inconsistent. For a Brownian process $B(\tau)$, $\sigma^2(B) = \tau$, and it is for this reason that one must be careful in formulating the equation to solve.

When an analytical relationship between $E(\Theta \diamond \Theta)$ and $E(\Theta^2)$ is not available, then one must expand the solution and the noise in series (Eq. (11a)) and project the solution onto the space, similar to the method used for polynomial chaos. An important point is that the expected value of the solution is simply the first term in the series, which corresponds to the deterministic solution based

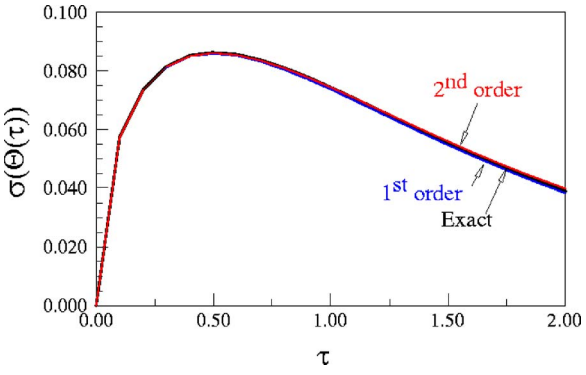

Fig. 6 Convergence of the Wick solution to Eq. (1) for white noise

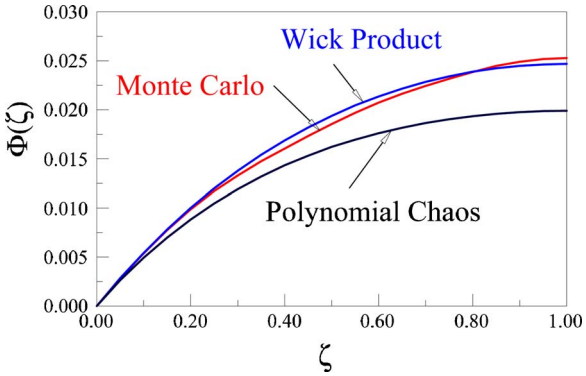

Fig. 8 Standard deviations of $\Phi(\zeta)$ for 10% noise compared to 5000 MC simulations

upon average values of the parameters. The equations for the other coefficients in the series are coupled to the first and to the preceding terms, not to subsequent terms. Thus, the solution can be obtained in a straightforward recursive way. Figure 6 illustrates the solution to Eq. (1).

One must also realize that the use of Wick products is not without questions. Kesse [15] points out the expected value is independent of the statistics of the process, contrary to some Monte Carlo simulation results. Benth and Theting [16] note that the validity of the Wick product needs to be confirmed mathematically and physically for each application.

The Fin Problem

Equation (2) for $\Phi(\zeta)$ was solved by both methods for C containing a white noise component. The fin was taken to have an insulated end and the solution based upon a finite element analysis using 40 isoparametric elements. Since there is no analytical solution available for the stochastic problem, we compare the results to a Monte Carlo simulation. Figure 7 illustrates the range of realizations observed.

Figure 8 compares the standard deviations estimated by the two methods. The Wick product estimation agrees very well with the Monte Carlo results. While the shape of the polynomial chaos solution is similar, it consistently underestimates $\sigma(\Phi)$, even when 40 terms were used in the *K-L* expansion. The reason for this underestimation is not known, but we are continuing to investigate this feature.

Conclusions

The polynomial chaos method can be used for random variables, fields, or white noise, but involves coupled equations of which the first, that for the mean response, is dependent upon the remaining equations, leading to high computing expense. In contrast, for white noise stochasticity, the Wick product yields a mean response, agreeing with equations derived from the Fokker-Planck equation, that depends only upon average properties. Different realizations using either method are relatively easy to compute by simply choosing random values of ξ and substituting into Eq. (11). This means a significant savings over the usual Monte Carlo approach.

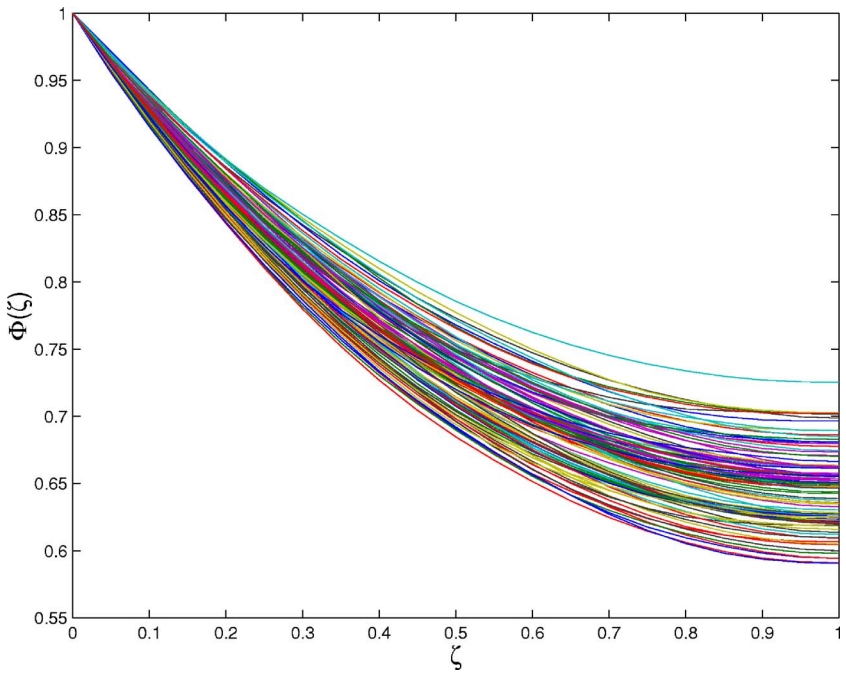

Fig. 7 Typical realizations obtained with the Monte Carlo solution to Eq. (2) for *C* having a white noise component, α=0.1

Because of the difficulties in establishing the relationship between the Wick product and the second moment, the closed form solution cannot be used and must be replaced by a sequence of first-order, but uncoupled, differential equations. The applicability of this method for general heat transfer problems remains to be seen. Theting [17] has used the Wick method to generate realizations for flow through porous media. A correlation of $C(\tau)$ to better represent reality can be introduced by using a smoothed white noise, w_ϕ, as described by Holden, who gives a simple relationship between $\exp \diamond w_\phi$ and $\exp \diamond w$ that enables a straightforward solution to Eq. (1) using Wick calculus.

Acknowledgment

This work was performed under the sponsorship of Sandia National Laboratories. The authors wish to acknowledge the technical direction of Dr. K. J, Dowding, The assistance of Prof. J. Uboe in helping us understand the intricacies of the Wick product approach is gratefully acknowledged.

Nomenclature

A = area
B = Brownian process
$\underline{C}$ = $hA/\rho cV$ or hP/kA
$\overline{C}$ = average value
$E[\,]$ = expected (average) value
f = probability density distribution
h = heat transfer coefficient
h_i = Hermite polynomial
H_i = generalized Hermite polynomial
k = thermal conductivity
N = number of terms
P = perimeter, probability, number of terms
t = time
w = white noise
x = coordinate
X = stochastic process
V = volume, random field vector
α = coefficient of variation
λ = eigenvalue
ω = realization
Φ = non-dimensional temperature for the fin
Ψ = function of two random variables
$\sigma[\,]$ = standard deviation
Θ = non-dimensional temperature for the cooling mass
τ = non-dimensional time
ξ = random value of zero mean and unit standard deviation
Ξ = random field vector
ζ = non-dimensional distance

Appendix: Relevant Equations for Stochastic Processes

Let ξ be a continuous random variable characterized by a probability density distribution $f(\xi)$. The expected value and standard deviation of ξ are given by

$$E[\xi] = \int \xi f(\xi) d\xi \tag{A1}$$

$$\sigma[\xi] = \int [\xi - E(\xi)]^2 f(\xi) d\xi \tag{A2}$$

Let $y = g(x,t,\xi)$ be a one-to-one transformation on ξ with the single inverse $\xi = u(y(x,t))$, which maps ξ into y. The probability density distribution of any function $g(x,t,\xi)$ is then given by

$$f[g(x,t,\xi)] = f(y) = f\{u[y(x,t)]\}|J| \tag{A3}$$

where $|J|$ is the absolute value of the Jacobian of the transformation from ξ to y, $J = du()/dy = d\xi/dy$. Consequently, the expected value and standard deviation of $g(x,t,\xi)$ are given by

$$E[g(x,t)] = \int y f(y) dy = \int g(x,t,\xi) f(\xi) |J| d\xi \tag{A4}$$

$$\sigma[g(x,t)] = \int (y - E[y])^2 f(y) dy$$

$$= \int \{g(x,t,\xi) - E[g(x,t,\xi)]\}^2 f(\xi) |J| d\xi \tag{A5}$$

Although it is not always possible to express $f(g(x,t,\xi))$ as an analytic function of $g(x,t)$, $E(g(x,t))$ and $\sigma(g(x,t))$ can always be found by numerical integration—although it may be difficult.

Non-one-to-one transformations are more complex and the appropriate development is discussed in Ref. [13].

References

[1] Emery, A. F., 2002, "Transient and Steady State Free Convection from a Horizontal Cylinder," *Proc. Inverse Problems in Engineering*, Agra dos Reis, Brazil.
[2] Bouleau, N., and Lepingle, D., 1993, *Numerical Methods for Stochastic Processes*, J. Wiley and Sons, New York.
[3] Ghanem, R., and Spanos, P., 1991, *Stochastic Finite Elements: A Spectral Approach*, Springer-Verlag Publ., New York.
[4] Ghanem, R., 1998, "Probabilistic Characterization of Transport in Heterogeneous Media," Comput. Methods Appl. Mech. Eng., **158**, pp. 199–220.
[5] Le Maitre, O. P., Knio, O. M., Najm, H. N., and Ghanem, R. G., 2001, "A Stochastic Projection Method for Fluid Flow," J. Comput. Phys., **173**, pp. 481–511.
[6] Holden, H., Oksendal, B., Uboe, J., and Zhang, T. S., 1995, *Stochastic Partial Differential Equations—A Modeling, White Noise Functional Approach*, Birkauser Publ., Boston, MA.
[7] Soong, T. T., 1973, *Random Differential Equations in Engineering and Science*, Academic Press, New York.
[8] Gard, T. C., 1988, *Introduction to Stochastic Differential Equations*, Marcel Dekker, New York.
[9] Oksendal, B., 1998, *Stochastic Differential Equations: An Introduction with Applications*, Springer, New York.
[10] Xiu, D., and Karniadakis, G. E., 2002, "The Wiener-Askey Polynomial Chaos for Stochastic Differential Equations," SIAM J. Sci. Comput. (USA), **24**(2), pp. 619–644.
[11] Sakamoto, S., and Ghanem, R., 2002, "Polynomial Chaos Decomposition for the Simulation of Non-Gaussian Non-stationary Stochastic Processes," J. Eng. Mech., **128**(2), pp. 190–201.
[12] Keese, A., and Matthies, H. G., 2002, "Efficient Solvers for Nonlinear Stochastic Problem," *Fifth World Congress on Computational Mechanics*, Vienna, Austria.
[13] Guttman, I., Wilks, S. S., and Hunter, J. S., 1982, *Introductory Engineering Statistics*, J. Wiley and Sons, New York.
[14] Ditlevsen, O., and Tarp-Johansen, N. J., 1999, "Choice of Input Fields in Stochastic Finite Elements," Probab. Eng. Mech., **14**, pp. 63–72.
[15] Keese, A., 2003, "A Review of Recent Developments in the Numerical Solution of Stochastic Partial Differential Equations (Stochastic Finite Elements)," http://opus.tu-bs.de/opus/volltexte/2003/504/pdf/review_sfern.pdf
[16] Benth, F. E., and Theting, T. G., 2000, Some Regularity Results for the Stochastic Pressure Equation of Wick-Type www.maphysto.dk/oldpages/publications/publications2000_static.htmlpp.
[17] Theting, T. G., 2000, "Solving Parabolic Wick-Stochastic Boundary Value Problems Using a Finite Element Method," Stochastics and Stochastics Reports, **75**(1–2), pp. 57–92.

An Experimental Study of the Friction Factor and Mass Transfer Performance of an Offset-Strip Fin Array at Very High Reynolds Numbers

Gregory J. Michna[1]
Department of Mechanical Engineering,
Iowa State University,
2078 H. M. Black Engineering Building,
Ames, IA 50011

Anthony M. Jacobi
Department of Mechanical Science and Engineering,
University of Illinois,
1206 West Green Street,
Urbana, IL 61801

Rodney L. Burton
Department of Aerospace Engineering,
University of Illinois,
104 South Wright Street,
Urbana, IL 61801

Thermal-hydraulic performance data for offset-strip fin arrays are readily available in the range $\mathrm{Re} < 10{,}000$*. However, in emerging applications in automotive and aerospace systems, where fan power is not a constraint and compactness is important, it may be desirable to operate offset-strip fin heat exchangers at very high Reynolds numbers. In this paper, friction factor and mass transfer performance of an offset-strip fin array at Reynolds numbers between 10,000 and 120,000 are characterized. A scale-model, eight-column fin array is used in pressure drop and naphthalene sublimation experiments, and the data are compared to predictions of performance given by available analytical models and extrapolations of the best available correlations. The friction factor data follow the correlation-predicted trend of decreasing monotonically as the Reynolds number is increased to 20,000. However, at higher Reynolds numbers, the friction factor increases as the Reynolds number increases and local maxima are observed in the data. Over the range investigated, the modified Colburn j factor decreases monotonically as the Reynolds number increases. For Reynolds numbers in the range* $10{,}000 < \mathrm{Re} < 120{,}000$*, well beyond that covered by state-of-the-art correlations, both the friction factor and Colburn j factor are roughly twice that predicted by extrapolating the best available correlations. The higher-than-predicted Colburn j factor at very high Reynolds numbers is encouraging for the use of offset-strip fin heat exchangers in emerging applications where compactness is of high importance.* [DOI: 10.1115/1.2739599]

Keywords: convective heat transfer, pressure drop, compact heat exchangers, offset-strip fin, turbulent flow, unsteady flow

1 Introduction

Compact heat exchangers are used in a wide variety of applications and are particularly common in air-cooling and heat-rejection systems for human comfort, food preservation, transportation, waste-heat recovery, and electronics cooling. The offset-strip fin geometry is frequently used in such systems to enhance the air-side performance of compact heat exchangers. Under normal operating conditions, the heat transfer enhancement stems from the restarting of the thermal boundary layers as the air flows through the fin array. Because boundary layer restarting decreases the average boundary layer thickness in the array compared to continuous-fin geometries, the convection coefficient increases. At Reynolds numbers larger than about 1,000 (depending on array geometry), vortex shedding is caused by the fin array; flow unsteadiness associated with vortex shedding also enhances heat transfer. At still higher Reynolds numbers, the flow in offset-strip arrays becomes turbulent. Both vortex shedding and turbulence in the arrays can enhance heat transfer significantly, but the pressure drop typically increases commensurately.

In most current applications, offset-strip fin heat exchangers are operated at low air-side Reynolds numbers to maintain low pressure drops and keep the required fan power low; therefore, vortex shedding and turbulence—and the attendant enhancements of heat transfer—are not present. The thermal-hydraulic performance of offset-strip fin heat exchangers operating above Reynolds numbers of about 10,000 has not been reported in the open literature. However, in emerging applications in automotive and aerospace systems, where fan power is not a constraint and compactness is important, it may be desirable to operate offset-strip fin heat exchangers at very high Reynolds numbers. The offset-strip fin geometry was chosen for this research because it is a well-known interrupted-fin geometry that provides excellent heat transfer performance with a lower pressure drop penalty than other interrupted-fin designs, such as multilouver fins. In addition, for some of the advanced aerospace applications, the heat exchanger is intended for use in the liquefaction of air, and the offset-strip fin geometry is superior to multilouver fins in terms of condensate management. The research reported here is focused on the measurement of the friction factor and mass transfer coefficient of an offset-strip array at very high Reynolds numbers, $10{,}000 < \mathrm{Re} < 120{,}000$.

The thermal-hydraulic performance of offset-strip fin heat exchangers has been studied extensively for low Reynolds number applications. Because a thorough review of the literature has been provided by Manglik and Bergles [1], only a brief discussion of the literature will be included here, with attention focused on the most germane articles.

A number of studies have investigated the structure of the flow through offset-strip arrays. Joshi and Webb [2] investigated the flow structure in offset-strip fin heat exchangers and observed four different flow regimes. At the lowest Reynolds numbers, the wake

[1]Corresponding author. e-mail: michna@iastate.edu

Contributed by the Heat Transfer Division of ASME for publication in the JOURNAL OF HEAT TRANSFER. Manuscript received June 27, 2006; final manuscript received January 22, 2007. Review conducted by Gautam Biswas.

from the upstream fin was smooth and laminar. At higher Reynolds numbers, oscillations occurred where the wake impinged on the downstream fin. The third regime was characterized by unsteadiness in the entire region between fins. At the highest Reynolds numbers, vortices were shed in the array. Mochizuki and Yagi [3] performed flow visualization experiments in offset-strip fin arrays for $Re < 12{,}000$. Vortices were first observed in the downstream section of the array, and as Reynolds numbers increased, the onset of vortex shedding moved upstream. They classified the flow into three different regimes: steady laminar, oscillating (vortex-shedding), and turbulent.

DeJong and Jacobi [4] performed an experimental study of the flow and heat transfer in offset-strip fin arrays. They performed flow visualization experiments in the range $360 < Re < 1060$ and mass transfer experiments in the range $300 < Re < 6000$ and presented local, row-by-row, and surface average behavior. They established a direct link between vortex shedding and heat transfer in the arrays. Using the flow visualization and row-by-row mass transfer data, they concluded that vortex shedding began in the downstream rows and occurred farther upstream as Reynolds number was increased. The mass transfer results were compared to the theoretical interrupted-plate solution. The mass transfer was lower than expected in the steady regime due to thermal wake effects. In the vortex-shedding regime, however, mass transfer was significantly higher than expected from the theoretical interrupted-plate solution.

A large number of experimental and numerical investigations have been reported for the friction factor and heat transfer performance of offset-strip fin arrays at air-side Reynolds numbers less than 10,000. Mochizuki and Yagi [5] performed experiments to measure the heat transfer and friction factor of seven different offset-strip fin heat exchangers in the range $1000 < Re < 8000$. They developed correlations relating Colburn j factor and friction factor to Reynolds number for these exchangers. They found that both j and f increased as the fin length decreased, owing to the more frequent boundary layer restarting that occurs with smaller lengths. Mochizuki et al. [6] investigated the performance of offset-strip arrays in the range $800 < Re < 10{,}000$. Because of markedly different heat transfer and friction factor behavior at the low and high Reynolds numbers of their experiments, two different sets of correlations were developed: the ranges of the correlations were $Re < 2000$ and $Re > 2000$.

Suzuki et al. [7] performed a combined numerical and experimental investigation of offset-strip fin heat exchangers operating at low Reynolds numbers. They paid special attention to the effect of fin thickness on performance in the range $Re < 1000$. For the Reynolds numbers under investigation, it was determined that increasing the fin thickness did not significantly increase the average Nusselt number. However, the average Nusselt number of the array increased as the fin length decreased for all of the Reynolds numbers investigated. Two-dimensional studies of inline fin arrays by Suzuki et al. [8] and Xi et al. [9] identified two mechanisms of heat transfer enhancement caused by vortex shedding. The first mechanism was the acceleration of the mixing of the thermal wake of upstream fins. The second was the transport of cool fluid toward the fin surface and of warm fluid away from the fin surface caused by the impingement of the vortices on the downstream fin.

Manglik and Bergles [1] performed a thorough review of the extant literature in 1995. They used the available data to develop correlations for the Colburn j factor and the friction factor that encompassed all three of the flow regimes that had been observed. They classified these regimes as laminar, transition (or vortex-shedding or oscillating), and turbulent flow. These correlations were accurate to within 20% for all three of the regimes and may be the best currently available general correlations for this type of array in the range of $200 < Re < 10{,}000$.

Muzychka and Yovanovich [10] developed analytical models for the Colburn j factor and friction factor for flow in offset-strip fin arrays. They claimed that the empirically based correlations of Manglik and Bergles [1] were unsuitable for use outside of the range $200 < Re < 10{,}000$ and that considerable uncertainty is expected if a new design does not fall into the range of parameters from which the correlations were developed. In the work of Muzychka and Yovanovich [10], models were developed for the flow in the laminar and turbulent regimes. The laminar friction factor model was obtained by superposition of the Blasius solution for a flat plate and the fully developed friction factor for a rectangular duct. The turbulent model was obtained by performing a force balance which assumes turbulent boundary layers. The laminar j factor model was obtained by combining the fully developed duct flow limit with the thermally developing flow asymptote. The turbulent model was obtained using the Reynolds analogy and the earlier determined turbulent skin friction relation. The laminar and turbulent models were then combined to form models ostensibly valid for all Reynolds numbers using the method of Churchill and Usagi [11], which required the use of one empirical parameter. The authors stated that the correlations of Manglik and Bergles [1] underpredicted both f and j for $Re < 200$ and $Re > 10{,}000$, although no experimental data were presented to verify this claim.

In most current applications, offset-strip fin heat exchangers are operated in the steady, laminar regime in order to manage fan power. By operating offset-strip fin heat exchangers in a vortex-shedding, turbulent regime, much higher convection coefficients are expected, but there have been no reported experimental studies of the performance of offset-strip fins operating in the range $Re > 10{,}000$. In the research reported in this paper, experiments were conducted to measure the mass transfer and pressure drop characteristics of an offset-strip fin array at much higher Reynolds numbers than have been previously investigated. These experiments were performed in the range $10{,}000 < Re < 120{,}000$, which is up to an order of magnitude larger in Reynolds number than that reported in prior work. The thermal-hydraulic performance of offset-strip fins at high Reynolds numbers, and especially the heat transfer enhancements expected at such flow rates, might make them attractive for new applications, where fan power is not a constraint and compactness is important.

While the experiments detailed in this paper involve only a single geometry of offset-strip fin, the array was chosen such that it has a canonical geometry. The fin pitch of the array studied is equal to the fin length. It can be reasonably expected that other geometries would exhibit similar behavior in this very high-Reynolds number range of operation, although the specific effects of fin thickness, fin length, etc., cannot be determined from these data.

2 Experimental Method

2.1 Experimental Apparatus. The pressure drop and mass transfer experiments were performed in an open loop wind tunnel. This tunnel was connected to a plenum/compressor system capable of continuously delivering dry air at 1 kg/s and 300 K, at pressures up to 6.8 atm. The air from this system entered the laboratory through a control valve, which was used to regulate the flow rate, and routed to the tunnel though a 76-mm-diameter pipe. Upon entering the wind tunnel, the flow passed through a radial diffuser and into a large settling chamber slightly above the laboratory pressure. The flow was conditioned by passing through a number of wire screens and a hexagonal honeycomb section and finally through an 11:1 flow-area contraction before entering the test section. Frontal velocities ranging from 2 m/s to 50 m/s could be achieved in the test section. A schematic of the wind tunnel is shown in Fig. 1.

The test section had a cross section of 152 mm × 152 mm, and was made from clear acrylic. The fins in the array had a height of 152 mm, a length of 25.4 mm, and a width of 3.18 mm, and the fin pitch was equal to the length of the fin as shown in Fig. 2. The hydraulic diameter of the array was calculated to be 35.0 mm. The

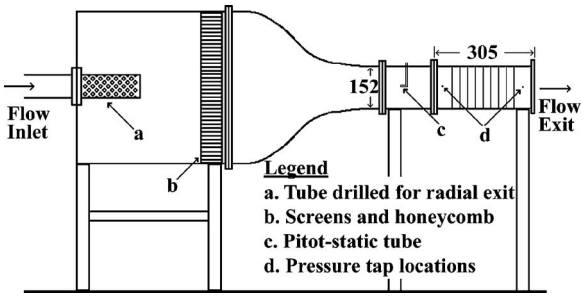

Fig. 1 Schematic of the wind tunnel used in the pressure drop and mass transfer experiments

top plate of the acrylic test section was partitioned to allow for fast installation and removal of these fins. Four static pressure taps, placed at the center of each side of the test section, were located just upstream and downstream of the test section. Each set of four taps was connected with tubing, and the tubing was connected to an inclined manometer to give an average reading of the pressure drop. A Pitot-static tube was inserted into the flow upstream of the test section. It was connected to a second inclined manometer and was used to measure the dynamic pressure of the air flow. A thermocouple was inserted into the large settling chamber to measure the temperature of the flow.

Solid aluminum fins were inserted into the test section for the pressure drop experiments, while different fins, made from low-carbon steel, were used in the mass transfer experiments. A cavity 0.8 mm deep was machined into each side of the fins into which naphthalene was cast. Geometric details of the fins are provided in Fig. 3.

2.2 Pressure Drop Experimental Procedure. Aluminum fins with no cavities for naphthalene were used in the pressure drop experiments, ensuring the geometry of the array did not change due to sublimation during the measurements. The air flow rate through the test section was set using the control valve, and the dynamic pressure, the temperature, the pressure drop across the array, and the room pressure were recorded for flows in the range $5000 < \mathrm{Re} < 120{,}000$.

2.3 Mass Transfer Experimental Procedure. The naphthalene sublimation method has been extensively used to determine mass transfer rates and infer heat transfer performance (see Goldstein and Cho [12] for a thorough review). The analogy between mass and heat transfer is direct and simple for laminar flows; the analogy is also direct for turbulent flows when the turbulent Lewis number is unity. Eckert [13] states in his analysis of the heat and mass transfer analogy that "all available experimental evidence

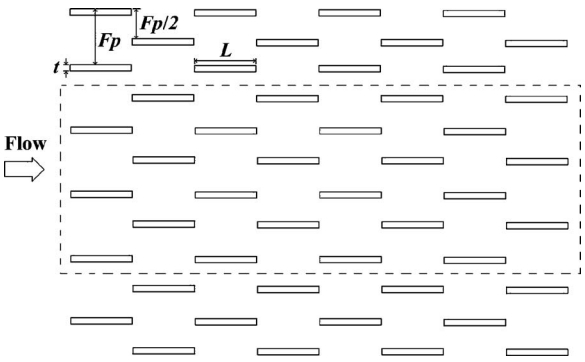

Fig. 2 Schematic of the experimental offset-strip fin array: L =25.4 mm, F_p=25.4 mm, t=3.18 mm, and w (into the page) =152 mm. The fins within the dotted box were used for the naphthalene sublimation mass transfer measurements.

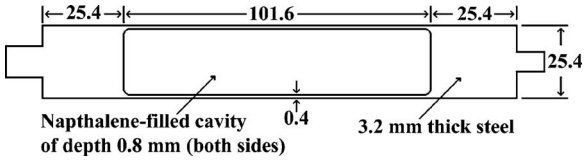

Fig. 3 Geometry of the fins used in the mass transfer experiments. All dimensions are in mm

points to the fact that $\mathrm{Sc}_t = \mathrm{Pr}_t$." Simpson and Field [14] have shown the turbulent Lewis number is unity for turbulent boundary layers over a flat plate. In addition, the heat and mass transfer analogy has been successfully applied in various turbulent flows. For example, Lewis [15] verified the heat and mass transfer analogy for turbulent flow through an annulus, and Goldstein and Cho [12] showed the analogy was valid for turbulent flows over square and circular cylinders. The application of the analogy to the current flow is therefore justified.

In preparation for the mass transfer experiments, the specimens were made by casting 99.9% pure naphthalene into the cavities of the fins shown in Fig. 3. The naphthalene was melted in a beaker, and the molten liquid was poured into the cavity until it was slightly overfull, ensuring that the naphthalene surface was at least as high as the fin surface after the shrinkage associated with solidification and cooling. After the naphthalene returned to lab temperature, the excess was removed with a razorblade using the cavity edges as a guide. The naphthalene surface was polished with fine-grit sandpaper for smoothness, if necessary, and visually inspected. The fins were then stored in a sealed, naphthalene-saturated box until used in the experiment.

Since a well-mixed flow was expected in the array, all 48 of the fins in the test section contained naphthalene-filled cavities on both sides, ensuring the free-stream naphthalene concentration was unaffected by the presence of nonparticipating fins. However, only the middle three rows, as indicated by the dotted box in Fig. 2, were used to obtain data for the mass transfer measurements. This approach avoided using the fins nearest the test section walls for measurements, in order to mitigate edge effects. The 24 fins that were not to be used for measurements were installed in the test section and the 24 fins that were to be used for mass transfer measurements were individually weighed on a precision balance. These fins were placed into the test section as quickly as possible through the opening of the top plate. The acrylic pieces covering the opening were replaced, room pressure was measured, and the wind tunnel was started.

The flow rate was set using the control valve, and in order to maintain a constant Reynolds number, the dynamic pressure, as measured by the Pitot-static tube, was held constant during the experiment. The temperature of the flow was recorded once per minute throughout the experiment. An average of this temperature was used to determine thermophysical properties of the air and the naphthalene.

The duration of the exposure time of the naphthalene fins was decided by estimating the mass transfer rate and calculating a sufficient exposure period to ensure that the amount of naphthalene sublimed would be large enough to result in a small measurement error in the change of mass of the fins. A Mettler AE 200 mass balance was used to measure the mass of the fins to ±0.05 mg, and the change of mass was chosen to be at least 100 mg. Therefore, the uncertainty in change of mass of the fins was less than 0.1%. The exposure period, however, had to be short enough that the geometry of the fins did not significantly change during the test. With the chosen exposure times, the thickness of the nominally 3.18-mm-thick fins changed by less than 0.1 mm during the experiments. Exposure times ranged from 8 min to 60 min. The range of Reynolds numbers in the mass transfer tests was approximately $10{,}000 < \mathrm{Re} < 120{,}000$, similar to the range in the pressure drop experiments.

3 Data Reduction

3.1 Pressure Drop Experiments. The properties of air were determined using the temperature recorded in the settling chamber of the wind tunnel and the average pressure of the air in the array. The frontal velocity of the air was determined from the dynamic pressure measured by the Pitot-static tube, and the average flow velocity in the array was calculated from the geometry of the test section. The Mach number for the highest flow velocity was calculated to be less than Ma=0.15. Therefore, compressibility effects were determined to be unimportant for this flow. The hydraulic diameter, D_h, was calculated using Eq. (1), where A_c is the minimum flow area through the array; A_t is the total heat transfer area; L_{array} is the length of the array; L is the fin length; and w is the fin height, and the Reynolds number reported here is based on hydraulic diameter, as is normally the case for offset-strip fin arrays:

$$D_h = \frac{4A_c}{(A_t/L_{\text{array}})} = \frac{2wL(F_p - t)}{w(L+t) + L(F_p - t)} \tag{1}$$

The Fanning friction factor, f, was calculated from the pressure drop measured across the array, ΔP_{array}, using Eq. (3), per Kays and London [16]. This equation accounts for pressure losses associated with the sudden contraction at the entrance to the heat exchanger, the sudden expansion at the exit, and the acceleration of the fluid due to the change in density. In this equation, ρ_1 represents the density of the air at the entrance to the fin array; ρ_2 represents the density at the exit of the fin array; ρ_m is the average density of air in the array; K_c is the pressure loss coefficient for a sudden contraction; K_e is the pressure loss coefficient for a sudden expansion; and σ is the ratio of the flow area in the test section to the frontal area, and was calculated using Eq. (2):

$$\sigma = \frac{F_p - t}{F_p} \tag{2}$$

$$\Delta P_{\text{array}} = \frac{\rho_1 U_c^2}{2}\left[(K_c + 1 - \sigma^2) + 2\left(\frac{\rho_1}{\rho_2} - 1\right) + f\left(\frac{4L_{\text{array}}}{D_h}\right)\frac{\rho_1}{\rho_m} - (1 - \sigma^2 - K_e)\frac{\rho_1}{\rho_2}\right] \tag{3}$$

The values of K_c and K_e were taken from Fig. 5-3 in Kays and London [16]. The values used were taken from the Re=∞ curves, as recommended by the authors for interrupted fin surfaces. In these experiments, the entrance- and exit-loss terms and the flow acceleration term in Eq. (3) accounted for 5–10% of the total pressure drop across the array.

3.2 Mass Transfer Experiments. An experiment was first performed to measure the sublimation associated with the weighing, installation, and removal of the fins from the test section. All of the experimental procedures for a mass transfer experiment were performed, except the wind tunnel was not started. The change in mass of each of the 24 fins was recorded, and the average mass sublimed during this time, Δm_{exp}, was used in the data reduction procedure as described below.

The freestream naphthalene vapor density, $\rho_{\text{nap},\infty}$, was zero at the entrance to the array; however, as the flow passed through the array the local mixing-cup species concentration increased due to sublimation from upstream fins. The local value of $\rho_{\text{nap},\infty}$ was calculated for each row of fins using the rate of sublimation from the upstream fins as shown in Eq. (4). In this equation, the index i represents the row number, $\overline{(dm/dt)_i}$ is the average mass transfer rate of a fin in the ith fin row, and $\dot{V}_{\text{air}}$ is the volumetric flow rate of air:

$$\rho_{\text{nap},\infty,n} = \sum_{i=1}^{n-1} \frac{6\overline{(dm/dt)_i}}{\dot{V}_{\text{air}}} \tag{4}$$

Following Sparrow and Hajiloo [17], a modified Colburn j factor was used for the mass transfer results. The modified Colburn j factor was calculated using Eqs. (5)–(7), where m_i is the initial mass of the fin; m_f is the final mass of the fin; A_{nap} is the area of the naphthalene on a fin; $\rho_{\text{nap},v}$ is the saturated vapor density of naphthalene; Δt is the duration of the experiment; h_m is the mass transfer coefficient; D_{na} is the diffusivity of naphthalene in air; Sc is the Schmidt number; and Sh is the Sherwood number. The sublimation associated with weighing, installation, and removal of the specimens, Δm_{exp}, is subtracted so the mass transfer coefficient reflects only the mass sublimed during the wind tunnel exposure:

$$h_m = \frac{(m_i - m_f) - \Delta m_{\text{exp}}}{A_{\text{nap}}(\rho_{\text{nap},v} - \rho_{\text{nap},\infty})\Delta t} \tag{5}$$

$$\text{Sh} = \frac{D_h h_m}{D_{\text{na}}} \tag{6}$$

$$j = \frac{\overline{\text{Sh}}}{\text{ReSc}^{0.4}} \tag{7}$$

The use of the heat and mass transfer analogy requires hydrodynamic similarity between the heat and mass transfer flows. A boundary condition for the heat transfer case is that the normal velocity at the wall is zero. In the mass transfer experiments discussed here, since naphthalene sublimes from the surface of the fin at some finite rate, this is not strictly true.

Eckert and Drake [18] used data taken by Hartnett and Eckert [19] to show that the temperature profile has the same shape as for flow with zero wall velocity as long as the inequality shown in Eq. (8) is true. Here, v_w is the wall velocity, which can be calculated using Eq. (9):

$$\left(\frac{v_w}{U_c}\right)\sqrt{\text{Re}_x} < 0.025 \tag{8}$$

$$v_w = \frac{\dot{m}}{\rho_w} \tag{9}$$

In this equation, $\dot{m}$ is the mass flux and ρ_w is the mixture density at the wall. Though this relation was developed from experiments studying the mass transfer from a flat plate in laminar flow, it has been used to justify the assumption of hydrodynamic similarity under turbulent conditions for other geometries. The value of the parameter on the left side of the inequality in Eq. (8) for the mass transfer experiments performed in this study varies from 3.1×10^{-4} for the lowest Reynolds number to 1.0×10^{-3} for the highest Reynolds number. Since this parameter for all experiments performed is much less than the limit of 0.025, the finite wall velocity does not significantly affect the similarity of the hydrodynamic conditions for the heat and mass transfer experiments.

3.3 Uncertainties. The propagation of uncertainties for reduced data followed standard methods [20]. The resulting uncertainty in the value of Re was determined to be less than 5% for Re>10,000. The uncertainty in the value of friction factor was always less than 10% for Re>10,000 and improved significantly as the Reynolds number increased. The uncertainty in the value of the modified Colburn j factor was less than 7% for all measurements.

4 Results and Discussion

4.1 Pressure Drop. The friction factor results are shown in Fig. 4. An extrapolation of the friction factor correlation from Manglik and Bergles [1] has been included in the figure. This correlation was developed from data at much lower Reynolds numbers (200<Re<10,000), and the geometry of the array investigated here is also slightly outside of the range of the corre-

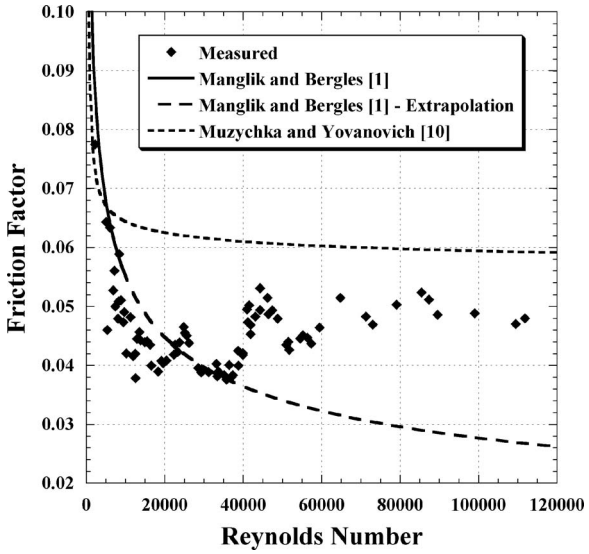

Fig. 4 Fanning friction factor of the offset-strip fin array. The correlation given by Manglik and Bergles [1] and the model developed by Muzychka and Yovanovich [10] are shown for comparison.

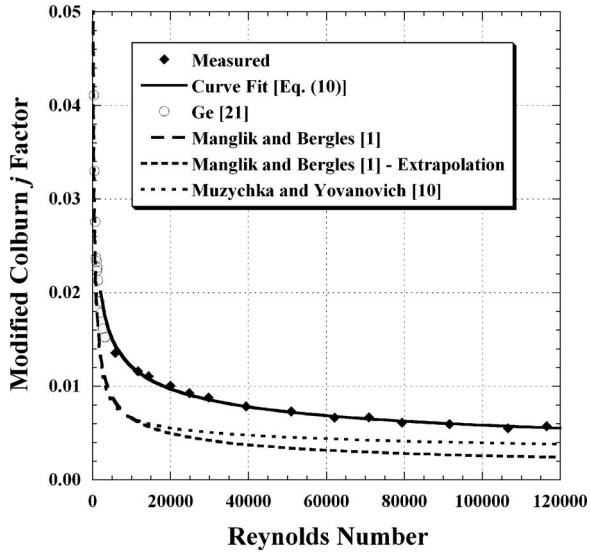

Fig. 5 Modified Colburn *j* factor of the offset-strip fin array. The curve fit has an R^2 value of 0.99. Previous work by Ge [21], the correlation given by Manglik and Bergles [1], and the model developed by Muzychka and Yovanovich [10] are shown for comparison.

lation. Nonetheless, this correlation is the best tool currently available to the offset-strip fin heat exchanger designer and is therefore included for comparison purposes. The prediction of the model developed by Muzychka and Yovanovich [10] is also shown in Fig. 4, since it was reported to be valid for the entire range of Reynolds numbers.

At low Reynolds numbers ($\mathrm{Re} < 20{,}000$), the friction factor behaves as expected from previous work, monotonically decreasing with Reynolds number. However, at higher Reynolds numbers the friction factor increases dramatically as the Reynolds number increases. For $\mathrm{Re} > 50{,}000$, the measured friction factor is approximately twice that predicted by the extrapolation of the correlation developed from low-Reynolds number data. The data are significantly over predicted by the model of Muzychka and Yovanovich [10].

As was noted in Sec. 1, transition to turbulence in the fin array is anticipated to ensue near Reynolds numbers of 1000, and a fully turbulent flow is anticipated for Reynolds numbers greater than about 10,000. While the correlation of Manglik and Bergles and the model of Muzychka and Yovanovich span these Reynolds numbers, neither of these earlier predictions captures the sudden increase in friction factor observed at a Reynolds number of about 40,000. The data suggest the nature of the flow changes significantly at high Reynolds numbers.

Interestingly, the data exhibit regular increases and decreases in friction factor with Reynolds numbers at high Reynolds numbers (such as the local maxima at $\mathrm{Re} = 25{,}000$, $\mathrm{Re} = 46{,}000$, and $\mathrm{Re} = 65{,}000$). The uncertainty in friction factor is very small (about the symbol size) at high Reynolds numbers, and thus these data reflect a real effect. These local maxima occurred at the same Reynolds numbers that a very loud acoustic noise was present in the wind tunnel, most likely from the valve used to regulate the flow rate. This behavior suggests that the vortex shedding in the array may "lock on" to the frequency of the acoustic noise when the vortex shedding frequency is close to the noise frequency. The resulting more vigorous or more intense vortex shedding could cause the increase in friction factor. However, since anemometry data are not presented, this explanation is currently only a hypothesis.

4.2 Mass Transfer. The results of the mass transfer experiments are shown in Fig. 5. The heat transfer correlation from Manglik and Bergles [1] and the model of Muzychka and Yovanovich [10] have again been included for comparison purposes. Results from previous work by Ge [21] using the same array geometry at low Reynolds numbers are also shown in Fig. 5. Since no such fits are available for the offset-strip fin geometry in this Reynolds number rage, a curve fit of the mass transfer data has been included. This fit has limited applicability. It is only valid for this particular offset-strip fin geometry in the range $10{,}000 < \mathrm{Re} < 120{,}000$. The fit is given in Eq. (10):

$$j = 0.2207 \cdot \mathrm{Re}^{-0.3153} \tag{10}$$

It can be seen that the correlation and model agree very well with the low-Reynolds number data. However, above a Reynolds number of about $\mathrm{Re} = 2000$, the data begin to diverge from both the correlation and the model. The modified Colburn *j* factor increases to approximately twice that predicted by the correlation in the range $\mathrm{Re} > 30{,}000$, and the model underpredicts the data by roughly 25%. The model of Muzychka and Yovanovich does not account for vortex shedding, and turbulent vortex shedding might occur at the Reynolds numbers of these experiments.

It is noteworthy that the modified Colburn *j* factor does not increase dramatically at $\mathrm{Re} \sim 40{,}000$, as does the friction factor; nor does the Colburn *j* factor reflect periodicity in the Reynolds number. The lack of correlation between *f* and *j* indicates breakdown of the Reynolds analogy, and such behavior could be indicative of important flow-separation effects on the friction factor.

Row-by-row mass transfer results are shown in Fig. 6. It is clear that throughout the Reynolds number range under study, the mass transfer coefficient on the first fin is lower than those for the rest of the fins. The second fin shows the highest heat transfer coefficient. This behavior is most evident at lower Reynolds numbers, but is present over the entire range. The increase in mass transfer coefficient from the first to second rows was also noted by DeJong and Jacobi [4] in their experiments at $\mathrm{Re} > 1000$. They also noted that the first row of fins was not observed to shed vortices from the leading edge and suggested that flow oscillations caused by vortex shedding from the trailing edge of the first row of fins caused the second row to shed from its leading edge, enhancing the mass transfer coefficient. This does not, however, explain why the second row mass transfer coefficient was larger than for the rows further downstream. One possible explanation is that because of the fin offset, there is no thermal wake to impinge

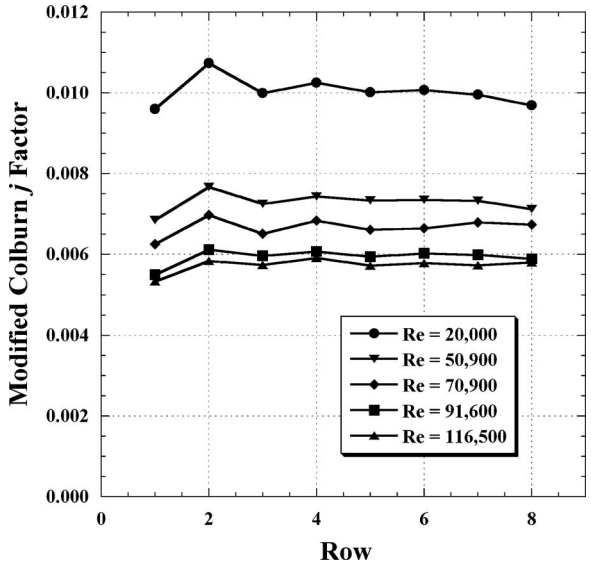

Fig. 6 Row-by-row modified Colburn *j* factor in the offset-strip fin array for a wide range of Reynolds numbers

on the second row, while all of the rows further downstream are directly affected by the thermal wake of at least one upstream fin.

5 Summary and Conclusions

An experimental study of the friction factor and mass transfer characteristics of an offset-strip fin array at very high Reynolds numbers was presented with the objective of developing an understanding of the flow and heat transfer performance at these Reynolds numbers. The study focused on the Reynolds number range $10,000 < \mathrm{Re} < 120,000$, which has not been investigated previously because the large pressure drops present at these flow rates are undesirable in traditional applications that require fan-power management. However, operation of offset-strip fin heat exchangers at these flow rates may be useful in emerging applications where compactness is the most highly valued characteristic of the heat exchanger.

The friction factor data monotonically decrease as Reynolds number increases in the range $\mathrm{Re} < 20,000$, agreeing well with previous work. However, as the Reynolds number increases beyond this point, the friction factor becomes less dependent on Reynolds number and increases suddenly at about $\mathrm{Re} = 40,000$. At higher Reynolds numbers, the friction factor is approximately twice that predicted by the correlation of Manglik and Bergles [1], but less than predicted by the model of Muzychka and Yovanovich [10]. In addition, regular increases and decreases of friction factor with Reynolds number appear at high Reynolds number. The breakdown of the analogy between momentum and mass transfer at high Reynolds numbers suggests that flow separation may be important to the unusual friction factor behavior.

The modified Colburn *j* factor decreases monotonically throughout the Reynolds number range. For $\mathrm{Re} > 30,000$, *j* is approximately twice that predicted by the extrapolation of the heat transfer correlation of Manglik and Bergles and is significantly underpredicted by the model of Muzychka and Yovanovich. Interestingly, *j* does not exhibit the same increases and decreases with Reynolds number manifested by the friction factor. The higher-than-predicted Colburn *j* factor at very high Reynolds numbers is encouraging for the use of offset-strip fin heat exchangers in emerging automotive and aerospace applications where compactness is important and fan power is not a constraint.

Acknowledgment

The authors thank undergraduate assistants Mary Lentz and Tom Coats for casting naphthalene specimens, and they gratefully acknowledge financial support from the Critical Research Initiative of the University of Illinois and the National Science Foundation.

Nomenclature

A_c = minimum flow area (m^2)
A_{nap} = area of naphthalene on fin (m^2)
A_t = total heat transfer area (m^2)
D_h = hydraulic diameter (m)
D_{na} = diffusivity of naphthalene in air ($m^2\ s^{-1}$)
$\overline{(dm/dt)_i}$ = average mass transfer rate of a fin in the *i*th fin row ($kg\ s^{-1}$)
f = Fanning friction factor
h_m = mass transfer coefficient ($m\ s^{-1}$)
j = modified Colburn *j* factor
L = length of fin (m)
L_{array} = length of array (m)
Ma = Mach number
$\dot{m}$ = wall mass flux ($kg\ m^{-2}\ s^{-1}$)
Δm_{exp} = mass sublimed during install/removal (kg)
m_f = final mass of fin (kg)
m_i = initial mass of fin (kg)
ΔP_{array} = pressure drop across the array (Pa)
Re = Reynolds number, based on hydraulic diameter unless noted
Sc = Schmidt number
$\underline{\mathrm{Sh}}$ = Sherwood number
$\overline{\mathrm{Sh}}$ = array averaged Sherwood number
Δt = time of exposure (s)
t = thickness of fin (m)
$\dot{V}_{air}$ = volumetric flow rate of air ($m^3\ s^{-1}$)
v_w = flow velocity normal to the wall ($m\ s^{-1}$)
w = height of fin (m)

Greek Symbols

ρ = density of air ($kg\ m^{-3}$)
ρ_w = mixture density at the wall ($kg\ m^{-3}$)
$\rho_{nap,v}$ = density of naphthalene vapor ($kg\ m^{-3}$)
$\rho_{nap,\infty}$ = density of naphthalene in the core flow ($kg\ m^{-3}$)

References

[1] Manglik, R. M., and Bergles, A. E., 1995, "Heat Transfer and Pressure Drop Correlations for the Rectangular Offset Strip Fin Compact Heat Exchanger," Exp. Therm. Fluid Sci., **10**(2), pp. 171–180.
[2] Joshi, H. M., and Webb, R. L., 1987, "Heat Transfer and Friction in the Offset Strip-Fin Heat Exchanger," Int. J. Heat Mass Transfer, **30**(1), pp. 69–84.
[3] Mochizuki, S., and Yagi, Y., 1982, "Characteristics of Vortex Shedding in Plate Arrays," *Flow Visualization II*, W. Merzkirch, ed., Hemisphere, Washington, D.C., pp. 99–103.
[4] DeJong, N. C., and Jacobi, A. M., 1997, "An Experimental Study of Flow and Heat Transfer in Parallel-Plate Arrays: Local, Row-by-Row, and Surface Average Behavior," Int. J. Heat Mass Transfer, **40**(6), pp. 1365–1378.
[5] Mochizuki, S., and Yagi, Y., 1977, "Heat Transfer and Friction Characteristics of Strip Fins," Heat Transfer-Jpn. Res., **6**(3), pp. 36–59.
[6] Mochizuki, S., Yagi, Y., and Yang, W.-J., 1987, "Transport Phenomena in Stacks of Interrupted Paralle-Plate Surfaces," Exp. Heat Transfer, **1**(2), pp. 127–140.
[7] Suzuki, K., Hirai, E., Miyake, T., and Sato, T., 1985, "Numerical and Experimental Studies on a Two-Dimensional Model of an Offset-Strip-Fin Type Compact Heat Exchanger Used at Low Reynolds Number," Int. J. Heat Mass Transfer, **28**(4), pp. 823–836.
[8] Suzuki, K., Xi, G. N., Inaoka, K., and Hagiwara, Y., 1994, "Mechanism of Heat Transfer Enhancement Due to Self-Sustained Oscillation for an In-Line Fin Array," Int. J. Heat Mass Transfer, **37**(1), pp. 83–96.
[9] Xi, G. N., Hagiwara, Y., and Suzuki, K., 1995, "Flow Instability and Augmented Heat Transfer of Fin Arrays," J. Enhanced Heat Transfer, **2**(1–2), pp. 23–32.

[10] Muzychka, Y. S., and Yovanovich, M. M., 1999, "Modeling the *f* and *j* Characteristics of the Offset Strip Fin Array," American Society of Mechanical Engineers, Heat Transfer Division, (Publication) HTD, No. 364-1, pp. 91–100.
[11] Churchill, S. W., and Usagi, R., 1972, "A General Expression for the Correlation of Rates of Transfer and Other Phenomena," AIChE J., **18**(6), pp. 1121–1128.
[12] Goldstein, R. J., and Cho, H. H., 1995, "A Review of Mass Transfer Measurements Using Naphthalene Sublimation," Exp. Therm. Fluid Sci., **10**(4), pp. 416–434.
[13] Eckert, E. R. G., 1976, "Analogies to Heat Transfer Processes," *Measurements in Heat Transfer*, E. R. G. Eckert and R. J. Goldstein, eds., McGraw–Hill, Washington, D.C., pp. 397–423.
[14] Simpson, R. L., and Field, R. L., 1972, "A Note on the Turbulent Schmidt and Lewis Numbers in a Boundary Layer," Int. J. Heat Mass Transfer, **15**(1), pp. 177–180.
[15] Lewis, J. S., 1971, "A Heat-Mass Transfer Analogy Applied to Fully Developed Turbulent Flow in an Annulus," J. Mech. Eng. Sci., **13**(4), pp. 286–292.
[16] Kays, W. M., and London, A. L., 1984, *Compact Heat Exchangers*, 3rd ed., McGraw–Hill, New York.
[17] Sparrow, E. M., and Hajiloo, A., 1980, "Measurements of Heat Transfer and Pressure Drop for an Array of Staggered Plates Aligned Parrallel to an Air Flow," J. Heat Transfer, **102**(3), pp. 426–432.
[18] Eckert, E. R. G., and Drake, R. M., 1972, *Analysis of Heat and Mass Transfer*, McGraw–Hill, New York.
[19] Hartnett, J. P., and Eckert, E. R. G., 1957, "Mass-Transfer Cooling in a Laminar Boundary Layer With Constant Fluid Properties," Trans. ASME, **79**(2), pp. 247–254.
[20] Kline, S. J., and McClintock, F. A., 1953, "Describing Uncertainties in Single-Sample Experiments," Mech. Eng. (Am. Soc. Mech. Eng.), **75**(1), pp. 3–8.
[21] Ge, H., 2002, "Air-Side Heat Transfer Enhancement for Offset-Strip Fin Arrays Using Delta Wing Vortex Generators," Ph.D. thesis, University of Illinois, Urbana, Ill.

Expansion Ratio Effects on Three-Dimensional Separated Flow and Heat Transfer Around Backward-Facing Steps

Aya Kitoh
Graduate Student
Department of Aerospace Engineering,
Tohoku University,
Sendai, Japan

Kazuaki Sugawara[1]
Former Graduate Student
Tohoku University,
Sendai, Japan

Hiroyuki Yoshikawa
Associate Professor
Department of Mechanical System Engineering,
Kumamoto University,
2-39-1 Kurokami,
Kumamoto 860-8555, Japan
e-mail: yoshi@kumamoto-u.ac.jp

Terukazu Ota
Professor
Department of Mechanical Systems and Design,
Tohoku University,
Sendai, Japan

Direct numerical simulation methodology clarified the three-dimensional separated flow and heat transfer around three backward-facing steps in a rectangular channel, especially effects of channel expansion ratio ER upon them. ER treated in the present study was 1.5, 2.0, and 3.0 under a step aspect ratio of 36.0. The Reynolds number Re based on the mean velocity at inlet and the step height was varied from 300 to 1000. The present numerical results for ER=2.0 were found to be in very good agreement with the previous experimental and numerical ones in the present Reynolds number range for both the steady and unsteady flow states. The time averaged reattachment length on the center line increases with a decrease of ER. The flow became unsteady at RE=700, 600, and 500 for ER=1.5, 2.0, and 3.0, respectively, accompanying the remarkable increase of the three-dimensionality of the flow and temperature fields in spite of a very large step aspect ratio of 36.0. The Nusselt number increases in the reattachment flow region, in the neighborhood of the sidewalls, and also in the far downstream depending on both Re and ER. [DOI: 10.1115/1.2739619]

Keywords: separated and reattached flow, forced convection, heat transfer, backward-facing step, DNS

Introduction

Prediction of the flow and heat transfer in the separated, reattached, and redeveloping regions around a backward-facing step is very important in relation to many types of fluid machinery and heat exchangers, and there have been numerous experimental and numerical works. Published papers have been reviewed thoroughly by several authors [1–5]. Since then, new results have been reported continuously [6–21]. However, there have been only a few works of the three-dimensional unsteady flow characteristics and their correlations with the heat transfer behaviors. Recent numerical simulations of the heat transfer in the three-dimensional separated and reattached flow regions [11,14,21] are concerned mainly with the cases at relatively low Reynolds number, in which the flow is steady.

On the other hand, investigations of the channel expansion ratio effects upon the flow and heat transfer characteristics have been noticed to be important in relation to the basic thermal and fluid mechanical aspects and engineering applications, and there have been several works [22–25] on fully developed turbulent flow. Durst and Tropea [22] and Ötügen [23] studied the expansion ratio effects upon the reattachment length. Kuehn [24] and Ra and Chang [25] measured the effects of pressure gradient downstream of the step. However, in these works some discrepant results are described. That is, the reattachment length increases with an increase of the expansion ratio in [22,24]. On the other hand, Ötügen [23] reported inverse results; i.e., the reattachment length is found to decrease with an increase of the step height [25]. Further, there have been only a few investigations of the laminar and transitional flow regimes [19].

The present authors have numerically studied the flow around the backward-facing step in order to clarify systematically its dependency on the Reynolds number and the step expansion ratio ER for three expansion ratios of 1.5, 2.0, and 3.0 [26,27]. In the case of ER=1.5, where the adverse pressure gradient downstream of the step is small, the development of flow instability needs an extraordinarily long streamwise distance, and a developing unsteady flow state is finally reached far downstream of the step. Three components of vorticity exhibit approximately an equal strength, resulting in a very wide region of three-dimensional flow structure. On the other hand, in the case of ER=3.0, where the adverse pressure gradient downstream of the step is noticeable, the shear layer transits quickly to the unsteady state just downstream of the separation point. The spanwise vorticity becomes very strong compared to other components, resulting in the flow structure similar to the two-dimensional one. In the case of ER=2.0, two characteristic flow features described above for ER=1.5, and 3.0 appeared simultaneously.

The purpose of the present study is to predict numerically the three-dimensional separated flow and heat transfer around three backward-facing steps in a rectangular channel for both the steady

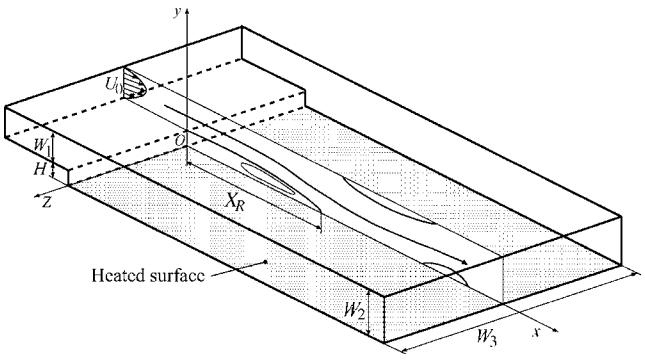

Fig. 1 Flow configuration and coordinates

[1]Presently, Shin Nippon Air Technologies Co., Ltd., Tokyo, Japan.

Contributed by the Heat Transfer Division of ASME for publication in the JOURNAL OF HEAT TRANSFER. Manuscript received March 20, 2006; final manuscript received September 28, 2006. Review conducted by Louis C. Burmeister.

Table 1 Conditions of numerical calculation

ER			1.5		2.0	3.0
AR				36.0		
Re		300	500	700, 1000	300, 500, 600, 700, 1000	300, 500, 700, 1000
Pr				0.7		
Time interval				$0.001H/U_0$		
Region	x/H	−10 to 50	−10 to 80	−10 to 150	−10 to 50	−10 to 50
	y/H		0 to 3.0		0 to 2.0	0 to 1.5
	z/H			−18 to 18		
Grid		291×91×221	421×91×221	701×91×221	291×61×221	291×45×221
Sampling time				$2000H/U_0$		
Sampling size				2×10^6		

and unsteady states. A direct numerical simulation methodology based on the finite difference method was employed in the calculations and the channel expansion ratio effects upon the flow and heat transfer features were minutely investigated. Figure 1 illustrates the flow configuration treated in the present study along with the coordinate system and main physical parameters. The channel height is W_1 in the upstream and W_2 in the downstream. The spanwise width of channel is W_3. The step height H is referred to as the reference length in the present paper. U_0 is the mean velocity at channel inlet. The downstream wall is heated at a constant temperature. It has been clarified in previous experimental studies [28] that the main separation bubble is naturally formed downstream of the step, but under certain flow conditions,

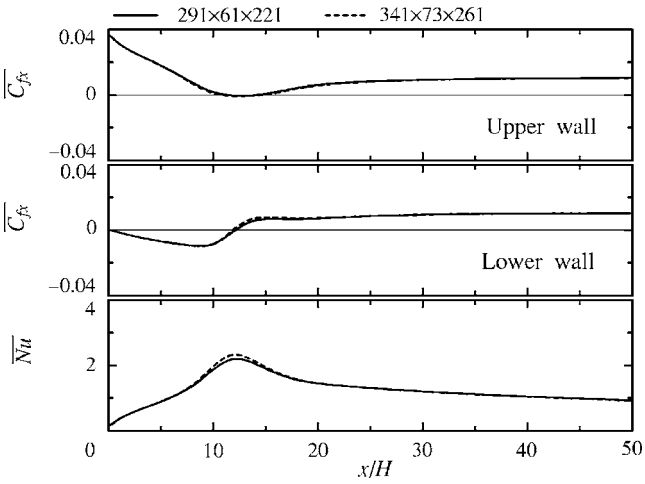

Fig. 2 Grid dependency (Re=300, ER=2.0, AR=36.0, and z/H=0)

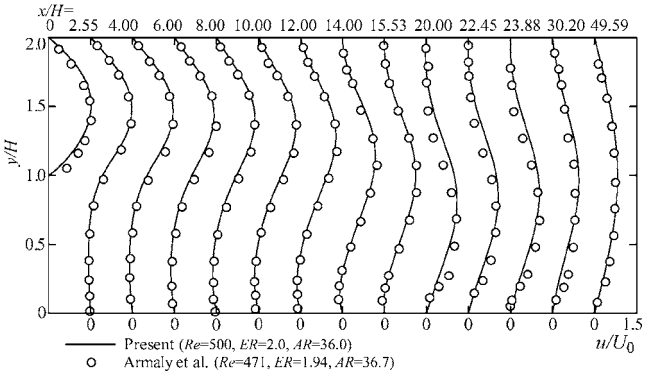

Fig. 3 Comparison of streamwise velocity (z/H=0)

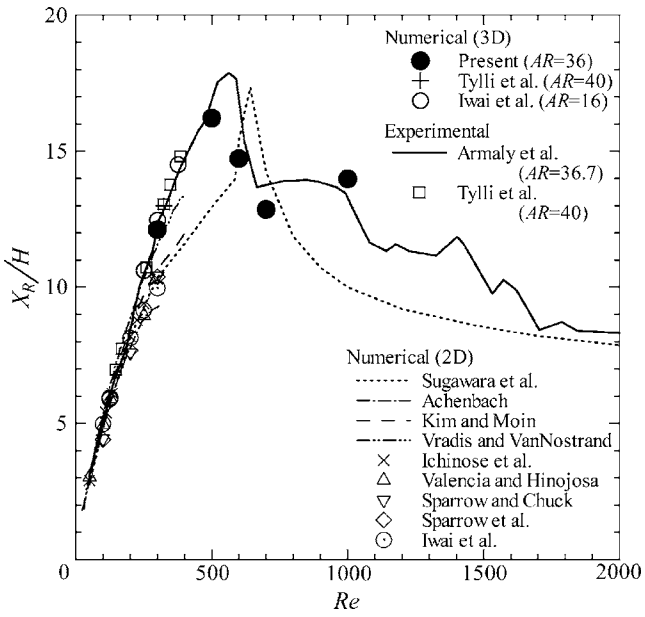

Fig. 4 Comparison of time averaged reattachment length (ER =2.0, and z/H=0)

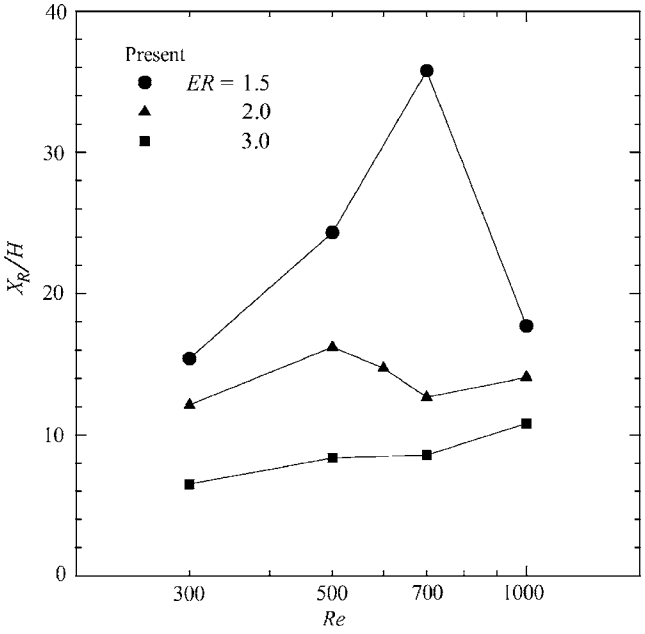

Fig. 5 Effect of ER upon time averaged reattachment length (z/H=0)

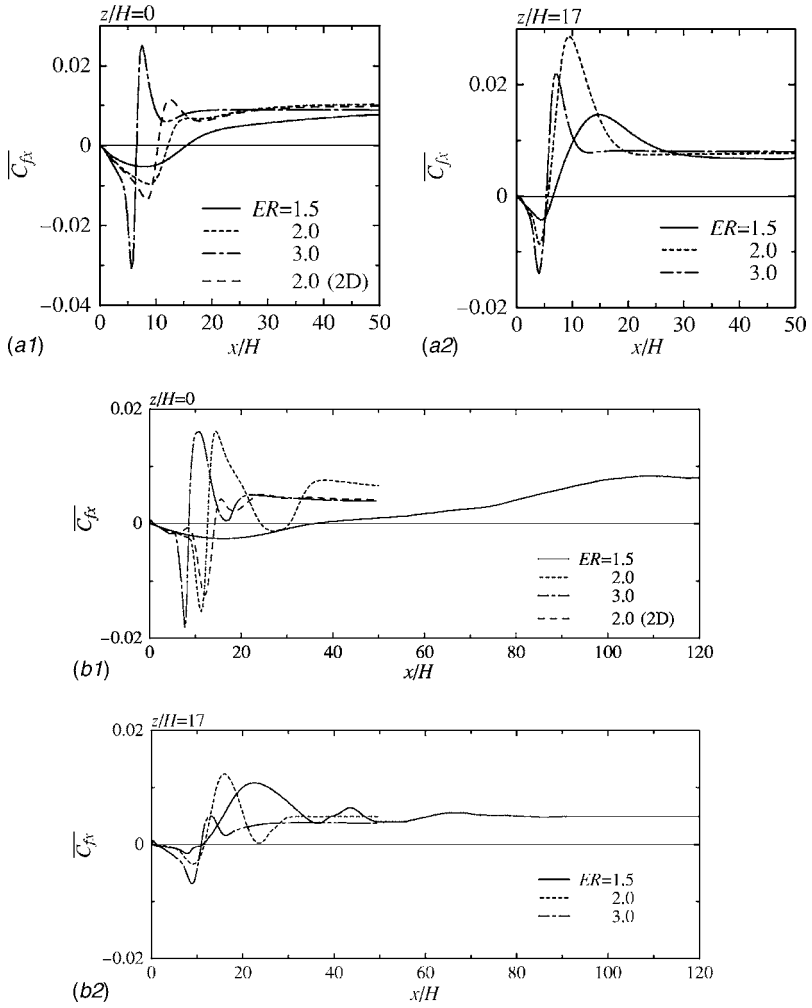

Fig. 6 Time averaged streamwise surface friction coefficient on lower wall: (*a*) Re=300; (*b*) Re=700

the second separation bubble is detected on the upper wall and the third separation bubble appeared downstream of the main bubble on the lower wall.

Fundamental Equations and Numerical Procedure

The fundamental equations analyzed are the continuity, momentum, and energy equations for a three-dimensional unsteady flow of incompressible viscous fluid with constant properties:

$$\nabla \cdot \boldsymbol{u} = 0 \tag{1}$$

$$\boldsymbol{u}_t + (\boldsymbol{u} \cdot \nabla)\boldsymbol{u} = -\nabla p + \frac{1}{\mathrm{Re}}\nabla^2 \boldsymbol{u} \tag{2}$$

$$\theta_t + (\boldsymbol{u} \cdot \nabla)\theta = \frac{1}{\mathrm{Re\,Pr}}\nabla^2 \theta \tag{3}$$

In these equations, physical quantities are nondimensionalized by $\boldsymbol{x}^* = \boldsymbol{x}/H, \boldsymbol{u}^* = \boldsymbol{u}/U_0$, $p^* = p/\rho U_0^2$, and $\theta^* = (\theta - \theta_0)/(\theta_w - \theta_0)$, respectively. The superscript "*" indicates nondimensional quantities, and it is omitted in the above equations. These equations are discretized on the non-uniform orthogonal grid by means of the finite difference method. In the time marching of Eq. (2), the second-order Crank-Nicholson method for the convective and viscous terms, and the first-order Euler backward difference for the pressure terms are employed, respectively. As for the space derivatives, the QUICK method is employed for the convection terms and the second-order central difference for the viscous and pressure terms, respectively. In the QUICK method, the artificial viscosity has been noticed to be large but it was employed in the present scheme for the stable calculations. Resulting finite difference equations were solved using the simplified marker and cell (SMAC) method [29]. The pressure was obtained by solving the Poisson equation for the pressure correction.

The boundary conditions are as follows. As for the velocity, the no-slip condition is assumed on the walls and the convection boundary condition is used at the outlet. At the inlet, the fully developed laminar channel flow calculated with an approximate formula by Chiang and Sheu [10] is presumed. As for the temperature, it is assumed to be uniform at the inlet, the lower wall downstream of the step is heated under the condition of uniform temperature θ_w, and other walls are adiabatic. At the outlet, the second derivative is presumed to be zero in the present scheme. The velocity correction equations are employed for the boundary condition of the Poisson pressure correction equation. Therefore, the boundary condition for the pressure is not necessary on the walls. In the present calculations, the usual symmetric boundary conditions are not used on the channel center plane, since the instantaneous velocity and temperature fields are considered not to be symmetric there in the unsteady state. Accordingly, the entire flow and temperature fields are treated in the calculations.

The numerical calculations were performed for three expansion ratios of ER$=W_2/W_1=1.5$, 2.0, and 3.0 under conditions of the step aspect ratio AR$=W_3/H=36.0$, the Reynolds number Re from

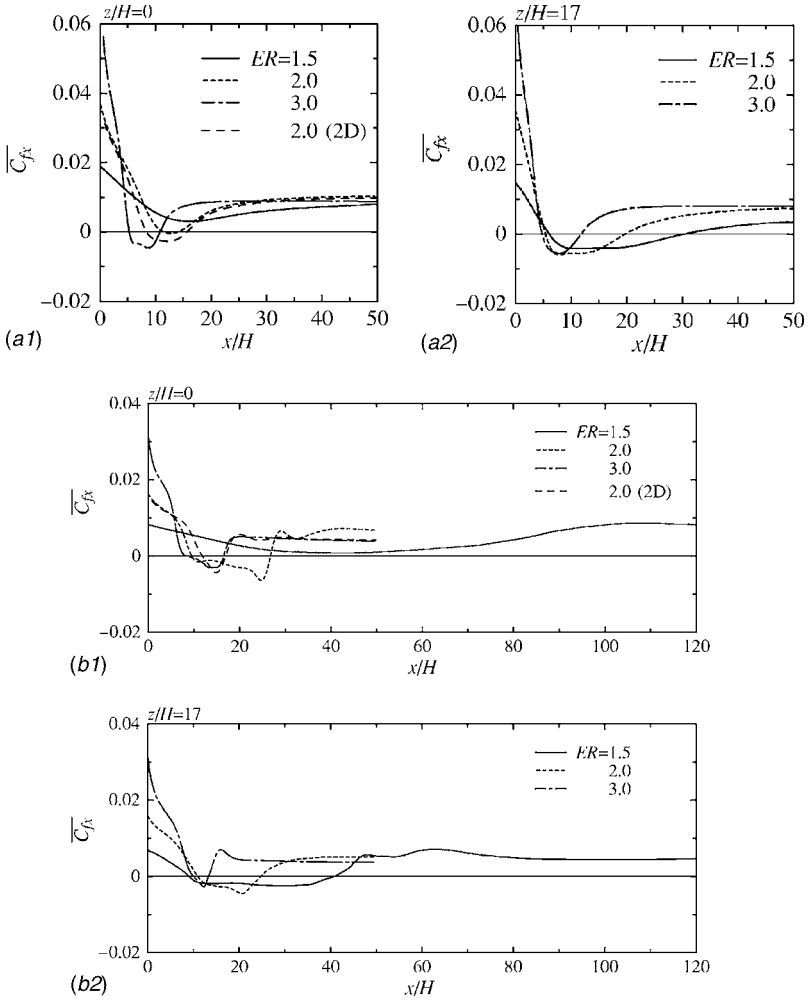

Fig. 7 Time averaged streamwise surface friction coefficient on upper wall: (*a*) Re=300; (*b*) Re=700

300 to 1000, and the Prandtl number Pr=0.7, respectively. The computational region extends from $10H$ upstream of the step to $50H$ downstream. In the case of ER=1.5, the computational region is extended to $80H$ for Re=500 and further to $150H$ for Re =700 and 1000, since the unsteady features are detected far downstream of the step. The calculations were made using a time interval of $0.001H/U_0$. The sampling time and size were $2000H/U_0$ and 2×10^6 for the mean quantities, respectively. The computational grids were generated using the orthogonal coordinates with non-uniform spacing in three directions, and the grids employed in the present calculations are summarized in Table 1, which includes other conditions for clearness.

Numerical Results and Discussion

In order to confirm the certainty of the present numerical results shown in the following, some preliminary calculations were made for a case of ER=2.0 and Re=300 using two grids of $291\times61\times221$ and $341\times73\times261$. The flow configuration treated was a backward-facing step of ER=2.0 and AR=36.0, since many previous experimental and numerical works investigated such a flow. The three components of velocity, two components of surface friction, and the Nusselt number on the channel center plane obtained with two grids described above were found to be in very good agreement with each other in the entire flow field, as shown in Fig. 2. Accordingly, the grid of $291\times61\times221$ was employed as a basic one of the computation. However, in the case of ER=3.0, the grid of $291\times45\times221$ was found to be sufficient. Further, in the case of ER=1.5, the streamwise calculation area was increased, since the unsteady features of the flow and temperature were detected to become remarkable far downstream at high Reynolds number greater than 700. Based on these findings, the streamwise grid points were increased, as shown previously in Table 1. The minimum grid spacings near the walls are 0.01 in three directions. This spacing is considered to be very small compared to the boundary layer thickness. Further, the present numerical results of the streamwise mean velocity profiles at several cross sections on the center plane for ER=2.0 and Re=500 obtained using the grid of $291\times61\times221$ were compared with the previous experimental ones [28] for ER=1.94, AR=36.7, and Re=471. Figure 3 shows their comparison, although the numerical and experimental conditions are slightly different from each other. It is very clear that the present numerical results are in very good agreement with the experimental ones in the whole flow field, indicating the certainty of the present calculation method including the grid employed.

Figure 4 represents the time averaged reattachment length X_R on the center line ($z/H=0$) for ER=2.0, as compared with several previous numerical and experimental ones [11,16,18,28,30–36]. In the present study, the time averaged reattachment point on the channel center line is defined as a point of zero streamwise surface friction. Published numerical and experimental results at low Reynolds number of $Re\leq300$ agree well with each other, although their difference increases at higher Reynolds number. It is clearly shown that our previous two-dimensional calculations [18]

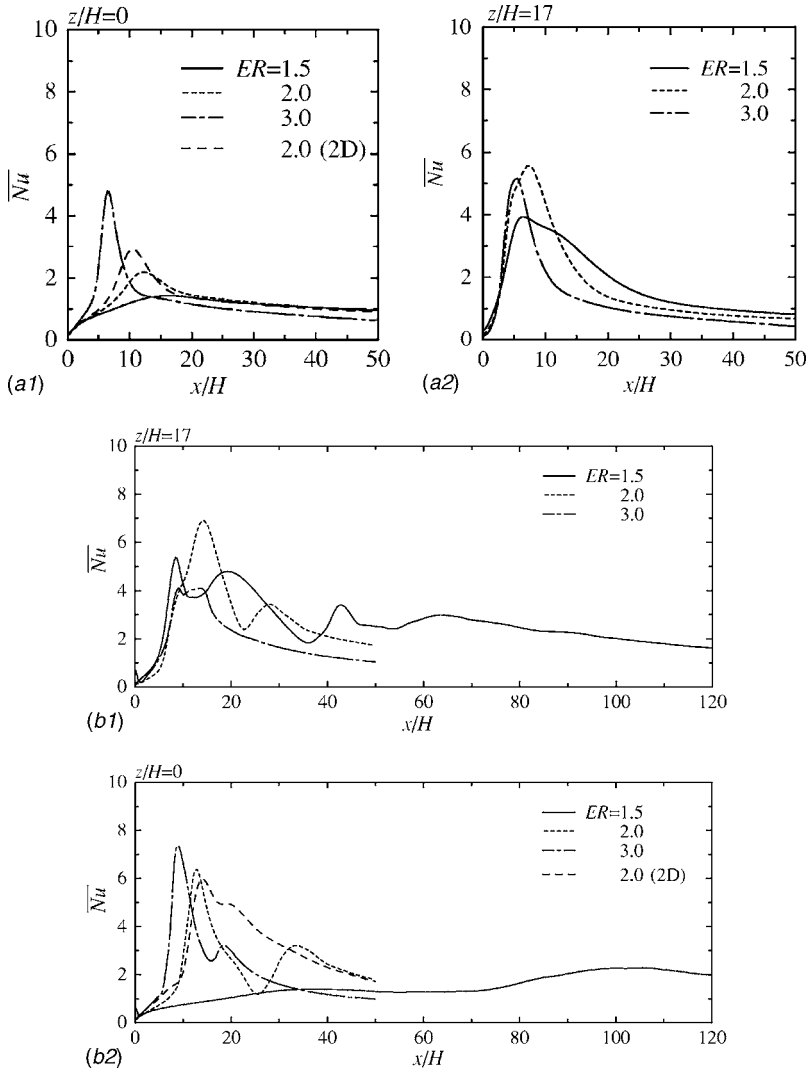

Fig. 8 Time averaged Nusselt number on lower wall: (*a*) Re=300; (*b*) Re=700

estimate reasonably well the experimental ones [28], including the maximum reattachment length and also its discontinuous decrease in the transitional Reynolds number regime of Re>500. The present three-dimensional simulation results are found to be in very good agreement with the experimental ones in a peak area of X_R and also in the transitional flow regime, where X_R decreases steeply with Re. The flow for ER=2.0 is detected to be steady up to Re=500 but becomes unsteady at Re=600. The difference between the two- and three-dimensional calculations increases with an increase of Re, especially in the high Reynolds number region where the flow is unsteady. These comparisons suggest that the two-dimensional calculation simulates reasonably well the steady flow at low Reynolds number; however, it estimates a quantitatively different flow at high Reynolds number in which the flow becomes unsteady.

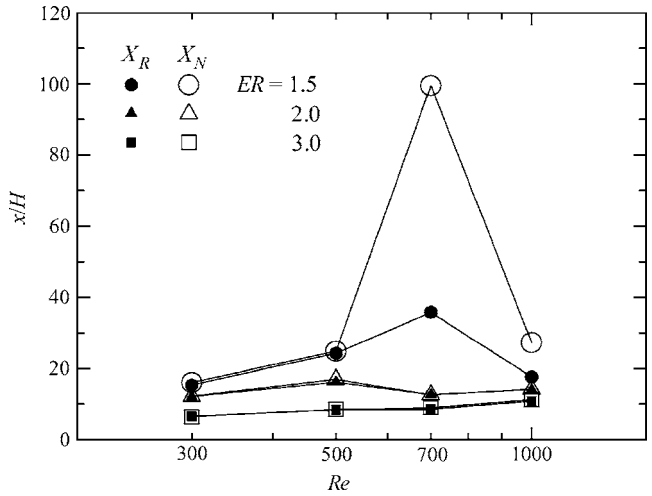

Fig. 9 Time averaged reattachment length and position of maximum Nusselt number (*z*/*H*=0)

Figure 5 illustrates the present numerical results of X_R on the center line for ER=1.5, 2.0, and 3.0. The flow becomes unsteady at Re=700, 600, and 500 for ER=1.5, 2.0, and 3.0, respectively. It is clearly represented that the reattachment length decreases greatly at some Reynolds number whose value depends on ER. That is, the separated shear layer transits to the unsteady one because of its instability and the transversal movement becomes severe, resulting in a sudden decrease of X_R. Such a transitional Reynolds number is easily found to be about 700 and 500 for ER=1.5 and 2.0, respectively. In the case of ER=3.0, there is no sudden variation of X_R in the present results. Further, it is very clear that the nondimensional reattachment length X_R/H increases with decreasing ER at low Reynolds number. In the case of the turbulent flow [22,24], X_R/H was found to increase with an increase of ER. On the other hand, Ötügen [23] reported the inverse

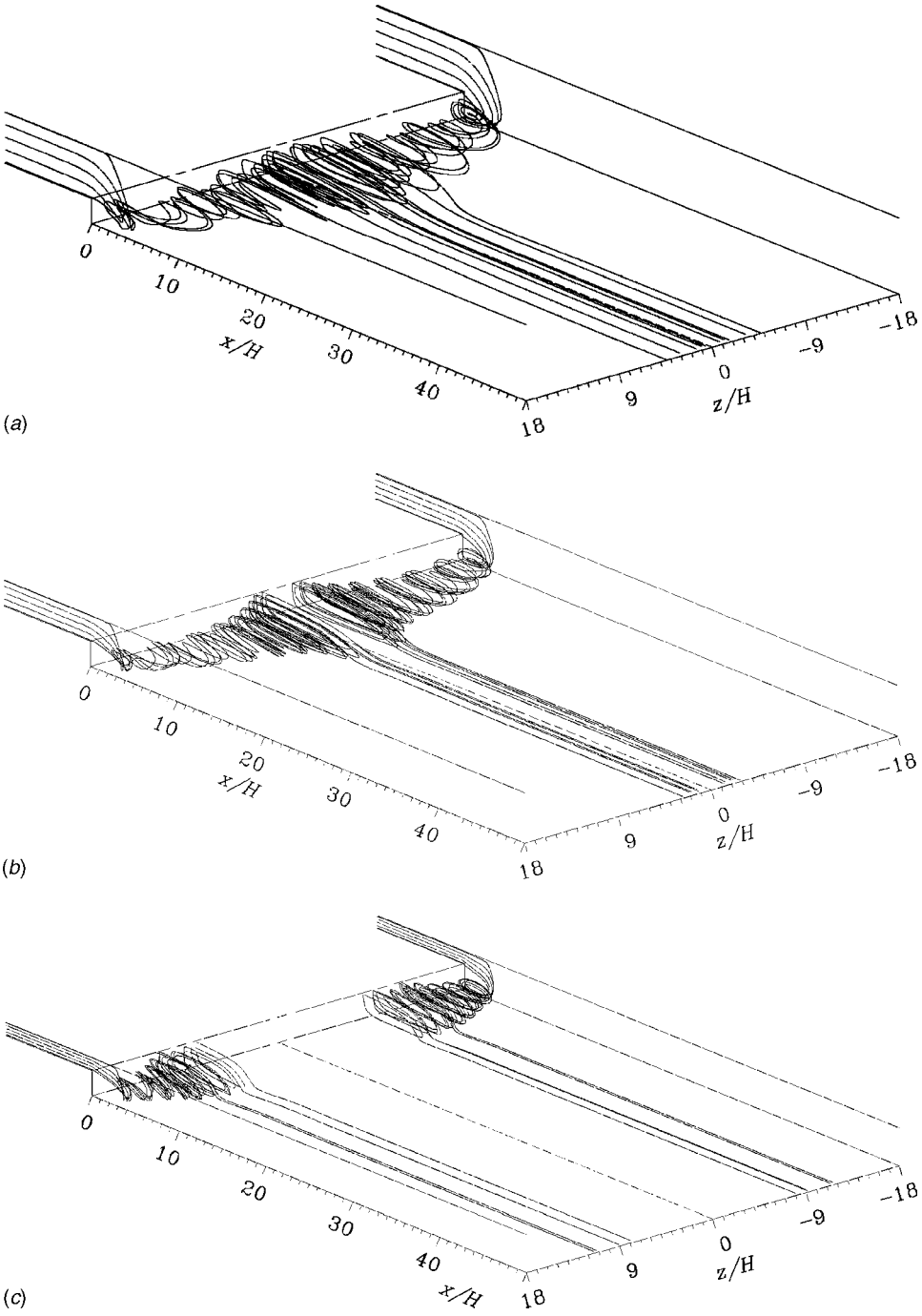

Fig. 10 Streamline (Re=300): (*a*) ER=1.5; (*b*) ER=2.0; (*c*) ER=3.0

results, and in the results by Ra and Chang [25], it is detected that X_R/H decreases with an increase of the step height H at the same pressure gradient. The reason for such a difference is not clear at present and further investigation is considered necessary.

Figures 6 and 7 summarize the time averaged streamwise surface friction on the upper and lower walls, respectively, at Re =300 and 700 for ER=1.5, 2.0, and 3.0. In order to clarify the details of the flow structure near the sidewalls, the results at $z/H=17$ very close to the sidewall are included along with those at $z/H=0$ in the figures. It is clear that the streamwise variation of $\overline{C_{fx}}$ depends greatly upon ER, Re, and also on the spanwise location. Further, their characteristic variations are naturally different on the upper and lower walls.

In the case of Re=300, there exists one negative region on the lower wall at both $z/H=0$ and 17 for all the expansion ratios, presenting one separation bubble and its streamwise length reduces to the sidewalls, as described later in Fig. 12, which shows the limiting streamlines. On the other hand, $\overline{C_{fx}}$ on the upper wall at $z/H=0$ shows a short region of negative value for ER=2.0 and 3.0, but is positive over the whole streamwise distance for ER =1.5. That is, the separation bubble is formed on the upper wall for ER=2.0 and 3.0 but is not formed there for ER=1.5. In the neighborhood of the sidewall of $z/H=17$, the reverse flow exists for ER=1.5, 2.0, and 3.0, and its streamwise length increases with a decrease of ER.

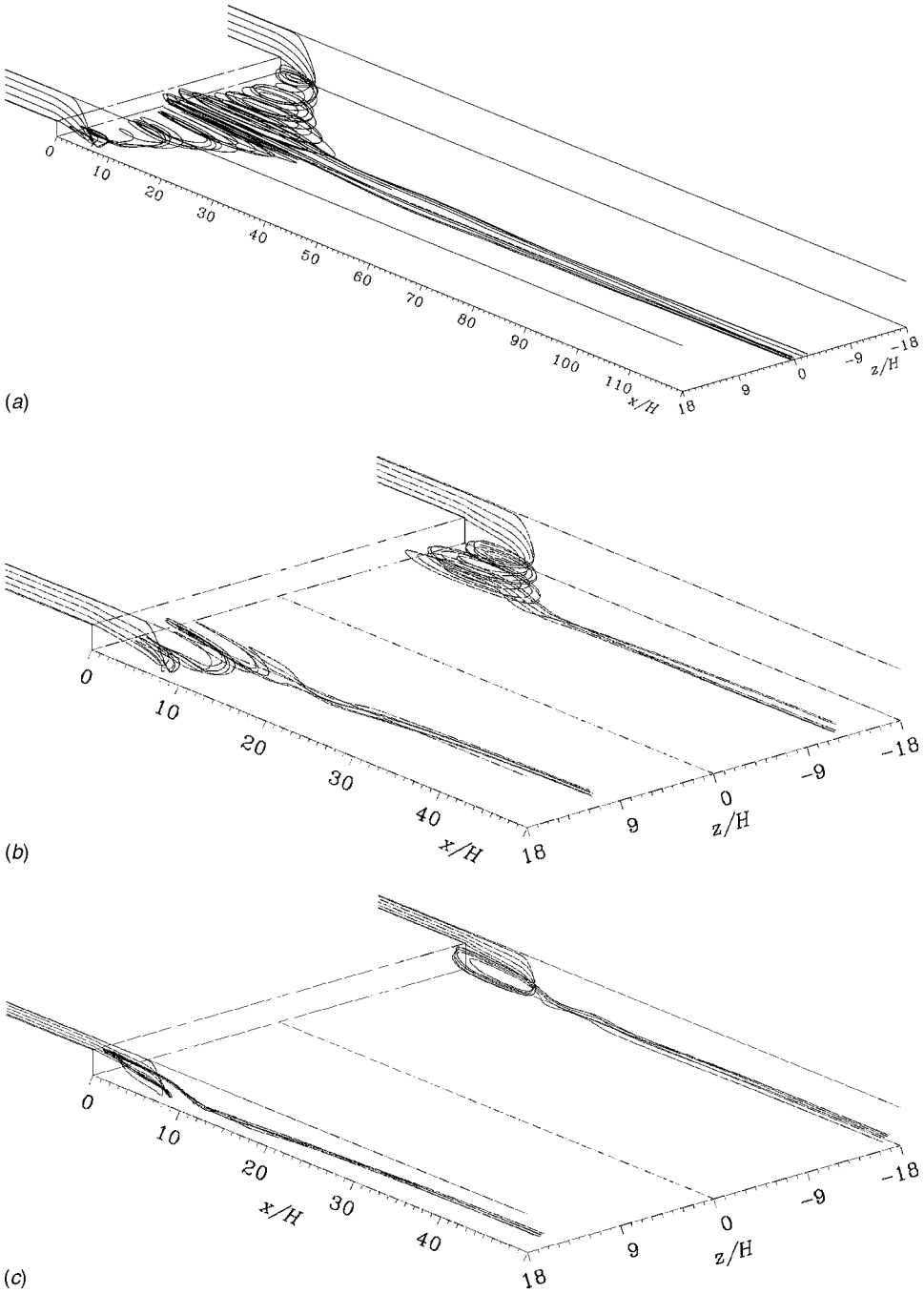

Fig. 11 Time averaged streamline (Re=700): (*a*) ER=1.5; (*b*) ER=2.0; (*c*) ER=3.0

In the case of Re=700, the streamwise variation of $\overline{C_{fx}}$ becomes complex. On the lower wall, the reverse flow region at $z/H=0$ increases with a decrease of ER and the third separation bubble is formed for the case of ER=2.0. The main separation bubble increases greatly for ER=1.5. It is very interesting that $\overline{C_{fx}}$ on the center line for ER=1.5 increases gently to the downstream even in the far downstream region. In the neighborhood of the sidewall of $z/H=17$, the roof eddy brings about a negative region of $\overline{C_{fx}}$ in the upstream part and its length shows no essential variation with ER. On the upper wall, $\overline{C_{fx}}$ at $z/H=0$ becomes negative for ER=2.0 and 3.0 in the upstream region but is positive in the whole region for ER=1.5. It shows that the secondary separation bubble on the upper wall is formed for ER=2.0 and 3.0 but is not formed for ER=1.5. However, in the neighborhood of the sidewall of $z/H=17$, the reverse flow is detected for three expansion ratios, and its streamwise length is the largest for ER=1.5 and the smallest for ER=3.0.

Figure 8 summarizes the time averaged Nusselt number on the lower wall at Re=300 and 700 for ER=1.5, 2.0, and 3.0. The results at $z/H=0$ and 17 are shown in the figure. In the case of Re=300, $\overline{\mathrm{Nu}}$ on the center line increases from the step corner to the downstream, attains the maximum near the reattachment point, and subsequently decreases monotonically in the redeveloping region. The maximum of $\overline{\mathrm{Nu}}$ increases with an increase of ER and its streamwise location shifts to the upstream. Such a variation is independent of ER. In the neighborhood of the sidewall of $z/H=17$, $\overline{\mathrm{Nu}}$ increases steeply from the step corner and reaches the maximum, the magnitude and location of which exhibit a small

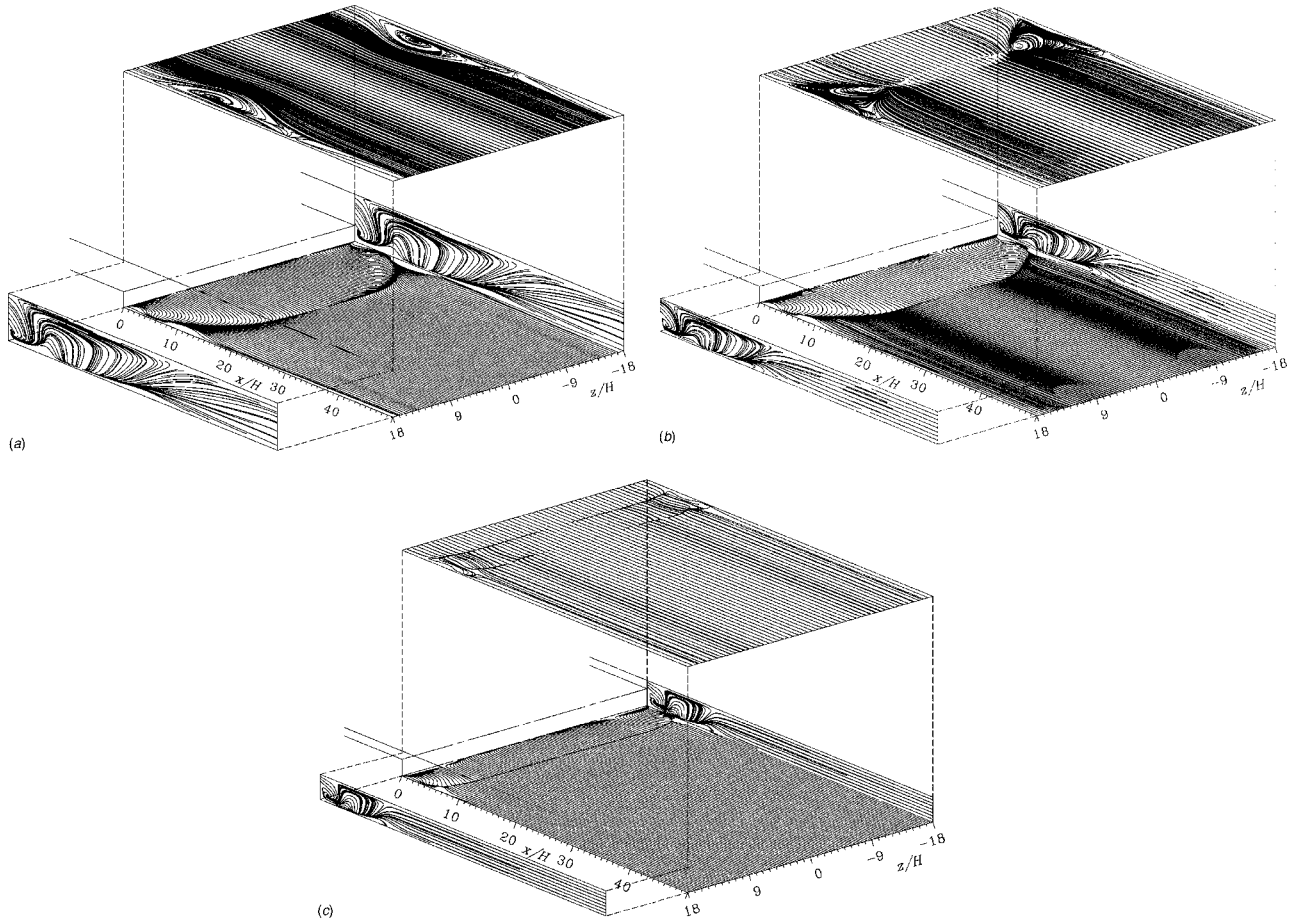

Fig. 12 Limiting streamline on four walls (Re=300): (*a*) ER=1.5; (*b*) ER=2.0; (*c*) ER=3.0

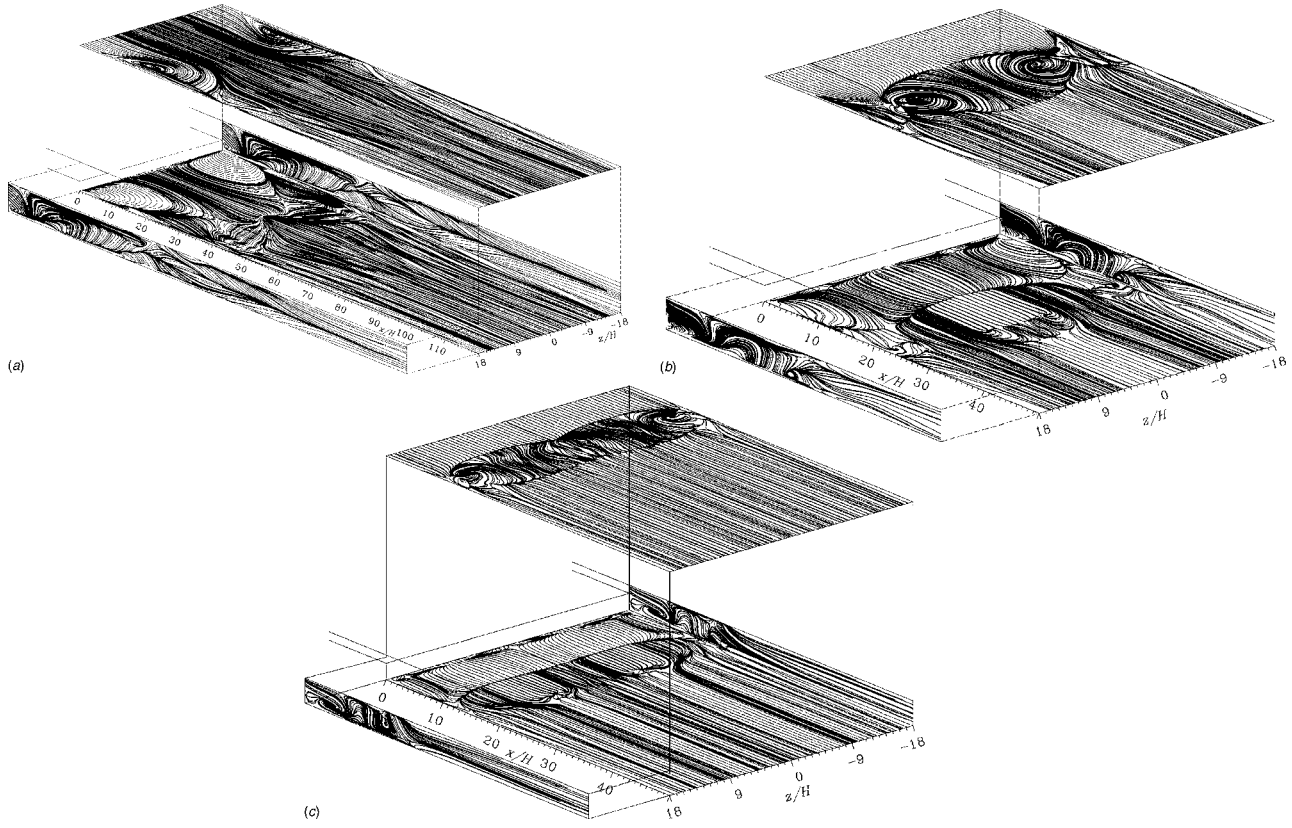

Fig. 13 Time averaged limiting streamline on four walls (Re=700): (*a*) ER=1.5; (*b*) ER=2.0; (*c*) ER=3.0

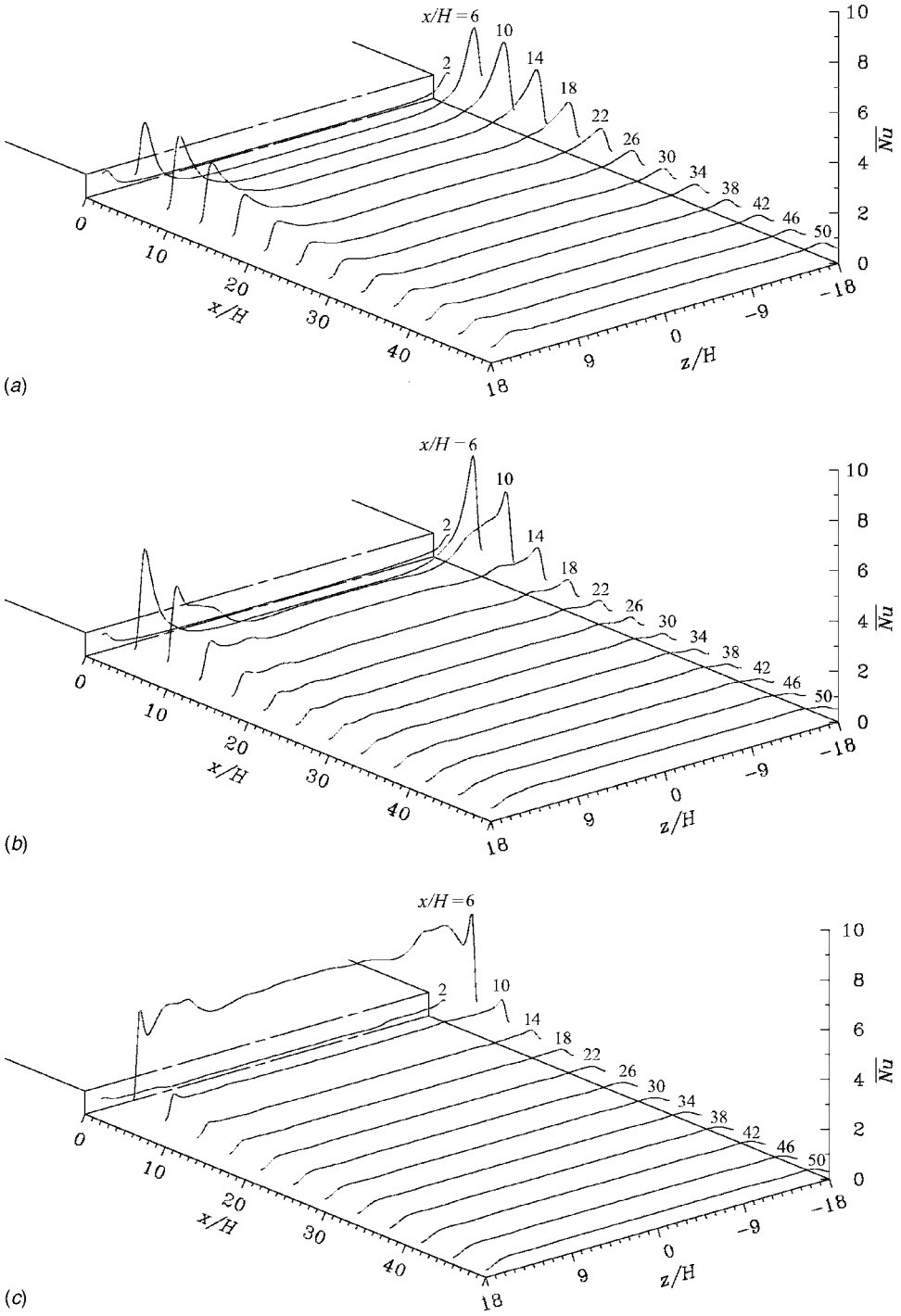

Fig. 14 Nusselt number on lower wall (Re=300): (*a*) ER=1.5; (*b*) ER=2.0; (*c*) ER=3.0

dependency upon ER. This is a different feature from that at $z/H=0$. Especially, the value of $\overline{\mathrm{Nu}}_{\max}$ is much larger than that at $z/H=0$ for ER=1.5 and 2.0.

In the case of Re=700, the results for ER=1.5 are extremely different from those for ER=2.0 and 3.0. On the center line of $z/H=0$, $\overline{\mathrm{Nu}}$ for ER=1.5 increases very slowly to the downstream and finally attains a maximum at about $x/H=100$, far away from the time averaged reattachment point. $\overline{\mathrm{Nu}}$ for ER=2.0 and 3.0 exhibits a second maximum around the reattachment point of the third separation bubble.

In the neighborhood of the sidewall of $z/H=17$, the results for ER=2.0 are very similar to those at $z/H=0$. However, $\overline{\mathrm{Nu}}$ for ER=3.0 shows no sharp peak but a plateau around $x/H=10$. Further, in the case of ER=1.5, four maxima are found in a streamwise region to about $x/H=60$. Such a complicated variation is presumed to be brought about by the longitudinal vortices formed near the sidewalls and their shedding to the downstream.

Figure 9 shows the time averaged reattachment length X_R and the streamwise location X_N of $\overline{\mathrm{Nu}}_{\max}$ on the center line as functions of Re for all the expansion ratios. In general, X_N is found to be nearly equal to X_R, presenting that the maximum Nusselt number on the center line is reached at a point very close to the reattachment one. An exceptional result is detected for ER=1.5 and Re=700. X_N is very much larger than X_R, as described previ-

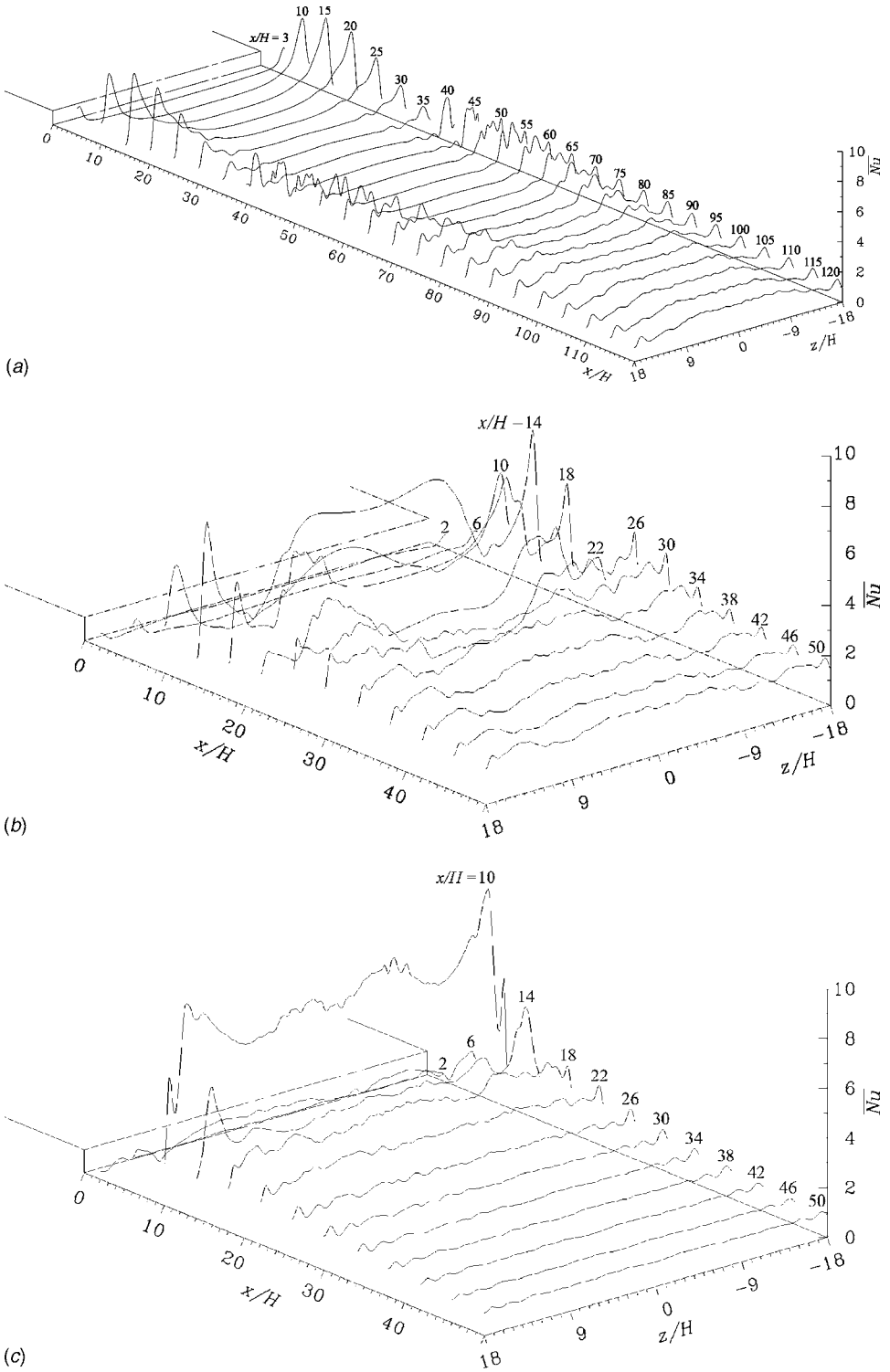

Fig. 15 Time averaged Nusselt number on lower wall (Re=700): (*a*) ER=1.5; (*b*) ER=2.0; (*c*) ER=3.0

ously. Both X_R and X_N are found to decrease with an increase of ER except the case of X_N for ER=1.5 and Re=700, in which X_N decreases greatly from about $100H$ for ER=1.5 to about $13H$ for ER=2.0. Such a complicated variation of X_N is brought about by the severe three-dimensional flow structure and also a very slow development to the unsteady flow state, which depends greatly upon both ER and Re. X_N at Re=1000 is also larger than X_R.

Figures 10 and 11 illustrate the streamlines at Re=300 and 700, respectively, for ER=1.5, 2.0, and 3.0. The flow is steady at Re =300 but unsteady at Re=700 for all the expansion ratios, respectively. The streamlines of fluid particles started from upstream of the step in the cross sections of $z/H=\pm 17$ are presented in the figures. In general, the fluid particles are greatly reflected into the lower corner of the step just after the flow separation, then flow spirally to the channel central region in the main separation bubble, and subsequently follow to the downstream for all the

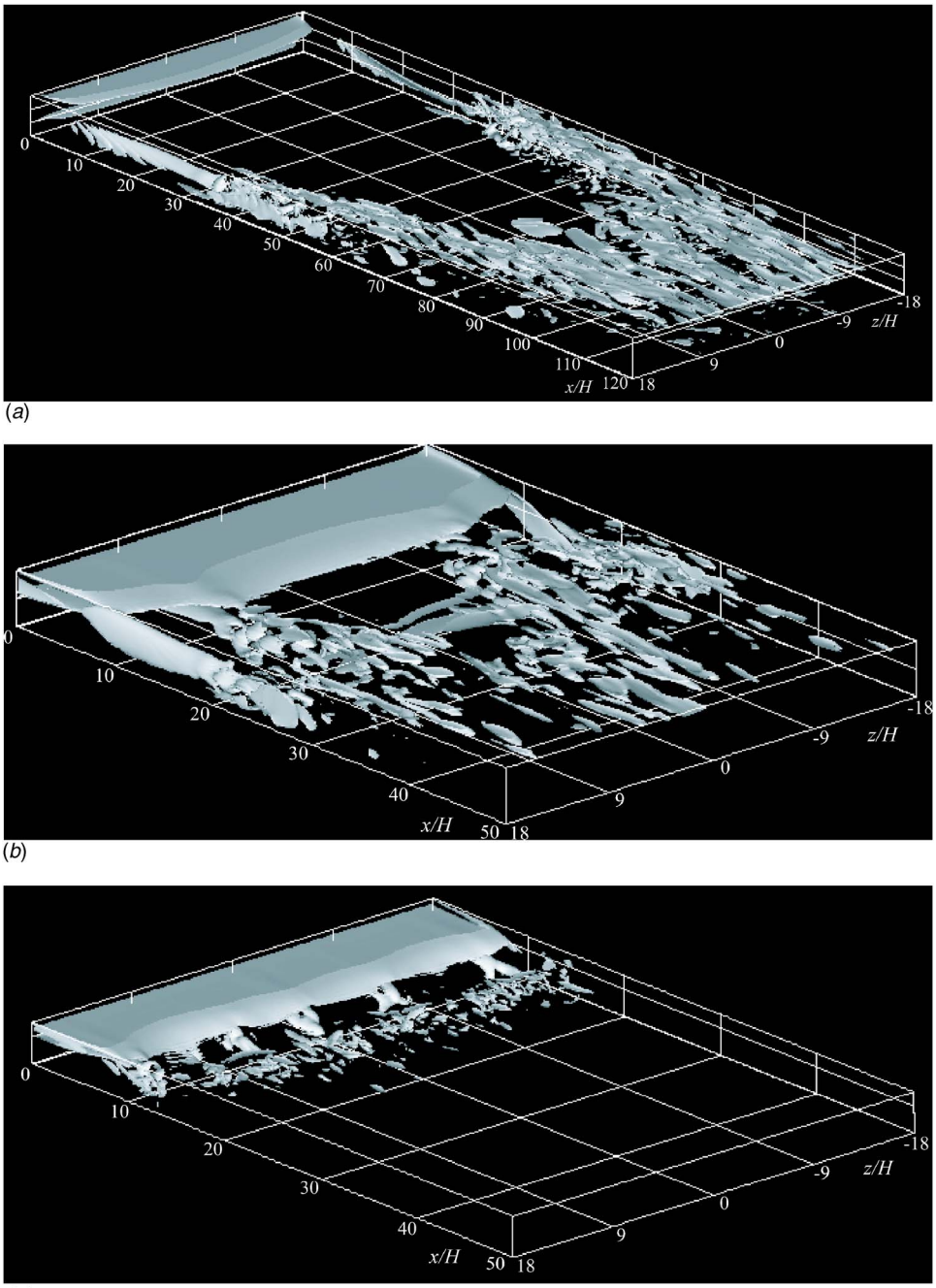

Fig. 16 Isosurface of instantaneous enstrophy (Re=700, $\Omega=2.0$, and $T=0$): (*a*) ER=1.5; (*b*) ER=2.0; (*c*) ER=3.0

cases. These results suggest the existence of a three-dimensional reverse flow near the sidewalls. However, the spanwise location from which the fluid particles move to the downstream depends strongly upon both ER and Re. That is, in the case of ER=2.0, the fluid particles move almost to the channel center line at Re=300; however, follow only to about $z/H=\pm 11$ at Re=700. Further, the region where the fluid particles spirally move increases with a decrease of ER, suggesting that the sidewall effects are severe for the channel of small expansion ratio.

Figures 12 and 13 present the limiting streamlines on the four walls downstream of the step at Re=300 and 700, respectively, for ER=1.5, 2.0, and 3.0. At Re=300, the flow structure in the separated and reattachment regions is rather simple except in the neighborhood of the sidewalls. The reattachment line of the separation bubble on the lower wall is clearly illustrated, and the recirculation region reduces near the sidewalls. The spanwise region of nearly two-dimensional flow is found to increase with an increase of ER. On the upper wall, the roof eddy is formed near the sidewalls and its size seems to increase with a decrease of ER. In the case of ER=2.0, the secondary separation bubble is clearly depicted and its spanwise border is connected to the roof eddy near the sidewall. The flow near the sidewall oncoming from upstream of the step is greatly deflected to the lower wall just downstream of the separation and follows spirally to the channel center. Such a flow situation creates locally the large adverse pressure gradient in the neighborhood of the upper corners of the channel, resulting in the formation of a roof eddy there.

As Re increases to 700 in which the flow is unsteady as de-

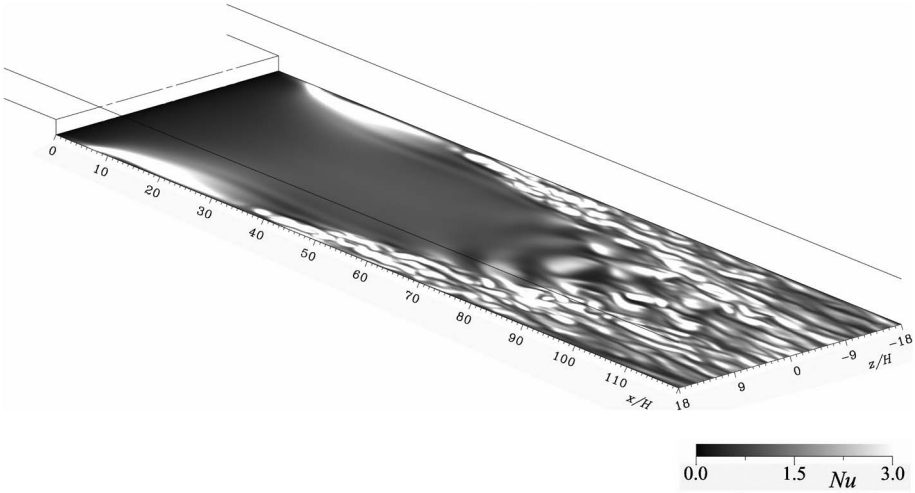

(a) $ER = 1.5$

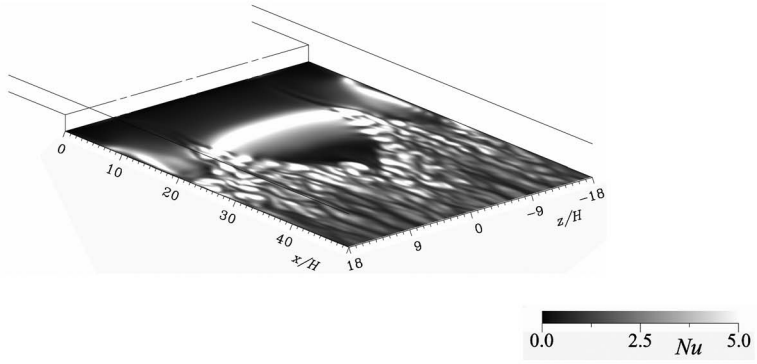

(b) $ER = 2.0$

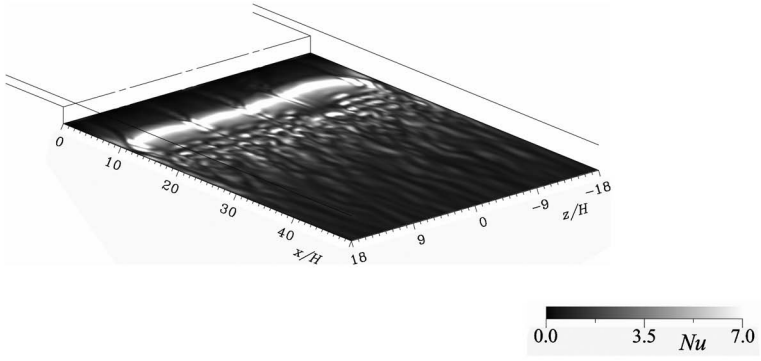

(c) $ER = 3.0$

Fig. 17 Instantaneous Nusselt number on lower wall (Re=700, *T*=0): (*a*) ER=1.5; (*b*) ER=2.0; (*c*) ER=3.0

scribed above, the flow structure in the separated and reattachment regions becomes extremely complicated, as shown in Fig. 13. The reattachment line on the lower wall and the secondary separation bubble on the upper wall are clearly depicted, but their flow structure is greatly different depending on ER. In particular the flow structure near the sidewalls is largely complex independent of ER. In the case of ER=1.5, the reattachment line is nearly parabolic and the separation bubble reduces to the sidewalls. The flow just downstream of the reattachment line also exhibits the complex features. The fluid particles near the channel center inside the

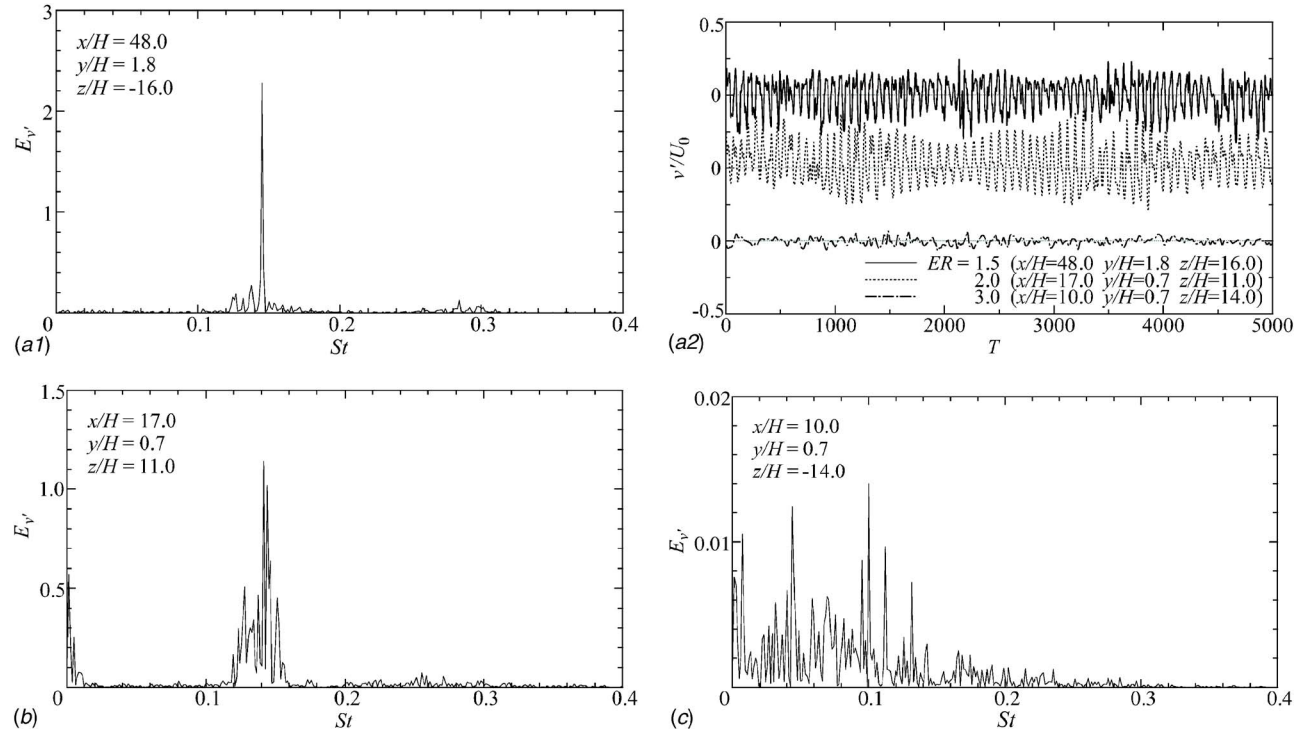

Fig. 18 Time variation and power spectrum of v' (Re=700): (*a*) ER=1.5; (*b*) ER=2.0; (*c*) ER=3.0

separation bubble follow from the reattachment point to the sidewalls, are rolled up there, flow spirally to the upstream, and subsequently are entrained into the separation bubble or into the longitudinal vortices near the sidewalls.

In the cases of ER=2.0 and 3.0, the separation bubble extends to the downstream near the sidewalls. The secondary separation bubble formed on the upper wall is clear for both cases. Its form is nearly an ellipse for ER=2.0; it extends the whole span for ER=3.0, but it is not clear for ER=1.5. The third separation bubble formed on the lower wall downstream of the main bubble exists in the central region for ER=2.0, but it shrinks to a very narrow one for ER=3.0 although its spanwise length increases. In general, the flow around the roof eddy on the upper wall exhibits no essential variation with Re. This flow structure on the upper wall is brought about by the longitudinal vortices formed near the sidewalls, which are estimated from the limiting streamlines on the sidewalls.

Figures 14 and 15 present the time averaged Nusselt number on the lower wall at Re=300 and 700, respectively, for ER=1.5, 2.0, and 3.0. Its spanwise and streamwise variations are evident in the figures. In general, $\overline{\mathrm{Nu}}$ attains the maximum very close to the sidewalls and it is brought about by the heat transfer enhancement of the longitudinal vortices. In the case of Re=300, $\overline{\mathrm{Nu}}$ varies gently in a very wide area except the near sidewall region. $\overline{\mathrm{Nu}}$ for ER=3.0 is exceptionally high in the reattachment region of about $x/H=6$ along the whole spanwise length.

As Re increases up to 700, the flow becomes unsteady for all the expansion ratios. In the case of ER=1.5, the vortices of several scales are shed from the longitudinal vortices near the sidewalls, extend to the downstream, and finally the unsteady flow state is reached over the whole spanwise region far downstream of the reattachment region. Accordingly, the streamwise variation of $\overline{\mathrm{Nu}}$ continues for a very long distance. In the cases of ER=2.0 and 3.0, the extremely high value of $\overline{\mathrm{Nu}}$ is attained in the reattachment region and just downstream. In the redeveloping flow region, the variation of $\overline{\mathrm{Nu}}$ is not severe.

Figures 16 and 17 represent instantaneous isosurfaces of the enstrophy ($\Omega=2.0$) and the corresponding instantaneous Nusselt number distributions, respectively, at Re=700 for ER=1.5, 2.0, and 3.0 in order to clarify the three-dimensional vortical structure in the flow and its correlation with the heat transfer characteristics. In the case of ER=1.5, the large scale longitudinal vortices exist steadily near the sidewalls, and the small scale vortices are shed from their downstream part around $x/H=30$. The whole span of the channel is finally covered by them at about $x/H=80$. On the other hand, in a very wide region, including the separation bubble, the reattachment region, and downstream (except for the sidewalls), there is no vortical flow structure. In the case of ER=2.0, the small scale vortices are radially shed from the two spanwise locations of about $z/H=\pm 10$ in the reattachment region. Some vortices are also shed from the longitudinal vortices, which locate steadily in the neighborhood of the sidewalls. Accordingly, the vortices of various scales are detected in the entire field in a region from $x/H=20$ to 30. In the case of ER=3.0, the small scale vortices are shed from the reattachment region at several spanwise locations and they diffuse quickly in the redeveloping flow region. It is very clear that the heat transfer is greatly enhanced in the regions where the vortices locate. The heat transfer is deteriorated in the separated flow region because of the steady stagnant flow there.

Figure 18 illustrates time variations of the velocity fluctuation v' and its power spectrum at the representative locations downstream of the reattachment point in order to show the severe unsteadiness of the flow at a high Reynolds number of Re=700 for ER=1.5, 2.0, and 3.0. It is very clear that the velocity fluctuates at high frequency and its amplitude is very large for ER=1.5 and 2.0, although the result for ER=3.0 presents a very small amplitude. The very large amount of the velocity fluctuation energy exists at a Strouhal number of about St=0.145, 0.142, and 0.105 for ER=1.5, 2.0, and 3.0, respectively. In the cases of ER=1.5 and 2.0, the large scale vortices are presumed to be shed from the longitudinal vortices near the sidewalls and from the reattachment region, respectively, as previously described in Fig. 16. In the case of ER=3.0, the fluctuation energy is very low, as suggesting the shedding of very small vortices from the reattachment region.

Concluding Remarks

The direct numerical simulation methodology with the finite difference method was employed to analyze the three-dimensional separated flow and heat transfer around three backward-facing steps in a rectangular channel. Effects of the channel expansion ratio upon the flow and heat transfer characteristics were minutely investigated. The channel expansion ratios treated were 1.5, 2.0, and 3.0 under a constant step aspect ratio of 36.0. The Reynolds number based on the mean velocity at the inlet and the step height treated in the calculations was varied from 300 to 1000 in order to investigate both the steady and also unsteady flow features. The main results obtained are as follows.

- It is found that the flow for ER=1.5, 2.0, and 3.0 becomes unsteady at the Reynolds number greater than 700, 600, and 500, respectively.
- The present time averaged reattachment length and the streamwise mean velocity on the center line for ER=2.0 are in very good agreement with the previous experimental ones, even in the unsteady flow state.
- The longitudinal vortices are formed in the neighborhood of two sidewalls and the vortices having large and small scales are shed to the downstream. These vortices influence largely the flow and heat transfer features in the neighborhood of the sidewalls and bring about the maximum Nusselt number very close to the sidewalls.
- The time averaged reattachment length on the center line increases with a decrease of ER in the present Reynolds number range for both the steady and unsteady flow states.
- The flow structure in the separated and reattachment regions is detected to exhibit a small dependency upon ER for the steady state but to vary greatly with ER for the unsteady state.
- The complexity of flow increases with a decrease of ER for the unsteady state. Especially, the case of ER=1.5 and Re=700 presents some very novel features, in which an extremely long streamwise distance is needed to develop to the developed flow and the maximum Nusselt number on the center line is finally attained at about $x/H=100$ far downstream of the time averaged reattachment point. Except for that case, the maximum Nusselt number on the center line is reached at the point that is nearly equal to the time averaged reattachment one.
- The heat transfer characteristics are found to depend greatly upon such a flow structure. In the case of small expansion ratios such as 1.5 and 2.0, the Nusselt number is very high near the sidewalls where the longitudinal vortices are formed and also in the far downstream where the large and small scale vortices shed from the reattachment flow region and the longitudinal vortices are united. In the case of ER=3.0, the highest Nusselt number is attained in a very small area of the flow reattachment region.
- Even in the case of a large step aspect ratio such as 36.0 treated in the present study, the three-dimensionality of the flow is severe and its effects upon the heat transfer are great, especially in the unsteady flow state.

Acknowledgment

The present calculations were conducted using the supercomputer SX-7 at Information Synergy Center, Tohoku University.

Nomenclature

AR = aspect ratio$=W_3/H$
C_f = surface friction coefficient$=\tau_w/(\rho U_0^2/2)$
ER = expansion ratio$=W_2/W_1$
E_x = power spectrum of x
f = frequency
H = step height
h = heat transfer coefficient$=q_w/(\theta_w-\theta_0)$
Nu = Nusselt number$=hH/\lambda$
Pr = Prandtl number
p = pressure
q_w = heat flux per unit area and unit time
Re = Reynolds number$=U_0H/\nu$
St = Strouhal number$=fH/U_0$
T = nondimensional time$=tU_0/H$
t = time
U_0 = mean velocity at inlet
$\boldsymbol{u}$ = velocity vector (u, v, w)
W_1 = upstream channel height
W_2 = downstream channel height
W_3 = channel width
X_N = streamwise location of $\overline{\mathrm{Nu}}_{\max}$
X_R = time averaged reattachment length
$\boldsymbol{x}$ = coordinates (x, y, z)
θ = temperature
θ_0 = uniform temperature at inlet
θ_w = wall temperature
λ = thermal conductivity
ν, ρ = kinematic viscosity and density, respectively
τ_w = wall friction stress
Ω = enstrophy$=|\omega|^2/2$
ω = vorticity vector

Subscripts

max = maximum
x, y, z = values along x, y, and z axes

Superscripts

— = time averaged
′ = unsteady fluctuating

References

[1] Fletcher, L. S., Briggs, D. G., and Page, R. H., 1974, "Heat Transfer in Separated and Reattached Flows: An Annotated Review," Isr. J. Technol., **12**, pp. 236–261.
[2] Aung, W., 1983, "Separated Forced Convection," *Proc. ASME-JSME Thermal Eng. Conf.*, Honolulu, HI, March 20–24, Vol. 2, pp. 499–515.
[3] Ota, T., and Nishiyama, H., 1987, "A Correlation of Maximum Turbulent Heat Transfer Coefficient in Reattachment Flow Region," Int. J. Heat Mass Transfer, **30**, pp. 1193–1200.
[4] Merzkirch, W., Page, R. H., and Fletcher, L. S., 1988, "A Survey of Heat Transfer in Compressible Separated and Reattached Flows," AIAA J., **26**, pp. 144–150.
[5] Ota, T., 2000, "A Survey of Heat Transfer in Separated and Reattached Flows," Appl. Mech. Rev., **53**, pp. 219–235.
[6] Kaiktsis, L., Karniadakis, G. E., and Orszag, S. A., 1996, "Unsteadiness and Convective Instabilities in a Two-Dimensional Flow Over a Backward-Facing Step," J. Fluid Mech., **321**, pp. 157–187.
[7] Le, H., Moin, P., and Kim, J., 1997, "Direct Numerical Simulation of Turbulent Flow Over a Backward-Facing Step," J. Fluid Mech., **330**, pp. 349–474.
[8] Williams, P. T., and Baker, A. J., 1997, "Numerical Simulations of Laminar Flow Over a 3D Backward-Facing Step," Int. J. Numer. Methods Fluids, **24**, pp. 1159–1183.
[9] Lee, T., and Mateescu, D., 1998, "Experimental and Numerical Investigation of 2D Backward-Facing Step Flow," J. Fluids Struct., **12**, pp. 703–716.
[10] Chiang, T. P., and Sheu, T. W. H., 1999, "A Numerical Revisit of Backward-Facing Step Flow Problem," Phys. Fluids, **11**, pp. 862–874.
[11] Iwai, H., Nakabe, K., and Suzuki, K., 2000, "Flow and Heat Transfer Characteristics of Backward-Facing Step Laminar Flow in a Rectangular Duct," Int. J. Heat Mass Transfer, **43**, pp. 457–471.
[12] Kaltenbach, H.-J., and Janke, G., 2000, "Direct Numerical Simulation of Flow Separation Behind a Swept Rearward-Facing Step at Re=3000," Phys. Fluids, **12**, pp. 2320–2337.
[13] Barkley, D., Gomes, M. G. M., and Henderson, R. D., 2002, "Three-Dimensional Instability in Flow Over a Backward-Facing Step," J. Fluid Mech., **473**, pp. 167–190.
[14] Nie, J. H., and Armaly, B. F., 2002, "Three-Dimensional Convective Flow Adjacent to Backward-Facing Step—Effects of Step Height," Int. J. Heat Mass Transfer, **45**, pp. 2431–2438.
[15] Ota, T., Fu, H.-G., and Yoshikawa, H., 2002, "Effects of Aspect Ratio on Turbulent Heat Transfer Around a Downward Facing Step," *Proc. 12th Int. Heat Transfer Conf.*, Grenoble, France, August 18–23, pp. 723–728.
[16] Tylli, N., Kaiktsis, L., and Ineichen, B., 2002, "Sidewall Effects in Flow Over a Backward-Facing Step: Experiments and Numerical Simulations," Phys. Flu-

ids, **14**, pp. 3835–3845.
[17] Armaly, B. F., Li, A., and Nie, J. H., 2003, "Measurements in Three-Dimensional Laminar Separated Flow," Int. J. Heat Mass Transfer, **46**, pp. 3573–3582.
[18] Sugawara, K., Kaihara, E., Yoshikawa, H., and Ota, T., 2003, "Numerical Simulation of Unsteady Separated Flow and Heat Transfer Around an Inclined Downward Step," *Proc. 6th ASME-JSME Thermal Eng. Jt. Conf.*, Honolulu, HI, March 16–20, Paper No. TED-AJ03-188.
[19] Biswas, G., Breuer, M., and Durst, F., 2004, "Backward-Facing Step Flows for Various Expansion Ratios at Low and Moderate Reynolds Numbers," ASME J. Fluids Eng., **126**, pp. 362–374.
[20] Nie, J. H., and Armaly, B. F., 2004, "Reverse Flow Regions in Three-Dimensional Backward-Facing Step Flow," Int. J. Heat Mass Transfer, **47**, pp. 4713–4720.
[21] Nie, J. H., and Armaly, B. F., 2004, "Convection in Laminar Three-Dimensional Separated Flow," Int. J. Heat Mass Transfer, **47**, pp. 5407–5416.
[22] Durst, F., and Tropea, C., 1981, "Turbulent, Backward-Facing Step Flows in Two-Dimensional Ducts and Channels," *Proc. 3rd Int. Symp. On Turbulent Shear Flows*, Davis, CA, September 9–11, pp. 18.1–18.6.
[23] Ötügen, M. V., 1991, "Expansion Ratio Effects on the Separated Shear Layer and Reattachment Downstream of a Backward Facing Step," Exp. Fluids, **10**, pp. 273–280.
[24] Kuehn, D. M., 1980, "Effects of Adverse Pressure Gradient on the Incompressible Reattaching Flow Over a Rearward-Facing Step," AIAA J., **18**, pp. 343–344.
[25] Ra, S. H., and Chang, P. K., 1990, "Effects of Pressure Gradient on Reattaching Flow Downstream of a Rearward-Facing step," J. Aircr., **27**, pp. 93–95.
[26] Sugawara, K., Kaihara, E., Yoshikawa, H., and Ota, T., 2005, "DNS of Three-Dimensional Unsteady Separated Flow and Heat Transfer Around a Downward Step," ASME Paper No. HT2005-72178.
[27] Kito, A., Sugawara, K., Yoshikawa, H., and Ota, T., 2005, "DNS of Expansion Ratio Effects on Three-Dimensional Unsteady Separated Flow and Heat Transfer Around a Downward Step," ASME Paper No. HT2005-72180.
[28] Armaly, B. F., Durst, F., Pereira, J. C. F., and Schönung, B., 1983, "Experimental and Theoretical Investigation of Backward-Facing Step Flow," J. Fluid Mech., **127**, pp. 473–496.
[29] Amsden, A. A., and Harlow, F. H., 1970, "A Simplified MAC Technique for Incompressible Fluid Flow Calculations," J. Comput. Phys., **6**, pp. 322–325.
[30] Achenbach, E., 1990, "Mass Transfer Downstream a Backward or a Forward-Facing Step," *Proc. 9th Int. Heat Transfer Conf.*, Vol. 5, pp. 305–310.
[31] Kim, J., and Moin, P., 1985, "Application of a Fractional-Step Method to Incompressible Navier-Stokes Equations," J. Comput. Phys., **59**, pp. 308–323.
[32] Vradis, G. C., and VanNostrand, L., 1992, "Laminar Coupled Flow Downstream of an Asymmetric Sudden Expansion," J. Thermophys. Heat Transfer, **6**, pp. 288–295.
[33] Ichinose, K., Tokunaga, H., and Satofuka, N., 1991, "Numerical Simulation of Two-Dimensional Backward-Facing Step Flows," Trans. Jpn. Soc. Mech. Eng., Ser. B, **57B**, pp. 3715–3721.
[34] Valencia, A., and Hinojosa, L., 1997, "Numerical Solutions of Pulsating Flow and Heat Transfer Characteristics in a Channel with a Backward-Facing Step," Heat Mass Transfer, **32**, pp. 143–148.
[35] Sparrow, E. M., and Chuck, W., 1987, "PC Solutions for Heat Transfer and Fluid Flow Downstream of an Abrupt, Asymmetric Enlargement in a Channel," Numer. Heat Transfer, **12**, pp. 19–40.
[36] Sparrow, E. M., Kang, S. S., and Chuck, W., 1987, "Relation Between the Points of Flow Reattachment and Maximum Heat Transfer for Regions of Flow Separation," Int. J. Heat Mass Transfer, **30**, pp. 1237–1246.

A Numerical Study of Flow and Heat Transfer Enhancement Using an Array of Delta-Winglet Vortex Generators in a Fin-and-Tube Heat Exchanger

A. Joardar[1]
e-mail: joardar@uiuc.edu

A. M. Jacobi

Department of Mechanical Science and Engineering,
University of Illinois,
158 Mechanical Engineering Building MC-244,
1206 West Green Street,
Urbana, Il 61801

This work is aimed at assessing the potential of winglet-type vortex generator (VG) "arrays" for multirow inline-tube heat exchangers with an emphasis on providing fundamental understanding of the relation between local flow behavior and heat transfer enhancement mechanisms. Three different winglet configurations in common-flow-up arrangement are analyzed in the seven-row compact fin-and-tube heat exchanger: (a) single–VG pair; (b) a 3VG-inline array (alternating tube row); and (c) a 3VG-staggered array. The numerical study involves three-dimensional time-dependent modeling of unsteady laminar flow $(330 \leqslant \mathrm{Re} \leqslant 850)$ *and conjugate heat transfer in the computational domain, which is set up to model the entire fin length in the air flow direction. It was found that the impingement of winglet redirected flow on the downstream tube is an important heat transfer augmentation mechanism for the common-flow-up arrangement of vortex generators in the inline-tube geometry. At* $\mathrm{Re}=850$ *with a constant tube-wall temperature, the 3VG-inline-array configuration achieves enhancements up to 32% in total heat flux and 74% in j factor over the baseline case, with an associated pressure-drop increase of about 41%. The numerical results for the integral heat transfer quantities agree well with the available experimental measurements.*
[DOI: 10.1115/1.2740308]

Keywords: vortex generator, fin-and-tube heat exchanger, enhanced heat transfer

1 Introduction

In numerous end-use energy applications, especially in heating, ventilation, air conditioning, and refrigeration (HVACR) systems, heat exchanger performance has been important in meeting efficiency standards with low cost and environmental impact. According to 2002 estimates by the US Department of Energy (EIA),[2] HVACR systems accounted for 58% of the energy used in residential buildings and 45% in the commercial buildings. This usage amounts to an annual expenditure of roughly 32 trillion dollars for energy consumed by HVACR systems alone. In the liquid-to-air and phase-change heat exchangers typical to HVACR systems, the air-side thermal resistance is the largest single contributor to the overall thermal resistance. For example, the air side can comprise 75% of the thermal resistance in an evaporator and 95% in a condenser for typical refrigeration applications. As an air-side heat transfer enhancement strategy, vortex generation (VG) has promise; this study is directed toward gaining a better understanding of the complex flow and heat transfer interactions that occur when implementing vortex generation in a fin-and-tube heat exchanger. With rising energy costs and new legislation aimed at efficiency and environmental protection, heat exchanger performance will continue to be very important. Achieving even a 10% performance enhancement in this type of heat exchanger geometry could have profound implications on the HVACR systems where it is commonly used.

Vortex generators introduce streamwise vortices in the flow field causing bulk fluid mixing, boundary-layer modification and potentially flow destabilization. Apart from these well known mechanisms of heat transfer enhancement, the placement and orientation of the VGs can yield additional augmentation through tube-wake management. The two most commonly reported VG placement strategies are the so called "common-flow-down" [1–3] and the "common-flow-up" approaches [4,5] for a single fin-tube element. Common-flow-up means the VGs in a pair are placed such that the resulting vortices counter-rotate in a way to move the fluid between them away from the fin on which they are mounted. Common-flow down means the flow shared by the two vortices (i.e., between them) is directed toward the mounting surface. In most of the prior work reported in the literature, when using a common-flow-down arrangement, the VGs are placed as a pair downstream of the tube in the near-wake region in order to introduce high-momentum fluid behind the tube and improve the poor heat transfer in the wake region. In the common-flow-up approach, the VGs are usually deployed further upstream adjacent to the tube such that the winglet forms a nozzle-like configuration with the tube, causing the fluid to accelerate in the near-tube region; this design is intended to delay separation on the tube surface and narrow the wake. It is interesting to note that the common-flow-down approach has been reported [2] to be more effective with an inline-tube geometry than with a staggered-tube geometry under identical test conditions; whereas the common-flow-up approach has been found to be less effective with an inline-tube pattern [5] than a staggered-tube pattern. However, it is not clear whether this observation remains valid for heat exchanger geometry and operating conditions different from those reported in these prior works.

[1]Corresponding author.
[2]See http://www.eia.doe.gov/

Contributed by the Heat Transfer Division of ASME for publication in the JOURNAL OF HEAT TRANSFER. Manuscript received September 14, 2006; final manuscript received December 6, 2006. Review conducted by Gautam Biswas.

The heat transfer enhancement due to vortex generation is usually accompanied by additional pressure loss and attendant pumping power increase, usually attributed to the form drag associated with the VG. However, some studies on scaled up models have reported improved pressure drop performance after deploying the VG [1,5]. Hence, the placement of VG with respect to tube position and the geometric parameters of the VG simultaneously influence both the overall heat transfer and the pumping power. Only a few systematic studies (by Feibig, Mitra, and their coworkers) have appeared in the literature, focused primarily on the common-flow-down configuration. Some general recommendations for the winglet position and geometric parameters have been made for the round tube heat exchanger geometry studied [1,2,4]. However, relatively fewer studies for the common-flow-up arrangement appear in the technical literature [4–6]. There are few reports of full-scale implementation and testing of vortex generators in heat exchangers under realistic operating conditions in the open literature (by Jacobi and his co-workers). Such studies are useful in evaluating the true potential of the enhancement strategies. El Sherbini and Jacobi [7] investigated the impact of leading-edge delta-wing vortex generators on a plain-fin-and-tube heat exchanger under dry-surface conditions. The ratio of wing to heat transfer area was 0.23%, and the wing had $\alpha=55$ deg and $\Lambda=1$. They measured a 31% heat transfer enhancement over the baseline, with a modest pressure drop penalty of 10%. Sherbini and Jacobi used an eight-row-deep, plain-fin-and-tube heat exchanger with a fin spacing of 5 mm. The first to-scale study of a vortex-enhanced heat exchanger under frosted-surface conditions was reported by Sommers and Jacobi [8]. The plain-fin-and-tube heat exchanger was eight rows deep and had a fin spacing of 8.5 mm. The delta-wing array was a four-row, staggered configuration and attached at intervals of 51 mm in an alternating single row, double row arrangement. The ratio of wing to heat transfer area was 3.1%, and the wing had $\alpha=55$ deg and $\Lambda=2$. For Re between 500 and 1300, the air-side thermal resistance was shown to decrease by 35–42%. Another important finding was that the average frost density increased in the enhanced case. The effects of relative humidity, air-side temperature, and refrigerant-side temperature on the heat exchanger performance under frosted-surface conditions were not considered. Joardar and Jacobi [9] studied the performance of leading edge delta wings in a flat tube, louvered-fin compact heat exchanger under both dry- and wet-surface conditions. They reported an average heat transfer (j factor) increase over the baseline case of 21% for dry conditions and 23.4% for wet conditions, with a pressure drop penalty smaller than 7%. The wing-to-fin area ratio was 0.48%, and the wing had $\alpha=45$ deg and $\Lambda=0.8$. Experimental studies aimed at optimizing vortex-enhanced fin-and-tube heat exchangers are expensive and time consuming because of large number of geometrical parameters involved.

In the early 1990s some of the first attempts were made to create three-dimensional (3D) numerical models of a single vortex-enhanced fin-and-tube element using the methods of computational fluid dynamics (CFD). At that time, multirow models were not feasible because of their excessive computing requirements. Biswas et al. [3] were among the first to numerically investigate the flow structure and heat transfer in a three-row fin-tube heat exchanger with built-in delta winglet pairs. The tube rows were arranged in a staggered design, and a punched-out delta winglet pair with an aspect ratio of 2 was located behind each tube at an attack angle of 45 deg. At a Reynolds number of 500, a local heat transfer increase of more than 240% was reported at a location about 12 times the channel height downstream of the inlet. The spanwise-average Nusselt number at Re=646 compared favorably to experimental results for the same geometry for most streamwise locations, although large discrepancies existed at some streamwise locations. It should be noted that the numerical modeling did not include the conjugate effects of conduction and convection from the fin surfaces. Instead, a constant temperature boundary condition was used for the fins—a condition not satisfied in the experimental work to which the authors compared their computations. Fiebig et al. [10] performed a 3D numerical calculation of conjugate convective and conductive heat transfer in a fin-tube element for different Reynolds numbers ($100 \leqslant \mathrm{Re} \leqslant 1000$) and fin efficiency parameter, $\mathrm{Fi}=(k_f/k)(\delta/H)$. Flow patterns, pressure distributions, Nusselt number distributions, heat flux distributions, and fin efficiency were presented for developing, laminar, steady flows. The Nusselt numbers were found to increase with increasing Re and with decreasing Fi. When the fin efficiency was small and Re was large, Feibig and co-workers found a region in the tube wake where the heat transfer reversed, degrading the heat exchanger performance. In a further study, Fiebig et al. [11] presented a solution to avoid the heat transfer reversal and augment the heat transfer by using a delta winglet pair vortex generator. Numerical calculations were carried out for Reynolds number of 250 and 300. The delta winglet pair, with an aspect ratio of 2 and an attack angle of 45 deg, was punched out of the fin surface downstream of the tube and placed in a common-flow-down arrangement. The numerical results showed that the longitudinal vortices greatly reduced the separated region in the tube wake. The authors reported a maximum global heat transfer enhancement of 31% due to the delta winglet pair. In 1999, Bastani Jahromi et al. [12] compared heat transfer performance of a periodic fin-and-tube element with a two-row element, both fitted with punched winglets in a common-flow-down arrangement. Their numerical results showed that at Re=400, the Nusselt number distribution on the second half of the two-row element is very similar to that of the periodic case. Recently, Jain et al. [13] studied the flow and heat transfer in a channel with circular tube, and winglet pair VG in a common-flow-up configuration. For Re=1000, the averaged Nusselt number for the enhanced case improved by 35% compared to the baseline case. The friction factor was not computed. Finally, some other numerical studies of plain fin-and-tube heat exchangers related to the current work should also be noted [14–16].

It is evident that very few papers have reported on vortex generator arrays in compact multirow heat exchangers for air-cooling and refrigeration applications. A number of important issues regarding how the generated vortices interact and their stability and spatial longevity in the presence of many tube rows still remain to be investigated. The impact of VG arrays in common-flow-up arrangements on overall heat transfer and pressure drop needs to be quantified. Furthermore, there is a large parameter space, both with respect to different placement strategies of the array and the VG geometry itself which needs to be explored to identify preferred VG arrangements in the context of multirow heat exchangers. Due to the large parameter space, experimental investigations are expensive and time consuming, and a numerical approach is more viable. With the rapid growth of computing power and advancements in CFD, it is now possible to obtain accurate time-dependent numerical solutions without significant simplifying assumptions.

The primary objective of this research is to understand the flow and heat transfer enhancement mechanisms associated with different delta-winglet array designs in a common-flow-up configuration for a fin-and-tube heat exchanger. The baseline heat exchanger is a seven-row inline-tube heat exchanger common in air-cooling and refrigeration applications. Commercial software is used for 3D numerical solution of the complete Navier–Stokes and energy equations in the heat exchanger—with and without VGs. In the present study, we consider three candidate winglet arrays in a common-flow-up orientation. The three configurations are: (a) a single-VG-pair (at the leading tube row); (b) 3VG-inline-array (alternating tube rows); and (c) a 3VG-staggered array. The computed results are compared to available experimental results to validate the numerical model. Through an understanding of the flow and heat transfer in this geometry, design guidance for

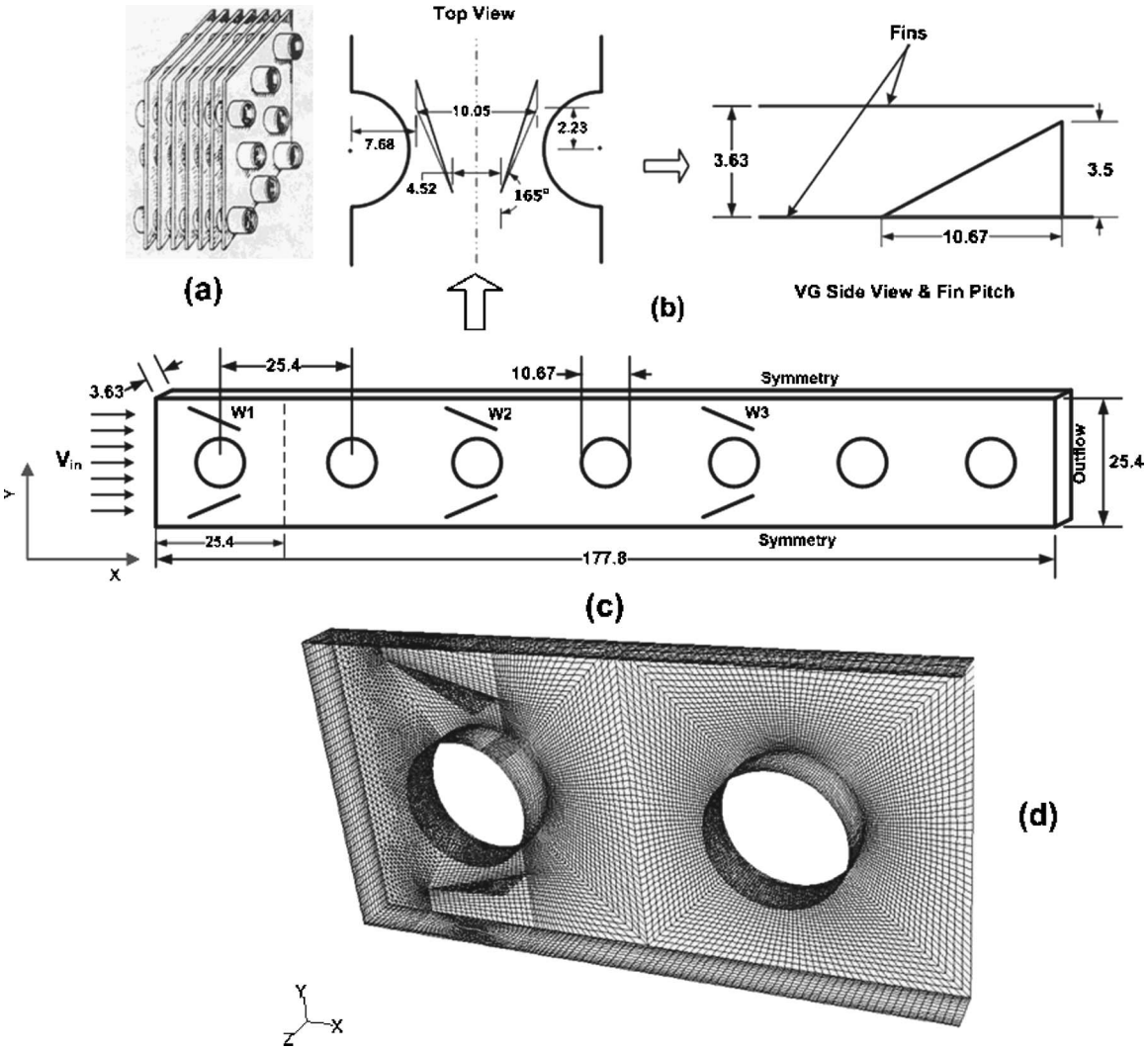

Fig. 1 Arrangement of vortex generators (3-row) on the fin-and-tube assembly: (*a*) schematic diagram showing core region of a plate fin-and-tube heat exchanger; (*b*) winglet vortex generator dimensions and the placement with respect to the tube; (*c*) coordinate system and computational domain comprising of single row of inline tubes mounted with winglets; and (*d*) typical computational mesh (all dimensions are in mm)

related geometries can be obtained. Moreover, the potential impact of VG enhancement is quantified for this important application.

2 Mathematical Formulation

A schematic diagram of the plain fin-and-tube heat exchanger is shown in Fig. 1(*a*). The heat exchanger being considered here is assembled by expanding the tube within the collars. Since the thermal contact resistance between the tube and fin collar is negligible, the CFD model will be developed without regard for the collar—the tube and collar are considered as one from a geometric viewpoint. Because of the relatively high heat transfer coefficient on the tube side, and the high thermal conductivity of the tube wall and collar, the tube temperature is assumed to be constant. However, the fin surface temperature distribution will be determined by solving the conjugate problem, in which the flow velocity and temperature distribution are found with simultaneous coupling to the temperature field in the solid surface of the fin. The vortex generator dimensions and their placement with respect to the tubes are shown in Fig. 1(*b*). The computational domain models a set of seven tubes as shown in Fig. 1(*c*), spanning from the inlet to the exit face of the heat exchanger. A back environment region (not shown here) is also added since the flow is recovering in the exit region. Two neighboring fins form a channel of height $H=3.6$ mm, width $B=7H$, and length $L=49H$. The first tube is centered at $X=3.5H$, and $Y=3.5H$. All subsequent tubes are located at even spacing of $7H$ from the nearest upstream tube. The fin material was aluminum and fin thickness was 0.18 mm. The VG arrangements for the three winglet configurations considered in this study are shown in Fig. 2. Computations have been carried out for Re=850 for each of these configurations since this Re corresponds to the actual operating condition of the heat exchanger under consideration.

2.1 Governing Equations. The fluid is considered Newtonian with constant properties, and the flow is assumed to incompressible, laminar, three dimensional, and unsteady with negligible viscous dissipation. The equations representing the conservation of mass, momentum, and energy (temperature) fields are the Navier–Stokes equations along with the incompressibility condition and the energy equation, as shown below

$$\nabla \cdot \vec{u} = 0 \quad \text{in} \quad D^3 \tag{1}$$

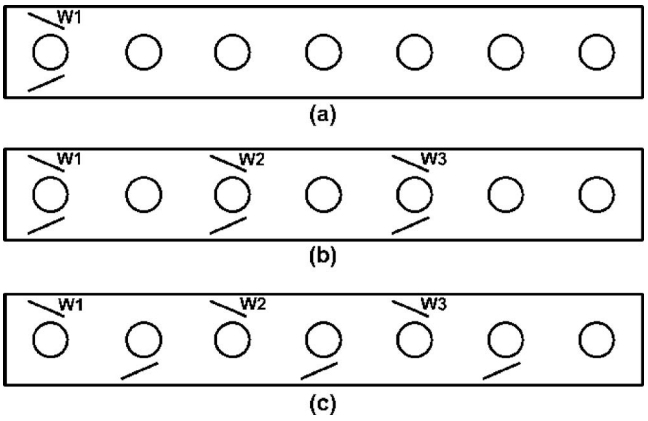

Fig. 2 Various configurations of the winglet pairs: (*a*) 1VG leading edge; (*b*) 3VG (alternate tube) inline array; and (*c*) 3VG staggered array

$$\frac{\partial \vec{u}}{\partial t} + \vec{u} \cdot \nabla \vec{u} = -\frac{1}{\rho} \nabla P + \nu \nabla^2 \vec{u} \quad \text{in} \quad D^3 \tag{2}$$

and

$$\frac{\partial T}{\partial t} + \vec{u} \cdot \nabla T = \alpha \nabla^2 T \quad \text{in} \quad D^3 \tag{3}$$

where D^3 denotes the computational domain as shown in Fig. 1(*b*); ρ represents the fluid density; ν is the kinematic viscosity; and α is the thermal diffusivity. Buoyancy forces are neglected; thus, it is assumed that $\mathrm{Gr}/\mathrm{Re}^2 \ll 1$.

The temperature distribution of the fin is described by the two-dimensional heat conduction equation, tacitly assuming $\mathrm{Bi} \ll 1$, so that the temperature variation across the fin thickness (z direction) can be neglected. The conduction equation for the fin can be expressed as

$$\frac{\partial T_f}{\partial t} = \alpha_f \nabla^2 T_f + \frac{\dot{q}}{(\rho c_p)_f} \quad \text{in} \quad D^2 \tag{4}$$

where the subscript f refers to fin and D^2 denotes the two-dimensional fin and VG surfaces. With no internal generation in the fin material, the source term on the right-hand side of Eq. (4) can be considered as solely due to convection from the fluid. Thus

$$\dot{q} = \frac{k}{t_f}\left(\frac{\partial T}{\partial z}\right)_{z=0}, \quad \text{for the fin mounted with VGs, i.e., at } z = 0 \tag{5a}$$

and

$$\dot{q} = -\frac{k}{t_f}\left(\frac{\partial T}{\partial z}\right)_{z=H}, \quad \text{for the fin without VGs, i.e., at } z = H. \tag{5b}$$

The energy equation, Eq. (3), for the fluid and the heat conduction equation, Eq. (4), are coupled by the heat flux equations, Eqs. (5*a*) and (5*b*). In this model, each fin is subject to convection from only one side, tacitly assuming the convective fluxes on both sides of the fin are identical and an adiabat exists at the midthickness of the fin. Because of symmetry, this assumption is correct for the baseline geometry; however, it might be violated when VGs are present. The success of this modeling approach will be addressed when the results are compared to experimental data (from Ref. [6]).

2.2 Boundary Conditions. The governing equations are elliptic in space and parabolic in time, necessitating initial conditions at time $t=0$ and well-posed boundary conditions at all surfaces. All flow variables are initialized to zero except the inlet velocity, inlet temperature, and tube temperature. A constant temperature difference ($\Delta T = 18.63$ K) between inlet air and the tube surfaces was maintained for all computations. For each fin, half of the actual thickness is specified and convective heat transfer occurs on one side as described above for $z=0$ and $z=H$ no-slip boundaries. The relevant boundary conditions for all other surfaces are as follows:

- Upstream of the inlet face ($x=0$) the velocity and temperature are constant

$$u = u_\infty \quad v = w = 0, \quad T = T_\infty \tag{6a}$$

- Downstream of the exit face ($x=L$) the streamwise gradients are zero

$$\frac{\partial u}{\partial x} = \frac{\partial v}{\partial x} = \frac{\partial w}{\partial x} = 0, \quad \frac{\partial T}{\partial x} = 0 \tag{6b}$$

- At side walls ($y=0$; $y=B$), symmetry condition holds

$$\frac{\partial u}{\partial y} = \frac{\partial w}{\partial y} = 0, \quad v = 0 \quad \text{(Symmetry) and} \quad \frac{\partial P}{\partial y} = 0$$

$$\frac{\partial T}{\partial y} = 0 \tag{6c}$$

- Fin, tube, and wing surfaces

$$u = v = w = 0 \text{ (no slip)} \quad \text{and} \quad \frac{\partial P}{\partial n} = 0$$

$$T = T_w \text{ (tube wall temperature)} \tag{6d}$$

2.3 Numerical Method. The Navier–Stokes and energy Eq. (1)–(5) along with the boundary conditions Eqs. (6*a*)–(6*d*) were solved using the commercial finite-volume based solver Fluent. The governing equations for momentum and energy in conservative form were discretized with finite-volume formulation using a fully implicit higher-order upwind differencing scheme. The scheme was second-order accurate in space and first-order accurate in time. The momentum equations are first solved implicitly with an estimated pressure field. Subsequently a pressure–velocity correction based on the SIMPLEC algorithm is performed until a divergence-free velocity field is obtained. A divergence-free criterion of 10^{-3} based on the scaled L_1 norm of the residual is prescribed for the computations. The largest absolute value of the residual in the last five iterations was typically used as the scale factor. The equations are integrated in time until a statistically stationary state for the area-averaged heat flux is reached. All computations were performed on four processors of an IBM p690 cluster with 128 GB RAM and 1.3 GHz CPUs at the National Center for Supercomputing Applications (NCSA).

2.4 Overall Friction Factor and Colburn *j* Factor Calculations. The overall heat transfer and pressure drop performance of the system for a given flow condition can be characterized by Colburn j factor and friction factor f, respectively. The flow condition is defined in terms of Reynolds number, $\mathrm{Re} = V_m D_h / \nu$, where V_m is the mean velocity at the minimum flow cross-sectional area, $A_{\min}$, and D_h is the hydraulic diameter. The f factor as the measure of pressure drop is given by

$$f = \frac{\Delta P}{\frac{\rho V_m^2}{2}\frac{A_T}{A_{\min}}} \tag{7}$$

where A_T is the total heat transfer surface area and ΔP is the pressure drop across the computational domain. The Colburn j factor is expressed as

$$j = \mathrm{St} \cdot \mathrm{Pr}^{2/3} \tag{8}$$

$$\mathrm{St} = \frac{h}{\rho V_m c_p} \tag{9}$$

The heat transfer coefficient, h, appearing in the Stanton number, is defined in terms of the area-weighted average heat flux, $q_{\mathrm{av}} = 1/A\int_{D^2} q\, dA$ and the logarithmic mean temperature difference (LMTD)

$$h = \frac{q_{\mathrm{av}}}{\mathrm{LMTD}}, \quad \mathrm{LMTD} = \frac{\Delta T_o - \Delta T_i}{\ln(\Delta T_o/\Delta T_i)} \tag{10}$$

$$\Delta T_i = T_{a,i} - T_w \tag{11}$$

and

$$\Delta T_o = T_{a,o} - T_w$$

where $T_{a,i}$ and $T_{a,o}$ are the mean air inlet and outlet temperatures and T_w is the specified tube wall temperature.

3 Validation of Numerical Results

Numerical accuracy and resolution are important issues in time-dependent calculations in complex geometries. The three-dimensional vortex enhanced multirow fin-and-tube geometry has the potential for generating highly complex velocity and thermal fields. Hence, the grid must be designed a priori with great care such that important scales (energy containing eddies) are appropriately captured, and the near-wall gradients are adequately resolved. The computational meshes were generated with Gambit-2.2.3 using multiblock hybrid approach. The computational domain was divided into several subdomains, and structured meshing was preferred (where feasible) since aligning the grid with flow has certain advantages in avoiding undesirable numerical diffusion. In general, mild stretching of the mesh was employed toward the fin walls and clustered in the vicinity of the tube where the gradients were expected to be large. The mesh topology was determined by refining the mesh until grid independence of the flow field solution was achieved. Grids consisting of about 110,000, 350,000, and 600,000 cells were tested for both baseline and vortex-enhanced cases. The overall area-weighted average heat flux was observed to change by only 3% between the two highest grid density solutions. The final mesh size used was about 560,000 control volumes for the baseline configuration and 670,000 for the winglet enhanced heat exchanger model (cf. Fig. 1(*d*)).

Apart from the grid independency study, we also compared the overall heat transfer performance with the available experimental results [6]. For the heat transfer, the predicted area-weighted heat fluxes were always within 7% of the experimental results, with 80% of the predictions within 5% of the experimental results. The Colburn j factor and friction factor predictions are compared to measured results in Fig. 3. The excellent agreement between the predicted and measured heat transfer results indicates that the simplifications associated with using Eq. (5) to model conjugate effects do not vitiate the predictive ability of the model. The f factor is consistently underpredicted by 14.6%. In the experimental study, the vortex generators were mounted on metallic strips (about 720) which were then glued to the fin surface. The numerical models did not take into account the finite thickness of the winglets and the metallic strips which contribute to extra pressure drop by increasing V_m and potentially by locally tripping the flow.

4 Results and Discussion

The flow and heat transfer behavior of the baseline fin-and-tube geometry with multiple tubes is well understood [11–13]. Here we focus on the flow and heat transfer characteristics of the winglet arrays in such a geometry. Prior to examining the thermal-hydraulic performance of the enhanced configurations, it is useful to analyze the dominant flow structures relevant to pressure drop and heat transfer in these heat exchangers. Details of the local

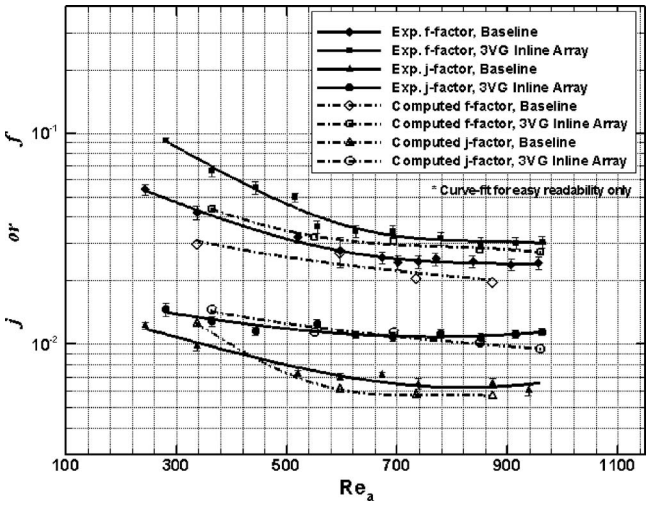

Fig. 3 Computed and measured (from Ref. [6]) friction factor and Colburn *j* factor at different air-side Reynolds number for baseline and 3VG array configuration

flow patterns around the winglets in a common-flow-up configuration for an inline tube geometry are discussed in the following subsections. Finally, local and overall heat transfer results are presented.

4.1 Longitudinal Vortex Systems. An effective way to visualize the flow is to consider the numerically generated pathlines, as shown in Fig. 4, capturing the swirling motion associated with the system of vortices generated by a winglet pair. As expected the flow in the region common to the two vortices is directed away from the fin ($z=0$) on which the winglets are mounted. The induced spanwise velocity of the vortex enhances transport from fluid in the tube wake to the mainstream regions and vice versa. The fluid in the recirculating wake regions is closer to the tube temperature than that in the mainflow, and these areas represent regions of low heat flux. The enhanced mixing between tube wake and mainstream by the swirling vortex flow is one important mechanism of heat transfer enhancement. Another important enhancement mechanism is the modification of near-wall temperature gradients due to the induced wall-normal flow. In the present winglet-pair configuration, for the fin mounted with winglets ($z=0$ wall), the region between the vortex cores and fin edge is the inflow region (downwash or flow toward the wall) where the heat

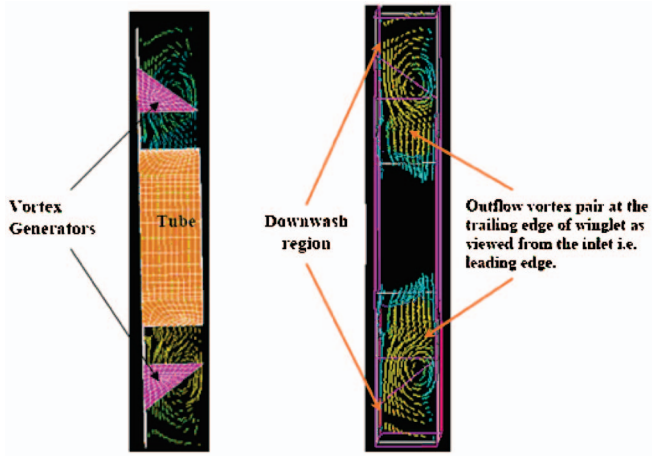

Fig. 4 Pathlines downstream of trailing edge of winglets showing the so called "outflow vortex pair"

transfer enhancement is manifest (see Fig. 4). Correspondingly, for the nonwinglet fin ($z=3.6$ mm), this region constitutes an outflow (upwash) region which is associated with decrease in heat transfer. Similarly, if we focus on the region between the cores of the two vortices, it constitutes an upwash region for the VG fin and a downwash for the non-VG fin. The heat transfer enhancement in downwash region, due to a larger temperature gradient, is greater than the degradation in the upwash regions; a net enhancement results. The situation is analogous to that which occurs in boundary layer flows with suction and blowing at the wall. For those flows it is well known that for the same value of wall-normal velocity the suction (downwash) case results in greater heat transfer enhancement than the degradation due to blowing (upwash). This observation has been attributed to the nonlinear nature of the convection–diffusion process. Although in the present geometry fully developed flow prevails, the heat transfer behavior is still governed by these processes, as discussed in more detail with the local heat transfer behavior.

In addition to the longitudinal vortices caused by the winglet pairs, horseshoe vortices are apparent near the tubes. For a single fin-and-tube junction, this well-known secondary flow occurs when the channel flow approaches the tube. The adverse pressure gradient upstream of the stagnation point on the tube acts on the approaching flow to decrease the local velocity. Fluid near the fins approaches this region with a lower velocity than does fluid near the channel centerline, and the adverse pressure gradient reverses the flow near the fins in the vicinity of the stagnation point on the tube. The result is the formation of a vortex system that is advected around the tube to form the horseshoe vortex. For an inline-tube arrangement the system is more complex, but the same interplay of pressure and inertia is the basis for vortex formation. In terms of Kelvin's circulation theorem, the transverse vorticity of the channel flow approaching the tube is conserved (except for small dissipation through viscous effects) and is carried around the tube and redirected into the streamwise direction. The horseshoe vortex system modifies the temperature field through the same mechanisms as winglet-generated vortices and can have a profound effect on local convection and wall shear. Vorticity magnitude contours, obtained from calculated velocity gradients along the channel centerline, are plotted in Fig. 5(*a*). For the sake of clarity, results are provided only for the first two tube rows, but the vortical systems associated with downstream tube rows are typical to those shown in the plot. The plots of vorticity magnitude clearly show that coherent vortical structures are formed by the winglet generators and the fin–tube junctions. The winglet-generated vortices persist for several wing spans downstream and act over large fin areas with relatively high-magnitude vorticity. The horseshoe vortices persist over the entire inter-tube space, likewise covering a large fin area. It is particularly important to note that the horseshoe vortex system exists in the baseline heat exchanger (Fig. 5(*b*)), and that the VG design adopted in this study does not destroy the naturally occurring horseshoe vortices. Deploying VGs in a way that destroys (or significantly reduces) the horseshoe vortices would vitiate the enhancement strategy. These flow features will be discussed quantitatively, as will their impact on heat transfer, later.

It is of considerable interest to know the effect of the inline tube pattern on the strength and longevity of the longitudinal vortex system in order to assess their efficacy in such geometry. For this purpose we examine the streamlines on the cross-stream planes at different axial locations for the single VG pair and 3VG-inline-array configurations as shown in Fig. 6. The axial locations are chosen at the minimum free flow areas corresponding to the tube centers as marked on the figure. Also indicated is the net circulation, or vortex strength. The total circulation was calculated by the area integral over magnitude of vorticity vector. The area integral was evaluated by summing the vorticity multiplied with the incremental area of the computational grid. The net circulation, or vortex strength, for the winglet-enhanced configurations were obtained by subtracting the total circulation of the baseline geometry from their respective total circulation. The circulation was defined in this manner because it is difficult to isolate the winglet induced main vortex from other vortical structures present (refer to Fig. 5(*a*)). The complex wake structure generated by a winglet has also been investigated in detail by Biswas et al. [17] for channel flows. These structures may have different rotational directions which could cancel while performing surface integral at any cross-sectional plane. The use of vorticity magnitude obviates this problem and the net circulation provides a meaningful way to eliminate wall contributions. A representative calculation, however, of the computed circulation of an isolated main vortex immediate downstream of the winglet showed a value of 3.4×10^{-3} m^2/s. Gentry and Jacobi [18] reported experimental values on the order of 2.0×10^{-4} m^2/s for the delta-wing induced tip vortex in channel flow at a higher Reynolds number. Differences in wing and channel geometry and the somewhat higher Reynolds number notwithstanding, the comparison lends indirect support to present calculations. For the single-VG pair, Fig. 6(*a*) indicates progressive decay in the vortex strength with the downstream distance from the winglet as would be expected. Streamlines at the second tube also reveal the presence of secondary flow structure but none is evident for tubes 3–7. For the 3VG-inline-array configuration, Fig. 6(*b*) shows streamlines on the cross-stream plane at the axial locations of 0.0381 m, 0.0889 m, 0.1397 m, and 0.1651 m from the leading edge which correspond to the center planes of nonVG tubes 2, 4, 6, and 7, respectively. From the figure it can be seen that the inline winglet array results in a more complex pattern of

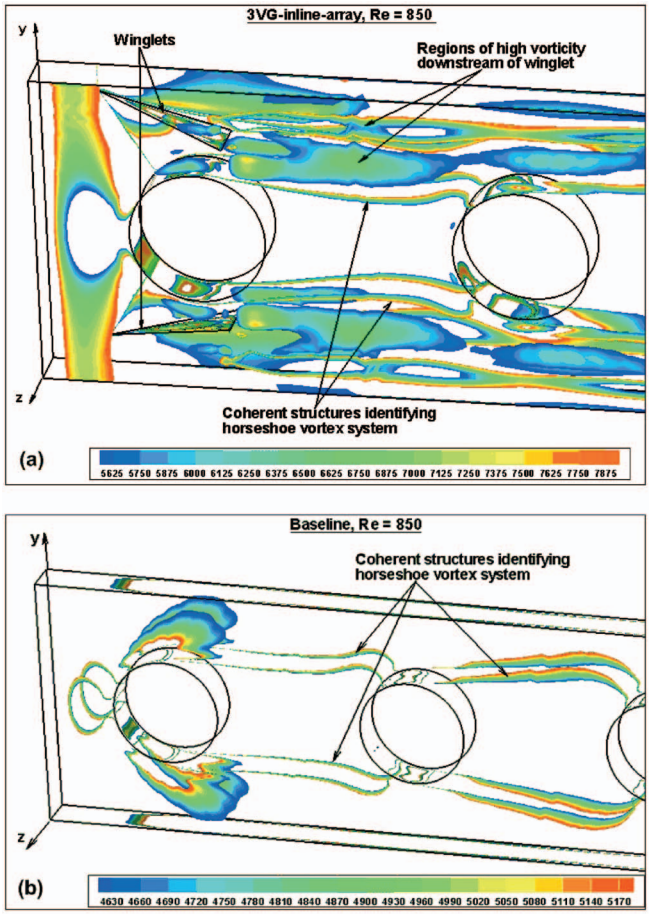

Fig. 5 3D iso-vorticity (magnitude) surfaces plotted in a selected range to identify the horseshoe vortex systems occurring at the junction of fin and tube for: (*a*) 3VG-inline array; and (*b*) baseline configurations

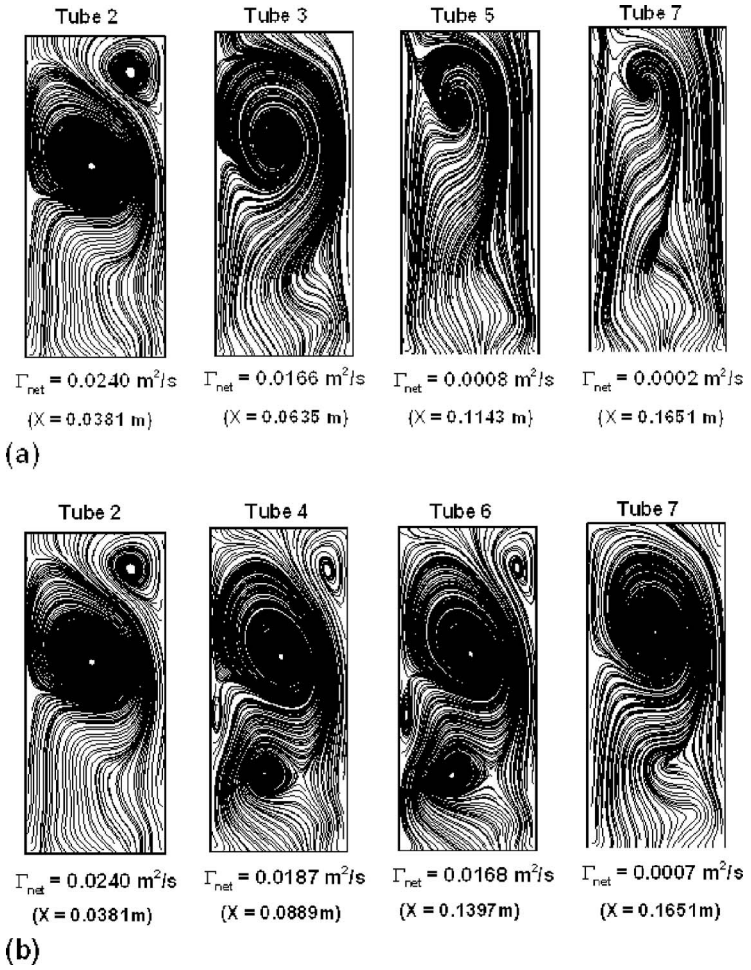

Fig. 6 Streamlines on the cross-sectional planes (top half only) at different axial locations coinciding with the indicated tube centers at Re=850: (*a*) single-VG-pair; and (*b*) 3VG-inline-array configuration

induced vortices compared to the single VG pair configuration. Such systems of multiple induced vortices are expected to be more effective for enhancing bulk fluid mixing and hence the convective heat transfer.

Plots showing change of circulation along the streamwise direction are presented in Fig. 7. The total circulation for the baseline and the three-enhanced configurations at Re=850 is shown in Fig. 7(*a*). The baseline curve shows distinct peaks corresponding to the increase in vorticity as the flow encounters the tubes and the horseshoe vortex forms. The circulation is then observed to drop sharply as the flow enters the decelerating region on the back half of the tube. In this region the vortex line can be imagined to undergo compression, destroying vorticity until it is strengthened when the flow encounters the upstream portion of the next tube. The enhanced configurations also exhibit similar behavior. The baseline circulation curve tends to increase in the flow direction which may be due to wall effects. In Fig. 7(*b*) the effects other than vortex generators are eliminated by subtracting total circulation of the baseline geometry and the net circulation so calculated is believed to be representative of only the winglet induced vortex strength. The following regimes may be distinguished. As the flow approaches the first winglet/pair, the vortex strength increases rapidly and reaches a maximum. The single-VG pair and 3VG-inline array have peaks at Γ_{net}=0.084 m^2/s, but the 3VG-staggered array peaks at approximately half that value at Γ_{net}=0.044 m^2/s since it has only one winglet at tube 1 and the other two configurations have a pair of winglets. Once the flow crosses the tube center plane, it decelerates and the vortex strength decreases rapidly due to vortex compression, followed by a slight increase before further decrease, until it reaches the next tube. The staggered array repeats the trend at the second tube due to the presence of a winglet. In the absence of any winglet at the second tube for the other two enhanced configurations, the vortex strength continues to decrease. It is interesting to note that for a single VG pair, the rate of decrease in Γ_{net} as the flow crosses the second tube is almost linear and significantly greater than that for the downstream tubes, 3–7. Because the vortex stretching, bending, and compression can be imagined as fairly periodic in passing from tube to tube, the overall decrease in the vortex strength can be attributed mainly to viscous diffusion due to the channel walls, tube walls, and possibly to other secondary flows. It is however clear that for inline-tube geometry with common-flow-up configuration of vortex generators, the overall impact of the presence of the tube downstream of a winglet is an accelerated decrease of the winglet vortex strength.

4.2 Tube Wake Flow. The motivation central to common-flow-up orientation of the winglet pair is to direct an accelerated flow toward the tube wake for the purposes of separation delay and wake modification. In order to assess this impact qualitatively and achieve a better understanding of the local flow structures, the streamlines on a plane parallel to z=0.1 mm—the so called limiting streamlines—are presented in Fig. 8. Such a plot allows for the identification of stagnation, separation, and other flow features relevant to the heat transfer. The first tube is mounted with a vortex generator in common-flow-up arrangement and the second

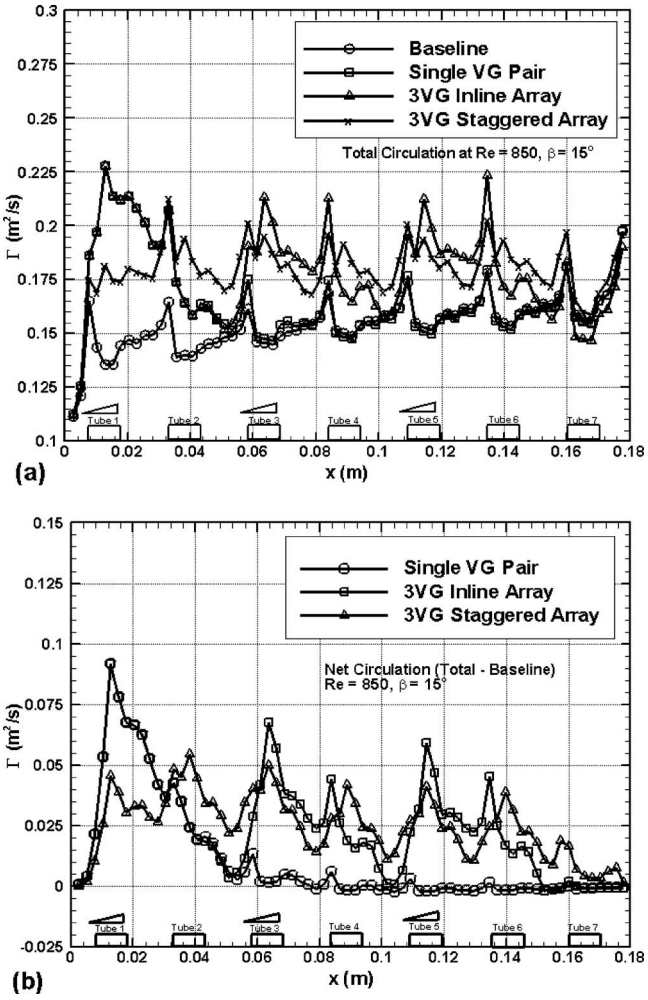

Fig. 7 Computed circulation (integral of vorticity magnitude) on the cross-stream planes at different axial locations for Re =850: (*a*) total circulation; and (*b*) net circulation for the enhanced configurations obtained by subtracting the baseline circulation from the total and is indicative of the winglet induced vortex strength

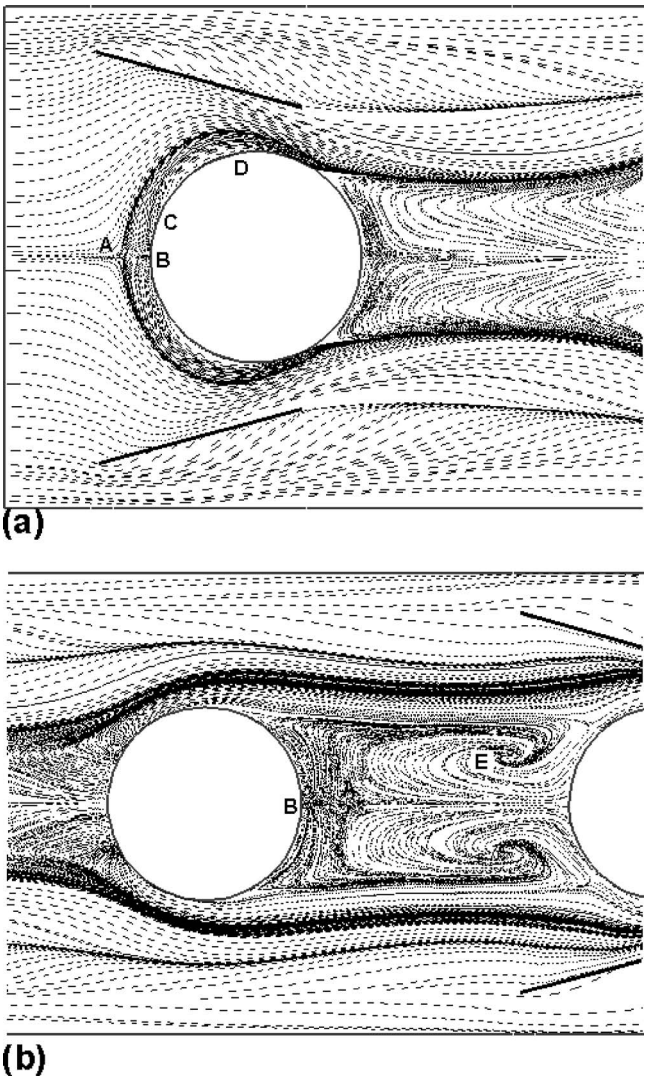

Fig. 8 Limiting streamlines on a plane close to the fin mounted with the vortex generators at Re=850 showing the singular points for flow in the vicinity of: (*a*) first tube; and (*b*) second tube: *A*=saddle point of separation, *B*=nodal point of attachment, and *E*=focus

tube is without a vortex generator. The streamlines were computed at Re=850. As the incoming flow approaches the tube, it reaches a stagnation or saddle point (labeled A) and bends around the tube to flow downstream. Horseshoe vortices are formed in the front of the tube near the bounded fin surface and can be identified in Fig. 8(*a*). A nodal point (labeled *B*) near the tube wall clearly indicates the presence of the horseshoe vortex. On either side of the tube, one finds a region of converging streamlines (labeled *D*). These are the traces of the horseshoe vortices. Behind the first tube, two symmetric zones of circulating flow are evident. The recirculating flow is separated from the main flow, and fluid in this region is thermally isolated, resulting in a region of lower heat transfer. In the region between the winglet and the tube (near *D*), the flow is accelerated by the nozzle-like geometry. This high-velocity fluid will impinge on the downstream tube, and result in a local heat transfer enhancement. In the absence of a vortex generator, the wake structure of the second tube, as shown in Fig. 8(*b*), markedly differs from the first row tube. The presence of the wake stagnation and a saddle point of separation in this zone are indicative of a reversed flow. When this flow encounters the tube downstream, the streamlines produce a focus (labeled *E*). A focus differs from a nodal point in that it has no common tangent line and infinite number of streamlines spiral around it. The focus here is on the separation type since the streamlines spiral into the singular point. The flow is characterized by an early separation from the tube and wider wake compared to the first row VG tube. Hence the common-flow-up orientation of the winglets as employed here acts to delay the separation from the tube resulting in reduction of the recirculation zone size. The reduced size of recirculation zone and the impingement of the winglet-induced accelerated flow on the downstream tube in turn augments heat transfer.

4.3 Heat Transfer and Pressure Drop Performance. Time-dependent simulations in the three-dimensional VG enhanced geometry were performed for a sample test case. No initial assumption was made regarding the development of flow and thermal conditions. The temporal evolution of the spatially averaged total surface heat flux was monitored and the simulations were terminated once it reached a statistically steady state. The steady-state heat transfer and pressure drop performance for the two vortex-enhanced configurations were compared to the baseline (no winglets) case. The computations were performed at air-side flow conditions corresponding to Re=850. The heat transfer parameters were selected from the experimental work as reported elsewhere [6]. The simulation parameters are summarized as follows:

(Re=850):

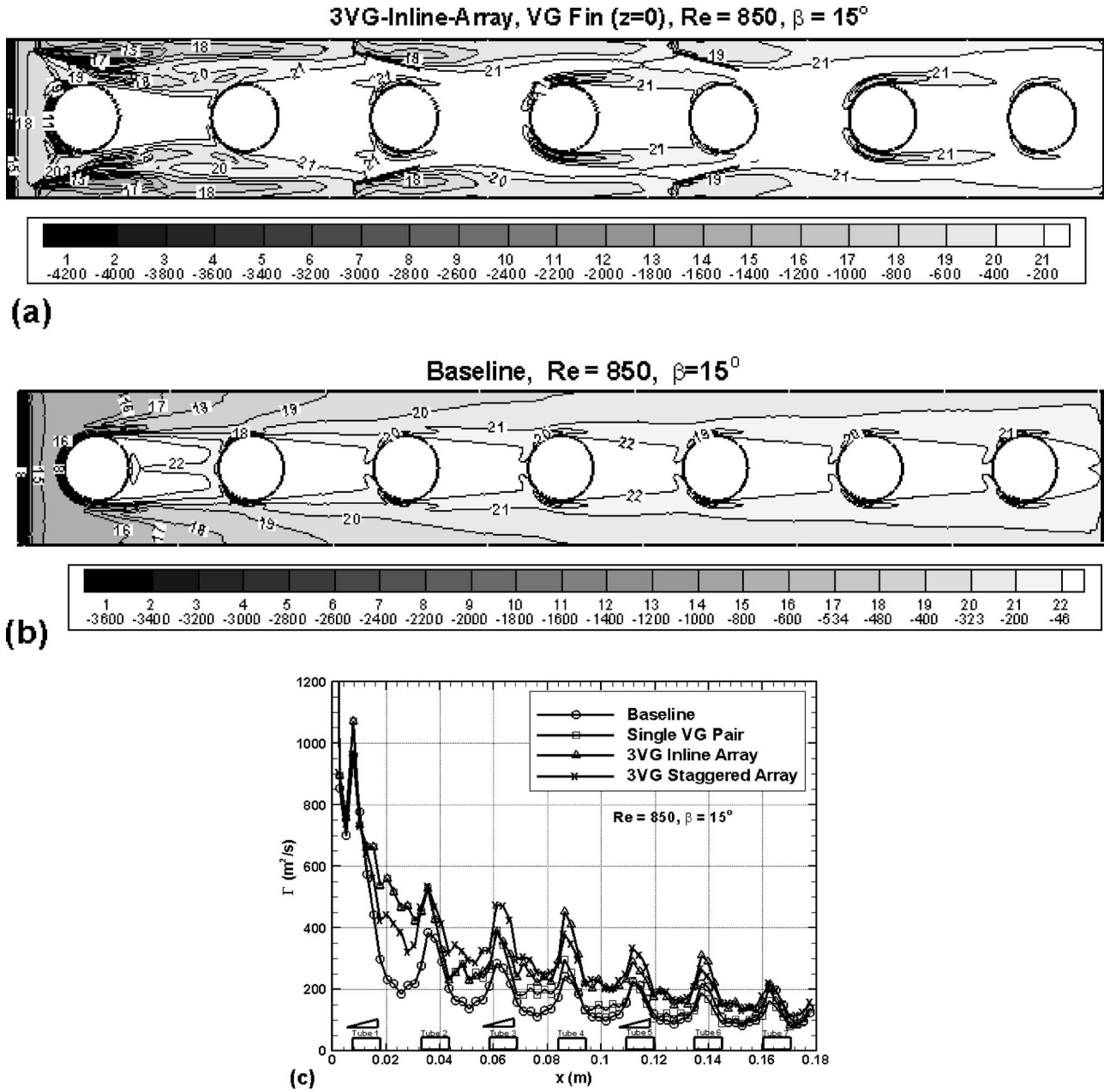

Fig. 9 Local heat flux distribution on the VG fin (*z*=0) for: (*a*) 3VG-inline-array configuration; and (*b*) baseline configuration at Re=850; (*c*) line-weighted average heat flux distribution at different axial locations on the VG fin for all four configurations

- air inlet velocity: 1.8 m/s;
- air inlet temperature: 310.6 K;
- tube temperature: 291.77 K (calculated from the mean coolant inlet and outlet temperatures and coolant side heat transfer coefficient); and
- time step size: 0.005 s

The local heat flux distribution on the VG mounted fin ($z=0$) for 3VG-inline-array configuration is shown in Fig. 9(*a*). A similar plot for baseline geometry is also shown for comparison at Fig. 9(*b*). Several distinct heat transfer regions can be distinguished as follows. At the leading edge of the fin, the heat flux starts with a very high value and then decreases rapidly. This behavior is attributable to the development of a thermal boundary layer on the fin wall. At the leading tube, a zone of high heat flux is observed at the front part of the fin–tube junction. This results from the formation of the horseshoe vortex system that consists of two slender counter-rotating longitudinal vortices as discussed earlier. The two legs of the horseshoe vortices wrap around the front half of the tube and extend to the rear of the tube leading to enhancement of local convective heat transfer. The local heat flux values at the finned region between the tube and winglet is observed to be lower than the outer region between the winglet and fin edge, which is contrary to what might be anticipated when considering the local acceleration of the flow. However, the vortex generated by the winglet causes a surface normal outflow (upwash) near the tube and an inflow (downwash) near the outer edge of the fin. As discussed earlier, these flow features have a profound effect on the local convective behavior, and that effect explains the flux distribution. Similar effects are also observed for second and third winglet pairs. The vortices bring about a better thermal mixing and boundary layer modification in the wake region which results in improved heat transfer. The front part of tubes downstream of the vortex generators, i.e., tubes 2, 4, and 6, are also seen to have

high heat flux compared to the surrounding areas. The accelerated fluid in the tube–winglet region impinges on the downstream tube to bring about heat transfer enhancement as discussed in more detail below.

The line-weighted average heat flux distribution on the VG-mounted fin ($z=0$) for the baseline and the three-vortex-generator enhanced configurations are compared in Fig. 9(c). The baseline curve shows distinct peaks at regular intervals in the streamwise direction, corresponding to the locations where a tube is approached by the flow. However, it is interesting to note that the peak value of q_{av} for the second tube is 384.4 W/m^2 as compared to 953.4 W/m^2 for the first tube. The decrease by about a factor of 2.5 for the first and second tube is comparatively larger than that between all subsequent tubes. This is primarily due to the high driving potential for heat transfer existing at the entrance region and also to the formation of horseshoe vortices as explained earlier. It may be noted that due to the inline pattern of the tubes, the second and all subsequent tubes are in the wake of their upstream tube. Up to the location of the leading edge of the winglets, the q_{av} distribution is almost the same for all the cases with and without winglets. However, beyond that location, the decrease is identical for 3VG-inline array and single-VG pair up to the leading edge of the third tube. After the third tube, the heat transfer performance of the single-VG pair gradually approaches that of the baseline case. In the case of 3VG-inline array, the peak value of q_{av} is observed to be high for tubes 2, 4, and 6 with lower values for tubes 3 and 5. In contrast, for the 3VG-staggered array, the peak q_{av} smoothly decreases from tubes 2–7. However, the net heat transfer for both the 3VG configurations is nearly the same.

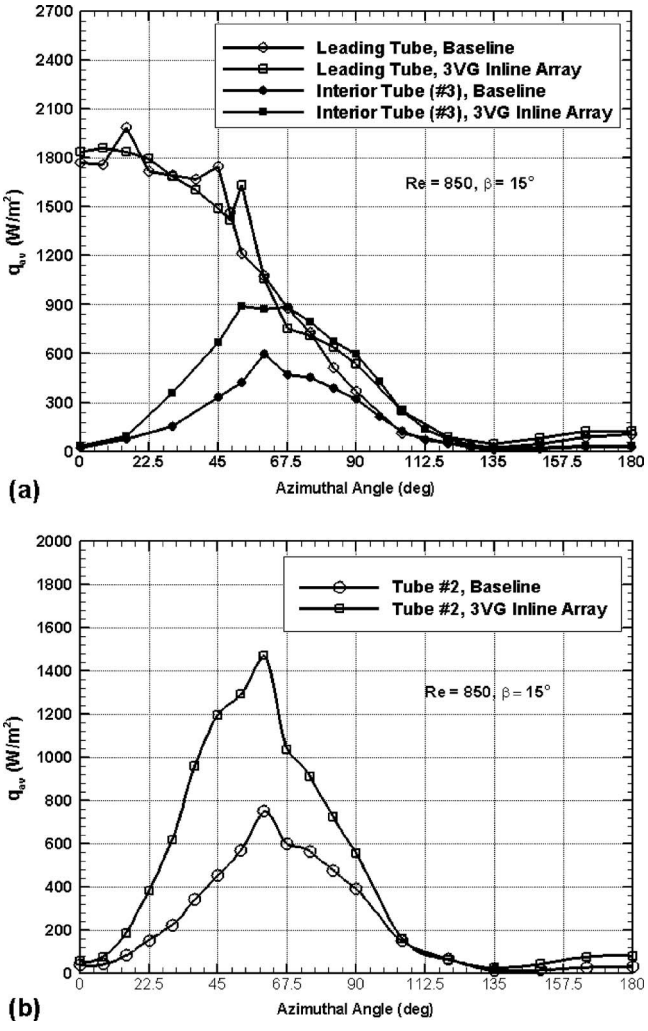

Fig. 10 Distribution of span-averaged tube surface heat flux along tube circumference for baseline and winglet—enhanced configurations at Re=850 (*a*) tube with VG, both leading and interior; and (*b*) tube downstream of VG

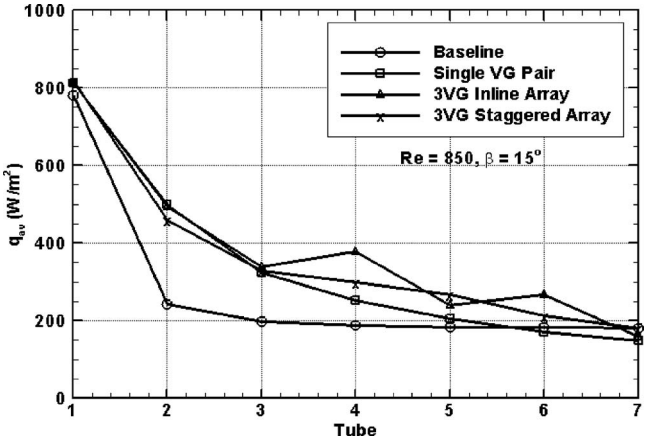

Fig. 11 Steady-state area-averaged total tube surface heat flux for baseline and different winglet—enhanced configurations at Re=850

The effect of vortex generators in common-flow-up orientation on the tube surface heat transfer is explored in Fig. 10 where the span-averaged (tube) heat flux distribution is shown along the circumference. The results pertaining to 3VG-inline array are compared to the baseline case. Of course, due to symmetry the conclusions are also valid for two other winglet configurations. Both, the leading tube and an internal tube (Third) case are shown in Fig. 10(a) for a winglet attack angle of 15 deg. It is clear that the influence of VG on the heat transfer performance of the leading tube is small. The formation of horseshoe vortices at the tube and wall junction, as explained earlier, and the existence of a high driving potential are dominant, and the effect of the winglets is not profound. However, winglet-induced effects on tube–surface heat transfer are important for an interior tube. Heat flux enhancements of up to 47% are observed. Figure 10(b) shows local heat transfer performance along the circumference of the tube immediately downstream of a winglet (Second tube). The effect of the winglet in common-flow up is more dramatic in this case—a finding not recognized in earlier studies. Both of the curves show very similar trends of azimuthally varying heat flux with a distinct peak at 16 deg. The maximum values of q_{av} are 749.7 W/m^2 and 1471.2 W/m^2 for the baseline and 3VG-inline array, amounting to a 96% enhancement. The flow passage between the winglet and the curved surface of the tube progressively narrows and geometrically resembles a nozzle-like configuration. The fluid accelerates in the constricted passage and impinges on the downstream tube. The significant enhancement observed in local heat transfer from the winglet-downstream tube surface is attributable to the flow impingement effect. The area-averaged heat fluxes from individual tubes for the baseline and the three enhanced configurations are presented in Fig. 11. The 3VG-inline array causes enhancements of about 105%, 72%, 102%, 30% and 46% for the 2nd–6th tubes, respectively. The heat transfer performance for the first and seventh tube is almost identical for all configurations. It is interesting to note that for the single-VG pair and the two 3VG-array cases, the heat transfer rates are equal at the third tube, even though the latter has a pair of winglets at that tube. Apparently the influence of the upstream winglet at the first tube is manifest at the third tube but does not have an important influence on the second tube. On the whole, these results indicate that the common-flow-up orientation has a significant impact on the heat transfer performance from the tube surface in addition to the fin surface

Table 1 Summary of overall heat transfer and pressure drop performance: test conditions: $u_\infty = 1.8$ m/s, $T_a = 310.6$ K, $T_w = 291.77$ K

	Computed results			% Increase in Capacity and friction factor	
	q (W/m^2)	j factor	f factor	$\Delta q/q_{\text{base}}$	$\Delta f/f_{\text{base}}$
Baseline	266.8	0.00573	0.02033	1	1
Single-VG pair	313.9	0.007427	0.02287	17.7%	12%
3VG-inline array	353.1	0.01000	0.02857	32.3%	41%
3VG-staggered array	351.6	0.00893	0.02694	31.8%	33%

enhancements.

Finally, the computational results, in terms of the overall area-weighted average surface heat flux and core pressure drop, are summarized in Table 1. The results show considerable enhancement of total surface heat fluxes with modest pressure-drop penalties. Interestingly, both 3VG array configurations show heat transfer augmentation of about 32%, but they have pressure-drop increases of 33% and 41% for the staggered and inline array, respectively. The leading-edge winglet pair resulted in heat transfer enhancements of 18.3% and a pressure-drop increase of 31%. These results demonstrate that vortex generator arrays in a common-flow-up orientation can cause significant augmentation in heat transfer capacity for multirow heat exchanger geometries. Using such enhancements, the heat exchangers could be designed to be more compact in size and economical in cost. If this potential area reduction is exploited by decreasing the flow depth of the heat exchanger, then the pressure-drop penalty can be reduced.

5 Conclusions

In this work, numerical simulations have been employed to explore the flow and heat transfer in multirow plain-fin-and-tube heat exchangers with an inline tube pattern. Apart from the baseline case, the three winglet enhanced configurations chosen for study were: (a) a single VG pair; (b) a 3VG-inline array (alternate tube); and (c) a 3VG-staggered array. The time-dependent, three-dimensional Navier–Stokes and energy equations were solved in a computational domain chosen to cover the entire fin length in the air flow direction. This approach has been shown to be a powerful tool in understanding the flow structure and predicting the thermal-hydraulic performance of the winglet-enhanced geometry. The major conclusions are summarized as follows:

1. Channel flow with a circular tube and delta-winglet vortex generators has been studied for a seven-row inline-tube pattern heat exchanger. Two systems of longitudinal vortices are generated: the horseshoe vortices that naturally form at the tube-and-fin junction, and the winglet-induced streamwise vortices. The heat transfer from the leading tube is significantly higher than for the other tubes, due to the horseshoe vortex system, locally high-temperature difference, and absence of an upstream tube wake. The horseshoe vortices are less important to heat transfer enhancement for downstream tubes.
2. The winglet-generated vortices are periodically subjected to accelerated and decelerated flow, due to flow confinement effects of the inline tube pattern. These local effects cause vortex straining and increased or decreased vortex strength, depending on whether the vortex is stretched or compressed.
3. The common-flow-up orientation of the winglet creates a constricted, nozzle-like passage between the winglet and tube surface. The flow accelerates in this region to suppress the wake and delay separation. These effects were small on the tube neighboring the winglets; however, it was found that the impingement of this accelerated flow on the downstream tube caused significant enhancement of local heat transfer.
4. The local distribution of the heat flux on the fin surface revealed good enhancement in the downwash regions of the vortices, near the winglet and extending a few chord lengths downstream.
5. At Re=850, the VG-enhancement strategies studied in this work can provide an overall heat transfer enhancement of about 32%, with a similar pressure-drop penalty. If the enhancement is exploited by reducing the flow length of the heat exchanger, the pressure-drop penalty can be reduced.

Acknowledgment

The authors would like to thank Mike Heidenreich (project monitor) and Advanced Heat Transfer, LLC, USA for financial support of this work. Supercomputing time on an IBM P690 machine was provided by the NSF PACI program through the Development Allocation Committee (DAC) of the National Center for Supercomputing Applications (NCSA) at the University of Illinois is also gratefully acknowledged.

Nomenclature

$A_{\min}$ = minimum flow cross-section area (m^2)
A_T = total heat transfer surface area (m^2)
b = span of delta wing (m)
B = transverse width of the fin (m)
Bi = Biot number
c = delta wing chord length (m)
c_p = specific heat at constant pressure (kJ/kg K)
D = computational domain
D_h = hydraulic diameter$=4A_{\min}L/A_T$ (m)
f = friction factor
Fi = fin efficiency parameter$=(k_f/k)(\delta/H)$
h = convective heat transfer coefficient (W/(m^2 K))
H = spanwise adjacent fin spacing (m)
j = Colburn j factor (Nu/RePr$^{1/3}$)
k = thermal conductivity (W/(m K))
L = fin length (m)
n = outward normal direction
P = total pressure (Pa)
ΔP = air-side pressure drop across the heat exchanger (Pa)
Pr = Prandtl number, ν/α
q = local heat flux (W/m^2)
q_{av} = area-averaged heat flux (W/m^2)
$\dot{q}$ = volumetric source term (W/m^3)
Re = Reynolds number based on hydraulic diameter
t = time (s)
t_f = fin thickness
T = temperature (K)

$\vec{u}$ = velocity in x, y, and z directions, u, v, w
U = overall heat transfer coefficient $(W/(m^2)\,K)$
V_m = mean velocity at $A_{min}(m/s)$

Greek Letters

α = thermal diffusivity (m^2/s)
β = wing angle of attack
ρ = mass density of fluid (kg/m^3)
ν = kinematic viscosity (m^2/s)
Γ = circulation or vortex strength (m^2/s)
Λ = wing aspect ratio $=2b/c$
Δ = increment

Subscripts

a = air
f = fin
i = inlet of heat exchanger
o = outlet of heat exchanger
w = tube wall
∞ = based on freestream

References

[1] Fiebig, M., Mitra, N., and Dong, Y., 1990, "Simultaneous Heat Transfer Enhancement and Flow Loss Reduction of Fin-Tubes," *Heat Transfer*, G. Hetsroni, ed., Vol., 3, Hemisphere, Washington, D.C., pp. 51–55.

[2] Fiebig, M., Valencia, A., and Mitra, N. K., 1993, "Wing-Type Vortex Generators for Fin-and-Tube Heat Exchangers," Exp. Therm. Fluid Sci., **7**, pp. 287–295.

[3] Biswas, G., Mitra, N. K., and Fiebig, M., 1994, "Heat Transfer Enhancement in Fin-Tube Exchangers by Winglet Type Vortex Generators," Int. J. Heat Mass Transfer, **37**, pp. 283–291.

[4] Torii, K., Kwak, K. M., and Nishino, K., 2002, "Heat Transfer Enhancement Accompanying Pressure-Loss Reduction With Winglet-Type Vortex Generators for Fin-Tube Heat Exchanger," Int. J. Heat Mass Transfer, **45**, pp. 3795—3801.

[5] Kwak, K. M., Torii, K., and Nishino, K., 2003, "Heat Transfer and Pressure-Loss Penalty for the Number of Tube Rows of Staggered Finned-Tube Bundles with a Single Transverse Row of Winglets," Int. J. Heat Mass Transfer, **46**, pp. 175—180.

[6] Joardar, A., Jacobi, and A. M., 2007, "Heat Transfer Enhancement by Winglet-Type Vortex Generator Arrays in Compact Plain-Fin-and-Tube Heat Exchangers," Int. J. Refrigeration, accepted.

[7] ElSherbini, A., and Jacobi, A. M., 2002, "The Thermal-Hydraulic Impact of Delta-Wing Vortex Generators on the Performance of a Plain-Fin-and-Tube Heat Exchanger," J. HVAC&R Res., **8**, pp. 357–370.

[8] Sommers, A. D., and Jacobi, A. M., 2005, "Air-Side Heat Transfer Enhancement of a Refrigerator Evaporator Using Vortex Generation," Int. J. Refrig., **28**(7), pp. 1006–1017.

[9] Joardar, A., and Jacobi, A. M., 2005, "Impact of Leading Edge Delta-Wing Vortex Generators on the Thermal Performance of a Flat Tube, Louvered-Fin Compact Heat Exchanger," Int. J. Heat Mass Transfer, **48**, pp. 1480–1493.

[10] Fiebig, M.,, Grosse-Gorgemann, A., Chen, Y., and Mitra, N. K., 1995, "Conjugate Heat Transfer of a Finned Tube Part A: Heat Transfer Behavior and Occurrence of Heat Transfer Reversal," Numer. Heat Transfer, Part A, **28**(2), pp. 133–146.

[11] Fiebig, M., Chen, Y., Grosse-Gorgemann, A., and Mitra, N. K., 1995, "Conjugate Heat Transfer of a Finned Tube Part B: Heat Transfer Augmentation and Avoidance of Heat Transfer Reversal by Longitudinal Vortex Generators," Numer. Heat Transfer, Part A, **28**(2), pp. 147–155.

[12] Bastani Jahromi, A. A., Mitra, N. K., and Biswas, G., 1999, "Numerical Investigations on Enhancement of Heat Transfer in a Compact Fin-and-Tube Heat Exchanger Using Delta Winglet Type Vortex Generators," J. Enhanced Heat Transfer, **6**(1), pp. 1–11.

[13] Jain, A., Biswas, G., and Maurya, D., 2003, "Winglet-Type Vortex Generators With Common-Flow-Up Configuration for Fin-Tube Heat Exchangers," Numer. Heat Transfer, Part A, **43**, pp. 201–219.

[14] Jang, J. Y., Wu, M. C., and Chang, W. J., 1996, "Numerical and Experimental Studies of Three Dimensional Plate-Fin-and-Tube Heat Exchangers," Int. J. Heat Mass Transfer, **39**(14), pp. 3057—3066.

[15] Tutar, M., and Akkoca, A., 2004, "Numerical Analysis of Fluid Flow and Heat Transfer Characteristics in Three Dimensional Plate Fin-and-Tube Heat Exchangers," Numer. Heat Transfer, Part A, **46**, pp. 301–321.

[16] Mendez, R. R., Sen, M., Yang, K. T., and McClain, R., 2000, "Effect of Fin Spacing on Convection in a Plate Fin and Tube Heat Exchanger," Int. J. Heat Mass Transfer, **43**, pp. 39–51.

[17] Biswas, G., Torii, K., Fujii, D., and Nishino, K., 1996, "Numerical and Experimental Determination of Flow Structure and Heat Transfer Effects of Longitudinal Vortices in a Channel Flow," Int. J. Heat Mass Transfer, **39**(16), pp. 3441–3451.

[18] Gentry, M. C., and Jacobi, A. M., 2002, "Heat Transfer Enhancement by Delta-Wing-Generated Tip Vortices in Flat-Plate and Developing Channel Flows," J. Heat Transfer, **124**, pp. 1158–1168.

Local Heat Transfer Coefficients Induced by Piezoelectrically Actuated Vibrating Cantilevers

Mark Kimber

Suresh V. Garimella[1]
e-mail: sureshg@purdue.edu

Arvind Raman

NSF Cooling Technologies Research Center,
School of Mechanical Engineering,
Purdue University,
585 Purdue Mall,
West Lafayette, IN 47907-2088

Piezoelectric fans have been shown to provide substantial enhancements in heat transfer over natural convection while consuming very little power. These devices consist of a piezoelectric material attached to a flexible cantilever beam. When driven at resonance, large oscillations at the cantilever tip cause fluid motion, which in turn results in improved heat transfer rates. In this study, the local heat transfer coefficients induced by piezoelectric fans are determined experimentally for a fan vibrating close to an electrically heated stainless steel foil, and the entire temperature field is observed by means of an infrared camera. Four vibration amplitudes ranging from 6.35 to 10 mm *are considered, with the distance from the heat source to the fan tip chosen to vary from 0.01 to 2.0 times the amplitude. The two-dimensional contours of the local heat transfer coefficient transition from a lobed shape at small gaps to an almost circular shape at intermediate gaps. At larger gaps, the heat transfer coefficient distribution becomes elliptical in shape. Correlations developed with appropriate Reynolds and Nusselt number definitions describe the area-averaged thermal performance with a maximum error of less than 12%.* [DOI: 10.1115/1.2740655]

Keywords: local heat transfer, piezoelectric fan, electronics cooling, vibrating cantilever, heat transfer enhancement

Introduction

A piezoelectric fan consists of a piezoelectric material bonded to a flexible cantilever blade. An alternating input signal causes the piezoelectric material to contract and expand, generating bending moments on the blade at the edges of the piezoelectric material. These moments produce oscillations at the free end of the cantilever blade, and when driven at the resonance frequency of the structure, the oscillations become large and serve to agitate and move the surrounding fluid, which enhances heat transfer when compared to natural convection alone. These fans consume very little power and can be built to meet different geometric constraints for many applications while remaining relatively noiseless. Because of this, piezoelectric fans offer an attractive electronics thermal management solution.

Various aspects of piezoelectric fans have been studied in the literature. A detailed analysis of the two-dimensional flow field generated from a vibrating cantilever beam was presented by Kim et al. [1]. Vortices were observed to be shed each time the beam passed the position of zero displacement, i.e., at twice the vibration frequency. The maximum fluid velocity was found to be roughly four times that of the maximum tip velocity. Açıkalın et al. [2] developed analytical models describing the streaming flow induced by a single vibrating piezoelectric fan and found good qualitative agreement between the predicted flow patterns and experimental visualizations for small displacements. Feasibility studies for implementing piezoelectric fans in electronic systems were conducted by Açıkalın et al. [3] and Wait et al. [4], where piezoelectric fans were placed within a laptop to further enhance the heat transfer performance of the rotary fan by increasing the fluid mixing in stagnant regions normally not accessed by the rotary fan. A simulated cell phone enclosure was also considered for which enhancements over natural convection were quantified for various piezoelectric fan orientations. Numerical modeling of the fluid flow and heat transfer induced by a piezoelectric fan has also been conducted [5]. The flow field generated by these fans was found to be extremely complex and highly dependent on the distance from fan tip to the heat source, as well as other boundary conditions.

The two-dimensional flow field generated from two flexible cantilevers was analyzed experimentally by Ihara and Watanabe [6]. They investigated the behavior for in-phase and out-of-phase vibration at three different pitches. The cantilevers were sandwiched between two large plates, thereby approximating a two-dimensional flow field. The results were compared to the flow field generated by a single cantilever in the same experimental setup, and the volumetric flow rate for in-phase vibration of two cantilevers was found to be approximately double that of a single cantilever. Mass transfer experiments on a vertical surface targeted by two piezoelectric fan blades were conducted by Schmidt [7] using the naphthalene sublimation technique. The fan blades vibrated out of phase and the fan pitch was kept constant. Power-law correlations were found to reasonably describe both maximum and surface-averaged Sherwood numbers for three separate distances from the vertical surface. In each case the Sherwood numbers formed contours symmetric about the midpoint of fan separation. Fluidic coupling between multiple fans was observed by Kimber et al. [8], who showed that as two fans operate in close proximity, their vibration characteristics are modified. Under in-phase vibration, this can lead to a decrease in viscous drag seen by the fans and yield a further increase in vibration amplitude; this in turn provides enhancement in the overall heat transfer. They considered multiple fan pitches for both in-phase and out-of-phase vibration, and discovered an optimal fan pitch to maximize the average heat transfer rates; this optimum was roughly equal to the vibration amplitude.

Bürmann et al. [9], Basak et al. [10], and Kim et al. [11] have explored the structural dynamics of these devices, particularly with regard to optimization by considering the mechanical work and maximum tip displacement that can be achieved, as functions of the geometric and material properties of the piezoelectric fan.

[1]Corresponding author.

Contributed by the Heat Transfer Division of ASME for publication in the JOURNAL OF HEAT TRANSFER. Manuscript received October 17, 2006; final manuscript received January 17, 2007. Review conducted by Bengt Sunden.

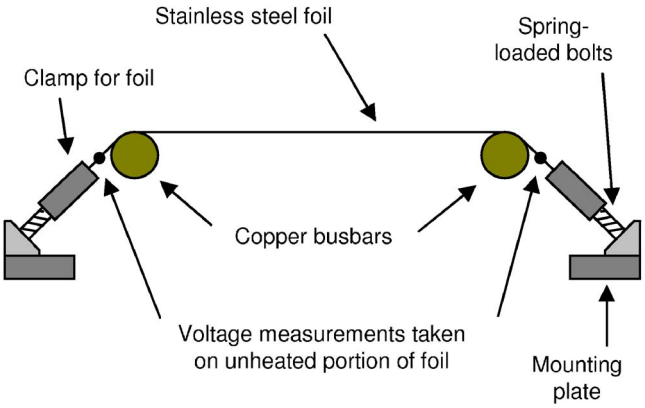

Fig. 1 Schematic diagram of constant heat flux surface

Açıkalın et al. [5] investigated a single piezoelectric fan vibrating near a small heat source to determine the conditions under which the average heat transfer could be optimized. The factors considered were fan length, vibration amplitude, frequency offset and distance from the heat source.

The present work aims at describing the behavior of the local heat transfer coefficients of flows generated from a piezoelectric fan. A detailed treatment of this topic is essential to providing insight into the underlying phenomena related to these fans, as well as to help in their implementation into practical designs.

Experimental Setup and Procedures

Details of the experimental setup for measurement of local temperature distributions are first presented, followed by methods for calculating the heat transfer coefficients and a description of the parameters of interest.

Experimental Setup. The experimental setup includes a flat, constant heat flux surface mounted in a vertical position on an optical table. Both sides of the heat source are exposed to ambient conditions. A piezoelectric fan is mounted normal to the heat source on one side (the "front" side) on a linear stage enabling precise positioning of the distance from the heat source. Only vibration in the horizontal direction is considered, and a laser displacement sensor (Keyence LK-G157) is positioned to capture the vibration signal of the fan tip. The heat source is coated on both sides with a thin layer of Krylon #1602 black paint having a known emissivity of 0.95 [12], and a thermal image of the back side of the heat source (i.e., side opposite from the fan) is captured with an infrared camera (ThermaCAM Merlin). A plexiglass enclosure is built around the entire setup to isolate it from extraneous flows within the room.

The constant-flux heat source design is similar to those in Refs. [13,14], and a schematic illustration is shown in Fig. 1. It consists of an electrically heated thin stainless steel (Type 302) foil stretched over two 25.4 mm diameter copper rods acting as busbar terminals. The foil is 0.051 mm thick and 101.6 mm wide. A power supply provides the required potential drop across the copper rods. The copper rods are located a distance of 203.2 mm apart, thereby providing a heated surface area of 101.6 mm $\times$ 203.2 mm. The unheated portions of the foil extending beyond the copper rods are clamped between two pieces of steel held together by three bolts traveling through holes in both the clamp and foil. The clamped foil is then attached to a mounting plate by means of spring-loaded bolts. The bolts are tightened to eliminate any slack at room temperature, and as the foil is heated, the springs accommodate the thermal expansion to maintain the heated foil in tension. A thick (25.4 mm) plexiglass frame holds the heater assembly together and also provides electrical isolation between the two extreme sides of the heater.

Due to the absence of an interface material or mechanical bond between the copper and stainless steel foil, the electrical contact resistance proved to be appreciable compared to the electrical resistance of the heated foil ($\sim$0.03 Ω). To account for this, voltage measurements are taken directly on the unheated ends of the foil as shown in Fig. 1, whereas the current input from the power supply is simultaneously monitored. Because current only flows through the portion of the foil between the busbars, no voltage drop occurs along the unheated length. Measuring voltage using contacts in the unheated portion avoids the problem of local cooling that would be caused if the probes were in contact with the heated portion of the foil. This method of voltage and current measurement adequately describes the power input to the heated portion of the foil without disturbing the heat transfer behavior of the heated surface.

Although the resistivity of stainless steel is temperature dependent (temperature coefficient of resistance measured to be 1.6 $\times 10^{-4}$ $\Omega/^{\circ}$C), measurements of the voltage at multiple points along the length of the heater revealed that this has no effect on the linearity of the voltage drop across the heater. As the voltage drop across the heater and the current supplied to the heater are used to calculate the local heat flux, any nominal change in resistance is accounted for, and will not have an adverse effect on the accuracy of the local heat flux estimation.

Lateral conduction effects leading to thermal smearing are estimated by analyzing the respective magnitudes of each mode of heat transfer (radiation and convective heat losses to both sides of the foil, and conduction heat transfer through the foil) compared to the overall heat generated at a specified location. Such an estimation revealed the heat transfer by lateral conduction to be less than 2% of the heat generated; smearing by lateral conduction is therefore negligible.

As the thermal conductivity of the copper busbars is much larger than that of the stainless steel, the copper can act as a local heat sink. This localized cooling effect is confined to a region close to the busbars; therefore, all the heat transfer results are reported for the portion of the heated foil sufficiently remote from the busbars. A span of foil 25.4 mm in length adjacent to each copper rod is excluded from the analysis, leaving a heated surface area of 101.6 mm $\times$ 152.4 mm that is considered in the measurements.

Local Heat Transfer Calculations. The electrically generated heat flux (q''_{gen}) is uniform across the entire heated surface, and is computed according to

$$q''_{\text{gen}} = \frac{V_s I_s}{A_{\text{heat}}} \tag{1}$$

A local flux balance is used to determine the convection coefficient due to the piezoelectric fans, as illustrated in Fig. 2. Radiation losses (q''_{rad}) on both sides of the heater are computed from the measured temperature field as

$$q''_{\text{rad}} = \varepsilon\sigma(T_s^4 - T_\infty^4) \tag{2}$$

and the heat loss by natural convection (q''_{nc}) on the side opposite the fans is found by first performing detailed experiments to determine the local natural convection coefficients (h_{nc}) and using them in:

$$q''_{\text{nc}} = h_{\text{nc}}(T_s - T_\infty) \tag{3}$$

The remaining component of the heat generated is dissipated as q''_{mix} by mixed convection with contributions from both forced convection (due to the piezoelectric fan) and natural convection. The relationship in such a regime can be expressed according to [15]:

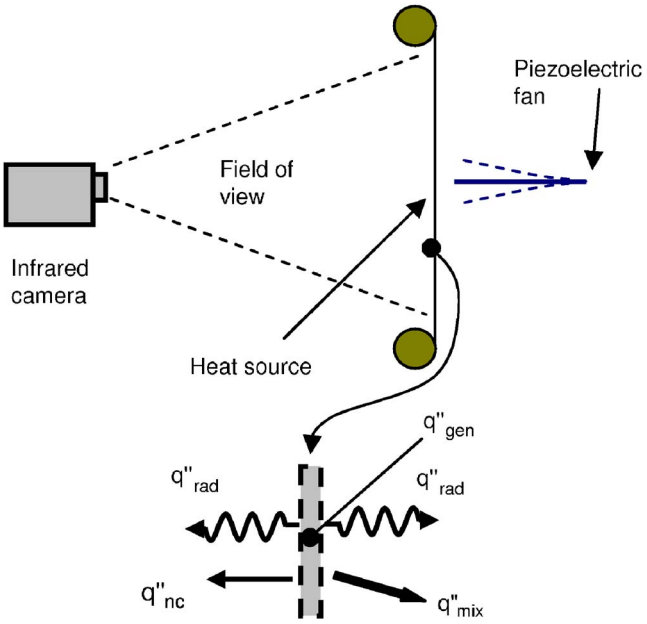

Fig. 2 Flux balance on foil (neglecting lateral conduction)

$$\mathrm{Nu}_{\mathrm{mix}}^3 = \mathrm{Nu}_{\mathrm{pz}}^3 + \mathrm{Nu}_{\mathrm{nc}}^3 \tag{4}$$

Taking each of these Nusselt numbers to be based on the same length scale, the convection coefficient attributed to the piezoelectric fan (h_{pz}) can be extracted according to

$$h_{\mathrm{pz}} = (h_{\mathrm{mix}}^3 - h_{\mathrm{nc}}^3)^{1/3} \tag{5}$$

where h_{mix} is directly found from:

$$h_{\mathrm{mix}} = \frac{q''_{\mathrm{gen}} - 2q''_{\mathrm{rad}} - q''_{\mathrm{nc}}}{T_s - T_\infty} \tag{6}$$

The convection coefficients reported in the results below exclusively represent the forced convective contribution from the piezoelectric fan (i.e., h_{pz}).

Experimental Parameters. The commercially available fans used in these experiments are made from a flexible mylar blade. As shown in Fig. 3, the overall fan length (L) is 64.0 mm, width (w) is 12.7 mm, and the fundamental resonance frequency of the fan is 60 Hz. Also illustrated in Fig. 3 are the two parameters varied during the heat transfer experiments: vibration amplitude (A), which is half the peak-to-peak amplitude, and gap distance (G) from fan tip to heater surface. Four different amplitudes are investigated ranging from 6.35 to 10 mm, where the lower number is half the fan width ($w/2$) and the higher number is the amplitude corresponding to the maximum input to the piezoelectric element below the depoling voltage (i.e., the voltage that causes a permanent change in polarization). It has previously been shown by Kimber et al. [16] that for small amplitudes and large gaps, the behavior is fundamentally different when compared to that seen at the opposite extreme (i.e., large amplitude and small gap). In light of this fact, the nondimensional quantity G/A is used to describe the gap distance. The range of this parameter and the four amplitudes considered within the experiments are given in Table 1. There are 21 different gaps for each amplitude, yielding a total of 84 experiments. The excitation frequency for each experiment is 60 Hz and the input signal magnitude was adjusted to obtain the desired vibration amplitude for each experiment; it may be noted that due to fluidic damping, a larger input voltage is required for fans vibrating close to a surface (small gaps). The power required to drive the fans varies across the experiments as a result, and ranges from 10 to 40 mW depending on the vibration amplitude. The tests thus compare performance for specified amplitude rather than for a given power consumption.

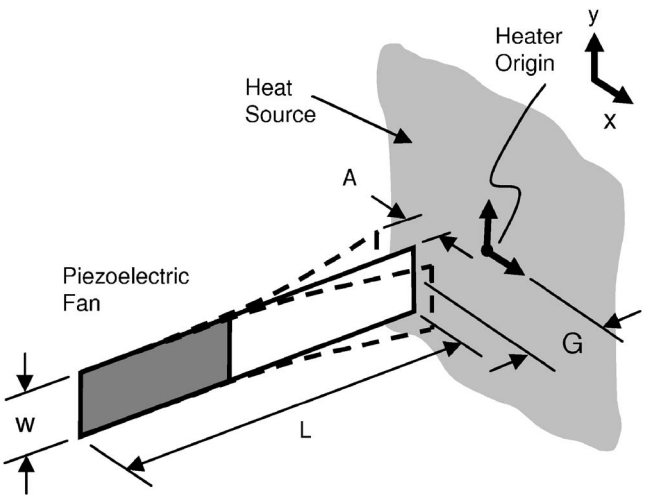

Fig. 3 Geometric parameters of fan: length (L) and width (w). Also shown are the parameters varied throughout experiments: vibration amplitude (A) and gap distance from heat source (G).

Table 1 Variable parameter values in the experiments

Parameter	Units	Values tested
Amplitude (A)	mm	6.35, 7.5, 8.5, 10
G/A	—	0.01–2.0 (21 values)

The uncertainty associated with the determination of convection coefficients has two primary contributions: Errors in temperature measurement and estimation of the generated heat flux. The uncertainty in the latter is caused by the resolution of the voltage and current measurements as well as uncertainties in the measurement of the heat source dimensions. The largest source of error is in the temperature measurement, which affects the estimation of the radiation flux, natural convection flux, and the mixed regime flux. The experimental error induced by the infrared camera was quantified using a blackbody emitter (SBIR 2004) with a temperature control within ±0.02°C. This revealed a temperature measurement error of ±1°C over a temperature range of 20–80°C. For the experiments, the heat input to the heater was chosen such that during forced convection, the minimum temperature observed was approximately 40°C, causing a worst-case error of ±2.5% in the temperature reading on the heated surface. Based on this analysis, the estimated uncertainty in forced convection coefficients is approximately ±8%.

Experimental Results

Accurate determination of the forced convection coefficient (h_{pz}) requires a thorough analysis of the setup under natural convection conditions. Natural convection heat transfer coefficients are first characterized followed by the forced convection coefficients.

Natural Convection. The temperature field in a representative natural convection experiment is shown in Fig. 4 where temperatures range from approximately 50°C at the leading edge (y =−50.8 mm) to 66°C at the top (y=50.8 mm) for a power input to the heater of 16 W. The near-horizontal nature of the isotherms is consistent with the behavior expected of natural convection on a heated vertical surface [17]. The temperature profile under such conditions is predicted to increase with vertical position to the 1/5

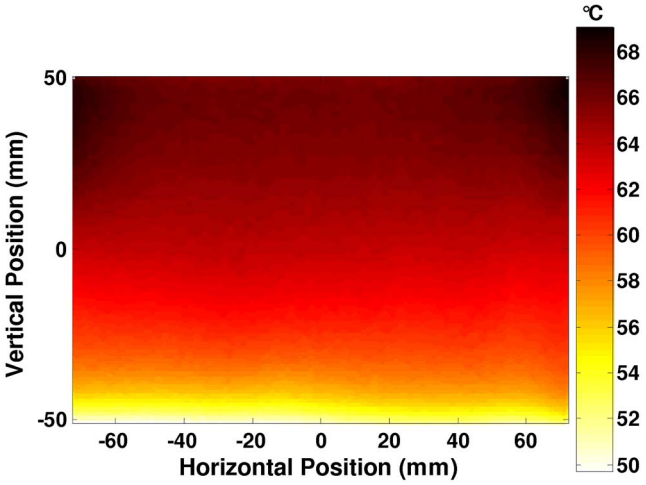

Fig. 4 Natural convection temperature distribution

power. The measured temperature profile is shown in Fig. 5 to conform to this dependence very well. The measured average convection coefficient is 5.3 $W/m^2 K$, which is also comparable with predicted value of 6.4 $W/m^2 K$ from the Vliet and Ross correlation [17].

The left and right edges near the top of the heater show slightly higher temperatures (by $\approx 3°C$) than at the center of the top edge. This is attributed to the disruption of the natural convection boundary layers by the copper rods, which is more pronounced as the boundary layers grow towards the top of the heated surface. However, the central area of the heater is isolated from these effects, and provides a robust experimental vehicle for the characterization of piezoelectric fan heat transfer.

Forced Convection. Local forced convection coefficient (h_{pz}) maps are presented in Fig. 6; the same scale is used in all the images to enable direct qualitative and quantitative comparison between the different cases. Twelve unique cases are shown (out of the total of 84 experiments conducted), with rows and columns representing changes in amplitude and gap, respectively. For each amplitude, results are shown at G/A values at which the temperature contours show a significant change in distribution. The fan is located in the middle of the heater and the vibration envelope is superimposed on each image. The solid vertical line in the center

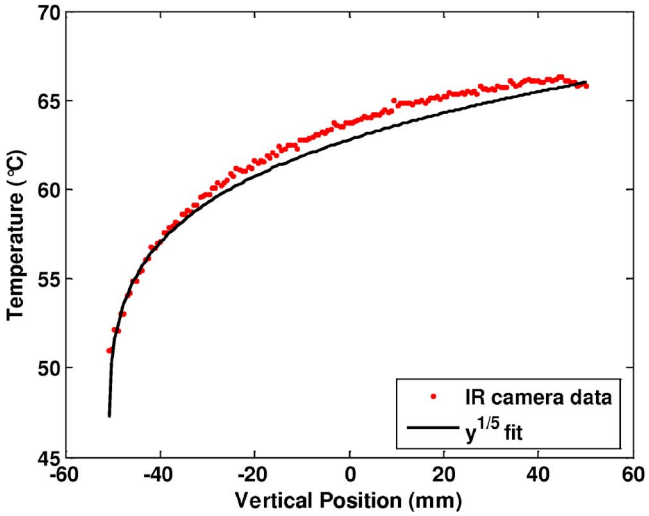

Fig. 5 Natural convection temperature profile in the vertical direction at the heat source center, $x=0$ mm

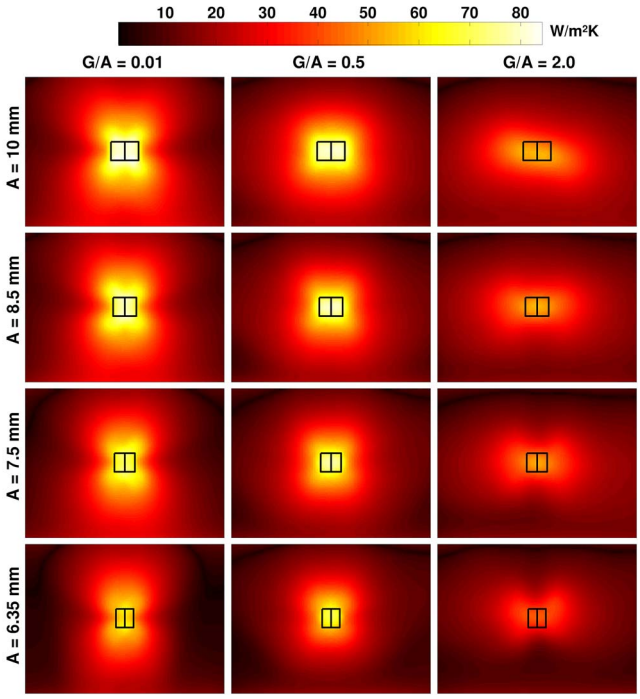

Fig. 6 Experimental convection coefficient (h_{pz}) for $A=10$ mm (top row), $A=8.5$ mm (second row), $A=7.5$ mm (third row), and $A=6.35$ mm (bottom row). Each column represents a different gap corresponding to $G/A=0.01$, 0.5, and 2.0. The heater size shown is 101.6 mm×152.4 mm.

represents the fan at its zero (undisplaced) position with the remaining lines illustrating the extent of the vibration envelope, whose overall dimensions are twice the vibration amplitude in the horizontal direction, and equal to the width of the fan in the vertical direction. The heater size shown is 101.6 mm×152.4 mm. The largest amplitude considered ($A=10$ mm) is shown along the top row of Fig. 6 for gaps of $G/A=0.01$, 0.5, and 2.0. A lobed pattern is generated when the fan vibrates close to the surface, and these lobes appear to be symmetric in both the vertical and horizontal directions, suggesting that the fluid agitation is roughly similar in the vibration direction and its orthogonal direction. This behavior transitions to a nearly circular (or rounded square) shape for the intermediate gaps, while the largest gap results in a distinctly different distribution of heat transfer coefficients. The fluid agitation at this gap is less influential in the vertical direction (orthogonal to the direction of vibration), yielding elliptical contours. The cooling effect is felt over a larger area in the horizontal direction in contrast to the somewhat localized behavior seen at small gaps. Although the magnitude of the heat transfer coefficients is lower for the largest gap, the horizontal extent over which the influence of the fan is felt is greater.

Results for $A=8.5$ mm and the same three G/A values as above are shown along the second row of Fig. 6. Again, distinct cooling regimes are observed and seem to have the same dependence on G/A as at the larger amplitude, transitioning from lobed contours at small gaps, to circular contours at intermediate gaps, and finally to elliptical contours at large gaps. A further decrease of amplitude (to $A=7.5$ mm) results in the distributions shown along the third row of Fig. 6, and show a similar trend. However it is interesting to observe the small differences in contours for $G/A=2.0$ between the three largest amplitudes. Although the behavior is similar in all three cases, a departure from elliptical behavior begins to appear as the amplitude decreases. A secondary pattern starts to form at the two extreme edges of the elliptical contours, forming two,

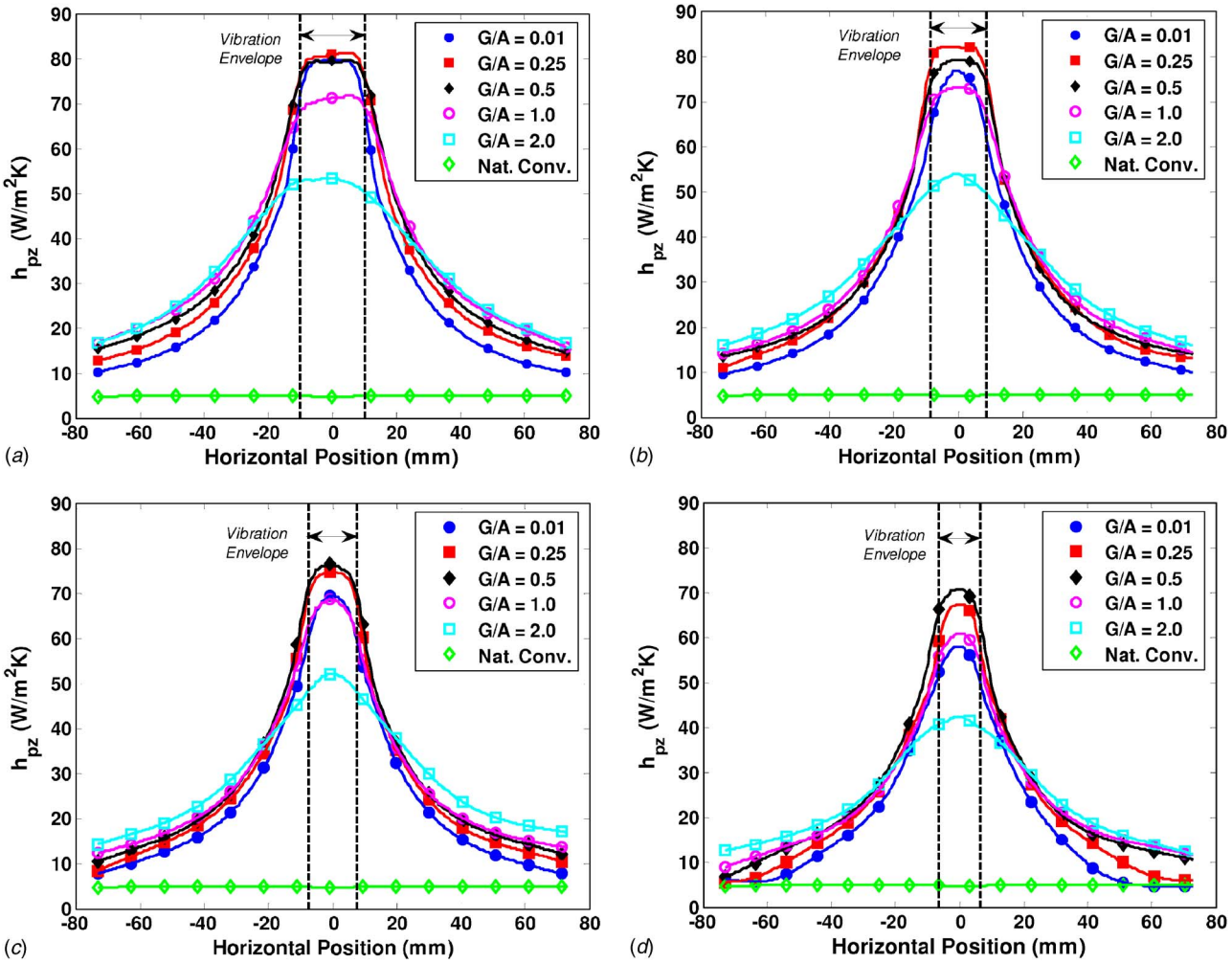

Fig. 7 Convection coefficient (h_{pz}) along horizontal direction ($y=0$) over range of nondimensional gaps ($G/A=0.01, 0.25, 0.5, 1.0, 2.0$) for: (*a*) $A=10$ mm, (*b*) $A=8.5$ mm, (*c*) $A=7.5$ mm, and (*d*) $A=6.35$ mm. For comparison, the natural convection profile is also shown.

slightly larger circular patterns. This suggests that although similar behavior is observed for different amplitudes at a given G/A, this behavior is slowly altered as the amplitude decreases.

This is even more apparent at the smallest amplitude ($A=6.35$ mm) as shown along the bottom row of Fig. 6. Notable differences relative to the larger amplitudes are seen at both the smallest and largest gaps. For $G/A=0.01$, the four distinct lobes observed at the higher amplitudes are now reduced to two, and the elliptical patterns typically seen at $G/A=2.0$ are also significantly altered. The regions with the greatest cooling are seen to have shifted from the stagnation region to just beyond the vibration envelope on either side. This is consistent with the observations in the literature regarding the fluid domain around a vibrating cantilever at small amplitudes [1], where vortices are shed as the fan tip passes the point of zero displacement and travel downstream. The heat transfer results suggest that these vortices are starting to form and impinge on the heater surface to create the observed areas of cooling on either side of the fan envelope. Previous results [16] showed that a further increase in G/A at small amplitudes ($G/A=4$, $A=5$ mm) generates two separate circular surface temperature contours on either side of the fan envelope, with very little cooling in the stagnation region. It appears that the reason for the differences observed in behavior between large and small amplitudes could be due to a change in flow/heat transfer regime. It is interesting to note that for various types of fluid flow including internal, external, and free streams, Bejan [18] has suggested that the *local* Reynolds number at which transition from laminar to turbulent flow occurs is of the order 10^2, regardless of the type of flow considered. The local Reynolds number (Re_l) for a vibrating cantilever can be defined as:

$$\mathrm{Re}_l = \frac{V_{\mathrm{rms}} A}{\nu} \tag{7}$$

It is interesting to compare the magnitude of Re_l for the two smallest amplitudes, which is 680 and 940 for $A=6.35$ and 7.5 mm, respectively. As the magnitude of Re_l changes from the order of 10^2–10^3, a transition would therefore be expected as is the case with the experimental observations. The area-averaged trends of heat transfer performance also suggest a change in regime, as will be shown in subsequent sections.

Temperature traces along the horizontal centerlines of the heater surface are analyzed next. These are shown for $A=10$, 8.5, 7.5, and 6.35 mm in Figs. 7(*a*)–7(*d*), respectively. Each plot includes five nondimensional gaps ranging from $G/A=0.01$ to 2.0 as well as the corresponding natural convection distribution for comparison. Also illustrated by two vertical dashed lines is the horizontal extent of the vibration envelope, decreasing in size as the amplitude is reduced. A number of important trends can be observed from this data. In general, the heat transfer coefficient near the stagnation region (within the vibration envelope) is nearly uniform, and drops in value beyond this region. The steep-

ness of this drop is dependent on the gap, with the steepest drop occurring at the smallest gap. Although the magnitude of convection coefficient is obviously different for the two extreme gaps ($G/A=0.01$ and 2.0), a more localized cooling zone is observed at smaller gaps in general, whereas the temperature profile flattens at large gaps. At small gaps, the fluid motion has limited physical space to diffuse before contacting the heat source, causing the observed localized cooling effect. Also inferred from these plots is the existence of an optimal gap that yields the highest stagnation-region heat transfer. At the largest amplitude (Fig. 7(*a*)), for example, the highest stagnation performance occurs for $G/A=0.25$, and decreases beyond $G/A=0.5$. For $A=8.5$ mm (Fig. 7(*b*)), the optimum gap is more distinct, with the maximum convection coefficients being 76.7, 82.0, and 79.2 $\mathrm{W/m^2\,K}$ for $G/A=0.01$, 0.25, and 0.5, respectively. As the amplitude is decreased to $A=7.5$ mm (Fig. 7(*c*)), the optimal gap is seen to occur at a larger G/A, where the maximum h_{pz} values are 69.3, 74.3, 76.4, and 68.6 $\mathrm{W/m^2\,K}$ for $G/A=0.01$, 0.25, 0.50, and 1.0, respectively. Similar results are observed for an amplitude of $A=6.35$ mm (Fig. 7(*d*)), where the maximum performance is 57.8, 67.2, 70.8, and 60.8 $\mathrm{W/m^2\,K}$ for $G/A=0.01$, 0.25, 0.50, and 1.0, respectively. It is interesting to note that for this amplitude, the performance for a gap as large as $G/A=1.0$ is better than the closest gap. Data from the two larger amplitudes ($A=10$ and 8.5 mm) suggest an optimal gap of $G/A\approx0.25$, whereas for the two smaller amplitudes ($A=7.5$ and 6.35 mm), $G/A\approx0.5$ appears to be the optimum. Relative to the closest gap, the benefit of operating at the optimum gap for the four cases shown in Fig. 7 ranges from only 2% at $A=10$ mm to over 20% at $A=6.35$ mm. A more detailed treatment of stagnation behavior follows in the next section.

Predictive Correlations for Thermal Performance of Piezoelectric Fans

In order to generalize the heat transfer performance obtained from the experiments, correlations are developed based on the key parameters involved. A number of similarities may be identified between the behavior of piezoelectric fans and impinging jets. Factors such as jet diameter, jet velocity, and spacing from the target are analogous to vibration amplitude, tip velocity, and gap distance, respectively. Although the flow generated by the oscillating piezoelectric fans is inherently unsteady, the results presented in this work are time-averaged convection coefficients. The heat transfer coefficient with piezofans is therefore expected to correlate with these parameters in a form similar to that in jet impingement. In the following, the applicable nondimensional parameters are first defined and predictive correlations then proposed.

Nondimensional Parameters. The appropriate length scale for the local Nusselt number is chosen to include both the vibration amplitude and fan width by employing the hydraulic diameter (D_{pz}) of the vibration envelope expressed as

$$D_{pz}=\frac{4Aw}{2A+w} \tag{8}$$

This is also consistent with the length scale used for noncircular impinging jets, and captures important behavior expected at the two extremes of $A\ll w$ and $A\gg w$. For the former extreme where a very wide fan is used $D_{pz}\approx4A$, and one would expect amplitude to be the dominant factor in describing heat transfer performance. In other words, an increase in width would not affect the magnitude of the local performance. The latter extreme would be realized for very thin fans with $D_{pz}\approx2w$. An increase in amplitude in this case would not have as great an effect on the fluid motion as would an increase in width. The local and area-averaged Nusselt numbers (Nu and $\overline{\mathrm{Nu}}$) are given as

$$\mathrm{Nu}=\frac{h_{pz}D_{pz}}{k},\quad \overline{\mathrm{Nu}}=\frac{\bar{h}_{pz}D_{pz}}{k} \tag{9}$$

where $\bar{h}_{pz}$ is determined from the size of an arbitrary heat source and is given as

$$\bar{h}_{pz}=\frac{1}{A_{eq}}\int_{A_{eq}}\int h_{pz}dA_{eq} \tag{10}$$

where A_{eq} is the area of the heat source. The stagnation Nusselt number (Nu_0) is the local Nusselt number at the geometric center of the vibration envelope which is based on the convection coefficient at that location (h_0) and is expressed as

$$\mathrm{Nu}_0=\frac{h_0D_{pz}}{k} \tag{11}$$

The Reynolds number for piezoelectric fans (Re_{pz}) is given below and is defined using the maximum tip velocity of the fan, or the product of frequency and amplitude (ωA), the kinematic viscosity (ν) of the working fluid, and the same length scale chosen for Nu:

$$\mathrm{Re}_{pz}=\frac{\omega AD_{pz}}{\nu} \tag{12}$$

Although the vibration amplitude appears in both Nu and Re_{pz}, a change in amplitude is manifested to a larger extent in Re_{pz} due to its direct influence in both the magnitude of tip velocity and hydraulic diameter. Nominal Re_{pz} values for the four amplitudes considered are 3550, 2810, 2370, and 1860 for $A=10$, 8.5, 7.5, and 6.35 mm, respectively.

Area-Averaged Nusselt Number. At small gaps the temperature contours indicate symmetric behavior in the horizontal and vertical directions, whereas at large gaps, better cooling is noticed in the horizontal direction. Thus, the optimum conditions for cooling appear to be strongly tied to the target area over which the heat transfer is averaged; different target area definitions could result in different optimal conditions. From the results obtained in this work, it was found that averaging over a square- and circular-shaped target area agreed to within 1–2% as long as the averaging area was identical; thus all the results in the following are area averaged over a circular area with a diameter of D_{eq}. The impact of increasing the diameter over which the heat transfer coefficient is averaged (by considering a larger subset of pixels within the thermal image) is illustrated in Fig. 8 for the largest amplitude $\mathrm{Re}_{pz}=3550$ over a range of gaps. The heater size is represented in terms of a nondimensional diameter (D_{eq}/A), where a value of 2 denotes a heater size with its diameter just inscribed within the horizontal extent of the vibration envelope. The area-averaged Nusselt number is approximately equal to the stagnation value for $D_{eq}/A<1$; well beyond this region ($D_{eq}/A>3$), the behavior transitions to an exponential decay. This type of behavior is comparable to that seen in jet impingement studies [19,20]. Correlations in the current work are thus based on the forms of the equations used in jet impingement studies [14,21] to account for the behavior at the two extremes and the transition in between:

$$\overline{\mathrm{Nu}}=\mathrm{Nu}_0(1+[a\exp\{b(D_{eq}/A)\}]^{-P})^{-1/P} \tag{13}$$

where a, b, and P are taken as variable parameters to be determined from a regression analysis. When the coefficient b takes a negative value, the appropriate behavior is captured for both small and large D_{eq}/A values.

The behavior of the average Nusselt number normalized with the stagnation-region value ($\overline{\mathrm{Nu}}/\mathrm{Nu}_0$) is compared for all four Re_{pz} (i.e., amplitudes) in Figs. 9(*a*) and 9(*b*) at the smallest ($G/A=0.01$) and largest ($G/A=2.0$) gaps, respectively. For $G/A=0.01$, the exponential decay observed for $D_{eq}/A>3$ seems to transition to a linear decay as Re_{pz} is decreased. The curvature

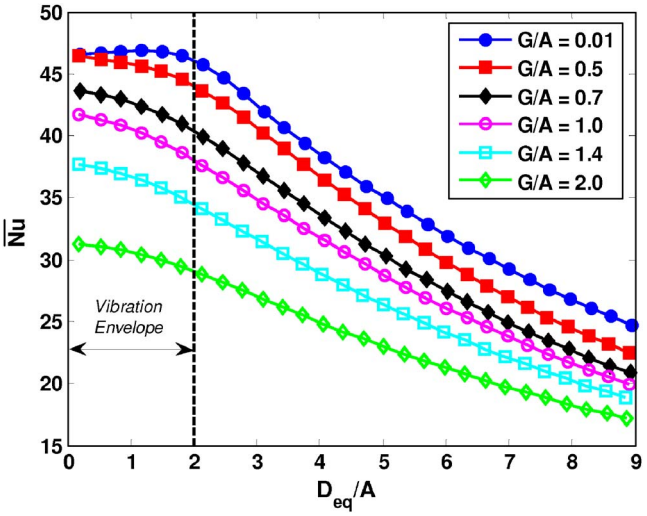

Fig. 8 Area-averaged Nusselt number ($\overline{Nu}$) versus nondimensional diameter of circular heater (D_{eq}/A) for Re_{pz}=3550 (A=10 mm) over range of nondimensional gaps (G/A=0.01–2.0)

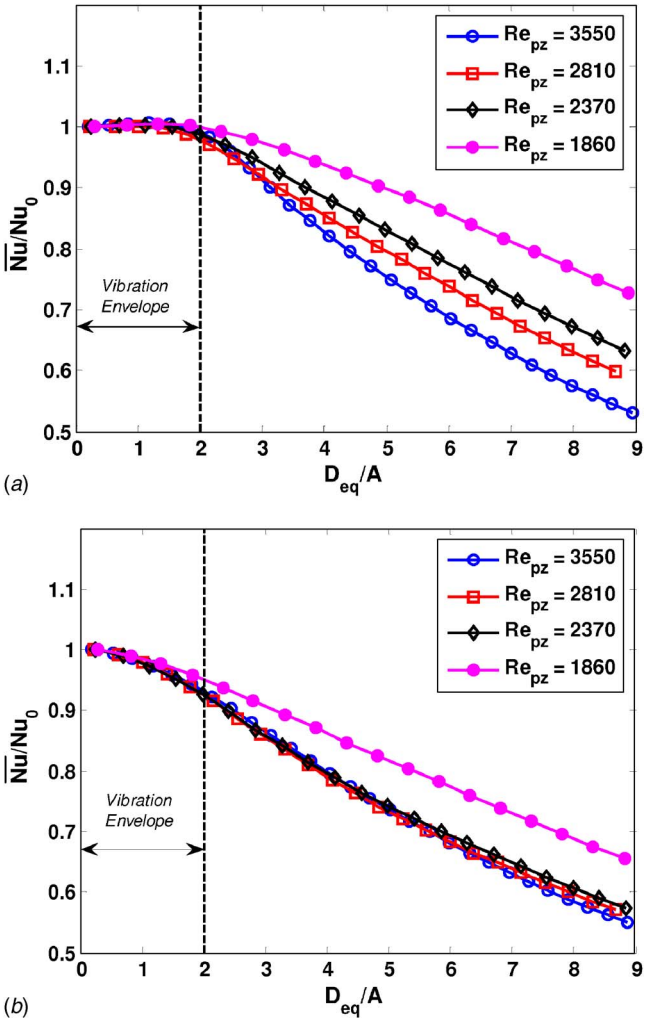

Fig. 9 Normalized area-averaged Nusselt numbers for four different Reynolds numbers (Re_{pz}=3550, 2810, 2370, and 1860 corresponding to A=10, 8.5, 7.5, and 6.35 mm, respectively) with (*a*) G/A=0.01 and (*b*) G/A=2.0

(second derivative) of the decay in this region is 0.007, 0.003, and 0.002 for Re_{pz}=3550, 2810, and 2370, respectively. The curvature then becomes negative (−0.002) at the smallest amplitude (Re_{pz}=1860). The transition from a four-lobe to a two-lobe pattern in the local heat transfer coefficient distributions in the first column of Fig. 6 are reflected in the results in Fig. 9 as well. For G/A=2.0 (Fig. 9(*b*)), the differences become more stark, where curves from the largest three Re_{pz} are nearly identical, but that for Re_{pz}=1860 exhibits a different behavior. Accordingly, results from the smallest Re_{pz} are not included in the correlations proposed in this work. However, the correlations developed can still be used for the smallest amplitude but would result in a somewhat greater deviation.

Stagnation Nusselt Number. The experimental stagnation Nusselt numbers for the three largest Re_{pz} are shown in Fig. 10 over the full range of gaps considered. A smooth fit is superimposed on each set of data to better reveal the trends. As observed earlier with the horizontal centerline profiles, the stagnation Nusselt number increases until an optimum G/A is reached, after which point, it decreases. For the largest amplitude (Re_{pz}=3550), the maximum Nu_0 occurs in the range of G/A between 0.1 and 0.2. As Re_{pz} is decreased, the maximum Nu_0 also decreases as is expected, but the corresponding optimum gap location increases. In contrast, the optimum spacing in the jet impingement literature has been suggested to be independent of Re_{pz}, with a value of $G/A \approx 10$ [15,19,20,22].

The size of the potential-core region (with an undisturbed velocity profile) in jets becomes smaller with increasing distance from the jet outlet, and disappears altogether at roughly five jet diameters, and is responsible for the independence of jet Reynolds number for the stagnation heat transfer. On the other hand, the velocity field is extremely complex for a vibrating cantilever [1,5,6] and its structure is highly dependent on the gap. The experimental trends suggest that when operating at the optimum gap, more of the energy of the excited fluid is used for cooling. The gap where this occurs is smaller for fluid of higher energy (large amplitudes) when compared to that of lower energy (small amplitudes). A rigorous analysis of the fluid domain at various gaps and amplitudes is underway to better understand the apparent trends of the optimal gap based on the underlying physics. The dependence of the optimum gap (G_{opt}) on Re_{pz} for the largest three Re_{pz} follows a power law relationship:

$$\frac{G_{opt}}{A} = 5.289\left(\frac{Re_{pz}}{1000}\right)^{-2.765} \tag{14}$$

The stagnation Nusselt number Nu_0 is correlated to Re_{pz} and G/A using the form:

$$Nu_0 = (Re_{pz})^q\left[C_1\left(\frac{G}{A}\right)^r + C_2\right] \tag{15}$$

where q, r, C_1, and C_2 are all considered variable parameters. The only modification introduced here relative to the form usually seen in jet impingement is the additional parameter (C_2), which accounts for the differences in the two flow situations. Only the region beyond the maximum ($G/A > G_{opt}/A$) is considered, consistent with jet impingement correlation efforts [22]; 48 experiments are included in the regression.

A least-squares approach was used to estimate the seven variable parameters in Eqs. (13) and (15), with the results listed in Table 2, yielding average and maximum deviations of 3.3% and 11.4%, respectively for the area-averaged Nusselt number. The quality of fit for the stagnation Nusselt number using Eq. (15) is illustrated in Fig. 11(*a*) where the correlation has average and maximum absolute deviations of 2.1% and 5.8%, respectively. The Reynolds number exponent (q) ranges between 0.39 and 0.47, which is comparable to those seen for jet impingement typically

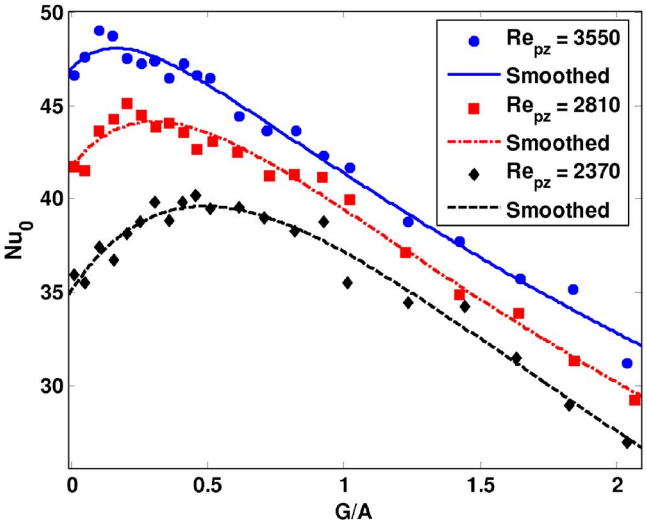

Fig. 10 Stagnation Nusselt number (Nu_0) behavior versus nondimensional gap (G/A) for three separate Reynolds numbers (Re_{pz}) corresponding to vibration amplitude of 10 mm (Re_{pz}=3550), 8.5 mm (Re_{pz}=2810), and 7.5 mm (Re_{pz}=2370)

between 0.3 and 0.5 [14]. The quality of fit for the average Nusselt number is found using the estimated stagnation Nusselt number from Eq. (15) as an input into Eq. (13); Fig. 11(*b*) shows that the correlation agrees quite well with the experimental data yielding average and maximum deviations of 3.3% and 11.4%. This correlation is valid for $G/A > G_{opt}/A$ (Eq. (14)) and for $2400 < Re_{pz} < 3500$ with the heater size $D_{eq}/A < 9$. The correlations can also be used for Re_{pz} as low as 1860 (the smallest amplitude considered); however the resulting accuracy is somewhat lower, yielding average and maximum deviations of 3.71% and 23.4%, respectively.

Conclusions

Local heat transfer coefficients are investigated for a single piezoelectric fan at various vibration amplitudes and gaps. The thermal maps exhibit a lobed-contour behavior at large gaps, transitioning to nearly circular (or rounded square) contours at intermediate gaps, and finally elliptical contours at small gaps. An optimal gap is noted both in the horizontal centerline profiles of local heat transfer coefficient and in the stagnation-region performance; the value of optimum gap is dependent on the vibration amplitude. Specifically, the optimum gap is small for large amplitudes and increases as the amplitude decreases. Predictive correlations are proposed for stagnation-region and area-averaged local Nusselt numbers. The experiments in this work were conducted with a single fan at a fixed fundamental resonance frequency, for different amplitudes and fan tip to heat source gap distances. The applicability of the Reynolds number definition in this work in describing flow conditions at higher (or lower) frequencies remains to be verified. Additional studies are currently underway to account for the additional factors not considered in this work such as the presence of additional fans, and the use of fans with different geometries and structural characteristics.

Table 2 Correlation coefficients from Eqs. (13) and (15) found from least squares analysis

Parameter	Value
a	1.132
b	−0.0899
P	25.13
q	0.440
r	1.451
C_1	−0.168
C_2	1.358
Average deviation (%)	3.3
Maximum deviation (%)	11.4

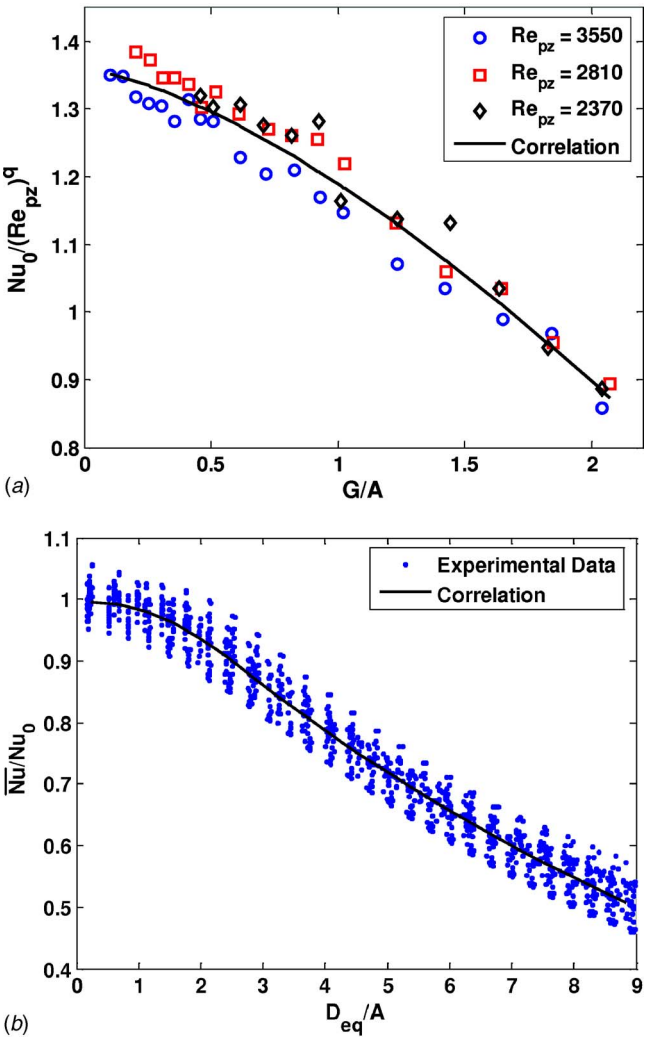

Fig. 11 Correlations with experimental data for (*a*) stagnation Nusselt number (Eq. (15)) with average and maximum deviations of 2.1% and 5.8%, respectively, and (*b*) area-averaged Nusselt number (Eq. (15) substituted in Eq. (13)) with average and maximum deviations of 3.3% and 11.4%, respectively

Acknowledgment

The authors acknowledge the financial support from members of the Cooling Technologies Research Center (www.ecn.purdue.edu/CTRC), a National Science Foundation Industry/University Cooperative Research Center and Purdue University.

Nomenclature

A = vibration amplitude (1/2 of peak to peak amplitude)
A_{heat} = area of heat source
D_{eq} = diameter of equivalent heat source
D_{pz} = hydraulic diameter of vibration envelope
G = gap distance

$\bar{h}$ = area-averaged forced convection coefficient
h = local forced convection coefficient
h_0 = stagnation forced convection coefficient
I_s = current from power supply
L = piezoelectric fan length
$\overline{\mathrm{Nu}}$ = area-averaged Nusselt number
Nu = local Nusselt number
Nu_0 = stagnation Nusselt number
q'' = heat flux
Re_l = local Reynolds number
$\mathrm{Re}_{\mathrm{pz}}$ = reynolds number for vibrating cantilever
T_s = surface temperature
T_∞ = ambient temperature
V_{rms} = root mean square velocity of fan tip
V_s = voltage drop across heater
w = piezoelectric fan width

Greek Symbols

ε = surface emissivity
ν = kinematic viscosity
σ = Stefan-Boltzmann constant
ω = vibration frequency

Subscripts

gen = energy generation
mix = mixed regime convection
nc = natural convection
pz = forced convection (under piezoelectric actuation)
rad = radiation

References

[1] Kim, Y., Wereley, S. T., and Chun, C., 2004, "Phase-Resolved Flow Field Produced by a Vibrating Cantilever Plate Between Two Endplates," Phys. Fluids, **16**(1), pp. 145–162.

[2] Açıkalın, T., Raman, A., and Garimella, S. V., 2003, "Two-Dimensional Streaming Flows Induced by Resonating, Thin Beams," J. Acoust. Soc. Am., **114**(4), pp. 1785–1795.

[3] Açıkalın, T., Wait, S. M., Garimella, S. V., and Raman, A., 2004, "Experimental Investigation of the Thermal Performance of Piezoelectric Fans," Heat Transfer Eng., **25**(1), pp. 4–14.

[4] Wait, S. M., Garimella, S. V., and Raman, A., 2007, "Piezoelectric Fans Using Higher Flexural Modes for Electronics Cooling Applications," IEEE Trans. Compon. Packag. Technol., **30**(1), pp. 119–128.

[5] Açıkalın, T., Garimella, S. V., Raman, A., and Petroski, J., "Characterization and Optimization of the Thermal Performance of Miniature Piezoelectric Fans," Int. J. Heat Fluid Flow (in press).

[6] Ihara, A., and Watanabe, H., 1994, "On the Flow Around Flexible Plates, Oscillating With Large Amplitude," J. Fluids Struct., **8**(6), pp. 601–619.

[7] Schmidt, R. R., 1994, "Local and Average Transfer Coefficients on a Vertical Surface Due to Convection From a Piezoelectric Fan," *International Society Conference on Thermal Phenomena*, Washington, D.C, pp. 41–49.

[8] Kimber, M., Garimella, S. V., and Raman, A., 2006, "An Experimental Study of Fluidic Coupling Between Multiple Piezoelectric Fans," *International Society Conference on Thermal Phenomena*, San Diego, CA, pp. 333–340.

[9] Bürmann, P., Raman, A., and Garimella, S. V., 2003, "Dynamics and Topology Optimization of Piezoelectric Fans," IEEE Trans. Compon. Packag. Technol., **25**(4), pp. 592–600.

[10] Basak, S., Raman, A., and Garimella, S. V., 2005, "Dynamic Response Optimization of Piezoelectrically Excited Thin Resonant Beams," ASME J. Vibr. Acoust., **127**, pp. 18–27.

[11] Kim, B., Rho, J., and Jung, H., 2005, "Optimal Design of Piezoelectric Cantilever Fan by Three-Dimensional Finite Element Analysis," KIEE International Transactions on Electrical Machinery and Energy Conversion Systems, **5-B**(1), pp. 90–94.

[12] NASA Jet Propulsion Laboratory Web Site, URL: http://masterweb.jpl.nasa.gov/reference/paints.htm

[13] Liu, X., Lienhard V, J. H., and Lombara, J. S., 1991, "Convective Heat Transfer by Impingement of Circular Liquid Jets," ASME J. Heat Transfer, **133**(3), pp. 571–582.

[14] Stevens, J., and Webb, B. W., 1991, "Local Heat Transfer Coefficients Under an Axisymmetric, Single-Phase Liquid Jet," ASME J. Heat Transfer, **113**(1), pp. 71–78.

[15] Incropera, F., and DeWitt, D., 2002, *Fundamentals of Heat and Mass Transfer*, 5th ed., Wiley, New York.

[16] Kimber, M., Garimella, S. V., and Raman, A., 2006, "Experimental Mapping of Local Heat Transfer Coefficients Under Multiple Piezoelectric Fans," ASME Paper No. IMECE2006–13922.

[17] Vliet, G. C., and Ross, D. C., 1975, "Turbulent Natural Convection on Upward and Downward Facing Inclined Constant Heat Flux Surfaces," ASME J. Heat Transfer, **97**(4), pp. 549–555.

[18] Bejan, A., 2004, *Convection Heat Transfer*, 3rd ed., Wiley, New York.

[19] Rice, R. A., and Garimella, S. V., 1995, "Confined and Submerged Liquid Jet Impingement Heat Transfer," ASME J. Heat Transfer, **117**(4), pp. 871–877.

[20] Garimella, S. V. and Schroeder, V. P., 2001, "Local Heat Transfer Distributions in Confined Multiple Air Jet Impingement," ASME J. Electron. Packag., **123**(3), pp. 165–172.

[21] Churchill, S. W., and Usagi, R., 1972, "A General Expression for the Correlation of Rates of Transfer and Other Phenomenon," AIChE J., **18**(6), pp. 1121–1128.

[22] Sun, H., Ma, C. F., and Nakayama, W., 1993, "Local Characteristics of Convective Heat Transfer From Simulated Microelectronic Chips to Impinging Submerged Round Water Jets," ASME J. Electron. Packag., **115**, pp. 71–77.

Laser Transmission Welding of a Lap-Joint: Thermal Imaging Observations and Three–Dimensional Finite Element Modeling

L. S. Mayboudi[1]
e-mail: mayboudi@me.queensu.ca

A. M. Birk
e-mail: birk@me.queensu.ca

G. Zak
e-mail: zak@me.queensu.ca

Mechanical and Materials Engineering Department,
Queen's University,
Kingston, Ont.,
K7L 3N6, Canada

P. J. Bates
Chemistry and Chemical Engineering Department,
Royal Military College,
Kingston, Ont.,
K7K 7B4, Canada
e-mail: bates-p@rmc.ca

Laser transmission welding (LTW) is a relatively new technology for joining plastic parts. This paper presents a three-dimensional (3D) transient thermal model of LTW solved with the finite element method. A lap-joint geometry was modeled for unreinforced polyamide (PA) 6 specimens. This thermal model addressed the heating and cooling stages in a laser welding process with a stationary laser beam. This paper compares the temperature distribution of a lap-joint geometry exposed to a stationary diode laser beam, obtained from 3D thermal modeling with thermal imaging observations. It is shown that the thermal model is capable of accurately predicting the temperature distribution when laser beam scattering during transmission through the polymer is included in the model. The weld dimensions obtained from the model have been compared with the experimental data and are in good agreement. [DOI: 10.1115/1.2740307]

Keywords: thermal imaging, finite element modeling (FEM), 3-D thermal modeling, ANSYS, laser transmission welding of thermoplastics (LTW), diode laser

Introduction

Plastics are extensively employed in manufacture of automotive components, consumer products, as well as electronic and medical devices. Their use continues to increase because of their good strength-to-weight ratio, low cost, and ease of recycling. Complex parts are often made of smaller parts that are molded and then joined together. Since making the same complex component in one piece is not always feasible, various joining techniques have been developed, including adhesive joining, mechanical fastening, and fusion bonding or welding. This paper will focus on thermal modeling of a fusion bonding technology known as laser transmission welding (LTW).

LTW involves clamping laser-transparent and laser-absorbent parts together. A laser beam passes through the laser-transparent part, and is absorbed by the laser-absorbent part near the weld interface. Heat generated at the interface is transfered back into the transparent part by conduction. This heat energy melts a thin layer of plastic in both parts. Molecular diffusion occurs and a solid joint is formed as the melt layer solidifies (Fig. 1).

The LTW approach known as contour welding is addressed in this paper. It refers to the use of a spot of laser energy that moves once along a preprogramed contour path. It creates a local melt film at the weld interface. This is different than quasi-simultaneous welding in which a quick oscillating movement of the laser beam spot creates a melt film over the entire weld area. Russek et al. review the existing LTW approaches and give several application examples [1]. The quasi-simultaneous technique has been used for manufacture of automotive sensors [2], while contour [3] and simultaneous (mask) welding [4] have been used to manufacture medical microfluidic devices.

The focus of this work was the development of a three-dimensional (3D) thermal model for a LTW process that can predict the spatial and temporal properties of parts being joined. It was our objective to have a model that can predict the detailed properties of the weld. Such a model is essential for good understanding of the process and subsequently its optimization.

Background

To form a strong bond, it is important that the weld interface is exposed to sufficient heat to melt the polymer while avoiding excessive energy which can cause polymer degradation. Delivery of the thermal energy by the laser beam is influenced by process parameters such as the laser power, speed, and beam spot size, as well as material properties such as absorptivity of the laser radiation, thermal conductivity, density, and specific heat. The presence of reinforcements and other additives can complicate the process by making the plastic properties anisotropic. The scattering of laser energy in the transparent part is of specific interest.

Several studies have tried to model the physical processes of melting and resolidification involved in welding. These studies concentrated on predicting the temperature distribution and heat flow during welding. An analytical thermal solution for a welding process was first suggested by Rosenthal [5]. He introduced a moving heat source applied to a highly conductive semi-infinite plate (metal). He ignored the dependence of thermal properties to temperature. Temperature-dependant properties cause nonlinearity that cannot be easily handled by analytical methods.

Potente et al. [6] analyzed the heating phase in LTW of polyamide (PA)6. They assumed the absorption coefficient of the absorbing part was high enough for the heat to be generated only at the interface and conducted equally into both parts. Subsequently, they obtained a symmetrical temperature distribution, with a peak temperature at the interface. Based on the above approximation,

[1]Corresponding author.

Contributed by the Heat Transfer Division of ASME for publication in the JOURNAL OF HEAT TRANSFER. Manuscript received July 27, 2006; final manuscript received January 23, 2007. Review conducted by Bengt Sunden. Paper presented at the 2006 ASME International Mechanical Engineering Congress (IMECE2006), Chicago, IL, USA, November 5–10, 2006.

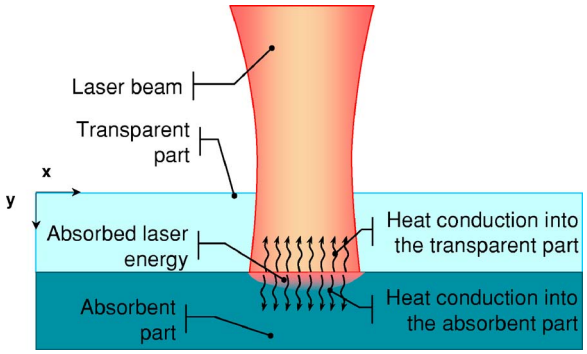

Fig. 1 LTW process for a lap joint

they applied an analytical heat transfer model of single-sided impulse welding to the LTW process. For an absorbing material with a low absorptivity, they defined a correction factor and supported their results by comparing the calculated and measured melt-layer thicknesses.

Several studies have modeled a moving laser heat source by a 2D model in the plane of the moving beam center line. By using a coordinate system moving together with a heat source, a quasi-steady state model is obtained. Grewell et al. [7] applied the model to laser transmission microwelding of plastics. The specimens were assumed to be semi-infinite with temperature-independent properties. Sato et al. [8] studied the effect of transmissivity and absorptivity of colored plastics on the temperature distribution within the welded parts. They assumed a semi-infinite workpiece, stationary laser beam, and moving workpiece. They applied the finite difference method (FDM) to model polystyrene plates in a lap-joint configuration. The main drawback of such 2D models is their inability to predict the temperature distribution in the joint, transverse to the beam travel direction.

In an earlier study conducted by this research group, Prabhakaran et al. [9] investigated a modified T-like joint exposed to a moving diode laser beam. Unreinforced PA6 was chosen for the experiments and 0.2% (weight) carbon black was added to the clear PA6 to make it absorbent. The effect of process parameters, such as weld pressure, as well as laser beam speed, power, and area, on meltdown, microstructure, and weld strength were investigated. A one-dimensional (1D) thermal FDM model was developed to predict the temperature distribution [10]. However, due to its 1D nature, the model could not predict the molten zone depth variation across the weld.

Mayboudi et al. [11] developed a 2D thermal model for LTW of a T-like joint geometry in their earlier studies. They presented the results for the case when an unreinforced PA6 (transparent) and an unreinforced PA6 with 0.2% (weight) added carbon black (absorbent) were joined under a small clamping pressure. Their model assumed that heat conduction in the direction along the beam travel was negligible. As a continuation to their study, Mayboudi et al. [12] presented a 3D thermal model for LTW of a T-like joint geometry exposed to a moving laser beam. The model was found to predict 7 °C lower peak temperatures in the joint than the earlier 2D model.

Few studies have been able to verify the LTW thermal models directly. They have mainly used indirect methods such as comparing the predicted and actual molten zone depth. Direct measurement by thermocouples inserted into the plastic are unreliable to the laser energy being directly absorbed by the wire and to errors introduced by high thermal conductivity of the wires (conduction errors). Noncontact surface temperature measurement by infrared thermal imaging offers one possible approach to thermal model verification for LTW. While use of thermal imaging in LTW has been reported [13], its application has focused on material optical property assessment and not on model verification. In their work, Haferkamp et al. [13] applied a thermographic method to plastics (polyamide and polybutylene) to assess their transmissivity by measuring the temperature difference of the sample surfaces exposed to a diode laser beam. They used the optical properties thus found in a finite element method (FEM) model. No details on the FEM modeling were given.

As a continuation to the authors' previous LTW study, this paper addresses the verification of the thermal model by a thermal imaging technique. A 3D transient heat transfer model of the specimen geometry used in this thermal imaging study was developed with ANSYS 10. The model represents a PA6 specimen in a lap-joint geometry configuration exposed to a stationary laser beam. Predicted temperature distributions were verified through thermal imaging observations of the specimen's surface.

Table 1 Thermo-physical properties of PA6 (Akulon F223-D) at the room temperature.[a]

Material Property	Value
Density (kg/m^3)	1130
Thermal conductivity (W/m°C)	0.2
Specific heat (J/kg°C)	1600
Melting temperature (°C)	220

[a]See Ref. [16].

Heat Transfer in LTW

Applying the energy conservation law to the LTW process results in a 3D transient conduction heat transfer equation [14]

$$\frac{\partial}{\partial x}\left(k_x(T)\frac{\partial T}{\partial x}\right)+\frac{\partial}{\partial y}\left(k_y(T)\frac{\partial T}{\partial y}\right)+\frac{\partial}{\partial z}\left(k_z(T)\frac{\partial T}{\partial z}\right)+q(x,y,z,t)=\rho(T)C(T)\frac{\partial T}{\partial t} \quad (1)$$

where k_x, k_y, and k_z are thermal conductivities along the x, y, and z axes, respectively; T is temperature; ρ is density; C is specific heat; t is time; and q is internal heat generation rate per unit volume.

In this analysis, the laser energy absorbed in the plastic is modeled as an internal heat generation term. The heat generation q (W/m^3) is defined in terms of the laser energy flux change caused by the absorption of the laser beam energy by the plastic and is a function of laser power, material absorption properties, laser beam cross-section dimensions, and laser beam power flux distribution. The rate of internal heat generation (W/m^3) is derived from the Bouguer–Lambert law [15] and is presented as a function of y

$$q(y)=KI_0e^{-Ky} \quad (2)$$

where I_0 is the laser energy flux (W/m^2) at the surface; y is distance from the surface within the material; and K is the total extinction coefficient caused by the laser beam absorption and scatter. In this study, radiation scatter was neglected unless otherwise mentioned.

Physical and Optical Properties

The material used in this study was PA6 with the commercial name of Akulon F223-D [16]. The temperature-dependant thermo-physical properties for this plastic were integrated into the model [11,12]. Table 1 shows values of the material properties at the room temperature [16].

The absorbent part contained 0.2% (weight) of carbon black. The absorption coefficient (total extinction coefficient) for the absorbent part was adopted from the authors' earlier study [11]. They suggested the absorption coefficient for the absorbing part could be predicted by modeling it as soot particles suspended in a transparent medium. This assumption leads to an absorption coef-

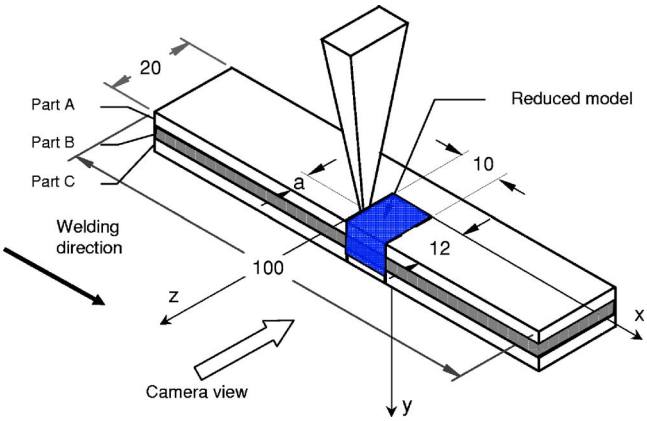

Fig. 2 3D model geometry (dimensions in mm, the thickness of each part is 3 mm)

ficient of 4.8 mm^{-1}. The absorption coefficient of the transparent part (0.21 mm^{-1}) was adopted from Prabhakaran [17], where the beam energy flux readings from a power meter before and after hitting the transparent part were obtained.

A Rofin-Sinar DL×16 diode laser with a power capacity of 160 W was used in this work. The diode laser beam has a rectangular cross section with the focal-plane dimensions of 1.4 mm ×0.7 mm [18]. The off focal-plane beam hits the transparent part 3 mm above the focal plane where the laser beam dimensions are slightly larger (1.5 mm×0.9 mm) [18]. The power flux distribution was assumed to be uniform. This approximated the energy distribution of unscattered beam focused at the interface. The long beam dimension (1.4 mm) was aligned with the z axis (Fig. 2).

Thermal Imaging

Thermal infrared (IR) imaging cameras are detector and precision optics platforms that produce a visual representation of the IR energy emitted and reflected by all objects. All objects above absolute zero (−273°C) radiate infrared energy. Thermal imaging was used to measure the surface temperature distribution of the welded components in order to compare the observed temperature to the predicted surface temperatures from the thermal model.

In this study the camera was directed at the exposed edge of the welded sample as shown in Fig. 2. The viewed direction was perpendicular to the laser beam axis.

The radiation measured by the camera depends on the object temperature, volume, and surface emissivity (ε), and surrounding conditions. The surroundings are important because they are partly reflected by the object. Volume emission and transmission are important because, if the material were not opaque, the camera would be able to see into the object. Surface emissivity affects the emission of thermal radiation by the object and the reflection of the surroundings. Radiation from the object is also influenced by the absorption in the atmosphere and any external optics that it passes through.

To measure the object temperature accurately, it is therefore necessary to compensate for the effects of these various parameters. If we want to measure the surface temperature distribution,

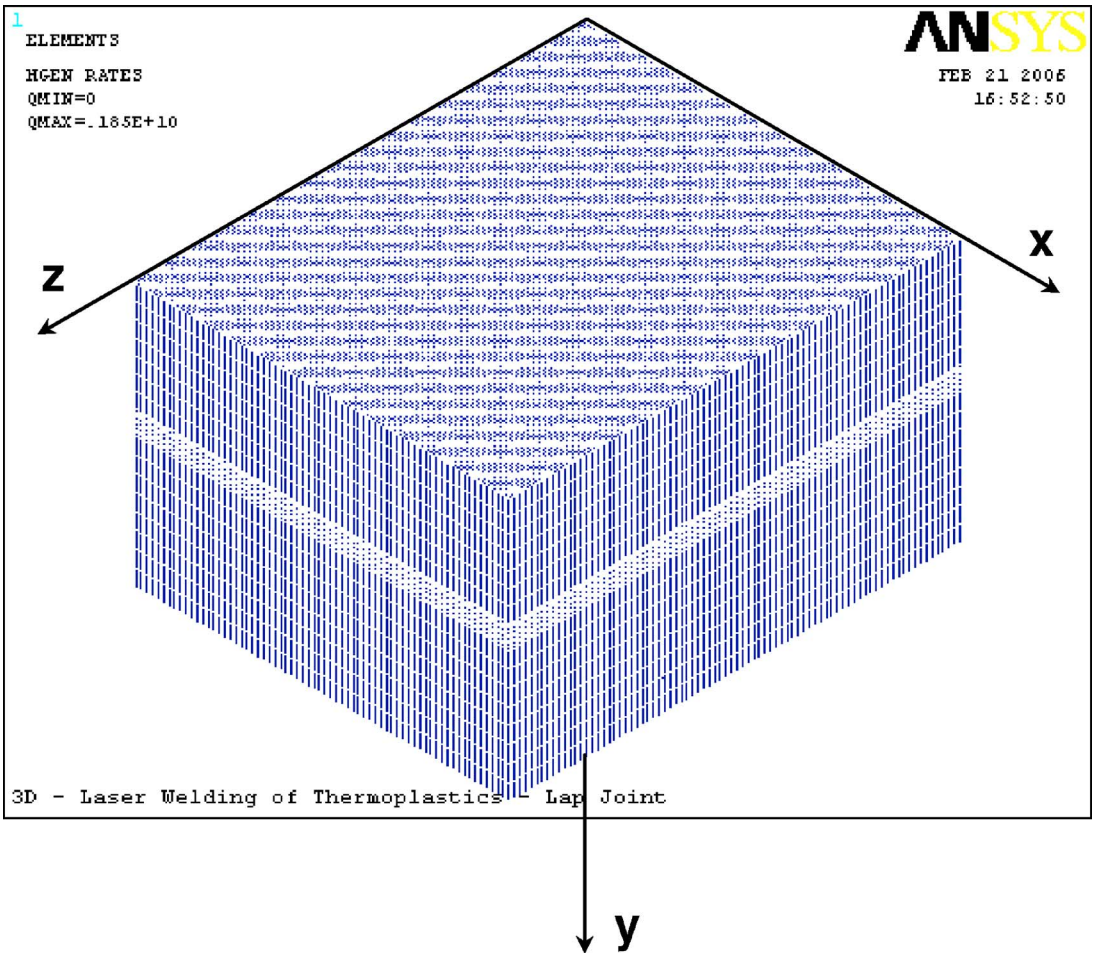

Fig. 3 The meshed model

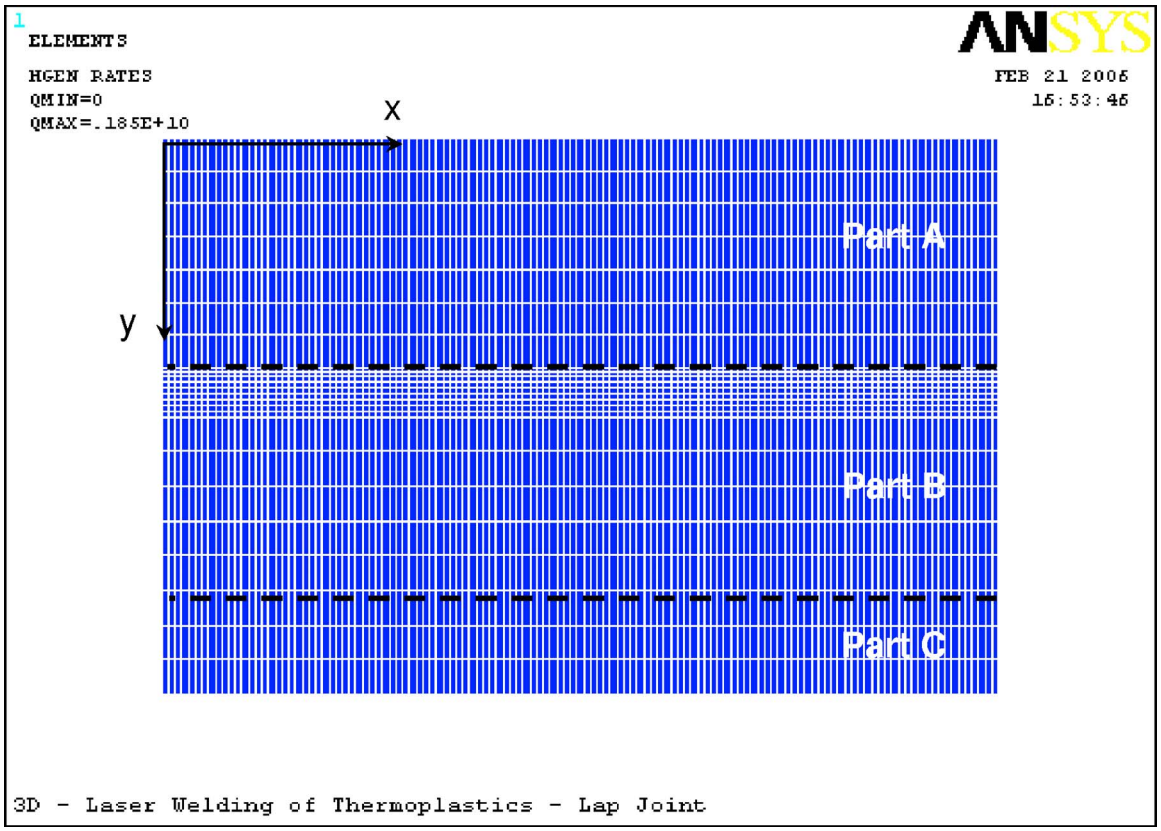

Fig. 4 Closeup of the meshed model (front view)

then it is highly desirable that the object be opaque. To minimize the effects of the surroundings, we want the surface emissivity to be near that of a blackbody (i.e., $\varepsilon = 1.0$).

Preliminary testing was done to determine the emission and transmission characteristics of the plastic. For the thermal imaging experiments to be accurate the plastic must be opaque to radiation in the wavelengths important in this study. The radiation wavelength depends on the temperature as described by the Planck function [15]. In this study we were interested in plastic surface temperatures up to approximately 70°C. We are also interested in radiation of the same wavelength as the laser (effective temperature 4500°C).

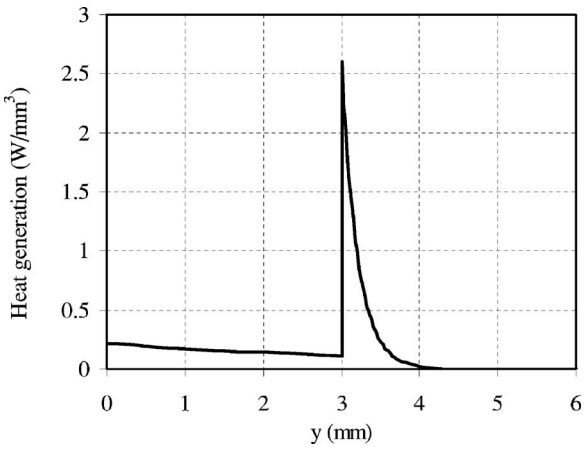

Fig. 5 Heat generation profile along the height of the geometry (energy flux: 1 w/mm^2)

The plastic surface emissivity was estimated by heating the transparent and absorbent PA6 plaques to a known temperature monitored by thermocouples embedded in the samples and then viewing the surfaces with the thermal imager. The surface emissivity setting in the camera was adjusted until the temperature indicated by the imager agreed with the known sample temperature. This method showed the emissivity of the plastic to be in the range of 0.9–0.95 for object temperatures from 22°C to 250°C, matching the thermocouples temperatures within 0.5°C.

We know that the transparent plastic part is transparent to the laser energy. Therefore we know that any scatter of the laser energy by the transparent part can be directed toward the imager to give a false temperature indication. Scatter has been ignored in the heat transfer analysis, but scatter in the thermal imaging measurements cannot be ignored. Therefore, the edge of the transparent part must be treated with a thin opaque coating such as carbon black. With this coating, the camera will not be affected by small amounts of scattered laser energy. If the coating is very thin, it should not affect the surface temperature significantly.

A 3-mm-thick sample of the transparent material was used to determine if the plastic (PA6) was opaque to the longer wavelength radiation from the lower temperatures expected from the internal heating process. A test was done using a soldering iron ($T = 400$°C). The soldering iron heated tip was held behind the 3-mm-thick sample and the sample was viewed by the thermal imager. This imager showed no trace of the soldering iron. From these tests it was concluded that the sample material is, in all practical terms, opaque to the thermal energy emitted by the plastic material.

One last concern was leakage of thermal radiation through a small gap between the two plastic pieces to be welded. This possibility was eliminated by joining the two plastic parts prior to thermal imaging. The parts were joined by making several parallel

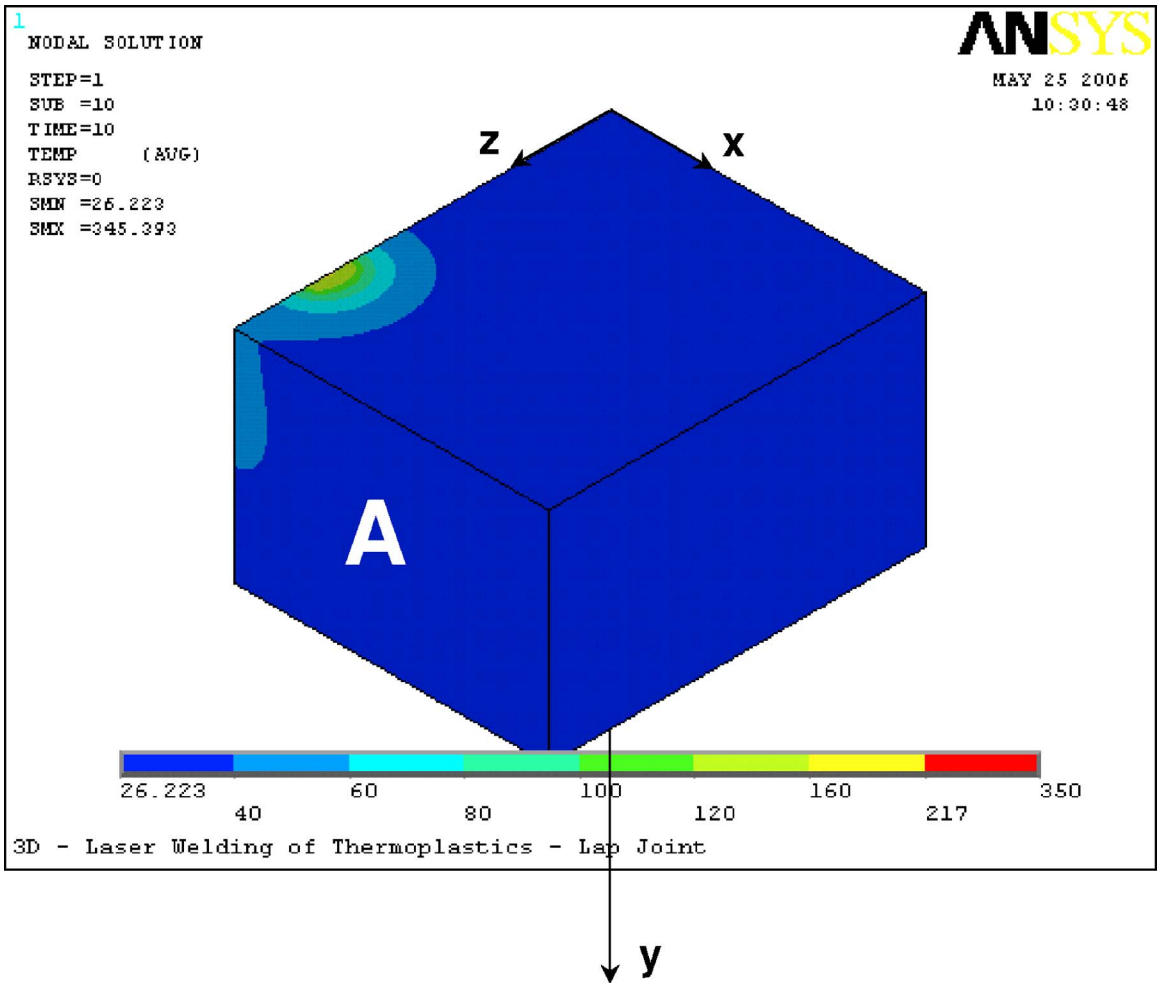

Fig. 6 Temperature contours at the end of the heating phase (t=10 s)

weld lines across the area where the stationary beam would be located for the thermal imaging test. These weld lines are visible as dark horizontal lines in Fig. 20.

An experimental plan was designed to verify the thermal model using a thermal imaging camera. In order to observe and record the temperature distribution during the LTW process, a thermal imaging camera (FLIR ThermaCAM SC1000) was mounted on a frame built inside the enclosure of the diode laser welding workstation (Rofin Sinar UW200). The camera has a spectral range of 3.4–5 μm and uses a 256×256 focal plane array of PtSi/complementary metal–oxide-semiconductor (CMOS) detectors. The laser in this study has a wavelength of 0.94 μm, which is outside the spectral range of the camera.

The thermal camera, equipped with a macro lens, had to be placed so that the lens was 2 cm from the geometry to achieve focus (Fig. 6, face A) and directed perpendicular to this face. The laser beam center (x=0 mm) was located at a distance "a" (Fig. 2) away from the front edge, ranging from 3 mm to 4 mm. It was assumed, based on the experiments described earlier, that the temperatures indicated by the camera on this surface were the true surface temperatures and were not affected by the scattered laser energy or by temperatures internal to the welded specimens.

Computational Methodology

ANSYS 10 was used in all stages of the thermal model including pre- and post-processing phases. The CPU time to process and solve the problem was approximately 12 h on a 3 GHz PC with 2 GB of RAM. The lap-joint used in the experiments (Fig. 2) was modeled in this study for verification purposes. It consists of two rectangular plaques ($100\times20\times3$ mm^3). The transparent part (part A in Fig. 2) is welded to the absorbent part (part B). It was assumed that the beam hits part A at the distance "a" away from the front edge (Fig. 2), the distance being measured to the beam center. A second absorbent plastic part, serving as an insulator from the aluminum fixture underneath part B, was added (part C). This extra part was partially included in the thermal model.

Modeling

The intent of this model was to simulate the LTW of a lap-joint geometry. Model run conditions were based on the experimental conditions unless otherwise mentioned. Due to the symmetry in the geometry and laser beam profile, the geometry was cut in the laser beam symmetry plane, at x=0, perpendicular to the x axis. Preliminary models with full-size geometry (Fig. 2) helped to identify where in the part the temperature gradients were sufficiently small to allow reduction of the model size to improve efficiency. The reduced model dimensions are $10\times12\times8$ mm^3 (Fig. 2). The top and front faces of the geometry were assumed to transfer heat by convection (h=5 W/m^2 K) to the environment since they are exposed to the surroundings. The rest of the surfaces were assumed to be insulated. The left vertical side is the plane of symmetry and thus insulated. The bottom face is in contact with another plastic part (part C) ($100\times20\times3$ mm^3), which insulates this face. 2 mm depth of this part was modeled to ac-

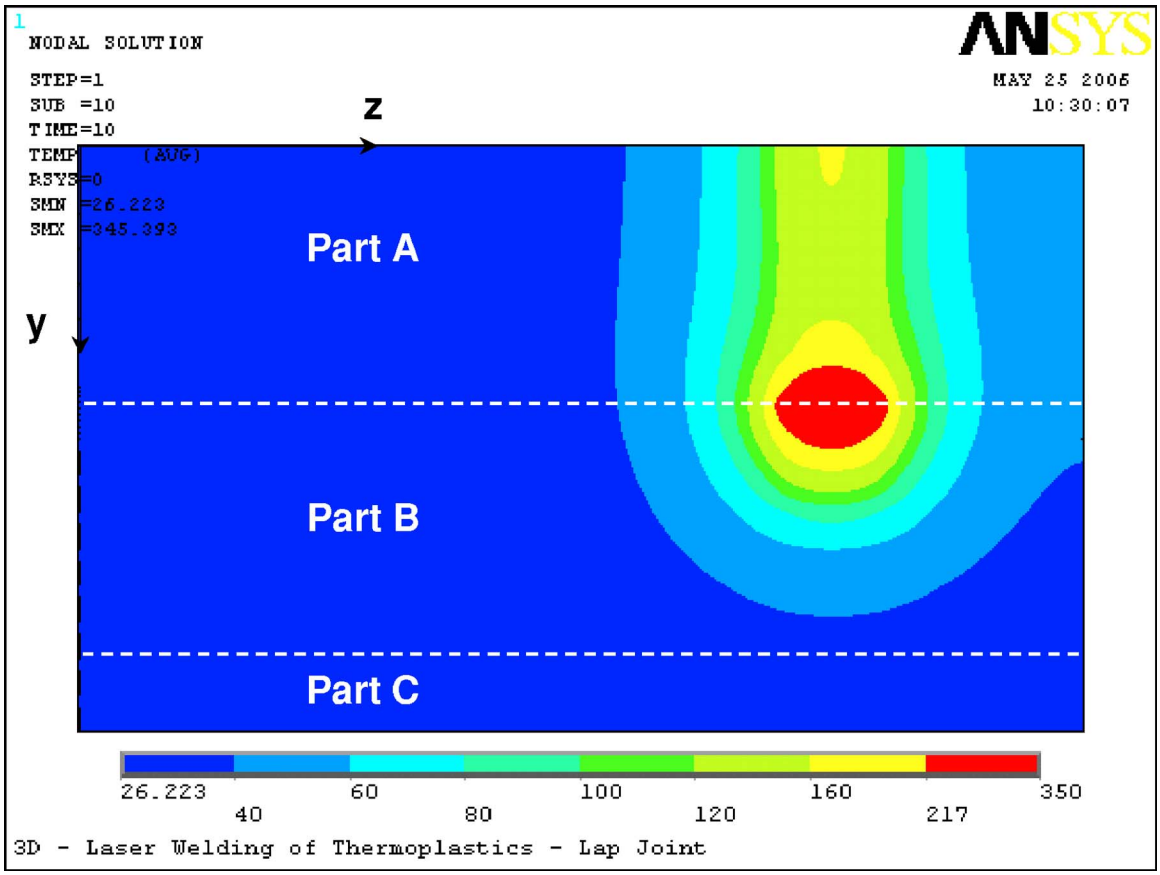

Fig. 7 Temperature contours at the symmetry plane at the end of the heating phase (t=10 s, x=0 mm)

count for the conduction heat transfer to this part. The model was meshed using Solid70 elements [19] (Figs. 3 and 4), a 3D element with heat conduction capabilities.

The element has eight nodes, with temperature as its single degree of freedom at each node. The element has the prism and tetrahedral options. An element size of 0.08 mm was used for the interface of parts A and B (Fig. 2) and the rest was meshed with 0.45 mm elements. Grid sensitivity analysis confirmed this choice of element size. Grid sensitivity analysis was performed by progressive reduction of element sizes both in the refined mesh area in part B near the joint interface and in the rest of the model. In the refined area, element sizes from 0.3 mm to 0.07 mm were tested while in the rest of the model, element sizes from 0.7 mm to 0.45 mm were tested. Mesh refinement was stopped when a change of less than 3 °C was observed within the molten zone. A range of time steps was explored starting from 2 s to 0.5 s. Time step of 1 s was chosen to satisfy solution convergence and stability.

Maximum heat generation happens at the contact surface of the parts. Heat generation was defined by an input ASCII file in the form of a 2D array and is a function of depth (y) and time (t). A MATLAB computer code was developed to create the heat generation input file as a function of beam dimensions, laser power, and absorption coefficient of the transparent and absorbent parts. An example of heat generation profile along the y axis is shown in Fig. 5 (Eq. (2)).

The model simulated a 10 s interval of laser–material interaction (i.e., heating), followed by 10 s cooling phase. The beam was stationary.

In laser welding of PA6 parts of similar dimensions, laser powers in the tens of watts, and speeds of 5–50 mm/s are used, which lead to laser–material interaction times of under 1 s. For this study, the heating process was prolonged and power was decreased to accommodate the thermal camera data acquisition speed limitations during the heating and cooling phases. As an example, the results obtained from a 10 s exposure of the rectangular plaques to a 1 W diode laser beam are presented in this study. When distributed uniformly over the beam area of 1.4 mm × 0.7 mm^2, this gives the energy flux of 1 W/mm^2. This value was used to generate the results presented in this paper, unless otherwise noted. While running a 160 W diode laser at a low power of 1 W leads to some degree of power fluctuation (±0.2 W), these fluctuations, as noted on the laser controller's display, were relatively fast (several per second) and average out to correct value over the much longer duration of the test (10 s). Accurate average power delivery was also verified prior to the tests by a calibration with a power meter.

Results and Discussion

The 3D temperature contours at the end of the heating stage (10 s) are shown in Fig. 6 for the case of an unscattered laser beam. Corresponding temperature contours on the symmetry plane of the geometry (x=0 mm) are shown in Fig. 7. The highest temperature of 345.4 °C was predicted at the symmetry plane and at 0.2 mm below the interface (y=3.2 mm). Given the melting point of PA6 (217 °C), the red area in the contour plot shows the molten volume of the plastic plaques. These data were supported by the experimental observations where the exposed plastic was molten at the interface.

Temperature as a function of time for different locations along the y axis at the symmetry plane (x=0 mm) and surface A (see

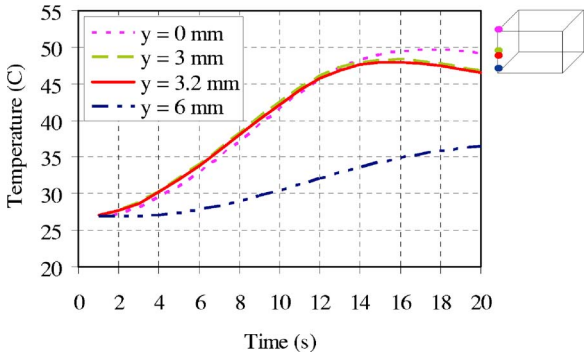

Fig. 8 Temperature versus time along the *Y* axis of the geometry (*x*=0 mm, *z*=12 mm, surface *A*)

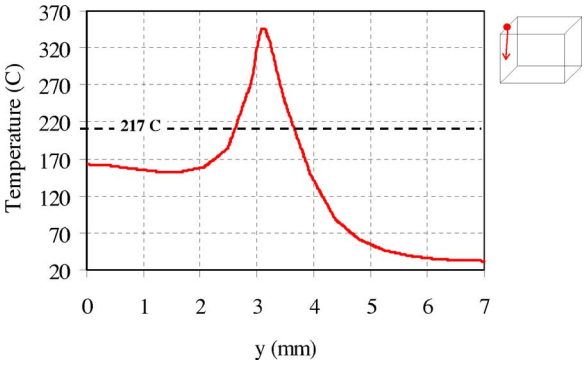

Fig. 11 Temperature distribution along the *y* axis (*t*=10 s, *x*=0 mm, *z*=9 mm, center of the beam)

Fig. 6) is shown in Fig. 8. Surface *A* is the surface observed by the thermal camera. The temperature increases up to a maximum value of 49.6°C at 17 s.

Figure 9 shows the temperature versus time at the center of the beam (z=9 mm) for different locations along the y axis. The temperature rises up to 345.4°C at 10 s and then decreases quickly at the joint interface (where the heat generation peaks). Temperature at the upper surface (y=0 mm) peaks at 162.3°C while temperature 3 mm below the joint interface remains below 38°C throughout the modeled time interval. From Fig. 9, the melting at the joint interface starts after 1.8 s and continues up to 10.8 s.

The temperature variation as a function of location along the x axis at the center of the beam and at the end of the heating phase (10 s) is shown in Fig. 10. A maximum temperature of 345.4°C was observed at the symmetry plane (x=0 mm). The temperature gradient is high up to x=2 mm and then decreases more considerably. Using Fig. 10, one can determine the weld width in the x direction. Using the melting temperature of PA6 (217°C), the weld half-width of 0.41 mm is obtained. This value is comparable with the weld half-width of 0.5 mm obtained from experimental studies (Fig. 20).

Temperature distribution along the y axis at the center of the beam, symmetry plane (x=0 mm), and at the end of the heating phase (10 s) is shown in Fig. 11. As can be seen from this figure, the temperature is highest (345.4°C) at 3.2 mm below the surface. This corresponds to 0.2 mm from the interface, inside the absorbent part. Using Fig. 11, one can determine the weld dimension in the y direction. Using the melting temperature of PA6 (217°C), the melt height of 0.99 mm is obtained.

Figure 12 shows the temperature distribution along the z axis at the center of the beam, symmetry plane (x=0 mm), and at the end of the heating phase (10 s). It is seen that the temperature increases as one gets closer to the center of the beam where maximum temperature of 345.4°C is observed. Using Fig. 12, one can determine the weld dimension in the z direction. Using the melting temperature of PA6 (217°C), the melt dimension of 1.35 mm is obtained. This value is comparable with the value of 1.5 mm obtained from experimental studies (Fig. 20). Figure 12 shows that the maximum temperature reached at surface *A* is 42.2°C.

Figure 13 shows the temperature variation for four different distances a of the laser beam center from the sample edge. The surface temperature is expected to increase as the laser is moved closer (shorter distance a). Figure 13 clearly shows how sensitive the edge temperature is to the position of the laser. When the beam was moved from 2 mm to 4 mm from the edge, the model-predicted peak face temperature decreased from 73°C to 37°C.

Note that all the results shown so far assumed the laser beam energy is uniformly distributed within the rectangular area of

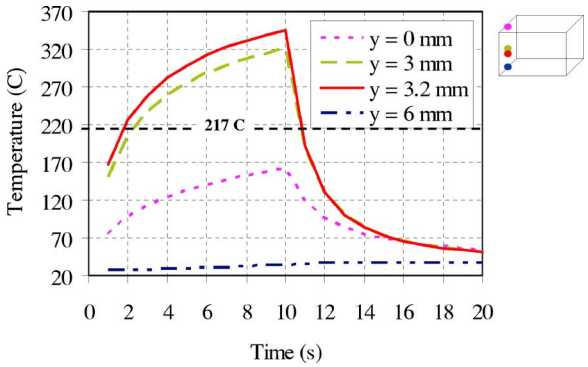

Fig. 9 Temperature versus time along the *Y* axis of the geometry (*x*=0 mm, *z*=9 mm, center of the beam)

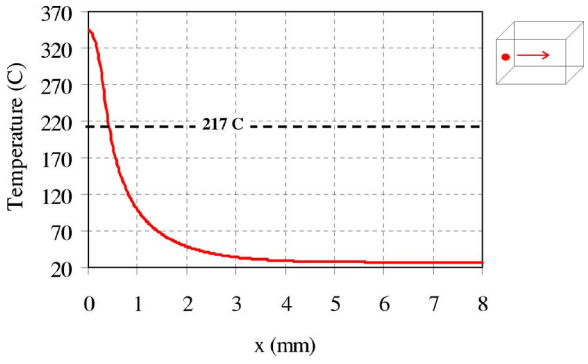

Fig. 10 Temperature distribution along the *x* axis (*t*=10 s, *y*=3.2 mm, *z*=9 mm, center of the beam)

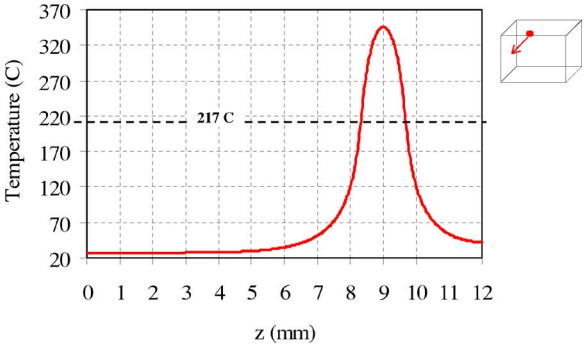

Fig. 12 Temperature distribution along the *z* axis (*t*=10 s, *x*=0 mm, *y*=3.2 mm)

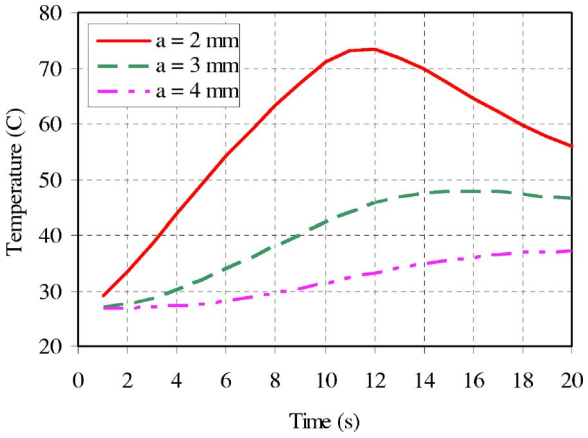

Fig. 13 Temperature versus time obtained from thermal modeling for different distances from the edge (*x*=0 mm, *y*=3 mm, *z*=12 mm, surface *A*)

1.4 mm × 0.7 mm^2. This uniform beam distribution serves as a first-order approximation of unscattered laser beam distribution in the focal plane.

Figures 14 and 15 show thermal images of the rectangular plaques exposed to a 1 W diode laser beam for 10 s where the beam center is located 3 mm from surface *A*. Figure 14 displays the temperature image at the end of the heating phase (10 s), where the temperature shows its maximum value (66°C) on the viewed surface. Figure 15 shows the temperature distribution after 10 s of cooling (20 s), where joint temperature drops to 55°C and heat conducts through the components.

Line *L*2 marks the top surface of part *A* (*y*=0 mm) and line *L*3 marks the lower surface of part *C* (*y*=9 mm). The image above line *L*3 shows the second absorbent plastic part (part *C*) that was mentioned earlier. As a reminder, the camera is looking at surface *A* (see Fig. 6). *L*1 marks the center line where the laser beam is located.

Figure 16 shows the temperature versus time obtained from thermal imaging presented in Figs. 14 and 15. It is seen that the temperature near the interface of the parts *A* and *B* increases during the heating stage (up to 66°C at 10 s) and then decreases during the cooling stage (down to 47°C at 20 s).

For comparison, Fig. 16 includes the thermal model prediction for temperature on surface *A* at the interface of parts *A* and *B* (Fig. 13, *a*=3 mm). It is clear that the observed surface temperatures do not agree with the 3D model predictions based on an unscattered and focused laser beam. The thermal model results show a smooth curve with no steep temperature gradient at the end of the heating stage. The thermal imager results show a sudden slope change when the laser is turned off at 10 s. This suggests that the laser beam is reaching much closer to the viewed surface than what would be expected from the unscattered laser.

The authors believe scattering is an important factor in a LTW process of PA6. Scattering causes the beam to be widened after hitting the transparent surface (part *A*). Therefore, the beam hitting the interface of the transparent and absorbent parts (parts *A* and *B*) is a larger distributed beam. To verify this theory, the beam was widened in the 3D thermal model to account for the scattering of the diode laser beam based on recently reported beam profiling studies [18] and ongoing experiments by the authors. Continuous and discretized beam profiles are shown in Fig. 17. This figure shows the measured normalized beam power flux after the beam passed through 3 mm of PA6 without carbon pigment. Clearly the beam has been broadened by scatter.

Figure 18 shows the results obtained from the thermal model where the discretized beam profile (Fig. 17) was implemented. In the *x* direction, energy was distributed uniformly over the beam half-width of 0.25 mm. The beam center was located at a distance *a*=3 mm from surface *A*, matching the experimental conditions. The results show that the thermal model predictions agree much better with the results obtained from the thermal imaging camera. The maximum predicted temperature of 67°C agrees very well with the observed peak temperature of 66°C thermal imaging experiments (Fig. 16).

Figure 19 compares the temperature versus time obtained from thermal modeling (points) and thermal imaging (lines) for different locations along the *y* axis on surface *A*. It is observed that the thermal imaging results support the thermal modeling results.

An additional way to validate a thermal model is to examine the

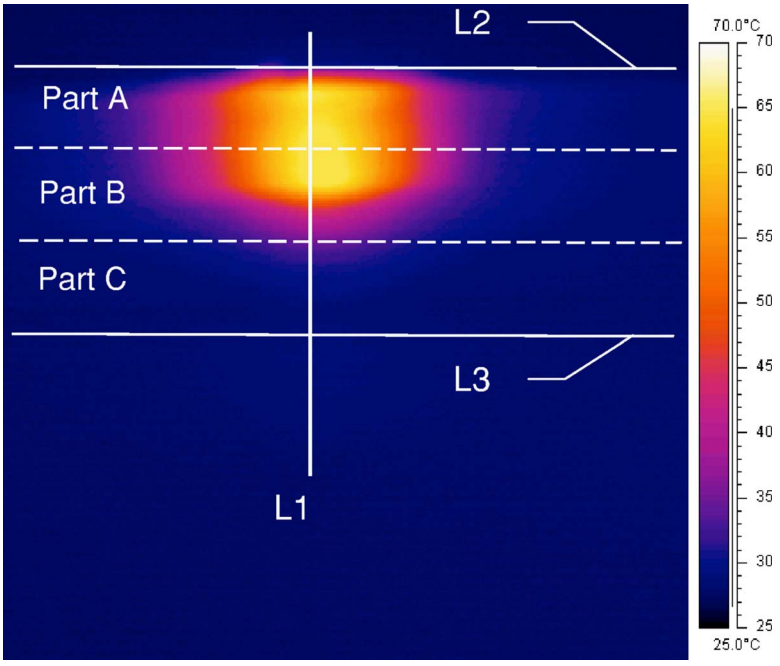

Fig. 14 Thermal imaging window at 10 s (laser on)

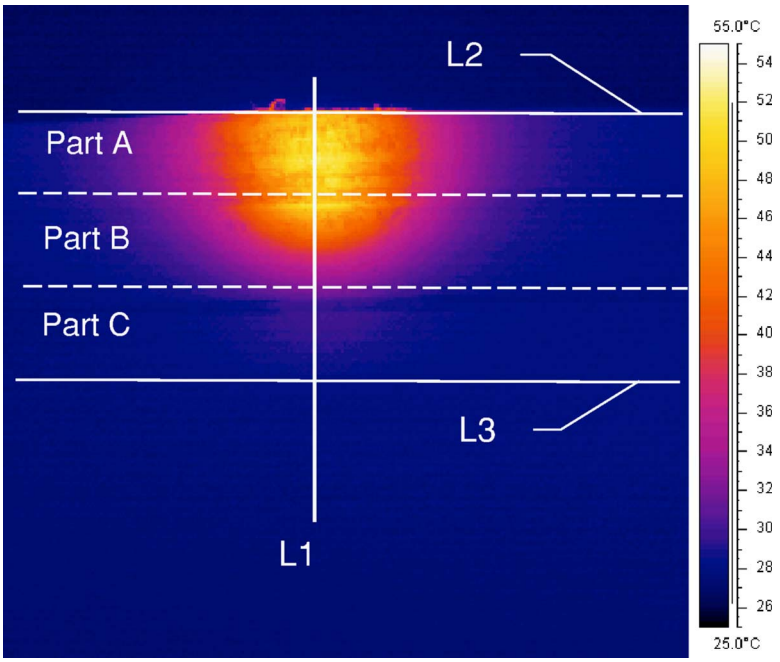

Fig. 15 Thermal imaging window at 20 s (laser off)

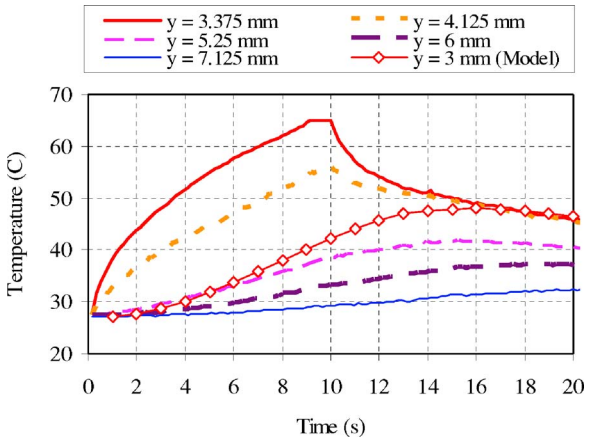

Fig. 16 Temperature versus time from thermal imaging experiments at different locations along the *y* axis (*x*=0 mm, *z*=12 mm, surface *A*)

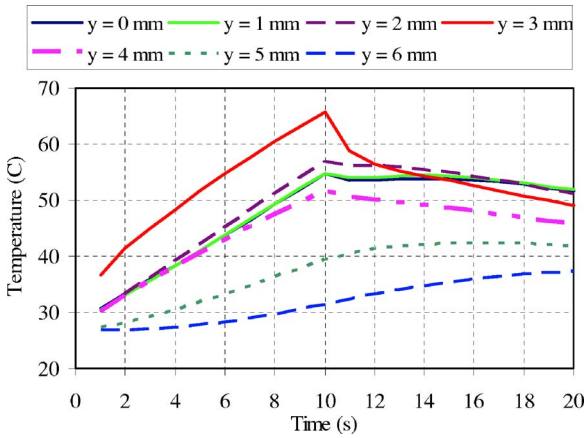

Fig. 18 Temperature versus time from thermal modeling at different locations along the *y* axis (*x*=0 mm, *z*=12 mm, surface *A*)

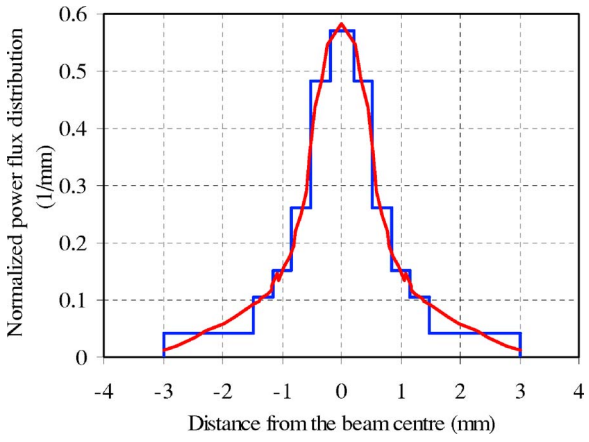

Fig. 17 Beam profile along the *z* axis

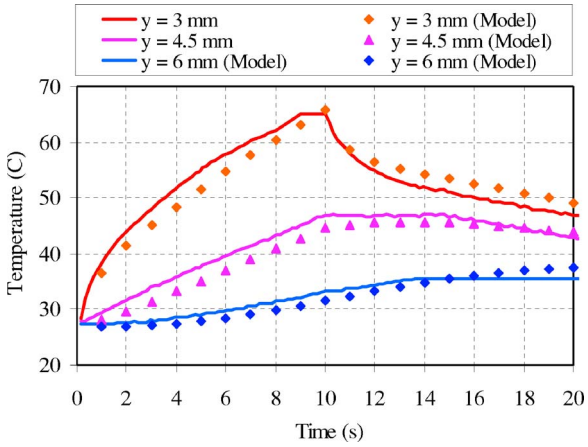

Fig. 19 A Comparison between the temperature versus time from thermal modeling and thermal imaging at different locations along the *y* axis (*x*=0 mm, *z*=12 mm, surface *A*)

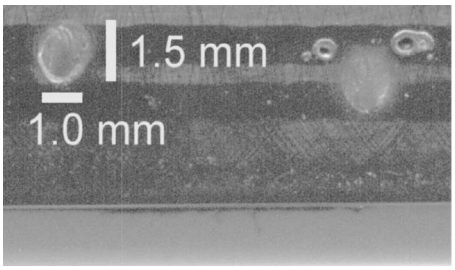

Fig. 20 Experimental molten spot dimensions

dimensions of the molten zone caused by the stationary beam. Upon separation of the two joined parts (A and B), this molten area was visible and its dimensions were found to be approximately 1.5 $mm^2 \times 1.0$ mm^2 (Fig. 20). These dimensions agree well with focused beam dimension (1.4 mm × 0.7 mm) suggesting that most of the laser power remains in the original beam.

Figure 21 shows the temperature distribution at 10 s along the x and z axes at the interface between parts A and B. Using the melting temperature of PA6 (217°C), the predicted molten zone dimension along the z axis is 1.23 mm and along the x axis, the half-width dimension is 0.29 mm (or 0.58 mm full width). This suggests the model is underpredicting the weld dimensions.

Conclusion

A 3D transient thermal model for a lap-joint exposed to a stationary diode laser was presented in this paper. The model was solved using the ANSYS FEM code. Results were presented for the case of a rectangular uniform beam energy distribution approximating unscattered and focused beam. The weld dimensions obtained from this model agreed well with the experimental weld dimensions. The temperature distribution obtained from the modeling results was compared to thermal imaging data from experiments and it was found that the model predictions did not agree well with the thermal imaging data. However, when scatter of the laser beam was accounted for in the thermal model, the agreement between the thermal imager and model was significantly improved. With scatter included, the thermal model tended to slightly underpredict the final weld dimensions. These results show that beam scatter is an important factor in thermal modeling of the LTW process.

Acknowledgment

The authors acknowledge the financial support of Natural Sciences and Engineering Research Council of Canada (NSERC).

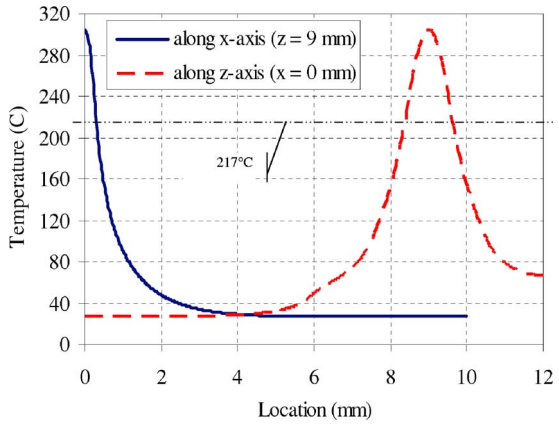

Fig. 21 Temperature as a function of location along the *x* and *z* axes at the center of the beam (*t*=10 s)

The authors appreciate the technical support for ANSYS provided by ROI Engineering Company and, in particular, Mr. Peter Budgell for technical assistance with the software. The authors acknowledge the contribution of Canada Foundation for Innovation (CFI) and Ontario Innovation Trust (OIT) toward the purchase of the diode laser system.

Nomenclature

C = specific heat (J/kg°C)
I = laser energy flux (W/mm^2)
K = extinction coefficient (mm^{-1})
T = temperature (°C)
dx = width increment (mm)
dy = depth increment (mm)
dz = height increment (mm)
k = thermal conductivity (W/m°C)
q = internal heat generation rate (W/mm^3)
t = time (s)
x, y, z = coordinate variables

Greek

ρ = density (kg/m^3), reflectivity

Subscripts

0 = initial condition
x = along the x axis
y = along the y axis
z = along the z axis

References

[1] Russek, U.-A., Poggel, M., Otto, G., and Koeppe, A. 2003, "Advances in Laser Beam Welding of Polymers and Automotive Prospects," *Proceedings of the 9th International Conference: TPOs in Automotive*, pp. 51–60.
[2] Cherdron, M. 2004, "Industrial Applications for Laser Welding of Plastics," SPE, ANTEC, pp. 1261–1264.
[3] Grewell, D., and Benatar, A. 2003, "Experiments in Micro-Welding of Polycarbonate With Laser Diodes," SPE, ANTEC, pp. 1039–1044.
[4] Chen, J. W., and Zybko, J. 2005, "Diode Laser Bonding of Planar Microfluidic Devices, Moems, Biomems, Diagnostic Chips and Microarrays," Proc. SPIE, **5718**, pp. 92–98.
[5] Rosenthal, D. 1941, "Mathematical Theory of Heat Distribution During Welding and Cutting," Weld. J. (Miami, FL, U.S.), **20**(5), pp. 220–234.
[6] Potente, H., Korte, J., and Becker, F. 1999, "Laser Transmission Welding of Thermoplastics: Analysis of the Heating Phase," J. Reinf. Plast. Compos., **18**(10), pp. 914–920.
[7] Grewell, D., and Benatar, A. 2003, "Modeling Heat Flow for a Moving Heat Source to Describe Scan Micro-laser Welding," SPE, ANTEC, pp. 1045–1050.
[8] Sato, K., Kurosaki, Y., Satio, T., and Satoh, I. 2002, "Laser Welding of Plastics Transparent to Near-Infrared Radiation," Proc. SPIE, **4637**, pp. 528–536.
[9] Prabhakaran, R., Kontopoulou, M., Zak, G., Bates, P. J., and Baylis, B., 2004, "Laser Transmission Welding of Unreinforced Nylon 6," SPE, ANTEC, pp. 1205–1209.
[10] Prabhakaran, R., Kontopoulou, M., Zak, G., Bates, P. J., and Sidiropoulos, V. 2005, "Simulation of Heat Transfer in Laser Transmission Welding," Int. Polym. Process., **20**(4), pp. 410–417.
[11] Mayboudi, L. S., Birk, A. M., Zak, G., and Bates, P. J. 2005, "A 2-D Model for Laser Transmission Welding of Thermoplastics," *Proceedings 25th International Congress on Applications on Lasers and Electro-Optics*, ICALEO, Laser Material Processing Conference, pp. 402–409.
[12] Mayboudi, L. S., Birk, A. M., Zak, G., and Bates, P. J. 2006, "A Three-Dimensional Finite Element Model for Laser Transmission Welding of Thermoplastics," *Proceedings 15th IASTED International Conference on Applied Simulation and Modelling*.
[13] Haferkamp, H., Von Busse, A., Hustedt, M., Bunte, J., Haberstroh, E., and Lutzeler, R. 2004, "Utilization of a Thermographic Process in Order to Determine the Laser Weldability of Plastics at Different Wavelengths," Welding and Cutting, **3**(1), pp. 43–49.
[14] Incropera, F. P., and DeWitt, D. P. 1996, *Introduction to Heat Transfer*, 3rd ed., Wiley, New York.
[15] Siegel, R., and Howell, J. R. 1992, *Thermal Radiation Heat Transfer*, 3rd ed., Taylor and Francis, London, UK.
[16] http://www.dsm.com/en_US/html/dep/MDAC_Selector.htm
[17] Prabhakaran, R. 2003, Laser Transmission Welding of Nylon 6, M.Sc. thesis, Queen's University, Canada.
[18] Mayboudi, L. S., Chen, M., Zak, G., Birk, A. M., and Bates, P. J. 2006, "Characterization of Beam Profile for High-Power Diode Lasers with Application to Laser Welding of Polymers," SPE, ANTEC, pp. 2274–2278.
[19] ANSYS® 10 Manual.

Temperature-Dependent Viscosity and Viscous Dissipation Effects in Simultaneously Developing Flows in Microchannels With Convective Boundary Conditions

C. Nonino[1]
e-mail: carlo.nonino@uniud.it

S. Del Giudice

S. Savino

Dipartimento di Energetica e Macchine,
Università degli Studi di Udine,
Via delle Scienze 208,
33100 Udine, Italy

The effects of viscous dissipation and temperature dependent viscosity in simultaneously developing laminar flows of liquids in straight microchannels are studied with reference to convective boundary conditions. Two different geometries, namely the circular tube and the parallel plate channel, are considered. Viscosity is assumed to vary with temperature according to an exponential relation, while the other fluid properties are held constant. A finite element procedure, based on a projection algorithm, is employed for the step-by-step solution of the parabolized momentum and energy equations. Axial distributions of the local overall Nusselt number and of the apparent Fanning friction factor are presented with reference to both heating and cooling conditions for two different values of the Biot number. Examples of radial temperature profiles at different axial locations and of axial distributions of centerline velocity and temperature are also shown. [DOI: 10.1115/1.2740306]

Keywords: microchannels, simultaneously developing flows, viscous dissipation, temperature dependent viscosity, convective boundary conditions

Introduction

The accurate solution of several heat transfer problems associated with microchannel flows requires that the thermal resistance of the channel wall is not disregarded. Moreover, in many situations of practical interest, fluid velocity and temperature fields develop simultaneously, resulting in overlapping hydrodynamic and thermal entrance regions. This occurs when fluid heating or cooling begins at the microchannel inlet, where the velocity boundary layer also starts developing. In such a situation, entrance effects on fluid flow and forced convection heat transfer cannot be neglected if, as it happens very often in laminar flows, the total length of the microchannel is comparable with that of the entrance region. Temperature dependence of fluid properties can also play an important role in the development of velocity and temperature fields. If, as it is assumed in this paper, the fluid is a liquid, viscosity is the property which exhibits the most relevant variations with respect to temperature. Therefore, the main effects of temperature dependent fluid properties can be retained even if only viscosity is allowed to vary with temperature, while the other properties are assumed constant. Finally, viscous dissipation effects often cannot be neglected in ducts with very small hydraulic diameters, like microchannels, even for ordinary liquids, characterized by moderate values of viscosity. It is worth noting that, with temperature dependent viscosity, viscous dissipation affects both temperature and velocity distributions along the microchannel. Even if all these aspects have already been considered in the past, to the authors' knowledge no systematic studies are reported in the literature taking into account the combination of wall thermal resistance, entrance, temperature dependent viscosity, and viscous dissipation effects. Only recently, the authors have presented a couple of papers where the influences of the last three factors are analyzed, but the wall thermal resistance is neglected [1,2]. It must be noticed, however, that a simplified way to account for it and, possibly, also for the external convection resistance, is represented by the specification of convective boundary conditions at the wall, with an appropriately defined heat transfer coefficient, when solving the energy equation. This approach is adopted in the present paper which, thus, represents an extension of the previous work.

In the past decades, many authors have investigated, both analytically and numerically, simultaneously developing flows in straight ducts of constant cross section. Comprehensive reviews of these theoretical studies, referring to ducts of different cross-sectional geometries, can be found in Refs. [3,4]. However, since a basic assumption made in almost all such studies is that fluid properties are constant, the corresponding solutions are adequate only for problems involving small temperature differences. In fact, experimental results for problems involving large temperature differences substantially deviate from constant property solutions [3,5].

As anticipated above, for most liquids, density, specific heat, and thermal conductivity are nearly independent of temperature, while viscosity markedly decreases with increasing temperature, in much the same manner as the Prandtl number does [5]. Thus, the assumption of constant properties, with the exception of viscosity, which is still allowed to vary with temperature, is adequate for most liquid flows, no matter how large temperature differences are. Because of the relative complexity of temperature dependent property problems, only a limited number of such solutions for laminar forced convection in simultaneously developing flow in ducts have appeared in the literature [3]. However, most of these studies are based on the assumption of a viscosity dependence on temperature given by a specific relation of empirical nature [5–9], leading to results which cannot be considered general and appli-

[1]Corresponding author.

Contributed by the Heat Transfer Division of ASME for publication in JOURNAL OF HEAT TRANSFER. Manuscript received July 25, 2006; final manuscript received December 11, 2006. Review conducted by Satish G. Kandlikar. Paper presented at the 4th International Conference on Nanochannels, Microchannels and Minichannels (ICNMM2006), Limerick, Ireland, UK, June 19–21, 2006.

cable to other liquids or for different temperature ranges. Similar considerations can be made with respect to studies concerning thermally or simultaneously developing flows in microchannels [10,11].

As already mentioned, viscous dissipation effects cannot be ignored in microchannel flows of ordinary fluids, having Prandtl numbers on the order of a few units, due to the very small values of the hydraulic diameter [12–17]. For such fluids, hydrodynamic and thermal entrance lengths are comparable, so that both fully developed and uniform velocity profiles can be assumed at the entrance of the heated/cooled part of the microchannel, resulting in thermally developing and hydrodynamically fully developed flow or in simultaneously developing flow, respectively. The first situation occurs when fluid heating/cooling begins at an axial position where hydrodynamically fully developed conditions have already been reached, the latter when both velocity and temperature boundary layers start developing at the microchannel inlet. Therefore, existing literature on viscous dissipation effects in microchannels not only considers fully developed forced convection [12,13,17] and thermally developing and hydrodynamically fully developed flow [18–20], but also simultaneously developing flow [10,11].

In this paper, we present the results of a parametric study on the simultaneously developing laminar flow of a liquid in straight microchannels. Two different cross-sectional geometries, namely the circular tube and the parallel plate channel, are considered. It must be pointed out that these cross-sectional geometries represent the limiting cases corresponding to the maximum and minimum values of the ratio of the wetted perimeter over the area of the cross section. Therefore, an intermediate behavior can be expected for ducts with different cross-sectional geometries. The effects of wall thermal resistance, temperature dependent viscosity, and viscous dissipation on pressure drop and heat transfer are investigated, while the other liquid properties are considered constant. A finite element procedure [21], based on a SIMPLE-like algorithm [22], is employed for the step-by-step solution of the parabolized momentum and energy equations [22,23] in a one-dimensional axial–symmetric domain corresponding to the cross section of the duct. Due to the high value of the ratio between the total length and the hydraulic diameter in microchannels, such an approach is very advantageous with respect to that based on the steady-state solution of the set of governing elliptic equations in a two-dimensional axial–symmetric domain corresponding to the whole microchannel. The above procedure has already been used, disregarding viscous dissipation effects, in the simulation of simultaneously developing flows of liquids with temperature dependent viscosity in straight ducts [24] and, on the additional assumptions of non-negligible viscous dissipation effects, in the study of thermally and simultaneously developing liquid flows in microchannels when prescribed constant temperature boundary conditions are applied to the rigid walls [1,2]. Here the same procedure is used to study a similar problem with reference to flows in microchannels with convective thermal boundary conditions. In all the cases studied here, viscosity is assumed to have an exponential variation with temperature in the range considered [5,8,9,25–27]. In order to allow a parametric investigation, a suitable dimensionless form of the assumed viscosity–temperature relation is used.

Mathematical Model

When the effects of axial diffusion can be neglected and there is no recirculation in the longitudinal direction, steady-state flow and heat transfer in straight microchannels of constant cross section are governed by the continuity and the parabolized Navier–Stokes and energy equations. Since the inverse of the Reynolds number is representative of the relative importance of diffusive and advective components of the axial momentum flow rate, while the inverse of the Péclet number is representative of the relative importance of conductive and advective components of the axial heat flow rate, the parabolic approximation of the Navier–Stokes and energy equations can be considered adequate, except for the immediate neighborhood of the inlet, for values of the Reynolds and Péclet numbers larger than 50 [3,28]. With reference to incompressible fluids with temperature dependent thermophysical properties, in the hypotheses of negligible body forces and significant effects due to viscous dissipation, the above mentioned equations can be written in the following form, valid for axial–symmetric geometries

$$\frac{\partial u}{\partial x} + \frac{1}{r}\frac{\partial}{\partial r}(rv) = 0 \tag{1}$$

$$\rho u\frac{\partial u}{\partial x} = \frac{1}{r}\frac{\partial}{\partial r}\left(\mu r\frac{\partial u}{\partial r}\right) - \rho v\frac{\partial u}{\partial r} - \frac{d\bar{p}}{dx} \tag{2}$$

$$\rho u\frac{\partial v}{\partial x} = \frac{2}{r}\left[\frac{\partial}{\partial r}\left(\mu r\frac{\partial v}{\partial r}\right) - \mu\frac{v}{r}\right] - \rho v\frac{\partial v}{\partial r} - \frac{\partial p}{\partial r} \tag{3}$$

$$\rho cu\frac{\partial t}{\partial x} = \frac{1}{r}\frac{\partial}{\partial r}\left(kr\frac{\partial t}{\partial r}\right) - \rho cv\frac{\partial t}{\partial r} + \mu\Phi_v \tag{4}$$

where

$$\Phi_v = \left(\frac{\partial u}{\partial r}\right)^2 + 2\left[\left(\frac{\partial v}{\partial r}\right)^2 + \left(\frac{v}{r}\right)^2\right] \tag{5}$$

According to the assumption of parabolic flow, all the derivatives in the axial direction are neglected in the diffusive terms of Eqs. (2)–(5) [23]. In the above equations, x and r are the axial and the radial coordinates, respectively; while u and v represent the axial and the radial components of velocity. Finally, t is the temperature; p is the deviation from the hydrostatic pressure; $\bar{p}$ is its average value over the cross section; while ρ, μ, c, and k represent density, dynamic viscosity, specific heat, and thermal conductivity of the fluid, respectively.

The solution domain can be bounded by rigid walls or by the symmetry axis. On rigid boundaries the usual no-slip conditions, that is, $u=v=0$, are imposed together with the convective boundary condition $q''=-k\partial t/\partial r=h_a(t-t_a)$, where h_a is the external convective heat transfer coefficient and t_a is the ambient fluid temperature. Instead, symmetry conditions at the symmetry axis are $\partial u/\partial r=0$, $v=0$, and $\partial t/\partial r=0$.

The model equations are solved using a finite element procedure which represents an extended version of one previously developed for the analysis of the forced convection of constant property fluids in the entrance region of straight ducts [21]. The added new features mainly consist of the possibility of taking into account the effects of temperature dependent properties and of viscous dissipation. The adopted procedure is based on a segregated approach which implies the sequential solution of momentum and energy equations on a one-dimensional domain corresponding to the cross section of the channel. A marching method is then used to move forward in the axial direction. The pressure–velocity coupling is dealt with using an improved projection algorithm already employed by one of the authors (C.N.) for the solution of the Navier–Stokes equations in their elliptic form [29].

Numerical Results

As stated above, the laminar forced convection in the entrance region of straight microchannels with convective boundary conditions is studied. The hypotheses made here are that viscous dissipation effects are not negligible and that liquid heating/cooling begins at the microchannel inlet, where also the velocity boundary layer starts developing. Therefore, at the entrance of the microchannel, uniform values of the velocity u_e and of the temperature t_e can be specified as the appropriate inlet conditions. At the mi-

crochannel wall the convective boundary condition $q''_w = h_a(t_w - t_a)$ is applied, where q''_w and t_w are the local wall heat flux and temperature, respectively.

The dynamic viscosity is assumed to vary with temperature and μ_e and μ_a are its values at t_e and t_a, respectively. The ratio of μ_e over μ_a gives an indication of the relevance of the temperature dependence of viscosity in the range between t_e and t_a. Exponential or Arrhenius type relations are usually employed to represent the temperature dependence of viscosity. The one adopted in this paper is the widely used exponential formula [5,8,9,25–27]

$$\mu = \mu_a \exp[-\beta(t - t_a)] \tag{6}$$

with $\beta = -(d\mu/dt)/\mu = \text{const}$. By means of simple manipulations, Eq. (6) can be cast in the following dimensionless forms

$$\frac{\mu}{\mu_a} = \exp(-BT) = \left(\frac{\mu_e}{\mu_a}\right)^T \tag{7}$$

where $T = (t - t_a)/(t_e - t_a)$ is the dimensionless temperature and $B = -\ln(\mu_e/\mu_a)$ is a dimensionless viscosity parameter.

It is worth noting that, since all the other thermophysical properties are assumed constant, we have $\mu_e/\mu_a = \mathrm{Pr}_e/\mathrm{Pr}_a = \mathrm{Re}_a/\mathrm{Re}_e$. Moreover, while the local Reynolds number $\mathrm{Re} = \rho u_e D_h/\mu$ and the local Prandtl number $\mathrm{Pr} = \mu c/k$ depend on temperature, the local Péclet number $\mathrm{Pe} = \mathrm{RePr} = \mathrm{Re}_e\mathrm{Pr}_e = \mathrm{Re}_a\mathrm{Pr}_a$ always has the same value. Since the viscosity of liquids decreases with increasing temperature, $\mathrm{Pr}_e/\mathrm{Pr}_a > 1$ corresponds to fluid heating ($t_e < t_a$) and $\mathrm{Pr}_e/\mathrm{Pr}_a < 1$ to fluid cooling ($t_e > t_a$), while $\mathrm{Pr}_e/\mathrm{Pr}_a = 1$ refers to isothermal flows ($t_e = t_a$) or to constant viscosity fluids. Moreover, the reference Brinkman number $\mathrm{Br}_m = \mu_m u_e^2/[k(t_e - t_a)]$, evaluated at the reference fluid temperature $t_m = (t_e + t_a)/2$, is negative for fluid heating and positive for fluid cooling.

In all the computations, the same values $\mathrm{Re}_m = \rho u_e D_h/\mu_m = 500$ and $\mathrm{Pr}_m = \mu_m c/k = 5$ of the Reynolds and Prandtl numbers at the reference temperature of the fluid $t_m = (t_e + t_w)/2$ have been assumed. The corresponding value of the Péclet number is $\mathrm{Pe} = 2500$. Therefore, for the values of the ratio $\mathrm{Pr}_e/\mathrm{Pr}_w = 1/2$, $2/3$, 1, $3/2$, and 2 considered here, minimum and maximum values of the local Reynolds number in the temperature range between t_e and t_w are 354 and 707, respectively, while the Prandtl number can vary between 3.54 and 7.07. In addition to $\mathrm{Br}_m = 0$, corresponding to negligible viscous dissipation, two reasonable nonzero values of the reference Brinkman number have been chosen, namely, $\mathrm{Br}_m = \pm 0.01$ and ± 0.1. Finally, two values of the Biot number $\mathrm{Bi} = h_a D_h/k = 5$ and 20 have been selected as representative of situations where convective boundary conditions should be specified.

In the following, numerical results concerning axial distributions of $f_{\mathrm{app}}\mathrm{Re}_m$ and of the local overall Nusselt number $\mathrm{Nu}_o = UD_h/k$ are presented. In these expressions f_{app} is the apparent Fanning friction factor defined as [3]

$$f_{\mathrm{app}} = \frac{(\bar{p}_e - \bar{p})D_h}{2\rho u_e^2 x} \tag{8}$$

while

$$U = \frac{q''_w}{t_b - t_a} \tag{9}$$

is the local overall heat transfer coefficient, where t_b is the bulk temperature [3,4]. The local overall heat transfer coefficient U can be expressed as [3,4]

$$U = \left(\frac{1}{h} + \frac{1}{h_a}\right)^{-1} \tag{10}$$

with the local convective heat transfer coefficient h defined as

$$h = \frac{q''_w}{t_b - t_w} \tag{11}$$

On the basis of Eq. (10), the local overall Nusselt number Nu_o can be expressed as

$$\mathrm{Nu}_o = \left(\frac{1}{\mathrm{Nu}} + \frac{1}{\mathrm{Bi}}\right)^{-1} \tag{12}$$

where $\mathrm{Nu} = hD_h/k$ is the local Nusselt number.

Two different cross-sectional geometries, namely the circular tube and the parallel plate channel, are selected as representative of the limiting situations corresponding to the minimum and maximum values of the ratio between the length of the wetted perimeter and the flow area. Both these cross-sectional geometries are axisymmetric, since the latter can be considered a particular case of concentric annular duct with $r_i/r_o = 1$, where r_i and r_o are the inner and the outer radii of the duct, respectively. In fact, even if the radii r_i and r_o are different, their ratio r_i/r_o tends to unity when they both tend to infinity. In such a case, the inner and the outer surfaces of the annular duct become flat as in a parallel plate channel.

The computational domains have been defined taking into account existing symmetries. Therefore, the circular and the parallel plate cross sections correspond to one-dimensional axisymmetric domains of lengths r_o and $r_o - r_i = 2a$, respectively, where a is the half-spacing of parallel plates. These domains have been discretized by means of three-node parabolic elements whose sizes gradually increase with increasing distance from the walls. A total of 40 elements and 81 nodal points have been used in the discretization of the domain corresponding to the circular cross section, and a total of 80 elements and 161 nodal points in that corresponding to the concentric annular cross section (parallel plates). Of course, preliminary test had been carried out to verify that all these discretizations are fine enough to give mesh-independent results. In all the computations, the axial step has gradually been increased from the starting value $\Delta x/D_h = 0.0001$ to the maximum value $\Delta x/D_h = 0.05$.

The procedure outlined in the previous section and employed for the numerical simulations had already been validated, on the assumptions of constant property fluid and negligible viscous dissipation, by comparing heat transfer and pressure drop results with existing literature data for laminar simultaneously developing flows in straight ducts, both three dimensional and axial–symmetric [21,24]. In order to assess the accuracy of the present computations, additional validation tests have been carried out. Asymptotic values of the Nusselt number $(\mathrm{Nu}_\infty)_c = h_\infty D_h/k$ and fully developed values of the Poiseuille number $(f\mathrm{Re})_c$ for a constant property fluid are compared here with available literature data for circular ducts and parallel plate channels. For circular ducts, the computed values $(\mathrm{Nu}_\infty)_c = 3.65680$ and 9.60000 for $\mathrm{Br}_m = 0$ and $\mathrm{Br}_m \neq 0$, respectively, are in excellent agreement with the corresponding literature values $(\mathrm{Nu}_\infty)_c = 3.65679$ and $48/5 = 9.6$ [3,30,31]. Moreover, the computed fully developed value of the Poiseuille number $(f\mathrm{Re})_c = 16.0000$ is coincident with the corresponding literature value $(f\mathrm{Re})_c = 16$ [3]. Similar comparisons can be carried out with reference to parallel plates. Also in this case, the computed values $(\mathrm{Nu}_\infty)_c = 7.54075$ and 17.50000 for $\mathrm{Br}_m = 0$ and $\mathrm{Br}_m \neq 0$, respectively, match very well the corresponding literature values $(\mathrm{Nu}_\infty)_c = 7.54070$ and 17.5 [3], while the computed fully developed value $(f\mathrm{Re})_c = 24.0000$ again coincides with the literature value $(f\mathrm{Re})_c = 24$ [3].

The procedure is also validated here on the assumption of nonnegligible viscous dissipation, with reference to thermally developing and hydrodynamically fully developed flows of constant property fluids in circular ducts with convective boundary conditions, for which an analytical solution exists [32]. As in Ref. [32], a fully developed (parabolic) axial velocity profile $u = 2\bar{u}[1 - (r/r_o)^2]$ and a uniform temperature profile $t = t_e$ are assumed at

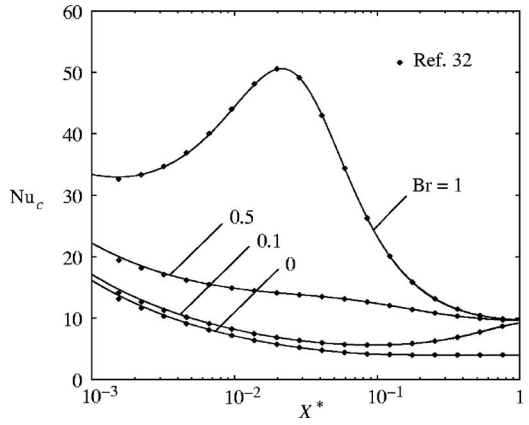

Fig. 1 Axial distributions of the Nusselt number Nu_c for thermally developing and hydrodynamically fully developed flows of constant property fluids in circular ducts with convective boundary conditions (Bi=4): comparisons of numerical results (solid lines) with analytical solutions by Lin et al. [32] (diamonds) for different values of the Brinkman number.

the inlet of the duct, while the convective boundary condition $q''_w=h_a(t_w-t_a)$ is specified at the wall. The axial velocity profile is assumed to remain the same along the whole duct length while, due to heat transfer and viscous dissipation, the temperature profile changes with the axial position until thermally developed flow conditions are reached. In our calculation, fluid properties and flow parameters are assumed to give the values $Re=\rho\bar{u}D_h/\mu=500$ and $Pr=\mu c/k=5$ of the Reynolds and Prandtl numbers, respectively. As in Ref. [32], three values of the Brinkman number $Br=\mu\bar{u}^2/[k(t_e-t_a)]=0.1$, 0.5, and 1 are considered here, to account for reasonable viscous dissipation effects. Axial distributions of computed Nusselt number $Nu_c=hD_h/k$ for the selected value of the Biot number $Bi=h_aD_h/k=4$ are in very good agreement with analytical results of Ref. [32], as can be seen in Fig. 1.

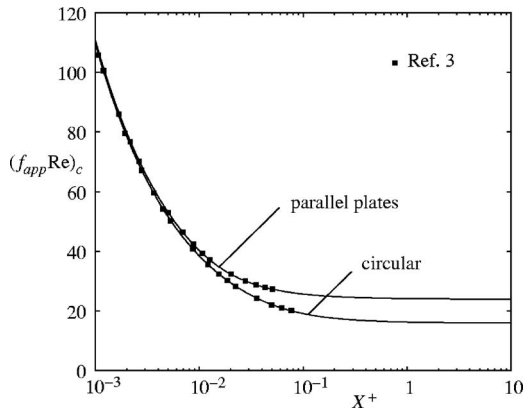

Fig. 2 Axial distribution of $(f_{app}\,Re)_c$ for simultaneously developing flows of constant property fluids in circular ducts and parallel plate channels: comparisons of numerical results (solid line) with literature data [3] (squares).

Finally, in order to complete the validation of the procedure, the axial distribution of computed $(f_{app}Re)_c$ for simultaneously developing flows of constant property fluids in circular and flat ducts is compared in Fig. 2 with available literature data from Ref. [3].

The influence of viscous dissipation on the local overall Nusselt number is illustrated in Figs. 3 and 4, where numerical results concerning axial distributions of $(Nu_o)_c$ for constant property flows ($Pr_e/Pr_a=1$) with different Biot and Brinkman numbers are presented. As expected, for a given value of the Biot number Bi the same asymptotic value of $(Nu_o)_c$ is reached for fully developed conditions with any value of Br_m, while Br_m strongly affects the Nusselt number in the intermediate range of X^*. The influence of Br_m is also significant for low values of X^*, where $(Nu_o)_c$ values are lower than those corresponding to $Br_m=0$ if $Br_m<0$ (fluid heating), and higher if $Br_m>0$ (fluid cooling). To explain the singularity appearing in the Nusselt number distributions for negative values of Br_m, we must consider that, because of viscous dissipation, when fully developed conditions are approached the bulk temperature also exceeds the wall temperature in fluid heating. At the axial location where the difference t_b-t_w goes to zero, the absolute value of the Nusselt number goes to infinity.

The influence of temperature dependent viscosity on the local overall Nusselt number is shown in Figs. 5 and 6, where axial distributions of the ratio $Nu_o/(Nu_o)_c$ for circular and flat microchannels with different Biot and Brinkman numbers are presented. As can be noticed, the ratio Pr_e/Pr_a significantly affects the Nusselt number as long as the flow develops, while its influence is rather small when fully developed conditions are reached. It must be observed that the very high values of the ratio $Nu_o/(Nu_o)_c$ found at intermediate X^* for heating ($Pr_e/Pr_a>1$) are not very significant, since they are simply due to a moderate axial shifting of curves representing axial distributions of Nu with respect to the constant property ones reported in Figs. 3 and 4. By comparing axial distributions of $Nu_o/(Nu_o)_c$ for different Brinkman numbers Br_m and the same Biot number Bi, it can be seen that, in simultaneously developing flows, the influence of temperature dependent viscosity is more evident than that of viscous dissipation.

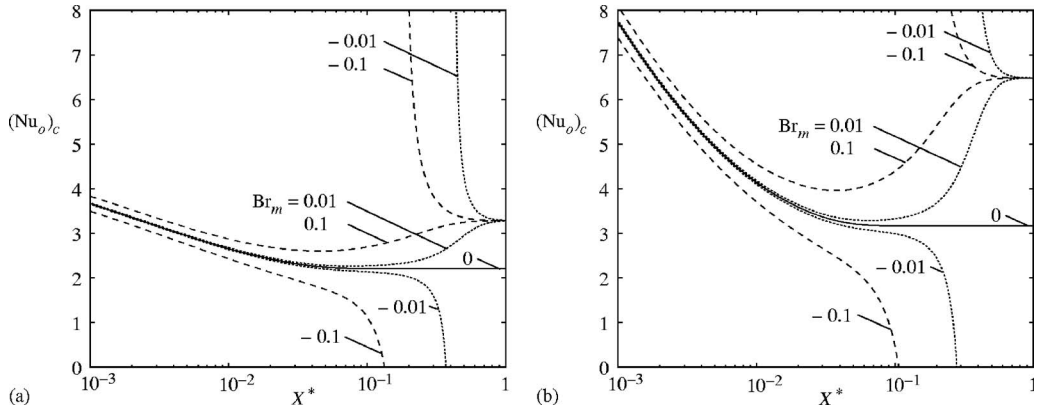

Fig. 3 Axial distributions of the local overall Nusselt number $(Nu_o)_c$ for simultaneously developing flows of constant property fluids with $Pr_m=5$ in microchannels of circular cross section with different Brinkman numbers Br_m: (*a*) Bi=5; and (*b*) Bi=20.

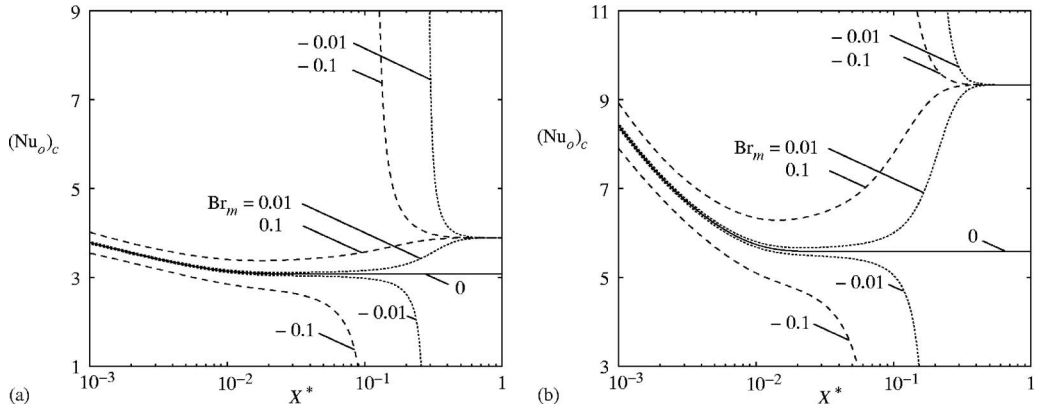

Fig. 4 Axial distributions of the local overall Nusselt number $(Nu_o)_c$ for simultaneously developing flows of constant property fluids with $Pr_m=5$ in flat microchannels with different Brinkman numbers Br_m: (*a*) Bi=5; and (*b*) Bi=20.

The combined effects of temperature dependent viscosity and viscous dissipation on pressure drop are illustrated in Figs. 7 and 8 with reference to axial distributions of the ratio $f_{app}Re_m/(f_{app}Re_m)_c$ for different Biot and Brinkman numbers. As can be seen, near the entrance the values of $f_{app}Re_m/(f_{app}Re_m)_c$ are more influenced by temperature dependence of viscosity than by viscous dissipation, while both effects increase and become comparable when fully developed conditions are approached. As expected, fully developed values of $f_{app}Re_m/(f_{app}Re_m)_c$ are larger than 1 for cooling and smaller than 1 for heating, while the opposite occurs near the entrance. Curves for heating and cooling cross each other because of the way the viscosity at the wall μ_w varies along the channel. In fact, we have $\mu_w > \mu_m$ near the entrance and $\mu_w < \mu_m$ in the fully developed region for fluid heating, while the opposite occurs in the case of fluid cooling. As can be seen, the axial positions where the crossing takes place get closer to the entrance as the Biot number increases.

The differences between the local values of $Nu_o/(Nu_o)_c$ and

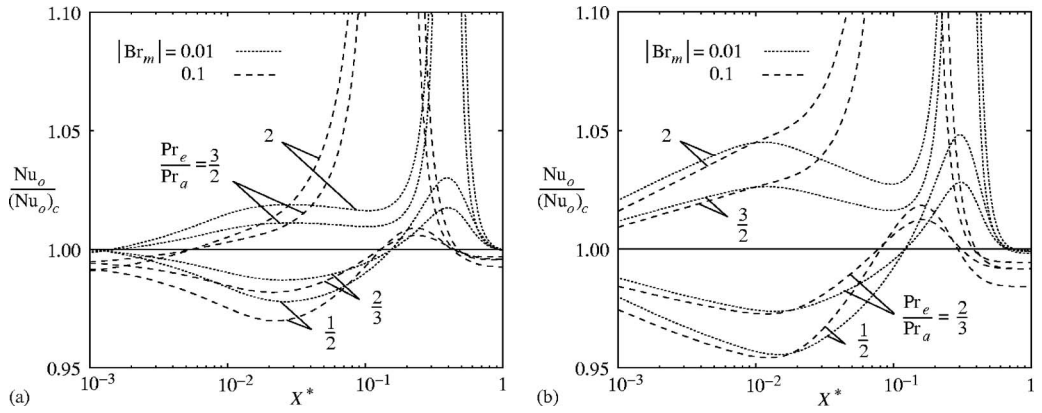

Fig. 5 Axial distributions of the ratio $Nu_o/(Nu_o)_c$ for microchannels of circular cross section with $Pr_m=5$ and different Brinkman numbers Br_m: (*a*) Bi=5; and (*b*) Bi=20.

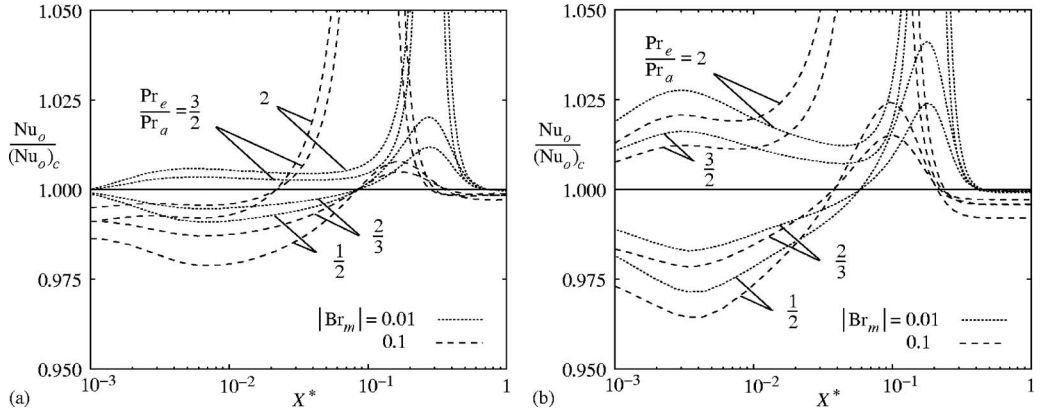

Fig. 6 Axial distributions of the ratio $Nu_o/(Nu_o)_c$ for flat microchannels with $Pr_m=5$ and different Brinkman numbers Br_m: (*a*) Bi=5; and (*b*) Bi=20.

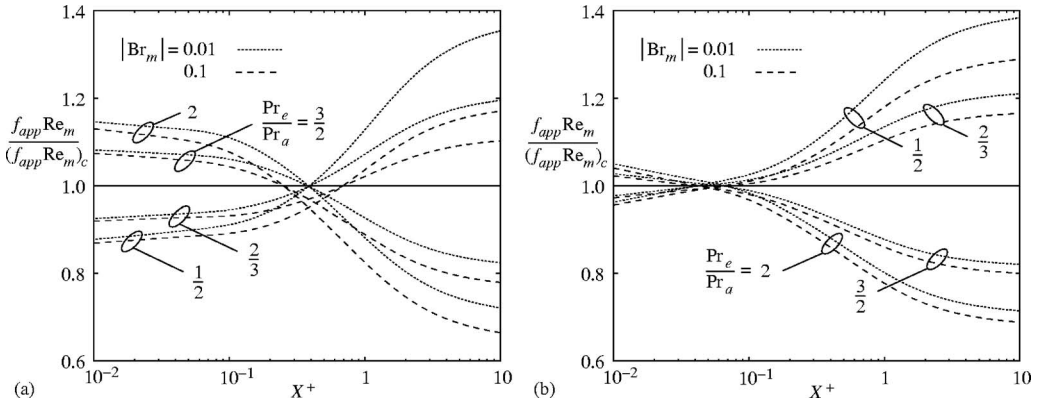

Fig. 7 Axial distributions of the ratio $f_{app}\,\mathrm{Re}_m/(f_{app}\,\mathrm{Re}_m)_c$ for microchannels of circular cross section with $\mathrm{Pr}_m=5$ and different Brinkman numbers Br_m: (*a*) Bi=5; and (*b*) Bi=20.

$f_{app}\,\mathrm{Re}_m/(f_{app}\,\mathrm{Re}_m)_c$ found for different values of the ratio $\mathrm{Pr}_e/\mathrm{Pr}_a$ can be explained taking into account the temperature distributions over the cross sections which, in turn, affect the velocity profiles. As an example, to show the effects of temperature dependent viscosity, radial or transverse profiles of the dimensionless temperature $T=(t-t_a)/(t_e-t_a)$ at selected axial locations are compared in Figs. 9 and 10 for flows with a temperature dependent viscosity fluid ($\mathrm{Pr}_e/\mathrm{Pr}_a=2$ for heating and 1/2 for cooling) and a constant property fluid in the case of Bi=5 and $|\mathrm{Br}_m|=0.1$. Symbols $R=r/D_h=r/(2r_o)$ and $Z=z/D_h=z/(4a)$ represent the dimensionless radial and transverse coordinates, respectively. It is worth noting that, when the fluid is heated ($\mathrm{Br}_m=-0.1$), the dimensionless temperature T can become negative since, because of viscous heating, the temperature of the fluid can exceed the ambient temperature t_a, while this is never possible when the fluid is cooled. Moreover, in the case of fluid heating, temperature profiles for intermediate axial positions exhibit a point of inflection due to the viscous dissipation effect which causes a reduction and, eventually, a change of sign of the temperature gradient at the wall. Of course, this cannot occur in the case of fluid cooling ($\mathrm{Br}_m=0.1$). It is also

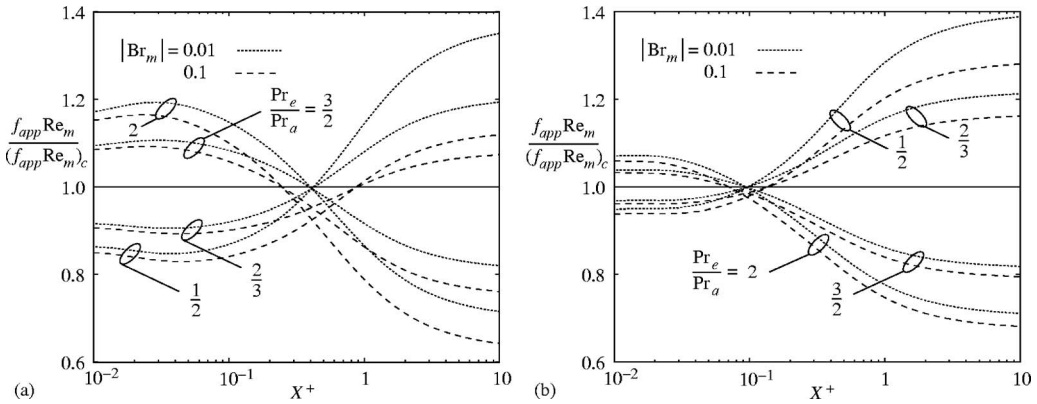

Fig. 8 Axial distributions of the ratio $f_{app}\,\mathrm{Re}_m/(f_{app}\,\mathrm{Re}_m)_c$ for flat microchannels with $\mathrm{Pr}_m=5$ and different Brinkman numbers Br_m: (*a*) Bi=5; and (*b*) Bi=20.

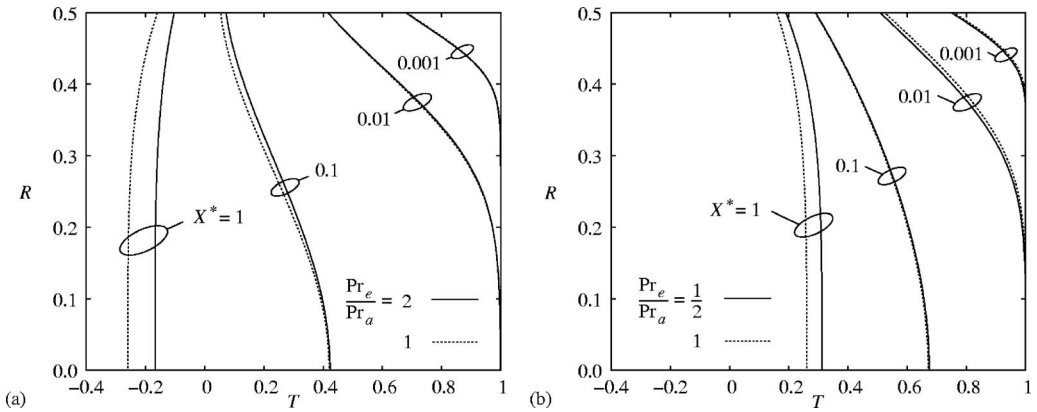

Fig. 9 Radial profiles of dimensionless temperature T at different axial locations for microchannels of circular cross section with $\mathrm{Pr}_m=5$, $|\mathrm{Br}_m|=0.1$, and Bi=5: (*a*) fluid heating; and (*b*) fluid cooling.

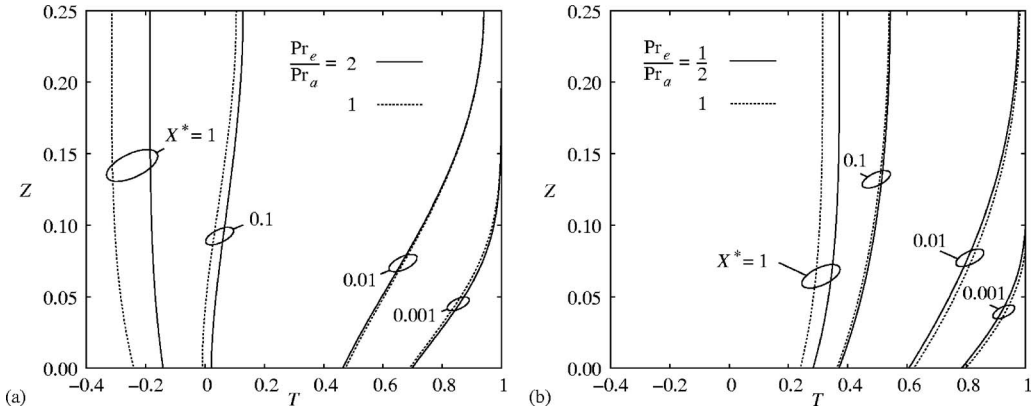

Fig. 10 Transverse profiles of dimensionless temperature *T* at different axial locations for flat microchannels with Pr_m=5, $|Br_m|$=0.1, and Bi=5: (*a*) fluid heating; and (*b*) fluid cooling.

apparent that the effect of temperature dependent viscosity increases with the distance from the entrance and is more relevant for fluid heating than for fluid cooling.

To show the influence of the temperature dependence of viscosity on the hydrodynamic entrance length, the axial distributions of dimensionless velocity $U_0'=u_0/u_e$ and temperature T_0 at the center of the cross section of circular and flat microchannels are presented in Fig. 11 for Bi=5, $|Br_m|$=0.1, and all the values of Pr_e/Pr_a considered. It is apparent that, with temperature dependent viscosity and non-negligible viscous dissipation, fully developed values of the dimensionless axial velocity component U_0' are reached at the distance from the inlet that appears to be nearly independent of the value of Pr_e/Pr_a and is about one order of magnitude larger than the hydrodynamic entrance length in the corresponding constant property flow [3,4]. We can also notice that the value of U_0' is lower than its asymptotic value everywhere in the case of fluid heating, while it exhibits an overshoot in the case of fluid cooling. Besides, the more the ratio Pr_e/Pr_a differs from 1, the larger the differences are between local values of U_0' for flows of fluids with temperature dependent viscosity and the corresponding values for flows of constant property fluids. Moreover, the asymptotic values of U_0' for temperature dependent viscosity flows are always larger than the corresponding value for a constant property fluid. In fact, when fully developed conditions are reached, the dimensional temperature of the fluid in the region near the wall is lower than that prevailing in the core of the flow both for fluid heating and cooling. The asymptotic values of the dimensionless temperature T_0, instead, are larger than zero for fluid cooling and lower than 0 for fluid heating, with values for constant property flows that are always lower than those for flows of temperature dependent viscosity fluids. It is also apparent in Fig. 11(*b*) that the asymptotic values of T_0 for circular microchannels are closer to zero than those for flat microchannels. This is due to the lower value of the ratio between the cross-sectional area and the length of the heated/cooled perimeter of the circular cross section.

Conclusions

The effects of viscous dissipation and temperature dependent viscosity in simultaneously developing laminar flows of liquids in straight microchannels have been studied. Two different geometries, namely the circular tube and the parallel plate channel, have been considered. Reference has been made to convective boundary conditions at the wall of the microchannels. Viscosity has been assumed to vary with temperature according to an exponential relation, while the other fluid properties have been held constant. Numerical results confirm that, in the laminar forced convection in the entrance region of straight microchannels, both temperature dependence of viscosity and viscous dissipation effects cannot be neglected in a wide range of operative conditions. In particular, it has been shown that, as compared to constant viscosity flows, the hydrodynamic entrance length is larger, the asymptotic Poiseuille number is higher or lower according to whether the fluid is cooled or heated while, because of viscous heating, the asymptotic Nusselt number is always lower. Radial temperature profiles are also influenced by viscous dissipation and temperature dependent viscosity and, in the case of fluid heating,

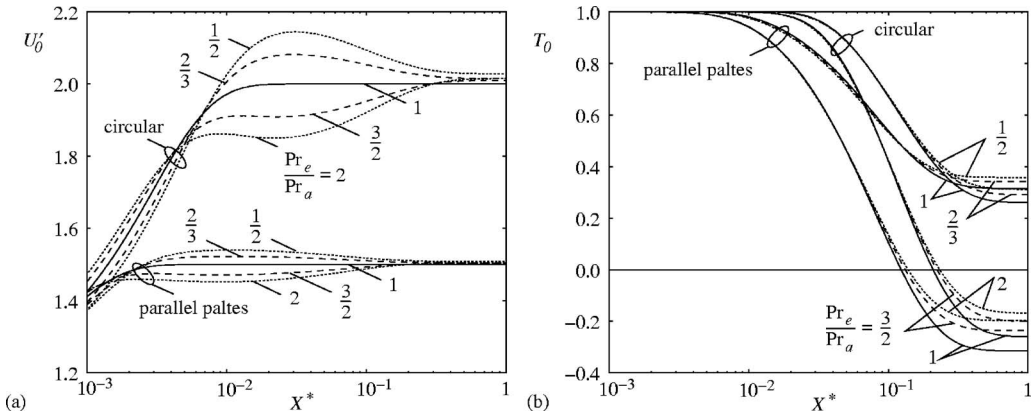

Fig. 11 Axial distributions of dimensionless velocity and temperature at the center of the cross section of circular and flat microchannels with Pr_m=5 and $|Br_m|$=0.1: (*a*) U_0', and (*b*) T_0.

present inflexion points. In the entrance region the effects of changing viscosity prevail over those of viscous dissipation.

Acknowledgment

This work was funded by MIUR (PRIN/COFIN 2005 project).

Nomenclature

a = half-spacing of parallel plates, m
B = parameter in Eq. (7), $B=-\ln(\mu_e/\mu_a)$
Bi = Biot number, $\mathrm{Bi}=h_a D_h/k$
Br = Brinkman number, $\mathrm{Br}=\mu u_e^2/[k(t_e-t_a)]$
c = specific heat, J/kg K
D_h = hydraulic diameter, m
f = Fanning friction factor
f_{app} = apparent Fanning friction factor
h = local convective heat transfer coefficient, $\mathrm{W/m^2\,K}$
h_a = external convective heat transfer coefficient, $\mathrm{W/m^2\,K}$
k = thermal conductivity, W/m K
Nu = local Nusselt number, $\mathrm{Nu}=hD_h/k$
Nu_o = local overall Nusselt number, $\mathrm{Nu}_o=UD_h/k$
Pe = Péclet number, Pe=RePr
Pr = Prandtl number, $\mathrm{Pr}=\mu c/k$
p = deviation from the hydrostatic pressure, Pa
q'' = heat flux, $\mathrm{W/m^2}$
R = dimensionless radial coordinate, $R=r/D_h=r/(2r_o)$
Re = Reynolds number, $\mathrm{Re}=\rho u_e D_h/\mu$
r,x = cylindrical coordinates, m
T = dimensionless temperature, $T=(t-t_a)/(t_e-t_a)$
U = local overall heat transfer coefficient, $\mathrm{W/m^2\,K}$
U' = dimensionless axial velocity, $U'=u/u_e$
t = temperature, °C
u,v = velocity components in x,r directions, m/s
X^+ = dimensionless axial coordinate, $X^+=x/D_h\mathrm{Re}_m$
X^* = dimensionless axial coordinate, $X^*=x/D_h\mathrm{Pe}$
Z = dimensionless transverse coordinate, $Z=z/D_h=z/(4a)$

Greek Symbols

β = parameter in Eq. (6), $\mathrm{K^{-1}}$
μ = dynamic viscosity, kg/m s
ρ = density, $\mathrm{kg/m^3}$
Φ_v = viscous dissipation term, $\mathrm{s^{-2}}$

Superscript

$-$ = average value over the cross section

Subscripts

a = ambient fluid, at the outer surface
b = bulk
c = constant property
e = entrance
i = inner
m = reference, evaluated at t_m
o = outer, overall
w = wall
0 = centerline
∞ = asymptotic value

References

[1] Del Giudice, S., Nonino, C., and Savino, S., 2005, "Thermally Developing Laminar Flow in Microchannels With Temperature Dependent Viscosity and Viscous Dissipation," *Proc. of the ECI ICHTFFM*, Castelvecchio Pascoli, Italy, September 25–30 (CD-ROM).

[2] Nonino, C., Del Giudice, S., and Savino, S., 2005, "Effects of Viscous Dissipation and Temperature Dependent Viscosity in Simultaneously Developing Laminar Flow in Microchannels," *Proc. of the ECI ICHTFFM*, Castelvecchio Pascoli, Italy, September 25–30 (CD-ROM).

[3] Shah, R. K., and London, A. L., 1978, *Laminar Flow Forced Convection in Ducts*, Academic, New York.

[4] Shah, R. K., and Bhatti, M. S., 1987, "Laminar Convective Heat Transfer in Ducts," *Handbook of Single-Phase Convective Heat Transfer*, S. Kakaç, R. K. Shah, and W. Aung, eds., Chap. 3, Wiley, New York.

[5] Kakaç, S., 1987, "The Effect of Temperature-Dependent Fluid Properties on Convective Heat Transfer," *Handbook of Single-Phase Convective Heat Transfer*, S. Kakaç, R. K. Shah, and W. Aung, eds., Chap. 18, Wiley, New York.

[6] Nouar, C., 1999, "Numerical Solution for Laminar Mixed Convection in a Horizontal Annular Duct: Temperature-Dependent Viscosity Effect," Int. J. Numer. Methods Fluids, **29**, pp. 849–864.

[7] Nóbrega, J. M., Pinho, F. T., Oliveira, P. J., and Carneiro, O. S., 2004, "Accounting for Temperature Dependent Properties in Viscoelastic Duct Flows," Int. J. Heat Mass Transfer, **47**, pp. 1141–1158.

[8] Shannon, R. L., and Depew, C. A., 1969, "Forced Laminar Flow Convection in a Horizontal Tube With Variable Viscosity and Free Convection Effects," J. Heat Transfer, **91**, pp. 251–258.

[9] Joshi, S. D., and Bergles, A. E., 1980, "Analytical Study of Heat Transfer to Laminar in-Tube Flow of Non-Newtonian Fluids," AIChE Symp. Ser., **76**(199), pp. 270–281.

[10] Toh, K. C., Chen, X. Y., and Chai, J. C., 2002, "Numerical Computation of Fluid Flow and Heat Transfer in Microchannels," Int. J. Heat Mass Transfer, **45**, pp. 5133–5141.

[11] Xu, B., Ooi, K. T., Mavriplis, C., and Zaghloul, M. E., 2003, "Evaluation of Viscous Dissipation in Liquid Flow in Microchannels," J. Micromech. Microeng., **13**, pp. 53–57.

[12] Morini, G. L., 2005, "Viscous Dissipation as Scaling Effect for Liquid Flows in Microchannels," *Proc. of the 3rd ICMM*, Toronto, Canada, June 13–16 (CD-ROM).

[13] Shen, P., Aliabadi, S. K., and Abedi, J. A., 2004, "Review of Single-Phase Liquid Flow and Heat Transfer in Microchannels," *Proc. of the 2nd ICMM*, Rochester, NY, June 17–19, pp. 213–220.

[14] Koo, J., and Kleinstreuer, C., 2003, "Liquid Flow in Microchannels: Experimental Observations and Computational Analyses of Microfluidics Effects," J. Micromech. Microeng., **13**, pp. 568–579.

[15] Herwig, H., and Hausner, O., 2003, "Critical View on New Results in Micro-Fluid Mechanics: An Example," Int. J. Heat Mass Transfer, **46**, pp. 935–937.

[16] Tso, C. P., and Mahulikar, S. P., 1998, "The Use of the Brinkman Number for Single Phase Forced Convective Heat Transfer in Microchannels," Int. J. Heat Mass Transfer, **41**, pp. 1759–1769.

[17] Morini, G. L., 2005, "Viscous Heating in Liquid Flows in Microchannels," Int. J. Heat Mass Transfer, **48**, pp. 3637–3647.

[18] Koo, J., and Kleinstreuer, C., 2004, "Viscous Dissipation Effects in Microtubes and Microchannels," Int. J. Heat Mass Transfer, **47**, pp. 3159–3169.

[19] Koo, J., and Kleinstreuer, C., 2004, "Analysis of Liquid Flow in Micro-Conduits," *Proc. of the 2nd ICMM*, Rochester, NY, June 17–19, pp. 191–198.

[20] Tunc, G., and Bayazitoglu, Y., 2001, "Heat Transfer in Microtubes With Viscous Dissipation," Int. J. Heat Mass Transfer, **44**, pp. 2395–2403.

[21] Nonino, C., Del Giudice, S., and Comini, G., 1988, "Laminar Forced Convection in Three-Dimensional Duct Flows," Numer. Heat Transfer **13**, pp. 451–466.

[22] Patankar, S. V., and Spalding, D. B., 1972, "A Calculation Procedure for Heat, Mass and Momentum Transfer in Three-Dimensional Parabolic Flows," Int. J. Heat Mass Transfer, **15**, pp. 1787–1806.

[23] Hirsh, C., 1988, *Numerical Computation of Internal and External Flows*, Vol. 1, Wiley, New York, p. 70.

[24] Nonino, C., Del Giudice, S., and Savino, S., 2006, "Temperature Dependent Viscosity Effects on Laminar Forced Convection in the Entrance Region of Straight Ducts," Int. J. Heat Mass Transfer, **49**, pp. 4469–4481.

[25] Lin, C. R., and Chen, C. K., 1994, "Effect of Temperature Dependent Viscosity on the Flow and Heat Transfer over an Accelerating Surface," J. Phys. D, **27**, pp. 29–36.

[26] Costa, A., and Macedonio, G., 2002, "Nonlinear Phenomena in Fluids With Temperature-Dependent Viscosity: An Hysteresis Model for Magma Flow in Conduits," Geophys. Res. Lett., **29**(10), pp. 1402.

[27] Costa, A., and Macedonio, G., 2003, "Viscous Heating for Fluids With Temperature Dependent Viscosity: Implications for Magma Flows," Nonlinear Processes Geophys., **10**, pp. 545–555.

[28] Javeri, V., 1977, "Heat Transfer in Laminar Entrance Region of a Flat Channel for the Temperature Boundary Condition of the Third Kind," Waerme- Stoffuebertrag., **10**, pp. 137–144.

[29] Nonino, C., 2003, "A Simple Pressure Stabilization for a SIMPLE-Like Equal-Order FEM Algorithm," Numer. Heat Transfer, Part B, **44**, pp. 61–81.

[30] Barletta, A., 1997, "Fully Developed Laminar Forced Convection in Circular Ducts for Power-Law Fluids With Viscous Dissipation," Int. J. Heat Mass Transfer, **40**, pp. 15–26.

[31] Zanchini, E., 1997, "Effect of Viscous Dissipation on the Asymptotic Behaviour of Laminar Forced Convection in Circular Tubes," Int. J. Heat Mass Transfer, **40**, pp. 169–178.

[32] Lin, T. F., Hawks, K. H., and Leidenfrost, W., 1983, "Analysis of Viscous Dissipation Effect on Thermal Entrance Heat Transfer in Laminar Pipe Flows With Convective Boundary Conditions," Waerme- Stoffuebertrag., **17**, pp. 97–105.

Natural Convection Heat Transfer From Horizontal Rectangular Ducts

Mohamed E. Ali
Mechanical Engineering Department,
King Saud University,
P. O. Box 800,
Riyadh 11421, Saudi Arabia
e-mail: mali@ksu.edu.sa

Experimental investigations have been reported on steady state natural convection from the outer surface of horizontal ducts in air. Five ducts have been used with aspect ratios (Γ=duct height/duct width) of 2, 1, and 0.5. The ducts are heated using internal constant heat flux heating elements. The temperatures along the surface and peripheral directions of the duct wall are measured. Longitudinal (circumference averaged) heat transfer coefficients along the side of each duct are obtained for laminar and transition regimes of natural convection heat transfer. Total overall averaged heat transfer coefficients are also obtained. Longitudinal (circumference averaged) Nusselt numbers are evaluated and correlated using the modified Rayleigh numbers for transition regime using the axial distance as a characteristic length. Furthermore, total overall averaged Nusselt numbers are correlated with the modified Rayleigh numbers, the aspect ratio, and area ratio for the laminar and transition regimes. The longitudinal or total averaged heat transfer coefficients are observed to decrease in the laminar region and to increase in the transition region. Laminar regimes are obtained only at very small heat fluxes, otherwise, transitions are observed. [DOI: 10.1115/1.2739623]

Keywords: natural convection, rectangular ducts, experimental heat transfer, laminar and transition regimes

1 Introduction

Steady state natural convection from rectangular and square ducts has many engineering applications in the cooling of electronic components, and design of solar collectors and heat exchangers. A survey of the literature shows that correlations for natural convection from a vertical plate (McAdams [1] and Churchill and Chu [2]) horizontal surface (Goldstein et al. [3] and Lloyd and Moran [4]) long horizontal cylinder (Morgan [5] and Churchill and Chu [6]), and spheres (Churchill [7]), have been reported for different thermal boundary conditions. Recently, fluid flow and heat transfer from an infinite circular cylinder have been reported for both isothermal and isoflux boundary conditions in Newtonian and power-law fluids by Khan et al. [8,9], respectively. Free convection simulation from an elliptic cylinder was studied by Badr and Shamsher [10] and by Mahfouz and Kocabiyik [11], and correlations for natural convection from helical coils were reported by Ali [12–15] for different Prandtl numbers. Furthermore, local and average mass transfer rates from a rectangular cylinder were measured using a naphthalene sublimation technique by Yoo and Park [16]. On the other hand, heat transfer and pressure drop characteristics of laminar flow of viscous oil through horizontal acrylic and stainless-steel rectangular and square ducts were reported by Saha and Mallick [17]. Moreover, analytical study of natural convection in a rectangular cavity with heat generation was conducted by Joshi et al. [18] for two different boundary conditions. Recently, the effects of buoyancy force and channel aspect ratio on heat transfer in two-pass rotating rectangular channel with smooth walls and 45 deg ribbed walls have been reported by Fu et al. [19].

On the other hand, there are limited correlations available in the literature for natural convection from the outer surface of such rectangular ducts, which motivates the current investigation. The approximation method suggested by Raithby and Hollands [20] to predict heat transfer from cylinders of various cross sections and for wide ranges of Prandtl and Rayleigh numbers was simplified by Hassani [21]. The free convection from a horizontal cylinder with cross section of arbitrary shape was theoretically analyzed for uniform surface temperature and uniform surface heat flux by Nakamura and Asako [22]. They have also checked their theoretical results by experiments in water on cylinders of modified triangular and square cross section. However, their experimental values of the mean heat transfer coefficient were about 10% to 30% higher than the analytical values. Hassani [21] has introduced a general correlation for predicting natural convection from isothermal two-dimensional bodies of arbitrary cross section. An experimental study was reported by Oosthuizen and Paul [23] for noncircular cylinders in air for single Rayleigh number using the transient method. Their results have showed significant effects of cross-section orientation and shape on heat transfer rate. Furthermore, another experimental study using the same method by Oosthuizen and Bishop [24] was made on mixed convection heat transfer from square cylinders in two different orientations. Their results included some limited data for free convection in air, which were correlated as

$$\overline{\mathrm{Nu}}_L = 0.424\ \mathrm{Ra}_L^{0.25} \quad 3.5 \times 10^5 \leq \mathrm{Ra}_L \leq 2.8 \times 10^6 \qquad (1)$$

Recently, Zeitoun and Ali [25] have reported numerical simulations of natural convection heat transfer from isothermal horizontal rectangular cross-section ducts in air. Their results show that as the aspect ratio increases, separation and circulation occur on the top surface of the cross-section duct at fixed Rayleigh number, and the corresponding behavior has observed through the isotherms. They have also obtained a general correlation using the aspect ratio as a parameter:

$$\overline{\mathrm{Nu}}_L = [0.9\Gamma^{-0.061} + 0.371\Gamma^{0.114}\mathrm{Ra}_L^{0.1445}]^2 \quad 700 \leq \mathrm{Ra}_L \leq 10^8 \qquad (2)$$

This paper presents the results of an experimental investigation of laminar and transition to turbulence natural convection heat transfer from the outer surface of rectangular ducts with their axis

Contributed by the Heat Transfer Division of ASME for publication in the JOURNAL OF HEAT TRANSFER. Manuscript received: May 15, 2006; final manuscript received December 2, 2006. Review conducted by Bengt Sunden.

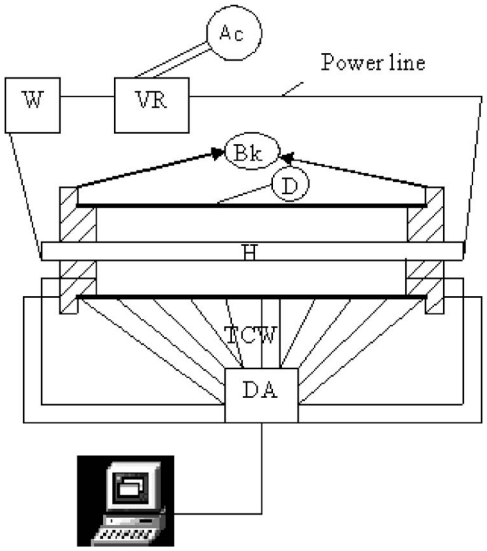

Fig. 1 Schematic of the experimental system showing the thermocouple locations in the longitudinal (TCW) direction (see text for details)

oriented horizontally. The study focuses on the determination of axial (circumference averaged) and overall averaged heat transfer coefficient in non-dimensional form of Nusselt numbers. General correlations using Nusselt numbers as function of Rayleigh numbers, aspect ratio, and surface area ratio are obtained. Furthermore, various general trends of laminar and transition convection heat transfer are discussed.

2 Experiment Setup and Procedure

Figure 1 shows a schematic cross-sectional view of the duct (D) and the thermocouple locations in the longitudinal (axial) direction (TCW) on three sides of the duct. The ducts (D) were made from steel (polished mild steel) with their dimensions listed in Table 1. An electrical heating element (H) (0.0066 m O.D.) was inserted into the center of the duct. Bakelite end plates (Bk, thermal conductivity=0.15 W/mK [26]) 0.0206 m thick were attached at both ends of each test duct (D) to reduce the rate of heat loss from the duct ends.

The surface temperature was measured at eleven points in the longitudinal direction of each duct at three different surfaces (lower, upper, and either side surface), as seen in Fig. 1. Thirty-five calibrated iron-constantan (type J) self-adhesive thermocouples (0.3 s time response with flattened bead) were stuck on the duct surfaces 0.1 m apart and two of them were stuck on the outer surface of the Bakelite end plates; one at each plate. Two thermocouples (0.01 in. or 0.25 mm diam., one at each plate) were inserted through the Bakelite thickness and leveled with its inside surface, as seen in Fig. 1. The ambient air temperature was measured by one more thermocouple mounted in the room.

The duct was oriented horizontally using two vertical stands in a room away from ventilation openings and air conditioning system to minimize any possible forced convection. Those thermocouples were connected to a 40-channel data acquisition system (DA), which in turn was connected to a computer where the measured temperatures were stored for further analysis.

Table 1 Physical dimensions of the used ducts 1 m long and 0.002 m thick

Duct no.	Height (A), m	Width (B), m	Aspect ratio Γ	Area ratio $\kappa=A_s/A_c$
1	0.07	0.07	1	57.143
2	0.08	0.04	2	75.0
3	0.06	0.03	2	100.0
4	0.04	0.04	1	100.0
5	0.02	0.04	0.5	150.0

The input electrical power (ac) to the heating element (H) is controlled by a voltage regulator (VR). The power consumed by the duct is measured by a wattmeter (W) and assumed uniformly distributed along the duct length. The heat flux per unit surface area of the duct is calculated by dividing the consumed power (after deducting the heat loss by axial conduction through the Bakelite end plates) over the duct outer surface area.

The input power to the duct increases for each duct from 10 to 350 W in two stages. In the first stage; the power increases in a step of 4 W up to 26 W for possible laminar natural convection regime. However, in the second stage it increases by 10 W, which presents the transition regime such that the maximum duct surface temperature does not exceed 160°C. In other words, the experiment is done thirteen times for each duct corresponding to the various input power. Temperature measurements are taken after 2 h of setting where the steady state should be reached. The procedure outlined above is used to generate natural convection heat transfer data in air (Prandtl number ≈0.69).

3 Analysis of Experiments

The heat generated inside the duct wall dissipates from the duct surface by convection and radiation in addition to the heat lost by axial conduction through the Bakelite end plates:

$$\text{EIP} = \text{Electrical input power} = A_s(q_c + q_r) + A_{\text{Bk}} q_{\text{Bk}} \tag{3}$$

where q_c and q_r, are the fraction of the heat flux dissipating from the duct surface by convection and radiation, respectively. The heat flux lost by radiation (q_r) and by axial conduction through the Bakelite end plates (q_{Bk}) can be calculated respectively as

$$q_r = \varepsilon\sigma(\bar{T}^4 - T_\infty^4) \quad q_{\text{Bk}} = k_{\text{Bk}}\frac{(T_{iB} - T_{oB})}{\delta} \tag{4}$$

It should be noted that q_r is estimated using the total overall averaged surface temperature $\bar{T}$ at each run of the duct and ε is the surface emissivity of the duct and it is estimated as 0.27 for polished mild steel [27]. Measurements show that, the fraction of radiated heat transfer is 25.5% of the total input power while the axial conduction heat lost through the Bakelite end plates is 1.5% at most. In the second term of Eq. (4); T_{iB} and T_{oB} are the measured inside and outside surface temperature of the Bakelite end plates, respectively, and k_{Bk} and δ present the Bakelite thermal conductivity and thickness, respectively.

3.1 Axial (Circumference Averaged) Heat Transfer Coefficient. In this case, the circumference averaged surface temperature at any station x in the longitudinal direction for each constant heat flux (run) is determined as

$$T_x = \sum_{j=1}^{3} T_{xj} \Big/ 3 \tag{5}$$

where j is the number of thermocouples in the circumference direction at any station x along the surface of the duct. The arithmetic mean surface temperature is calculated along the axial direction for each run as

$$\theta_x = 0.5(T_x + T_\infty) \quad x = 1,2,\ldots,11 \tag{6}$$

Therefore, for each heat flux (run) there are 11 T_x longitudinal temperature measurements. Consequently, once the electrical input power to the duct is measured, q_r and q_{Bk} from Eq. (4) and q_c from Eq. (3), then the axial (circumference averaged) heat transfer coefficient h_x can be calculated from

$$h_x = \frac{q_c}{T_x - T_\infty} \quad x = 1,2,3,\ldots,11 \tag{7}$$

Hence, the non-dimensional Nusselt and the modified Rayleigh numbers are obtained as

$$\mathrm{Nu}_x = \frac{h_x x}{k}, \quad \mathrm{Ra}_x^* = \frac{g\beta q_c x^4}{\nu k \alpha} \tag{8}$$

All physical properties are evaluated at the axial circumference averaged mean temperature θ_x for each q_c.

3.2 Total Overall Averaged Heat Transfer Coefficient. In this case the circumference averaged heat transfer coefficient h_x is first evaluated at each station x as in Eq. (7) and then the overall longitudinal average $\bar{h}_1$ is obtained as

$$\bar{h}_1 = \sum_{x=1}^{11} h_x \Big/ 11 \tag{9}$$

Therefore, each heat flux q_c is presented by only one overall averaged heat transfer coefficient on contrary to the case (3.1), where q_c is presented by 11 h_x along the longitudinal direction given by Eq. (7). All circumference averaged physical properties are first obtained at θ_x, and then the overall averaged properties are obtained the same way following Eq. (9). The non-dimensional overall averaged Nusselt and the modified Rayleigh numbers are defined using the characteristic length $L=A+B$ as

$$\overline{\mathrm{Nu}}_L = \frac{\bar{h}_1 L}{k} \quad \mathrm{Ra}_L^* = \frac{g\beta q_c L^4}{\nu k \alpha} \tag{10}$$

In order to compare the present results with similar previously published results; another method of averaging results using the overall average temperature is also used. In this way the temperature is first the circumference averaged following Eq. (5), and then the overall average temperature is obtained as

$$\bar{T} = \sum_{x=1}^{11} T_x \Big/ 11 \tag{11}$$

All physical properties are obtained in this case at the arithmetic mean surface temperature

$$T_{\mathrm{mean}} = 0.5(\bar{T} + T_\infty) \tag{12}$$

The overall average heat transfer coefficient for constant heat flux is determined from

$$\bar{h}_2 = \frac{q_c}{(\bar{T} - T_\infty)} \tag{13}$$

and Nusselt and Rayleigh numbers using $L=A+B$ as a characteristic length are defined in this case as

$$\overline{\mathrm{Nu}}_L = \frac{\bar{h}_2 L}{k}, \quad \mathrm{Ra}_L = \frac{g\beta(\bar{T} - T_\infty)L^3}{\nu\alpha} \tag{14}$$

3.3 Experimental Uncertainty. In this section, the experimental uncertainty is to be estimated in the calculated results on the basis of the uncertainties in the primary measurements. It should be mentioned that, some of the experiments are repeated more than twice to check the calculated results and the general trends of the data especially in the laminar range of the experiment. The errors in measuring the temperature, estimating the emissivity, and in calculating the surface area are ±0.2 °C, ±0.02, and ±0.003 m^2, respectively. The accuracy in measuring the voltage is taken from the manual of the wattmeter is 0.5% of reading ±2 counts with a resolution of 0.1 V and the corresponding one for the current is 0.7% of reading ±5 counts +1 mA with a resolution of 1 mA.

At each run, 40 scans of the temperature measurement are made by the data acquisition system for each channel and the mathematical average of these scans is obtained. Furthermore, since the input power, as mentioned earlier, has two stages (one for laminar and the other for transition), then using the abovementioned errors turns to maximum itemized uncertainties of the calculated results shown in Table 2 for each range using the method recommended by Moffat [28]. Table 2 shows, in general, that the uncertainty of the quantities in the laminar regime is higher than that in transition regime, which is expected since both the input power and the temperature range are very small.

Table 2 The maximum percentage uncertainties of various quantities in the laminar and transition regimes

Quantity	Laminar range, %	Transition range, %
EIP	3.8	2.1
q_{Bk}	5.4	3.8
q_r	17.7	3.1
q_c	7.1	4.4
h	12.2	4.6
Nu_x	10.9	4.6
Ra_x^*	7	4.4
$\overline{\mathrm{Nu}}_L$	12.2	4.7
Ra_L^*	7.9	5.8

4 Results and Discussions

Experimental data points are obtained for rectangular ducts oriented horizontally in air. Figure 2 shows the axial circumference averaged surface temperature normalized by the ambient temperature T_∞ versus the non-dimensional axial (longitudinal) duct length for three selected values of q_c using duct number 2. As seen in Fig. 2(*a*), the temperature distribution at low heat flux is almost unaffected by the end effects where the heat lost through the Bakelite end plates is minimum. As the heat flux inside the duct increases, the surface temperature increases and the end effects become more distinguishable. The distance between the dashed lines in Fig. 2(*a*) shows that the temperature is almost uniform and least affected by the end effects. Therefore, in order to avoid the end effects, the test section of the duct is chosen to be between these two dashed lines where the study is focused. Figure 2(*b*) shows the axial temperature distributions as in Fig. 2(*a*), but for lower values of heat flux corresponding to the laminar regime, as will be discussed in Fig. 3(*b*).

Comparison between the axial circumference averaged heat transfer coefficient (▲) and the overall average heat transfer coefficient (solid lines) are presented in Fig. 3 for duct number 2. Figure 3(*a*) shows the transition regime where heat transfer coefficient increases as the heat flux increases. However, in Fig. 3(*b*), heat transfer coefficient decreases as the heat flux increases, which confirms that laminar regime is achieved. It is worth mentioning that other symbols are used in Fig. 3(*b*) only for clarifying the figure, but all the data are for duct number 2 and corresponding to the temperature distributions given in Fig. 2(*b*). It should be mentioned that other ducts in Table 1 give similar effects.

The axial circumference averaged Nusselt numbers versus the modified Rayleigh numbers are shown in Fig. 4 corresponding to the test section defined by the dashed lines in Fig. 2 using all ducts for all heat fluxes. Since the modified Rayleigh number is function of q_c and x^4 then the following observations can be drawn from this figure:

(i) At any fixed station x along the duct length, as the heat flux increases the Nusselt number decreases up to a minimum critical value then increases as q_c increases,
(ii) The decrease in Nu_x at fixed x and at different heat flux corresponds to an increase in Ra_x^*, as indicated by the downward inclined arrow,

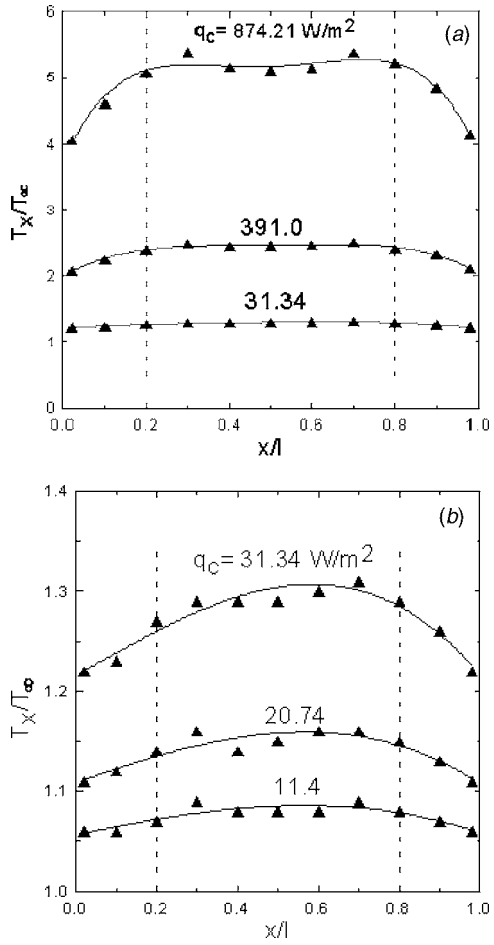

Fig. 2 Circumference averaged dimensionless axial temperature distributions along the duct surface for some selected heat fluxes for duct number 2; (*a*) associated with transition regime and (*b*) corresponding to laminar regime

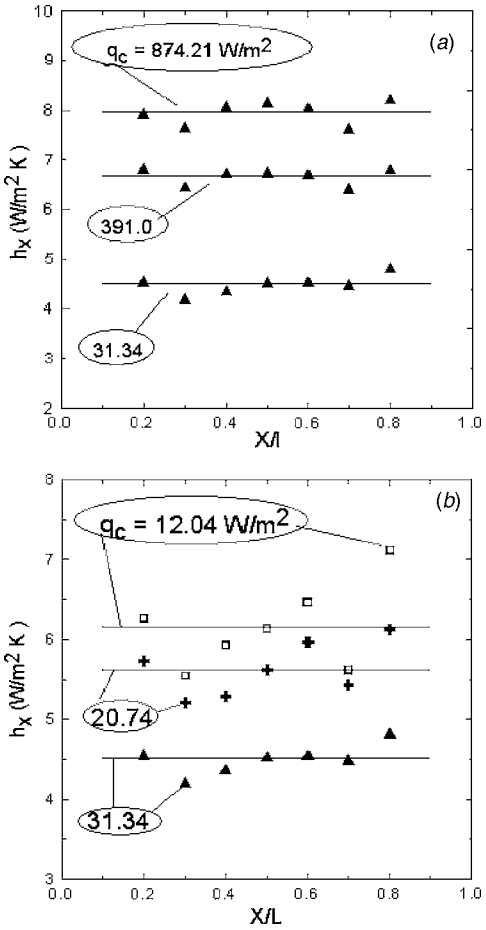

Fig. 3 Axial circumference averaged heat transfer coefficient along the duct surface for some selected heat fluxes for duct number 2; (*a*) associated with transition regime and (*b*) corresponding to laminar regime (different symbols are assigned for each heat flux only for clarity)

(iii) At fixed heat flux as x increases along the duct surface Nu_x increases, which corresponds to an increase in Ra_x^*, as indicated by the upward inclined arrow,

(iv) Below the solid line, all the data are less sensitive to be distinguished either for q_c or x and are collapsed on each other with general trends of increasing Nu_x as Ra_x^* increases. Therefore, this region can be characterized as a transition region, as will be seen in Fig. 5,

(v) The data above the solid line, as mentioned earlier, can be identified either by q_c or x and cannot be collapsed on each other. Hence, the general trend is Nu_x decreases as Ra_x^* increases at fixed location on the duct surface for different heat fluxes. Therefore, this region is defined as a laminar region and will be treated on the overall averaged basis, as will be seen in Figs. 6 and 7.

Figure 5 is constructed to obtain a correlation in the transition region for the data below the solid line in Fig. 4. A least-squares power law fit through the data set yields the following correlation:

$$\mathrm{Nu}_x = 0.355(\mathrm{Ra}_x^*)^{0.237} \quad 1.9 \times 10^8 \le \mathrm{Ra}_x^* \le 7.0 \times 10^{11} \quad (15)$$

with a correlation coefficient (R^2) of 96.5% with an error band of ±15%, where 94.8% of the data fall within this band. The overall averaged results using the definitions of $\overline{\mathrm{Nu}}_L$ and Ra_L^* given by Eq. (10) are shown in Fig. 6, where the laminar and transition regions are characterized by a decrease or increase in the heat transfer coefficient, respectively, since $\bar{h} \propto \overline{\mathrm{Nu}}_L$ for each duct. The dashed

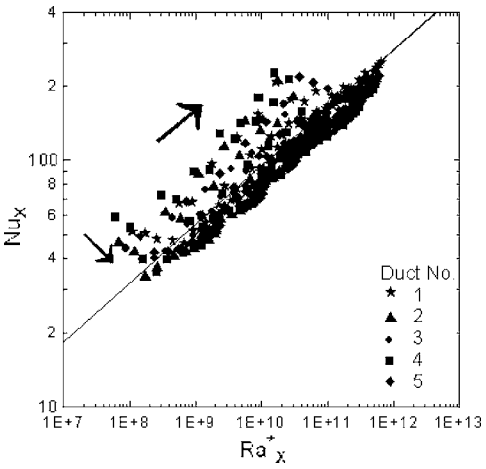

Fig. 4 Local circumference averaged Nusselt numbers versus the modified Rayleigh numbers; solid line separating the laminar data (above the line) and the transition data (below the line). The inclined upward arrow shows the transition direction while the downward arrow presents the laminar direction.

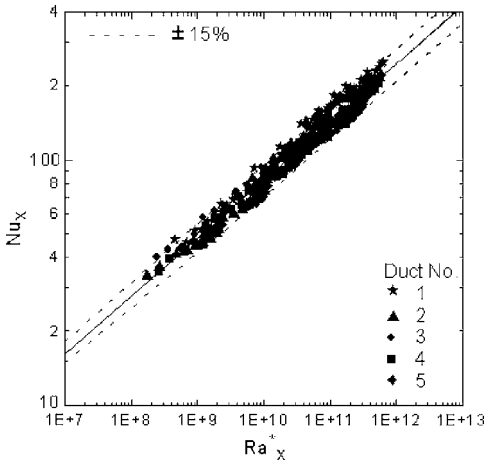

Fig. 5 Local circumference averaged Nusselt numbers versus the modified Rayleigh numbers for the transition regime. Solid line present the data fit given by Eq. (15).

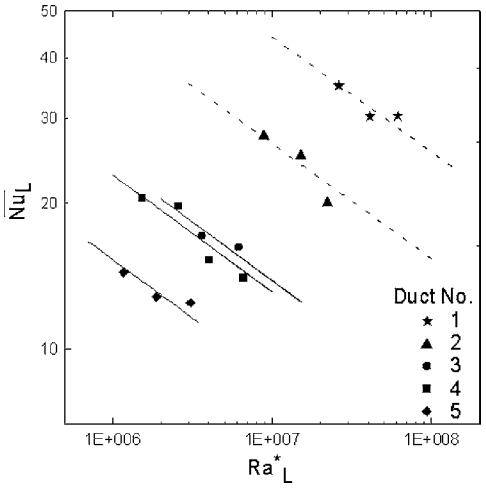

Fig. 7 The overall averaged Nusselt numbers for the laminar regime; dashed lines are the fitting data given by Eq. (17) and solid lines are those given by Eq. (18)

line presents the fitting locus of the critical points segregating the laminar and transition regimes, where the exact critical points are circled for each duct. The correlation of the fitting locus is given by

$$\overline{\mathrm{Nu}}_L = 0.168(\mathrm{Ra}_x^*)^{0.287} \tag{16}$$

with a correlation coefficient of 95.93%.

Figure 7 shows the overall average Nusselt numbers versus the modified Rayleigh numbers, where the laminar data is correlated using the aspect ratio Γ and the area ratio $\kappa=(A_s/A_c)$. Dashed lines present the fitting correlation for duct numbers 1 and 2, which is given by

$$\overline{\mathrm{Nu}}_L = 12.414(\mathrm{Ra}_L^*)^{-0.237}\kappa^{1.259}\Gamma^{-1.226}$$
$$\text{for } \kappa < 100 \quad 8\times 10^6 \le \mathrm{Ra}_L^* \le 6\times 10^7 \tag{17}$$

with an error band of +7% and −8%, where all the data fall within this band. However, for duct numbers 3, 4, and 5, where the area ratio $\kappa \ge 100$, the fitting correlation presented by the solid lines is given by

$$\overline{\mathrm{Nu}}_L = 33,633.84(\mathrm{Ra}_L^*)^{-0.241}\kappa^{-0.860}\Gamma^{0.0779}$$
$$\text{for } \kappa \ge 100 \quad 1\times 10^6 \le \mathrm{Ra}_L^* \le 7\times 10^6 \tag{18}$$

with an error band of +9% and −7%, where all the data fall within this band. It should be noticed that in this figure and in the next one, two geometrical parameter ratios are needed to effectively correlate the data. The aspect ratio is taking care of the horizontal orientation of the rectangular ducts and the difference between the rectangular and square ducts. However, the area ratio is used to differentiate between ducts having the same aspect ratio. The transition regimes of the overall averaged data are correlated in terms of Nusselt and the modified Rayleigh numbers using the aspect ratio and the area ratio as parameters, as shown in Fig. 8. The correlation covering ducts 1 and 2 is presented by dashed lines as

$$\overline{\mathrm{Nu}}_L = 0.256(\mathrm{Ra}_L^*)^{0.179}\kappa^{0.367}\Gamma^{-0.385}$$
$$\text{for } \kappa < 100 \quad 3\times 10^7 \le \mathrm{Ra}_L^* \le 6\times 10^8 \tag{19}$$

with an error band of ±5%, where all the data fall within this band. The correlation covering duct numbers 3, 4, and 5 is presented by solid lines as

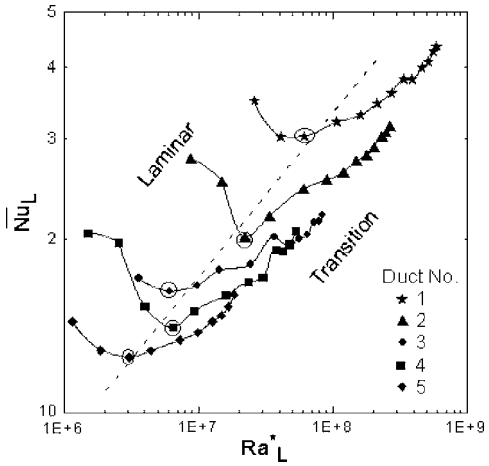

Fig. 6 The overall averaged Nusselt number profiles. Dashed line presents the data fit (Eq. (16)) through the critical points marked by circles.

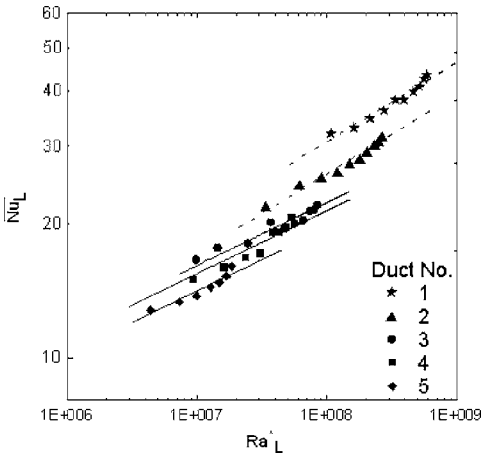

Fig. 8 The overall averaged Nusselt numbers for the transition regime; dashed lines are the fitting data given by Eq. (19) and solid lines are those given by Eq. (20)

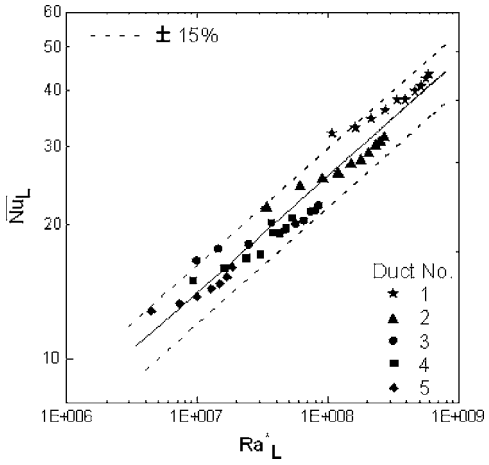

Fig. 9 The overall averaged Nusselt numbers for the transition regime; solid line presents the fitting through the data given by Eq. (21)

$$\overline{\mathrm{Nu}}_L = 2.664(\mathrm{Ra}_L^*)^{0.142}\kappa^{-0.114}\Gamma^{0.0617}$$
$$\text{for } \kappa \geq 100 \quad 4\times 10^6 \leq \mathrm{Ra}_L^* \leq 9\times 10^7 \qquad (20)$$

with an error band of ±7%, where all the data fall within this band.

On the other hand, if the aspect ratio and the area ratio at transition regime are relaxed and the overall averaged data to be correlated using Nusselt numbers as function of the modified Rayleigh numbers, only then the following correlation is developed:

$$\overline{\mathrm{Nu}}_L = 0.213(\mathrm{Ra}_L^*)^{0.260} \quad 4\times 10^6 \leq \mathrm{Ra}_L^* \leq 6\times 10^8 \qquad (21)$$

and shown as a solid line in Fig. 9, with correlation coefficient R^2=94.5%. Dashed lines in Fig. 9 present the error band width ±15%, where 95.6% of the points fall within this band. It should be noticed that a correlation such as (21) could not be obtained with a reasonable accuracy for the laminar case shown in Fig. 7 due to the diversity in the data and their dependence on the area ratio and the aspect ratio.

Figure 10 was constructed in order to compare the present results of isoflux surface with those of isothermal surface of Hassani [21] and Zeitoun and Ali [25]. Overall averaged Nusselt numbers versus Rayleigh numbers, given by Eq. (14), are shown in Fig. 10

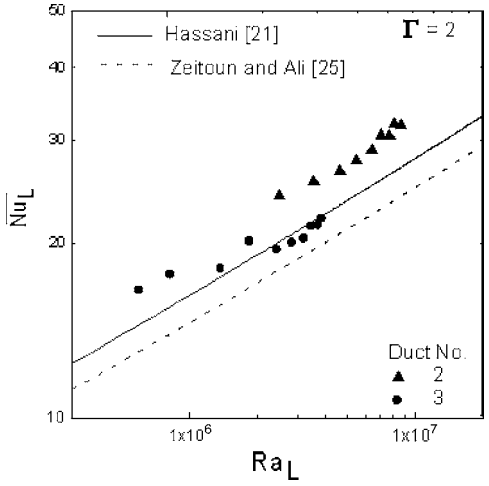

Fig. 10 Comparison of the overall averaged Nusselt numbers for the isoflux surface ducts (symbols) with the analytical (solid line) and the computational (dashed line) having isothermal duct surface

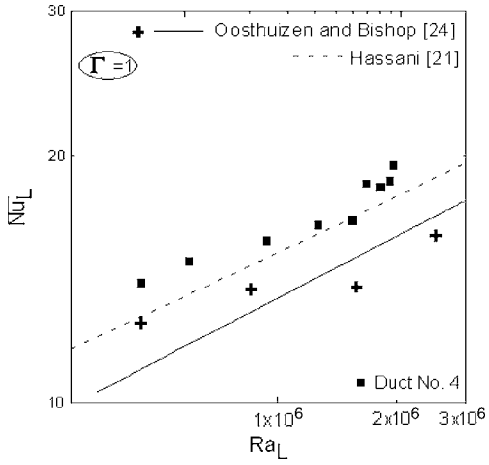

Fig. 11 Comparison of the overall averaged Nusselt numbers for the isoflux surface ducts (square symbols) with the experimental (+ symbols and solid line) and the analytical (dashed line) having isothermal duct surface

for Γ=2 for ducts 2 and 3. The present results are higher by 20% than the analytical prediction of Hassani [21] (solid line) and by 30% than the computational simulation by Zeitoun and Ali [25] (dashed line), keeping in mind that their correlations are for an isothermal duct surface, whereas the present analyses are for an isoflux surface. It should be mentioned that Nakamura and Asako [22] have performed a similar experiment, but in water using isoflux duct surface for single short square duct, and their results were higher by 10–30% than their analytical predicted solution. It is worth mentioning that a comparison of constant heat flux values with constant wall temperature values reveals that the isoflux Nusselt number is about 15% higher in the case of free convection from a vertical plate (Kays [29]), which compares with ratios of about 36% for laminar forced convection boundary layers (Kays [29]). Furthermore, the same comparison in the case of internal flow through horizontal square, circular, and rectangular ducts shows ratios of 25.6%, 19.23%, and 15.0% higher, respectively (Bejan [30]).

Another comparison is made with the empirical correlation obtained by Oosthuizen and Bishop [24] for isothermal short square ducts using the transient method for heating in air for Γ=1 in Fig. 11. The present experimental isoflux results are higher by 27% than those of [24]. Their exact experimental data points + are shown in Fig. 11 for comparison. Furthermore, the analytical correlation of Hassani [21] for isothermal square duct with Γ=1 is also plotted as a dashed line in Fig. 11. The present experimental data points are higher by only 10% than the analytical correlation of Hassani.

5 Conclusions

Experimental study has been made of natural convection heat transfer from horizontal rectangular ducts in air. Two distinct flow regimes are observed; namely, laminar and transition to turbulence. A laminar regime is obtained for low values of convection heat flux and characterized by a decrease in Nusselt numbers at any fixed longitudinal station x on the duct's surface. However, Nusselt numbers increase as x increases along the duct's surface for any value of the heat flux, and the regime is characterized as transition to turbulence. General correlation using the local circumference average transition to turbulence heat transfer data is obtained where Nusselt numbers are correlated using the modified Rayleigh numbers (Eq. (15)). Furthermore, on the overall average basis, the following conclusions can be drawn:

- Correlation covering the locus of critical points segregating the laminar and transition regimes is obtained using the modified Rayleigh number (Eq. (16)).
- Laminar heat transfer data are aspect ratio and area ratio dependent, as correlated using the modified Rayleigh numbers (Eqs. (17) and (18)).
- Transition regime data are less sensitive to the aspect ratio and the area ratio; therefore, they could be correlated either by using aspect ratio and area ratio as seen by Eqs. (19) and (20) or using the modified Rayleigh numbers only, as given by Eq. (21).

Comparisons with the available data in the literature show that Nusselt numbers for ducts of a uniform surface heat flux are always higher by about 10%–30% than that of an isothermal surface. This agrees with the general trends found in the literature for other flow configurations.

Nomenclature

A = duct height, m
A_c = duct cross-section area, (AB), m^2
A_s = duct surface area, $2(A+B)l$, m^2
A_{Bk} = end plate cross-section area, m^2
B = duct width, m
EIP = electrical input power, W
h = heat transfer coefficient, $W\,m^{-2}\,K^{-1}$
k = thermal conductivity, $W\,m^{-1}\,K^{-1}$
L = characteristic length, $=A+B$, m
l = duct length, m
Nu = Nusselt number, hL/k or hx/k
q_c = convection heat flux, W/m^2
q_r = radiation heat flux, W/m^2
q_{Bk} = heat lost by conduction through the Bakelite end plates, W/m^2
Ra_L = Rayleigh number, $g\beta(\bar{T}-T_\infty)L^3\nu^{-1}\alpha^{-1}$
Ra^* = the modified Rayleigh number, $g\beta q_c x^4\nu^{-1}\alpha^{-1}k^{-1}$ or $g\beta q_c L^4\nu^{-1}\alpha^{-1}k^{-1}$
T = temperature, K
T_{iB} = inside surface temperature of the Bakelite end plate, K
T_{oB} = outside surface temperature of the Bakelite end plate, K
T_{mean} = arithmetic mean temperature, K
x = axial or longitudinal distance, m

Greek Symbols

Γ = aspect ratio$=A/B$
α = thermal diffusivity, $m^2\,s^{-1}$
β = coefficient for thermal expansion, K^{-1}
δ = Bakelite thickness
ϵ = emissivity
θ = arithmetic mean temperature defined by Eq. (6), K
κ = area ratio, A_s/A_c
ν = kinematics viscosity, $m^2\,s^{-1}$
σ = Boltzmann constant $(=5.67\times10^{-8}\ W\,m^2\,K^4)$

Subscripts

Bk = Bakelite
j = indices in the circumference direction ranging from 1 to 3
L = characteristic length
x = indices in the axial direction ranging from 1 to 11
x = characteristic length
∞ = ambient condition

Superscript

$-$ = average quantity

Acknowledgment

This experimental investigation is supported by Saudi Arabian Basic Industrial Company (SABIC) and the Research Center, College of Engineering at King Saud University under project No. 33/426. This support is highly appreciated and acknowledged.

References

[1] McAdams, W. H., 1954, *Heat Transmission*, 3rd ed., McGraw-Hill, New York, Chap. 7.
[2] Churchill, S. W., and Chu, H. H., 1975, "Correlating Equations for Laminar and Turbulent Free Convection From a Vertical Plate," Int. J. Heat Mass Transfer, **18**, pp. 1323–1329.
[3] Goldstein, R., Sparrow, E. M., and Jones, D. C., 1973, "Natural Convection Mass Transfer Adjacent to Horizontal Plates," Int. J. Heat Mass Transfer, **16**, pp. 1025–1037.
[4] Lloyd, J. R., and Moran, W. R., 1974, "Natural Convection Adjacent to Horizontal Surfaces of Various Planforms," ASME Paper 74-WA/HT-66.
[5] Morgan, V. T., 1975, "The Overall Convective Heat Transfer From Smooth Circular Cylinders," in *Advances in Heat Transfer*, T. F. Irvine and J. P. Hartnett, eds., Academic Press, New York, Vol. 11, pp. 199–264.
[6] Churchill, S. W., and Chu, H. H., 1975, "Correlating Equations for Laminar and Turbulent Free Convection From a Horizontal Cylinder," Int. J. Heat Mass Transfer, **18**, pp. 1049–1053.
[7] Churchill, S. W., 1983, "Free Convection Around Immersed Bodies," *Heat Exchanger Design Handbook*, E. U. Schlünder, ed., Hemisphere Publishing, New York, Sec. 2.5.7.
[8] Khan, W. A., Culham, J. R., and Yovanovich, M. M., 2005, "Fluid Flow Around and Heat Transfer From an Infinite Circular Cylinder," ASME J. Heat Transfer, **127**(7), pp. 785–790.
[9] Khan, W. A., Culham, J. R., and Yovanovich, M. M., 2006, "Fluid Flow and Heat Transfer in Power-Law Fluids Across Circular Cylinder: Analytical Study," ASME J. Heat Transfer, **128**(9), pp. 870–878.
[10] Badr, H. M., and Shamsher, K., 1993, "Free Convection From an Elliptic Cylinder With Major Axis Vertical," Int. J. Heat Mass Transfer, **36**(14), pp. 3593–3602.
[11] Mahfouz, F. M., and Kocabiyik, S., 2003, "Transient Numerical Simulation of Buoyancy Driven Flow Adjacent to an Elliptic Tube," Int. J. Heat Fluid Flow, **24**, pp. 864–873.
[12] Ali, M. E., 1994, "Experimental Investigation of Natural Convection From Vertical Helical Coiled Tubes," Int. J. Heat Mass Transfer, **37**(4), pp. 665–671.
[13] Ali, M. E., 1998, "Laminar Natural Convection From Constant Heat Flux Helical Coiled Tubes," Int. J. Heat Mass Transfer, **41**(14), pp. 2175–2182.
[14] Ali, M. E., 2004, "Free Convection Heat Transfer From the Outer Surface of Vertically Oriented Helical Coils in Glycerol Water Solution," Heat Mass Transfer, **40**(8), pp. 615–620.
[15] Ali, M. E., 2006, "Natural Convection Heat Transfer From Vertical Helical Coils in Oil," Heat Transfer Eng., **27**(3), pp. 79–85.
[16] Yoo, S. Y., and Park, J. H., 2003, "An Experimental Study on Heat/Mass Transfer From a Rectangular Cylinder," ASME J. Heat Transfer, **125**(6), pp. 1163–1169.
[17] Saha, S. K., and Mallick, D. N., 2005, "Heat Transfer and Pressure Drop Characteristics of Laminar Flow in Rectangular and Square Plain Ducts and Ducts With Twisted-Tape Inserts," ASME J. Heat Transfer, **127**(9), pp. 966–977.
[18] Joshi, M. V., Gaitonde, U. N., and Mitra, S. K., 2006, "Analytical Study of Natural Convection in a Cavity With Volumetric Heat Generation," ASME J. Heat Transfer, **128**(2), pp. 176–182.
[19] Fu, W. L., Wright, L. M., and Han, J. C., 2006, "Rotational Buoyancy Effects on Heat Transfer in Five Different Aspect-Ratio Rectangular Channels With Smooth Walls and 45 Degree Ribbed Walls," ASME J. Heat Transfer, **128**(11), pp. 1130–1141.
[20] Raithby, G. D., and Hollands, K. G. T., 1975, "A General Method of Obtaining Approximate Solutions to Laminar and Turbulent Free Convection Problems," *Advances in Heat Transfer*, T. F. Irvine, Jr. and J. P. Hartnett, eds., Academic Press, New York, Vol. 11, pp. 265–315.
[21] Hassani, V., 1992, "Natural Convection Heat Transfer From Cylinders of Arbitrary Cross Section," ASME J. Heat Transfer, **114**, pp. 768–773.
[22] Nakamura, H., and Asako, Y., 1978, "Laminar Free Convection From a Horizontal Cylinder with Uniform Cross Section of Arbitrary Shape," Bull. JSME, **21**(153), pp. 471–478.
[23] Oosthuizen, P. H., and Paul, J. T., 1984, "An Experimental Study of Free Convective Heat Transfer From Horizontal Non-circular Cylinders," *The 22nd National Heat Transfer Conference*, Niagara Falls, NY, ASME, New York, Vol. 32, pp. 91–97.
[24] Oosthuizen, P. H., and Bishop, M., 1987, "An Experimental Study of Mixed Convective Heat Transfer From Square Cylinders," AIAA 22nd Thermophysics Conf., Honolulu, June 8–10, Paper No. AIAA-87-1592.
[25] Zeitoun, O., and Ali, M., 2006, "Numerical Investigation of Natural Convec-

tion Around Isothermal Horizontal Rectangular Ducts," Numer. Heat Transfer, Part A, **50**, pp. 189–204.
[26] Callister, W. D., Jr., 2003, *Materials Science and Engineering An Introduction*, 6th ed., John Wiley and Sons, New York, Chap. 19, p. 660.
[27] Siegel, R., and Howell, J. R., 1992, *Thermal Radiation Heat Transfer*, 3rd ed., McGraw-Hill, New York.
[28] Moffat, R. J., 1988, "Describing Uncertainties in Experimental Results," Exp. Therm. Fluid Sci., **1**(1), pp. 3–7.
[29] Kays, W. M., and Crawford, M. E., 1993, *Convective Heat and Mass Transfer*, 3rd ed., McGraw Hill, Singapore, Chap. 17, p. 403.
[30] Bejan, A., 1993, *Convection Heat Transfer*, John Wiley and Sons, New York, p. 78.

Laminar Mixed Convection in the Entrance Region of Horizontal Semicircular Ducts With the Flat Wall at the Top

Y. M. F. El. Hasadi[1]

A. A. Busedra

I. M. Rustum

Mechanical Engineering Department,
University of Garyounis,
Benghazi, Libya

Laminar mixed convection in the entrance region for horizontal semicircular ducts with the flat wall on top is investigated theoretically. The governing momentum and energy equations are solved numerically using a marching technique with the finite control volume approach following the SIMPLER algorithm. Results are obtained for the thermal boundary conditions of uniform heat input axially with uniform wall temperature circumferentially at any cross section (H1 boundary condition) with Pr=0.7 *and a wide range of Grashof numbers. These results include the velocity and temperature distributions at different axial locations, axial distribution of local Nusselt number, and local average wall friction factor. It is found that Nusselt number values are close to the forced convection values near the entrance region and then decrease to a minimum as the distance from the entrance increases and then rise due to the effect of free convection before reaching constant value (fully developed). As the Grashof number increases the Nusselt number and the average wall friction factor increase in both developing and fully developed regions and the location of the onset of the secondary flow moves upstream.* [DOI: 10.1115/1.2739612]

Keywords: laminar mixed convection, entrance region, fully developed, semicircular duct, numerical, horizontal, SIMPLER

Introduction

Laminar combined forced and free convection flows in ducts have received much attention in recent years because of their wide range of applications, such as compact heat exchangers and chemical process. This paper is concerned with the problem of laminar mixed convection in the entrance region of horizontal semicircular ducts, with uniform heating which is a particular case of multipassage tubes. Due to the large amount of literature on fully developed laminar mixed convection of different cross sections, consideration will be given to the geometry of semicircular ducts only. Nandakumar et al. [1] studied numerically the problem of fully developed laminar mixed convection flow in horizontal semicircular ducts, for the case of uniform heat input axially with uniform peripheral wall temperature (*H*1 thermal boundary condition), with the flat wall at the bottom for Pr=0.7 and 5 corresponding to air and water, respectively. They found that a dual solution of two and four vortex coexist and decreasing Pr delays the appearance of the four vortex solution. Law et al. [2] studied the same problem considered in Ref. [1] by insulating the curved wall and imposing a uniform heat flux on the flat wall. They obtained a four vortex solution for the case of Pr=5 but they could not obtain a four vortex solution for the case of Pr=0.7. They concluded that increasing Pr appeared to aid the formation of four vortex flow. Lei and Trupp [3] also solved the same problem considered in Ref. [1] with the flat wall on top for Pr=5. They reported approximately the same results of Nusselt number as for the flat wall at the bottom (Ref. [1]). Chinporncharoepong et al. [4] studied the effect of orientation by rotating the horizontal semicircular duct from 0 deg (the flat wall on top) to 180 deg (the flat wall at the bottom) with incremental angle of 45 deg for Pr =4. Busedra and Soliman [5] investigated the effect of duct inclination on laminar mixed convection in inclined semicircular ducts under buoyancy assisted and opposed conditions for Pr=7. They oriented the flat wall of the duct in a vertical position using two thermal boundary conditions, *H*1 thermal boundary condition (uniform heat input axially with uniform wall temperature circumferentially at any cross section) and uniform heat input axially with uniform wall heat flux circumferentially (*H*2 thermal boundary condition).

The literature on combined free and forced convection in the entrance region is few in comparison with the fully developed case. Most of the results for laminar mixed convection in the entrance region are available for vertical rectangular ducts [6–8], and for vertical circular tubes [9–11]. Other results for horizontal ducts are also available for rectangular ducts [12] concentric annulus [13], and circular tubes [14,15]. For the case of laminar mixed convection, the thermal entrance region of the horizontal semicircular duct was experimentally investigated by Lei and Trupp [16]. The heat input was uniformly generated along the duct test section with the flat wall on top. They used water as the working fluid. They obtained results for the local and fully developed Nusselt number for a wide range of flow parameters. Busedra and Soliman [17] studied experimentally the same problem considered in Ref. [16] by inclining the semicircular duct upward and downward with $\alpha=\pm 20$ deg while the flat wall was in a vertical position. They noted that the axial variation of the Nusselt number followed the same trend observed in Ref. [16] for the horizontal and upward inclinations. Theses values of Nusselt number increased with Grashof number and angle of inclination. Although they reported that a small variation in the circumferential wall temperature occurred at $Gr > 10^7$ along the duct length, their comparison with the theoretical results of Ref. [5] for the case of $\alpha=0$ deg was found to be in good agreement. El. Hasadi et al.

[1]Corresponding author.

Contributed by the Heat Transfer Division of ASME for publication in the JOURNAL OF HEAT TRANSFER. Manuscript received February 6, 2006; final manuscript received November 14, 2006. Review conducted by Louis C. Burmeister.

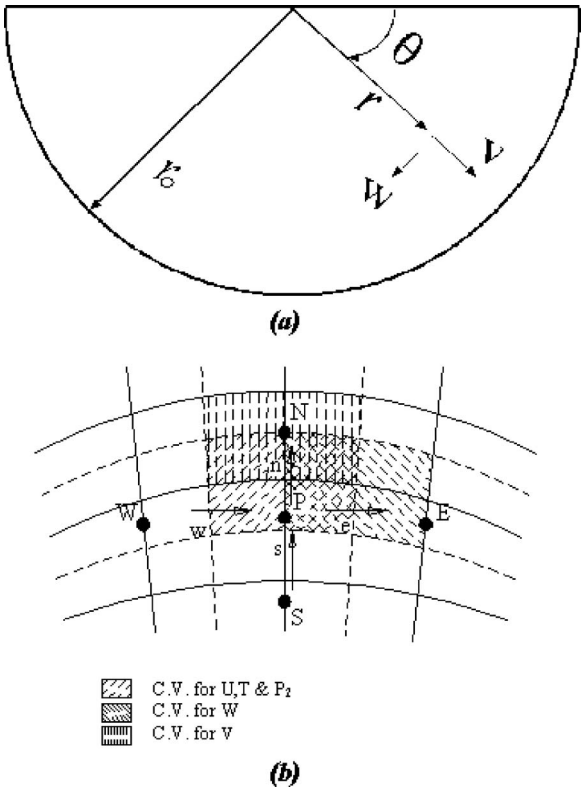

Fig. 1 Geometrical configuration system and control volumes

[18] investigated numerically the laminar mixed convection in the entrance region of circular sector ducts for Pr=0.7 and 7 with the $H1$ thermal boundary condition.

Numerical studies for the case of laminar mixed convection in the entrance region of horizontal semicircular ducts with the flat wall on top are, to the knowledge of the authors, nonexistent. The present investigation, therefore, is concerned with buoyancy effects on laminar mixed heat transfer of simultaneously developing hydrodynamically and thermally for horizontal semicircular ducts with the $H1$ thermal boundary condition. These effects are to be examined over a wide range of Gr. The calculated parameters are local Nusselt number and wall friction factor, as well as the development of axial velocity and temperature profiles.

Mathematical Model

Figure 1(a) shows the geometry of a semicircular duct with radius r_0 with the flat surface on top. The fluid enters the duct with uniform velocity equal to u_e and a uniform temperature equals to t_e. The circumferential average heat rate per unit length is constant at any cross section along the flow axis of the duct and equal to $\bar{q}$. The flow is assumed to be laminar and simultaneously developing hydrodynamically and thermally with the $H1$ thermal boundary condition. The problem is analyzed for constant fluid properties with negligible viscous dissipation. The variation of density is taken into account only in the body forces (Boussinesq approximation). All terms containing the second derivative of any quantity with respect to X are neglected. The fluid pressure decomposition which was used is given by Ref. [19]

$$p(x,r,\theta) = \bar{p}_1(x) + p_2(r,\theta) \tag{1}$$

where $\overline{p_1}$ is the cross-sectional average pressure, which is assumed to vary only in the x direction and p_2 provides the driving force for the secondary flow within the cross section. This decoupling of pressure makes it possible to solve the three-dimensional problem by using the marching technique in which the solution is progressed stepwise in the axial direction with a two-dimensional elliptic system (in the r and θ directions) to be solved at each axial step. The governing Navier–Stokes equations and the energy equation in cylindrical coordinates can be written in the nondimensional form as

1. **Continuity**

$$\frac{\partial}{\partial R}(RV) + \frac{\partial W}{\partial \theta} + \left(\frac{\pi+2}{2\pi}\right)^2 \frac{R}{\mathrm{Pr}}\frac{\partial U}{\partial X} = 0 \tag{2}$$

2. **Axial momentum**

$$\left[V\frac{\partial U}{\partial R} + \frac{W}{R}\frac{\partial U}{\partial \theta} + \left(\frac{\pi+2}{2\pi}\right)^2 \frac{U}{\mathrm{Pr}}\frac{\partial U}{\partial X}\right] = -\frac{1}{\mathrm{Pr}}\frac{d\bar{P}_1}{dX}\left(\frac{\pi+2}{2\pi}\right) + \nabla^2 U \tag{3}$$

3. **Radial momentum**

$$\left[V\frac{\partial V}{\partial R} + \frac{W}{R}\frac{\partial V}{\partial \theta} + \left(\frac{\pi+2}{2\pi}\right)^2 \frac{U}{\mathrm{Pr}}\frac{\partial V}{\partial X}\right] = \nabla^2 V - \left[\frac{2}{R^2}\frac{\partial W}{\partial \theta} + \frac{V}{R^2}\right] + \frac{W^2}{R} - \frac{\partial P_2}{\partial R} - \mathrm{Gr}\, T \sin\theta \tag{4}$$

4. **Angular momentum**

$$\left[V\frac{\partial W}{\partial R} + \frac{W}{R}\frac{\partial W}{\partial \theta} + \left(\frac{\pi+2}{2\pi}\right)^2 \frac{U}{\mathrm{Pr}}\frac{\partial W}{\partial X}\right] = \nabla^2 W + \left[\frac{2}{R^2}\frac{\partial V}{\partial \theta} - \frac{W}{R^2}\right] - \frac{WV}{R} - \frac{1}{R}\frac{\partial P_2}{\partial \theta} - \mathrm{Gr}\, T \cos\theta \tag{5}$$

5. **Energy**

$$\mathrm{Pr}\left[V\frac{\partial T}{\partial R} + \frac{W}{R}\frac{\partial T}{\partial \theta} + \left(\frac{\pi+2}{2\pi}\right)^2 \frac{U}{\mathrm{Pr}}\frac{\partial T}{\partial X}\right] = \nabla^2 T \tag{6}$$

where

$$\nabla^2 = \frac{1}{R}\frac{\partial}{\partial R}\left(R\frac{\partial}{\partial R}\right) + \frac{1}{R^2}\frac{\partial^2}{\partial \theta^2} \tag{7}$$

The dimensionless parameters are defined as follows

$$R = \frac{r}{r_0}, \quad X = \frac{x}{D_h \mathrm{PrRe}}, \quad V = \frac{v r_0}{\nu}, \quad W = \frac{w r_0}{\nu}, \quad U = \frac{u}{u_b}$$

$$T = \frac{t - t_e}{\bar{q}/k}, \quad \bar{P}_1 = \frac{\bar{p}_1^*}{\rho u_b^2}, \quad P_2 = \frac{p_2^* r_0^2}{\rho \nu^2}$$

$$\mathrm{Re} = \frac{D_h u_b}{\nu}, \quad \mathrm{Pr} = \frac{\rho \nu C_p}{k}, \quad \mathrm{Gr} = \frac{g\beta \bar{q} r_0^3}{k\nu^2}, \quad D_h = \left(\frac{2\pi}{\pi+2}\right) r_0 \tag{8}$$

The dimensionless initial and boundary conditions are

At $X=0$

$$U = 1 \quad \text{for all } R \text{ and } \theta$$

$$T = 0 \quad \text{for all } R \text{ and } \theta$$

$$\bar{P}_1 = \bar{P}_0 \quad \text{for all } R \text{ and } \theta$$

$$V = W = P_2 = 0 \quad \text{for all } R \text{ and } \theta \tag{9a}$$

At $X>0$

$$U = V = W = 0 \quad \text{at the walls}$$

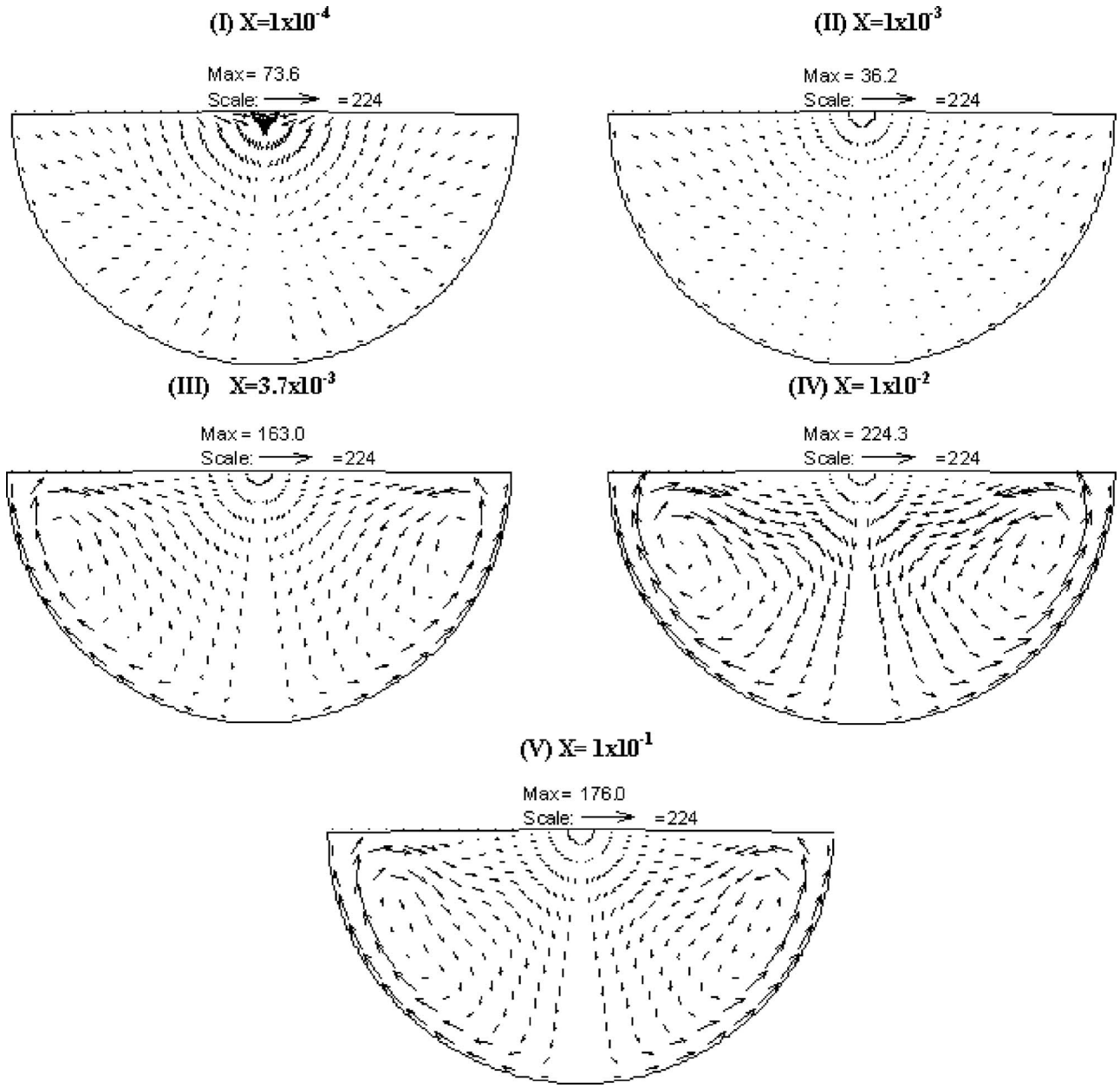

Fig. 2 Secondary flow pattern for different axial stations at Gr=10^7

$$T = T_w \quad \text{at the walls} \tag{9b}$$

The parameter T_w in Eq. (9*b*) is the dimensionless wall temperature, which is a function of X; however, its value is not known a priori. The method used for determining T_w at each axial location X is similar to the one used by Paraksh and Liu [20]. Starting from a uniform flow at the inlet of the duct (defined by Eq. (9*a*)) the solution for U, V, W, $\bar{P}_1$, P_2, and T is to be determined as a function of X, R, and θ. The solution is to be progressed along X until $X=0.4$ for all Gr. This distance is sufficient to ensure that the fully developed region has been reached.

The Nusselt number in dimensionless form

$$\mathrm{Nu}_x = \frac{hD_h}{k} = \frac{2\pi}{(\pi+2)^2}\frac{1}{(T_w - T_b)} \tag{10}$$

The product $f\mathrm{Re}$ where the friction factor f is defined by

$$f = \frac{\bar{\tau}_w}{(1/2)\rho u_b^2} \tag{11}$$

The parameter $\bar{\tau}_w$ was calculated by averaging the wall shear stress around the circumference of the duct. Thus, the average wall friction factor is given by the following relation

$$f\mathrm{Re} = \frac{4\pi}{(\pi+2)^2}\left[\int_0^1 \left(\frac{\partial U}{R\partial\theta}\right)_{\theta=0} dR - \int_0^1 \left(\frac{\partial U}{R\partial\theta}\right)_{\theta=\pi} dR - \int_0^\pi \left(\frac{\partial U}{\partial R}\right)_{R=1} d\theta\right] \tag{12}$$

Solution Procedure

The numerical method employed to solve these equations is based on the SIMPLER method of Patankar [21] with the march-

Table 1 Effects of grid size on local Nusselt number for case of Gr=5×10^5

	Station			
	Nu_x			
$M\times N$ (ΔX)	(I) 10^{-4}	(II) 10^{-3}	(IV) 10^{-2}	(V) 10^{-1}
30×50 ($1\times10^{-5}-1\times10^{-3}$)	43.49	16.61	6.58	6.38
40×60 ($1\times10^{-5}-1\times10^{-3}$)	43.62	16.60	6.58	6.38
20×40 ($1\times10^{-5}-1\times10^{-3}$)	42.80	16.71	6.58	6.41
30×50 ($6\times10^{-6}-1\times10^{-3}$)	43.19	16.63	6.61	6.39
30×50 ($7\times10^{-6}-1\times10^{-3}$)	43.3	16.62	6.60	6.39

ing method of Patankar and Spalding [19]. For the discretization of the governing Eqs. (2)–(6), the power law-scheme suggested by Patankar [21] was used. The pressure equation and the pressure–correction equation have been derived from the continuity. The discretized equations were solved simultaneously for each radial line using the tridiagonal matrix algorithm (TDMA) and the domain was covered by sweeping line by line in the angular direction. At the end of each iteration a correction procedure was applied to the values of U and $d\bar{P}_1/dX$ in order to ensure that the mean value of the dimensionless axial velocity U_b is equal to 1.

The mesh used to solve the governing equations was a three-dimensional mesh staggered in the radial and angular directions (see Fig. 2(*b*)), with uniform divisions in the radial and angular directions and nonuniform divisions in the axial direction. The control volumes adjacent to solid walls were subdivided into two subdivisions in order to capture the steep gradient in the velocity and temperature, and the axial step size was taken as $\Delta X=10^{-5}$ near the duct inlet. Then ΔX was increased by 5% for each consecutive step until ΔX reaches the value of 10^{-3} which was kept constant. The grid points used in radial and angular directions are selected to be 30(M) and 50(N), respectively. To examine the grid size effects, Table 1 presents the local Nusselt number at Gr=5 $\times10^5$ for various grid arrangements. A very small deviation appears in the first station for local Nusselt number values. This deviation is within 1.5%.

The present results of $f\mathrm{Re}_{fd}$ and Nu_{fd} for the fully developed forced convection (Gr=0) have been compared with the exact results obtained from Lei and Trupp [22,23]. These values are within 0.1% and 0.12% for $f\mathrm{Re}_{fd}$ and Nu_{fd}, respectively. For a fully developed mixed convection, a comparison of Nu_{fd} and $f\mathrm{Re}_{fd}$ has been made with the results of Lei [24] for horizontal semicircular ducts with the flat wall on top and Pr=0.7. These results are presented in Table 2.

Results and Discussion

The numerical investigations were obtained for the entrance region of horizontal semicircular ducts with the flat wall on top and Pr=0.7. A wide range of Gr was covered providing the results for the development of the secondary flow, axial velocity, and temperature profiles, and the development of overall quantities Nu_x and $f\mathrm{Re}$.

Table 2 Comparison of fully developed Nu_{fd} and $f\mathrm{Re}_{fd}$ with Ref. [24] at Pr=0.7

	Nu_{fd}		$f\mathrm{Re}_{fd}$	
Gr	Present	Ref. [24]	Present	Ref. [24]
1×10^6	7.161	7.293	22.839	23.145
1×10^7	10.918	11.377	32.070	33.110

Development of Secondary Flow

Figure 2 shows the development of the secondary flow at Gr $=10^7$ for five selected axial stations. In Station I ($X=10^{-4}$) the effects of free convection are negligible and the development of the hydrodynamic and thermal boundary layers is essential as in pure forced convection. In Station II ($X=10^{-3}$) signs of upward flow are observed near the curved wall. The secondary flow begins to particularly destroy the hydrodynamic boundary layer. Further downstream with Station III ($X=3.7\times10^{-3}$) the appearance of two counter-rotating cells in the upper part of the duct near the curved wall are partially established. In Station IV ($X=10^{-2}$) the two counter-rotating cells strengthened along the curved wall. Their effects on the thermal field now become important, as shown later. Contrasted with the velocities at Station II the two vortex flow in Station IV is significantly magnified with maximum cross stream velocities, from 36.2 to 224.3. At the last Station V ($X=10^{-1}$) the hydrodynamic and thermal fields remain essentially the same, indicating that the fully developed flow is well established. It can be seen that the intensity of the secondary flow is lower than that of Station IV. This is consistent with Ref. [14]. It should be mentioned that Lei [24] showed, by solving the fully developed model for $\mathrm{Gr}\geqslant10^6$, the occurrence of bifurcated solution for different values of Pr. However, the four-vortex result for Pr=0.7 was less noticeable and the heat transfer enhancement was not important. The present results correspond to a two-vortex solution for developing and fully developed flow, indicating that the two-vortex solution is the only stable solution. This is consistent with the findings of Orfi et al. [25] for horizontal and inclined tubes with $H2$ thermal boundary condition.

Development of Axial Velocity

The development of the axial velocity is represented by the isovels for the case of pure forced convection, as shown in Fig. 3. It can be seen that the maximum velocity has moved toward the center of the duct as the flow approaching the fully developed state due to the absence of the free convection. The isovels for the case of Gr=10^7 are shown in Fig. 4. In the absence of buoyancy effects, the isovels are seen to be very much similar to those of pure forced convection. The velocity is constant in most of the flow domain with sharp changes very near the duct walls, as shown in Stations I and II. As the flow proceeds further downstream in Station III the effect of free convection begins to appear by distorting the isovels, particularly in the upper part of the duct due to the intensity of the secondary flow near the corners. In Station IV the isovels are distorted along the upper part of the curved wall, while the maximum velocity is confined at the middle bottom of the duct. In Station V the fully developed state is reached and the maximum velocity shifted downward toward the lower portion of the curved wall.

Development of Temperature

The development of temperature is represented by the isotherms for the case of forced convection as shown in Fig. 5. The flow is symmetric and the minimum temperature moves toward the center of the duct as the flow proceeds toward the fully developed state. Figure 6 shows the isotherms for the case of Gr=10^7. It is clear that, in Stations I and II, the fluid temperature is nearly uniform except at very near the wall, indicating that the heat did not reach the core of the fluid in the duct cross section. In Station III, the effect of the secondary flow becomes important, especially near the upper corners. However, the isotherms are still concentric. Further downstream in Station IV the isotherms are shown to fill the whole fluid in the cross section, indicating that the heat has penetrated to the core of the fluid. At this station the intensity of

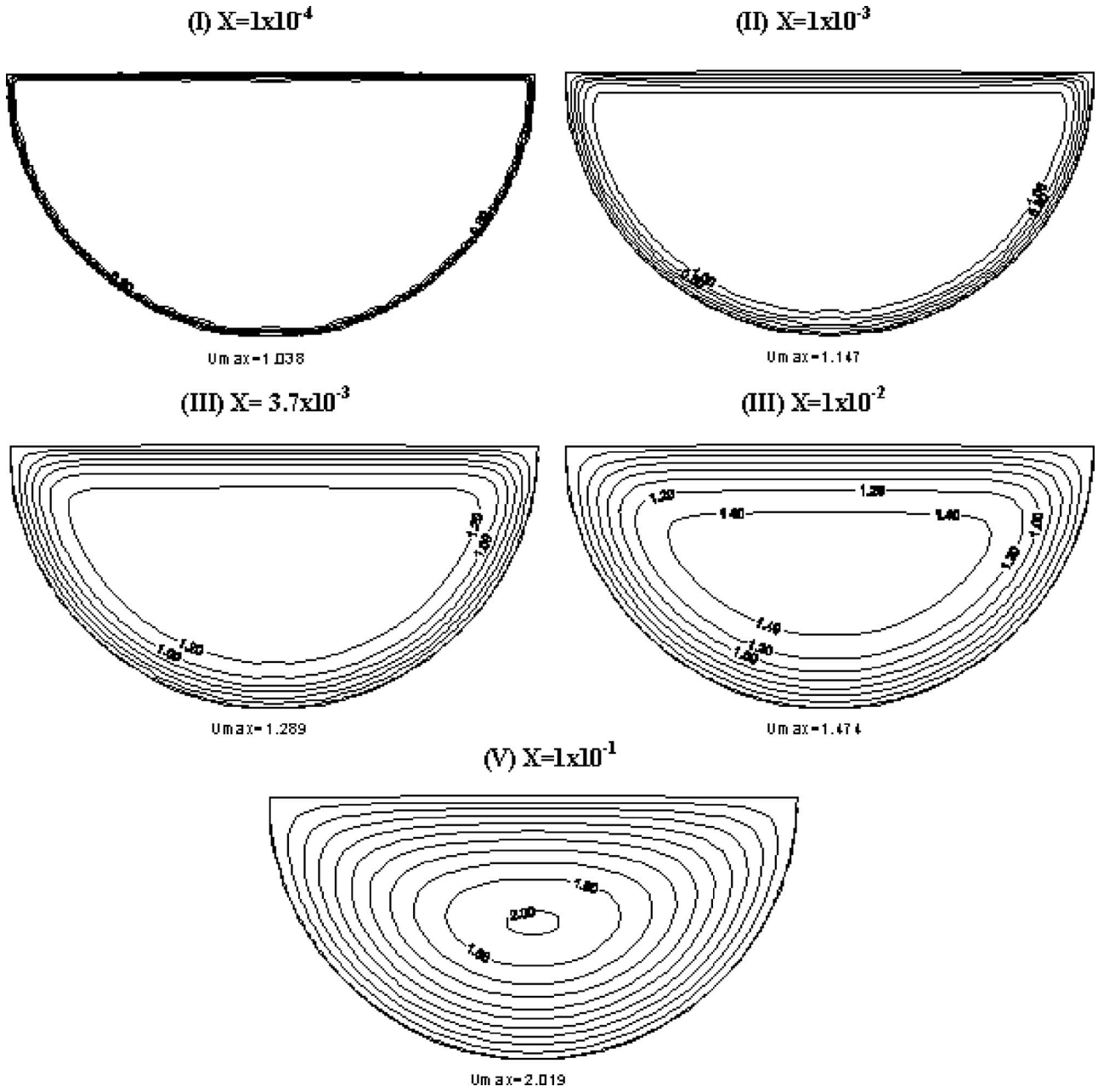

Fig. 3 Axial velocity contours for different axial stations at Gr=0

the secondary flow increases and its effects on the distortion of the temperature become significant. These effects are shown to shift the minimum temperature near the bottom of the duct cross section. At Station V the flow becomes fully developed and the minimum temperature is still confined at the bottom.

Local Nusselt Number and Friction Factor

Figure 7 shows the development of Nu_x for different Gr. The Nu_x is close to the forced convection values at smaller values of X due to the absence of the free convection. As X increases Nu_x decreases to a minimum due to the balance between the entrance and free convection effects, and then rises up to the fully developed value due to the generation of strong currents of the secondary flow. Further, as Gr increases the minimum Nu_x shifts upstream and the thermal entrance length decreases. This behavior was predicted experimentally by Refs. [16,17,26] and numerically by Ref. [12] for rectangular ducts. The increase in Gr enhances Nu_x in the developing and fully developed regions. The corresponding values of Nu_x at Stations IV and V at $Gr=1\times10^7$ are 9.628 and 10.918, respectively, which are 144% and 263% higher than those of forced convection at the same axial locations.

Figure 8 shows the development of $f\mathrm{Re}$ for different Gr. The results show behavior similar to that of Nu_x discussed above. The corresponding values of $f\mathrm{Re}$ at Stations IV and V at $Gr=1\times10^7$ are 30.643 and 32.071, respectively, which are 142% and 202% higher than those of forced convection at the same axial stations. The enhancement of $f\mathrm{Re}$ is less as compared with Nu_x. Table 3 presents the fully developed values of Nu_{fd} and $f\mathrm{Re}$ for the whole range of Gr considered in this study. Further, the thermal entrance length, L_{th}, represents the axial distance in which Nu_x deviates from the fully developed value by 5%. It should be noted that for mixed convection the values of Nu_x plunge below the value of Nu_{fd} and then rise to approach the fully developed from below, as shown in Fig. 6.

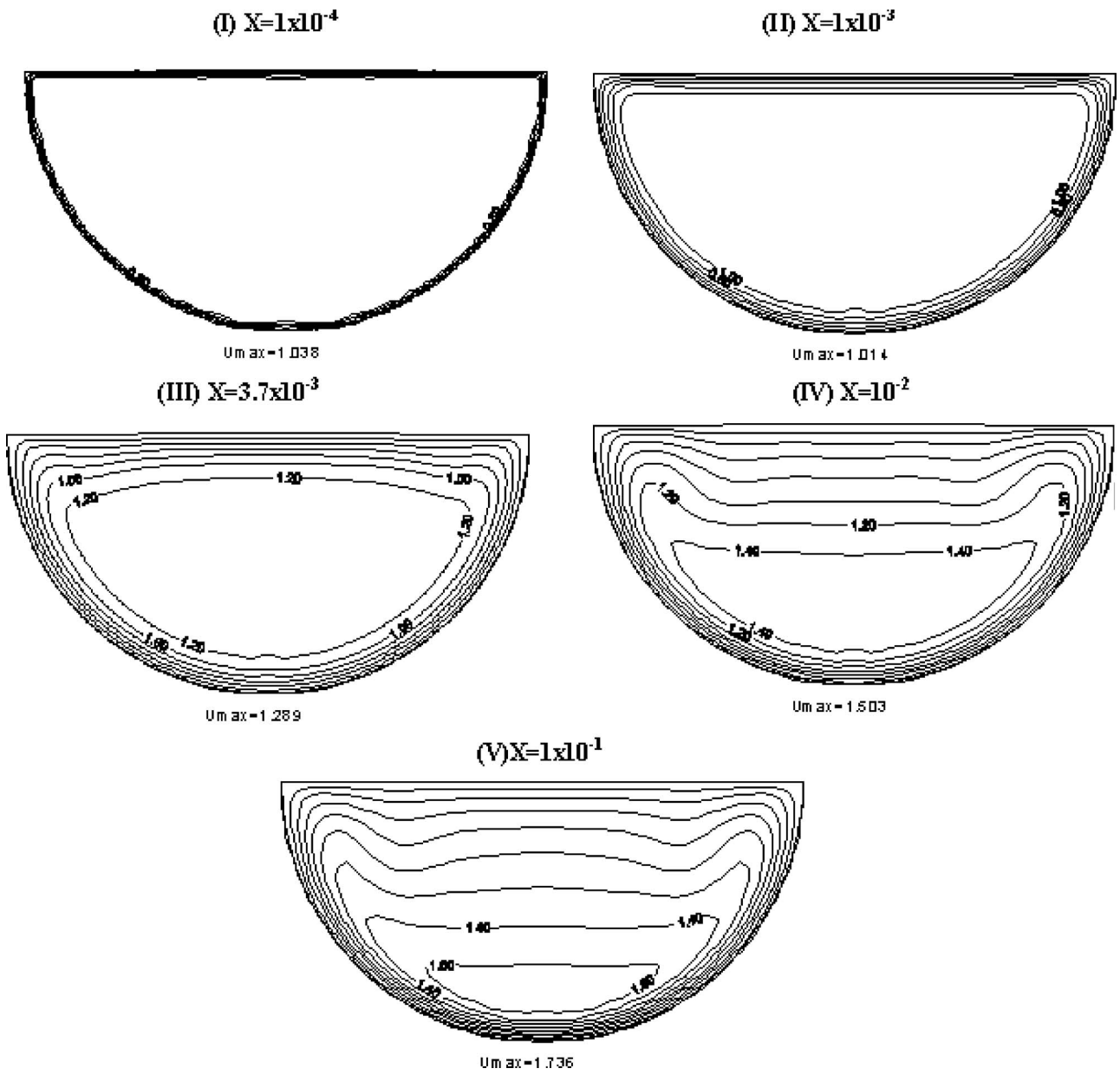

Fig. 4 Axial velocity counters for different axial stations Gr=10^7

Onset of the Secondary Flow

The location of the onset of secondary flow is defined as the axial distance where the local Nu_x value first exceeds the forced convection value by 5%. Results for the location of the onset of the secondary flow are tabulated in Table 4. It is clear that as Gr increases the location of the onset of the secondary flow moves upstream.

Conclusions

Laminar mixed convection in the entrance region of horizontal semicircular ducts with the flat wall on top has been studied numerically. The effects of free convection on the development of the hydrodynamic and thermal boundary layers are clearly established. Nu_x and fRe in the developing and fully developed regions increased with Gr. The axial variation of Nu_x follows the trend noted in the previously published results for horizontal ducts. The enhancement of Nu_x is found to be greater than fRe in the developing and fully developed regions. Further, as Gr increases the location of the onset of the secondary flow moves upstream.

Nomenclature

C_p = specific heat, J kg^{-1} K^{-1}
D_h = hydraulic diameter, m
f = friction factor defined by Eq. (11)
g = gravitational acceleration, ms^{-2}
Gr = Grashof number defined by Eq. (8)
h = average heat transfer coefficient, W m^{-2} K^{-1}
k = thermal conductivity, W m^{-1} k^{-1}
L_{th} = dimensionless thermal entrance length
Nu_x = local Nusselt number defined by Eq. (10)
$\bar{p}_1$ = cross-sectional average pressure, N m^{-2}
p_2 = cross-sectional excess pressure, N m^{-2}
$\bar{P}_1$ = dimensionless cross—sectional average pressure defined by Eq. (8)
P_2 = dimensionless cross—sectional excess pressure defined by Eq. (8)
Pr = Prandtl number defined by Eq. (8)
$\bar{q}$ = rate of heat input per unit length, W m^{-1}
r = radial coordinate, m

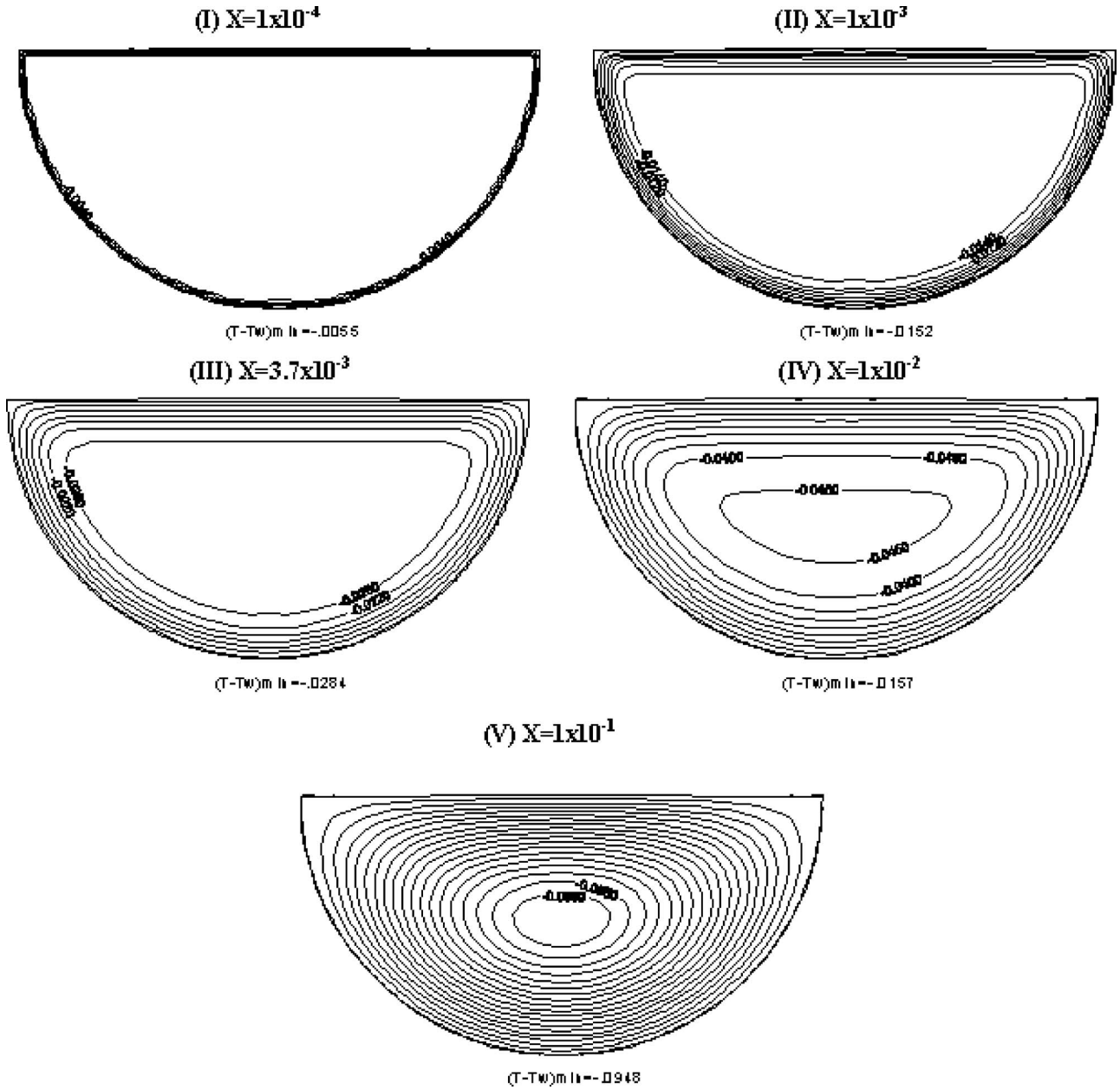

Fig. 5 ($T-T_w$) **temperature contours for different axial stations at Gr=0**

r_0 = radius of circular wall, m
R = dimensionless radial coordinate defined by Eq. (8)
Re = Reynolds number defined by Eq. (8)
t = temperature, K
t_e = temperature at the inlet, K
T = dimensionless temperature defined by Eq. (8)
T_b = dimensionless bulk temperature
T_w = dimensionless wall temperature
u = axial velocity, m s^{-1}
u_b = mean axial velocity, m s^{-1}
U = dimensionless axial velocity defined by Eq. (8)
v = radial velocity, m s^{-1}
V = dimensionless radial velocity defined by Eq. (8)
w = angular velocity, m s^{-1}
W = dimensionless angular velocity defined by Eq. (8)
x = axial coordinate, m
X = dimensionless axial coordinate define by Eq. (8)
$H1$ = corresponding to the $H1$ boundary condition
$H2$ = corresponding to the $H2$ boundary condition

Greek Symbols

β = coefficient of thermal expansion of fluid, K^{-1}
θ = angular coordinate
ν = kinematic viscosity, m^2 s^{-1}
ρ = density, kg m^{-3}
τ = shear stress, N m^{-2}

Subscripts

fd = fully developed state
e = refers to the Entrance

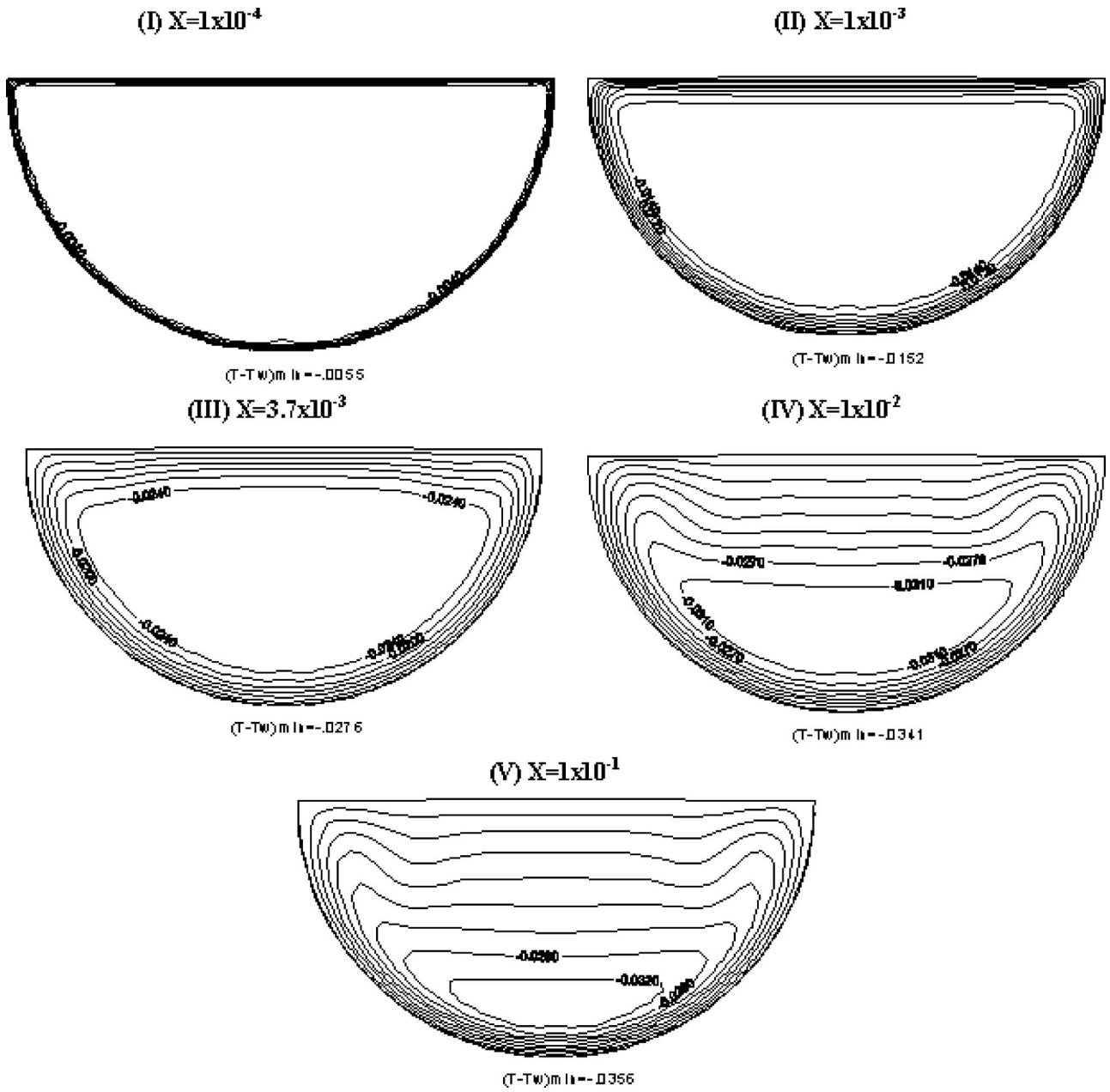

Fig. 6 ($T - T_w$) **temperature contours for different axial stations at Gr=10^7**

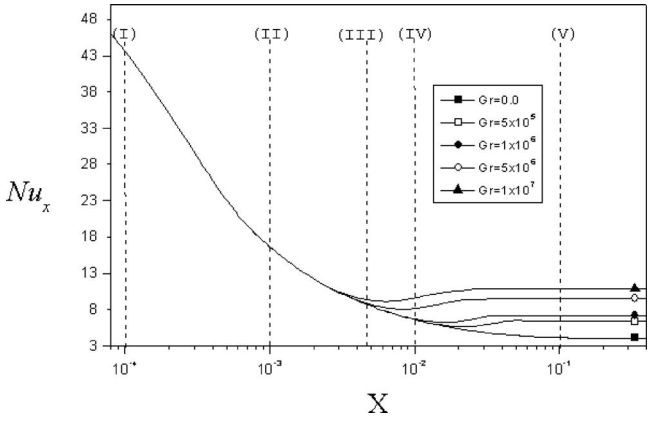

Fig. 7 Effect of Gr on the axial development of Nu_x

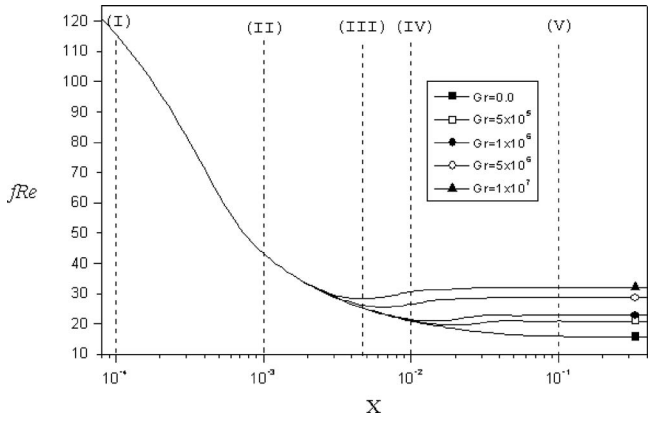

Fig. 8 Effect of Gr on the axial development of *f*Re

Table 3 Fully developed values of Nu_{fd}, fRe_{fd}, and L_{th} for different Gr

Gr	Nu_{fd}	fRe_{fd}	L_{th}
0.0	4.084	15.748	0.0664
5×10^5	6.389	21.032	0.0344
1×10^6	7.161	22.839	0.0274
5×10^6	9.551	28.653	0.0176
1×10^7	10.918	32.070	0.0159

Table 4 Locations of the onset of the secondary flow at different Gr

Gr	Location of the onset of the secondary flow
5×10^5	1.94×10^{-2}
1×10^6	1.37×10^{-2}
5×10^6	5.88×10^{-3}
1×10^7	4.11×10^{-3}

References

[1] Nandakumar, K., Masliyah, J. H., and Law, H. S., 1985, "Bifurcation in Steady Laminar Mixed Convection Flow in Horizontal Ducts," J. Fluid Mech., **152**, pp. 145–161.

[2] Law, H. S., Masliyah, J. H., and Nandakumar, K., 1987, "Effect of Nonuniform Heating on Laminar Mixed Convection in Ducts," ASME J. Heat Transfer, **109**, pp. 131–137.

[3] Lei, Q. M., and Trupp, A. C., 1990, "Predictions of Laminar Mixed Convection in Horizontal Semicircular Duct," *Proceedings of the 6th International Symposium on Heat and Mass Transfer*, Miami, FL, pp. 10–12.

[4] Chinpruncharoenpong, C., Trupp, A. C., and Soliman, H. M., 1993, "Effect of Gravitational Force Orientation on Laminar Mixed Convection for a Horizontal Semicircular Duct," *Proceedings of the 3rd World Conference on Experimental Heat Transfer, Fluid Mechanics and Thermodynamics*, Vol. 109, Elsevier, New York, pp. 131–137.

[5] Busedra, A. A., and Soliman, H. M., 1999, "Analysis of Laminar Mixed Convection in Inclined Semicircular Ducts Under Buoyancy-Assisted and –Opposed Conditions," Numer. Heat Transfer, Part A, **36**, pp. 527–544.

[6] Cheng, C. H., Lin, C. H., and Aung, W., 2000, "Predictions of Developing Flow With Buoyancy-Assisted Flow Separation in Vertical Rectangular Duct: Parabolic Model Versus Elliptic Model," Numer. Heat Transfer, Part A, **37**, pp. 567–586.

[7] Cheng, C. H., Anug, W., and Weng, C. J., 2000, "Buoyancy-Assisted Flow Reversal and Convective Heat Transfer in Entrance Region of a Vertical Rectangular Duct," Int. J. Heat Fluid Flow, **21**, pp. 403–411.

[8] Cheng, C. H., Huang, S. Y., and Aung, W., 2002, "Numerical Predictions of Mixed Convection and Flow Separation in a Vertical Duct With Arbitrary Section," Numer. Heat Transfer, Part A, **41**, pp. 491–514.

[9] Nesreddin, H., Galanis, N., and Nguyen, C. T., 1998, "Effects of Axial Diffusion on Laminar Heat Transfer With Low Pelect Numbers in the Entrance Region of Thin Vertical Tubes," Numer. Heat Transfer, Part A, **33**, pp. 247–266.

[10] Zeldin, B., and Schmidt, F. W., 1972, "Developing Flow With Combined Forced—Free Convection in an Isothermal Vertical Tube," ASME J. Heat Transfer, **94**, pp. 211–223.

[11] Behzadmehr, A., Galanis, N., and Laneville, A., 2002, "Laminar-Turbulent Transition for Low Reynolds Number Mixed Convection in a Uniformly Heated Vertical Tube," Int. J. Numer. Methods Heat Fluid Flow, **12**, pp. 839–854.

[12] Mahaney, H. V., Incropera, F. P., and Ramadhyani, S., 1987, "Development of Laminar Mixed Convection Flow in a Horizontal Rectangular Duct With Uniform Bottom Heating," Numer. Heat Transfer, **12**, pp. 137–155.

[13] Nazrul, I., Gatonde, U. N., and Sharma, G. K., 2001, "Mixed Convection Heat Transfer in the Entrance Region of Horizontal Annuli," Int. J. Heat Mass Transfer, **44**, pp. 2107–2120.

[14] Nguyen, C. T., and Galanis, N., 1986, "Combined Forced and Free Convection for the Developing Laminar Flow in Horizontal Tubes Under Uniform Heat Flux," Numerical Numerical Methods in Thermal Problems Conference, Montreal, Canada, 5, Part 1, pp. 414–425.

[15] Mare, T., Galanis, N., Pretot, S., and Miriel, J., 2005, "Mixed Convection With Flow Reversal in the Entrance Region of Inclined Tubes," Int. J. Numer. Methods Heat Fluid Flow, **15**, pp. 740–756.

[16] Lei, Q. M., and Trupp, A. C., 1991, "Experimental Study of Laminar Mixed Convection in the Entrance Region of a Horizontal Semicircular Duct," Int. J. Heat Mass Transfer, **34**(9) pp. 2361–2372.

[17] Busedra, A. A., and Soliman, H. M., 2000, "Experimental Investigation of Laminar Mixed Convection in an Inclined Semicircular Duct Under Buoyancy Assisted and Opposed Conditions," Int. J. Heat Mass Transfer, **43**, pp. 1103–1111.

[18] El. Hasadi, Y. M. F., 2006, "Numerical Prediction of Laminar Mixed Convection in the Entrance Region Horizontal Circular Sector Ducts," M.Sc. thesis, University of Garyounis, Benghazi, Libya.

[19] Patankar, S. V., and Spalding, D. B., 1972, "A Calculation Procedure for Heat, Mass and Momentum Transfer in Three-Dimensional Parabolic Flows," Int. J. Heat Mass Transfer, **15**, pp. 1787–1806.

[20] Prakash, C., and Liu, Ye-Di., 1985, "Analysis of Laminar Flow and Heat Transfer in the Entrance Region of an Internally Finned Circular Duct," ASME J. Heat Transfer, **107**, pp. 84–91.

[21] Pantakar, S. V., 1980, *Numerical Heat Transfer and Fluid Flow*, Mc Graw–Hill, New York.

[22] Lei, Q. M., and Trupp, A. C., 1989, "Maximum Velocity Location and Pressure Drop of Fully Developed Laminar Flow in Circular Sector Ducts," ASME J. Heat Transfer, **111**, pp. 1085–1087.

[23] Lei, Q. M., and Trupp, A. C., 1989, "Further Analyses of Laminar Flow Heat Transfer in Circular Sector Ducts," ASME J. Heat Transfer, **111**, pp. 1088–1090.

[24] Lei, Q. M., 1990, "Numerical and Experimental Study of Laminar Mixed Convection in a Horizontal Semicircular Duct," Ph.D. thesis, University of Manitoba, Winnipeg, Canada.

[25] Orfi, J., Galanis, N., and Nguyen, C. T., 1999, "Bifurcation in Steady Laminar Mixed Convection Flow in Uniformly Heated Inclined Tubes," Int. J. Numer. Methods Heat Fluid Flow, **9**, pp. 543–567.

[26] Maghan, J. R., and Incropera, F. P., 1987, "Experiments on Mixed Convection Heat Transfer for Airflow in a Horizontal and Inclined Channel," Int. J. Heat Mass Transfer, **30**, pp. 1307–1318.

Dual Solutions in Magnetohydrodynamic Mixed Convection Flow Near a Stagnation-Point on a Vertical Surface

A. Ishak

R. Nazar[1]
e-mail: rmn72my@yahoo.com

School of Mathematical Sciences,
Faculty of Science and Technology,
Universiti Kebangsaan Malaysia,
43600 UKM Bangi, Selangor, Malaysia

N. M. Arifin
Department of Mathematics,
Universiti Putra Malaysia,
43400 UPM Serdang, Selangor, Malaysia

I. Pop
Faculty of Mathematics,
University of Cluj,
R-3400 Cluj CP 253, Romania

The steady magnetohydrodynamic (MHD) mixed convection stagnation-point flow toward a vertical heated surface is investigated in this study. The external velocity impinges normal to the vertical surface and the surface temperature are assumed to vary linearly with the distance from the stagnation point. The governing partial differential equations are transformed into a system of ordinary differential equations, which is then solved numerically by a finite-difference method. The features of the flow and heat transfer characteristics for different values of the governing parameters are analyzed and discussed. Both assisting and opposing flows are considered. It is found that dual solutions also exist for the assisting flow, besides that usually reported in the literature for the opposing flow.
[DOI: 10.1115/1.2740645]

Keywords: magnetohydrodynamic, mixed convection, stagnation-point, dual solutions

1 Introduction

The existence of dual solutions in mixed convection over a horizontal plate was reported by Afzal and Hussain [1] when they reconsidered the problem posted by Schneider [2]. This discovery is in agreement with the statement mentioned in the "note added in proofs" by Schneider [2]. The lower branch solutions obtained by Afzal and Hussain [1] terminate at the points where the skin friction coefficient is zero. On the other hand, the complete lower branch solutions were reported by de Hoog et al. [3] for Prandtl number Pr=0.5, 1, and 2. de Hoog et al. [3] showed that the lower branch solutions terminate at a point where the buoyancy is zero. The same problem for a micropolar fluid was recently considered by Ishak et al. [4], and the results presented in that paper are in agreement with those obtained by de Hoog et al. [3], i.e., dual solutions exist in the opposing flow regime and the solutions terminate at a point where the buoyancy is zero.

The study of free (natural) convection, forced convection or the combination of both convections (mixed convection) has attracted many investigations until recently, see, e.g., Refs. [5–7]. Ramachandran et al. [8] studied the steady laminar mixed convection in two-dimensional stagnation flows around vertical surfaces by considering both cases of an arbitrary wall temperature and arbitrary surface heat flux variations. They found that a reverse flow develops in the buoyancy opposing flow region, and dual solutions are found to exist for a certain range of the buoyancy parameter. This work was then extended by Devi et al. [9] to the unsteady case and by Lok et al. [10] to a vertical surface immersed in a micropolar fluid. Dual solutions were found to exist by these authors for certain range of buoyancy parameter, when the buoyancy is opposing. The lower branch solutions terminate at various points and not attracted to a single point as mentioned earlier. Ingham [11] probably is the first to find dual solutions for the assisting flow case, and Ridha [12] for both the opposing and assisting cases. In his paper, Ridha [12] showed that dual solutions exist in the opposing flow regime and they continue into that of the assisting flow regime, i.e., when the buoyancy force acts in the same direction as the inertia force. Very recently, Merrill et al. [13] improved the results obtained by Nazar et al. [14] on the existence of dual solutions. They found that dual solutions exist for all values of the buoyancy parameter $\lambda > \lambda_c$, where λ_c is the value of λ for which the upper branch solution meets the lower branch solution.

In this paper, we investigate whether or not the dual solutions reported by Ramachandran et al. [8] exist also for the flow near the stagnation point on a vertical heated flat plate when there is a constant magnetic field applied normal to the plate. Both assisting and opposing flows are considered.

2 Basic Equations

Consider the steady, two-dimensional flow of a viscous and incompressible electrically conducting fluid near the stagnation-point on a vertical heated flat plate placed in the plane $y=0$ of a Cartesian coordinate system Oxy with the x-axis along the plate as shown in Fig. 1. It is assumed that the velocity of the flow external to the boundary layer $U(x)$ and the temperature $T_w(x)$ of the plate are proportional to the distance x from the stagnation point, i.e., $U(x)=ax$ and $T_w(x)=T_\infty+bx$, where a and b are constants. A uniform magnetic field of strength B_0 is assumed to be applied in the positive y-direction normal to the plate. The induced magnetic field is assumed to be small compared to the applied magnetic field, and is neglected. Under these assumptions along with the Boussinesq and boundary-layer approximations, the governing equations which model the boundary-layer flow are given by

$$\frac{\partial u}{\partial x}+\frac{\partial v}{\partial y}=0 \tag{1}$$

$$u\frac{\partial u}{\partial x}+v\frac{\partial u}{\partial y}=\nu\frac{\partial^2 u}{\partial y^2}-\frac{1}{\rho}\frac{dp}{dx}-\frac{\sigma B_0^2}{\rho}u\pm g\beta(T-T_\infty) \tag{2}$$

[1]Corresponding author.

Contributed by the Heat Transfer Division of ASME for publication in the JOURNAL OF HEAT TRANSFER. Manuscript received October 4, 2006; final manuscript received January 17, 2007. Review conducted by Louis C. Burmeister.

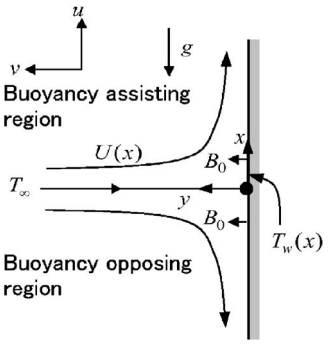

Fig. 1 Physical model and coordinate system

$$u\frac{\partial T}{\partial x}+v\frac{\partial T}{\partial y}=\alpha\frac{\partial^2 T}{\partial y^2} \tag{3}$$

subject to the boundary conditions

$$u=0,\ v=0,\ T=T_w(x) \quad \text{at } y=0$$

$$u\to U(x),\ T\to T_\infty \quad \text{as } y\to\infty \tag{4}$$

All symbols are defined in the Nomenclature. The last term on the right-hand side of Eq. (2) represents the influence of the thermal buoyancy force on the flow field, with "+" and "−" signs pertaining to the buoyancy assisting and the opposing flow regions, respectively. Figure 1 illustrates such a flow field for a vertical, heated surface with the upper half of the flow field being assisted and the lower half of the flow field being opposed by the buoyancy force. The reverse trend will occur if the plate is cooled below the ambient temperature.

By employing the generalized Bernoulli's equation, in free-stream, Eq. (2) becomes

$$U\frac{dU}{dx}=-\frac{1}{\rho}\frac{dp}{dx}-\frac{\sigma B_0^2}{\rho}U \tag{5}$$

Eliminating dp/dx in Eqs. (2) and (5) gives

$$u\frac{\partial u}{\partial x}+v\frac{\partial u}{\partial y}=\nu\frac{\partial^2 u}{\partial y^2}+U\frac{dU}{dx}+\frac{\sigma B_0^2}{\rho}(U-u)\pm g\beta(T-T_\infty) \tag{6}$$

We introduce now the following similarity variables:

$$\eta=\left(\frac{U}{\nu x}\right)^{1/2}y,\quad f(\eta)=\frac{\psi}{(U\nu x)^{1/2}},\quad \theta(\eta)=\frac{T-T_\infty}{T_w-T_\infty} \tag{7}$$

where ψ is the stream function defined as $u=\partial\psi/\partial y$ and $v=-\partial\psi/\partial x$ so as to identically satisfy Eq. (1). Substituting Eq. (7) into Eqs. (6) and (3), we get the following ordinary differential equations:

$$f'''+ff''+1-f'^2+M(1-f')+\lambda\theta=0 \tag{8}$$

$$\frac{1}{\mathrm{Pr}}\theta''+f\theta'-f'\theta=0 \tag{9}$$

where the primes denote differentiation with respect to η, $M=\sigma B_0^2/(\rho a)$ is the magnetic parameter, $\lambda=\pm\mathrm{Gr}_x/\mathrm{Re}_x^2$ [with "±" sign has the same meaning as in Eq. (2)] is the buoyancy or mixed convection parameter and $\mathrm{Pr}=\nu/\alpha$ is the Prandtl number. Further, $\mathrm{Gr}_x=g\beta(T_w-T_\infty)x^3/\nu^2$ and $\mathrm{Re}_x=Ux/\nu$ are, respectively, the local Grashof number and the local Reynolds number. We notice that λ is a constant, with $\lambda=\mathrm{Gr}_x/\mathrm{Re}_x^2>0$ and $\lambda=-\mathrm{Gr}_x/\mathrm{Re}_x^2<0$ correspond to the assisting flow and opposing flow, respectively, whereas $\lambda=0$ represents the case when the buoyancy force is absent (pure forced convection flow). The boundary conditions (4) now become

$$f(0)=0,\quad f'(0)=0,\quad \theta(0)=1$$

$$f'(\infty)\to 1,\quad \theta(\infty)\to 0 \tag{10}$$

It is worth mentioning that when $M=0$ (magnetic field is absent), Eqs. (8)–(10) reduce to those found by Ramachandran et al. [8] for the case of an arbitrary surface temperature with $n=1$ in their paper.

The physical quantities of interest are the skin friction coefficient C_f and the local Nusselt number Nu_x, which are defined by

$$C_f=\frac{\tau_w}{\rho U^2/2},\quad \mathrm{Nu}_x=\frac{xq_w}{k(T_w-T_\infty)} \tag{11}$$

where the skin friction τ_w and the heat transfer from the plate q_w are given by

$$\tau_w=\mu\left(\frac{\partial u}{\partial y}\right)_{y=0},\quad q_w=-k\left(\frac{\partial T}{\partial y}\right)_{y=0} \tag{12}$$

with μ and k being the dynamic viscosity and thermal conductivity, respectively. Using the similarity variables (7), we get

$$\tfrac{1}{2}C_f\,\mathrm{Re}_x^{1/2}=f''(0),\quad \mathrm{Nu}_x/\mathrm{Re}_x^{1/2}=-\theta'(0) \tag{13}$$

3 Results and Discussion

The system of equations (8)–(10) was solved numerically for some values of the buoyancy parameter λ and magnetic parameter M, whereas the Prandtl number Pr is fixed to be unity (Pr=1), except for comparisons with previously reported cases. The nonlinear ordinary differential equations were solved using the Keller-box method by integrating forwards in η until a predetermined large value of η is reached, η_∞ say, where we assume the infinity boundary condition may be enforced. The Keller-box method is very well described in the book by Cebeci and Bradshaw [15].

We notice that the results presented in this study are valid only in the small region near the stagnation line, and are not applicable outside the region. The values of the dimensionless skin friction coefficient $f''(0)$ and local Nusselt number $-\theta'(0)$ are obtained and compared with previously reported cases. This comparison is

Table 1 Values of $f''(0)$ for various values of Pr when $M=0$ (for upper branch solution)

	Ramachandran et al. [8]		Lok et al. [10]		Present results	
Pr	λ=−1	λ=1	λ=−1	λ=1	λ=−1	λ=1
0.7	0.6917	1.7063	0.691693	1.706376	0.6917	1.7063
7	0.9235	1.5179	0.923528	1.517952	0.9235	1.5179
20	1.0031	1.4485	1.003158	1.448520	1.0031	1.4485
40	1.0459	1.4101	1.045989	1.410094	1.0459	1.4101
60	1.0677	1.3903	1.067703	1.390311	1.0677	1.3903
80	1.0817	1.3774	1.081719	1.377429	1.0817	1.3774
100	1.0918	1.3680	1.091840	1.368070	1.0918	1.3680

Table 2 Values of $-\theta'(0)$ for various values of Pr when $M=0$ (for upper branch solution)

	Ramachandran et al. [8]		Lok et al. [10]		Present results	
Pr	$\lambda=-1$	$\lambda=1$	$\lambda=-1$	$\lambda=1$	$\lambda=-1$	$\lambda=1$
0.7	0.6332	0.7641	0.633269	0.764087	0.6332	0.7641
7	1.5403	1.7224	1.546374	1.722775	1.5403	1.7224
20	2.2683	2.4576	2.269380	2.458836	2.2683	2.4576
40	2.9054	3.1011	2.907781	3.103703	2.9054	3.1011
60	3.3527	3.5514	3.356338	3.555404	3.3527	3.5514
80	3.7089	3.9095	3.713824	3.914882	3.7089	3.9095
100	4.0097	4.2116	4.015974	4.218462	4.0097	4.2116

shown in Tables 1 and 2. It is seen that the present values of $f''(0)$ and $-\theta'(0)$ are in very good agreement with both results obtained by Ramachandran et al. [8] and Lok et al. [10]. Therefore, it can be concluded that the developed code can be used with great confidence to study the problem discussed in this paper.

The variations of the skin friction coefficient $f''(0)$ and the local Nusselt number $-\theta'(0)$ with buoyancy parameter λ for $M=0$ and $M=1$ are shown in Figs. 2 and 3, respectively, for Pr=1. Figures 2 and 3 show that it is possible to obtain dual solutions of the similarity equations (8)–(10) also for the assisting flow ($\lambda>0$), apart of those for the opposing flow ($\lambda<0$), that have been reported by Ramachandran et al. [8] and Lok et al. [10]. For $\lambda>0$, there is a favorable pressure gradient due to the buoyancy forces, which results in the flow being accelerated and consequently there is a larger skin friction coefficient than in the nonbuoyant case ($\lambda=0$). For negative values of λ, there is a critical value λ_c, with two branches of solutions for $\lambda>\lambda_c$, a saddle-node bifurcation at $\lambda=\lambda_c$ and no solutions for $\lambda<\lambda_c$. The boundary-layer separated from the surface at $\lambda=\lambda_c$, thus we are unable to get the solution for $\lambda<\lambda_c$ by using the boundary-layer approximations. To obtain the solutions beyond this value, the full Navier-Stokes equations have to be used. Based on our computations, we found that $\lambda_c=-2.364$ for $M=0$, and $\lambda_c=-3.850$ for $M=1$. This value of λ_c for $M=0$ is different from those reported by Lok et al. [10], as they were using Pr=0.7 in their paper. The boundary-layer separation occurs at $\lambda=\lambda_c$ where $f''(0)<0$, a different result from the classical boundary-layer theory where separation occurs when $f''(0)=0$. This observation is in agreement with both cases reported by Ramachandran et al. [8] and Lok et al. [10].

Further, it is seen from Fig. 2 that the upper branch solution has a higher value of $f''(0)$ for a given λ than the lower branch solution. For the assisting flow, dual solutions are found to exist for all positive values of λ considered, to much higher values than shown in Fig. 2. Figure 2 also shows that the critical value $|\lambda_c|$ increases as the magnetic parameter M is increased, suggesting that the magnetic field increases the range of existence of solutions to Eqs. (8)–(10), i.e., the boundary-layer separation can be delayed by introducing the effect of magnetic field. The results shown in Fig. 3 for the heat transfer rate at the surface, $-\theta'(0)$, suggest that for the lower branch solution, $-\theta'(0)$ becomes unbounded as $\lambda\to0^-$ and as $\lambda\to0^+$.

Figures 4 and 5 illustrate the samples of velocity and temperature profiles for the assisting flow, $\lambda=1$, whereas the corresponding opposing flow results, $\lambda=-1$, are shown in Figs. 6 and 7, all for Pr=1. In Figs. 6 and 7, the solid lines are for the upper branch solution and the dash lines for the lower branch solution, respec-

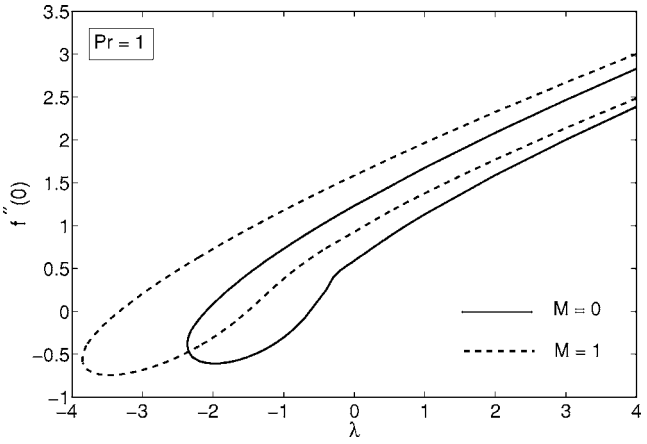

Fig. 2 Variation of the skin friction coefficient $f''(0)$ with λ for $M=0,1$ when Pr=1

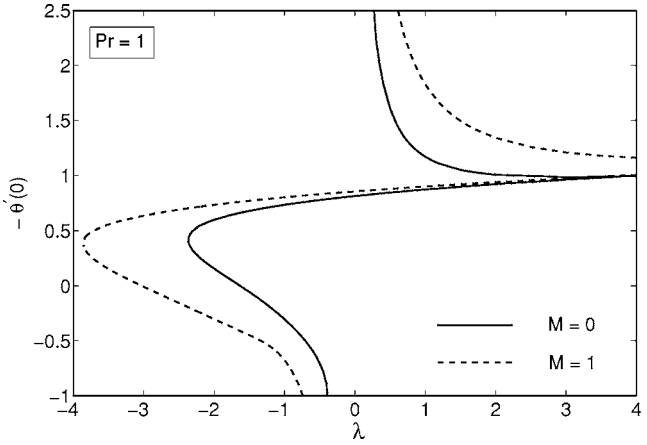

Fig. 3 Variation of the local Nusselt number $-\theta'(0)$ with λ for $M=0,1$ when Pr=1

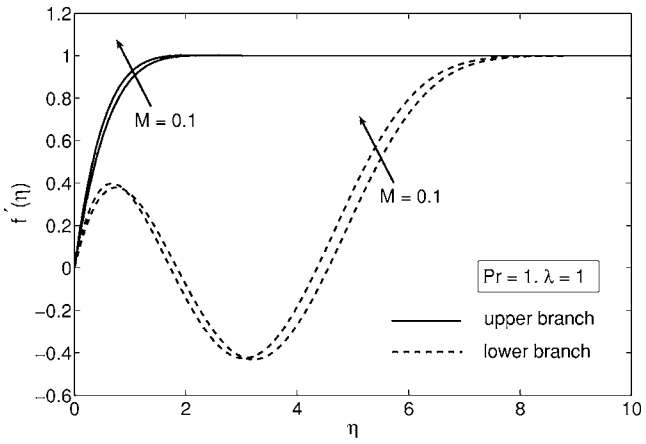

Fig. 4 Velocity profiles $f'(\eta)$ for $M=0,1$ when Pr=1 and $\lambda=1$ (assisting flow)

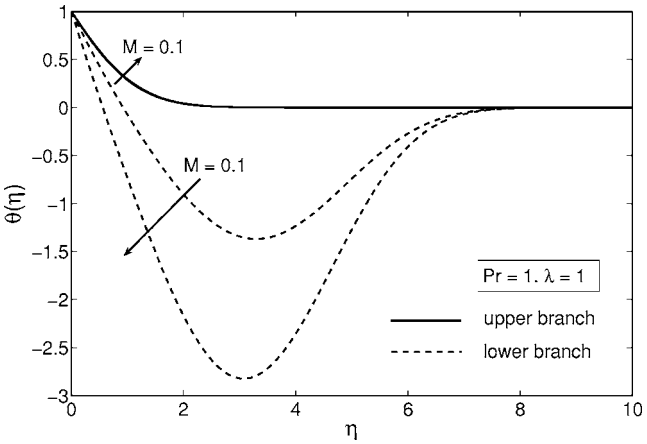

Fig. 5 Temperature profiles $\theta(\eta)$ for M=0,1 when Pr=1 and λ=1 (assisting flow)

tively. As seen in Figs. 4–7, there are dual solutions both when $\lambda=1$ and $\lambda=-1$. When $\lambda=1$, the velocity gradient at the wall is positive for the solutions on both branches (see Fig. 4), which is in agreement with the curves of $f''(0)$ shown in Fig. 2. For $\lambda=-1$ (see Fig. 6), the velocity profiles for the upper branch solution have a positive velocity gradient at the wall, while for the lower branch solution, the velocity gradient at the wall is positive when

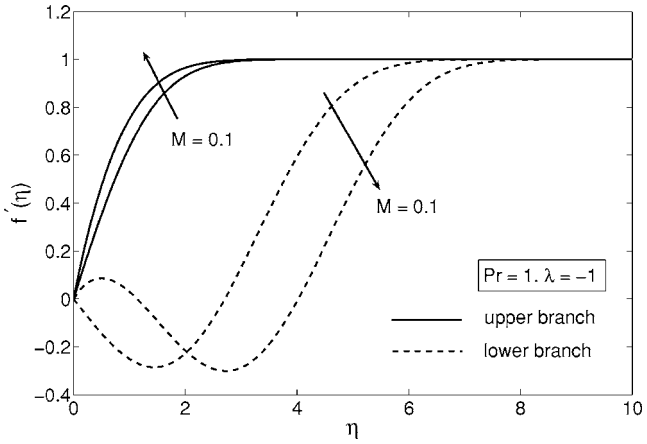

Fig. 6 Velocity profiles $f'(\eta)$ for M=0,1 when Pr=1 and λ=−1 (opposing flow)

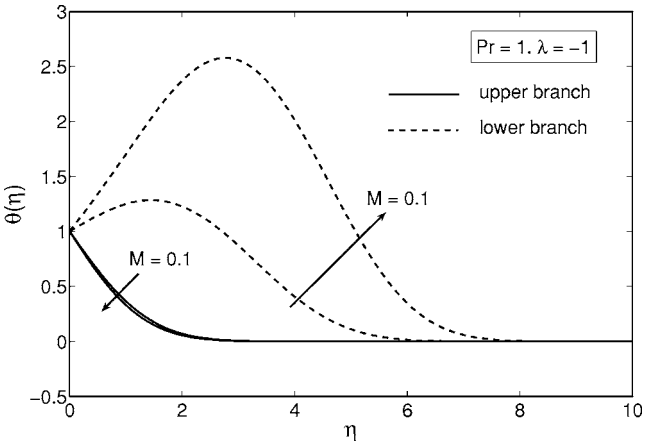

Fig. 7 Temperature profiles $\theta(\eta)$ for M=0,1 when Pr=1 and λ=−1 (opposing flow)

$M=1$ and negative when $M=0$. Again, this observation is in agreement with the curves shown in Fig. 2. Further, the solution on the lower branch for both cases $\lambda=\pm1$ has a region of reversed flow (has $f'(\eta)<0$) located away from the wall (η=0). In Fig. 5, we see that the temperature profiles are negatives for the lower branch solution, away from the wall (η=0). As discussed by Ridha [12], those solutions for which $\theta(\eta)<0$ for any η have no physical sense. This can be explained by using the definition of the dimensionless temperature $\theta(\eta)$ given in Eq. (7) that requires T must be less than the ambient temperature T_∞ to give $\theta(\eta)<0$, since $T_w>T_\infty$ (heated plate). This is in contradiction with the fact that the heat is transferred from the plate to the fluid, but the temperature of the fluid in the boundary layer is less than the ambient temperature T_∞. For the case of opposing flow, the lower branch temperature profiles as presented in Fig. 7 show there exists a region in the boundary layer where $\theta(\eta)>\theta(0)$ that seems to contradict the second law of thermodynamics. Thus, the lower branch solutions in this case also may be not physically acceptable.

Finally, Figs. 4–7 show that the boundary conditions (10) are satisfied, which support the validity of the present results, besides support the dual nature of the solution to the boundary-value problem (8)–(10).

4 Conclusions

We have studied the similarity solutions for the steady MHD mixed convection flow near the stagnation point on a vertical heated surface immersed in an incompressible viscous fluid. The governing nonlinear ordinary differential equations were solved numerically using the Keller-box method. We discussed the effects of the magnetic parameter M and the buoyancy parameter λ on the fluid flow and heat transfer characteristics. For convenience, we considered Prandtl number unity. A new feature to emerge from our results is the existence of a reversed flow region, in addition to a dual solution in the assisting flow regime ($\lambda>0$). Previous works for nonmagnetic effect [8] and for a micropolar fluid [10] had failed to notice that the lower branch solution could be continued into the assisting flow regime. We found that the lower branch solution of $f''(0)$ remains continuous, whereas $-\theta'(0)$ has a discontinuity at $\lambda=0$. In the assisting flow case, solutions could be obtained for all positive values of λ, while in the opposing case the solution terminated with a saddle-node bifurcation at $\lambda=\lambda_c$ ($\lambda_c<0$). The value of $|\lambda_c|$ increases with an increase in M, thus the magnetic parameter increases the range of similarity solutions, which in turn delays the boundary-layer separation.

Acknowledgment

The authors wish to express their very sincere thanks to the reviewers for their valuable time spent reading this paper and for their valuable comments and suggestions. This work is supported by a research grant (IRPA Project Code No 09-02-02-10038-EAR) from the Ministry of Science, Technology and Innovation (MOSTI), Malaysia.

Nomenclature

a, b = constants
B_0 = uniform magnetic field
C_f = skin friction coefficient
f = dimensionless stream function
Gr_x = local Grashof number
g = acceleration due to gravity
k = thermal conductivity
M = magnetic parameter
Nu_x = local Nusselt number
Pr = Prandtl number
p = fluid pressure

q_w = heat transfer from the plate
Re_x = local Reynolds number
T = fluid temperature
$T_w(x)$ = plate temperature
T_∞ = ambient temperature
$U(x)$ = velocity of the external flow
u, v = velocity components along the x and y directions, respectively
x, y = Cartesian coordinates along the plate and normal to it, respectively

Greek Symbols

α = thermal diffusivity
β = thermal expansion coefficient
η = similarity variable
θ = dimensionless temperature
λ = buoyancy or mixed convection parameter
μ = dynamic viscosity
ν = kinematic viscosity
ρ = fluid density
σ = electrical conductivity
τ_w = skin friction
ψ = stream function

Subscripts

w = condition at the plate surface
∞ = condition far from the plate

Superscript

$'$ = differentiation with respect to η

References

[1] Afzal, N., and Hussain, T., 1984, "Mixed Convection Over a Horizontal Plate," ASME J. Heat Transfer, **106**, pp. 240–241.

[2] Schneider, W., 1979, "A Similarity Solution for Combined Forced and Free Convection Flow Over a Horizontal Plate," Int. J. Heat Mass Transfer, **22**, pp. 1401–1406.

[3] de Hoog, F. R., Laminger, B., and Weiss, R., 1984, "A Numerical Study of Similarity Solutions for Combined Forced and Free Convection," Acta Mech., **51**, pp. 139–149.

[4] Ishak, A., Nazar, R., and Pop, I., 2006. "The Schneider Problem for a Micropolar Fluid," Fluid Dyn. Res., **38**, pp. 489–502.

[5] Saeid, N. H., 2006, "Natural Convection From Two Thermal Sources in a Vertical Porous Layer," ASME J. Heat Transfer, **128**, pp. 104–109.

[6] Roy, S., and Anilkumar, D., 2006, "Unsteady Mixed Convection From a Moving Vertical Slender Cylinder," ASME J. Heat Transfer, **128**, pp. 368–373.

[7] Ishak, A., Nazar, R., and Pop, I., 2007. "Mixed Convection on the Stagnation Point Flow Towards a Vertical, Continuously Stretching Sheet," ASME J. Heat Transfer (accepted for publication).

[8] Ramachandran, N. T. S., Chen, T. S., and Armaly, B. F., 1988, "Mixed Convection in Stagnation Flows Adjacent to Vertical Surfaces," ASME J. Heat Transfer, **110**, pp. 373–377.

[9] Devi, C. D. S., Takhar, H. S., and Nath, G., 1991, "Unsteady Mixed Convection Flow in Stagnation Region Adjacent to a Vertical Surface," Heat Mass Transfer, **26**, pp. 71–79.

[10] Lok, Y. Y., Amin, N., Campean, D., and Pop, I., 2005, "Steady Mixed Convection Flow of a Micropolar Fluid Near the Stagnation Point on a Vertical Surface," Int. J. Numer. Methods Heat Fluid Flow, **15**, pp. 654–670.

[11] Ingham, D. B., 1986, "Singular and Non-Unique Solutions of the Boundary-Layer Equations for the Flow Due to Free Convection Near a Continuously Moving Vertical Plate," ZAMP, **37**, pp. 559–572.

[12] Ridha, A., 1996, "Aiding Flows Non-Unique Similarity Solutions of Mixed-Convection Boundary-Layer Equations," ZAMP, **47**, pp. 341–352.

[13] Merrill, K., Beauchesne, M., Previte, J., Paullet, J., and Weidman, P., 2006, "Final Steady Flow Near a Stagnation Point on a Vertical Surface in a Porous Medium," Int. J. Heat Mass Transfer, **49**, pp. 4681–4686.

[14] Nazar, R., Amin, N., and Pop, I., 2004, "Unsteady Mixed Convection Boundary Layer Flow Near the Stagnation Point on a Vertical Surface in a Porous Medium," Int. J. Heat Mass Transfer, **47**, pp. 2681–2688.

[15] Cebeci, T., and Bradshaw, P., 1988, *Physical and Computational Aspects of Convective Heat Transfer*, Springer, New York.

Convective Heat Transfer in Open Cell Metal Foams

Ken I. Salas[1]

Anthony M. Waas[2]

Department of Aerospace Engineering,
The University of Michigan,
Ann Arbor, MI 48109

Convective heat transfer in aluminum metal foam sandwich panels is investigated with potential applications to actively cooled thermal protection systems in hypersonic and re-entry vehicles. The size effects of the metal foam core are experimentally investigated and the effects of foam thickness on convective transfer are established. Four metal foam specimens are utilized with a relative density of 0.08 and pore density of 20 pores per inch (ppi) in a range of thickness from 6.4 mm to 25.4 mm*, in increments of approximately* 6 mm*. An exact-shape-function finite element model is developed that envisions the foam as randomly oriented cylinders in cross flow with an axially varying coolant temperature field. A fully developed velocity profile is obtained through a semi-empirical, volume-averaged form of the momentum equation for flow through porous media, and used in the numerical analysis. The experimental results show that larger foam thicknesses produce increased heat transfer levels, but that this effect diminishes for thicker foams. The finite element simulations capture the thickness dependence of the heat transfer process and good agreement between experimental and numerical results is obtained for larger foam thicknesses.* [DOI: 10.1115/1.2739598]

Keywords: convective heat transfer, metal foams, active cooling, experimental, finite elements

1 Introduction

Metal foam sandwich panels have been proposed as alternative multifunctional materials for structural thermal protection systems in hypersonic and re-entry vehicles [1]. This type of construction offers numerous advantages over other actively cooled concepts because of the unique properties of metal foams. These materials, when brazed between metallic face sheets, are readily suited to allow coolant passage without the addition of alien components that may compromise structural performance. Moreover, the mechanical properties can be varied to suit different structural needs by varying the foam relative density. From a heat transfer point of view, these materials have been shown to be exceptional heat exchangers primarily due to the increased surface area available for heat transfer between the solid and fluid phases, and the turbulence created in the flow by the presence of the metal foam.

The thermo-mechanical response of metal foam sandwich panels has been recently studied and characterized [1]. In particular, it has been shown that using air as coolant at sufficiently high velocities, the strain due to buckling of these structures under thermo-mechanical loads can be virtually eliminated. The implementation of these materials in thermal protection systems, however, requires that a proper heat transfer model exists that allows the coupling between the thermo-mechanical and heat transfer problems to be properly analyzed. In other words, it is necessary to understand how different foam properties such as relative density, pore density, and foam thickness will affect the heat loads that this type of structural component can remove.

The improvements produced by the presence of porous media on heat exchanger systems has been the topic of extensive research over the years. Lagé et al. [2–4] studied the effect of placing a porous aluminum material inside a phased-array radar slat in the forced convection properties of this system. It was shown that this material greatly improved the heat transfer process by decreasing the temperature difference between the two sides of the slat by as much as 700%. Mohamad et al. [5–8] have studied the heat transfer enhancements produced by porous media on heat exchanger systems. In particular, they carried out experiments using metallic porous inserts on heated pipes. Their results suggested that the presence of the porous material produced higher heat transfer levels for an acceptable increase in the pressure drop through the pipe; moreover, it was shown that larger porosities produced better heat transfer performance. Boomsma and Paulikakos [9–11] performed experiments using aluminum foams and water as the cooling medium; their study focused on a comparing the performance of metal foams to other commercially available heat exchangers. It was reported that, using these materials instead of other available options, the thermal resistance of the system could be reduced by nearly a factor of two for the same amount of pumping power. Lu et al. [12] developed an analytical model envisioning the foam as an array of mutually perpendicular cylinders subjected to cross-flow. In their study, a closed-form expression for the convective coefficient of a foam-filled channel with constant wall temperatures was presented, based on foam geometry and material and fluid properties. These authors reported that the simplifying assumptions used in their analysis were likely to lead to an overprediction of the actual heat transfer level. This model has been partially validated by Bastawros and Evans [13] who performed forced convection experiments on aluminum foams adhered to silicon substrate face sheets. These authors reported that the predictions of [12] regarding the dependence of the convective coefficient on coolant velocity and strut diameter were qualitatively consistent with their observations, but that the foam thickness effects were not adequately modeled. In particular, they reported that, for a fixed value of the free stream air velocity, the heat dissipation rate and convective coefficient decreased with increasing foam thickness. Moreover, they introduced an empirical modification to this model based on a tetrakaidecahedral unit cell and their experimental results. These modifications, however, did not completely solve the qualitative limitations of the model.

Calmidi and Mahajan [14] also carried out experimental studies on forced convection in aluminum metal foams, using air as the cooling medium. Their study focused on porosity and pore density in an effort to quantify thermal dispersion and thermal nonequi-

[1]E-mail: ksalas@umich.edu
[2]Corresponding author. e-mail: dcw@umich.edu

Contributed by the Heat Transfer Division of ASME for publication in the JOURNAL OF HEAT TRANSFER. Manuscript received March 26, 2006; final manuscript received December 8, 2006. Review conducted by Jose L. Lage. Paper presented at the Joint AIAA/ASME/ASCE SDM Conference, Newport, RI, USA, May 1–5, 2006.

librium effects in metal foams. In their numerical analysis, they used a semi-empirical form of the momentum equation governing the flow of fluid through porous media to obtain the velocity profile in the foam-filled channel. This profile was then used in solving a volume-averaged form of the energy equation, which yielded models for the foam thermal dispersion conductivity and interstitial heat transfer coefficient. They showed that for air as the cooling medium, thermal dispersion effects were very low. Their results reportedly agree favorably with their experimental data and those published in the open literature.

The literature review performed by the present authors did not yield a definite model that properly includes the effects of foam thickness on the convective heat transfer of metal foams. As a result, the objective of this study is to experimentally investigate these size effects, and to numerically model them using a finite element approach. Four different foam thicknesses are investigated to determine the dimensions at which size effects disappear and metal foams can be considered as a continuum for heat transfer. In the analysis, the metal foam is envisioned as an array of cylinders in cross-flow but a highly ordered structure is not assumed, as has been previously done. The velocity profile inside the foam-filled duct is calculated using the approach of Refs. [14,15] along with the permeability and inertial coefficient determined experimentally. The governing equation for cylinders in cross-flow is then used to derive a weak form that yields the necessary element effective conductivity matrix and heat flux vector. These results are later used to calculate the temperature distribution on the surfaces of the sandwich panel.

2 Experimental Procedures

Four metal foam sandwich panels were used to experimentally study the effect of foam thickness on the convective heat transfer coefficient of aluminum metal foams. The sandwich construction consists of a metal foam core brazed to two aluminum face sheets. The face sheets are constructed of aluminum T6061-T6, whereas the metal foam core alloy is T6101-T6. The panels used belong to the Duocel family of metal foams manufactured by ERG Materials and Aerospace Corporation. The set of specimens used consisted of four different foam thicknesses ranging from 6.4 mm to 25.4 mm in increments of 6.4 mm. In addition, the ratio of foam thickness to face sheet thickness was maintained constant, at approximately 6:1, to ensure that thermal resistance effects were similar in all cases. The length and width of each specimen were kept constant at 203.5 mm and 51.0 mm, respectively. In order to properly isolate the thickness effects, the foam relative density and pore density were maintained constant at 0.08 and 20 pores per inch (ppi), respectively (values provided by manufacturer). A schematic of a typical specimen is shown in Fig. 1.

Each specimen was placed inside a custom-built Plexiglas case which provided insulation from the ambient conditions, as well as a means to prevent airflow bypass. Low conductivity styrofoam ($k=0.037$ W/m K) was placed on the sides of the case to prevent and measure existing heat losses. The top of each specimen was insulated using insulating melamine foam. A sample insulated specimen is shown in Fig. 2. The specimens were heated on the top side using four patch heaters (Minco Inc, HK913P), as shown in Fig. 3. The upper side was heated so as to obtain a stable temperature gradient [16]. The lower side of the panel was insulated using a Plexiglas sheet. The heat entering each panel was controlled by specifying the voltage supplied to the heaters using an adjustable Variac, which allowed only a fraction of the available voltage to be used, and measured through Ohm's law. Temperature measurements were taken at three axial locations on both the top and bottom face sheets using type K thermocouples (Omega Engineering, 5SC-TT-K-36-36), which were then connected to a data acquisition system for recording.

Forced convection was achieved by running air at different velocities through the metal foam. The flow rate was measured using

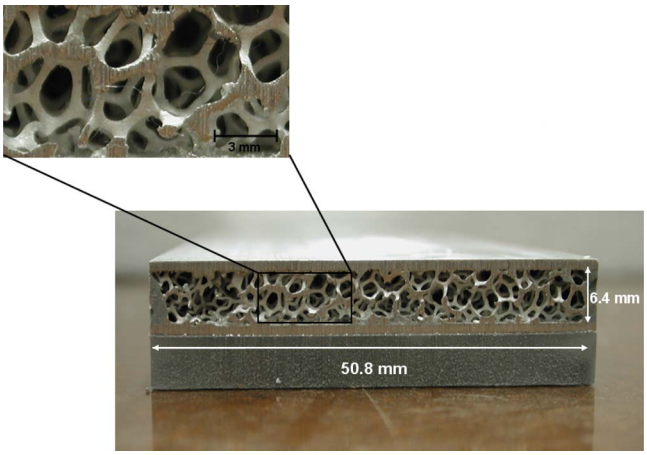

Fig. 1 Geometry of a sample metal foam sandwich panel used in the present study. The specimen shown has a foam thickness of 6.4 mm and a face sheet thickness of approximately 1.1 mm.

an in-line pneumatic flow meter (Omega Engineering, FL6711A), and the average air velocity was then calculated using this value and the foam cross-sectional area. A schematic of the overall experimental set up is shown in Fig. 4. For each specimen a range of velocities between 0 m/s and 10 m/s was covered, while in some cases the velocity was increased until 19 m/s. The temperature and pressure of the air entering and exiting the foam core were also measured. A typical experimental run started with the application of a heat flux on the upper surface of the sandwich panel using the heaters. The voltage supplied to the heaters was kept constant by using only 20% of the available 110 V; this resulted in a constant heat flux setting of 730 W/m^2 for all the experimental cases run. The temperature of the heated surface was monitored at one sample per second, and when its value reached approximately 50°C active cooling was started by running high-pressure air through the metal foam core; the particular velocity under examination was set through the volumetric flow rate, which was measured downstream of the sandwich panel. Each experiment lasted until all temperatures reached steady-state conditions.

The uncertainty in the air velocity was determined based on the uncertainty of the volumetric flow rate and the uncertainty in the cross-sectional area measurement. The resolution of the flow

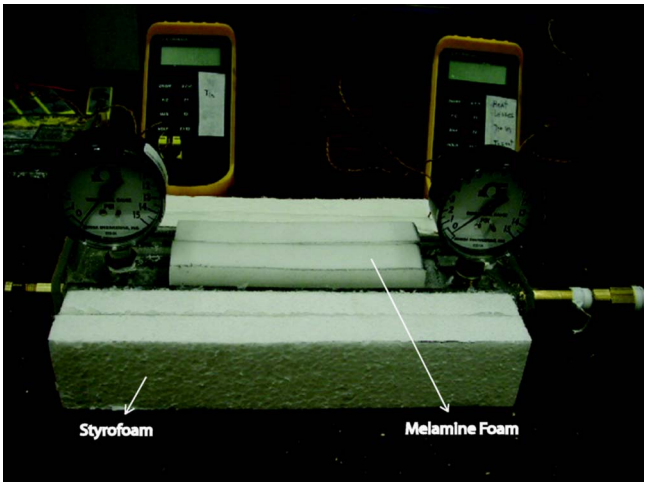

Fig. 2 Detail of fully insulated metal foam sandwich panel specimen

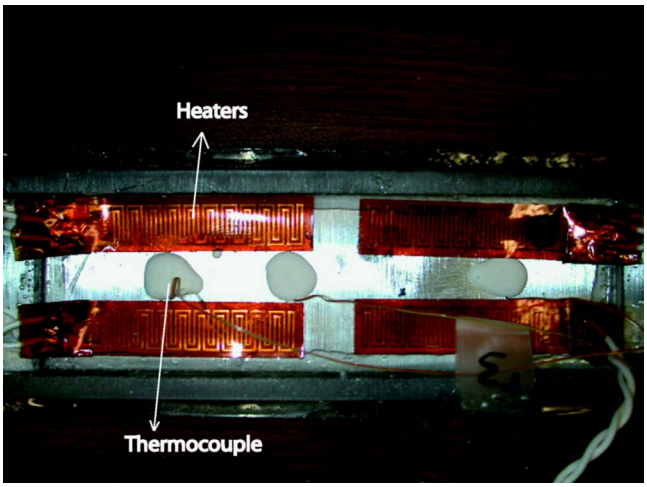

Fig. 3 Detail of heated surface in metal foam sandwich panel specimen. Each heater has dimensions of 76 mm long by 15 mm wide.

meter was 5 scfm, while the resolution in length measurement was 0.1 mm. These values result in an air velocity uncertainty estimate of 13%. The uncertainty in the experimental values measured are reported through error bars, which represent the standard deviation of the specific parameter under consideration. The heat losses through the sides were calculated using the temperature reading from two thermocouples embedded in the insulating styrofoam, along with this material's thermal conductivity and thickness. This procedure has been shown to accurately represent the lateral heat losses in this type of experimental arrangement [15].

The average convective coefficient, $\bar{h}$, was calculated using the average temperature of the heated surface, the temperature of the incoming air, and the geometry of the foam through

$$\bar{h} = \frac{Q}{LW\Delta T} \tag{1}$$

The heat entering the sandwich panel and the temperature difference, defined in Eq. (2), are based on the resistance summary of these data see Table 1) as well as the losses through the sides. The term k_s represents the thermal conductivity of the styrofoam; A_l the lateral foam area; b the thickness of the styrofoam; and ΔT_{loss} is the difference in the readings of the thermocouples embedded in the insulation.

Table 1 Resistance of heaters used in experiments

Heater number	Resistance (Ω)
1	64.7
2	65.5
3	63.0
4	64.1

$$\Delta T = \frac{1}{3}\left(\sum_{n=1}^{3} T_n\right) - T_\infty \tag{2a}$$

$$Q = V^2 \sum_{i=1}^{4} \frac{1}{R_i} - k_s A_l \left(\frac{\Delta T_{\text{loss}}}{b}\right) \tag{2b}$$

3 Experimental Results

Figures 5 and 6 show, respectively, a typical set of experimental results for the temperature distribution of the heated and unheated sides of the sandwich panel as a function of time. The temperature of both surfaces increases with axial position indicating that the cooling fluid does not reach a constant temperature shortly after entering the foam duct. The effect of thickness on the temperature difference between top and bottom surfaces is illustrated in Fig. 7. In this figure, as well as in all subsequent figures showing experimental results, average values are reported and the corresponding standard deviations are represented through error bars. Clearly, as the foam thickness is increased, the difference between both surfaces increases. This trend indicates that heat transfer increases with increasing thickness, as a lower temperature implies that more heat has been carried away by the cooling fluid; this has its physical basis on the fact that an increased metallic surface area is available for heat transfer. This result is also consistent with the convective coefficient trends presented below for the same reasons. It is important to mention that the temperature difference decreases with increasing air velocity due to the constant heat flux boundary condition. If a constant temperature were prescribed at the heated surface, we would observe an increase in the temperature difference with increasing air velocity.

The experimental results obtained for the convective heat transfer coefficient are summarized in Fig. 8. The results show that increasing the average velocity of the cooling fluid increases the convective coefficient. As the fluid velocity increases, and assuming that it is far downstream so that the velocity profile is fully

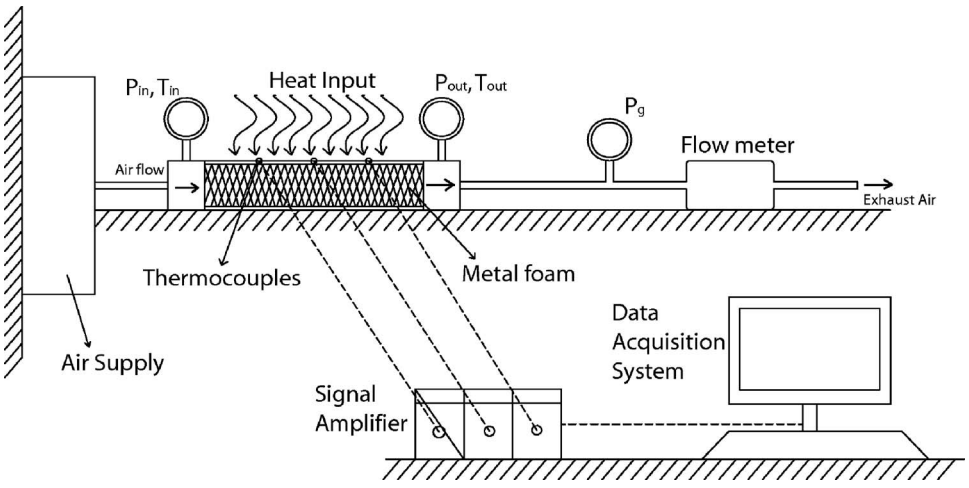

Fig. 4 Diagram of experimental setup

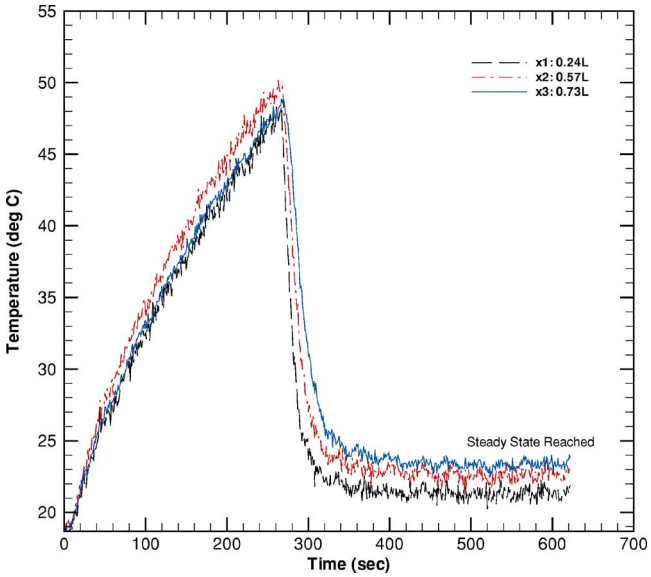

Fig. 5 Sample thermocouple readings for heated side. The air velocity is 12.1 m/s, the foam thickness is 12.7 mm, and the voltage setting is 22 V resulting in a heat flux of 730 W/m^2.

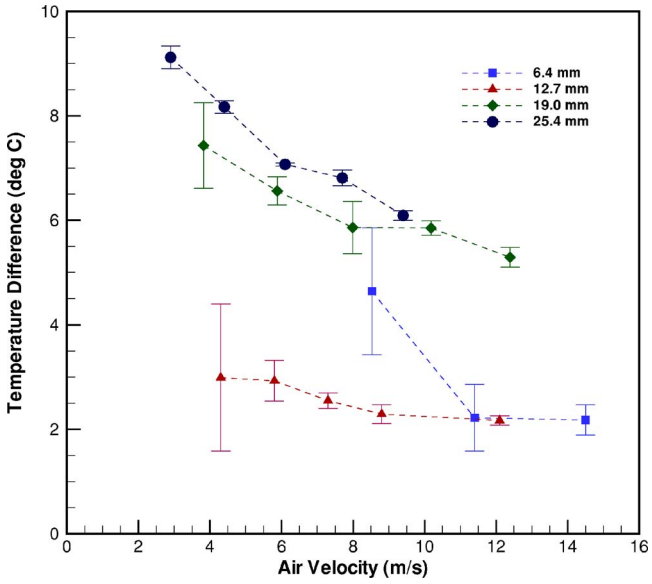

Fig. 7 Effect of thickness on temperature difference across metal foam. The voltage setting was kept constant in all cases at 22 V resulting in a heat flux of 730 W/m^2.

developed, a larger velocity leads to a larger rate of interaction between the fluid and the solid struts in the metal foam. This leads to better heat transfer and therefore a higher heat transfer coefficient, as shown in Fig. 8. Nevertheless, this trend is not without bound since the proximity of the metal struts limits the interaction, and dictates the velocity at which the trend seems to level off. Furthermore, it is possible that the increased convective coefficient observed for higher flow velocities is due to thermal boundary layer development. For a fully developed thermal boundary layer, the convective coefficient would not be as sensitive to the flow velocity. However, this process usually requires a larger entrance length, and since the specimens used in this study were relatively short, it is possible that it was never completed for the range of velocities studied.

The effect of foam thickness is also evident from the figure: an increased convective coefficient is observed for larger foam thicknesses. This trend, although relatively weak, is expected, because a greater foam thickness implies a larger amount of effective surface area available for heat transfer. The trends observed in these results are inconsistent with those presented in Ref. [13] where the convective coefficient reached a maximum value at approximately 2 m/s and steadily decreased thereafter, and where this coefficient was observed to decrease with increasing foam thickness. A nondimensional form of these results is presented in Fig. 9. Since the average convective coefficient for the sandwich panel is obtained, the Nusselt number, Nu, was defined based on the foam thickness and thermal conductivity of air at 20°C through

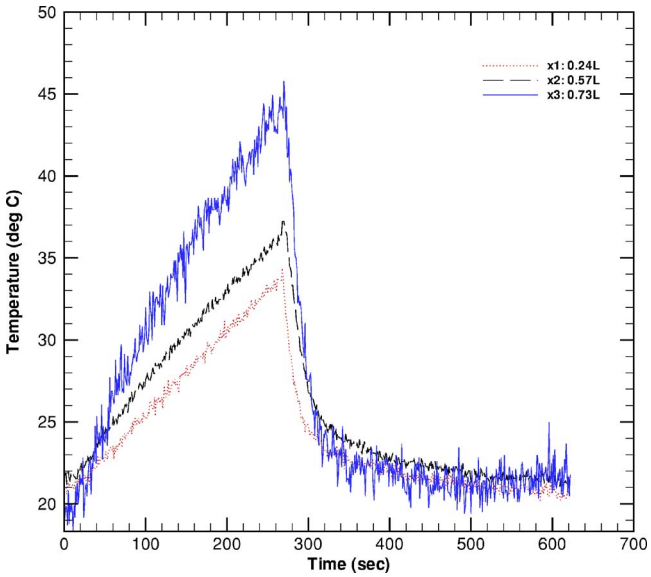

Fig. 6 Sample thermocouple readings for insulated side. The air velocity is 12.1 m/s, the foam thickness is 12.7 mm, and the voltage setting is 22 V, resulting in a heat flux of 730 W/m^2.

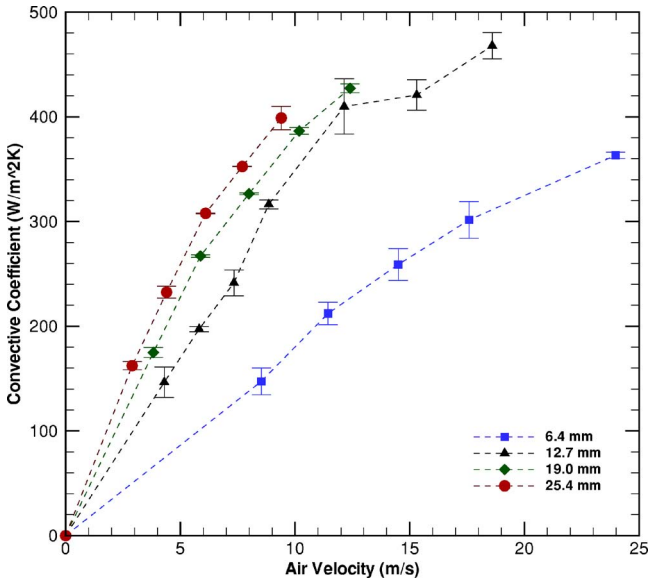

Fig. 8 Dependence of average convection coefficient of metal foam on foam thickness. The voltage setting was kept constant in all cases at 22 V resulting in a heat flux of 730 W/m^2.

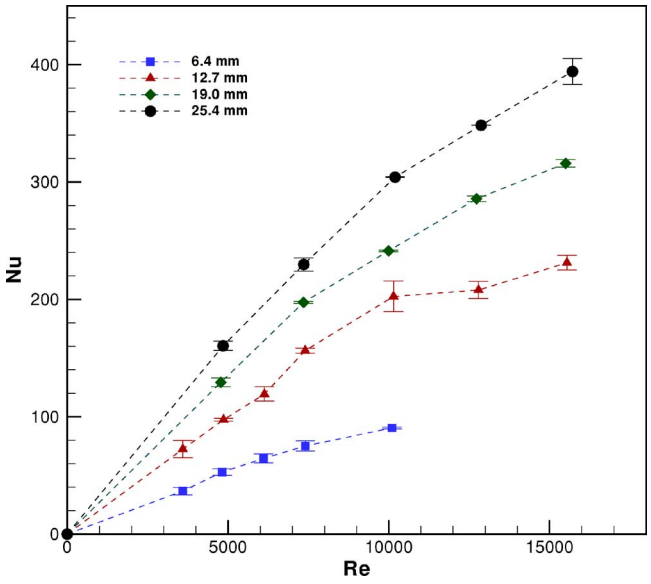

Fig. 9 Nondimensional average convection coefficient of metal foam. Re and Nu calculated based on foam thickness. The voltage setting was kept constant in all cases at 22 V resulting in a heat flux of 730 W/m^2.

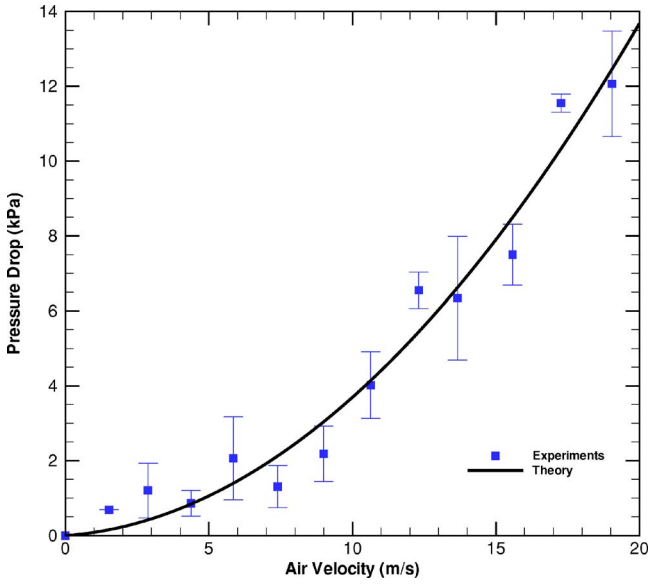

Fig. 11 Pressure drop across 12.7-mm-thick metal foam core

$$\mathrm{Nu} = \frac{\bar{h}t}{k_{\mathrm{air}}} \tag{3}$$

The properties of air at 20°C were chosen since this is a representative value of the inlet air temperature observed in the experiments. Furthermore, the range of inlet temperatures covered spanned 4°C, and air properties do not show appreciable differences in this small range. Similarly, the Reynolds number, Re, was calculated based on the foam thickness and air density and dynamic viscosity at the same air temperature as before through

$$\mathrm{Re} = \frac{\rho u t}{\mu} \tag{4}$$

The experimental results obtained for the pressure drop across the sandwich panels are shown in Figs. 10–12. It is important to note from the experimental results that the foam thickness effect becomes less pronounced as the thickness is increased. Furthermore, the results seem to indicate that for sandwich panels with thicker foams this effect will be negligible; this conclusion is based on the fact that the convective coefficient curves lie closer and closer together for larger foam thicknesses. The nondimensional version of the results also support this trend, albeit in a weaker form. This observation has important implications for engineering applications of these materials, in particular for the case of multifunctional structures as the one considered in this paper. If used as part of a thermal protection system for hypersonic and re-entry vehicles, metal foam sandwich panels would need to carry mechanical loads, while at the same time protecting the inner components of the vehicle from the high temperatures resulting from aerodynamic heating, through convection with a cooling fluid. It is then important to know that the convective coefficient has an upper bound which is achieved for a certain foam thickness. This would therefore allow a designer more flex-

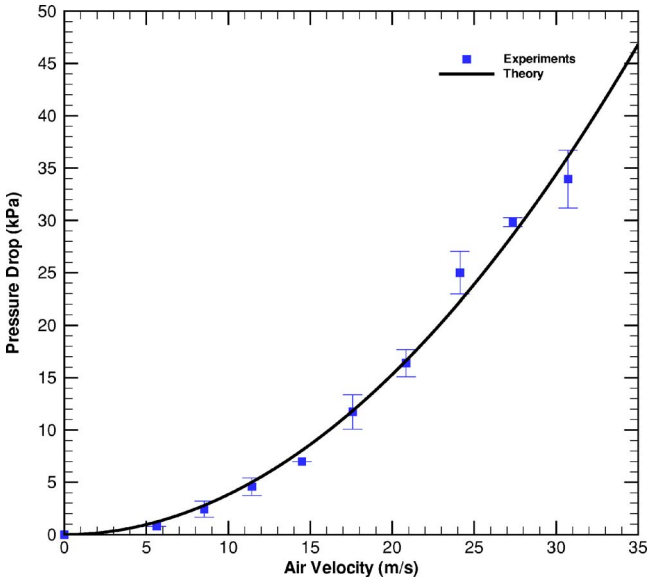

Fig. 10 Pressure drop across 6.4-mm-thick metal foam core

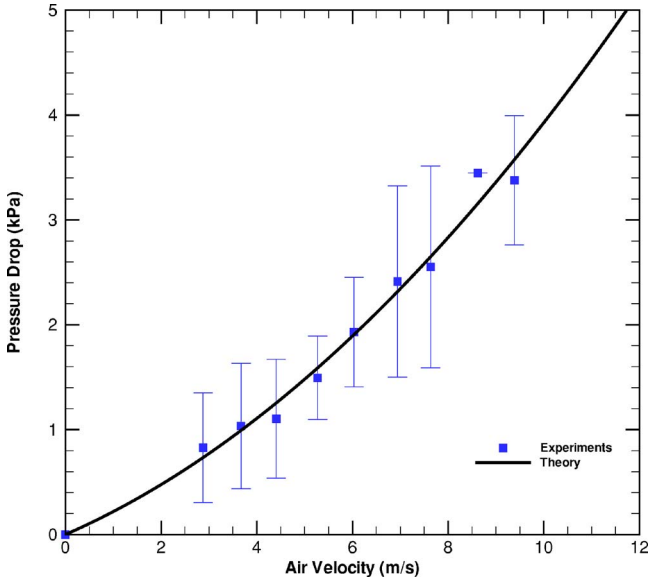

Fig. 12 Pressure drop across 25.4-mm-thick metal foam core

ibility in choosing the foam parameters based on structural or other suitable considerations. In conclusion, while the foam thickness at which size effects disappear has not been identified, it has been experimentally shown that this effect weakens for thicker foams.

4 Numerical Model

In this section, the governing differential equation for a cylinder in cross-flow is used to derive a weak form that allows a solution to the convective heat transfer problem using a finite element approach. This description is more suited to metal foams as its constituent struts can be easily envisioned as individual components, that is, the method will not lead to the discretization of a continuous structure, as in the case of a beam or a plate, but will instead embrace the nature of metal foams in their description. Additional advantages of this approach include:

- easy calculation of properties using cylinders of different orientations as all calculations take place in the local coordinate system;
- networks of cylinders with different geometries (lengths and diameter) can be easily modeled;
- cylinders with different material properties can be employed, thereby describing functionally graded foams; and
- the discretization of the medium allows the introduction of an axially varying temperature field for the coolant phase.

4.1 Derivation of Element Matrices. The convective heat transfer model proposed in this study envisages the metallic foam as an array of randomly oriented cylinders subjected to cross-flow. To develop the temperature distribution of such a cylinder, a standard fin analysis is used regarding the heat flux as a negative source that is proportional to the cylinder's geometry and convective coefficient. For a cylinder with diameter d, thermal conductivity k_{pm}, and local convective coefficient h, subjected to cross-flow of a coolant with temperature T_∞, the governing energy equation has the form

$$k_{pm}\frac{d^2T}{dz'^2} - \frac{4h}{d}(T - T_\infty) = 0 \tag{5}$$

Equation (5) is used to derive a weak form that will allow the determination of the corresponding element effective conductivity matrix and heat flux vector. To find this weak form, Eq. (5) is multiplied by a small temperature variation δT and integrated over the length, l, of one cylinder

$$\int_0^l \left(k_{pm}\frac{d^2T}{dz'^2}\delta T - \frac{4h}{d}T\delta T\right)dz' = -\int_0^l \frac{4h}{d}T_\infty \delta T\, dz' \tag{6}$$

Using integration by parts on the first term of the left hand side, the following is obtained

$$-\frac{1}{2}\int_0^l \left[k_{pm}\left(\frac{dT}{dz'}\right)^2 - \frac{4h}{d}T^2\right]dz' + \frac{1}{2}\int_0^l \frac{4h}{d}T_\infty T dz' = \text{constant} \tag{7}$$

The description of the problem using a finite element approach considers each cylinder as a one-dimensional finite element. As a result, the temperature distribution is expressed in terms of two interpolating functions, N_1 and N_2, as well as the temperature at each end of the cylinder, T_1 and T_2. These temperatures correspond to the degrees of freedom since the cylinder ends are considered as the element's nodes. In this way, the temperature distribution inside the element is expressed as

$$T(z') = [N_1(z')N_2(z')]\begin{Bmatrix} T_1 \\ T_2 \end{Bmatrix} = \mathbf{NT} \tag{8}$$

Defining $\mathbf{T}$ as the vector of temperature degrees of freedom and $\mathbf{N}$ as the shape function vector, Eq. (7) takes the form

$$\int_0^l \left(k_{pm}\mathbf{T^T N'^T N' T} + \frac{4h}{d}\mathbf{T^T N^T N T} - \frac{4h}{d}\mathbf{T^T N^T}\right)dz' = 0 \tag{9}$$

It is important to note that the first term in Eq. (9) contains the temperature derivatives which are expressed in terms of the shape function derivatives ($\mathbf{N'}$) as

$$\frac{dT}{dz'} = \begin{bmatrix} \frac{dN_1}{dz'} & \frac{dN_2}{dz'} \end{bmatrix}\begin{Bmatrix} T_1 \\ T_2 \end{Bmatrix} = \mathbf{N'T} \tag{10}$$

One clear advantage of using a finite element approach is now introduced. The interpolation functions N_1 and N_2 are defined as the solution to the homogenous form of the governing equation thereby becoming "exact" shape functions. As a result, we have

$$N_1 = \frac{\exp(-\sqrt{\Psi}z') - \exp(-2\sqrt{\Psi}l)\exp(\sqrt{\Psi}z')}{1 - \exp(-2\sqrt{\Psi}l)} \tag{11}$$

$$N_2 = \frac{\exp(-\sqrt{\Psi}l)\exp(\sqrt{\Psi}z') - \exp(-\sqrt{\Psi}l)\exp(-\sqrt{\Psi}z')}{1 - \exp(-2\sqrt{\Psi}l)} \tag{12}$$

The parameter Ψ is defined for simplicity as

$$\Psi = \frac{4h}{k_{pm}d} \tag{13}$$

The solution to the problem follows from Eq. (9) as

$$\mathbf{KT - P = 0} \tag{14}$$

In Eq. (14), $\mathbf{K}$ represents the element effective conductivity matrix which contains both conduction and convection contributions; and $\mathbf{P}$ corresponds to the element heat flux vector. Note that in order to have a simpler solution every term in Eq. (9) has been normalized by the thermal conductivity, k_{pm}, which results in the units of $\mathbf{K}$ and $\mathbf{P}$ becoming $[\text{length}]^{-1}$ and $[\text{temperature}]\times[\text{length}]^{-1}$, respectively. The components of these terms follow from substitution of Eqs. (11) and (12) into Eq. (9) and can be expressed as

$$K_{11} = K_{22} = \frac{[\exp(2\sqrt{\Psi}l) + 1]\sqrt{\Psi}}{\exp(2\sqrt{\Psi}l) - 1} \tag{15a}$$

$$K_{12} = K_{21} = \frac{-2\sqrt{\Psi}\exp(\sqrt{\Psi}l)}{\exp(2\sqrt{\Psi}l) - 1} \tag{15b}$$

$$P_{11} = P_{21} = \frac{\sqrt{\Psi}T_\infty[\exp(\sqrt{\Psi}l) - 1]}{\exp(\sqrt{\Psi}l) + 1} \tag{15c}$$

The calculation of the heat removed by each element is easily carried out as [17]

$$q_e = h_e(T^e_{\text{av}} - T_\infty)A_{sf} \tag{16}$$

In Eq. (16), the term h_e is the convective coefficient associated with each element, A_{sf} is the surface area through which heat transfer takes place, and the average temperature of each cylinder is defined as

$$T^e_{\text{av}} = \frac{1}{l}\int_0^l (T_1N_1 + T_2N_2)dz' \tag{17}$$

This matrix and heat flux vector are used to assemble the global effective conductivity matrix, $\mathbf{K_g}$, and global heat flux vector, $\mathbf{P_g}$, which are used to obtain the temperature distribution through the thickness of the foam. This assembly is carried out following a standard procedure from finite element analysis, starting the element numbering on the heated surface. In order to obtain a unique solution, boundary conditions consistent with those applied experimentally must be used in the numerical simulations. The heat flux boundary condition is specified by setting the first entry of the

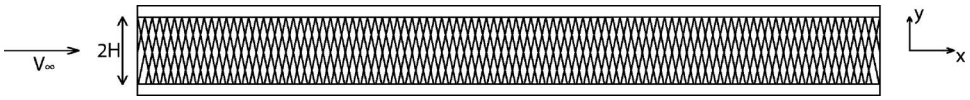

Fig. 13 Geometry of metal foam sandwich panel used in nondimesionalization of momentum equation

vector $\mathbf{P_g}$ equal to the heat flux used experimentally divided by the thermal conductivity, or by setting the last entry of this vector equal to zero if the insulated condition is used instead. These positions are based on the fact that the element numbering begins at the upper facesheet which corresponds to the heated surface. Since the metal foam is modeled using randomly oriented cylinders, the heat flux boundary conditions are applied only at the corresponding cylinder nodes and not in the spaces between them since these do not form part of the discretization domain. The second condition to be enforced is necessarily a temperature condition so that a unique solution is obtained. This condition is applied using the elimination approach from standard finite element analysis. This procedure, therefore, eliminates the rows and columns of the effective conductivity matrix where the temperature degrees of freedom are known. The temperature values are then determined by matrix multiplication of the inverse reduced effective conductivity matrix and the heat flux vector.

The finite element result for the average heat transfer coefficient, $\bar{h}$, is calculated using an equation similar to Eq. (1). The fundamental difference is that the value of Q is replaced with the total heat removed by the cooling fluid. This value is determined by summing the heat removed from each cylinder using Eq. (16), and then summing over all the elements. This may be stated as

$$Q_{\text{fluid}} = \sum_{i=1}^{n} q_e^{(i)} \tag{18}$$

so that the average convective coefficient results in

$$\bar{h}^{\text{fem}} = \frac{Q_{\text{fluid}}}{LW\Delta T} \tag{19}$$

It is important to mention that this analysis is valid because steady-state conditions have been reached. Hence, conservation of energy may be used to show that the amount of heat entering the foam duct must be equal to the amount of heat removed by the cooling fluid.

4.2 Development of Velocity Profile. The velocity of the cooling fluid plays a critical role in the convective heat transfer coefficient associated with a cylinder in cross flow (see Sec. 4.3), and therefore its accurate representation is essential in the present analysis. In order to determine what the velocity of the fluid is, the steady volume-averaged momentum equation describing the flow through a porous medium (Eq. (20)) is utilized, following the approach presented by Calmidi and Mahajan [14].

$$\frac{\rho}{\epsilon^2}\nabla\cdot\mathbf{uu} = -\nabla p + \frac{\mu}{\epsilon}\nabla^2\mathbf{u} - \frac{\mu}{K}\mathbf{u} - \frac{\rho f}{\sqrt{K}}\|\mathbf{u}\|\mathbf{u} \tag{20}$$

The authors in Ref. [14] reported that the linear superposition of the Darcy term accounting for the drag due to the metallic struts, and the nonlinear correction term representative of form drag and flow separation used in Eq. (20) is semi-empirical, but nevertheless produces good agreement with experimental results. Equation (20) describes the full three-dimensional velocity field based on the properties of the medium such as its permeability (K), inertia coefficient (f), and porosity (ϵ). In the present analysis, only the one-dimensional velocity distribution along the thickness of the foam is necessary. This is a consequence of the assumption of a fully developed coolant velocity (parallel flow). Using only the axial component of the velocity and neglecting changes along the axial direction, Eq. (20), can be simplified into the following scalar equation

$$\frac{\mu}{\epsilon}\frac{\partial^2 u}{\partial y^2} - \frac{dp}{dx} - \frac{\mu}{K}u - \frac{\rho f}{\sqrt{K}}u^2 = 0 \tag{21}$$

Following the approach of Vafai and Tien [18], Eq. (21) is nondimensionalized using the foam half-duct height (H) and the centerline velocity u_∞ (see Fig. 13 for a description of the geometry used in this process)

$$u^* = \frac{u}{u_\infty} \tag{22a}$$

$$y^* = \frac{y}{H} \tag{22b}$$

In this way, Eq. (21) can be expressed in nondimensional form as follows

$$\frac{\partial^2 u^*}{\partial y^{*2}} = \frac{1}{\text{Da}}(u^* - 1) + \frac{\Lambda}{\sqrt{\text{Da}}}(u^{*2} - 1) \tag{23}$$

Following Ref. [18] the Darcy number, Da, and inertia function, Λ, are defined as

$$\text{Da} = \frac{K}{H^2\epsilon} \tag{24a}$$

$$\Lambda = \frac{\sqrt{\epsilon} f \text{Hu}_\infty}{\nu} \tag{24b}$$

The exact solution to Eq. (23) is derived in Ref. [18] and is reproduced below

$$u^* = 1 - \frac{A+B}{A}\,\text{sech}^2[D(y^* + C)] \tag{25}$$

For simplicity, the following constants are defined

$$A = \frac{2\Lambda}{3\sqrt{\text{Da}}} \tag{26}$$

$$B = \frac{1}{\text{Da}} + \frac{4\Lambda}{3\sqrt{\text{Da}}} \tag{27}$$

$$D = \frac{\sqrt{A+B}}{2} \tag{28}$$

$$C = -\frac{1}{D}\,\text{sech}^{-1}\left(\sqrt{\frac{A}{A+B}}\right) - 1 \tag{29}$$

Note that the term corresponding to the pressure gradient in Eq. (21) is not explicitly shown in Eq. (25) since it was expressed in terms of the flow velocity outside the momentum boundary layer, u_∞, in the solution process [18]. It is important to mention that the use of Eq. (25) requires the centerline velocity of the fluid in the foam-filled channel to be specified. As was mentioned in Sec. 2, the experimental results only yield the average velocity in the duct. In order to resolve this, a mass balance calculation is performed in which an initial value for the centerline velocity is

Table 2 Summary of foam thermophysical properties.

Foam thickness (mm)	Permeability (K, m^2)	Inertia coefficient (f)
6.4	1.9e−6	0.2084
12.7	6.7e−8	0.0327
25.4	9.1e−8	0.0048

specified (usually equal to the average velocity since the centerline value is expected to be larger [19]). This value is then used to integrate a modified version of Eq. (25) until the mass flow rate is equal to the one obtained using the average velocity. This process is mathematically stated as

$$\int_{-H}^{H} u_c u^* \, dy = 2u_0 H \tag{30}$$

The implementation of the equations presented above requires the foam permeability, K, and inertia coefficient, f, to be specified. These foam properties are determined from the experimental results for the pressure drop by fitting the data to a Forchheimer extended Darcy's equation [15,20]. In this way, the pressure drop is expressed as

$$-\frac{dp}{dx} = \frac{\mu}{K}u + \frac{\rho f}{\sqrt{K}}u^2 \tag{31}$$

Therefore, the experimental data is fitted to an equation of the form

$$\frac{|p_{\text{in}} - p_{\text{out}}|}{L} = c_1 u + c_2 u^2 \tag{32}$$

where the constants c_1 and c_2 are found through a least squares procedure. Setting these values equal to their counterparts in Eq. (31), the permeability and inertia coefficient are determined. A summary of these results for three of the foam specimens used is presented in Table 2. Note that this model for the pressure drop does not account for the effect of temperature on the viscosity of the cooling fluid. Lagé et al. [21], proposed a model to include this effect, and showed that it is more pronounced for large power settings. As has been previously mentioned, the voltage setting in the experiments presented in this work was 22 V, and therefore it can be safely assumed that these effects are negligible.

A sample velocity profile obtained using Eqs. (25) and (30) is shown in Fig. 14. The boundary layer thickness is very small due to the low permeability of the medium. The significance of this result and its impact on the heat transfer rate across the thickness of the foam is clear from the figure: the velocity at the ends is zero, thereby enforcing the condition that only conduction occurs at both ends. Neglecting the viscous effects of the flow through the foam, would mean that the heat transfer rate at the foam–facesheet joints is assumed to be equal to that at any other point, which could in turn overpredict the actual heat transfer level.

4.3 Effect of Cylinder Orientation. The final piece necessary to complete the description and obtain a solution for the problem using the finite element model developed above is to account for the orientation of each element, which is here assumed to be random. This parameter may also be determined from microscopic examination of the metal foam samples. The orientation of the cylinder is introduced through the velocity of the cooling fluid, which is vectorially decomposed into its parallel and perpendicular components with respect to the cylinder coordinate system based on the angle, θ, that it makes with its local vertical. This procedure is illustrated in Fig. 15. Even though the determination of the convective coefficient for a cylinder in cross flow is still an active area of research, several semi-empirical correlations have been proposed [16] and are adopted in the present analysis.

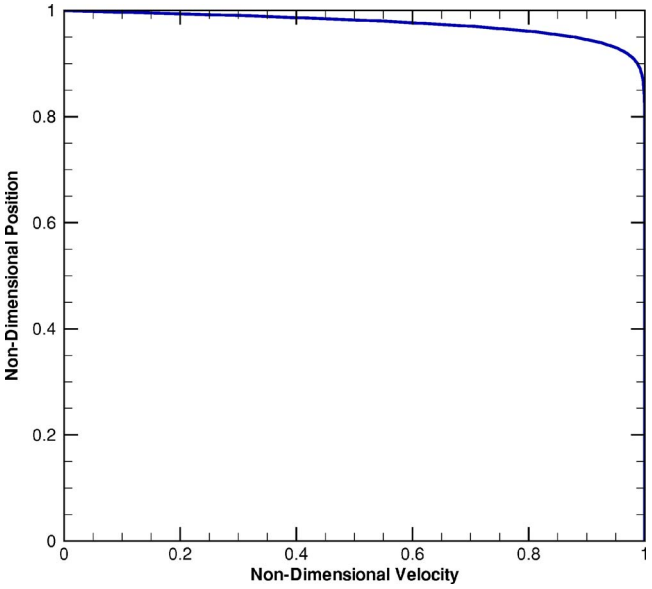

Fig. 14 Sample velocity profile across metal foam

Most of these results indicate that the convective coefficient is proportional to the fluid Prandtl and Reynolds numbers as

$$h = \frac{C\lambda \, \text{Re}_D^m \, \text{Pr}^{1/3}}{d} \tag{33}$$

In Eq. (33), Re_D is the Reynolds number based on the cylinder diameter and pore velocity. The constants m and C are empirical coefficients that have been shown to depend on the geometry of the cylinder, in particular, its specific cross-sectional shape. In the analysis presented in this paper the following semi-empirical correlation will be used

$$h = \frac{1.8\lambda \, \text{Re}_D^{0.55} \, \text{Pr}^{1/3}}{d} \tag{34}$$

The only variable in Eq. (34) becomes the Reynolds number which will vary along the length of the cylinder according to the solution of the momentum equation through porous media (Eq. (25)). Since the velocity of the cooling fluid is only included in this term, the modification mentioned above is included in the Reynolds number, so that the effective h which takes into account the orientation of the cylinder is

$$h_{\text{eff}} = \frac{1.8\lambda \, \text{Re}_D^{0.55} \cos(\theta)^{0.55} \, \text{Pr}^{1/3}}{d} \tag{35}$$

One important assumption made in the analysis is clear from Eq. (35); heat transfer in the axial cylinder direction is assumed to be zero, that is, heat transfer of the cylinder in longitudinal flow is not included. The implications of this assumption are discussed in Sec. 5.

4.4 Numerical Implementation of Finite Element Model. In the implementation of the finite element model developed above, each metal foam sandwich panel is discretized into 160 sections along its axial dimension. This number was determined based on the porosity and length of the foam samples. Each section consists of an arrangement of cylinders oriented at different angles as shown in Fig. 16. It is important to note that this method of discretization does not include interactions among cylinders from adjacent axial sections.

The inputs required by the finite element model are the parameters necessary to assemble the element effective conductivity matrix and the heat flux vectors. The local convective coefficient for each element is determined based on the velocity profile obtained

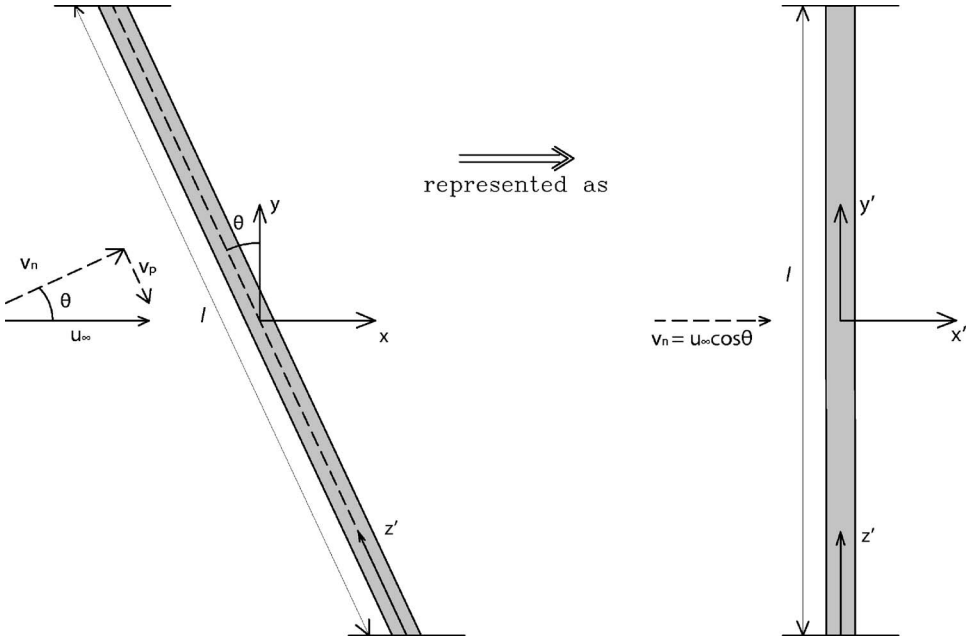

Fig. 15 Decomposition of flow velocity into parallel and perpendicular components with respect to cylinder axis

in Sec. 4.2 and the semi-empirical form adopted in Sec. 4.3. In this way, the coordinates of the two nodes of each element are used to calculate the velocity of the fluid at the element's midpoint, and this result is later used in determining the convective coefficient. The fluid properties used correspond to those of air at 20°C. The reason for this choice is similar to the one explained in Sec. 2. Note that since the velocity profile is assumed to be fully developed, it is the same for every axial section.

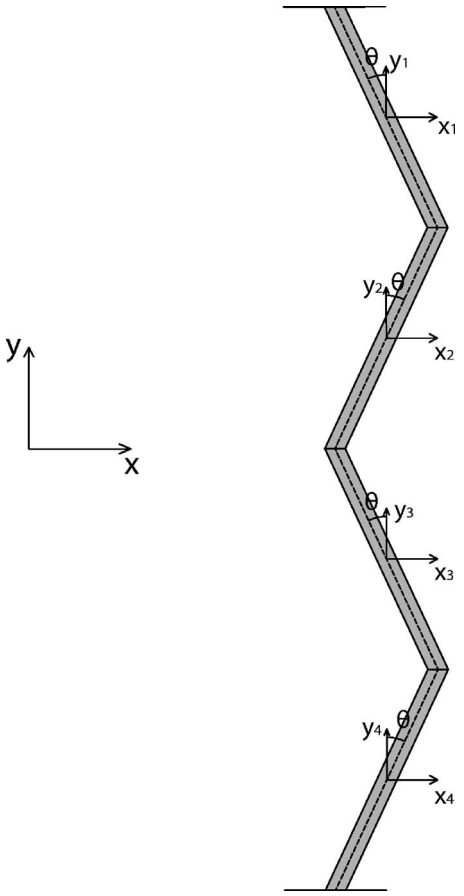

Fig. 16 Illustration of sample through-the-thickness cylinder arrangement used in finite element simulations for each axial section

The thermal conductivity value used corresponds to the parent aluminum alloy. Since we are interested in isolating the thickness effects, the diameter of each cylinder was maintained constant for all finite element simulations. This value was an average obtained from measurement of strut diameters in the different foam samples. The length of each cylinder is determined based on its particular orientation, and the number of elements used. As the primary objective is to model the heat transfer through the thickness of the foam, a large number of elements is desired in this direction. However, caution must be exercised to ensure that the total thickness of the foam is equal to the one of the sample under consideration. This is enforced by selecting the element length so that its component along the foam thickness equals the value of the foam thickness divided by the number of elements. This may be stated as

$$l_i \cos(\theta_i) = \frac{t}{n} \tag{36}$$

so that

$$\sum_{i=1}^{n} l_i \cos(\theta_i) = t \tag{37}$$

Note that this requirement is simply a geometric constraint, and does not imply that only the length of the cylinder along the thickness direction is used. In all simulations performed, 100 elements were used through the thickness of the foam. The final input necessary is the temperature of the cooling fluid. This parameter is specified at each axial section by assuming a linear distribution along the length of the foam, using the air temperature at the entrance and exit of the foam duct to determine the necessary constants. For a summary of the input parameters see Table 3.

The solution process begins by assembling the global effective conductivity matrix and global heat flux vector for the first axial

Table 3 Properties of sandwich panel and metal foam

Parameter	Description	Value used
L	Sandwich panel length	0.203 m
w	Width	0.051 m
d	Diameter of foam strut	0.00044 m
λ	Thermal conductivity	218 W/m^2 K

section, which corresponds to the entrance of the foam duct. Once this procedure has been completed, boundary conditions need to be specified. In the calculation of the temperature of the heated side, the boundary conditions used are the applied experimental heat flux, and the experimentally measured temperature distribution of the insulated side. Therefore, the first entry of the global heat flux vector is set equal to the experimental value used, while the last entry of the global temperature vector is given a value corresponding to the specific position of the station. This value is extrapolated by using a linear approximation of the temperatures measured experimentally. In the calculation of the temperature of the insulated side, the boundary conditions used are the experimentally measured temperature distribution of the heated side and zero heat flux on the insulated side. These values are implemented following a procedure similar to the one outlined above. The temperature value at all nodes in the axial section is then found from matrix multiplication of the inverse reduced effective conductivity matrix and heat flux vector, as explained in Sec. 4.1. The same procedure is followed for every axial section, which yields the temperature distribution along the thickness and length of the foam.

5 Results and Discussion

Figures 17–20 show the results obtained for all the foam specimens used. It can be seen that the predictions of the finite element model become more accurate as the foam thickness is increased. For the 6.4 mm panel the slope of the temperature profile produced numerically is somewhat deviated from the slope of the temperature profile obtained experimentally, especially for the temperature of the insulated side. Because of the small thickness

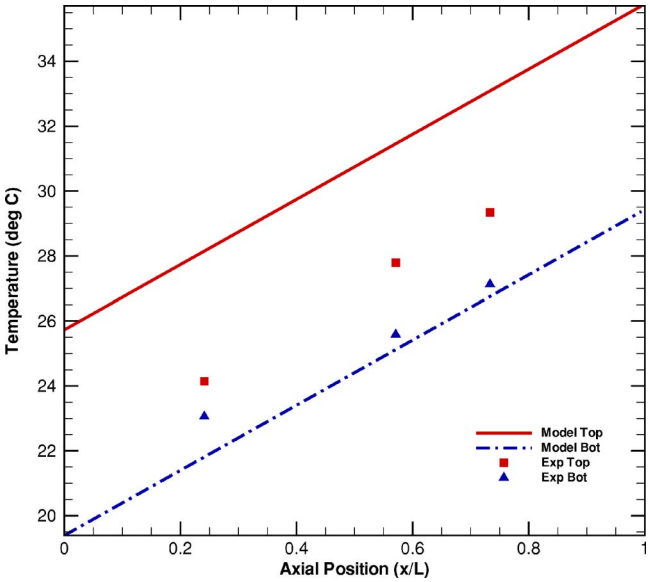

Fig. 18 Comparison of finite element model prediction and experimental results for temperature distribution on sandwich panel. The foam thickness is 12.7 mm, the air velocity is 5.9 m/s, and the voltage setting is 22 V resulting in an applied heat flux of 730 W/m^2. Random cylinder orientation.

of the metal foam, it is possible that size effects are predominant in this case, in other words, since the two facesheets are so close together it is likely that the entire heat transfer process is dominated by boundary layer effects. The hypothesis that the physical process governing the heat transfer in the thin panel is not completely similar to that in the other specimens is also apparent in Fig. 8, where the results for the convective coefficient of the 6.4 mm panel lie considerably far from the others. The results obtained for the foam permeability and inertia coefficient also support this hypothesis. As is shown in Table 2, the foam permeability for the 6.4 mm panel is two orders of magnitude smaller

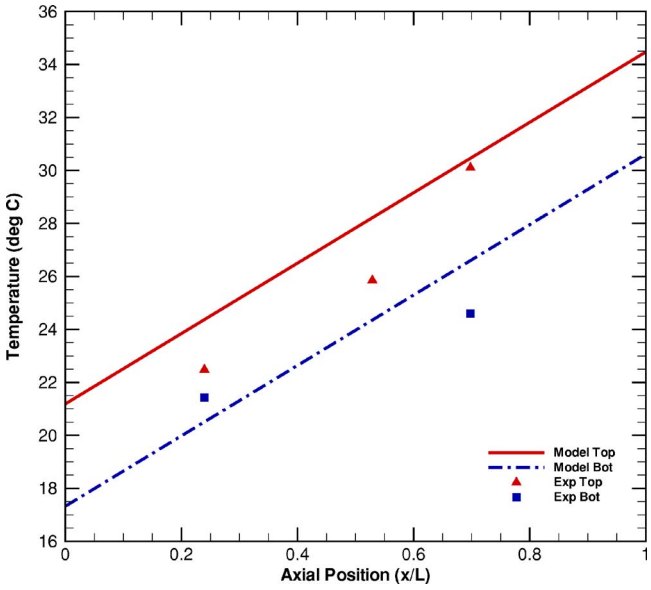

Fig. 17 Comparison of finite element model prediction and experimental results for temperature distribution on sandwich panel. The foam thickness is 6.4 mm, the air velocity is 17.6 m/s, and the voltage setting is 22 V resulting in an applied heat flux of 730 W/m^2. Random cylinder orientation.

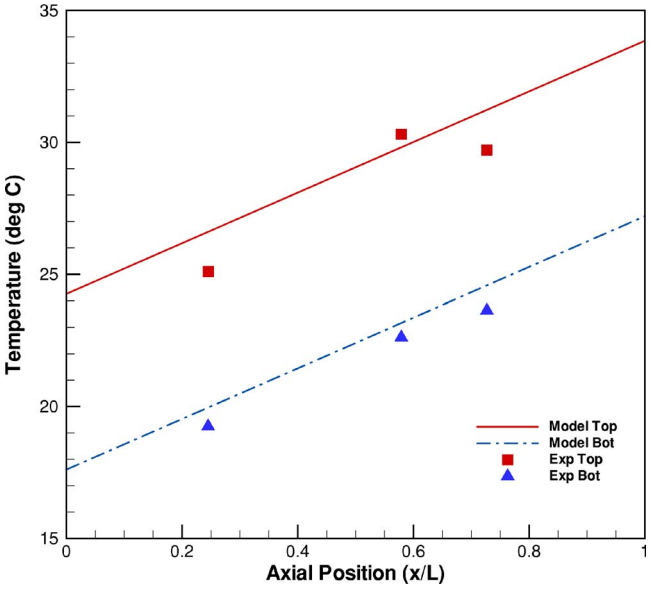

Fig. 19 Comparison of finite element model prediction and experimental results for temperature distribution on sandwich panel. The foam thickness is 19.0 mm, the air velocity is 5.8 m/s, and the voltage setting is 22 V resulting in an applied heat flux of 730 W/m^2. Random cylinder orientation.

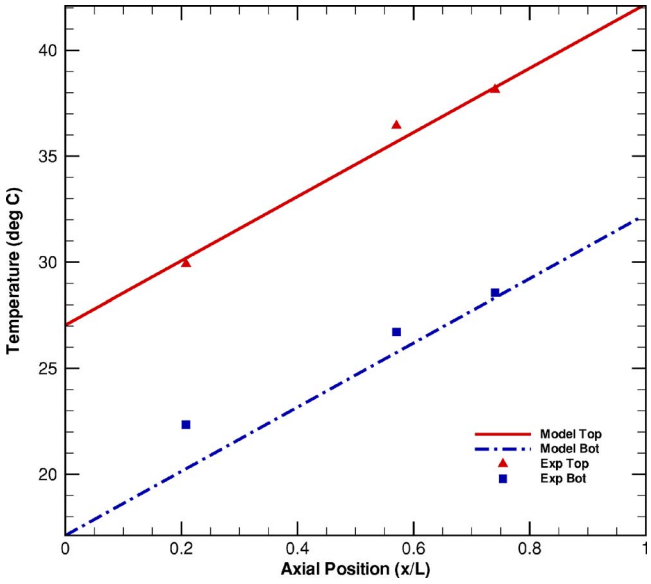

Fig. 20 Comparison of finite element model prediction and experimental results for temperature distribution on sandwich panel. The foam thickness is 25.4 mm, the air velocity is 2.9 m/s, and the voltage setting is 22 V resulting in an applied heat flux of 730 W/m^2. Random cylinder orientation.

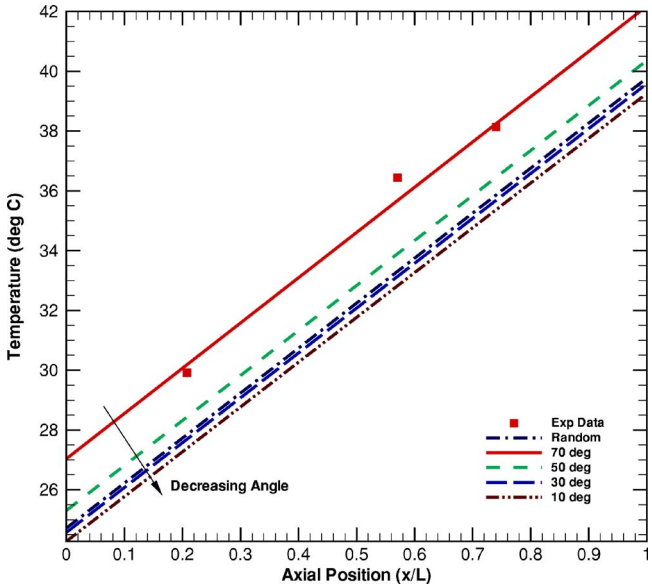

Fig. 21 Effect of varying cylinder angle on model prediction. The foam thickness is 25.4 mm, the air velocity is 2.9 m/s, and the voltage setting is 22 V resulting in a heat flux of 730 W/m^2. Heated side.

than that of the remaining specimens. Since these foams have the same porosity and relative density, it would be reasonable to expect this parameter to be within the same order for all the samples. It is likely that this difference is due to the fact that the model used to determine this parameter (Eq. (32)) does not adequately describe the physical phenomenon. It should be noted that the entire velocity formulation presented in Sec. 4.2 excludes any interaction between the two viscous boundary layers from the two facesheets [18].

As the thickness is increased we observe a significant improvement in the agreement between the experimental and numerical results, especially for the insulated side. Figure 18 shows that for the 12.7-mm-thick panel the model predictions are within 0.5°C of the experimental results for the insulated side at two axial locations. Figure 19 shows that for the 19.0-mm-thik specimen the experimental and numerical results are in good agreement for both the heated and insulated surfaces. It should be noted that the experimental data for the pressure drop obtained for this panel was not sufficient to adequately determine its permeability and inertia coefficient; as a result, the arithmetic mean of the properties for the 12.7 mm and 25.4 mm foam was used in the numerical simulations for this sample. This assumption is reasonable as these properties are expected to be similar for all the samples, as was previously explained. Finally, Fig. 20 shows how for the largest foam thickness tested the results agree very well.

Figures 21–24 show the effect of varying the cylinder orientation on the numerical results for the temperature of both surfaces. The cylinder orientation is defined through the angle that it makes with its local vertical, as shown in Fig. 15. In the tests performed, a random cylinder orientation was compared with several regular configurations, i.e., by selecting a particular angle and assuming the cylinders were arranged in a "zig-zag" manner alternating between positive and negative values of this angle. It is important to note that in this type of arrangement, the resulting geometry is equivalent to a single cylinder connecting both facesheets of the sandwich panel oriented at the angle θ; however, this is not the case for the random configuration where each cylinder has a different orientation. As expected, increasing the angle that the cylinder makes with its local vertical, produces a decreased heat transfer level (as the axis of the cylinder becomes parallel to the flow) which is evident from the higher temperatures resulting for the 70°C case in all thicknesses. The figures also show that altering the orientation of the cylinder has a stronger effect on the temperature of the heated surface, as the envelope of temperatures is thinner for the insulated part. Additionally, the variations that occur in cylinder configuration from specimen to specimen are also clear from these results, as different sandwich panels require different angle configurations to closely match the experimental results. Although angle variations produce different results, the magnitude of these differences is in most cases smaller than 15%, indicating that the exact configuration of the metal foam is not a crucial factor in determining its heat transfer properties. Other

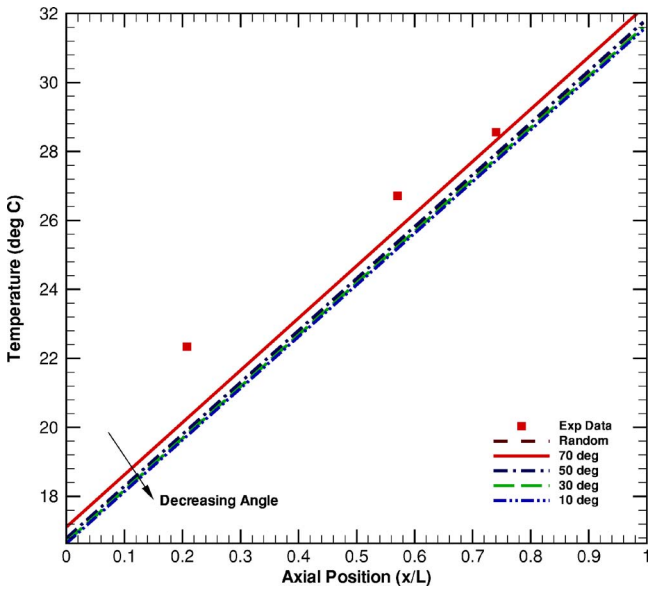

Fig. 22 Effect of varying cylinder angle on model prediction. The foam thickness is 25.4 mm, the air velocity is 2.9 m/s, and the voltage setting is 22 V resulting in a heat flux of 730 W/m^2. Insulated side.

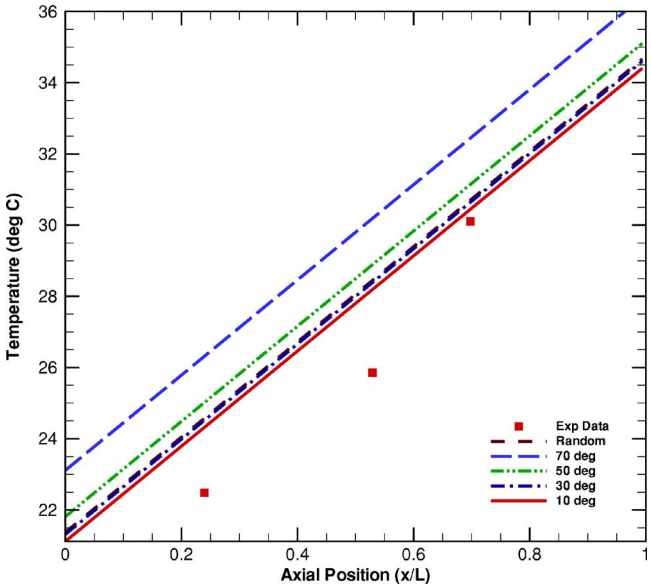

Fig. 23 Effect of varying cylinder angle on model prediction. The foam thickness is 6.4 mm, the air velocity is 17.6 m/s, and the voltage setting is 22 V resulting in a heat flux of 730 W/m^2. Heated side.

foam parameters, in particular its thickness and strut size, appear to have a much more important influence on the performance of these materials as heat exchangers.

Finite element results for the convective heat transfer coefficient, based on the approach presented in Sec. 4.1, were calculated for the 25.5-mm-thick foam. This foam thickness was selected because it provided the best match with experimental data for the temperature distributions, as shown in Fig. 20. It was found that for low velocities, there was good agreement between numerical and experimental results. In particular, for a free stream air velocity of 2.9 m/s, the finite element simulations predicted a convective coefficient of 152 W/m^2 K, which compared well with 162 W/m^2 K obtained experimentally. However, as the air velocity was increased, a significant disagreement between both solutions developed, with the finite element analysis underpredicting the convective coefficient. This difference may be partially attributed to the fact that heat transfer along the length of the cylinder is neglected in the analysis. This contribution may become increasingly important for larger air velocities, which contributes to the disagreement between the model and experiments. The development of a refined heat transfer model that considers both the normal (to a strut element) and axial heat transfer processes would significantly improve predictions, and is left for future work.

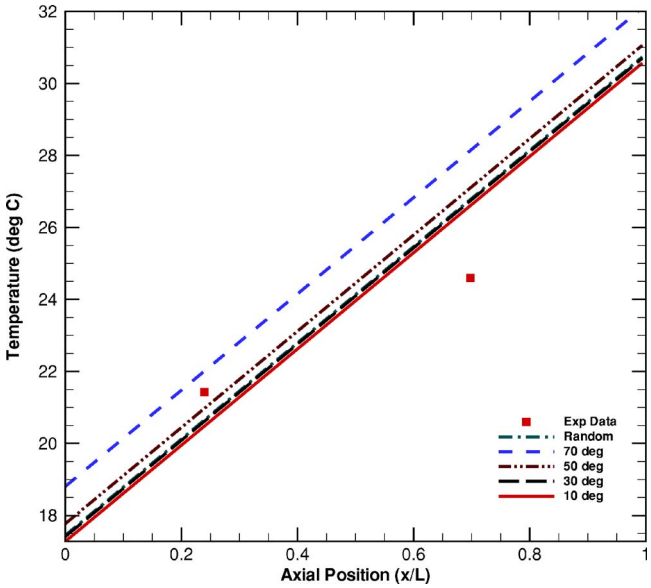

Fig. 24 Effect of varying cylinder angle on model prediction. The foam thickness is 6.4 mm, the air velocity is 17.6 m/s, and the voltage setting is 22 V resulting in a heat flux of 730 W/m^2. Insulated side.

6 Concluding Remarks

The effect of foam thickness on the convective heat transfer of metal foam sandwich panels has been experimentally investigated and modeled using a finite element approach. Four different foam thickness ranging from 6.4 mm to 25.4 mm have been tested, and results for the convective heat transfer coefficient have been obtained. It has been determined that increasing the foam thickness produces an increased heat transfer level, as revealed by a larger convective coefficient and a larger temperature difference between both foam surfaces. Moreover, it was observed that this effect weakens as the thickness of the foam increases. The heat transfer process in the foam has been modeled using a finite element approach that accomodates metal struts of different orientations. These results have been shown to agree favorably with experimental data. Both the experimental results and the numerical predictions indicate that size effects are present in the heat transfer properties of metal foams, as revealed by the substantial differences between the 6.4-mm-thick panel and the rest of the specimens. The numerical predictions capture the appropriate trend of increased heat transfer with increasing foam thickness, and indicate that the exact orientation of the foam struts is of secondary importance, while the foam thickness and strut size are the dominant properties on convective heat transfer.

Nomenclature

A = area (m^2)
b = styrofoam thickness (m)
d = cylinder diameter (m)
Da = Darcy number
f = Inertia coefficient
h = convective coefficient (W/m^2 K)
H = metal foam half thickness (m)
k = thermal conductivity (W/m K)
K = foam permeability (m^2)
L = sandwich panel length (mm)
l = cylinder length (mm)
N_j = shape function
p = pressure (kPa)
q = heat flux (W/m^2)
Q = heat input (W)
R_i = resistance
Re = Reynolds number
t = foam thickness (mm)
T_j = temperature degree of freedom
u = axial velocity in foam duct (m/s)
V = voltage (V)
W = foam width (m)
x = coordinate along foam length
y = coordinate along foam thickness
z' = coordinate along cylinder length

Greek Symbols

Δ = difference
ϵ = foam porosity
μ = fluid viscosity
ρ = fluid density (kg/m^3)
θ = cylinder orientation

Subscripts

e = element
i = resistance index, $i=1,2,3,4$
j = shape function index, $j=1,2$
l = lateral
∞ = free stream conditions
n = thermocouple index, $n=1,2,3$
pm = foam parent material
s = styrofoam
sf = cylinder surface
∞ = free stream conditions

Superscript

— = average property

References

[1] Rakow, J. F., and Waas, A. M., 2005, "Thermal Buckling of Metal Foam Sandwich Panels for Convective Thermal Protection Systems," J. Spacecr. Rockets, **42**(5), pp. 832–844.

[2] Weber, R. M., Lage, J. L., Price, D. C., and Weinert, A. K., 1996, "Numerical Study of a Low Permeability Microporous Heat Sink for Cooling Phased-Array Radar Systems," Int. J. Heat Mass Transfer, **39**, pp. 3633–3647.

[3] Price, D. C., Antohe, B. V., Lage, J. L., and Weber, R. M., 1996, "Numerical Characterization of MicroHeat Exchanges using Experimentally Tested Porous Aluminum Layers," Int. J. Heat Fluid Flow, **19**, pp. 594–603.

[4] Porneala, D. C., Lage, J. L., Narasimhan, A., and Price, D. C., 2004, "Experimental Study of Forced Convection through Microporous Enhanced Heat Sinks: Enhanced Heat Sinks for Cooling Airborne Microwave Phased-Array Radar Antenas," *Emerging Technologies and Techniques in Porous Media*, Vol. 28, Kluwer, Dordrecht, The Netherlands, pp. 433–452.

[5] Pavel, B. I., and Mohamad, A. A., 2004, "Experimental Investigation of the Potential of Metallic Porous Insert in Enhancing Forced Convective Heat Transfer," ASME J. Heat Transfer, **126**, pp. 540–545.

[6] Pavel, B. I., and Mohamad, A. A., 2004, "An Experimental and Numerical Study on Heat Transfer Enhancement for Heat Exchangers Fitted With Porous Media," Int. J. Heat Mass Transfer, **47**, pp. 4939–4952.

[7] Mohamad, A. A., 2003, "Heat Transfer Enhancements in Heat Exchangers Fitted With Porous Media, Part i: Constant Wall Temperature," J. Therm. Sci., **42**, pp. 385–395.

[8] Mohamad, A. A., 2003, "Porous Media Utilizations for Heat Transfer Enhancements," Proceedings of the NATO Advanced Study Institute on Porous Media, Neptum-Olimp, Romania, June 9–20, pages 358–367.

[9] Poulikakos, D., Boomsma, K., and Zwick, F., 2003, "Metal Foams as Compact High Performance Heat Exchangers," Mech. Mater., **35**, pp. 1161–1176.

[10] Boomsma, K., and Poulikakos, D., 2002, "The Effects of Compression on Pore Size Variation on the Liquid Flow Characteristics in Metal Foams," ASME J. Fluids Eng., **124**, pp. 263–272.

[11] Poulikakos, D., Boomsma, K., and Ventikos, Y., 2003, "Simulations of Flow through Open Cell Metal Foams Using an Idealized Periodic Cell Structure," Int. J. Heat Fluid Flow, **24**, pp. 825–834.

[12] Stone, H. A., Lu, T. J., and Ashby, M. F., 1998, "Heat Transfer in Open-Cell Metal Foams," Acta Mater., **46**(10), pp. 3619–3635.

[13] Bastawros, A. F., and Evans, A. G., 1997, "Characterisation of Open-Cell Aluminum Alloy-Foams as Heat Sinks for High Power Electronic Devices," Proceedings of the Symposium on the Application of Heat Transfer in Microelectronics Packaging IMECE, Dallas, TX.

[14] Calmidi, V. V., and Mahajan, R. L., 1999, "Forced Convection in High Porosity Metal Foams," ASME J. Heat Transfer, **122**, pp. 557–565.

[15] Calmidi, V. V., Bhattacharya, A., and Mahajan, R. L., 2002, "Thermophysical Properties of High Porosity Metal Foams," Int. J. Heat Mass Transfer, **45**, pp. 1017–1031.

[16] Incropera, F. P., and DeWitt, D. P., 2002, *Fundamentals of Heat and Mass Transfer*, 5th ed., J Wiley, New York.

[17] Chandrupatla, T., and Belegundu, A., 1997, *Introduction of Finite Elements in Engineering*, 2nd ed., Prentice–Hall, Upper Saddle River, NJ.

[18] Vafai, K., and Kim, S. J., 1989, "Forced Convection in a Channel Filled with a Porous Medium: An Exact Solution," ASME J. Heat Transfer, **111**, pp. 1103–1106.

[19] White, F. M., 1991, *Viscous Fluid Flow*, 2nd ed., McGraw–Hill, New York.

[20] Price, D. C., Antohe, B. V., Lage, J. L., and Weber, R. M., 1997, "Experimental Determination of Permeability and Inertia Coefficients of Mechanically Compressed Aluminum Porous Matrices," ASME J. Fluids Eng., **119**, pp. 404–412.

[21] Nield, D. A., Lage, J. L., Narasimhan, A., and Porneala, D. C., 2001, "Experimental Verification of Two New Theories Predicting Temperature-Dependent Viscosity Effects on the Forced Convection in a Porous Channel," ASME J. Fluids Eng., **123**, pp. 948–951.

Forced Convective Heat Transfer in Parallel Flow Multilayer Microchannels

M. H. Saidi[1]

Reza H. Khiabani

Center of Excellence in Energy Conversion,
School of Mechanical Engineering,
Sharif University of Technology,
P.O. Box 11365-9567,
Tehran, Iran

In this paper, the effect of increasing the number of layers on improving the thermal performance of microchannel heat sinks is studied. In this way, both numerical and analytical methods are utilized. The analytical method is based on the porous medium assumption. Here, the modified Darcy equation and the energy balance equations are used. The method has led to an analytical expression presenting the average dimensionless temperature field in the multilayer microchannel heat sink. The effects of different parameters such as aspect ratio, porosity, channel width, and the solid properties on the thermal resistance are described. The results for single layer and multilayer heat sinks are compared to show the effectiveness of using multilayer microchannels.
[DOI: 10.1115/1.2739600]

Keywords: microcooling, microchannel heat sink, multi layer channels, porous medium

1 Introduction

In the current state of fast developing electronic equipment, having high speeds and at the same time high heat generation rates, researchers are trying to find an effective microcooling method. The main problem in the cooling of microdevices is their high heat generation rate in a limited space. In this way, much research has been conducted on the analysis of different novel microcooling methods such as microheat pipes, microjet impingements, microcapillary pumped loops, microelectrohydrodynamic coolers, and microchannel heat sinks. Among the different microcooling devices the microchannel heat sink has been of special consideration due to its capabilities such as high capacity of heat removal. The use of microchannel heat sink was first introduced by Tuckerman and Pease in 1981 [1]. Their research was based on an experiment where they showed that high heat rates of 790 W/cm^2 could be removed by microchannel heat sinks. Currently, research in the field of microchannels is going on in three aspects of experimental methods [2,3], numerical methods [4], and analytical methods [5]. The experimental method has its own values and the new developments in the micromachining techniques help the researchers to perform precise experiments, but because of its high cost it fails to be commonly applied [6]. The numerical method is being used vastly to simulate the performance of microchannels like other fields of heat transfer [7–9]. There has been much effort to analytically model the microchannel heat sink [10,11]. Knight et al. [12] used empirical correlations to evaluate the performance of a microchannel heat sink. Koh and Colony [13] first modeled microstructures as a porous medium using Darcy's law. Later on Tien and Kuo [14] developed a model for heat transfer in microchannels using the modified Darcy equation and the two-equation model. Another method to model the microchannel heat sink analytically is to use the fin and plate theory. In this way, the solid walls are assumed to be as fins that are connected to the base plate. Applying this assumption, the thermal resistance and other thermal characteristics of the system could be derived using the fin and plate heat transfer relations. The results of such an analysis fail to predict some effects in comparison with the numerical results or the porous medium approach results [11].

Recently, the effect of using multilayer microchannel heat sink is introduced even to increase the thermal capacities of microchannel heat sinks. Vafai et al., using a numerical analysis, have shown that the two layer microchannel heat sink has more advantages compared with the single layer microchannel [7]. The advantage of multilayer channels is that they can remove more heat having the same area in contact with the heat generating component.

In this paper, the porous medium approach is used to derive a novel expression for describing the average dimensionless temperature in a multilayer microchannel heat sink. The results are first introduced for a single layer microchannel and then the method has been extended to the multilayer case. The concept of overall thermal resistance has been introduced and applied to compare the thermal performance of microchannels. The usefulness of the definition of the thermal resistance is described based on the concept of entropy generation minimization. The effect of important parameters such as aspect ratio, porosity, and the number of layers on the overall thermal resistance of multilayer microchannels is studied.

2 Problem Definition and Overview

Figure 1 shows a single layer microchannel heat sink. A microchannel heat sink consists of several parallel channels in which the working fluid flows through. The solid part is made of a material such as silicon with high thermal conductivity and the working fluid usually is water. The length, L, of the microchannel is usually much larger than its width, W, and the channel height, H, or the channel width, w_c. The bottom of the heat sink is connected to a heat generating surface. The heat generating surface usually is an electronic component. The top surface is assumed to be insulated. It is seen that there is a limited area available between the heat sink and the heat generating surface. Therefore, the heat dissipation rate per unit area is very high and the heat removal capacity of the current heat sinks is limited. A possible method to resolve this problem is to use multilayer heat sinks to increase the heat removal capacity per unit area. Figure 2 presents a schematic of a multilayer microchannel heat sink. It is constructed of several rows of a single layer microchannel heat sink. The problem of concern in this research is to study the forced convective heat

[1]Corresponding author. E-mail: saman@sharif.edu
Contributed by the Heat Transfer Division of ASME for publication in the JOURNAL OF HEAT TRANSFER. Manuscript received September 27, 2005; final manuscript received August 30, 2006. Review conducted by Jose L. Lage.

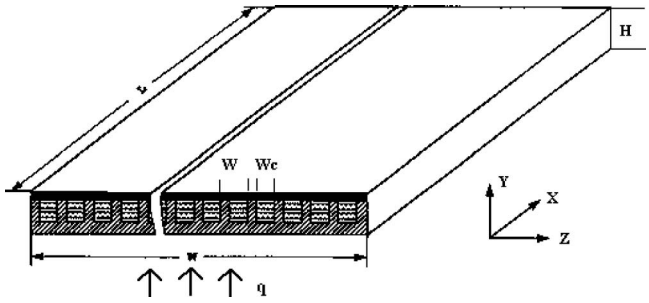

Fig. 1 Schematic of a single layer microchannel

transfer and fluid flow in multilayer microchannel heat sinks and compare the effect of increasing the number of layers in the thermal performance of the microheat sink. In the parametric analysis, the conditions of laminar fully developed, incompressible, steady flow and constant thermo-physical properties, e.g., viscosity and thermal conductivity, are assumed. In this study, the microchannel heat sink is assumed to be a porous medium filled with working fluid as in the work of Tien and Kuo [14]. Volume averaging is applied to the fluid flow and heat transfer equations. For volume averaging to be valid, the averaging volume should be much longer than the channel width and the direction of averaging should be independent of the flow and heat transfer path [15]. Here, the averaging is done in the z direction for a small volume of which its dimensions in x and y directions are small compared to the z direction. On the other hand, the flow is in the x direction and the heat transfer can be assumed in the x and y directions. Therefore, these conditions are considered in this approach and the volume-averaged equations can be applied to microchannels [10].

3 Governing Equations

In this paper, the approach is to model the microchannel heat sink as a fluid saturated porous medium. To study the heat transfer and fluid flow the extended Darcy equation and the volume averaged heat transfer equations are used [14]. The extended Darcy equation is developed to describe the fluid flow in the porous media [16]. This equation considers the boundary effects in the convection problems, so it is more appropriate to use this equation instead of the Darcy equation in the study of forced convection in microchannels [17]. In the next sections, first the model has been developed for a single layer heat sink and then the solution method has been extended to a multilayer microchannel.

3.1 Single Layer Microchannel Heat Sink. The volume averaged extended Darcy equation and the corresponding boundary conditions for a microchannel heat sink, such as Fig. 1, are [16]

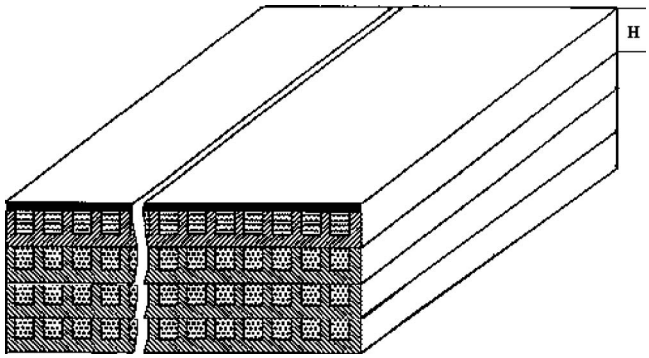

Fig. 2 Schematic of a multilayer microchannel

$$\frac{d}{dx}\langle P\rangle_f = \mu\frac{d^2}{dx^2}\langle u\rangle_f - \varepsilon\frac{\mu}{K}\langle u\rangle_f \tag{1}$$

$$\langle u\rangle_f = 0 \quad \text{at } y = 0, H \tag{2}$$

Applying the energy balance, the following equations and boundary conditions can be derived for the temperature field

$$\varepsilon\rho\langle u\rangle_f c_f\frac{\partial\langle T\rangle_f}{\partial x} = ha(\langle T\rangle_s - \langle T\rangle_f) + k_{fe}\frac{\partial^2\langle T\rangle_f}{\partial y^2} \tag{3}$$

$$k_{se}\frac{\partial^2\langle T\rangle_s}{\partial y^2} = ha(\langle T\rangle_s - \langle T\rangle_f) \tag{4}$$

$$\langle T\rangle_s = \langle T\rangle_f = T_w \quad \text{at } y = 0 \tag{5}$$

$$\frac{\partial\langle T\rangle_s}{\partial y} = \frac{\partial\langle T\rangle_f}{\partial y} = 0 \quad \text{at } y = H \tag{6}$$

where e is porosity; K is permeability; $a=1/w$ is the wetted area per volume; k_{fe} is the fluid effective thermal conductivity; k_{se} is the solid effective thermal conductivity, and $\langle\rangle$ denotes a volume averaged quantity. The characteristic parameters for a microchannel can be defined as [18]

$$\varepsilon = \frac{w_c}{w}, \quad K = \frac{\varepsilon w_c^2}{12}$$

$$k_{se} = (1-\varepsilon)k_s$$

$$k_{fe} = \varepsilon k_f$$

$$C = \frac{\varepsilon k_f}{(1-\varepsilon)k_s} \tag{7}$$

where C is the effective conductivity ratio. As mentioned earlier in Sec. 2, the volume averaging is done in the z direction and the dimension of the averaging volume in the z direction is much longer than the others. Therefore, considering that the fully developed flow is in the x direction, the permeability is selected based on the Hagen–Poiseuille flow between two parallel plates. In Eq. (7), the hydraulic diameter of the channel may be used instead of w_c [14], but the results of current selection of the permeability show very good agreement with the exact analytical solution for the velocity profile [10]. The selection of effective thermal conductivities is based on the same direction for averaging of the temperature field.

Considering the fully developed conditions and the energy balance in the microchannel, the following dimensionless parameters can be defined to nondimensionalize the equations, as done in much research after the report of Kim and Kim [10,11]

$$q_w = \varepsilon\rho_f c_f u_m H\frac{\partial\langle T\rangle_f}{\partial x} \tag{8}$$

$$Y = \frac{y}{H}, \quad U = \frac{\langle u\rangle_f}{u_m}, \quad \mathrm{Da} = \frac{K}{\varepsilon H^2}$$

$$P = \frac{K}{\varepsilon\mu_f u_m}\frac{d\langle P\rangle_f}{dx}, \quad \theta = \frac{\langle T\rangle - T_w}{\dfrac{q_w H}{(1-\varepsilon)k_s}} \tag{9}$$

Applying these assumptions, the nondimensional form of Eq. (1) and the boundary conditions (2) are obtained as

$$U = \mathrm{Da}\frac{d^2U}{dY^2} - P \tag{10}$$

$$U = 0 \quad \text{at } Y = 0, 1 \tag{11}$$

Utilizing separate temperatures for the solid and the fluid phases makes the problem very complicated. The resulting statements contain many parameters and it makes it impossible to extend the method to multilayer channels [10]. To mitigate the difficulties another approach is used that makes the problem less complicated. The idea is to use an average value, T, to describe the average temperature of the fluid and the solid. The temperature field resulting in this method accurately presents the average temperature in the heat sink, while decreasing the Darcy number even improves its accuracy [19]. Therefore, a single equation for the heat transfer can be obtained by adding Eqs. (3) and (4). Applying these assumptions, the nondimensional heat transfer equation and the boundary conditions are obtained as

$$U = (1 + C)\frac{\partial^2 \theta}{\partial Y^2} \tag{12}$$

$$\theta = 0 \quad \text{at } Y = 0 \tag{13}$$

$$\frac{\partial \theta}{\partial Y} = 0 \quad \text{at} \quad Y = 1 \tag{14}$$

In this case, i.e., single layer microchannel, the velocity, pressure and temperature fields can be obtained with some mathematical manipulations as

$$U = P\left\{\text{Cosh}\left(\sqrt{\frac{1}{\text{Da}}}Y\right) + A\ \text{Sinh}\left(\sqrt{\frac{1}{\text{Da}}}Y\right) - 1\right\} \tag{15}$$

$$P = \frac{\text{Sinh}\left(\sqrt{\frac{1}{\text{Da}}}\right)}{2\sqrt{\text{Da}}\left\{\text{Cosh}\left(\sqrt{\frac{1}{\text{Da}}}Y\right) - 1\right\} - \text{Sinh}\left(\sqrt{\frac{1}{\text{Da}}}\right)} \tag{16}$$

$$\theta = \frac{P}{1 + C}\left[\text{Da Cosh}\left(\sqrt{\frac{1}{\text{Da}}}Y\right) + A\ \text{Da Sinh}\left(\sqrt{\frac{1}{\text{Da}}}Y\right) - \frac{1}{2}Y^2 + mY + s\right] \tag{17}$$

where the constant parameters can be obtained as

$$A = \frac{1 - \text{Cosh}\left(\sqrt{\frac{1}{\text{Da}}}\right)}{\text{Sinh}\left(\sqrt{\frac{1}{\text{Da}}}\right)}, \quad s = -\text{Da}$$

$$m = 1 - \sqrt{\text{Da}}\ \text{Sinh}\ \sqrt{\frac{1}{\text{Da}}} - A\sqrt{\text{Da}}\ \text{Cosh}\ \sqrt{\frac{1}{\text{Da}}} \tag{18}$$

It is seen that for a particular flow regime there are a limited number of independent parameters that affect the dimensionless velocity and temperature fields. The main parameters are Darcy number and the effective conductivity ratio. Furthermore, there are a few constant parameters which make it possible to extend the solution to the case of multilayer microchannels.

3.2 Multilayer Microchannel Heat Sink. The solution can be extended to the multilayer heat sink by applying Eqs. (10) and (12) for each layer. It should be noted that different coordinate systems should be used for each layer. Therefore, the origin of the y axis is placed in the bottom of each channel. Furthermore, the reference for nondimensional parameter Y, is the height of a channel, H. Utilizing the approach, the velocity and the pressure fields are obtained in each layer and can be described as is done in Eqs. (15) and (16). The energy balance equation in different layers is the same as Eq. (12) and can be summarized as

$$U = (1 + C)\frac{\partial^2 \theta_i}{\partial Y_i^2} \tag{19}$$

Solving Eq. (19), the dimensionless temperature field and its derivative can be derived as

$$\frac{\partial \theta_i}{\partial Y_i} = \frac{P}{1 + C}\left[\sqrt{\text{Da}}\ \text{Sinh}\left(\sqrt{\frac{1}{\text{Da}}}Y_i\right) + A\sqrt{\text{Da}}\ \text{Cosh}\left(\sqrt{\frac{1}{\text{Da}}}Y_i\right) - Y_i + m_i\right] \tag{20}$$

$$\theta_i = \frac{P}{1 + C}\left[\text{Da Cosh}\left(\sqrt{\frac{1}{\text{Da}}}Y_i\right) + A\ \text{Da Sinh}\left(\sqrt{\frac{1}{\text{Da}}}Y_i\right) - \frac{1}{2}Y_i^2 + m_i Y_i + s_i\right] \tag{21}$$

However, the boundary conditions should be modified so that the new physical domain could be described mathematically. That is

$$\theta_i = 0 \quad \text{at } Y_i = 0 \tag{22}$$

$$\theta_i(\text{at } Y_i = 1) = \theta_{i+1} \quad \text{at } Y_{i+1} = 0$$

$$\frac{\partial \theta_i}{\partial Y_i}(\text{at } Y_i = 1) = \frac{\theta_{i+1}}{\partial Y_{i+1}} \quad \text{at } Y_{i+1} = 0 \tag{23}$$

$$\frac{\partial \theta_n}{\partial Y_n} = 0 \quad \text{at } Y_n = 1 \tag{24}$$

The boundary conditions in Eqs. (22) and (24) stand for the conditions of constant heat flux in the bottom and the thermal isolation in the top. Relations (23) are used to describe the continuity in the temperature field. Applying the boundary conditions Eqs. (22)–(24) into Eqs. (20) and (21), a recursive relation between the constant parameters s_i and m_i can be obtained as

$$s_1 = G_1$$

$$s_i - s_{i+1} - m_{i-1} = G_2 \quad 1 \leqslant i < n$$

$$m_i - m_{i+1} = G_3 \quad 1 \leqslant i < n$$

$$m_n = G_4 \tag{25}$$

where

$$G_1 = -\text{Da}$$

$$G_2 = \text{Da Cosh}\left(\sqrt{\frac{1}{\text{Da}}}\right) + A\ \text{Da Sinh}\left(\sqrt{\frac{1}{\text{Da}}}\right) - \text{Da} - \frac{1}{2}$$

$$G_3 = 1 + A\sqrt{\text{Da}} - \sqrt{\text{Da}}\ \text{Sinh}\left(\sqrt{\frac{1}{\text{Da}}}\right) - A\sqrt{\text{Da}}\ \text{Cosh}\left(\sqrt{\frac{1}{\text{Da}}}\right)$$

$$G_4 = 1 - \sqrt{\text{Da}}\ \text{Sinh}\ \sqrt{\frac{1}{\text{Da}}} - A\sqrt{\text{Da}}\ \text{Cosh}\ \sqrt{\frac{1}{\text{Da}}} \tag{26}$$

The system of $2n$ Eqs. (25) can be rewritten in the matrix form to simplify the solution process, and then the parameters can be obtained using Gauss technique. It is shown in the following matrix relation

$$\begin{bmatrix} 1 & 0 & 0 & \dots & 0 & 0 & 0 & \dots & 0 & 0 \\ 1 & 1 & 0 & \dots & 0 & -1 & 0 & \dots & 0 & 0 \\ 0 & -1 & 1 & 0 & \dots & 0 & \dots & \dots & 0 & 0 \\ \vdots & 0 & \vdots & \ddots & \cdots & \cdots & \vdots & \vdots & \vdots & \vdots \\ 0 & \cdots & 0 & -1 & 1 & 0 & \cdots & 0 & -1 & 0 \\ 0 & \cdots & \cdots & \cdots & 0 & 1 & -1 & 0 & \cdots & 0 \\ \vdots & \vdots & \vdots & \cdots & 0 & 0 & \ddots & \cdots & \vdots & \vdots \\ 0 & 0 & \cdots & \cdots & \cdots & \cdots & 0 & 1 & -1 & 0 \\ 0 & 0 & \vdots & \vdots & \cdots & \cdots & \vdots & 0 & 1 & -1 \\ 0 & 0 & 0 & \cdots & 0 & 0 & \cdots & \cdots & 0 & 1 \end{bmatrix} \times \begin{bmatrix} s_1 \\ s_2 \\ \vdots \\ \vdots \\ s_n \\ m_1 \\ m_2 \\ \vdots \\ \vdots \\ m_n \end{bmatrix}$$

$$= \begin{bmatrix} G_1 \\ G_2 \\ G_2 \\ \vdots \\ G_2 \\ G_3 \\ G_3 \\ \vdots \\ G_3 \\ G_4 \end{bmatrix}$$

$$m_i = G_4 + (n-i)G_3$$

$$s_i = G_1 + G_2 + (i-1)G_4 + (i-1)\left(n - \frac{i}{2}\right)G_3 \tag{27}$$

Applying Relations (27) into Relation (21) the dimensionless temperature field in each layer can be determined.

4 Thermal Performance Analysis

The entropy generated in a control volume can be obtained from Eq. (28)

$$\dot{S}_{\text{gen}} = \frac{dS}{dt} - \sum_{i=0}^{n} \frac{Q_i}{T_i} - \sum_{\text{in}} \dot{m}s + \sum_{\text{out}} \dot{m}s \tag{28}$$

Using thermodynamic relations and assuming that the temperature difference in the fluid is smaller than the fluid average temperature, Eq. (28) can be simplified for a microchannel as [5]

$$\dot{S}_{\text{gen}} \cong \frac{\dot{q}\Delta T}{T_f^2} + \frac{\dot{m}}{\rho T_f}\left(-\frac{dP}{dx}\right) \tag{29}$$

Considering Eq. (29), it is seen that the generated entropy is mainly due to the heat transfer and the friction effects. Considering the common relation for the pressure drop in a channel, $dP = f(L/D_h)(u_m)^2/2g$, where $f = \text{const}/\text{Re}$, it is clear that the pressure drop is proportional to the mean velocity u_m. The second right-hand term in Eq. (29) is proportional to the pumping power. The pumping power is obtained as

$$W_p = \Delta P \cdot Q \tag{30}$$

The volume flow rate, Q, is proportional to the cross section and the mean velocity. Therefore, in a constant flow rate, increasing the number of microchannel layers results in decreasing the mean velocity in each channel that will decrease the pressure drop and the required pumping power. It will decrease the generated entropy. However, in the case of constant pumping power, which is an appropriate assumption based on the current limitations in the pumping power in the microscale, the decrease in the entropy generation is mainly related to the temperature difference, ΔT. It is important to note that decreasing the temperature difference in the heat sink decreases the generated entropy. This shows the importance of minimizing the absolute thermal resistance that is commonly defined as

$$R_{\text{thermal}} = \frac{\Delta T}{q} \tag{31}$$

where, ΔT is the difference between the inlet fluid temperature and the temperature of the bottom of the channel in the outlet. It is shown in the following sections that increasing the number of layers of a microchannel heat sink will result in decreasing the thermal resistance. For the case of microchannel heat sink, the thermal resistance can be defined as

$$R_{\text{thermal}} = R_{\text{flow}} + R_{\text{solid}} \tag{32}$$

where R_{flow} is due to the thermal capacity of the fluid and R_{solid} is due to heat transfer through and between the solid walls. Therefore, the value of these thermal resistances can be determined based on the system characteristics as

$$R_{\text{flow}} = \frac{1}{\dot{m}c_f} \tag{33}$$

where $m = \rho u_m A = \rho w_c^2 \alpha_s \varepsilon W / w_c u_m$; and $\alpha_s = H/w_c$ is aspect ratio, and

$$R_{\text{solid}} = \frac{1}{hA_{\text{fs}}} = \frac{T_w - T_b}{q_w LW} = -\frac{w_c \alpha_s \int_0^1 U\theta\, dY}{(1-\varepsilon)k_s LW} \tag{34}$$

where A_{fs} is the are between the fluid and the solid.

Here, the absolute thermal resistance is used to introduce the optimum values for the microchannel heat sinks and to compare the performance of the single layer and multilayer heat sinks. Considering the above equations, it is known that three parameters of aspect ratio, porosity, and channel width affect the thermal resistance.

5 Numerical Simulation

A numerical simulation is used to verify the above results and assumptions. The results also show that assuming fully developed flow in the analytical solution does not result in a significant error. In this regard, a three-dimensional model of the problem is simulated using numerical methods and considering laminar flow and constant thermophysical properties. A heat generating area of 1 cm × 1 cm for the electronic device with a heat flux of 200 W/cm^2 is considered. The cooling media is water at 223.5 °C and the solid body is made of silicon. The symmetric boundary condition is applied at the sidewalls. The channel dimensions are 365 mm × 57 mm similar to the experimental set of Tuckerman and Pease [1]. The SIMPLEC method is used for numerical solution and staggered control volumes are used. To interpolate the convective terms, the QUICK method is used. Figure 3 presents the temperature field in x planes in the direction of channel length. Table 1 compares the value of the thermal resistance resulting from the numerical simulation with the results of the parametric study. There exists an excellent agreement between the results of different methods.

6 Results and Discussion

The results show that three parameters of aspect ratio, porosity, and the channel width affect the thermal resistance of a particular microchannel heat sink. Figure 4 presents the effect of aspect ratio on the thermal resistance. It is seen that when the other characteristics are constant, the thermal resistance decreases with increasing aspect ratio. It is due to increasing both the channel cross section and the surface between the fluid and solid that decreases both terms in the thermal resistance relation, i.e., Eq. (32). There-

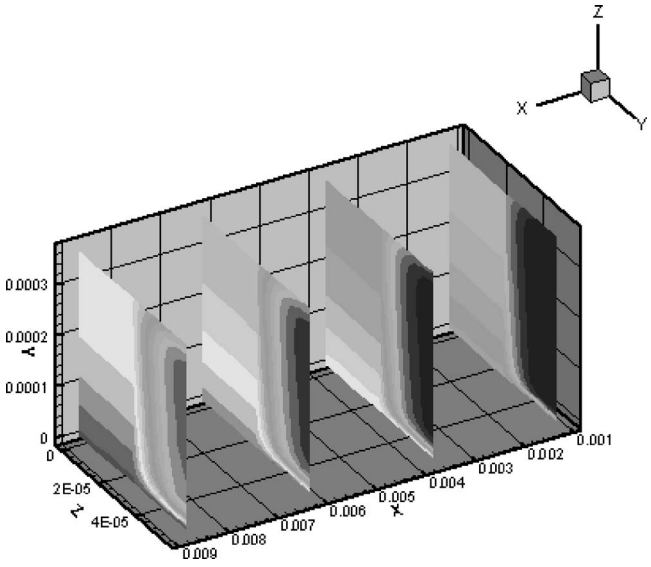

Fig. 3 Temperature field in *x* planes in the direction of channel length

fore, there is no optimum value for the aspect ratio to minimize the thermal resistance and selecting an aspect ratio depends on the construction limitations.

Figure 5 presents the effect of porosity on the thermal resistance for different values of the aspect ratio. When the porosity increases, the surface between the channel base and the fluid increases; as a result, the heat transfer rate to the fluid increases. At the same time, the heat transfer in the direction of the channel height decreases due to the decreasing surface between the walls and the channel base. Therefore, it is seen that there is an optimum value for the porosity that minimizes the thermal resistance. The optimum value changes slightly with the aspect ratio, but for a general case it can be estimated to be about 0.5, as it is mentioned in previous research [1].

The effect of the channel width on the overall thermal resistance is shown in Fig. 6. Increasing the channel width, while the other characteristics are constant, increases the channel cross section and therefore the flow rate that according to Eq. (33) decreases the first term of Eq. (32). On the other hand, increasing the channel width results in the second term of Eq. (32) to increase according to Eq. (34). This term estimates the thermal resistance of the solid section. Therefore, it can be seen that the thermal resistance decreases with increasing channel width until it reaches a minimum value and then it increases again. On the other hand, the optimum value for the channel width increases with increasing aspect ratio.

Table 1 Results of different methods proposed for the thermal resistance.

ε	α_s	w_c (mm)	R_{reported} (°C/W)	$R_{\text{analytical}}$ (°C/W)	$R_{\text{numerical}}$ (°C/W)
0.504	5.8	61	0.077[12]	0.072	0.080
0.5	5.9	61	0.070[10]	0.071	0.076
0.5	6.4	59	0.075[10]	0.069	0.08

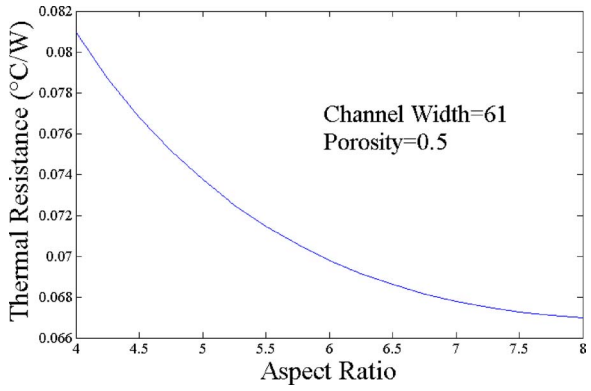

Fig. 4 The effect of aspect ratio on the thermal resistance

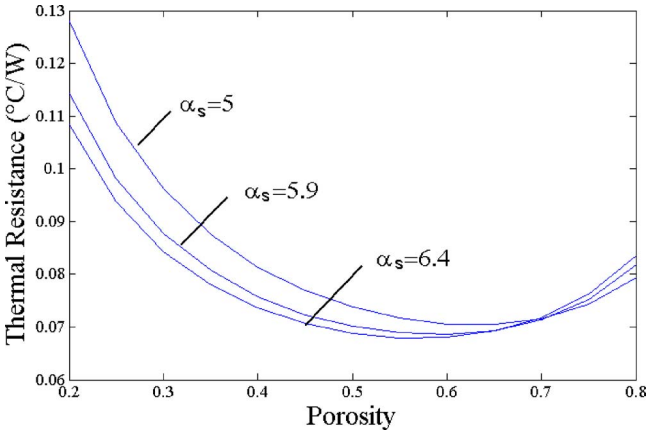

Fig. 5 The effect of porosity on the thermal resistance

6.1 The Effect of Increasing the Number of Layers. Using multilayer microchannel heat sinks decreases the overall thermal resistance and therefore the generated entropy.

The effect of increasing the number of layers on the thermal resistance of a microchannel heat sink in the condition of constant pressure drop is compared in Fig. 7. The applied assumptions are: $\rho=885.8$ kg/m^3, $\nu_f=0.883\times10^{-6}$, $k_s=148$ W/m K, $w_c=71$ μm, $\alpha_s=6$, and $\Delta p=0.1$ bar.

The reference values are derived applying a different method [20]; however, it is seen that there is a good agreement between the predicted values from both methods. The reference results are derived applying the assumption of fin and plate that has its limitations such as a high amount of calculations. In this method, the solid walls are assumed as fins and the overall thermal resistance is determined applying a thermal resistance network analysis. Figure 7 shows that increasing the number of layers decreases the thermal resistance effectively. For example, thermal resistance of the two layer microchannel is about half of the thermal resistance of the single layer case. Furthermore, it is inferred from Fig. 7 that the increase in the number of layers above four or five layers is not as effective. The increase in the number of layers decreases

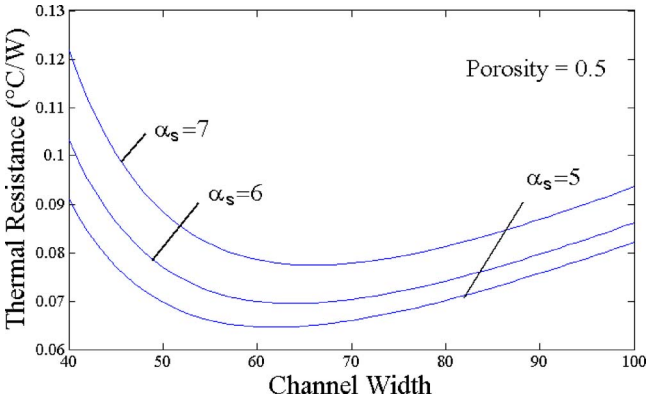

Fig. 6 The effect of channel width on the thermal resistance

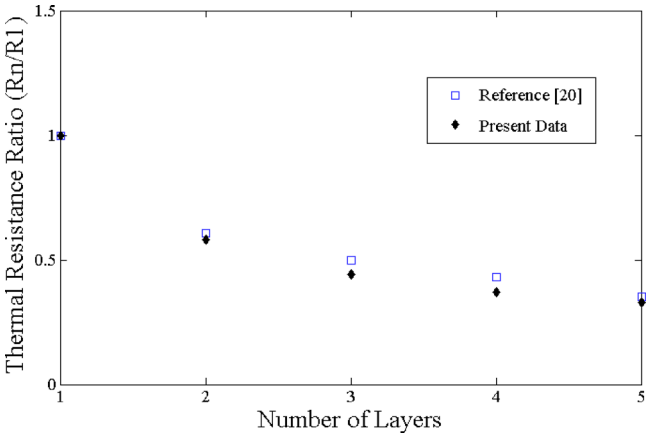

Fig. 7 Effect of number of layers on thermal performance in fixed pressure drop

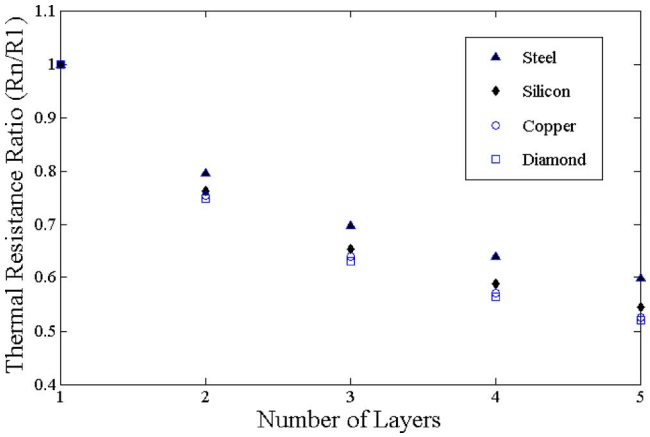

Fig. 9 Effect of solid properties on the thermal resistance of multilayer microchannel

the thermal resistance because it causes the flow rate to increase and at the same time increases the thermal resistance of the solid section. The effects are balanced in the layers above five.

To account for the present limitations of micropumps it is more practical to apply the assumption of constant pumping power. Most of the current micropumps can be applied in a limited pumping power that confines the choice for the limit of pressure drop and flow rate in the microchannels. Figure 8 compares the effect of increasing the number of layers on the thermal resistance of a microchannel heat sink in the condition of constant pumping power equal to 0.002 W/cm^2. The results predict that the thermal resistance decreases as the number of layers increases. In this condition, the effect of the decrease in the heat transfer coefficient occurring due to the decrease in the mean velocity has been compensated for with the effect of the increase in the wetted area. Similar to Fig. 7 it is shown that the increase in the number of layers above four or five is not as effective. This is due to the role of thermal resistance of the solid section in the overall thermal resistance.

6.2 The Effect of Solid Properties. The thermal characteristics of the solid and fluid sections affect the overall thermal performance of the microchannel heat sink. Here, the effect of thermal conductivity of the solid material on the effectiveness of increasing the number of layers is compared. The applied materials are steel (k_s=50 W/Km), silicon (k_s=148 W/Km), copper (k_s=400 W/Km), and diamond (k_s=1200 W/Km).

Figure 9 compares the effect of using the four different solid materials in the condition of constant pumping power. It is shown that as the thermal conductivity of the solid increases, the effectiveness of applying multilayer channels increases. Therefore, the decrease in the thermal resistance with increasing number of layers in the steel microchannel is less than the other materials.

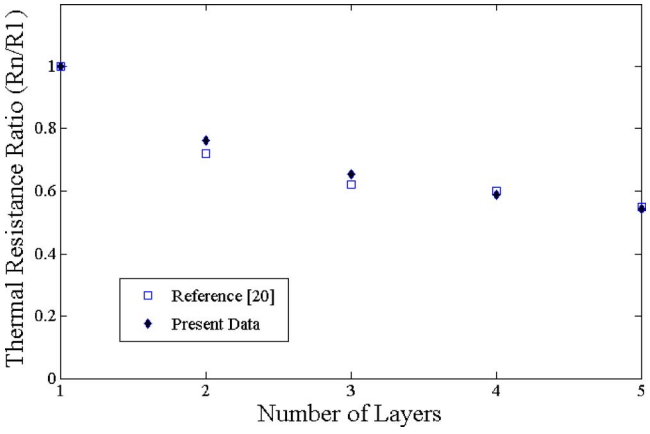

Fig. 8 Effect of number of layers on thermal performance in fixed pumping power

7 Conclusions

A parametric study on the heat transfer and fluid flow in the microchannel heat sink has been done using the porous medium assumption. The study has led to the derivation of a novel model to describe the average dimensionless temperature in the multilayer microchannel heat sink. The results are used to analytically describe the overall thermal resistance. The results are compared with the results of other works and the present numerical results. The effect of increasing the number of layers on the thermal resistance of the microchannel heat sink is studied for the conditions of constant pressure drop and constant pumping power. Results show that increasing the number of layers effectively decreases the overall thermal resistance. The effectiveness of applying multilayer microchannels increases by using solid materials with high thermal conductivity. However, it is shown that increasing the number of layers above four or five is not as effective.

Nomenclature

D = diameter
Da = Darcy number
h = convective heat transfer coefficient
H = channel height
K = permeability
L = length
Nu = Nusselt number
p = pressure
P = dimensionless pressure
q = heat flow
Q = volume flow rate
R = thermal resistance
Re = Reynolds number
t = thickness
T = temperature
u = horizontal velocity
U = dimensionless horizontal velocity
W = width
Y = height

Greek Symbols

α = aspect ratio
ε = porosity
ρ = density

θ = dimensionless temperature
ω = width
ν = kinematic viscosity
μ = viscosity
$\langle\rangle$ = mean value along z axis

Subscripts

b = base
c = channel
f = fluid
h = hydraulic
m = mean
s = solid
t = thermal, local
w = wall

References

[1] Tuckerman, D. B., and Pease, R. F. W., 1981, "High-Performance Heat Sinking for VLSI," IEEE Electron Device Lett., **2**, pp. 126–129.

[2] Jang, S. P., Kim, S., and Paik, K. W., 2003, "Experimental Investigation of Thermal Characteristics for a Microchannel Heat Sink Subject to an Impinging Jet, Using a Micro Thermal Sensor Array," Sens. Actuators, A, **105**, pp. 211–224.

[3] Chen, Y., Kang, S., Tuh, W., and Hsiao, T., 2004, "Experimental Investigation of Fluid Flow and Heat Transfer in Microchannels," Tamkang Journal of Science and Engineering, **7**(1), pp. 11–16.

[4] Qu, W., and Mudawar, I., 2002, "Analysis of Three-Dimensional Heat Transfer in Micro-Channel Heat Sinks," Int. J. Heat Mass Transfer, **45**, pp. 3973–3985.

[5] Saidi, M. H., Salehi, M., and Khiabani, R. H., 2005, "An Approach to the Optimum Design of Two Layered Microchannel Heat Sinks," Proceeding of 9th UK heat Transfer Conference, Manchester, UK, September 5–6.

[6] Zhang, H. Y., Pinjala, D., Womg, T. N., Toh, K. C., and Joshi, Y. K., 2005, "Single Phase Liquid Cooled Microchannel Heat Sink foe Electronic Packages," Appl. Therm. Eng., **25**, pp. 1472–1487.

[7] Vafai, K., and Zhu, L., 1999, "Analysis of Two Layered Microchannel Heat Sink Concept in Electronic Cooling," Int. J. Heat Mass Transfer, **31**, pp. 1176–1186.

[8] Kulkarni, P., and Das, D., 2005, "Analytical and Numerical Studies on Microscale Heat Sinks for Electronic Applications," Appl. Therm. Eng., **25**, pp. 2432–2449.

[9] Gamrat, G., Marinet, M., and Asendrych, D., 2005, "Conduction and Entrance Effects on Laminar Liquid Flow and Heat Transfer in Rectangular Microchannels," Int. J. Heat Mass Transfer, **48**, pp. 2943–2954.

[10] Kim, S. J., and Kim, D., 1999, "Forced Convection in Microstructures for Electronic Equipment Cooling," ASME J. Heat Transfer, **121**, pp. 639–645.

[11] Zhao, C. Y., and Lu, T. J., 2002, "Analysis of Microchannel Heat Sinks for Electronics Cooling," Int. J. Heat Mass Transfer, **45**, pp. 4857–4869.

[12] Knight, R. W., Goodling, J. S., and Hall, D. J., 1991, "Optimal Thermal Design of Forced Convection Heat Sinks," ASME J. Electron. Packag., **113**, pp. 313–321.

[13] Koh, J. C. Y., and Colony, R., 1986, "Heat Transfer of Micro Structures for Integrated Circuits," Int. Commun. Heat Mass Transfer, **13**, pp. 89–98.

[14] Tien, C. L., and Kuo, S. M., 1987, "Analysis of Forced Convection in Microstructures for Electronic Systems Cooling," Proc. Int. Symp. Cooling Technology for Electronic Equipment, Honolulu, HI, August 31–September 2, pp. 217–226.

[15] Kaviany, M., 1995, *Principles of Heat Transfer in Porous Media*, Springer, New York.

[16] Vafai, K., and Tien, C. L., 1981, "Boundary and Inertia Effects on Flow and Heat Transfer in Porous Media," Int. J. Heat Mass Transfer, **24**, pp. 195–203.

[17] Lee, D. Y., and Vafai, K., 1999, "Analytical Characterization and Conceptual Assessment of Solid and Fluid Temperature Differentials in Porous Media," Int. J. Heat Mass Transfer, **42**, pp. 423–435.

[18] Bejan, A., 1995, *Convection Heat Transfer*, 2nd ed., Wiley, New York.

[19] Saidi, M. H., Salehi, M., and Khiabani, R. H., 2005, "Performance of Micro Channel Heat Sink Used in Integrated Micro Cooling Devices," Proceeding of IIR International Conferences: Thermophysical Properties and Transfer Processes of Refrigerants, Vicenza, Italy, March 18–21.

[20] Wei, X., and Joshi, Y., 2004, "Stacked Microchannel Heat Sinks for Liquid Cooling of Microelectronic Components," J. Electron. Packag., **126**, pp. 60–66.

A. G. Straatman
Mem. ASME
Department of Mechanical and Materials Engineering,
The University of Western Ontario,
London, ON, N6A 5B9, Canada

N. C. Gallego
Metals and Ceramics Division,
Oak Ridge National Laboratory,
Oak Ridge, TN 37831

Q. Yu
Thermalcentric Inc.,
24 Ravenglass Cres.,
London, ON, Canada, N6J 3J5

L. Betchen
Department of Mechanical and Materials Engineering,
The University of Western Ontario,
London, ON, N6A 5B9, Canada

B. E. Thompson
Thermalcentric Inc.,
24 Ravenglass Cres.,
London, ON, Canada, N6J 3J5

Forced Convection Heat Transfer and Hydraulic Losses in Graphitic Foam

Experiments and computations are presented to quantify the convective heat transfer and the hydraulic loss that is obtained by forcing water through blocks of graphitic foam (GF) heated from one side. Experiments have been conducted in a small-scale water tunnel instrumented to measure the pressure drop and the temperature rise of water passing through the foam and the base temperature and heat flux into the foam block. The experimental data were then used to calibrate a thermal non-equilibrium finite-volume model to facilitate comparisons between GF and aluminum foam. Comparisons of the pressure drop indicate that both normal and compressed aluminum foams are significantly more permeable than GF. Results of the heat transfer indicate that the maximum possible heat dissipation from a given surface is reached using very thin layers of aluminum foam due to the inability of the foam to entrain heat into its internal structure. In contrast, graphitic foam is able to entrain heat deep into the foam structure due to its high extended surface efficiency and thus much more heat can be transferred from a given surface area. The higher extended surface efficiency is mainly due to the combination of moderate porosity and higher solid-phase conductivity. [DOI: 10.1115/1.2739621]

Keywords: graphitic foam, forced convection, thermal non-equilibrium, thermal dispersion

1 Introduction

Porous materials have been studied in the past to understand their application in convective heat transfer. In general, porous materials include packed particle beds wherein the solid phase is discontinuous, sintered-particle porous materials in which the solid phase is continuous but the voids are small and often not interconnected, and porous materials that are produced by casting or foaming. Cast or foamed materials, such as aluminum, copper, and carbon, typically have an open, interconnected void structure that enables fluid exposure to internal surface area and thus the potential for significant convective heat transfer. Thus, such materials have the potential for application in energy exchange and electronics cooling.

Graphitic foam (hereafter referred to as GF) is produced by a process of foaming, carbonization, and subsequent graphitization of a carbon-based precursor material [1]. GF has a high effective (stagnant) conductivity (40–160 [W/m K]) [2] due to the high conductivity of the graphite material (800–1900 [W/m K]) and moderate porosity[1] (75–90%). In comparison, aluminum foams have effective conductivities of 2–26 [W/m K], resulting from material conductivities in the range of 140–237 W/m K (for various aluminum alloys) [3] and high porosity (90–96%). The combination of high solid-phase conductivity and moderate porosity enables GF to entrain heat deep into the solid structure of the foam to be swept away by passing fluid. Another significant advantage of GF over aluminum or other reticulated metal foams is the high internal surface area that results from the foaming process. The internal surface area, which can be as high as 5,000–50,000 m^2/m^3, serves to reduce the convective resistance thereby fostering energy exchange at the pore level. It is this combination of high material conductivity, moderate porosity, and high internal surface area that makes GF attractive as a heat transfer material for both single and multiphase applications.

While literature is available quantifying the pressure losses and convective heat transfer in open cell metal foams, there is relatively little information available on the characterization of GF. Concerning metal foams, Antohe et al. [4], Paek et al. [3], and Boomsma and Poulikakos [5] all reported on the hydraulic losses of normal and compressed aluminum foams and provided information quantifying the permeability and form drag coefficients for foams of different porosity so that pressure losses could be characterized using the classical Darcy-Forchheimer law. Calmidi and Mahajan [6] studied forced (air) convection in high porosity aluminum foams using experiments and computational fluid dynamics. In their experiments, large (196 mm × 63 mm × 45 mm thick) aluminum foam blocks of various porosities were inserted into a channel and heated from one side while air was forced through the internal structure of the foam. Since the effective conductivity was relatively low (maximum 7.4 W/m K), the extended-surface efficiency of the blocks was very low and convective heat transfer only occurred in a thin layer of foam adjacent to the heater. Boomsma et al. [7] studied the effect of foam-compression on the flow and heat transfer characteristics of aluminum foams. Compression of the foam increased the internal area to volume ratio of the foam and was an attempt to reduce the internal convective resistance and thereby reduce the volume of foam required to remove a given amount of energy. In this case, 40 mm × 40 mm × 2 mm thick blocks of foam were heated from one side while water was forced through the foam structure. Compression of the foam was shown to increase the heat transfer effectiveness by up to a factor of 2, however, with an associated increase in the pressure drop.

Gallego and Klett [2] provided some of the first data on the pressure drop and heat transfer for GF. Their study provided estimates of the influence of configuration on the heat transfer and pressure drop, but not enough detail was provided to assess the influence of porosity, pore diameter, and Reynolds number. To

[1]Porosity is defined in units of percent as the void fraction of the porous material.

Contributed by the Heat Transfer Division of ASME for publication in the JOURNAL OF HEAT TRANSFER. Manuscript received April 24, 2006; final manuscript received December 1, 2006. Review conducted by Jose L. Lage.

Table 1 Summary of properties for the carbon foam specimens tested

Specimen	Porosity, %	Average void dia., μm	Standard deviation of void dia., μm	β, m^2/m^3	k_{eff}, W/m K
219-3	86	350	105	6850	72
219-3-3	88	400	138	5640	61
218-3	88	400	121	5640	61
POCO™	82	500	193	5240	120

facilitate the development of heat transfer and hydraulic models for GF, Yu et al. [8] proposed a sphere-centered unit-cube geometry model to characterize the internal structure of a spherical void-phase porous material. Their model provides expressions for the internal and external surface areas, and the effective conductivity as a function of the porosity and the average void diameter, and can be used in combination with heat transfer data to obtain estimates of the internal convective heat transfer in GF. The model developed by Yu et al. [8] is utilized in combination with experimental data in the present work to quantify the convective heat transfer and pressure drop obtained by forcing a fluid through the internal structure of GF. The data are then used to calibrate a numerical model to facilitate comparisons between GF and aluminum foams.

Comparisons of the thermal and hydraulic performance are most efficiently done computationally since it is not practical to obtain measurements for all of the different variations of available foams. Furthermore, details of the energy transfer inside the porous metals must be explored computationally, since it is not possible to measure temperature variations inside foam blocks. Energy transfer in porous materials is typically studied by invoking the assumption of local thermal equilibrium between the solid and fluid phases, however, for porous metals and GF, this assumption is not valid due to the large difference between the solid and fluid phase thermal conductivities. To this end, Calmidi and Mahajan [6] used a thermal non-equilibrium model to carry out calculations of forced convection in uncompressed aluminum foams. In their study, models for interstitial convective exchange and thermal dispersion were proposed and then used to simulate the heat transfer for several different samples of aluminum foam. Betchen et al. [9] developed a complete three-dimensional conjugate heat transfer code for studying fluid/porous/solid domains, which also incorporates a thermal non-equilibrium model inside the porous domain. The models for interstitial exchange and thermal dispersion proposed by Calmidi and Mahajan [6] were implemented in the code and simulations of uncompressed aluminum foam confirmed the validity of the code and the accuracy of the models.

The purpose of the present work is to provide information quantifying the heat transfer and pressure drop observed when passing fluid through the internal structure of GF and to compare these results to similar results for aluminum foam. Experiments are described that establish the hydraulic losses and convective heat transfer obtained by passing water through heated GF blocks of different porosity and pore diameter. The results are used to calibrate the thermal non-equilibrium finite-volume code for conjugate heat transfer developed by Betchen et al. [9]. The computational model is then used to make detailed comparisons between the thermal and hydrodynamic performance of GF and aluminum foams. The remaining sections describe the GF specimens used in the experiments, theory, and the results of the experimental and computational studies.

2 The Carbon Foam Specimens

Four different GF specimens have been considered in the present experiments. The geometric properties and effective thermal conductivities of the specimens are summarized in Table 1.

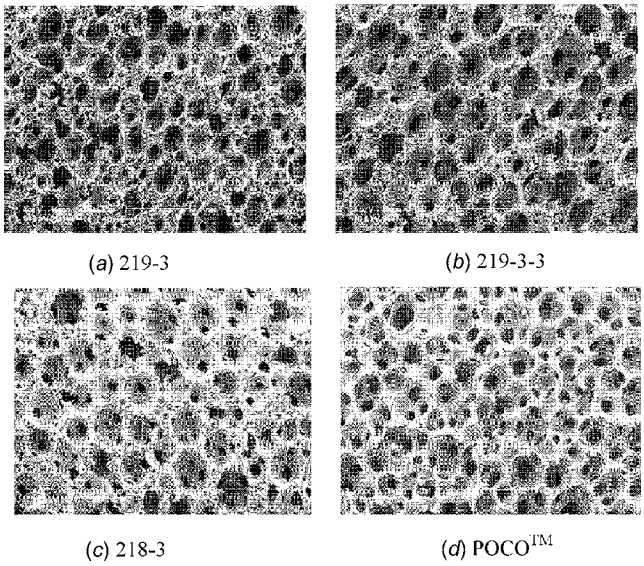

Fig. 1 Scanning electron microscope images of the graphitic foam specimens tested

The porosity of the specimens was obtained using the ratio of the specimen density and the solid ligament density and is expressed in Table 1 in terms of void fraction (in percent). The average pore diameter of the foam specimens was obtained by analysis of scanning electron microscope (SEM) images of the foam specimens given in Fig. 1. The standard deviation of the pore diameter is included in Table 1 to give an indication of the range of pore sizes present in a given specimen. Estimates of the internal surface area and effective conductivity were obtained using the expressions developed by Yu et al. [8].

The images in Fig. 1 indicate that there are significant differences between the foams in terms of the size of the cell windows connecting the pores. The cell windows provide the interconnectivity between the voids and thus afford access to the internal surface area of the foam. From the point of view of heat transfer, it is best to have small cell windows to maximize the internal surface area available for convection. However, from the point of view of flow into the foam, small cell windows will lead to much higher pressure drops due to the hydrodynamic loss associated with the severe contraction/expansion. Something the SEM images in Fig. 1 do not show, because of the high magnification, is the porosity gradient that can occur in the foaming process. The gradient is due to gravity, is typically only in the foaming (vertical) direction, and can account for porosity differences as high as 12% across a 25.4 mm thick specimen. The images in Fig. 1 also show some random lateral non-uniformity, which is most pronounced in the 219-3 foam. For the present experiments, test specimens were machined such that the (gravity) gradient was aligned with the vertical coordinate of the channel (normal to the flow direction) with the denser side of the foam specimen always placed adjacent to the heating element. Foam specimens were cut such that the nominal plan dimensions were 50.8 mm $\times$ 50.8 mm and the nominal thickness was 6 mm, to minimize porosity gradient effects while ensuring a suitable number of pores across the channel. Approximately 0.2 mm was added to each nominal dimension (except for the length in the flow direction) so that the specimens could be pressed into the test rig to ensure a good thermal contact and to avoid fluid bypass. Unpublished tests on the contact resistance between graphite foam and aluminum or copper substrates showed two things: first that contact pressure was as good as any bonding material or thermal epoxy for minimizing contact resistance, and second that the contact resistance did not vary strongly with contact pressure once a small deformation of the graphite was observed. Since the foam specimens were

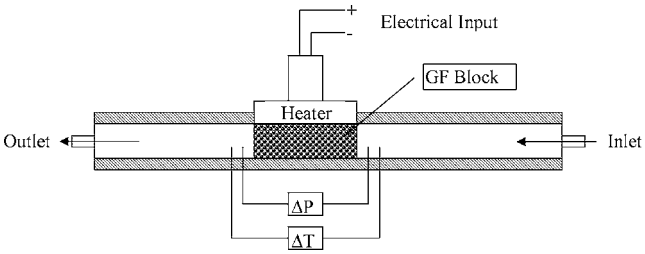

Fig. 2 Schematic of experimental setup showing the position and orientation of the graphitic foam, the fluid inlet and outlet, and the heat input

pressed into the test section, no mechanical bonding was used between the heating element and the foam block.

3 The Experiments

3.1 Experimental Setup. Experiments were conducted using a small-scale test rig to measure the pressure drop and heat transfer obtained by passing water through blocks of GF. The test setup, shown in Fig. 2, consists of a channel with a water inlet and outlet, a heating element, and instrumentation to measure the flow rate, fluid pressure drop, heat input, and temperature across the foam specimen (from position 1 to 2), and the base temperature of the heating element. The flow channel was 50.8 mm wide by 6 mm high and was machined to an accuracy of ±0.08 mm. Foam specimens, described in the previous section, were pressed into the test section of the channel. After assembly, the upper 50.8 mm × 50.8 mm surface of the foam was pressed firmly against a heating element and the lower surface was adjacent to a phenolic composite (garolite) to minimize heat loss. The lateral edges of the channel were also insulated to avoid heat loss. In this configuration, the foam specimens represent 50.8 mm × 50.8 mm cross-section extended surfaces (of 6 mm height) heated from one side.

The heating element consisted of two cartridge heaters inserted into a 50.8 mm × 50.8 mm copper block that was pressed firmly against the foam specimens during the experiments. The electrical power input to the heating element was monitored using a voltmeter and a clamp-on ammeter. The power input was adjusted using a variac.

The water flow rate was measured using a Yokogawa, Model AM102AG magnetic flow meter that was located upstream of the channel inlet. The flow meter was calibrated prior to the experiments and was deemed to be accurate to within ±1% over the range of flow rates considered. The pressure difference across the GF specimen was measured using a differential pressure transducer. Pressure probes were inserted into the channel 50.8 mm upstream of the GF specimen and 50.8 mm downstream of the specimen beyond the rapid mixing region just past the outlet of the foam. Because of the large pressure differences across the GF, errors associated with the positioning of the pressure probes in the channel were considered negligible. The pressure differences were measured to within ±1.5% over the range considered.

The base plate temperature was measured using six type-T thermocouples, which were pressed into holes that were drilled to within 1 mm of the copper-foam interface. The holes were drilled to achieve an interference fit and were filled with conductive paste prior to inserting the thermocouples to ensure a good thermal contact between the thermocouple and the base plate. The water inlet and outlet temperatures were monitored using type-T thermocouples which were placed 300 mm up- and downstream of the test section. The inlet temperature varied slightly from test to test, but was approximately 18 °C. Properties of the water were obtained at the average of the inlet and outlet bulk temperatures using tabulated data from Incropera and Dewitt [10]. The thermocouples used had an error of ±1 °C.

An estimate of the experimental error can be made based on the uncertainties of the individual measured quantities. Estimates of the uncertainty of the derived quantities are discussed in the next section and presented in conjunction with the processed data.

For each GF specimen, tests were initially run without heating to establish the pressure drop as a function of flow for ambient (cold) conditions. The tests were then repeated for several power densities to establish the heat transfer under different flow and heating conditions. For each flow/heating condition considered, the fluid pressure drop and the temperatures of the fluid outlet, inlet, and the heater base were carefully monitored to ensure that steady state was achieved before any measurements were recorded.

The maximum flow condition was established on the basis of the maximum pressure drop that the water pumping system could support. The more *closed* foams generated high pressure drops at relatively low flow conditions, while the *open* foams could be run at higher flow conditions without reaching the maximum pressure. The maximum heating condition was established on the basis of the power input supplied to the cartridge heaters at the maximum temperature that could be tolerated by the test apparatus (~100 °C).

3.2 Processing of Experimental Results. Pressure data from the experiments was used to derive permeability and form drag coefficients used in the classical Darcy-Forchheimer law for porous media:

$$\frac{\Delta P}{L} = \frac{\mu}{K}U + \frac{c_f}{\sqrt{K}}\rho U^2 \tag{1}$$

Here, ΔP is the pressure drop across the foam specimen, L is the length of the specimen in the flow direction (50.8 mm in the present work), U is the filter (clear channel) velocity, and K and c_f are the permeability and Forchheimer (form drag) coefficient, respectively. The permeability and form drag coefficient are evaluated simultaneously for a given GF specimen by considering the whole Re range at the tested conditions. The coefficients were obtained using the least-squares method described by Antohe et al. [4]. Uncertainties in the estimation of K and c_f were also calculated using the method described by Antohe et al. [4] and are included in forthcoming tabulated data.

The heat transfer results are cast in terms of a Nusselt number that incorporates geometric and thermal properties of the GF. Care is taken here to ensure that the Nusselt number is not cast in a manner that is dependent upon the physical dimensions of the specimen tested, as is the case in previous work. On the assumption that the temperature at a given distance away from the base plate is approximately uniform, fluid temperature increases can be approximated using the log-mean temperature difference, and the Nusselt number can be defined as (Straatman et al. [11])

$$\mathrm{Nu} = \frac{h_{sf}D}{k_{fa}} = \frac{q}{A_{\mathrm{eff}}\Delta T_{\mathrm{LM}}}\frac{D_e}{k_{fa}} \tag{2}$$

where h_{sf} is the pore-level heat transfer coefficient, D_e is the equivalent particle diameter, k_{fa} is the thermal conductivity of the fluid evaluated at the average fluid temperature, A_{eff} is the effective surface area, ΔT_{LM} is the log-mean temperature difference, $\Delta T_{\mathrm{LM}} = (\Delta T_{\mathrm{out}} - \Delta T_{\mathrm{in}})/\ln(\Delta T_{\mathrm{out}}/\Delta T_{\mathrm{in}})$, where reference is taken to the base temperature of the foam, and q is the heat transfer obtained from an energy balance on the water (and from the power input to the heater). For processing purposes, cases where a difference of more than 10% between electrical power input and the enthalpy rise of the fluid were discarded. In most cases the difference between the electrical input to the heater and the enthalpy rise was less than 5%, indicating that losses from the system were small. The equivalent particle diameter D_e is the solid particle diameter that preserves the interior surface area of a single spherical void and is obtained as (Yu [8])

$$D_e = \frac{6(1-\varepsilon)}{\beta} \tag{3}$$

D_e is chosen as the length scale for the present study because it characterizes the internal structure of the GF. The effective surface area is obtained as

$$A_{\text{eff}} = \eta A_f + A_{bf} \tag{4}$$

where A_f is the interior wall surface area of the foam specimen obtained from $A_f = \beta V$, where β is the area factor (Yu [8]) and V is the volume of the specimen. The area A_{bf} is the bare surface area of the heater that is not covered by the porous foam and is obtained from $A_{bf} = \varepsilon A_b$, where the base area is simply $A_b = 50.8 \times 50.8 = 2580.64$ mm^2. As such, $A_f + A_{bf}$ is the total surface area available for energy exchange. The equivalent micro-fin efficiency η is applied to the interior wall surface area and is used to account for the temperature variation inside the foam. The equivalent micro-fin efficiency of the foam is obtained using (Taylor [12])

$$\eta_f = \frac{\tanh\left(\sqrt{\frac{2h_{sf}}{k_{sf}t}}H\right)}{\sqrt{\frac{2h_{sf}}{k_{sf}t}}H} \tag{5}$$

where k_{sf} is the thermal conductivity of the solid phase of the GF evaluated at the film temperature and t is the thickness of the equivalent micro-fin determined by

$$t = \frac{(1-\varepsilon)}{\varepsilon}\sqrt{\frac{12K}{\varepsilon}} \tag{6}$$

The Taylor model preserves the solid volume fraction of the porous media and determines the fin thickness and number by preserving the hydraulic resistance based on the permeability of the porous media. As such, a connection exists between the thermal and hydraulic resistance due to their interdependence on internal surface area.

Using the equivalent particle diameter, effective surface area, and the log-mean temperature difference to formulate the Nusselt number ensures that the values obtained are not dependent upon the dimensions of the specimen considered and are thus constant for a given foam structure and Reynolds/Prandtl number (Straatman et al. [11]), as should be expected. The forthcoming section on computational modeling confirms this statement by comparing Nu_{De} computed using Eq. (2) for foams of different thicknesses.

4 Experimental Results

Results for the pressure drop as a function of U are shown in Fig. 3 for the GF specimens described in Table 1. The measured results of pressure drop are shown as symbols while the curves have been generated using Eq. (1) with the permeability and form drag coefficients derived and shown in Table 2. It is clear from Table 2 and Fig. 3 that the permeability and thus the pressure drop are very different for the four specimens tested, with the 219-3 foam having the highest fluid pressure drop and POCO™ having the lowest. The large differences in pressure drop between the foam specimens can only be reconciled by considering the properties in Table 1 and the images in Fig. 1. Consider, for example, the difference between the 219-3 and POCO™ foams. The porosity of the 219-3 is higher, which might otherwise indicate a lower pressure drop, but the void diameter of 219-3 is smaller and consequently the internal area is larger, thereby increasing the internal resistance to fluid flow. However, the 20% increase in internal surface area does not alone account for the more-than-twofold increase in pressure drop. From Fig. 1, it is also clear that the cell windows in the 219-3 foam are, on average, considerably smaller than those in the POCO™ foam, and thus there is a much higher hydraulic loss in the 219-3 foam due to the sudden contraction/expansion of fluid through the pore windows. A similar argument can be formed to describe the differences in pressure drop between the 219-3-3 and 218-3 foams.

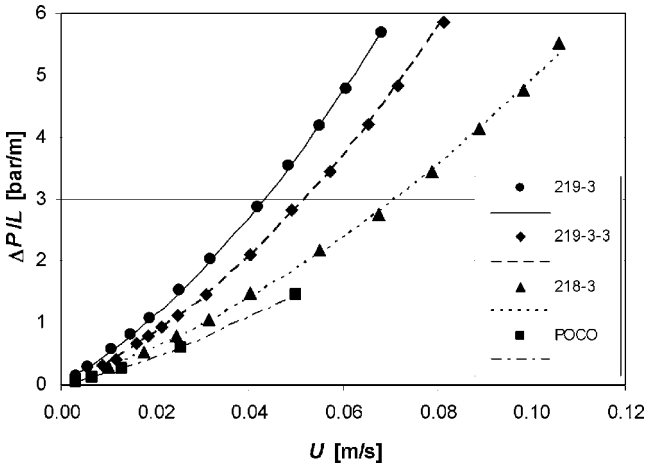

Fig. 3 Plot showing the pressure drop as a function of the filter velocity for the GF specimens considered. The symbols are measured data and the curves are generated from Eq. (1) using the values of permeability and form drag summarized in Table 2.

Since the high pressure losses observed for the GF specimens considered are due mainly to the large hydraulic loss associated with the cell windows that link the spherical voids, it is of interest to modify the foaming process for GF to provide larger and smoother cell windows to decrease c_f and thereby decrease the pressure drop across the foam at the expense of reduced internal surface area. Note that the estimates of internal surface area in Table 1 are derived from the unit-cube geometry model and thus, variations in the area due to cell window size are not accounted for.

The Nusselt number is plotted in Fig. 4 as a function of the Reynolds number, i.e., $\text{Re}_{De} = \rho U D_e / \mu$, where ρ and μ are the density and dynamic viscosity, respectively, of the water. The figure indicates that for most conditions, the 219-3-3 and POCO™ foams have the highest internal heat transfer followed by 219-3 and 218-3. The differences between the specimens can be reconciled by considering the different geometric parameters and effective conductivities summarized in Table 1, and by considering the images in Fig. 1. The largest difference in heat transfer occurs between the 219-3 and 219-3-3 foams. On the basis of internal surface area and effective conductivity, the 219-3 foam might be expected to give the highest heat transfer for a given flow rate, however, an examination of images in Figs. 1(*a*) and 1(*b*) suggests that the difference is likely due to differences in the *available* internal surface area. Plot (*a*) shows a scattering of large pores surrounded by many smaller pores that appear to be noninterconnected (isolated or dead-end). Plot (*b*) shows a more uniform distribution of large pores and fewer isolated or dead-end

Table 2 Summary of permeability and Forchheimer coefficients for the carbon foam specimens tested

Specimen	Permeability K, m^2	Uncertainty of K, ±%	Forchheimer coefficient c_f	Uncertainty of c_f, ±%
219-3	2.41×10^{-10}	8.0	0.7444	6.6
219-3-3	3.47×10^{-10}	9.4	0.7932	6.5
218-3	4.46×10^{-10}	7.9	0.4548	5.7
POCO™	6.13×10^{-10}	7.5	0.4457	8.4

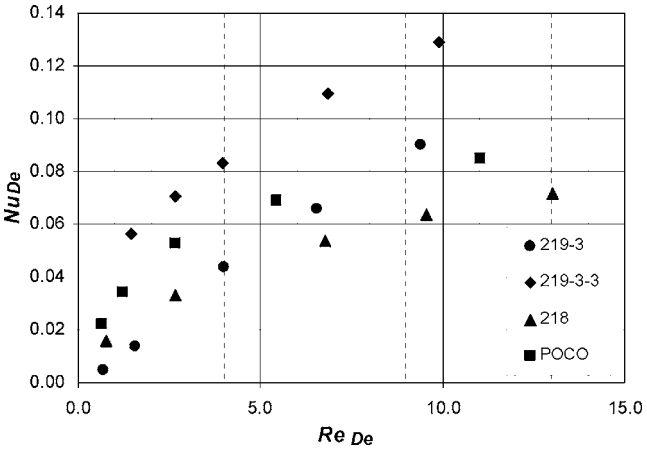

Fig. 4 Plot showing the Nusselt number as a function of Reynolds number based on D_e and A_{eff} for the four GF specimens tested experimentally

pores. Thus, even though the unit-cube approximation for β suggests that 219-3 has a larger internal area, Fig. 1 shows that the 219-3-3 foam has more internal area *available* for convective exchange, and thus a higher heat transfer, as reflected in Fig. 4. While the difference in effective conductivity between the 219-3 and 219-3-3 foams would serve to maintain a higher temperature difference inside the 219-3 foam, the difference is evidently not large enough to offset the difference in available surface area.

Considering the 219-3-3 and POCO™ foams, differences in the geometric and thermal properties are substantial, while the difference in heat transfer is not. Comparing the SEM images, it is clear that the 219-3-3 foam has more available internal surface area: the 219-3-3 foam contains mainly large pores with small cell windows and the POCO™ foam has relatively uniform large pores with larger cell windows. Thus, the difference in internal surface area given in Table 1 is reasonable. In this case, the higher thermal conductivity of the POCO™ foam is enough to offset the difference in internal area and the foams have a similar thermal performance. Because of the higher effective conductivity, the POCO™ foam would yield a higher performance for thicker specimens owing to the higher equivalent micro-fin efficiency.

Of the specimens tested, the POCO™ foam offers the best combination of hydrodynamic and thermal performance and is considered as the GF benchmark in the forthcoming section on computational modeling where GF is compared to aluminum foam.

5 Computational Modeling

To facilitate comparisons between the GF considered herein and aluminum foam, simulations have been carried out using the three-dimensional finite-volume code developed by Betchen et al. [9]. In this formulation, the volume averaged continuity equation is expressed in the form

$$\rho_f(\nabla \cdot \langle \mathbf{u} \rangle) = 0 \tag{7}$$

where ρ_f is the fluid density, $\mathbf{u}$ is the velocity vector and $\langle\rangle$ indicates an extrinsically averaged quantity; i.e., the average is taken over a representative volume containing both fluid and solid constituents. The extrinsic form of the momentum equation in the porous region is given by

$$\rho_f \frac{\partial \langle \mathbf{u} \rangle}{\partial t} + \frac{\rho_f}{\varepsilon} \nabla \cdot (\langle \mathbf{u} \rangle \langle \mathbf{u} \rangle) = -\varepsilon \nabla \langle P \rangle^f + \mu_f \nabla^2 \langle \mathbf{u} \rangle - \frac{\varepsilon \mu_f}{K} \langle \mathbf{u} \rangle - \frac{\varepsilon \rho_f c_f}{\sqrt{K}} |\langle \mathbf{u} \rangle| \langle \mathbf{u} \rangle \tag{8}$$

where ε is the porosity, which is defined as $\varepsilon = V_f/V$ (volume occupied by fluid/total volume), and μ_f is the dynamic viscosity of the fluid. The second term on the right hand side of Eq. (8) represents the macroscopic viscous effects, and is historically referred to as the Brinkman term. While the Brinkman viscosity might be expected to be larger than the fluid viscosity to account for momentum dispersion, determination of this value remains an open problem and thus, the fluid viscosity is used herein to account for viscous effects. Previous work (see [6] and [9]) has shown this to be a suitable assumption. The third and fourth terms are the familiar Darcy and Forchheimer terms that describe, respectively, the viscous and form drag interaction between the fluid and solid constituents that is lost in volume averaging the velocity field. In these terms, the permeability K and the drag coefficient c_f, are required as inputs to characterize the porous region.

Because of the large differences in solid phase conductivity between the solid and fluid constituents, the heat transfer problem in the porous region is treated under the assumption of local thermal non-equilibrium; i.e., we do not assume that $\langle T_f \rangle^f = \langle T_s \rangle^s = \langle T \rangle$ at a given point. This gives rise to extrinsic volume averaged energy equations of the form

$$\rho_f c_{p,f} \left[\varepsilon \frac{\partial \langle T_f \rangle^f}{\partial t} + \nabla \cdot (\langle \mathbf{u} \rangle \langle T_f \rangle^f) \right] = k_{fe} \nabla^2 \langle T_f \rangle^f + h_i A_{sf} (\langle T_s \rangle^s - \langle T_f \rangle^f) \tag{9}$$

$$(1-\varepsilon) \rho_s c_s \frac{\partial \langle T_s \rangle^s}{\partial t} = k_{se} \nabla^2 \langle T_s \rangle^s - h_i A_{sf} (\langle T_s \rangle^s - \langle T_f \rangle^f) \tag{10}$$

for the fluid (f) and solid (s) constituents, respectively. Here, T is the temperature and k_{fe} is the conductivity, which includes both molecular diffusion and thermal dispersion components. The heat exchange between the fluid and solid constituents is modeled using an interstitial convective exchange model (last term in Eqs. (9) and (10)). It is important to note that interstitial exchange is not equivalent to bulk convective heat transfer unless thermal dispersion is negligible, and this is not the case herein. Thermal dispersion arises in the fluid energy equation as a result of volume averaging and accounts essentially for transport effects due to fluctuations in the temperature field about the volume-averaged temperature. In essence, thermal dispersion distributes energy within the porous continuum, such that higher temperature differences and thus higher interstitial exchange occurs. Thermal dispersion is modeled as an enhancement to the molecular conductivity of the fluid and can thereby contribute significantly to the bulk convective heat transfer of a porous media. Thermal dispersion is modeled herein using the expression developed by Calmidi and Mahajan [6]. Since thermal dispersion is a hydrodynamic effect that can be affected by the internal structure of a porous material, the validity of the Calmidi and Mahajan [6] model for GF is discussed in terms of the present results. The interstitial convective exchange coefficient h_i is obtained locally from an expression of the form

$$\mathrm{Nu}_L = \frac{h_i L}{k_f} = C\,\mathrm{Re}^m\,\mathrm{Pr}^n, \tag{11}$$

which can be calibrated using experimental results to give the correct overall heat transfer for any type of porous media. In Eq. (11), L is simply the length scale used for the definition of the Nusselt number. For simulations of aluminum foam, the expression for internal surface area and the parameters C, m, and n were obtained from Calmidi and Mahajan [6] and are listed in Table 3; the length scale used was the ligament diameter. For simulations of GF, the internal surface area was obtained using $A = \beta V$ (Yu et al. [8]), where V is the volume of the cell, and the parameters C, m, and n were obtained by calibration with the results for POCO™ foam (described below). In this case the length scale used was the equivalent particle diameter D_e. Darcy and Forchheimer coefficients for aluminum foam were obtained from Boomsma et al. [7]

Table 3 Parameters for the interstitial exchange model for aluminum foam and GF

Source	Material	C	m	n
Calmidi and Mahajan [6]	Aluminum foam	0.520	0.50	0.37
Present experiments	GF	0.018	0.27	0.33

and for GF from Table 2. Readers are directed to Betchen et al. [9] for a detailed description of the discretization procedure used.

Computations were carried out for the domain shown in Fig. 5. A conjugate domain that included upstream and downstream sections was also considered, but differences in overall heat transfer were less than 2% and changes in pressure drop were less than 1% between the foam-only and conjugate domains, with differences concentrated to a very short (less than 1 mm) region adjacent to the inlet of the foam. Thus, the computational domain was 50.8 $\times$6 mm in cross section and 50.8 mm long, the exact dimensions of the GF specimens tested experimentally. A uniform velocity profile combined with a pressure extrapolation was imposed at the inlet boundary, while a pressure value and zero-velocity gradients were imposed on the outlet plane. The lateral and lower walls of the channel were considered to be no-slip, impenetrable, and adiabatic. The upper wall was also no-slip and impenetrable, with the addition of a constant temperature condition. Calculations were conducted on grids of $20\times20\times20$ and $30\times30\times30$ non-uniform grids to ensure that the results were independent of grid density. In both cases, volumes were concentrated towards the solid boundaries where velocity and temperature gradients were expected to be highest. The reported results are grid independent to within 0.5% for both heat transfer and pressure drop.

The first step in the computational modeling was calibration of the computational model for POCO™ foam. While the values of K and c_f were simply obtained from Table 2, calibration of the interstitial exchange model was done by systematically adjusting C and m ($\mathrm{Pr}^{0.33}$ was set since only one Pr was tested) and running the model over the full range of Re_{De} considered until the difference between the predicted overall heat transfer and the measured heat transfer was minimized. For each case computed in the calibration step, the flow rate, the temperature difference between the heated base of the foam and the fluid inlet, and the overall heat transfer were obtained from experiments on POCO™ foam. Figure 6 compares the computed and measured results obtained using the calibrated values of C, m, and n listed in the second row of Table 3. The results shown in Fig. 6 are for the pore-level Nusselt number described in Eq. (2) and obtained using the approach described in Sec. 3.1. The fact that there is excellent agreement between the computed and experimental results does not alone confirm that the interstitial exchange and thermal dispersion models are accurate. To validate that the interstitial convection and augmentation due to thermal dispersion in the computational fluid

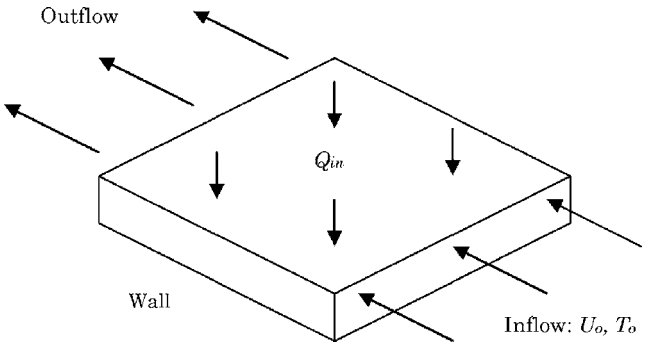

Fig. 5 Schematic of computational domain for porous plug computations

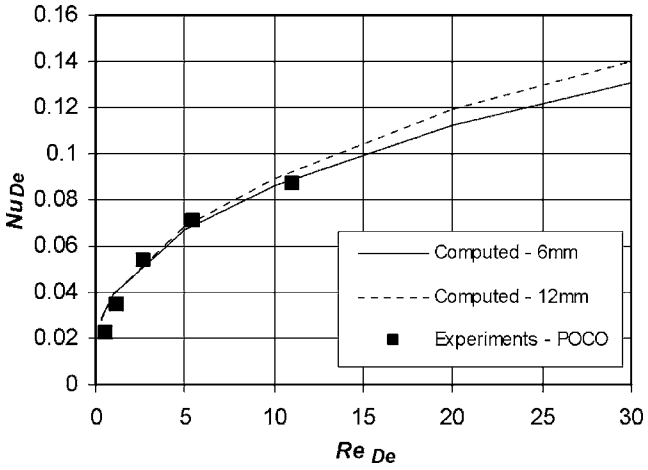

Fig. 6 A comparison of the computed and measured results for Nusselt number as a function of Reynolds number for calibration of the computational model

dynamics model are correct, a second test case was run in which the thickness of the foam was doubled to 12 mm (the grid for this test case was also doubled to maintain the density of the original case). For this set of simulations, the bulk velocity and the temperature difference of the original test cases were maintained so that differences between the results could be related solely to the increase in foam thickness. Results for the 12 mm thick GF block are also shown in Fig. 6 and are observed to be essentially the same as the results for the 6 mm thick block over the full range of Re_{De} considered (at the highest Re_{De} considered, the difference in Nu_{De} is less than 3.7%). That the results for Nu_{De} are essentially the same independent of the block thickness considered confirms that the interstitial exchange and thermal dispersion are approximately correct for the GF simulations. To explain, if the local thermal dispersion conductivity was too large, the temperature difference between the solid and fluid phases would be artificially too large, resulting in high heat transfer rates near the heated wall, but an artificially poor distribution of heat away from the wall. Because of the poor use of internal area, this would result in a lower overall heat transfer and ultimately an overall Nusselt number that is too low. The opposite would be true if the thermal dispersion model produced values of k_{ef} that were too low. Since the Nusselt number based on the overall heat transfer is predicted to be essentially the same independent of the foam thickness, it is reasonable to assume that the temperature distributions of the fluid and solid phases inside the foam and the models for interstitial exchange and thermal dispersion are also approximately correct.

The calibrated model is now used to explore differences between POCO™ foam and the aluminum foams considered by Calmidi and Mahajan [6] and by Boomsma et al. [7]. Figures 7 and 8 show the pressure drop and heat transfer as a function of filter (clear channel) velocity for POCO™ foam and for an uncompressed aluminum T-6201 foam with a porosity of 90% and effective conductivity 7.19 W/m K, as reported in Calmidi and Mahajan. The plots are shown in terms of the filter velocity instead of Re_{De} to make the differences at a given flow condition more clear. Even though the Reynolds and Nusselt numbers (based on D_e) give the most compact characterization of the material, differences between the internal structures of GF and aluminum foam yield very different ranges of values, which make direct comparisons difficult. For the comparisons shown in Figs. 7 and 8, the foam blocks were simulated for the same heating condition (set using a specified base and inlet temperature) over a range of bulk velocities to expose differences between the hydraulic and thermal characteristics of the materials. On the basis of Fig. 7, it is clear that the aluminum foam has a considerably lower

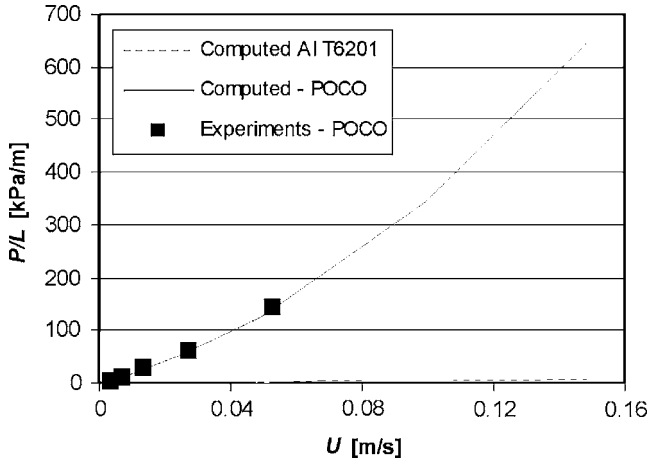

Fig. 7 Plot of the pressure drop as a function of the filter velocity for POCO™ foam and for Al T6201 foam

pressure drop than GF over the entire range tested. This is largely due to differences between the porosities and internal structures of the aluminum foam and GF: the aluminum foam has a high porosity and is comprised of thin fused strands and large open cell windows, but relatively little internal surface area. The GF has a moderate porosity and is comprised of spherical voids and small(er) cell windows, but with a lower porosity and much larger internal surface area.

Figure 8 shows the heat transfer for 6 mm thick and 12 mm thick blocks of POCO™ and Al T-6201 foams computed using the same bulk velocity and heating conditions. At a 6 mm thickness, the Al T-6201 foam has a higher heat transfer across the full range of conditions considered. However, when the thickness of the Al T-6201 foam is doubled, no increases in heat transfer are realized at any flow rate. In contrast, doubling the thickness of the POCO™ foam leads to increases in heat transfer from 85% at low velocity to 50% at high velocity. These observations can be explained by considering the balance between heat conduction (or entrainment) into the foam and the convective exchange between the foam and the fluid. For aluminum foam, the entrainment into the foam is limited by the solid-phase conductivity of the aluminum material and by the small amount of material available for conduction. However, the convective heat transfer coefficient for aluminum (and other reticulated foams) is quite high due to the pore-level ligament structure. Thus, even though heat is only entrained a small distance into the foam, the convective resistance is quite

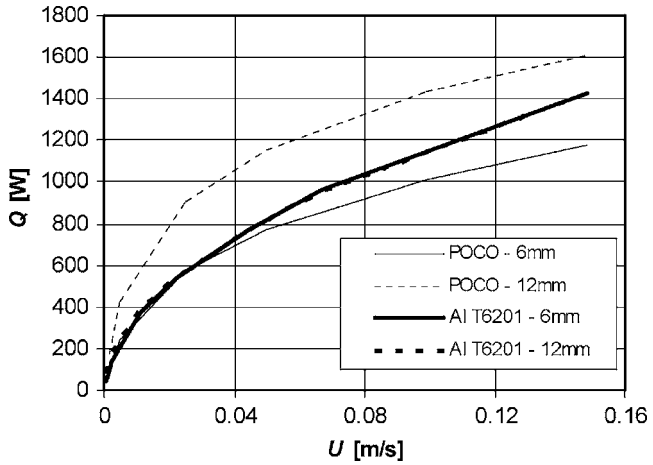

Fig. 8 Plot of the heat transfer as a function of filter velocity for POCO™ foam and for Al T6201 foam

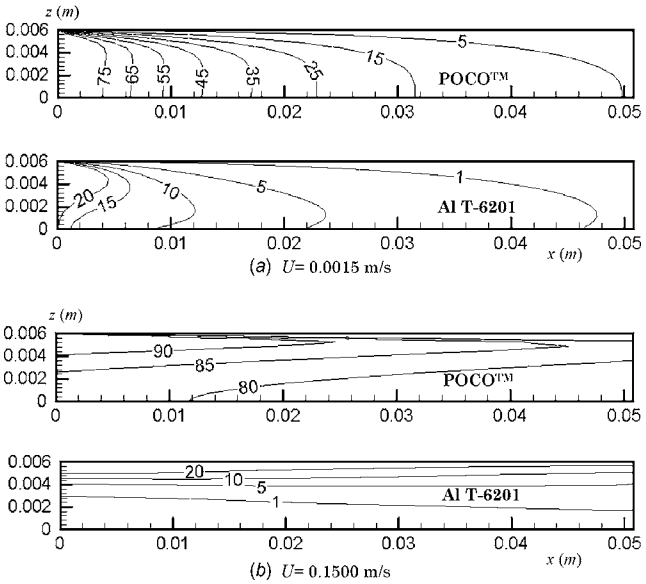

Fig. 9 Local thermal non-equilibrium distributions on the *x-z* center plane for (*a*) *U*=0.0015 m/s, and (*b*) *U*=0.1500 m/s. The local thermal non-equilibrium is defined as: $(T_s-T_f)/(T_b-T_o)\times 100$.

small resulting in reasonably good heat transfer. The fact that doubling the thickness results in no increases in heat transfer confirms that heat is not entrained deeply into the foam and that the maximum possible heat transfer for a given base surface area is achieved using a very thin layer of aluminum foam. For POCO™ foam, the pore-level convective heat transfer coefficient is considerably smaller than that for aluminum foam, but the lower porosity and much higher conductivity serve to entrain heat much deeper into the foam, thereby making use of much more available surface area. At 6 mm thick, POCO™ foam removes less heat than Al T-6201 foam, but at 12 mm, the heat transfer has increased above that of aluminum foam, without yet reaching its maximum possible heat dissipation.

To further elucidate on the differences between the internal heat transfer in aluminum foam and GF, Fig. 9 shows plots of the thermal non-equilibrium on the lateral center-plane of the POCO™ and aluminum foams at low (*a*) and high (*b*) bulk velocities. The local thermal non-equilibrium is defined as: $(T_s-T_f)/(T_b-T_o)\times 100$, where T_b-T_o is the difference between the temperature of the heater base and the inlet fluid and represents the maximum temperature difference in the system. As such, the contour values in Fig. 9 represent the fraction of the maximum temperature difference in percent. The plots show that for both low and high velocity, there is a substantial temperature difference throughout the POCO™ foam, and thus a very well distributed heat transfer potential. For the uncompressed aluminum foam, significant temperature differences only occur near the heated surface, which indicates that heat transfer is restricted to a very thin layer of foam even under low flow conditions. The plots for the aluminum foam suggest that the foam could be made even thinner without significantly degrading the net heat transfer.

Comparisons are also made to the compressed aluminum specimens considered by Boomsma et al. [7] by conducting simulations of $40\times 40\times 2$ mm thick blocks of POCO™ foam and processing the predicted pressure drops and Nusselt numbers as done in [7]. Comparisons are done in this manner because no expressions for interstitial exchange exist to facilitate computational modeling of compressed aluminum foams. Figure 10 compares the pressure drop of POCO™ with that of three different compressed aluminum foams: 92-02, 92-03, and 92-06, where the $-0X$ indicates the compression ratio based on the volume. Figure 10 makes it clear that

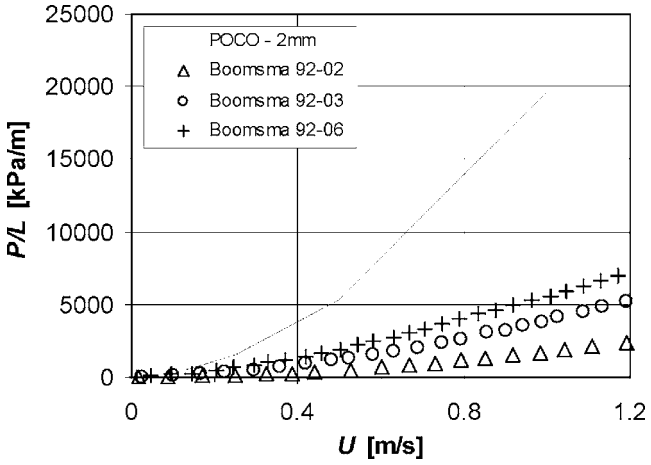

Fig. 10 Plot of the pressure drop as a function of filter velocity for POCO™ foam compared to three different compressed aluminum foams as reported in Boomsma et al. [7]

compression decreases the permeability of the foam and increases the Forchheimer coefficient c_f, but the pressure drop is still significantly lower than that of POCO™ over the same range of bulk velocities, again owing to the large hydraulic loss associated with the contraction/expansion of fluid through the cell windows. Figure 11 shows the Nusselt number based upon the heated area and the temperature difference between the heated base and the fluid inlet. The heat transfer for the compressed aluminum samples is seen to approach that of POCO™ foam for high compression ratios. It is expected that under compression, the local convective heat transfer coefficient decreases, but this is offset by the increase in available internal surface area, thereby yielding a lower net thermal resistance. On the basis of Figs. 10 and 11, it appears that the highly compressed aluminum offers an equivalent heat transfer for a significantly lower pressure drop, but it is important to note that this will only be the case for very thin layers of foam. As shown in the comparison with uncompressed aluminum foams, if the thickness of the samples was doubled or tripled, the POCO™ foam would yield significantly higher heat transfer than any derivative of compressed aluminum foam due to its high extended surface efficiency.

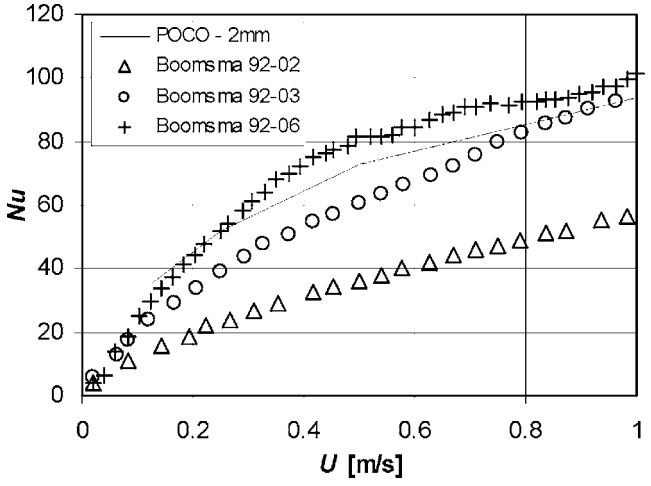

Fig. 11 Plot of the Nusselt number (as defined in Boomsma et al. [7]) as a function of filter velocity for POCO™ foam compared to three different compressed aluminum foams as reported in Boomsma et al. [7]

On the basis of the comparisons given in this section, it is evident that GF (POCO™ in particular) in its existing form has heat transfer characteristics that offer a significant advantage over uncompressed and compressed aluminum, however, at the cost of a higher hydraulic resistance. It is clear from the present work that there is a severe limitation in maximum heat dissipation from a given base surface area when using aluminum foam due to the combination of very high porosity and low solid-phase conductivity. Graphitic foams with their moderate porosity and much higher conductivity transcend this heat transfer limitation and thus, provide much higher heat dissipation for a given base surface area. The advantages of using GF as a heat transfer material would become even more impressive if the permeability of the foam is increased since this will serve to decrease the pressure drop and potentially increase the pore-level convective heat transfer.

6 Closing Remarks

Measurements of the pressure drop and heat transfer obtained by forcing water through blocks of porous carbon foam are reported. The pressure drop is seen to mainly be affected by the size of the cell windows connecting the spherical pores, due to the large hydrodynamic loss associated with the fluid contracting/expanding through the windows. Of the specimens tested, POCO™ foam offers the best combination of hydrodynamic and thermal performance. The experimental results for POCO™ foam were used to calibrate a numerical model such that comparisons could be made with existing literature on normal and compressed aluminum foams. The computed results indicate that both normal and compressed aluminum foams produce significantly lower pressure drops than POCO™ for equivalent flow rates. The results also show that the extended surface efficiency of POCO™ foam is much higher than any aluminum foam due to the high solid phase conductivity and moderate porosity of GF. The comparisons suggest that while the current aluminum foams have good thermal performance for thin layers, the graphitic foams offer a significant overall advantage for cases where a significant amount of heat needs to be removed from a given base surface area.

Acknowledgment

This work has been sponsored by the Automotive Propulsion Materials Program, DOE Office of FreedomCAR and Vehicle Technology Program, under contract DE-AC05-00OR22725 with UT-Battelle, LLC, and by the Natural Science and Engineering Research Council of Canada (NSERC).

References

[1] Klett, W. J., Hardy, R., Romine, E., Walls, C., and Burchell, T., 2000, "High-Thermal Conductivity, Mesophase-Pitch-Derived Carbon Foam: Effect of Precursor on Structure and Properties," Carbon, **38**, pp. 953–973.
[2] Gallego, C. N., and Klett, W. J., 2003, "Carbon Foams for Thermal Management," Carbon, **41**, pp. 1461–1466.
[3] Paek, W. J., Kang, H. B., Kim, Y. S., and Hyum, M. J., 2000, "Effective Thermal Conductivity and Permeability of Aluminum Foam Materials," Int. J. Thermophys., **21**(2), pp. 453–464.
[4] Antohe, B. V., Lage, J. L., Price, D. C., and Weber, R. M., 1997, "Experimental Determination of Permeability and Inertia Coefficients of Mechanically Compressed Aluminum Porous Matrices," ASME J. Fluids Eng., **119**, pp. 404–412.
[5] Boomsma, K., and Poulikakos, D., 2002, "The Effects of Compression and Pore Size Variations on the Liquid Flow Characteristics in Metal Foams," ASME J. Fluids Eng., **124**, pp. 263–272.
[6] Calmidi, V. V., and Mahajan, R. L., 2000, "Forced Convection in High Porosity Metal Foams," ASME J. Heat Transfer, **122**, pp. 557–565.

[7] Boomsma, K., Poulikakos, D., and Zwick, F., 2003, "Metal Foams as Compact High Performance Heat Exchangers," Mech. Mater., **35**, pp. 1161–1176.
[8] Yu, Q., Thompson, B. E., and Straatman, A. G., 2006, "A Unit-Cube Based Model for Heat Transfer and Pressure Drop in Porous Carbon Foam," ASME J. Heat Transfer, **128**, pp. 352–360.
[9] Betchen, L. J., Straatman, A. G., and Thompson, B. E., 2006, "A Non-Equilibrium Finite-Volume Model for Conjugate Fluid/Porous/Solid Domains," Numer. Heat Transfer, Part A, **49**, pp. 543–565.
[10] Incropera, M., and Dewitt, F., 2003, *Fundamentals of Heat and Mass Transfer*, Wiley, New York.
[11] Straatman, A. G., Gallego, N. C., Yu, Q., and Thompson, B. E., 2006, "Characterization of Porous Carbon Foam as a Material for Compact Recuperators," ASME Paper No. GT2006-90598.
[12] Taylor, G. I., 1971, "A Model for the Boundary Condition of a Porous Material. Part 1," J. Fluid Mech., **49**, pp. 319–326.

S. S. Sazhin[1]
T. Kristyadi

School of Engineering,
University of Brighton,
Cockcroft Building,
Brighton BN2 4GJ, U.K.

W. A. Abdelghaffar
Mechanical Engineering Department,
Faculty of Engineering,
Alexandria University,
Alexandria 21544, Egypt

S. Begg
M. R. Heikal

School of Engineering,
University of Brighton,
Cockroft Building,
Brighton, BN2 4GJ, U.K.

S. V. Mikhalovsky
S. T. Meikle
O. Al-Hanbali[2]

School of Pharmacy and Biomolecular Sciences,
University of Brighton,
Cockcroft Building,
Brighton BN2 4GJ, U.K.

Approximate Analysis of Thermal Radiation Absorption in Fuel Droplets

The values of absorption coefficients of gasoline fuel (BP Pump Grade 95 RON ULG (research octane number unleaded gasoline)), 2,2,4-trimethylpentane $(CH_3)_2CHCH_2C(CH_3)_3$ *(iso-octane) and 3-pentanone* $CH_3CH_2COCH_2CH_3$ *have been measured experimentally in the range of wavelengths between* 0.2 μm *and* 4 μm. *The values of the indices of absorption, calculated based on these coefficients, have been compared with those previously obtained for low sulphur ESSO AF1313 diesel fuel. These values are generally lower for pure substances (e.g., iso-octane and 3-pentanone) than for diesel and gasoline fuels. The values of the average absorption efficiency factor for all fuels are approximated by a power function* aR_d^b, *where* R_d *is the droplet radius. a and b in turn are approximated by piecewise quadratic functions of the radiation temperature, with the coefficients calculated separately in the ranges of droplet radii* 2–5 μm, 5–50 μm, 50–100 μm, *and* 100–200 μm *for all fuels. This new approximation is shown to be more accurate compared with the case when a and b are approximated by quadratic functions or fourth power polynomials of the radiation temperature, with the coefficients calculated in the whole range* 2–200 μm. *This difference in the approximations of a and b, however, is shown to have little effect on modeling of fuel droplet heating and evaporation in conditions typical for internal combustion engines, especially in the case of diesel fuel and 3-pentanone.*
[DOI: 10.1115/1.2740304]

Keywords: absorption efficiency factor, fuel droplets, thermal radiation, heating, evaporation

1 Introduction

The importance of droplet and particle radiative heating in various engineering applications has been extensively discussed in the literature (e.g., Refs. [1–4]). A more specific analysis of the effects of thermal radiation on the processes in diesel engines were reported in Refs. [5–8]. In the later paper, it was indicated that the effect of thermal radiation on droplet heating in diesel engines is expected to be particularly strong if the fuel injection takes place at a time when autoignition has already occurred. In this case, the temperature of the remote flame, responsible for droplet radiative heating, is much higher than the ambient gas temperature, responsible for droplet convective heating.

In a series of papers, simplified yet accurate models describing the thermal radiation absorption in diesel fuel droplets have been developed. In the model suggested in Ref. [9] and further developed in Ref. [10], detailed Mie calculations were replaced by the approximation of the absorption efficiency factor for droplets with an analytical formula aR_d^b, where R_d is the droplet radius and a and b are polynomials (quadratic functions in most cases) of the gas temperature. The coefficients of these polynomials were found by comparison with rigorous computations for realistic diesel fuel droplets, assuming that these droplets are irradiated by blackbody thermal radiation. This model allowed the authors to attain a reasonable compromise between accuracy and computational efficiency. This is particularly important for the implementation of the thermal radiation model into multidimensional computational fluid dynamics (CFD) codes designed to simulate combustion processes in diesel engines [11].

In Refs. [12–15] more advanced models for radiation absorption in diesel fuel droplets have been developed. These take into account the distribution of absorption inside droplets. None of these models, however, seem to be suitable for implementation into CFD codes due to excessive CPU requirements [16–19]. Therefore in practical applications, implementing the distribution of radiation absorption inside droplets seems to be of limited potential. There are two main shortcomings in the model developed in Refs. [9,10]. First, the analysis of these papers was focused only on diesel fuels (although various types of these fuels were considered in Ref. [10]). Second, the accuracy of the aforementioned approximation of the absorption efficiency factor was shown to be rather poor when the range of droplet radii was large (typical values of droplet radii in diesel engines are in the range 2–200 μm). The focus of this paper is mainly to address these matters.

The results of experimental studies of the optical properties of

[1]Corresponding author. e-mail: S.Sazhin@brighton.ac.uk
[2]Presently at: Faculty of Pharmacy, An-Najah National University, P. O. Box-7, Jordan, e-mail: othman4791@hotmail.com
Contributed by the Heat Transfer Division of ASME for publication in the JOURNAL OF HEAT TRANSFER. Manuscript received June 23, 2006; final manuscript received January 18, 2007. Review conducted by A. Haji-Sheikh.

gasoline fuel (BP Pump Grade 95 RON ULG), 3-pentanone, and 2,2,4-trimethylpentane (iso-octane) are presented and discussed in Sec. 2. The results are compared with the results for diesel fuel reported earlier in Ref. [10]. A new approximation for the efficiency factor of absorption of all these fuels in a wide range of droplet radii is suggested and discussed in Sec. 3. The results predicted by various approximations are compared in Sec. 4. In Sec. 5 the new approximation for the efficiency factor of absorption is applied to simulate heating and evaporation of fuel droplets. The main results of the paper are summarized in Sec. 6.

2 Optical Properties of Fuels

Three fuels (i) gasoline fuel (BP Pump Grade 95 RON ULG); (ii) iso-octane $(CH_3)_2CHCH_2C(CH_3)_3$; and (iii) 3-pentanone $CH_3CH_2COCH_2CH_3$ were used for the analyses. Iso-octane and 3-pentanone are most often used in experimental studies of gasoline fuel sprays and mixture preparation: iso-octane is 100 RON gasoline and 3-pentanone is used as a fluorescent dopant for laser induced fluorescence (LIF). The results were compared with the earlier results for low sulphur ESSO AF1313 diesel fuel, hereafter referred to as diesel fuel. The absorption coefficients of fuels were measured in the ranges 0.2–0.8 μm and 0.4–4 μm. Ultraviolet (UV)-visible spectra (0.2–0.8 μm) were obtained using a UV-visible spectrophotometer Shimadzu, model 1601. The spectra were recorded in a 1 cm quartz cell for samples diluted with *n*-hexane. In the range 0.4–4 μm the absorption coefficients were measured using a Fourier transform infrared (FTIR) spectrometer, (Nicolet FT-IR Avatar). A resolution of 8 cm^{-1} was used, recording 32 scans in a NaCl cell with an optical pathlength of 0.025 mm. The background was recorded as the empty NaCl cell. All samples were diluted with chloroform and all measurements were carried out at room temperature. In all cases, the dilution was used when the value of the absorption coefficient exceeded the measuring limit of the instrument. The corrections for dilutions were made. In contrast to the case previously reported in Ref. [10], infrared spectra (4–6 μm) could not be measured, as the FTIR spectrometer (Nicolet FT-IR Nexus) was not operational. The measurement error for the absorption coefficient was approximately 5% across the whole range of wavelengths.

In the range 0.4–0.8 μm the difference between the results obtained using these methods was generally small. Over this range the results obtained using a UV-visible spectrophotometer were considered to be more reliable than those obtained using a Fourier transform infrared spectrometer. The reason for this is that as one approaches the upper and lower measurement limits of the spectrometer the signal to noise ratio decreases, leading to incorrect readings.

Results of the calculation of the indices of absorption for all three fuels, based on the measurements of the corresponding absorption coefficient, are presented in Fig. 1. In the same figure, the previously reported plot in Ref. [10] of κ versus λ for diesel fuel is reproduced. About 2300 individual measurements were used for presenting each of these plots. As can be seen in Fig. 1, the dependence of κ on the type of fuel is noticeable, and there are a number of similarities between the plots. For all fuels, the region of semi-transparency in the range 0.5 μm $<\lambda<$ 1 μm is evident. The index of absorption increases by approximately three orders of magnitude when λ increases from 0.5 μm to 1.5 μm. At the same time, some noticeable differences between the indices of absorption of the fuels can be identified. For example, the peak of absorption of diesel fuel at $\lambda \approx 3.4$ μm is much more pronounced than the corresponding peaks of absorption of the other fuels. Also the value of λ when this peak is observed is shifted from 3.4 μm for diesel fuel to approximately 3.0 μm for other fuels.

Strong peaks at around 3.5 μm are related to C–H stretch vibrations of nonaromatic molecules, occurring in the range of 3.3–3.5 μm. Less intense peaks at around 3.0 μm are most likely due to the presence of aromatic hydrocarbons, in which C–H stretch vibrations from benzene rings are expected. This is supported by the absorbance at around 0.25 μm which is characteristic of the $\pi-\pi$ electron transitions in the aromatic benzene ring. Aromatic hydrocarbons are added to gasoline to increase its octane number.

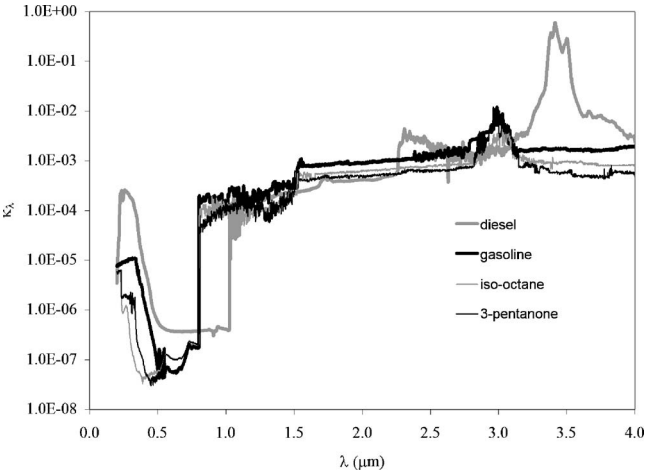

Fig. 1 Indices of absorption of four types of fuel (low sulphur ESSO AF1313 diesel fuel, gasoline fuel (BP Pump Grade 95 RON ULG), 2,2,4-trimethylpentane (iso-octane), and 3-pentanone) versus wavelength λ. The results for diesel fuel are reproduced from Ref. [10].

The differences in the optical properties of the fuels shown in Fig. 1 are expected to produce different values of the average absorption efficiency factors of fuel droplets (see Sec. 3).

Index of refraction measurements were conducted using the ABBE 60 direct reading refractometer at room temperature. This index was measured by turning a dual prism combination through an angle, which is proportional to the refractive index of liquid placed between the two prisms. The light source was white. It was emitted from a tungsten lamp. The angle of light emerging from the combination of prisms was measured using a telescope that moved over a calibrated refractive index scale. The telescope was focused on the edge of the light beam, which showed up as a dark edge in the field of view. The values of refractive indices for the three fuels were: gasoline ($n=1.394\pm0.001$); iso-octane ($n=1.389\pm0.001$), and 3-pentanone ($n=1.390\pm0.001$). The measurement of the index of refraction for diesel fuel was $n=1.460$ with similar error except in the region of strong absorption ($\lambda \approx 3.4$ μm) [20]. The relatively weak dependence of n on λ for diesel fuel has only a minor effect on the efficiency factor of absorption of this fuel [20]. Therefore, this dependence can be ignored when this factor is calculated for diesel fuel [10]. We assume that this conclusion remains valid for other fuels.

3 Average Efficiency Factor of Absorption

Following Refs. [9,10,21] the absorption efficiency factor of droplets Q_a at a given wavelength λ obtained using detailed Mie calculations, is approximated as

$$Q_a = \frac{4n}{(n+1)^2}[1-\exp(-4\kappa x)] \tag{1}$$

where $x=2\pi R_d/\lambda$ is the droplet diffraction parameter (cf. Fig. 1 of Ref. [9]). This equation gives a better approximation for Q_a when compared with that used in Ref. [9].

As in Refs. [9,10], it is assumed that the dependence of the incoming radiation intensity on λ is close to that of a blackbody. Using Eq. (1) the averaged (over wavelengths) absorption efficiency factor of droplets is calculated as

$$\overline{Q_a} = \frac{4n}{(n+1)^2}\left\{1 - \left[\int_{\lambda_1}^{\lambda_2} \frac{\exp\left(-\frac{8\pi\kappa R_d}{\lambda}\right)}{\lambda^5[\exp(C_2/(\lambda\theta_R)) - 1]}d\lambda \Big/ \int_{\lambda_1}^{\lambda_2} \frac{d\lambda}{\lambda^5[\exp(C_2/(\lambda\theta_R)) - 1]}\right]\right\} \quad (2)$$

where $C_2 = 1.439 \times 10^4$ μm K and θ_R is the radiation temperature. This temperature is equal to the external temperature responsible for radiative heating, T_{ext}, in the case of an optically thin gas and to gas temperature, T_g, in the case of an optically thick gas.

The accuracy of Eq. (2) increases with the increased separation between λ_1 and λ_2. The separation is limited by the available experimental facilities. In our case this range is between 0.2 μm and 4 μm. This, however, is not the major limitation of the model; over the range of the most important radiation temperatures for diesel engine applications (1000–3000 K), the values of λ at which the intensity of blackbody radiation is maximum (λ_{max}), lie in the range between 0.97 μm and 2.90 μm. Since these values of λ_{max} lie in the range of wavelengths at which the measurements were performed and the intensity of thermal radiation decreases rapidly when $|\lambda - \lambda_{max}|$ increases, it can be assumed that limits 0.2 μm and 4 μm for λ provide reasonably accurate values of $\overline{Q_a}$ as predicted by Eq. (2).

To illustrate the effect of the range of λ on the value of $\overline{Q_a}$, the calculations have been performed for low sulphur ESSO AF1313 diesel fuel in the range 0.2–4 μm, using data for κ shown in Fig. 1 and for the same fuel in the range 0.2–6 μm, using data for κ reported in Ref. [10]. The results of these calculations are shown in Fig. 2 in the form of the plots of $\overline{Q_a}$ versus droplet radius, for three radiation temperatures: 1000 K, 2000 K, and 3000 K. The curves calculated in these ranges are close for all three temperatures. Except for the smallest droplet radii, the deviation between these curves does not exceed 10%. This is comparable with the errors introduced by a number of other assumptions in the model. These include errors introduced by approximation (1) (see Ref. [9] for the analysis of the accuracy of this approximation) and errors introduced by the assumption that the external radiation is that of a blackbody.

The contribution of thermal radiation absorption at $\lambda < 0.2$ μm can be safely ignored for all three temperatures (it is well below 0.03%). The maximal possible contribution of thermal radiation absorption at $\lambda > 6$ μm (assuming that all external radiation at these wavelengths is absorbed in droplets) is expected to be 26% for $\theta_R = 1000$ K, 5% for $\theta_R = 2000$ K, and 2% for $\theta_R = 3000$ K. A more realistic contribution of thermal radiation absorption in this range of λ is expected only from a strong absorption band in the 6.8–7.5 μm region. In the case of $\theta_R = 1000$ K, $\theta_R = 2000$ K, and $\theta_R = 3000$ K, the maximal contribution from the later range is estimated to be 3.8%, 0.9%, and <0.3%, respectively. This is well below the errors shown in Fig. 2. Hence, the application of data presented in Fig. 1 for calculation of $\overline{Q_a}$ based on Eq. (2) can be justified.

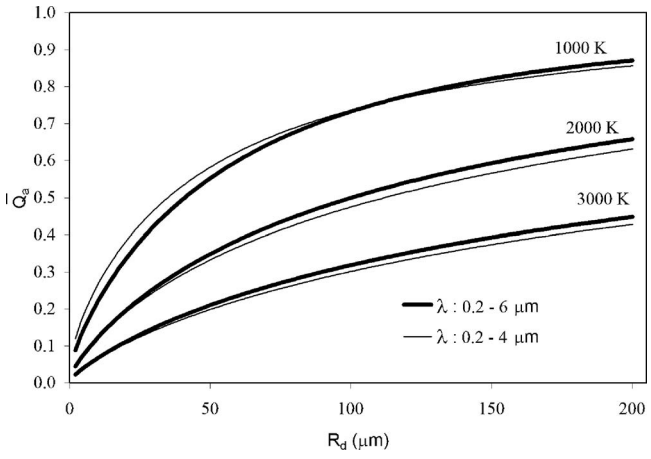

Fig. 2 Plots $\overline{Q_a}$ versus droplet radius for diesel fuel and three radiation temperatures: 1000 K, 2000 K, and 3000 K (indicated near the curves), as calculated from Eq. (2). Thick solid curves are based on the values of κ in the range 0.2–6 μm, as reported in Ref. [10]. Thin solid curves are based on the values of κ in the range 0.2–4 μm, as shown in Fig. 1.

Following Refs. [9,10], the results of the calculation of $\overline{Q_a}$ based on Eq. (2) are approximated by the following expression

$$\Lambda = aR_d^b \quad (3)$$

where

$$a = \sum_{i=0}^{N} a_i \left(\frac{\theta_R}{1000}\right)^i \quad (4)$$

$$b = \sum_{i=0}^{N} b_i \left(\frac{\theta_R}{1000}\right)^i \quad (5)$$

θ_R is in K, R_d is in μm, a_i is in $\mu m^{-b}\,K^{-i}$, and b_i is in K^{-i}.

In Ref. [9], it was assumed that $N=2$. In Ref. [10] both $N=2$ and $N=4$ were considered and it was shown that the fourth-order approximation is particularly important when the radiation temperatures are less than 1000 K (when the overall contribution of the thermal radiation in the process of droplet heating is small). For radiation temperatures equal to or greater than 1000 K, approximations (4) and (5) with $N=2$ were used.

The coefficients a_i and b_i in Eqs. (4) and (5) were obtained by curve fitting and direct comparison of the values of Λ predicted by Eq. (3) and $\overline{Q_a}$ predicted by Eq. (2). Approximation (3) for $N=2$ shows good agreement with Eq. (2) for R_d in the range 5–50 μm, but less so for R_d in the range 2–200 μm.

Here, in contrast to Refs. [9,10], approximations (4) and (5) are not used for the entire range of droplet radii (2–200 μm), but in subranges over R_d. Taking $N=2$, the values of coefficients a_i and b_i in various subranges over R_d and various fuels have been calculated. The results are shown in Table 1.

For $N=4$, approximations (4) and (5) with the same coefficients a_i and b_i were used in the entire range of droplet radii 2–200 μm. The corresponding values of coefficients a_i and b_i are shown in Table 2. Finally, approximations (4) and (5) for $N=2$ with the same coefficients a_i and b_i were used in the entire range of droplet radii 2–200 μm. The corresponding values of coefficients a_i and b_i are shown in Table 3. Note that the values of these coefficients for diesel fuel differ slightly from the values given in Ref. [10]. This is attributed to different ranges of λ used in the current analysis.

The values of Λ predicted by Eq. (3) and $\overline{Q_a}$ predicted by Eq. (2) for various approximations of a and b are compared in Sec. 4.

Table 1 The coefficients a_i and b_i calculated for various ranges of R_d and various fuels, assuming that $N=2$ and R_d is in μm.

Type of fuel	R_{min} (μm)	R_{max} (μm)	a_0	a_1	a_2	b_0	b_1	b_2
	2	5	0.177537	−0.111821	0.019098	0.340153	0.163354	−0.020202
Diesel (low sulphur ESSO AF1313)	5	50	0.181243	−0.117208	0.020356	0.299978	0.232538	−0.032668
	50	100	0.358073	−0.243320	0.043437	0.070587	0.308590	−0.043973
	100	200	0.635142	−0.440123	0.079431	−0.075184	0.339893	−0.048833
	2	5	0.020400	−0.005650	0.000450	0.957600	0.011450	−0.001450
Gasoline (BP Pump Grade 95 RON ULG)	5	50	0.029100	−0.009300	0.000900	0.771800	0.052950	−0.005850
	50	100	0.092600	−0.038400	0.004800	0.455900	0.096050	−0.008350
	100	200	0.276800	−0.125450	0.016550	0.215500	0.108950	−0.006950
	2	5	0.010310	−0.001990	0.000090	0.985320	0.002500	−0.002990
2,2,4-Trimethylpentane	5	50	0.013100	−0.003150	0.000150	0.874900	0.023450	−0.002250
	50	100	0.030500	−0.009750	0.000850	0.650100	0.050350	−0.003150
	100	200	0.076900	−0.027300	0.002600	0.451000	0.055600	−0.000100
	2	5	0.013100	−0.004000	0.000370	0.940590	0.022660	−0.003220
3-Pentanone	5	50	0.019200	−0.007250	0.000850	0.736400	0.092500	−0.012800
	50	100	0.038400	−0.016450	0.002150	0.537500	0.125010	−0.015700
	100	200	0.065100	−0.024950	0.002750	0.440200	0.088950	−0.006850

4 Comparison of the Results

The plots of $\overline{Q_a}$ and three approximations Λ for diesel fuel versus R_d are shown in Fig. 3 for the range 2–200 μm. As can be seen from this figure, the piecewise quadratic approximation for coefficients a and b accurately predicts the values of Λ. The values of Λ based on quadratic and fourth-power approximations over the whole range of R_d are noticeably different from $\overline{Q_a}$. The piecewise quadratic approximation for coefficients a and b is therefore expected to be of use in practical engineering applications, including CFD codes.

The same conclusion was drawn for gasoline (Fig. 4), iso-octane (Fig. 5), and 3-pentanone (Fig. 6). Note that the temperature effect on $\overline{Q_a}$ is greatest for diesel fuel. The maximum values of $\overline{Q_a}$ are greater for diesel and gasoline fuels than for iso-octane and 3-pentanone. For all fuels, the values of $\overline{Q_a}$ decrease with increasing external temperature in agreement with the results reported earlier in Refs. [9,10].

5 Applications

To illustrate the effect of thermal radiation on diesel fuel droplet heating and evaporation, the time evolution of radius and surface temperature of a droplet was considered. A droplet at room temperature ($T_{d0}=300$ K) and with initial radius equal to 10 μm was injected into air with ambient temperature of 600 K and pressure of 3 MPa. The initial velocity of the droplet was taken to be 1 m/s. The overall volume of injected liquid fuel was taken as

Table 2 The coefficients a_i and b_i calculated for R_d in the range 2–200 μm and various fuels, assuming that $N=4$ and R_d is in μm.

Coefficients\Fuel	Diesel (low sulphur ESSO AF1313)	Gasoline (BP 95 RON ULG)	2,2,4-Trimethylpentane	3-Pentanone
a_0	0.143452	0.074546	0.035479	0.045995
a_1	−0.016510	−0.049511	−0.034435	−0.047760
a_2	−0.058531	0.023057	0.023033	0.029250
a_3	0.027674	−0.006836	−0.007777	−0.009075
a_4	−0.003661	0.000829	0.000964	0.001065
b_0	0.482037	0.406702	0.429499	0.327158
b_1	−0.249135	0.334640	0.625147	0.686807
b_2	0.286669	−0.208455	−0.462004	−0.463508
b_3	−0.094873	0.068515	0.152989	0.147149
b_4	0.010658	−0.008410	−0.018322	−0.017281

Table 3 The coefficients a_i and b_i calculated for R_d in the range 2–200 μm and various fuels, assuming that $N=2$ and R_d is in μm.

Coefficients\Fuel	Diesel (low sulphur ESSO AF1313)	Gasoline (BP 95 RON ULG)	2,2,4-Trimethylpentane	3-Pentanone
a_0	0.252827	0.05220	0.02010	0.02590
a_1	−0.167207	−0.020890	−0.00610	−0.010400
a_2	0.029404	0.002710	0.000500	0.001290
b_0	0.160138	0.575405	0.721815	0.620380
b_1	0.274847	0.081630	0.048190	0.112250
b_2	−0.038919	−0.008300	−0.005300	−0.015710

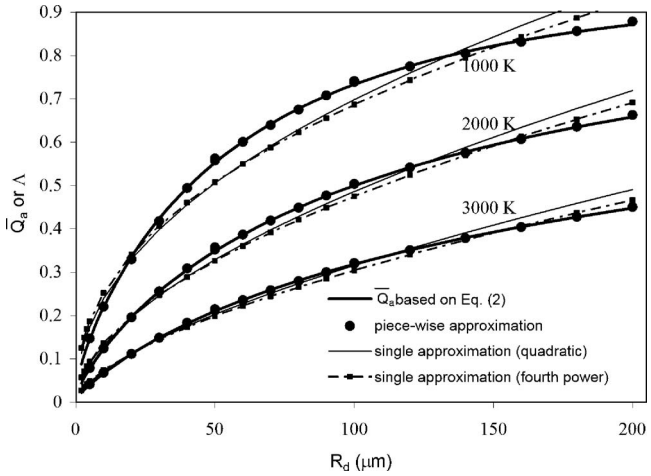

Fig. 3 Plots $\overline{Q}_a$ and its three approximations Λ versus droplet radius for diesel fuel. Three radiation temperatures: 1000 K, 2000 K, and 3000 K (indicated near the curves) were considered. Thick solid curves refer to the values of $\overline{Q}_a$ as calculated from Eq. (2). Thick dots refer to piecewise approximation for Λ, as calculated from Eq. (3). Thin solid curves refer to a single quadratic approximation for Λ. Dashed–dotted curves refer to a singe fourth power approximation for Λ.

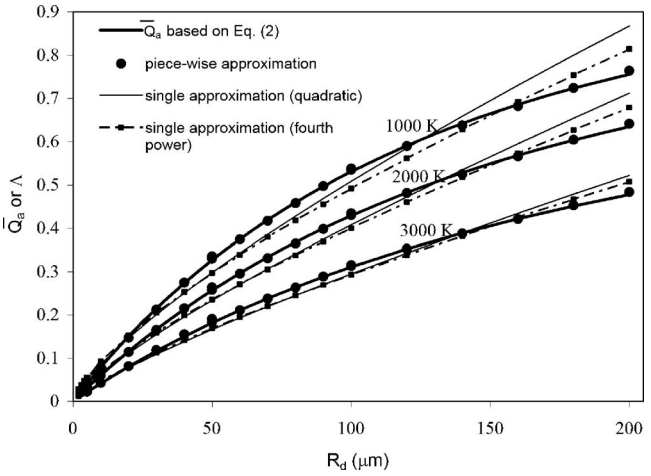

Fig. 5 The same as Figs. 3 and 4 but for iso-octane

1 mm^3. The volume of air, where the fuel was injected, was taken equal to 639 mm^3. This volume was calculated using the assumption that diesel fuel can be approximated as *n*-dodecane ($C_{12}H_{26}$) and that the initial gas temperature is equal to 600 K. In this case, provided that all fuel is evaporated without combusting, the fuel vapor/air mixture is expected to become close to stoichiometric [22]. The temperature dependence of all transport coefficients and density was taken into account. The relevant approximations are presented and discussed in Ref. [22]. The droplet was irradiated homogeneously from all directions by external thermal radiation from a source at temperatures in the range from 1000 K to 3000 K.

This is a rather idealized case, as in diesel engines the droplets are likely to be irradiated from one side only [23] (see Ref. [14] for a detailed mathematical analysis of this case). To take into account the effect of asymmetrical irradiation of droplets, the actual power absorbed by droplets could be halved, compared with the case of homogeneous irradiation. Alternatively, this effect can be accounted for by the corresponding adjustment of the radiation temperature. The integral effect of symmetrical radiative heating of droplets by the source at temperature θ_R is approximately equivalent to the effect of asymmetrical droplet heating by a source at temperature $\theta_{R(\text{eff})}=2^{1/4}\theta_R=1.19\theta_R$. As pointed out in Refs. [17,18,24], the effect of nonhomogeneous, but spherically symmetrical, distribution of the radiative heating inside a droplet is insignificant when the radiative heating of droplets takes place simultaneously with convective heating. We anticipate that this conclusion is valid in the case of asymmetrical droplet radiative heating.

The effect of thermal radiation was taken into account using the new model based on the piecewise approximation of the coefficients *a* and *b* in Eq. (3) (see Table 1) for $T_{\text{ext}}=1000$ K, 2000 K, and 3000 K, and the model based on the single quadratic approximations of these coefficients (see Table 3) for $T_{\text{ext}}=3000$ K. The predictions of the model based on the single fourth power approximations are expected to lie between the predictions of these two models.

The liquid and gas phase models used in the analysis are summarized in Appendix A. The solutions in both these phases are fully coupled.

The plots of T_s and R_d for diesel fuel versus time with and without taking into account the effect of thermal radiation are shown in Fig. 7. The droplet radius initially increases due to thermal expansion of liquid fuel, until the effect of evaporation dominates. In the case of $T_{\text{ext}}=1000$ K, the effect of thermal radiation on droplet evaporation is small. This effect visibly increases when

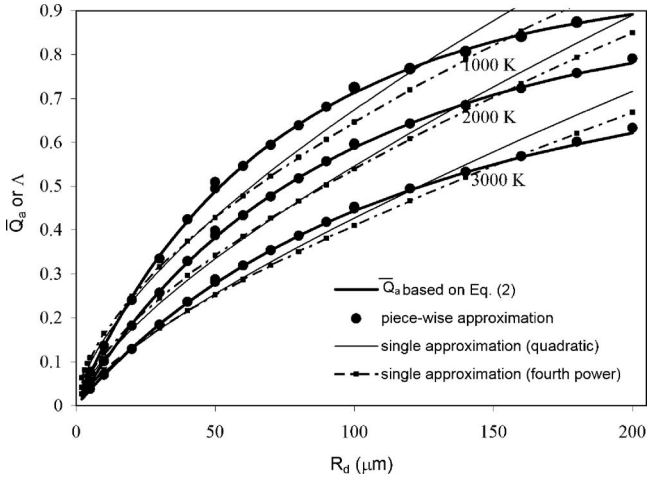

Fig. 4 The same as Fig. 3 but for gasoline fuel

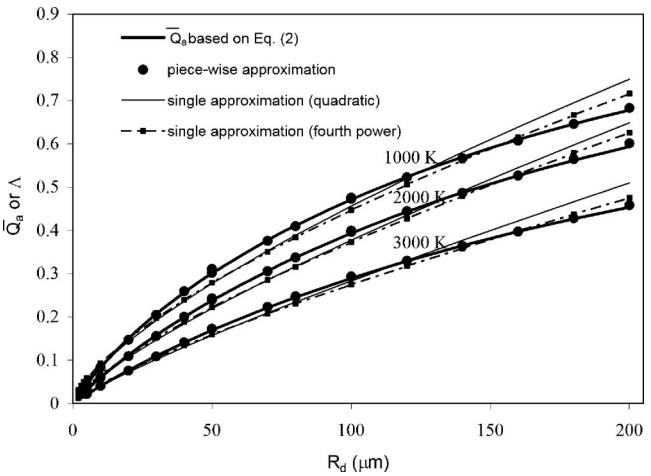

Fig. 6 The same as Figs. 3–5 but for 3-pentanone.

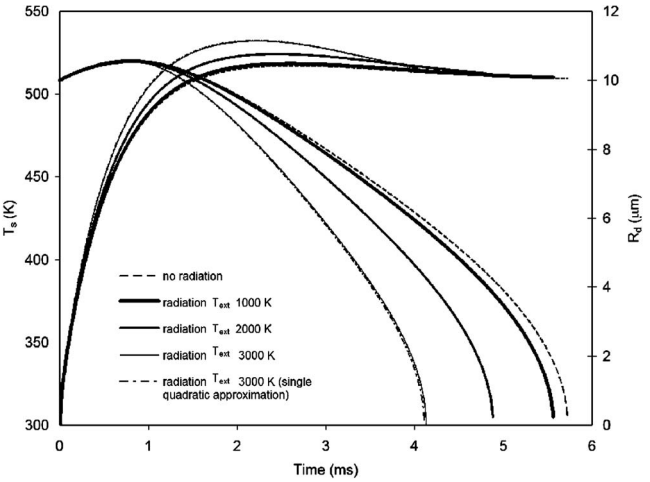

Fig. 7 Plots of T_s and R_d for a diesel fuel droplet versus time for an initial air temperature T_{g0}=600 K, air pressure p_{g0}=3 MPa, droplet temperature T_{d0}=300 K, radius R_{d0}=10 μm, and velocity v_{d0}=1 m/s. The overall volume of injected liquid fuel was taken equal to 1 mm^3, and the volume of air was equal to 639 mm^3. The results were obtained based on the effective thermal conductivity (ETC) model and the analytical solution of the heat conduction equation inside the droplet [22]. Dashed curves refer to the case when the effects of thermal radiation are ignored. Thick, intermediate, and thin solid curves refer to the case when the thermal radiation is generated by a source with external temperatures 1000 K, 2000 K, and 3000 K, respectively, and calculated using the model based upon a piecewise approximation of the coefficients *a* and *b* in Eq. (3). Dashed-dotted curves refer to the case when the thermal radiation is generated by a source with external temperatures of 3000 K and the model based on single quadratic approximations of these coefficients.

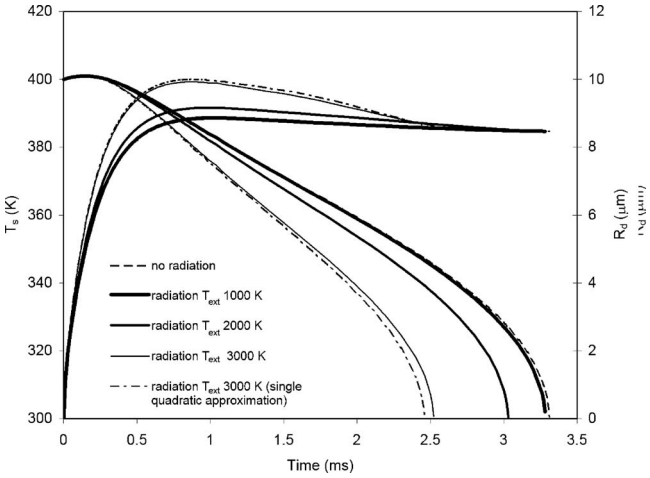

Fig. 8 The same as Fig. 7 but for gasoline fuel, injected into a gas volume equal to 620 mm^3

the external temperature increases to 2000 K and 3000 K (the lifetime of a droplet becomes shorter). In the case without radiation, the droplet surface temperature monotonically increases until it reaches the wet bulb temperature. When the effect of thermal radiation is taken into account, the surface temperature reaches a maximum value before it reduces to the same wet bulb temperature. This effect was discussed in detail in Ref. [24].

The plots calculated using the model based on the piecewise approximation of the coefficients *a* and *b* in Eq. (3) and the model based on the single quadratic approximations of these coefficients are nearly coincident for T_{ext}=3000 K. These curves are expected to be even closer for lower external temperatures. This happens despite the fact that the values of the average absorption efficiency factors predicted by these models are visibly different (see Fig. 3). Thus, in many practical applications, including modeling of heating and evaporation of droplets, the high accuracy of the approximation of the average absorption efficiency factor, provided by the model based on a piecewise approximation of the coefficients *a* and *b*, is not always required. However, since the computer requirements of the implementation of this new model are all but the same as those of the model based on the single quadratic approximations of these coefficients, the application of the new model is recommended in all cases.

Plots similar to those shown in Fig. 7 but for gasoline fuel are presented in Fig. 8. The physical properties of the gasoline fuel used in our study are shown in Appendix B. In contrast to diesel fuel, gasoline fuel is injected into a gas volume of 620 mm^3. The volume was calculated under the assumption that gasoline fuel can be approximated as $C_{7.9}H_{17.8}$. In this case, provided that all gasoline fuel is evaporated without combusting, the fuel vapor/air mixture is expected to become close to stoichiometric, as in the case of diesel fuel. The general shapes of the curves shown in Figs. 7 and 8 are rather similar, except that the difference between the curves calculated using the model based on the piecewise approximation of the coefficients *a* and *b* in Eq. (3) and the model based on the single quadratic approximations of these coefficients, is more pronounced in the case of Fig. 8 than Fig. 7. This justifies the application of the new model in the case of gasoline.

The iso-octane and 3-pentanone cases are presented in Figs. 9 and 10, respectively. The physical properties of iso-octane and 3-pentanone are shown in Appendix B. These fuels were injected into gas volumes of 625 mm^3 and 712 mm^3, respectively. Comparison of Figs. 9 and 10 and Figs. 7 and 8 shows that the effect of radiation on heating and evaporation of iso-octane and 3-pentanone is noticeably weaker than in the case of diesel fuel and gasoline. This agrees with the results presented in Figs. 3–6. Also, the choice of the approximation of the average absorption efficiency factor is more important for iso-octane than for 3-pentanone.

Note that we can draw a parallel between the results presented in Figs. 7–10 of this paper and some earlier results obtained in our group and well known results. As already mentioned, the droplet heating and evaporation in realistic diesel engine conditions was shown to be practically independent of the detailed distribution of radiative heating inside the droplets [17,18,24]. Also, the replacement of the actual distribution of temperature inside droplets by a

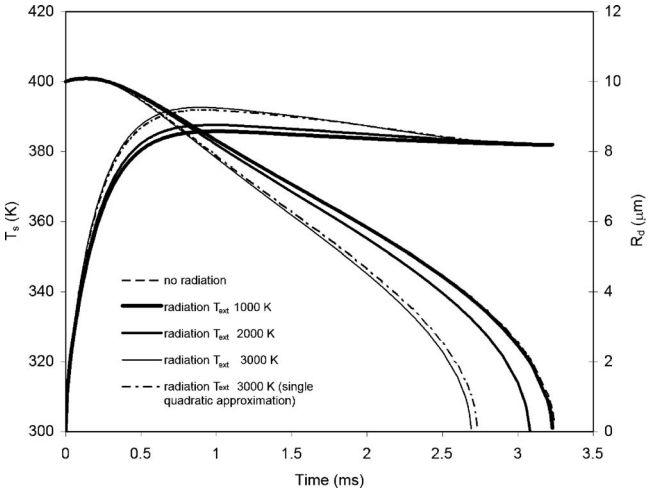

Fig. 9 The same as Figs. 7 and 8 but for iso-octane, injected into a gas volume equal to 625 mm^3

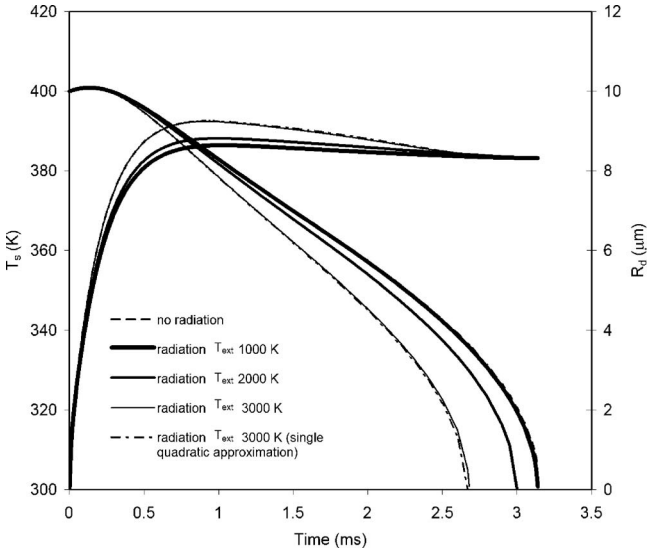

Fig. 10 The same as Figs. 7–9 but for 3-pentanone, injected into a gas volume equal to 712 mm^3

rather crude parabolic approximation was shown to lead to insignificant changes of the predicted droplet heating and evaporation [18,25]. Similar phenomenon is well known in the boundary layer theory, when the details of the velocity profile near the boundaries have relatively small effects of the integral characteristics such as drag and lift forces [26]. This property of the boundary layers is widely used in CFD codes when a detailed calculation of the velocity profiles near the boundaries is replaced by modeling these profiles [27]. All abovementioned phenomena allow us to shift the focus of the research from the development of the most accurate submodels to finding a compromise between the accuracy of modeling and computational efficiency. Returning to our problem of finding an approximation for the absorption efficiency factor we can say that the relatively weak dependence of droplet heating and evaporation on the accuracy of this approximation gives us an additional argument in favor of using an approximate formula (1) instead of the detailed Mie calculations of the distribution of thermal radiative absorption inside droplets. In contrast to the model described in this paper, the implementation of the model, based on Mie calculations, into CFD codes would be infeasible.

6 Conclusions

The values of absorption coefficients of gasoline fuel (BP Pump Grade 95 RON ULG), 2,2,4-trimethylpentane (iso-octane) and 3-pentanone have been measured experimentally in the range of wavelengths 0.2–4 μm. Ultraviolet – visible spectra (0.2–0.8 μm) have been obtained using an UV-visible spectrophotometer Shimadzu, model 1601. In the range 0.4–4 μm the absorption coefficients have been measured using a Fourier transform infrared spectrometer (Nicolet FT-IR Avatar). The values of the indices of absorption calculated based on these coefficients have been shown to be similar to those obtained earlier for low sulphur ESSO AF1313 diesel fuel. For all fuels, the region of semi-transparency in the range $0.5\ \mu\text{m} < \lambda < 1\ \mu\text{m}$ is illustrated. The index of absorption increases by approximately three orders of magnitude when λ increases from 0.5 μm to 1.5 μm. At the same time, noticeable differences between the indices of absorption of the fuels can be identified. For example, the peak of absorption of diesel fuel at $\lambda \approx 3.4\ \mu$m is much more pronounced than the corresponding peaks of absorption of other fuels. Also, the value of λ when this peak is observed is close to 3.4 μm for diesel fuel, and close to approximately 3.0 μm for other fuels. The values of this index tend to be lower for pure substances (e.g., iso-octane and 3-pentanone) than for diesel and gasoline fuels.

It has been shown that the main contribution to the average absorption efficiency factor is expected to come from radiation at wavelengths less than 4 μm for the range of external temperatures between 1000 K and 3000 K. The value of this factor has been approximated by a power function aR_d^b, where R_d is the droplet radius. Coefficients a and b are approximated by piecewise quadratic functions of the radiation temperature, with the coefficients calculated separately in the ranges of radii 2–5 μm, 5–50 μm, 50–100 μm, and 100–200 μm for all fuels. This new approximation has been shown to be more accurate when compared with the case when a and b are approximated by quadratic functions or fourth power polynomials of the radiation temperature, with the coefficients calculated over the entire range 2–200 μm. This difference in the approximations of a and b, however, have been shown to have little effect on the modeling of fuel droplet heating and evaporation in conditions typical for internal combustion engines, especially in the case of diesel fuel and 3-pentanone.

Acknowledgment

The authors are grateful to the Indonesian government (TPSDP, Batch III) and the European Regional Development Fund Franco-British INTERREG IIIa (Project Ref. No. 162/025/247) for financial support of the work on this project.

Nomenclature

a = coefficient introduced in Eq. (4)
a_i = coefficient introduced in Eq. (4) (K^{-i})
b = coefficient introduced in Eq. (5)
b_i = coefficient introduced in Eq. (5) (K^{-i})
B_M = Spalding mass transfer number
B_T = Spalding heat transfer number
c = specific heat capacity (J/kg K)
C_2 = coefficient in the Planck function (μm K)
D_{Fa} = binary diffusion coefficient of fuel vapor in air ($m^2/(s)$)
$F(B_{M,T})$ = functions introduced in Eqs. (A6) and (A7)
h = convection heat transfer coefficient ($W/(m^2\,K)$)
h_0 = $(hR_d/k_l)-1$
h_m = mass transfer coefficient (m/s)
k = thermal conductivity (W/(m K))
L = specific heat of evaporation (J/(kg))
m = mass (kg)
n = index of refraction
Nu = Nusselt number
q_n = coefficients introduced in formula (A4)
Q_a = efficiency factor of absorption
p = pressure (Pa)
p_n = coefficients introduced in formula (A4)
$P(R)$ = normalized power generated in unit volume (K/s)
$\tilde{P}(R)$ = variable introduced in formula (A4)
Pe_d = Péclet number
Pr_d = Prandtl number
R = distance from the center of the droplet (m)
R_d = radius of the droplet (m) or (μm)
Re = Reynolds number
Sc = Schmidt number
Sh_0 = Sherwood number of nonevaporating droplets
t = time (s)
T = temperature (K)
$\tilde{T}_0(R)$ = variable introduced in formula (A4)
$v_n(R)$ = eigenfunctions used in formula (A4)
$\|v_n(r)\|$ = parameter introduced in formula (A4)

x = droplet diffraction parameter
Y = mass fraction

Greek Symbols

ε/k = fuel vapor parameter (K)
θ_R = radiation temperature (K)
κ = index of absorption
κ_d = $k_l/(c_l\rho_l R_d^2)$
κ_l = liquid thermal diffusivity (m^2/s)
λ = wavelength (μm)
λ_n = eigenvalues used in formula (A4)
μ = dynamic viscosity K(N s/m^2)
$\mu_0(t)$ = $hT_{\text{eff}}(t)R_d/k_l$
ρ = density (kg/m^3)
σ = fuel vapor parameter (K)
χ = coefficient introduced in the definition of k_{eff}

Subscripts

cr = critical
d = droplet
eff = effective
ext = external
f = fuel
f_s = saturated fuel vapor
g = gas
l = liquid
max = maximal
p = constant pressure
s = surface
v = vapor
∞ = ambient gas

Superscripts

— = average
~ = normalized

Appendix A: Liquid and Gas Phase Models

Liquid Phase Model. Assuming that droplet heating is spherically symmetric, the transient heat conduction equation inside droplets is written as

$$\frac{\partial T}{\partial t} = \kappa_l\left(\frac{\partial^2 T}{\partial R^2} + \frac{2}{R}\frac{\partial T}{\partial R}\right) + P(R) \tag{A1}$$

where $\kappa_l = k_l/(c_l\rho_l)$ is the liquid thermal diffusivity; k_l is the liquid thermal conductivity; $T = T(R,t)$ is the droplet temperature; R is the distance from the center of the droplet; and $P(R)$ is the normalized power generated in unit volume inside the droplet due to thermal radiation (in K/s).

Assuming that the droplet is heated by convection from the surrounding gas, and cooled due to evaporation, the energy balance equation at the droplet surface ($R = R_d$) is written as

$$h(T_g - T_s) = -\rho_l L\dot{R}_d + k_l \left.\frac{\partial T}{\partial R}\right|_{R=R_d}$$

where $h = h(t)$ is the convection heat transfer coefficient; T_s is the droplet's surface temperature; and L is the specific heat of evaporation. This is complemented by the boundary condition at $R = 0$: $\partial T/\partial R|_{R=0} = 0$ and the initial condition: $T(t=0) = T_0(R)$. This equation can be rearranged to

$$T_{\text{eff}} - T_s = \frac{k_l}{h}\left.\frac{\partial T}{\partial R}\right|_{R=R_d} \tag{A2}$$

where

$$T_{\text{eff}} = T_g + \frac{\rho_l L\dot{R}_d}{h}$$

The value of $\dot{R}_d$ is controlled by fuel vapor diffusion from the droplet surface. It is found from the equation [28]

$$\dot{m}_d = 4\pi R_d^2\dot{R}_d\rho_l = 2\pi\bar{\rho}_g D_{Fa}R_d\text{Sh}_0\ln(1+B_M) \tag{A3}$$

where $\bar{\rho}_g$ is the average gas (mixture of air and fuel vapor) density; D_{Fa} is the binary diffusion coefficient of fuel vapor in air; $\text{Sh}_0 \equiv 2h_m R_d/D_{\text{Fa}}$ is the Sherwood number of nonevaporating droplets; h_m is the mass transfer coefficient: $B_M = (Y_{fs} - Y_\infty)/(1 - Y_{fs})$ is the Spalding mass trans number; and Y_{fs} and $Y_{f\infty}$ is the mass fraction of vapor near the droplet surface and at large distances from the droplet, respectively. They are calculated from the Clausius–Clapeyron equation. Approximations for Sh_0 depend on the modeling or approximations of the processes in the gas phase. These will be discussed in the next subsection. The limitations of the hydrodynamic model, on which the equation for $\dot{m}_d$ is based, are discussed in Refs. [19,29,30].

In the case when $h(t) = h =$ const, the solution of Eq. (A1) with $R_d =$ const and the corresponding boundary and initial conditions, as discussed above, is presented as

$$T(R,t) = \frac{R_d}{R}\sum_{n=1}^{\infty}\left\{\frac{p_n}{\kappa_d\lambda_n^2} + \exp[-\kappa_d\lambda_n^2 t]\left(q_n - \frac{p_n}{\kappa_d\lambda_n^2}\right)\right.$$
$$- \frac{\sin\lambda_n}{\|v_n\|^2\lambda_n^2}\mu_0(0)\exp[-\kappa_d\lambda_n^2 t] - \frac{\sin\lambda_n}{\|v_n\|^2\lambda_n^2}\int_0^t \frac{d\mu_0(\tau)}{d\tau}$$
$$\left.\times\exp[-\kappa_d\lambda_n^2(t-\tau)]d\tau\right\}\sin(\lambda_n R/R_d) + T_{\text{eff}}(t) \tag{A4}$$

where

$$\mu_0(t) = \frac{hT_{\text{eff}}(t)R_d}{k_l}, \quad h_0 = (hR_d/k_l) - 1,$$

$$\|v_n\|^2 = \frac{1}{2}\left(1 + \frac{h_0}{h_0^2 + \lambda_n^2}\right), \quad \kappa_d = \frac{k_l}{c_l\rho_l R_d^2}$$

$$p_n = \frac{1}{R_d\|v_n\|^2}\int_0^{R_d}\tilde{P}(R)v_n(R)dR, \quad q_n = \frac{1}{R_d\|v_n\|^2}\int_0^{R_d}\tilde{T}_0(R)v_n(R)dR$$

$$\tilde{P}(R) = RP(R)/(c_l\rho_l R_d), \quad \tilde{T}_0(R) = RT_0(R)/R_d,$$

$$v_n(R) = \sin(\lambda_n R/R_d) \quad (n = 1,2,\ldots)$$

a set of positive eigenvalues λ_n numbered in ascending order ($n = 1,2,\ldots$) is found from the solution of the following equation

$$\lambda_n\cos\lambda_n + h_0\sin\lambda_n = 0$$

The dependence of P on R is ignored. Remembering Eq. (3), $P(R)$ is approximated as

$$P(R) = 3\times 10^6 a\sigma R_{d(\mu\text{m})}^{b-1}\theta_R^4/(c_l\rho_l) \tag{A5}$$

where θ_R is the radiation temperature; and $R_{d(\mu\text{m})}$ is the droplet radius in μm.

The solution Eq. (A4) can be generalized to take into account the internal recirculation inside the droplets. This is achieved by replacing the thermal conductivity of liquid k_l by the so called effective thermal conductivity $k_{\text{eff}} = \chi k_l$, where [28]

$$\chi = 1.86 + 0.86\tanh[2.225\log_{10}(\text{Pe}_d/30)]$$

Pe_d is the droplet Péclet number.

Gas Phase Model. The choice of the gas phase model controls the values of the Sherwood number Sh_0, introduced in Eq. (A3), and the Nusselt number Nu. Following Abramzon and Sirignano [28] these numbers are calculated from the following equations

$$\mathrm{Sh}_0 = 2\left(1 + \frac{(1+\mathrm{Re}_d\mathrm{Sc}_d)^{1/3}\max[1,\mathrm{Re}_d^{0.077}]-1}{2F(B_M)}\right) \quad \text{(A6)}$$

$$\mathrm{Nu} = 2\frac{\ln(1+B_T)}{B_T}\left(1 + \frac{(1+\mathrm{Re}_d\mathrm{Pr}_d)^{1/3}\max[1,\mathrm{Re}_d^{0.077}]-1}{2F(B_T)}\right) \quad \text{(A7)}$$

where

$$F(B_{M,T}) = (1+B_{M,T})^{0.7}\frac{\ln(1+B_{M,T})}{B_{M,T}}$$

B_T is Spalding heat transfer number.

Numerical Scheme. If the time step over which droplet temperature and radius are calculated is small, we can assume that $h(t)$= const over this time step. In this case we calculate $\dot{R}_d(t=0)$ from Eq. (A3) and $T_{\mathrm{eff}}(t=0)$. Then the initial condition at $t=0$ will allow us to calculate $T(R,t)$ at the end of the first time step ($T(R,t_1)$) using Eq. (A4). $R_d(t_1)$ is calculated based on Eq. (A3) with the correction swelling of the droplet. The same procedure is repeated for all the following time steps until the droplet is evaporated. The number of terms in the series in Eq. (A4), which needs to be taken into account, depends on the timing of the start of droplet heating and the time when the value of droplet temperature is calculated. For parameters relevant to the diesel engine environment, just three terms in the series have been used with possible errors of not more than about 1%.

Appendix B: Physical Properties of Fuels

Following Ref. [22], the temperature dependence of the physical properties of fuels is presented in the form of their dependence upon the normalized temperature

$$\tilde{T} = \frac{T-T_0}{T_0}$$

where T_0=300 K. The estimate of the physical properties of mixtures is the same as in Ref. [22]. The values of physical parameters are presented for $\tilde{T}<\tilde{T}_{\mathrm{cr}}$, unless stated otherwise.

Physical Properties of Gasoline Fuel (BP Pump Grade 95 RON ULG). Using data presented in Ref. [31], the latent heat of evaporation is approximated as

$$L = 3.48\times10^5 - 1.64\times10^5\tilde{T} + 2.88\times10^4\tilde{T}^2 - 1.61\times10^5\tilde{T}^3 \text{ J/kg}$$

when $\tilde{T}<\tilde{T}_{\mathrm{cr}}$=0.883 and zero otherwise.

Using data presented in Refs. [31,32], the specific heat capacities of liquid and vapor at constant pressure are approximated as

$$c_l = 2058 + 1200\tilde{T} \text{ J/kg K}$$

$$c_{pv} = 2.5077\times10^3 + 7.2076\times10^2\tilde{T} - 13.8415\tilde{T}^2 + 2.1111\tilde{T}^3 \text{ J/kg K}$$

The saturated vapor pressure is approximated as [31]

$$p_s = (0.353 - 4.051\tilde{T} + 72.812\tilde{T}^2 - 164.867\tilde{T}^3 + 178.985\tilde{T}^4)10^5 \text{ N/m}^2$$

Using data presented in Refs. [31,33], the density and the thermal conductivity of liquid are approximated as

$$\rho_l = 720.02 - 222.22\tilde{T} \text{ kg/m}^3$$

$$k_l = 0.1251 - 0.0462\tilde{T} - 0.2047\tilde{T}^2 + 0.4575\tilde{T}^3 - 0.3579\tilde{T}^4 \text{ W/m K}$$

when $\tilde{T}<\tilde{T}_{\mathrm{cr}}$ and zero otherwise. Using data presented in Refs. [31,34], the dynamic viscosity of liquid and vapor are approximated as

$$\mu_l = (4.50 - 14.85\tilde{T} + 16.45\tilde{T}^2 - 8.84\tilde{T}^3)10^{-4} \text{ N s/m}^2$$

$$\mu_v = (5.0555 + 6.0455\tilde{T} - 0.6356\tilde{T}^2 + 0.0014\tilde{T}^3)10^{-6} \text{ N s/m}^2$$

The binary diffusion coefficient of fuel vapor in air was calculated based on the following fuel vapor parameter values [34]

$$\varepsilon/k = 320 \text{ K}; \quad \sigma = 7.451 \text{ Å}$$

Physical Properties of Iso-octane. Using data presented in Ref. [35], the latent heat of evaporation is approximated as

$$L = 3.49\times10^5 + 4.37\times10^3\tilde{T} - 5.64\times10^4\tilde{T}^2 + 2.72\times10^4\tilde{T}^3 - 5.23\times10^3\tilde{T}^4 \text{ J/kg}$$

when $\tilde{T}<\tilde{T}_{\mathrm{cr}}$=0.888 and zero otherwise.

Using data presented in Ref. [36], the specific heat capacities of liquid and vapor at constant pressure are approximated as

$$c_l = 2224.12 + 930.43\tilde{T} + 602.23\tilde{T}^2 - 311.12\tilde{T}^3 \text{ J/kg K}$$

$$c_{pv} = 1697.61 + 1339.81\tilde{T} - 162.68\tilde{T}^2 - 18.85\tilde{T}^3 \text{ J/kg K}$$

The saturated vapor pressure is approximated in Ref. [33] as

$$p_s = (0.03 - 0.09\tilde{T} + 0.99\tilde{T}^2 - 0.82\tilde{T}^3 + 0.34\tilde{T}^4)10^5 \text{ N/m}^2$$

Using data presented in Ref. [37], the density and the thermal conductivity of liquid are approximated as

$$\rho_l = 725.56 - 33.12\tilde{T} - 56.16\tilde{T}^2 + 28.33\tilde{T}^3 - 5.61\tilde{T}^4 \text{ kg/m}^3$$

$$k_l = 0.141 - 0.042\tilde{T} - 0.027\tilde{T}^2 \text{ W/m K}$$

when $\tilde{T}<\tilde{T}_{\mathrm{cr}}$ and zero otherwise. Using data presented in Ref. [37], the dynamic viscosity of liquid and vapor are approximated as

$$\mu_l = (5.61 - 24.79\tilde{T} + 67.61\tilde{T}^2 - 78.75\tilde{T}^3)10^{-4} \text{ N s/m}^2$$

$$\mu_v = (6.41 + 0.88\tilde{T} + 10.76\tilde{T}^2 - 6.93\tilde{T}^3)10^{-6} \text{ N s/m}^2$$

The binary diffusion coefficient of fuel vapor in air was calculated based on the following fuel vapor parameter values [38]

$$\varepsilon/k = 456.627 \text{ K}; \quad \sigma = 6.52 \text{ Å}$$

Physical Properties of 3-Pentanone. Using data presented in Ref. [39], the latent heat of evaporation is approximated as

$$L = 3.889515\times10^5 - 65.22\tilde{T} - 1.8962545\times10^4\tilde{T}^2 + 1.7642231\times10^5\tilde{T}^3 - 3.84512\times10^4\tilde{T}^4 \text{ J/kg}$$

when $\tilde{T}<\tilde{T}_{\mathrm{cr}}$=0.87 and zero otherwise.

The temperature dependence of the specific heat capacities of liquid is ignored in our analysis. It is assumed equal to that at room temperature [39]: c_l=2219.86 J/kg K. Using data presented in Ref. [40], the specific heat capacity of vapor at constant pressure is approximated as

$$c_{pv} = 1486.16 + 972.88\tilde{T} - 68.16\tilde{T}^2 \text{ J/kg K}$$

The saturated vapor pressure is approximated as [39]

$$p_s = (0.11034 - 0.20556\tilde{T} + 2.15673\tilde{T}^2 + 1.05622\tilde{T}^3 + 0.15395\tilde{T}^4)10^5 \text{ N/m}^2$$

Using data presented in Ref. [41], the liquid density is approximated as

$$\rho_l = 815.17 - 61.341\tilde{T} - 88.184\tilde{T}^2 + 91.16\tilde{T}^3 - 26.112\tilde{T}^4 \text{ kg/m}^3$$

Using data presented in Ref. [39], the liquid thermal conductivity is approximated as

$$k_l = 0.144 - 0.0467\tilde{T} - 0.00019\tilde{T}^2 \text{ W/m K}$$

when $\tilde{T} < \tilde{T}_{cr}$, and zero otherwise.

The temperature dependence of the vapor dynamic viscosity is ignored in our analysis. It is assumed equal to that at room temperature [42]: $\mu_v = 9.16 \times 10^{-6}$ N s/m^2.

Using data presented in Ref. [39], the dynamic viscosity of liquid is approximated as

$$\mu_l = (4.44 - 5.56\tilde{T} + 15.00\tilde{T}^2)10^{-4} \text{ N s/m}^2$$

The binary diffusion coefficient of fuel vapor in air was calculated based on the following fuel vapor parameter values [34]

$$\varepsilon/k = 351.562 \text{ K}; \quad \sigma = 4.22 \text{ Å}$$

References

[1] Tuntomo, A., 1990, "Transport Phenomena in a Small Particle with Internal Radiant Absorption," Ph.D. dissertation, University of California at Berkeley, Berkeley, CA.

[2] Tuntomo, A., Tien, C. L., and Park, S. H.,1991, "Internal Distribution of Radiant Absorption in a Spherical Particle," ASME J. Heat Transfer, **113**, pp. 402–412.

[3] Modest, M. F., 2003, *Radiative Heat Transfer*, 2nd ed., Academic, Amsterdam, The Netherlands.

[4] Viskanta, R., 2005, *Radiative Transfer in Combustion Systems: Fundamentals & Applications*, Begel House, Inc., New York, Wallingford, UK.

[5] Chapman, M., Friedman, M. C., and Aghan, A., 1983, "A Time-Dependent Spatial Model For Heat Transfer in Diesel Engines," SAE Paper No. 831725.

[6] Mengüc, M. P., Viskanta, R., and Ferguson, C. R., 1985, "Multidimensional Modeling of Radiative Heat Transfer in Diesel Engines," SAE Paper No. 850503.

[7] Dombrovsky, L. A., 2002, "Spectral Model of Absorption and Scattering of Thermal Radiation by Diesel Fuel Droplets," High Temp., **40**, pp. 242–248.

[8] Sazhina, E. M., Sazhin, S. S., Heikal, M. R., and Bardsley, M. E. A., 2000, "The P-1 Model for Thermal Radiation Transfer: Application to Numerical Modeling of Combustion Processes in Diesel Engines," *Proceedings of the 16th IMACS World Congress 2000 on Scientific Computation, Applied Mathematics and Simulation*, Lausanne, Switzerland, 21–25 August, (CD) Paper No. 125-10.

[9] Dombrovsky, L. A., Sazhin, S. S., Sazhina, E. M., Feng, G., Heikal, M. R., Bardsley, M. E. A., and Mikhalovsky, S. V., 2001, "Heating and Evaporation of Semi-transparent Diesel Fuel Droplets in the Presence of Thermal Radiation," Fuel, **80**(11), pp. 1535–1544.

[10] Sazhin, S. S., Abdelghaffar, W. A., Sazhina, E. M., Mikhalovsky, S. V., Meikle, S. T., and Bai, C., 2004, "Radiative Heating of Semi-transparent Diesel Fuel Droplets," ASME J. Heat Transfer, **126**, pp. 105–109; 2004, , **126**, pp. 490–491.

[11] Sazhin, S. S., Dombrovsky, L. A., Krutitskii, P. A., Sazhina, E. M., and Heikal, M. R., 2002, "Analytical and Numerical Modeling of Convective and Radiative Heating of Fuel Droplets in Diesel Engines," *Proceedings of the 12th International Heat Transfer Conference*, Grenoble, France, August 18–23, Editions Scientifique et Medicale, Elsevier SAS, Vol. 1, pp. 699–704.

[12] Lage, P. L. C., and Rangel, R. H., 1993, "Single Droplet Vaporization Including Thermal Radiation Absorption," J. Thermophys. Heat Transfer, **7**(3), pp. 502–509.

[13] Dombrovsky, L. A., and Sazhin, S. S., 2003, "Absorption of Thermal Radiation in a Semi-transparent Spherical Droplet: A Simplified Model," Int. J. Heat Fluid Flow, **24**(6), pp. 919–927.

[14] Dombrovsky, L. A., and Sazhin, S. S., 2004, "Absorption of External Thermal Radiation in Asymmetrically Illuminated Droplets," J. Quant. Spectrosc. Radiat. Transf., **87**, pp. 119–135.

[15] Dombrovsky, L. A., 2004, "Absorption of Thermal Radiation in Large Semi-transparent Particles at Arbitrary Illumination of a Polydisperse System," Int. J. Heat Mass Transfer, **47**, pp. 5511–5522.

[16] Sazhin, S. S., Krutitskii, P. A., Abdelghaffar, W. A., Sazhina, E. M., Mikhalovsky, S. V., Meikle, S. T., and Heikal, M. R., 2004, "Transient Heating of Diesel Fuel Droplets," Int. J. Heat Mass Transfer, **47**, pp. 3327–3340.

[17] Sazhin, S. S., Abdelghaffar, W. A., Krutitskii, P. A., Sazhina, E. M., and Heikal, M. R., 2005, "New Approaches to Numerical Modeling of Droplet Transient Heating and Evaporation," Int. J. Heat Mass Transfer, **48**(19–20), pp. 4215–4228.

[18] Abramzon, B., and Sazhin, S., 2005, "Droplet Vaporization Model in the Presence of Thermal Radiation," Int. J. Heat Mass Transfer, **48**, pp. 1868–1873.

[19] Sazhin, S. S., 2006, "Advanced Models of Fuel Droplet Heating and Evaporation," Prog. Energy Combust. Sci., **32**(2), pp. 162–214.

[20] Dombrovsky, L. A., Sazhin, S. S., Mikhalovsky, S. V., Wood, R., and Heikal, M. R., 2003, "Spectral Properties of Diesel Fuel Droplets," Fuel, **82** pp. 15–22.

[21] Dombrovsky, L. A., 2002, "A Spectral Model of Absorption and Scattering of Thermal Radiation by Diesel Fuel Droplets," High Temp., **40**(2), pp. 242–248.

[22] Sazhin, S. S., Kristyadi, T., Abdelghaffar, W. A., and Heikal, M. R., 2006, "Models for Fuel Droplet Heating and Evaporation: Comparative Analysis," Fuel, **85**(12–13), pp. 1613–1630.

[23] Flynn, P. F., Durrett, R. P., Hunter, G. L., zur Loye, A. O., Akinyemi, O. C., Dec, J. E., and Westbrook, C. K., 1999, "Diesel Combustion: An Integrated View Combining Laser Diagnostics, Chemical Kinetics, and Empirical Validation," SAE Report No. 1999-01-0509.

[24] Abramzon, B., and Sazhin, S., 2006, "Convective Vaporization of Fuel Droplets with Thermal Radiation Absorption," Fuel, **85**(1), pp. 32–46.

[25] Dombrovsky, L. A., and Sazhin, S. S., 2003, "A Parabolic Temperature Profile Model for Heating of Droplets," ASME J. Heat Transfer, **125**, pp. 535–537.

[26] Schlichting, H., and Gersten, K., 2000, *Boundary Layer Theory*, Springer, Berlin, Germany.

[27] Versteeg, H. K., and Malalasekera, W., 1999, *An Introduction to Computational Fluid Dynamics*, Longman, Harlow, UK.

[28] Abramzon, B., and Sirignano, W. A., 1989, "Droplet Vaporization Model for Spray Combustion Calculations," Int. J. Heat Mass Transfer, **32**, pp. 1605–1618.

[29] Shishkova, I. N., and Sazhin, S. S., 2007, "A Numerical Algorithm for Kinetic Modelling of Evaporation Processes," J. Comput. Phys., **218**, pp. 635–653.

[30] Sazhin, S. S., Shishkova, I. N., Kryukov, A. P., Levashov, V., Yu, and Heikal, M. R., 2007, "Evaporation of Droplets into a Background Gas: Kinetic Modelling," Int. J. Heat Mass Transfer, **50**, pp. 2675–2691.

[31] Chin, J. S., and Lefebvre, A. H., 1985, "The Role of the Heat-up Period in Fuel Drop Evaporation," Int. J. Turbo Jet Engines, **2**, pp. 315–325.

[32] Handbook of Aviation Fuel Properties, 1984, American Petroleum Institute CRC Technical Report No. 530.

[33] Reid, R. C., and Sherwood, T. K., 1958, *The Properties of Gases and Liquids*, McGraw–Hill, London, U.K.

[34] Hirschfelder, J. O., Curtiss, C. F., and Bird, R. B., 1967, *Molecular Theory of Gases and Liquids*, 4th ed., Wiley, New York.

[35] Maxwell, J. B., 1950, *Data Book on Hydrocarbons: Application to Process Engineering*, van Nostrand, New York.

[36] Touloukian, Y. S., and Makita, T., 1970, *Specific Heat. Nonmetallic Liquids and Gases*, IFI/Plenum, New York.

[37] Raznjevic, K., 1976, *Handbook of Thermodynamics: Tables and Charts*, McGraw-Hill, London, U.K.

[38] Paredes, M. L. L., Nobrega, R., and Tavares, F. W., 2000, "A Completely Analytical Equation of State for Mixture of Square-Well Chain Fluid of Variable Well Width," *Proceedings 19th Inter American Congress of Chemical Engineering*, Agios de Sao Pedro, Brazil, 24–27 September, Paper No. 396.

[39] *CRC Handbook of Chemistry and Physics*, 86th ed., 2005, Taylor & Francis, Boca Raton, FL, pp. 6-35–6-190.

[40] Hales, J. L., 1967, "Thermodynamic Properties of Organic Oxygen Compounds. Part 18. Vapour Heat Capacities and Heats of Vaporization of Ethyl Ketone, Ethyl Propyl Ketone, Methyl Isopropyl Ketone, and Methyl Phenyl Ether," Trans. Faraday Soc., **63**, pp. 1876–1879.

[41] Lee, L., and Chuang, M., 1997, "Excess Volumes of Cyclohexane with 2-Propanone, 2-Butanone, 3-Pentanone, 4-Methyl-2-Penthanone, 1-Propanoland 2-Propanol and Ethanoic Acid + 1-Propanol Systems," J. Chem. Eng. Data, **42**, pp. 850–853.

[42] Fermeglia, M., Lapasin, R., and Torriano, G., 1990, "Excess Volumes and Viscosities of Binary Systems Containing 4-Methyl-3-Penthanone," J. Chem. Eng. Data, **35**, pp. 260–265.

A Fully Wet and Fully Dry Tiny Circular Fin Method for Heat and Mass Transfer Characteristics for Plain Fin-and-Tube Heat Exchangers Under Dehumidifying Conditions

Worachest Pirompugd[1]
Department of Mechanical Engineering,
Faculty of Engineering,
Burapha University,
Saensook, Muang,
Chonburi 20131, Thailand

Chi-Chuan Wang
Energy and Environment Lab.,
Industrial Technology Research Institute,
Hsinchu, Taiwan 310, R.O.C.

Somchai Wongwises[2]
Department of Mechanical Engineering,
Fluid Mechanics,
Thermal Engineering
and Multiphase Flow Research Lab. (FUTURE),
King Mongkut's University of Technology,
Thonburi, Bangmod,
Bangkok 10140, Thailand

This study proposes a new method, namely the "fully wet and fully dry tiny circular fin method," for analyzing the heat and mass transfer characteristics of plain fin-and-tube heat exchangers under dehumidifying conditions. The present method is developed from the tube-by-tube method proposed in the previous study by the same authors. The analysis of the fin-and-tube heat exchangers is carried out by dividing the heat exchanger into many tiny segments. A tiny segment will be assumed with fully wet or fully dry conditions. This method is capable of handling the plain fin-and-tube heat exchanger under fully wet and partially wet conditions. The heat and mass transfer characteristics are presented in dimensionless terms. The ratio of the heat transfer characteristic to mass transfer characteristic is also studied. Based on the reduced results, it is found that the heat transfer and mass transfer characteristics are insensitive to changes in fin spacing. The influence of the inlet relative humidity on the heat transfer characteristic is rather small. For one and two row configurations, a considerable increase of the mass transfer characteristic is encountered when partially wet conditions take place. The heat transfer characteristic is about the same in fully wet and partially wet conditions provided that the number of tube rows is equal to or greater than four. Correlations are proposed to describe the heat and mass characteristics for the present plain fin configuration. [DOI: 10.1115/1.2739589]

Keywords: fully wet and fully dry tiny circular fin method, dehumidifying conditions, heat transfer characteristic, mass transfer characteristic, plain fin-and-tube heat exchangers

1 Introduction

Generally the heat exchange process between two fluids that take place at different temperatures and is separated by a solid wall. Typical applications involving heat exchange may be found in air conditioning, refrigeration, power production, waste heat recovery, and chemical processing. The device used to implement the heat exchange process is called a heat exchanger. For residential air conditioning and refrigeration application, the most widely used heat exchangers take the form of a fin-and-tube configuration. Fin-and-tube heat exchangers generally consist of tubes in a block of parallel continuous fins. Depending on the application, fin-and-tube heat exchangers can be produced with one or more rows. The fin patterns can be in continuous form such as plain or wavy or in interrupted form such as louver or slit. Among the fin patterns being used, the plain fin-and-tube heat exchangers are the most widely used for their long term reliability, and the plain fin-and-tube heat exchangers can be exploited as condensers or evaporators. For application as an evaporator, the surface temperature of the fins is normally below the dew point temperature. As a result, simultaneous heat and mass transfer occurs on the fin surfaces.

Many studies have been published on the heat and mass transfer characteristics of fin-and-tube heat exchangers under dehumidifying conditions. For instance, ARI Standard 410 [1] has been used by the industry for over 40 years (since 1964). McQuiston [2,3] presented experimental data for five plate fin-and-tube heat exchangers, and developed a well-known heat transfer and friction correlation for both dry and wet surfaces. Mirth and Ramadhyani [4,5] investigated the heat and mass characteristics of wavy fin heat exchangers. Their results showed that the Nusselt number was very sensitive to changes of the inlet dew point temperature, and that the Nusselt number decreased with an increase of dew point temperature. Similar results were reported by Fu et al. [6] in dehumidifying heat exchangers having a louver fin configuration. They reported a pronounced decrease of the wet sensible heat transfer coefficient with the rise of the inlet relative humidity. Contrary to this, the experimental data of Seshimo et al. [7] indicated that the Nusselt number was relatively independent of the inlet conditions. Wang et al. [8] studied the effects of the fin pitch, the number of tube rows, and the inlet relative humidity on the heat transfer performance under dehumidification, concluding that the sensible heat transfer characteristic was relatively independent of the inlet humidity. The differences in the existing literature are attributed to the different reduction methodologies. Pirompugd et al. [9,10] presented a new reduction method, namely the "tube-

[1]Currently with Department of Mechanical Engineering, Fluid-Mechanics, Thermal Engineering and Multiphase Flow Research Lab, King Mongkut's University of Technology Thonburi, Bangmod, Bangkok 10140, Thailand.

[2]Corresponding author e-mail: somchai.won@kmutt.ac.th

Contributed by the Heat Transfer Division of ASME for publication in the JOURNAL OF HEAT TRANSFER. Manuscript received March 23, 2006; final manuscript received December 2, 2006. Review conducted by Anthony M. Jacobi.

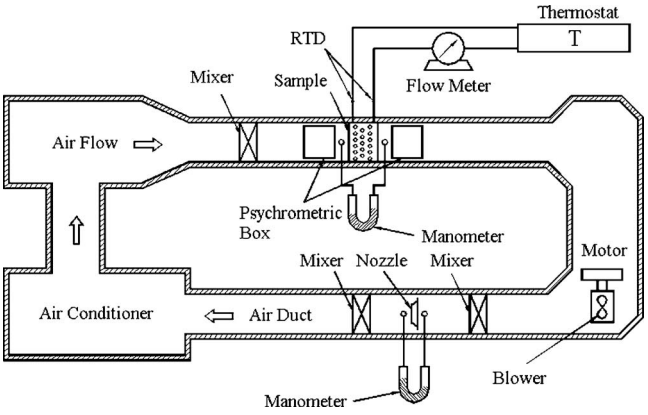

Fig. 1 Schematic diagram of experimental apparatus

by-tube method," for calculation of the heat and mass transfer characteristics for fin-and-tube heat exchangers under dehumidifying conditions. Their results showed that the heat and mass transfer characteristics were relatively independent of fin spacing and relative humidity.

In practice, the fin surfaces may be in wet or dry conditions depending on the temperature difference of the dew point temperature and surface temperature. Notice that if the dew point temperature of moist air is above the outside tube (including collar) temperature, there is only sensible heat transfer and it is termed the fully dry condition. However, if the dew point temperature of moist air is lower than the fin tip temperature, sensible and latent heat transfer occur at the same time for all fin surfaces. This condition is regarded as the fully wet condition. It is found that most of the available literature concerning the heat transfer characteristic is either related to fully dry conditions or to completely wet surfaces. There are very few papers addressing the heat transfer performance of the heat exchangers under partially wet surface conditions. For example, Xia and Jacobi [11] formulated the logarithmic-mean temperature difference (LMTD) and logarithmic-mean enthalpy difference (LMED) methods for fully dry, fully wet, partially wet, and frosted surface conditions. In view of the lack of research in this area, it is the objective of this study to provide a detailed method for analyzing the partially wet condition.

2 Experimental Apparatus

The schematic diagram of the experimental air circuit assembly is shown in Fig. 1. It consists of a closed-loop wind tunnel in which air is circulated by a variable speed centrifugal fan (7.46 kW, 10 HP). The air duct is made of galvanized sheet steel and has an 850 mm $\times$ 550 mm cross section. The dry-bulb and wet-bulb temperatures of the inlet air are controlled by an air ventilator that can provide a cooling capacity of up to 21.12 kW (6RT). The air flow-rate measurement station is an outlet chamber set up with multiple nozzles. This setup is based on the ASHRAE 41.2 standard [12]. A differential pressure transducer is used to measure the pressure difference across the nozzles. The air temperatures at the inlet and exit zones across the sample heat exchangers are measured by two psychrometric boxes based on the ASHRAE 41.1 standard [13].

The working medium for the tube side is cold water. A thermostatically controlled reservoir provides cold water at selected temperatures. The temperature differences on the water side are measured by two precalibrated resistance temperature detectors (RTDs). The water volumetric flow rate is measured by a magnetic flow meter with a ±0.001 L/s precision. All the temperature measuring probes are resistance temperature devices (Pt100), with a calibrated accuracy of ±0.05°C. In the experiments, only the data that satisfy the ASHRAE 33 [14] requirements (namely, the energy balance condition, $|\dot{Q}_a - \dot{Q}_w|/\dot{Q}_{\text{avg}}$, are less than 0.05, where $\dot{Q}_a$ is the air-side heat transfer rate; $\dot{Q}_w$ is the water-side heat transfer rate; and $\dot{Q}_{\text{avg}}$ is the average heat transfer rate between air side and water side) are considered in the final analysis. Detailed geometry used for the present plain fin-and-tube heat exchangers is tabulated in Table 1. The test fin-and-tube heat exchangers are tension wrapped having a "L" type fin collar. The test conditions of the inlet-air are as follows:

- Dry-bulb temperature of the air: 27±0.5°C;
- Inlet relative humidity for the incoming air: 50% and 90%;
- Inlet-air velocity: from 0.3 m/s to 4.5 m/s;
- Inlet-water temperature: 7±0.5°C; and
- Water velocity inside the tube: 1.5–1.7 m/s.

The test conditions approximate those encountered with typical fan coils and evaporators of air conditioning applications. Uncertainties reported in the present investigation, following the single-sample analysis proposed by Moffat [15], are tabulated in Table 2.

Table 1 Geometric dimensions of the sample plain fin-and-tube heat exchangers

No.	F_p (mm)	t (mm)	S_p (mm)	D_c (mm)	P_t (mm)	P_l (mm)	N
1	1.19	0.115	1.075	8.51	25.4	19.1	1
2	1.75	0.120	1.630	10.34	25.4	22.0	1
3	2.04	0.115	1.925	8.51	25.4	19.1	1
4	2.23	0.115	2.115	10.23	25.4	19.1	1
5	2.50	0.120	2.380	10.34	25.4	22.0	1
6	1.23	0.115	1.115	8.51	25.4	19.1	2
7	1.70	0.120	1.580	8.62	25.4	19.1	2
8	2.06	0.115	1.945	8.51	25.4	19.1	2
9	2.24	0.130	2.110	10.23	25.4	22.0	2
10	3.20	0.130	3.070	10.23	25.4	22.0	2
11	1.23	0.115	1.115	10.23	25.4	19.1	4
12	1.55	0.115	1.435	10.23	25.4	19.1	4
13	2.03	0.130	1.900	10.23	25.4	22.0	4
14	2.23	0.130	2.100	10.23	25.4	22.0	4
15	3.00	0.130	2.870	10.23	25.4	22.0	4
16	1.85	0.130	1.720	10.23	25.4	22.0	6
17	2.21	0.130	2.080	10.23	25.4	22.0	6
18	3.16	0.130	3.030	10.23	25.4	22.0	6

Table 2 Summary of estimated uncertainties

Primary measurements		Derived quantities		
Parameter	Uncertainty	Parameter	Uncertainty $Re_{Dc}=400$ (%)	Uncertainty $Re_{Dc}=5000$ (%)
$\dot{m}_a$	0.3–1%	Re_{Dc}	±1.0	±0.57
$\dot{m}_w$	0.5%	Re_{Di}	±0.73	±0.73
ΔP	0.5%	$\dot{Q}_w$	±3.95	±1.22
T_w	0.05°C	$\dot{Q}_a$	±5.5	±2.4
T_a	0.1°C	j_h, j_m	±11.4	±5.9

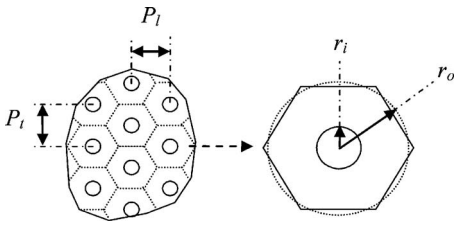

Fig. 3 Comparison between the data obtained from the present method and those obtained from the method of Threlkeld

3 Mathematical Model

The total heat transfer rate used in the calculation is the average of $\dot{Q}_a$ and $\dot{Q}_w$, namely

$$\dot{Q}_a = \dot{m}_a(i_{a,\text{in}} - i_{a,\text{out}}) - \dot{m}_a(W_{a,\text{in}} - W_{a,\text{out}})i_{w,f} \approx \dot{m}_a(i_{a,\text{in}} - i_{a,\text{out}}) \tag{1}$$

$$\dot{Q}_w = \dot{m}_w C_{p,w}(T_{w,\text{out}} - T_{w,\text{in}}) \tag{2}$$

$$\dot{Q}_{\text{avg}} = \frac{\dot{Q}_a + \dot{Q}_w}{2} \tag{3}$$

In this study, a new method, namely the "fully wet and fully dry tiny circular fin method" is proposed to evaluate the performances of plain fin-and-tube heat exchangers, instead of the conventional lump approach. Analysis of the plain fin-and-tube heat exchangers is first carried out by dividing the heat exchangers into many tiny segments (number of tube rows × number of tube passes per row × number of fins) as shown in Fig. 2. For calculation of the fin efficiency, the equivalent circular area method, as shown in Fig. 3, is adopted. Two heat transfer modes are identified in the heat transfer surface. The first one is the fully dry condition, in which the dew point temperature of the moist air is lower than the tube surface (including collar) temperature (as shown in Fig. 4(*a*)). As a result, only sensible heat transfer occurs on the whole area of this tiny segment. The other case is the fully wet condition, in which the dew point temperature of moist air is higher than the fin tip temperature (as shown in Fig. 4(*b*)). Both sensible and latent heat transfer take place along the area of each tiny segment.

3.1 Tiny Circular Fin Under Fully Wet Conditions

3.1.1 Heat Transfer. The new method for the plain fin-and-tube heat exchangers is based on the method of Threlkeld [16]. The overall heat transfer coefficient, U_i, is based on the enthalpy potential and is given as follows

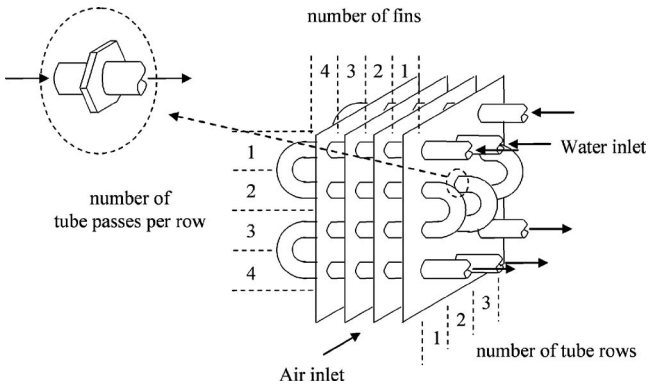

Fig. 2 Fully wet and fully tiny circular fin method

$$\dot{Q}_{\text{wet}} = U_i A_{\text{tot}} \Delta i_{m,\text{cf}} F \tag{4}$$

The term of $\Delta i_{m,\text{cf}}$ can be shown as

$$\Delta i_{m,\text{cf}} = i_{a,m,\text{cf}} - i_{r,m,\text{cf}} \tag{5}$$

According to Bump [17] and Myers [18], for the counter flow configuration, the mean enthalpy difference is

$$i_{a,m,\text{cf}} = i_{a,\text{in}} + \frac{i_{a,\text{in}} - i_{a,\text{out}}}{\ln\left(\frac{i_{a,\text{in}} - i_{r,\text{out}}}{i_{a,\text{out}} - i_{r,\text{in}}}\right)} - \frac{(i_{a,\text{in}} - i_{a,\text{out}})(i_{a,\text{in}} - i_{r,\text{out}})}{(i_{a,\text{in}} - i_{r,\text{out}}) - (i_{a,\text{out}} - i_{r,\text{in}})} \tag{6}$$

$$i_{r,m,\text{cf}} = i_{r,\text{out}} + \frac{i_{r,\text{out}} - i_{r,\text{in}}}{\ln\left(\frac{i_{a,\text{in}} - i_{r,\text{out}}}{i_{a,\text{out}} - i_{r,\text{in}}}\right)} - \frac{(i_{r,\text{out}} - i_{r,\text{in}})(i_{a,\text{in}} - i_{r,\text{out}})}{(i_{a,\text{in}} - i_{r,\text{out}}) - (i_{a,\text{out}} - i_{r,\text{in}})} \tag{7}$$

For a tiny segment, $i_{r,\text{in}}$ is nearly equal to $i_{r,\text{out}}$. Because the temperature of the water flowing in the tube side is almost constant, F can be approximated to unity [16]. The overall heat transfer coefficient is related to the individual heat transfer resistances [18], i.e., the water side thermal resistance for the convection heat transfer, the thermal resistance of the tube (including very tiny collar) for the conduction heat transfer, and the moist air side thermal resistance for the simultaneous heat and mass transfer as follows

$$\frac{1}{U_i} = \frac{b'_r A_{\text{tot}}}{h_{c,\text{in}} A_{p,\text{in}}} + \frac{b'_p A_{\text{tot}} \ln\left(\frac{D_{p,\text{out}}}{D_{p,\text{in}}}\right)}{2\pi k_p L_p} + \frac{1}{\frac{h_{c,\text{wf},p,\text{out}} A_{p,\text{out}}}{b'_{\text{wf},p,\text{out}} A_{\text{tot}}} + \frac{h_{c,\text{wf},f} A_f \eta_{f,\text{wet}}}{b'_{\text{wf},f} A_{\text{tot}}}} \tag{8}$$

Note that the water film is very thin, then

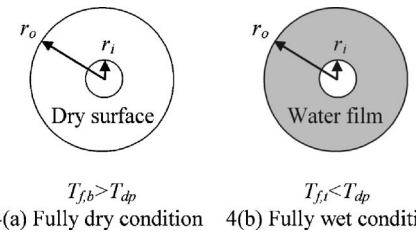

Fig. 4 Comparison between the data obtained from the present method and those obtained from the tube-by-tube method (Pirompugd et al. (2005))

$$h_{c,\mathrm{wf},f} = \frac{1}{\dfrac{C_{p,a}}{b'_{\mathrm{wf},f} h_{c,\mathrm{out}}} + \dfrac{y_{\mathrm{wf}}}{k_{\mathrm{wf}}}} \tag{9}$$

$$h_{c,\mathrm{wf},p,\mathrm{out}} = \frac{1}{\dfrac{C_{p,a}}{b'_{\mathrm{wf},p,\mathrm{out}} h_{c,\mathrm{out}}} + \dfrac{y_{\mathrm{wf}}}{k_{\mathrm{wf}}}} \tag{10}$$

y_{wf} in Eqs. (9) and (10) represents the thickness of the water film. A constant of 0.013 cm was proposed by Myers [18]. In practice, $y_{\mathrm{wf}}/k_{\mathrm{wf}}$ accounts for only 0.5–5% compared to $C_{p,a}/b'_{\mathrm{wf},f} h_{c,\mathrm{out}}$ and $C_{p,a}/b'_{\mathrm{wf},p,\mathrm{out}} h_{c,\mathrm{out}}$, and has often been neglected by previous investigators. As a result, this term is not included in the final analysis. The water-side heat transfer coefficient was presented by Gnielinski [19]

$$h_{c,\mathrm{in}} = \frac{(f_{\mathrm{in}}/2)(\mathrm{Re}_{\mathrm{in}} - 1000)\mathrm{Pr}_{\mathrm{in}}}{1.07 + 12.7\sqrt{f_{\mathrm{in}}/2}(\mathrm{Pr}_{\mathrm{in}}^{2/3} - 1)} \cdot \frac{k_w}{D_{p,\mathrm{in}}} \tag{11}$$

and the friction factor, f_i is

$$f_{\mathrm{in}} = \frac{1}{(1.58 \ln \mathrm{Re}_{\mathrm{in}} - 3.28)^2} \tag{12}$$

The Reynolds number used in Eqs. (11) and (12) is based on the inside tube diameter. In Eq. (8) b'_p, b'_r, $b'_{\mathrm{wf},f}$, and $b'_{\mathrm{wf},p,\mathrm{out}}$ are the ratios of enthalpy to temperature that must be evaluated. The quantities b'_p and b'_r can be calculated as

$$b'_r = \frac{i_{r,p,\mathrm{in},m,\mathrm{cf}} - i_{r,m,\mathrm{cf}}}{T_{p,\mathrm{in},m,\mathrm{cf}} - T_{r,m,\mathrm{cf}}} \tag{13}$$

$$b'_p = \frac{i_{r,p,\mathrm{out},m,\mathrm{cf}} - i_{r,p,\mathrm{in},m,\mathrm{cf}}}{T_{p,\mathrm{out},m,\mathrm{cf}} - T_{p,\mathrm{in},m,\mathrm{cf}}} \tag{14}$$

The values of $b'_{\mathrm{wf},f}$ and $b'_{\mathrm{wf},p,\mathrm{out}}$ denote the slopes of the saturated moist air enthalpy curved evaluated at the mean water film temperatures of the fin and outside tube surfaces, respectively. Without loss of generality, $b'_{\mathrm{wf},f}$ and $b'_{\mathrm{wf},p,\mathrm{out}}$ can be approximated by the slope of the saturated moist air enthalpy curved at the mean fin surface temperature ($T_{f,m,\mathrm{cf}}$) and the mean outside tube surface temperature ($T_{p,\mathrm{out},m,\mathrm{cf}}$) [8]. With the assumption of the small range of temperature, the enthalpy of saturated air may be represented as the linear function of the temperature. Then, the slope of the saturated moist air enthalpy can be calculated [16]. However, the evaluation of $b'_{\mathrm{wf},f}$ requires a trial and error procedure and needs the information of wet fin efficiency. Notice that the wet fin efficiency ($\eta_{f,\mathrm{wet}}$) is based on the enthalpy difference proposed by Threlkeld [16]

$$\eta_{f,\mathrm{wet}} = \frac{i_{a,m,\mathrm{cf}} - i_{r,f,m,\mathrm{cf}}}{i_{a,m,\mathrm{cf}} - i_{r,p,\mathrm{out},m,\mathrm{cf}}} \tag{15}$$

The use of the enthalpy potential equation greatly simplifies the fin efficiency calculation as illustrated by Kandlikar [20]. However, the original formulation of the wet fin efficiency by Threlkeld [16] was for straight fin configuration. For a circular fin, the wet fin efficiency is [8]

$$\eta_{f,\mathrm{wet}} = \frac{2r_i}{M_T(r_o^2 - r_i^2)}\left[\frac{K_1(M_T r_i)I_1(M_T r_o) - K_1(M_T r_o)I_1(M_T r_i)}{K_1(M_T r_o)I_0(M_T r_i) + K_0(M_T r_i)I_1(M_T r_o)}\right] \tag{16}$$

where

$$M_T = \sqrt{\frac{2h_{c,\mathrm{wf},f}}{k_f t}} \tag{17}$$

Evaluation of $b'_{\mathrm{wf},f}$ requires a trial and error procedure. For the trial and error procedure, $i_{r,f,m,\mathrm{cf}}$ must be calculated using the following equation

$$i_{r,f,m,\mathrm{cf}} = i_{a,m,\mathrm{cf}} - \eta_{f,\mathrm{wet}}\left(1 - U_i A_{\mathrm{tot}}\left[\frac{b'_r}{h_{c,\mathrm{in}} A_{p,\mathrm{in}}} + \frac{b'_p \ln\left(\dfrac{D_{p,\mathrm{out}}}{D_{p,\mathrm{in}}}\right)}{2\pi k_p L_p}\right]\right)\Delta i_{m,\mathrm{cf}} \tag{18}$$

An algorithm for solving the heat transfer characteristic for the fully wet condition is given as follows:

1. Based on the information, calculate the average heat transfer rate ($\dot{Q}_{\mathrm{avg}}$) using Eq. (3);
2. Assume a $h_{c,\mathrm{out}}$ for all elements;
3. Calculate the heat transfer characteristic for each segment with the following procedures:
   - 3.1 Calculate the water-side heat transfer coefficient of $h_{c,\mathrm{in}}$ using Eq. (11);
   - 3.2 Assume an outlet moist air enthalpy of the calculated segment;
   - 3.3 Calculate $i_{a,m,\mathrm{cf}}$ and $i_{r,m,\mathrm{cf}}$ by Eqs. (6) and (7);
   - 3.4 Assume $T_{p,\mathrm{in},m,\mathrm{cf}}$ and $T_{p,\mathrm{out},m,\mathrm{cf}}$;
   - 3.5 Calculate $b'_r/h_{c,\mathrm{in}}A_{p,\mathrm{in}}$ and $b'_p \ln(D_{p,\mathrm{out}}/D_{p,\mathrm{in}})/2\pi k_p L_p$;
   - 3.6 Assume a $T_{f,m,\mathrm{cf}}$;
   - 3.7 Calculate the $\eta_{f,\mathrm{wet}}$ using Eq. (16);
   - 3.8 Calculate U_i from Eq. (8);
   - 3.9 Calculate $i_{r,f,m,\mathrm{cf}}$ by Eq. (18);
   - 3.10 Calculate $T_{f,m,\mathrm{cf}}$ from $i_{r,f,m,\mathrm{cf}}$;
   - 3.11 If $T_{f,m,\mathrm{cf}}$, calculated in Step 3.10, is not equal to that assumed in step 3.6, the calculation Steps 3.7–3.10 will be repeated with $T_{f,m,\mathrm{cf}}$ calculated in Step 3.10 until $T_{f,m,\mathrm{cf}}$ is constant;
   - 3.12 Calculate the heat transfer rate ($\dot{Q}$) of this segment;
   - 3.13 Calculate $T_{p,\mathrm{in},m,\mathrm{cf}}$ and $T_{p,\mathrm{out},m,\mathrm{cf}}$ from the water-side convection heat transfer and the conduction heat transfer of the tube;
   - 3.14 If $T_{p,\mathrm{in},m,\mathrm{cf}}$ and $T_{p,\mathrm{out},m,\mathrm{cf}}$, calculated from Step 3.13, are not equal to the assumed values in Step 3.4, the calculation of Steps 3.5–3.13 will be repeated with $T_{p,\mathrm{in},m,\mathrm{cf}}$ and $T_{p,\mathrm{out},m,\mathrm{cf}}$ being calculated in Step 3.13 until $T_{p,\mathrm{in},m,\mathrm{cf}}$ and $T_{p,\mathrm{out},m,\mathrm{cf}}$ are fixed;
   - 3.15 Calculate the outlet moist air enthalpy by Eq. (1) and the outlet water temperature by Eq. (2); and
   - 3.16 If the outlet moist air enthalpy calculated in Step 3.15 is not equal to that assumed value in Step 3.2, the calculation Steps 3.3–3.15 will be repeated with the outlet moist air enthalpy calculated from Step 3.15 until the outlet moist air enthalpy is fixed.
4. If the summation of the heat transfer rate ($\dot{Q}$) for all elements is not equal to $\dot{Q}_{\mathrm{avg}}$, $h_{c,\mathrm{out}}$ will be assumed with a new value and the calculation Step 3 will be repeated until the summation of the heat transfer rate ($\dot{Q}$) for all elements is equal to $\dot{Q}_{\mathrm{avg}}$.

3.1.2 Mass Transfer. For the fully wet condition, the cooling and dehumidifying of the moist air by a cold surface involves the simultaneous heat and mass transfer and can be described by the process line equation (SI unit) from Threlkeld [16]

$$\frac{di_a}{dW_a} = R\frac{(i_a - i_{\mathrm{wf}})}{(W_a - W_{\mathrm{wf}})} + (i_{w,g} - 2501R) \tag{19}$$

and

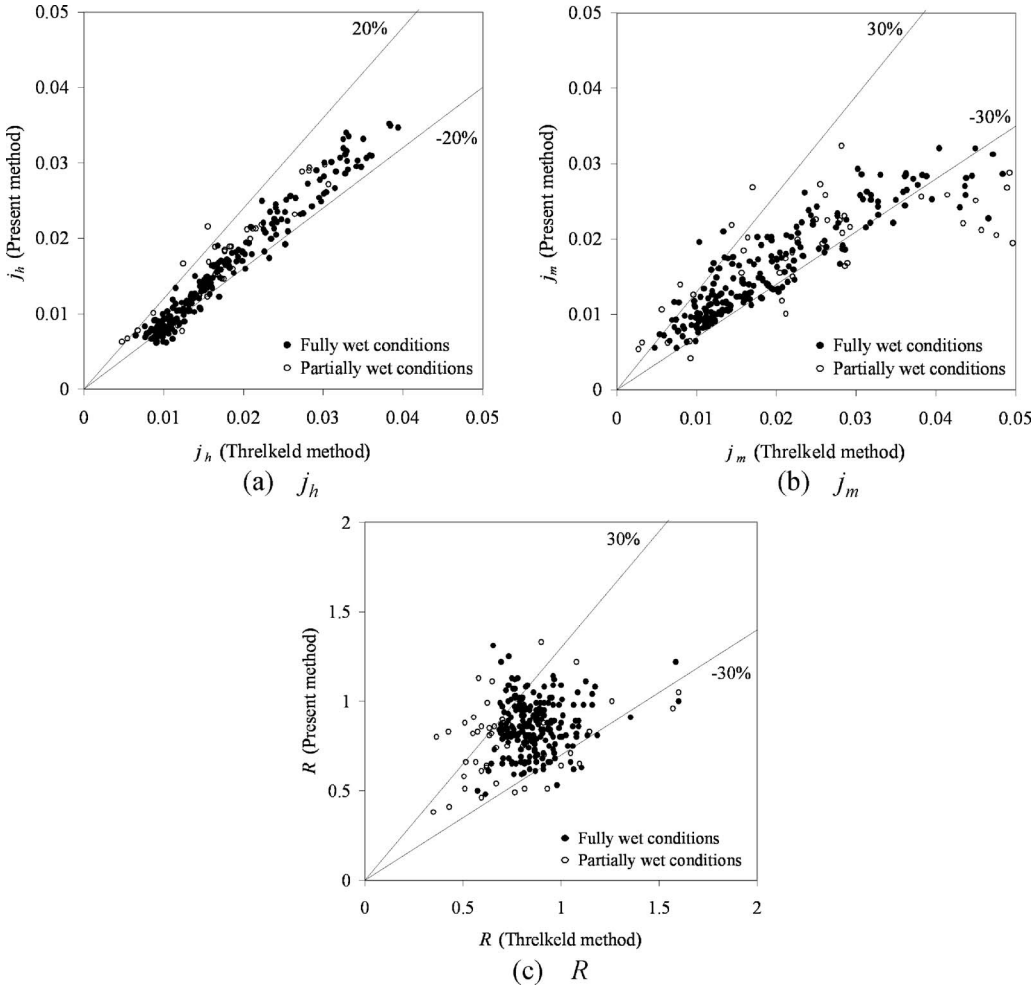

Fig. 5 j_h and j_m obtained from the present method

$$R = \frac{h_{c,\text{out}}}{h_{d,\text{out}} C_{p,a}} \tag{20}$$

However, for the present fin-and-tube heat exchanger, Eq. (19) did not correctly describe the dehumidification process on the psychrometric chart. This is because the saturated moist air enthalpy (i_{wf}) at the mean water film temperature on the fin surface is different from that at the outside tube surface. In this regard, a modification of the process line on the psychrometric chart corresponding to the fin-and-tube heat exchangers is made. From the energy balance of the dehumidification, the rate equation can be arrived at by following expression

$$\dot{m}_a di_a = \frac{h_{c,\text{out}}}{C_{p,a}} dA_{p,\text{out}} (i_{a,m} - i_{r,p,\text{out},m}) + \frac{h_{c,\text{out}}}{C_{p,a}} dA_f (i_{a,m} - i_{r,f,m}) \tag{21}$$

Note that the first term on the right-hand side denotes the heat transfer for the outside tube part, whereas the second term is the heat transfer for the fin part. Conservation of the water condensate gives

$$\dot{m}_a \, dW_a = h_{d,\text{out}} \, dA_{p,\text{out}} (W_{a,m} - W_{r,p,\text{out},m}) + h_{d,\text{out}} \, dA_f (W_{a,m} - W_{r,f,m}) \tag{22}$$

Dividing the equation of the heat transfer rate (Eq. (21)) by the equation of the mass transfer rate (Eq. (22)) yields

$$\frac{di_a}{dW_a} = \frac{R \cdot (i_{a,m} - i_{r,p,\text{out},m}) + R \cdot (\varepsilon - 1) \cdot (i_{a,m} - i_{r,f,m})}{(W_{a,m} - W_{r,p,\text{out},m}) + (\varepsilon - 1) \cdot (W_{a,m} - W_{r,f,m})} \tag{23}$$

where

$$\varepsilon = \frac{A_{\text{tot}}}{A_{p,\text{out}}} \tag{24}$$

By assuming a value of the ratio of heat transfer to mass transfer, R, and by integrating Eq. (23) with an iterative algorithm, the moist air-side convective mass transfer performance can be obtained. Analogous procedures for obtaining the mass transfer characteristic are given as

1. Obtain $W_{r,p,\text{out},m}$ and $W_{r,f,m}$ from $i_{r,p,\text{out},m}$ and $i_{r,f,m}$ from those calculations of the heat transfer;
2. Assume a value of R;
3. Calculations are performed from the first element to the last element, employing the following procedures:
   - 3.1 Assume an outlet moist air humidity ratio;
   - 3.2 Calculate the outlet moist air humidity ratio of each element by Eq. (23); and
   - 3.3 If the outlet moist air humidity ratio obtained from Step 3.2 is not equal to the assumed value of Step 3.1, the calculation Steps 3.1–3.2 will be repeated.
4. If the average of the outlet moist air humidity ratio for all elements of the last row is not equal to the total outlet moist

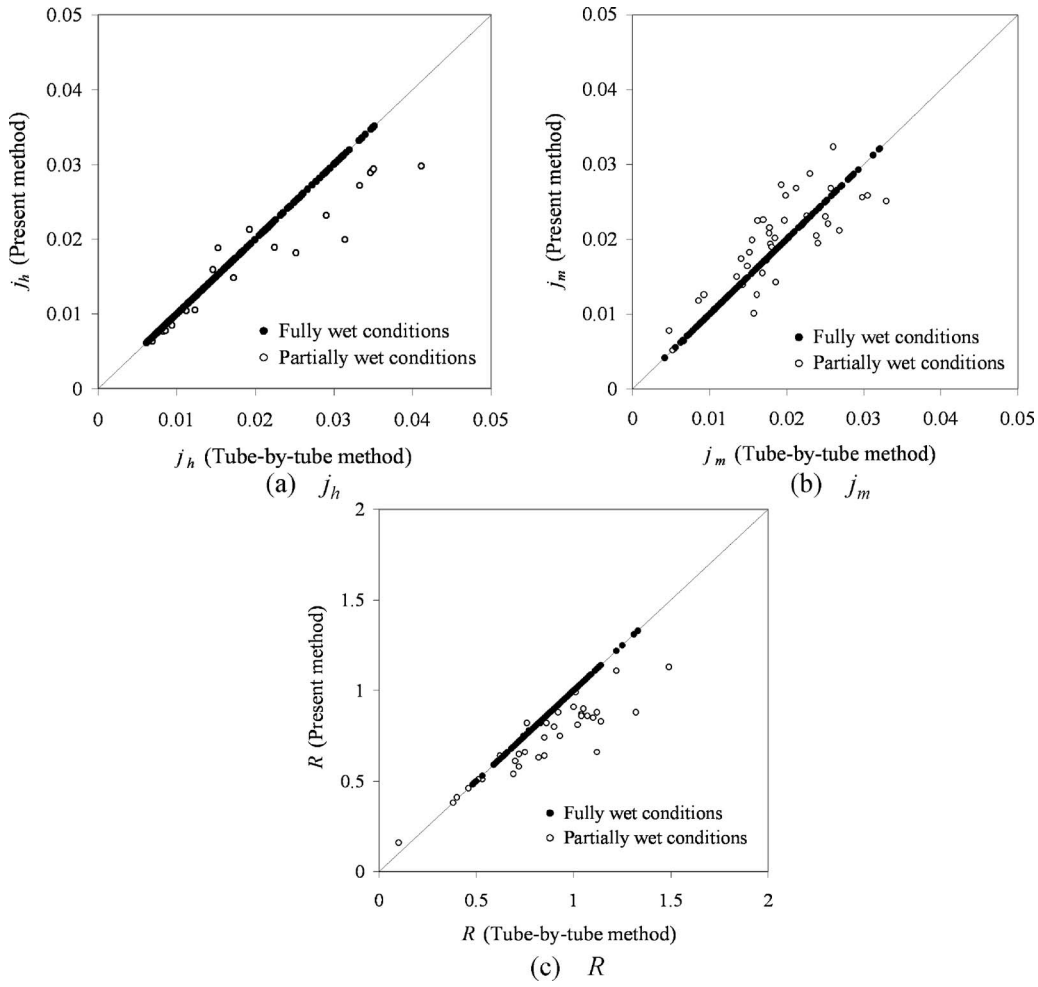

Fig. 6 Comparison between predicted data and experimental data

air humidity ratio, assume a new R value and the calculation Step 3 will be repeated until the average of the outlet moist air humidity ratio of the last row is equal to the outlet moist air humidity ratio.

3.2 Tiny Circular Fin Under Fully Dry Condition

3.2.1 Heat Transfer. The total rate of heat transfer used in the calculation is averaged from the air side ($\dot{Q}_a$) and the water side ($\dot{Q}_w$) as shown in Eq. (3). For the fully dry condition, the overall heat transfer coefficient, U_T, is based on the temperature difference and given as follows

$$\dot{Q}_{\text{dry}} = U_T A_{\text{tot}} \Delta T_{m,\text{cf}} F \tag{25}$$

The term of $\Delta T_{m,\text{cf}}$ can be shown as

$$\Delta T_{m,\text{cf}} = T_{a,m,\text{cf}} - T_{w,m,\text{cf}} \tag{26}$$

According to Bump [17], for the counter flow configuration, the mean temperature difference is

$$T_{a,m,\text{cf}} = T_{a,\text{in}} + \frac{T_{a,\text{in}} - T_{a,\text{out}}}{\ln\left(\dfrac{T_{a,\text{in}} - T_{w,\text{out}}}{T_{a,\text{out}} - T_{w,\text{in}}}\right)} - \frac{(T_{a,\text{in}} - T_{a,\text{out}})(T_{a,\text{in}} - T_{w,\text{out}})}{(T_{a,\text{in}} - T_{w,\text{out}}) - (T_{a,\text{out}} - T_{w,\text{in}})} \tag{27}$$

$$T_{w,m,\text{cf}} = T_{w,\text{out}} + \frac{T_{w,\text{out}} - T_{w,\text{in}}}{\ln\left(\dfrac{T_{a,\text{in}} - T_{w,\text{out}}}{T_{a,\text{out}} - T_{w,\text{in}}}\right)} - \frac{(T_{w,\text{out}} - T_{w,\text{in}})(T_{a,\text{in}} - T_{w,\text{out}})}{(T_{a,\text{in}} - T_{r,\text{out}}) - (T_{a,\text{out}} - T_{w,\text{in}})} \tag{28}$$

In the analysis, F can be approximated to unity. The overall heat transfer coefficient is related to the individual heat transfer resistances, which are the water-side thermal resistance for the convection heat transfer, the thermal resistance of the tube (including very tiny collar) for the conduction heat transfer, and the air-side thermal resistance as follows

$$\frac{1}{U_T} = \frac{A_{\text{tot}}}{h_{c,\text{in}} A_{p,\text{in}}} + \frac{A_{\text{tot}} \ln\left(\dfrac{D_{p,\text{out}}}{D_{p,\text{in}}}\right)}{2\pi k_p L_p} + \frac{1}{\dfrac{h_{c,\text{out}} A_{p,\text{out}}}{A_{\text{tot}}} + \dfrac{h_{c,\text{out}} A_f \eta_{f,\text{dry}}}{A_{\text{tot}}}} \tag{29}$$

The water-side heat transfer coefficient is determined from the Gnielinski semi-empirical correlation [19]. The dry fin efficiency ($\eta_{f,\text{dry}}$) is based on the temperature difference shown as

$$\eta_{f,\text{dry}} = \frac{T_{a,m,\text{cf}} - T_{f,m,\text{cf}}}{T_{a,m,\text{cf}} - T_{p,\text{out},m,\text{cf}}} \tag{30}$$

The dry fin efficiency for a circular fin is determined by the formula proposed by Kern and Kraus[21] as follows

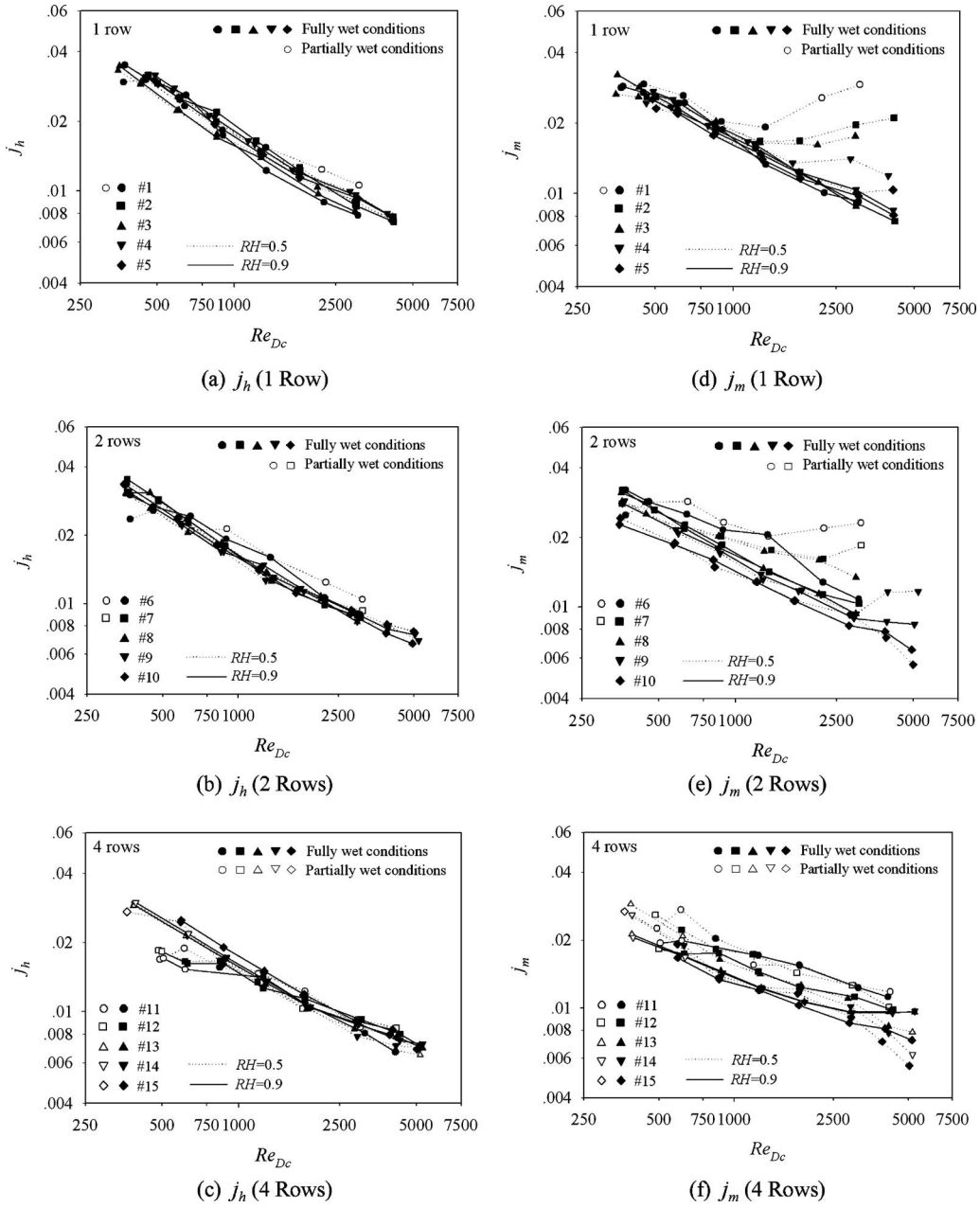

Fig. 7 j_h and j_m obtained from the present method

$$\eta_{f,\mathrm{dry}} = \frac{2r_i}{M_m(r_o^2 - r_i^2)}\left[\frac{K_1(M_m r_i)I_1(M_m r_o) - K_1(M_m r_o)I_1(M_m r_i)}{K_1(M_m r_o)I_0(M_m r_i) + K_0(M_m r_i)I_1(M_m r_o)}\right] \tag{31}$$

where

$$M_m = \sqrt{\frac{2h_{c,\mathrm{out}}}{k_f t}} \tag{32}$$

An algorithm for solving the heat transfer characteristic for the fully dry condition is given as follows:

1. Based on the information, calculate the average heat transfer rate ($\dot{Q}_{\mathrm{avg}}$) using Eq. (3);
2. Assume a $h_{c,\mathrm{out}}$ for all elements;
3. Calculate the heat transfer characteristic for each segment with the following procedures:

- 3.1 Calculate the tube-side heat transfer coefficient of h_i using Eq. (11);
- 3.2 Assume an outlet-air enthalpy of the calculated segment;
- 3.3 Calculate $T_{a,m,\mathrm{cf}}$ and $T_{w,m,\mathrm{cf}}$ by Eqs. (27) and (28);
- 3.4 Calculate $1/h_{c,\mathrm{in}}A_{p,\mathrm{in}}$ and $\ln(D_{p,\mathrm{out}}/D_{p,\mathrm{in}})/2\pi k_p L_p$;
- 3.5 Calculate the $\eta_{f,\mathrm{dry}}$ using Eq. (31);
- 3.6 Calculate U_T from Eq. (29);
- 3.7 Calculate $\dot{Q}_{\mathrm{dry}}$ from Eq. (25) of this segment;
- 3.8 Calculate the outlet-air enthalpy and the outlet-water temperature from $\dot{Q}_{\mathrm{dry}}$ obtained in Step 3.7; and
- 3.9 If the outlet-air enthalpy obtained in Step 3.8 is not equal to that assumed in Step 3.2, the calculation Steps 3.3–3.8 will be repeated with the outlet-air enthalpy obtained in Step 3.8 until the outlet-air enthalpy reaches a constant value.

4. If the summation of the heat transfer rate ($\dot{Q}$) for all elements is not equal to $\dot{Q}_{avg}$, $h_{c,out}$ will be assumed with a new value and the calculation Step 3 will be repeated until the summation of the heat transfer rate ($\dot{Q}$) for all elements is equal to $\dot{Q}_{avg}$.

3.3 Chilton–Colburn *j*-Factor for Heat and Mass Transfer (j_h and j_m). The heat and mass transfer characteristics for the plain fin-and-tube heat exchangers from the experimentation will be presented in the forms of the dimensionless groups

$$j_h = \frac{h_{c,out}}{G_{a,max} C_{p,a}} \mathrm{Pr}_{out}^{2/3} \tag{33}$$

$$j_m = \frac{h_{d,out}}{G_{a,max}} \mathrm{Sc}_{out}^{2/3} \tag{34}$$

4 Results and Discussion

The heat and mass transfer characteristics for the plain fin-and-tube heat exchangers are presented in terms of the dimensionless parameters j_h and j_m, respectively. The test results are first compared with the original Threlkeld method. The comparisons are shown in Figs. 5(*a*), 5(*b*), and 5(*c*). For the heat transfer characteristic, one can see in Fig. 5(*a*) that the original lumped approach is in fair agreement with the present discretized approach (77.86% of j_h within ±20%). However, the j_h obtained by the present method is slightly lower than that obtained by the Threlkeld method. There are two reasons for this result. The first one is because the j_h obtained by the present method is based on a discretized approach. In addition, the original Threlkeld method is applicable for fully wet surfaces only. For those data that are in partially wet conditions, an underestimation of the wet fin efficiency by the lumped Threlkeld method gives rise to a higher heat transfer coefficient, thereby yielding a higher j_h value accordingly. For the reduced results of the mass transfer characteristic, shown in Fig. 5(*b*), one can see a much larger departure to the original Threlkeld method relative to the present method (76.72% of j_m within ±30%). This is attributed to the original Threlkeld method being more suitable for counter flow arrangements. By comparison with the tube-by-tube method proposed by Pirompugd et al.[9], as shown in Figs. 6(*a*), 6(*b*), and 6(*c*), the heat and mass transfer characteristics obtained by the present method for the fully wet conditions are equal to those obtained by the tube-by-tube method. However, for the partially wet conditions, the heat and mass transfer characteristics obtained by the present method are different from those obtained from the tube-by-tube method. This is because the present method takes into account partially wet conditions, whereas the tube-by-tube method is more suitable for fully wet conditions.

A typical plot for examination of the influence of the inlet relative humidity and the fin spacing on the heat and mass transfer characteristics are shown in Fig. 7. As seen in Figs. 7(*a*)–7(*c*), the heat transfer characteristic is relatively insensitive to the inlet relative humidity and fin spacing. For the influence of fin spacing on the heat transfer characteristic having $N=1$ or $N=2$, Wang and Chi[22] showed that the results are different from those in fully dry conditions. Based on the numerical simulation by Torikoshi et al.[23], they found that the vortex forming behind the tube can be suppressed and the entire flow region can be kept steady and laminar when the fin spacing is small enough. A further increase of fin spacing would result in a noticeable increase of cross-stream width of the vortex region behind the tube. As a result, the heat transfer characteristic decreases with the increase of fin spacing for the one-row configuration, indicating a detectable influence of fin spacing. However, it can be seen that the effect of fin spacing on the heat transfer characteristic is comparatively small for the wet fin surface. Apparently it is attributed to the presence of condensate that provides a good air flow mixing even at larger fin spacing. In fact, the difference in the heat transfer characteristic becomes even more negligible when the number of tube rows is increased. With the increase in the number of tube rows, the condensate blow-off phenomenon from the preceding row is blocked by the subsequent row.

As seen in Figs. 7(*d*)–7(*f*), the influence of the inlet relative humidity on the mass transfer characteristics is rather small when the fin spacing is sufficiently large (>2.0 mm). However, at a smaller fin spacing (sample Nos. 1–3, 6–8, and 11–13) one can observe a slight decrease of j_m when the inlet relative humidity is increased from 50% to 90%. The slight decrease in the mass transfer characteristic with the inlet relative humidity at dense fin spacing may be described with the condensate retention phenomenon. Yoshii et al.[24] conducted a flow pattern observation of the air flow across tube bank, their results indicating that the blockage of the tube rows by the condensate retention may hinder the performance of the heat exchangers. Thus, one can see a slight drop in the mass transfer characteristic. However, a considerable increase in the mass transfer characteristic is encountered when relative humidity (RH)=0.5 and $\mathrm{Re}_{Dc} > 1000$. This is attributed to the blow-off condensate by flow inertia which makes more room for water vapor to condense along the surface.

The dehumidifying process involves heat and mass transfer simultaneously. If mass transfer data are unavailable, it is convenient to employ the analogy between the heat and mass transfer. The existence of the heat and mass analogy is due to the fact that conduction and diffusion in a liquid are governed by physical laws of identical mathematical forms. Therefore, for an air–water vapor mixture, the ratio of $h_{c,o}/h_{d,o}C_{p,a}$ is generally around unity. The term in Eq. (20) is approximately equal to unity for dilute mixtures like water vapor in air near the atmospheric pressure (temperature well below the corresponding boiling point). The validity of this approximation relies heavily on the mass transfer rate. The experimental data of Hong and Webb [25] indicated that this value was between 0.7 and 1.1, Seshimo et al.[7] gave a value of 1.1. Eckels and Rabas [26] also reported a similar value of 1.1–1.2 for their test results of fin-and-tube heat exchangers having plain fin geometry. The aforementioned studies all showed the applicability of the approximation. In the present study, we notice that the values of $h_{c,o}/h_{d,o}C_{p,a}$ are generally between 0.6 and 1.2.

It is obvious from the test results shown that no single curve can describe the j_h and j_m factors. As a result, using a multiple linear regression technique in a range of experimental data. ($300 < \mathrm{Re}_{Dc} < 5500$), the appropriate correlations of j_h and j_m based on the present data are as follows

1. –1 row and fully wet condition

$$j_{h,1} = 0.6189\left(\frac{S_p}{D_c}\right)^{-0.4176}\left(\frac{P_l}{D_c}\right)^{-0.7834}\left(\frac{P_t}{D_c}\right)^{0.9802}\mathrm{Re}^{\left(0.3232\frac{S_p}{D_c}+0.04332\frac{P_l}{D_c}-0.07983\frac{P_t}{D_c}-0.6125\right)} \tag{35}$$

$$j_{m,1} = 0.2094\left(\frac{S_p}{D_c}\right)^{-0.3507}\left(\frac{P_l}{D_c}\right)^{-1.6856}\left(\frac{P_t}{D_c}\right)^{1.9988}\mathrm{Re}^{\left(0.3264\frac{S_p}{D_c}+0.09569\frac{P_l}{D_c}-0.09808\frac{P_t}{D_c}-0.5523\right)} \tag{36}$$

$$R_1 = 2.8804\left(\frac{S_p}{D_c}\right)^{0.00973}\left(\frac{P_l}{D_c}\right)^{0.6203}\left(\frac{P_t}{D_c}\right)^{-0.8043}\mathrm{Re}^{\left(-0.0671\frac{S_p}{D_c}-0.0295\frac{P_l}{D_c}+0.00847\frac{P_t}{D_c}-0.06323\right)} \quad (37)$$

2. –1 row and partially wet condition ($70\% < A_{wet}/A_{tpt} < 100\%$)

$$j_{h,1,p} = 1.5638 j_{h,1}\left(\frac{A_{wet}}{A_{tot}}\right)^{-0.5554}\mathrm{Re}^{\left(0.1132\frac{S_p}{D_c}-0.01953\frac{P_l}{D_c}+0.003906\frac{P_t}{D_c}-0.02734\right)} \quad (38)$$

$$j_{m,1,p} = 0.3384 j_{m,1}\left(\frac{A_{wet}}{A_{tot}}\right)^{-0.5072}\mathrm{Re}^{\left(0.09427\frac{S_p}{D_c}-0.00001\frac{P_l}{D_c}+0.04688\frac{P_t}{D_c}-0.00001\right)} \quad (39)$$

$$R_{1,p} = 1.5165 R_1\left(\frac{A_{wet}}{A_{tot}}\right)^{-0.04714}\mathrm{Re}^{\left(0.02054\frac{S_p}{D_c}-0.02344\frac{P_l}{D_c}+0.03906\frac{P_t}{D_c}-0.01563\right)} \quad (40)$$

3. –2, 4 and 6 rows and fully wet condition

$$j_{h,N} = 0.3301 j_{h,1}\left(\frac{S_p}{D_c}\right)^{0.4683}\left(\frac{P_l}{D_c}\right)^{0.3549}\left(\frac{P_t}{D_c}\right)^{0.8906}\mathrm{Re}^{\left(-0.3611\frac{S_p}{D_c}-0.01713\frac{P_l}{D_c}-0.01710\frac{P_t}{D_c}+0.2514\right)} \quad (41)$$

$$j_{m,N} = 0.08575 j_{m,1}\left(\frac{S_p}{D_c}\right)^{0.2051}\left(\frac{P_l}{D_c}\right)^{0.8187}\left(\frac{P_t}{D_c}\right)^{1.425}\mathrm{Re}^{\left(-0.3503\frac{S_p}{D_c}-0.03997\frac{P_l}{D_c}-0.054360\frac{P_t}{D_c}+0.4086\right)} \quad (42)$$

$$R_N = 5.0207 R_1\left(\frac{S_p}{D_c}\right)^{0.1977}\left(\frac{P_l}{D_c}\right)^{-0.2889}\left(\frac{P_t}{D_c}\right)^{-1.0349}\mathrm{Re}^{\left(0.04954\frac{S_p}{D_c}+0.01036\frac{P_l}{D_c}+0.06751\frac{P_t}{D_c}-0.2272\right)} \quad (43)$$

4. –2, 4 and 6 rows and partially wet condition ($60\% < A_{wet}/A_{tpt} < 100\%$)

$$j_{h,N,p} = 1.1833\left(\frac{j_{h,N}}{j_{h,1}}\right)\left(\frac{A_{wet}}{A_{tot}}\right)^{-0.1258}\mathrm{Re}^{\left(0.0749\frac{S_p}{D_c}-0.01844\frac{P_l}{D_c}-0.00865\frac{P_t}{D_c}-0.56937\right)} \quad (44)$$

$$j_{m,N,p} = 0.4406\left(\frac{j_{m,N}}{j_{m,1}}\right)\left(\frac{A_{wet}}{A_{tot}}\right)^{-0.3742}\mathrm{Re}^{\left(0.2132\frac{S_p}{D_c}-0.03656\frac{P_l}{D_c}+0.02305\frac{P_t}{D_c}-0.4906\right)} \quad (45)$$

$$R_{N,p} = 2.1662\left(\frac{R_N}{R_1}\right)\left(\frac{A_{wet}}{A_{tot}}\right)^{0.2434}\mathrm{Re}^{\left(-0.1486\frac{S_p}{D_c}+0.01579\frac{P_l}{D_c}-0.03139\frac{P_t}{D_c}-0.05805\right)} \quad (46)$$

Detailed comparisons of the proposed correlations against the experimental data are shown in Figs. 8(*a*), 8(*b*), and 8(*c*). It is found that Eqs. (35), (38), (41), and (44) can describe 96.95% of j_h within ±20%. Equations (36), (39), (42), and (45) can describe 77.49% of j_m within ±20%. Equations (37), (40), (43), and (46) can describe 80.92% of R within ±20%.

5 Conclusions

This study experimentally examines the heat and mass characteristics of 18 fin-and-tube heat exchangers having plain fin geometry. On the basis of previous discussions, the following conclusions are made:

1. A fully wet and fully dry tiny circular fin method is proposed in this study for reducing the test results. This predictive ability of the proposed method is superior to previous studies;
2. It is found that the reduced results for the heat transfer characteristic by the present method are insensitive to changes of the inlet humidity. The effect of the fin spacing on the mass transfer characteristic is rather small when the fin spacing is larger than 2.0 mm. However, at a smaller fin spacings, j_m decreases slightly when the relative humidity increases;
3. Comparatively, the heat transfer characteristic is independent of the fin spacing. This is because the presence of condensate plays a role in altering the air flow pattern within the heat exchanger, resulting in better mixing characteristics. For $N \geq 4$, the heat transfer characteristic is about the same, even when the fin surface is partially wet;
4. For one and two row configurations, the effect of the relative humidity on the mass transfer characteristic becomes more pronounced when the partially wet condition has taken place; and
5. Correlations are proposed for the present fin-and-tube heat exchanger having plain fin configurations. These correlations can describe 96.95% of j_h within ±20%, 77.49% of j_m within ±20%, and 80.92% of R within ±15%.

Acknowledgment

The authors are indebted to the Thailand Research Fund (TRF) and the Energy R&D Foundation funding from the Bureau of Energy of the Ministry of Economic Affairs, Taiwan for supporting this study.

Nomenclature

A_f = surface area of the fin, m^2
$A_{p,in}$ = inside surface area of the tube, m^2
$A_{p,out}$ = outside surface area of the tube, m^2
A_{tot} = total surface area that is the summation of A_f and $A_{p,out}$, m^2
A_{wet} = wet fin surface area, m^2
b'_p = slope of the saturated moist air enthalpy curved between the mean inside and outside tube surface temperatures, $J\,kg^{-1}\,K^{-1}$
b'_r = slope of the saturated moist air enthalpy curved between the mean water temperature and the mean inside tube surface temperature, $J\,kg^{-1}\,K^{-1}$

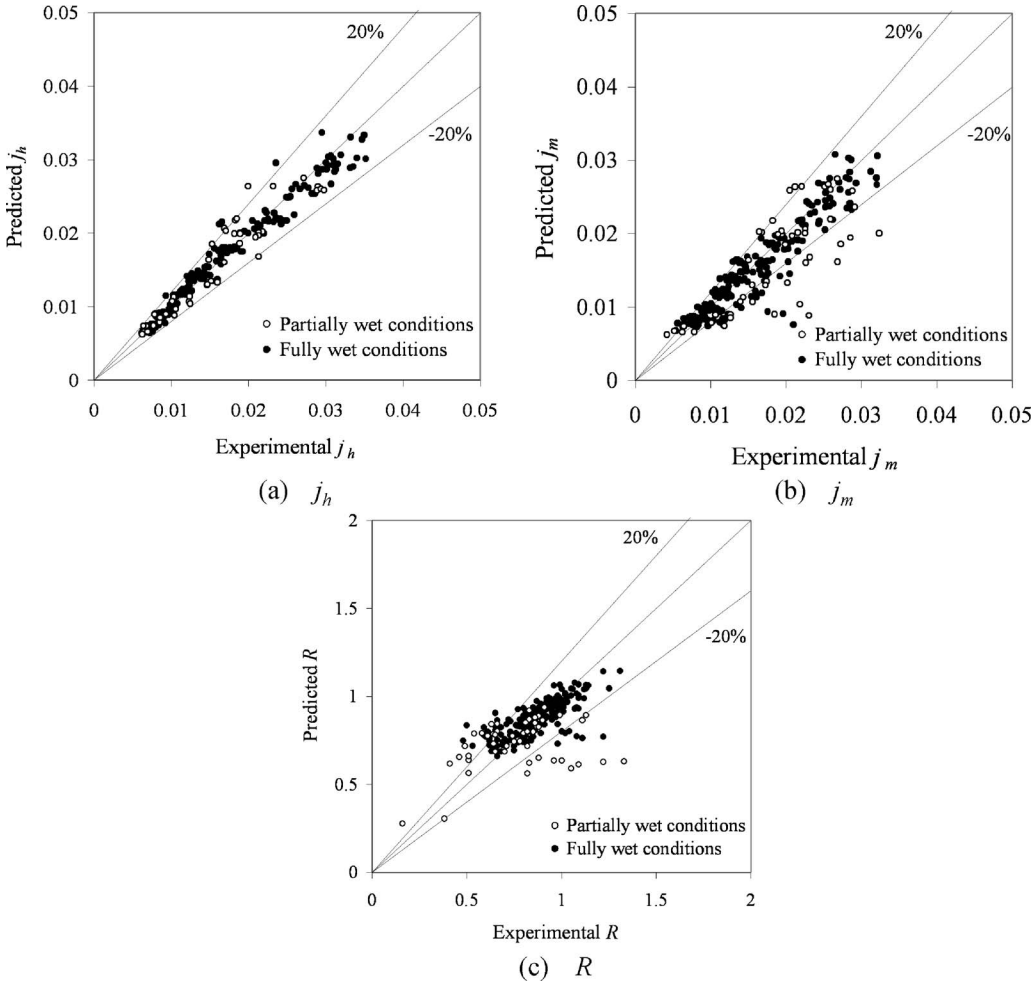

Fig. 8 Comparison between predicted data and experimental data

$b'_{\mathrm{wf},f}$ = slope of the saturated moist air enthalpy curved at the mean water film temperature of the fin surface, J kg^{-1} K^{-1}

$b'_{\mathrm{wf},p,\mathrm{out}}$ = slope of the saturated moist air enthalpy curved at the mean water film temperature of the outside tube surface, J kg^{-1} K^{-1}

$C_{p,a}$ = moist air specific heat at constant pressure, J kg^{-1} K^{-1}

$C_{p,w}$ = water specific heat at constant pressure, J kg^{-1} K^{-1}

D_c = collar diameter, m

$D_{p,\mathrm{in}}$ = inside tube diameter, m

$D_{p,\mathrm{out}}$ = outside tube diameter (include very tiny collar) that is equal to the collar diameter, m

F = correction factor

F_p = fin pitch, m

f_{in} = water side friction factor

$G_{a,\max}$ = moist air maximum mass velocity based on the minimum flow area, kg m^{-2} s^{-1}

$h_{c,\mathrm{in}}$ = water side convection heat transfer coefficient, W m^{-2} K^{-1}

$h_{c,\mathrm{out}}$ = moist air side convection heat transfer coefficient, W m^{-2} K^{-1}

$h_{c,\mathrm{wf},f}$ = heat transfer coefficient for the heat transfer between the moist air and fin surface, W m^{-2} K^{-1}

$h_{c,\mathrm{wf},p,\mathrm{out}}$ = heat transfer coefficient for the heat transfer between the moist air and outside tube surface, W m^{-2} K^{-1}

$h_{d,\mathrm{out}}$ = moist air side convection mass transfer coefficient, kg m^{-2} s^{-1}

I_0 = modified Bessel function solution of the first kind, order 0.

I_1 = modified Bessel function solution of the first kind, order 1.

i_a = moist air enthalpy, J kg^{-1}

$i_{a,\mathrm{in}}$ = inlet moist air enthalpy, J kg^{-1}

$i_{a,m}$ = mean moist air enthalpy, J kg^{-1}

$i_{a,m,\mathrm{cf}}$ = mean moist air enthalpy for the counter flow configuration, J kg^{-1}

$i_{a,\mathrm{out}}$ = outlet moist air enthalpy, J kg^{-1}

$i_{r,f,m}$ = mean saturated moist air enthalpy at the mean fin surface temperature, J kg^{-1}

$i_{r,f,m,\mathrm{cf}}$ = mean saturated moist air enthalpy at the mean fin surface temperature for the counter flow configuration, J kg^{-1}

$i_{r,\mathrm{in}}$ = saturated moist air enthalpy at the inlet water temperature, J kg^{-1}

$i_{r,m,\mathrm{cf}}$ = mean saturated moist air enthalpy at the mean water temperature for the counter flow configuration, J kg^{-1}

$i_{r,\text{out}}$ = saturated moist air enthalpy at the outlet water temperature, J kg^{-1}

$i_{r,p,\text{in},m,\text{cf}}$ = mean saturated moist air enthalpy at the mean inside tube surface temperature for the counter flow configuration, J kg^{-1}

$i_{r,p,\text{out},m}$ = mean saturated moist air enthalpy at the mean outside tube surface temperature, J kg^{-1}

$i_{r,p,\text{out},m,\text{cf}}$ = mean saturated moist air enthalpy at the mean outside tube surface temperature for the counter flow configuration, J kg^{-1}

i_{wf} = saturated moist air enthalpy at the water film temperature, J kg^{-1}

$i_{w,f}$ = specific enthalpy of the saturated water liquid, J kg^{-1}

$i_{w,g}$ = specific enthalpy of the saturated water vapor, J kg^{-1}

j_h = Colburn heat transfer group or Chilton–Colburn j factor for the heat transfer

j_m = Colburn mass transfer group or Chilton–Colburn j factor for the mass transfer

K_0 = modified Bessel function solution of the second kind, order 0

K_1 = modified Bessel function solution of the second kind, order 1

k_f = thermal conductivity of the fin, W m^{-1} K^{-1}

k_p = thermal conductivity of the tube, W m^{-1} K^{-1}

k_{wf} = thermal conductivity of the water, W m^{-1} K^{-1}

k_{wf} = thermal conductivity of the water film, W m^{-1} K^{-1}

L_p = tube length, m

$\dot{m}_a$ = moist air mass flow rate, kg/s

$\dot{m}_w$ = water mass flow rate, kg/s

N = number of tube rows

P_l = longitudinal tube pitch, m

Pr_{in} = water-side Prandtl number

Pr_{out} = moist air-side Prandtl number

P_t = transverse tube pitch, m

$\dot{Q}_a$ = moist air-side heat transfer rate, W

$\dot{Q}_{\text{avg}}$ = average heat transfer rate between the moist air and water sides, W

$\dot{Q}_w$ = water-side heat transfer rate, W

$\dot{Q}_{\text{wet}}$ = heat transfer rate for a fully wet segment, W

R = ratio of the convection heat transfer characteristic to the convection mass transfer characteristic for the simultaneous convection heat and mass transfer

Re_{Dc} = moist air-side Reynolds number based on the collar diameter

Re_{in} = water-side Reynolds number

RH = inlet relative humidity of the moist air

r_i = inside fin radius for the equivalent circular fin equal to the outside tube (include collar) radius, m

r_o = outside fin radius for the equivalent circular fin, m

Sc_{out} = moist air-side Schmidt number

S_p = fin spacing, m

T_a = moist air temperature, K

$T_{a,\text{in}}$ = inlet moist air temperature, K

$T_{a,m,\text{cf}}$ = mean moist air temperature for the counter flow configuration, K

$T_{a,\text{out}}$ = outlet moist air temperature, K

T_{dp} = dew point temperature of the moist air, K

$T_{f,b}$ = fin base temperature, K

$T_{f,t}$ = fin tip temperature, K

$T_{f,m,\text{cf}}$ = mean fin temperature, K

$T_{p,\text{in},m,\text{cf}}$ = mean inside-tube surface temperature for the counter flow configuration, K

$T_{p,\text{out},m,\text{cf}}$ = mean outside-tube surface temperature for the counter flow configuration, K

$T_{r,m,\text{cf}}$ = mean water temperature for the counter flow configuration, K

T_w = water temperature, K

$T_{w,\text{in}}$ = inlet water temperature, K

$T_{w,\text{out}}$ = outlet water temperature, K

$T_{w,m,\text{cf}}$ = mean water temperature for the counter flow configuration, K

t = fin thickness, m

U_i = overall heat transfer coefficient based on the mean enthalpy difference, kg m^{-2} s^{-1}

U_T = overall heat transfer coefficient based on the mean temperature difference, W m^{-2} K^{-1}

W_a = moist air humidity ratio

$W_{a,\text{in}}$ = inlet moist air humidity ratio

$W_{a,m}$ = mean moist air humidity ratio

$W_{a,\text{out}}$ = outlet moist air humidity ratio

$W_{r,f,m}$ = mean saturated moist air humidity ratio at the mean fin surface temperature

$W_{r,p,\text{out},m}$ = mean saturated moist air humidity ratio at the mean outside tube surface temperature

W_{wf} = saturated moist air humidity ratio at the water film temperature

y_{wf} = thickness of the water film, m

$\eta_{f,\text{dry}}$ = dry fin efficiency

$\eta_{f,\text{wet}}$ = wet fin efficiency

$\Delta i_{m,\text{cf}}$ = logarithmic mean enthalpy difference across the heat exchanger for the counter flow double-pipe configuration with hot and cold fluid enthalpies, J kg^{-1}

ΔP = difference pressure, Pa

$\Delta T_{m,\text{cf}}$ = logarithmic mean temperature difference across the heat exchanger for the counter flow double-pipe configuration with hot and cold fluid temperatures, K

References

[1] ARI, 2001, "Forced Circulation Air-Cooling and Air-Heating Coils," Air Conditioning and Refrigeration Institute, VA, Standard No. 410.

[2] McQuiston, F. C., 1978, "Heat Mass and Momentum Transfer Data for Five Plate-Fin Tube Transfer Surface," ASHRAE Trans., **84**, pp. 266–293.

[3] McQuiston, F. C., 1978, "Correlation of Heat, Mass and Momentum Transport Coefficients for Plate-Fin-Tube Heat Transfer Surfaces With Staggered Tubes," ASHRAE Trans., **84**, pp. 294–309.

[4] Mirth, D. R., and Ramadhyani, S., 1993, "Prediction of Cooling-Coils Performance Under Condensing Conditions," Int. J. Heat Fluid Flow, **14**(4), pp. 391–400.

[5] Mirth, D. R., and Ramadhyani, S., 1994, "Correlations for Predicting the Air-Side Nusselt Numbers and Friction Factors in Chilled-Water Cooling Coils," Exp. Heat Transfer, **7**, pp. 143–162.

[6] Fu, W. L., Wang, C. C., and Chang, C. T., 1995, "Effect of Anti-Corrosion Coating on the Thermal Characteristics of a Louvered Finned Heat Exchanger Under Dehumidifying Condition," *Advances in Enhanced Heat/Mass Transfer and Energy Efficiency*, ASME HTD, Vol. 320/PID-Vol. 1, pp. 75–81.

[7] Seshimo, Y., Ogawa, K., Marumoto, K., and Fujii, M., 1988, "Heat and Mass Transfer Performances on Plate Fin and Tube Heat Exchangers With Dehumidification," Trans. Jpn. Soc. Mech. Eng., Ser. A, **54**(499), pp. 716–721.

[8] Wang, C. C., Hsieh, Y. C., and Lin, Y. T., 1997, "Performance of Plate Finned Tube Heat Exchangers Under Dehumidifying Conditions," J. Heat Transfer, **119**, pp. 109–117.

[9] Pirompugd, W., Wongwises, S., and Wang, C. C., 2005, "A Tube-by-Tube Reduction Method for Simultaneous Heat and Mass Transfer Characteristics for Plain Fin-and-Tube Heat Exchangers in Dehumidifying Conditions," Heat Mass Transfer, **41**(8), pp. 756–765.

[10] Pirompugd, W., Wongwises, S., and Wang, C. C., 2006, "Simultaneous Heat and Mass Transfer Characteristics for Wavy Fin-and-Tube Heat Exchangers Under Dehumidifying Conditions," Int. J. Heat Mass Transfer, **49**, pp. 132–143.

[11] Xia, Y., and Jacobi, A. M., 2005, "Air-Side Data Interpretation and Performance Analysis for Heat Exchangers With Simultaneous Heat and Mass Transfer: Wet and Frosted Surfaces," Int. J. Heat Fluid Flow, **48**, pp. 5089–5102.

[12] ASHRAE, 1987, "Standard Methods for Laboratory Air-Flow Measurement,"

American Society of Heating, Refrigerating and Air-Conditioning Engineers, Inc., Atlanta, GA, Standard No. 41.2.
[13] ASHRAE, 1986, "Standard Method for Temperature Measurement," American Society of Heating, Refrigerating and Air-Conditioning Engineers, Inc., Atlanta, GA, Standard No. 41.1.
[14] ASHRAE, 2000, "Method of Testing Forced Circulation Air Cooling and Air Heating Coils," American Society of Heating, Refrigerating and Air-Conditioning Engineers, Inc., Atlanta, GA, Standard No. 33, pp. 33–78.
[15] Moffat, R. J., 1988, "Describing the Uncertainties in Experimental Results," Exp. Therm. Fluid Sci., **1**, pp. 3–17.
[16] Threlkeld, J. L., 1970, *Thermal Environmental Engineering*, Prentice–Hall, New York.
[17] Bump, T. R., 1963, "Average Temperatures in Simple Heat Exchangers," ASME J. Heat Transfer, **85**(2), pp. 182–183.
[18] Myers, R. J., 1967, "The Effect of Dehumidification on the Air-Side Heat Transfer Coefficient for a Finned-Tube Coil," M.S. thesis, University of Minnesota, Minneapolis, MN.
[19] Gnielinski, V., 1976, "New Equation for Heat and Mass Transfer in Turbulent Pipe and Channel Flow," Int. Chem. Eng., **16**, pp. 359–368.
[20] Kandlikar, S. G., 1990, "Thermal Design Theory for Compact Evaporators," *Compact Heat Exchangers—A Festschrift for A. L. London*, R. K. Shah, A. D. Kraus, and D. Metzger, eds., Hemisphere, New York, pp. 245–286.
[21] Kern, D. Q., and Kraus, A. D., 1972, *Extended Surface Heat Transfer*, McGraw–Hill, New York, pp. 102–106.
[22] Wang, C. C., and Chi, K. U., 2000, "Heat Transfer and Friction Characteristics of Plain Fin-and-Tube Heat Exchangers: Part I: New Experimental Data," Int. J. Heat Mass Transfer, **43**, pp. 2681–2691.
[23] Torikoshi, K., Xi, G., Nakazawa, Y., and Asano, H., 1994, "Flow and Heat Transfer Performance of a Plate-Fin and Tube Heat Exchanger (1st Report: Effect of Fin Pitch)," *Proceedings 10th International Heat Transfer Conference*, Brighton, UK, August 14–18, Paper No. 9-HE-16, pp. 411–416.
[24] Yoshii, T., Yamamoto, M., and Otaki, M., 1973, "Effects of Dropwise Condensate on Wet Surface Heat Transfer of Air Cooling Coils," *Proceedings of the 13th Int. Congress of Refrigeration*, Washington, DC, August 27, pp. 285–292.
[25] Hong, T. K., and Webb, R. L., 1996, "Calculation of Fin Efficiency for Wet and Dry Fins," HVAC&R Res., **2**(1), pp. 27–41.
[26] Eckels, P. W., and Rabas, T. J., 1987, "Dehumidification on the Correlation of Wet and Dry Transport Process in Plate Finned-Tube Heat Exchangers," ASME J. Heat Transfer, **109**, pp. 575–582.

Heat Exchanger Efficiency

Ahmad Fakheri
Professor
Department of Mechanical Engineering,
Bradley University,
Peoria, IL 61625
e-mail: ahmad@bradley.edu

This paper provides the solution to the problem of defining thermal efficiency for heat exchangers based on the second law of thermodynamics. It is shown that corresponding to each actual heat exchanger, there is an ideal heat exchanger that is a balanced counter-flow heat exchanger. The ideal heat exchanger has the same UA, the same arithmetic mean temperature difference, and the same cold to hot fluid inlet temperature ratio. The ideal heat exchanger's heat capacity rates are equal to the minimum heat capacity rate of the actual heat exchanger. The ideal heat exchanger transfers the maximum amount of heat, equal to the product of UA and arithmetic mean temperature difference, and generates the minimum amount of entropy, making it the most efficient and least irreversible heat exchanger. The heat exchanger efficiency is defined as the ratio of the heat transferred in the actual heat exchanger to the heat that would be transferred in the ideal heat exchanger. The concept of heat exchanger efficiency provides a new way for the design and analysis of heat exchangers and heat exchanger networks.
[DOI: 10.1115/1.2739620]

Keywords: heat exchangers, efficiency, heat exchanger efficiency, entropy minimization, arithmetic mean temperature difference (AMTD), log-mean temperature difference (LMTD), effectiveness-NTU

1 Introduction

The concept of efficiency is used in many areas, particularly engineering, to assess the performance of real components and systems. Efficiency is a comparison between the actual (real) and ideal (best) performances and is typically defined to be less than or at best equal to 1. The ideal behavior is generally known from modeling, and the limitations dictated by physical laws, particularly the second law of thermodynamics. Knowing the ideal performance, the actual performance can be determined if expressions for the efficiency as a function of the system characteristics and the operating conditions are known. Efficiency provides a clear and intuitive measure of a system's performance by showing how close an actual system comes to the best that it can be and if further improvements are feasible and justified. Despite much effort, the application of the second law to heat exchangers has not yielded a consistent method for assessing the performance of heat exchangers.

Two of the more widely used approaches for analyzing heat exchangers are the log-mean temperature difference method (LMTD) and effectiveness NTU (ε-NTU) method. In the LMTD method

$$F = \frac{q}{UA\text{LMTD}} \tag{1}$$

where the term in the denominator is the maximum rate of heat transfer, which takes place in a counter-flow heat exchanger having the same UA and the same inlet and exit temperatures as the heat exchanger under consideration. Expressions and charts are available to determine F for different heat exchangers. These correlations are typically a function of two parameters P and R that depend solely on the inlet and exit temperatures. The LMTD approach is generally used for solving heat exchanger problems where the inlet and the exit temperatures are known and the size of the heat exchanger is to be determined (sizing problems).

In the ε-NTU approach, the heat exchanger effectiveness is defined as

$$\varepsilon = \frac{q}{C_{\min}(T_1 - t_1)} \tag{2}$$

where the term in the denominator is the absolute maximum heat that can be transferred from a fluid at T_1 to another fluid at t_1. This maximum amount of heat transfer can only occur in a heat exchanger whose area approaches infinity. Expressions and charts are available to determine the effectiveness of different heat exchangers, and are typically a function of two variables (C_r and NTU). The ε-NTU method is mostly used in situations where the size of the heat exchanger and the inlet temperatures are known and the heat transfer rate and the fluid exit temperatures are sought (the rating problem), although sizing problems can also be solved with this method.

The author recently introduced the concept of heat exchanger efficiency [1–4]. The heat exchanger efficiency is defined as the ratio of the actual rate of heat transfer in the heat exchanger (q) to the optimum rate of heat transfer (q_{opt}):

$$\eta = \frac{q}{q_{\text{opt}}} = \frac{q}{UA(\bar{T} - \bar{t})} \tag{3}$$

The optimum (maximum) rate of the heat transfer is the product of UA of the heat exchanger under consideration and its arithmetic mean temperature difference (AMTD), which is the difference between the average temperatures of hot and cold fluids. The rate of heat transfer in any heat exchanger with the same UA and AMTD is always less than the optimum value of the heat transfer rate ($\eta \leq 1$) [1]. Furthermore, the optimum heat transfer rate takes place in a balanced counter-flow heat exchanger [1].

The efficiency of a number of commonly used heat exchangers is given by the general expression

$$\eta = \frac{\tanh\,(\text{Fa})}{(\text{Fa})} \tag{4}$$

where Fa, the fin analogy number, is the nondimensional group that characterizes the performance of different heat exchangers. This is a remarkable expression in that the efficiency of a wide variety of heat exchangers has the same functional form as the efficiency of a constant area insulated tip fin. The expressions for Fa for some of the commonly used heat exchangers are given in Table 1.

Contributed by the Heat Transfer Division of ASME for publication in the JOURNAL OF HEAT TRANSFER. Manuscript received April 13, 2006; final manuscript received November 16, 2006. Review conducted by Ramendra P. Roy.

Table 1 Fin analogy number of various heat exchangers

Counter	Parallel	Single stream	Single shell
$\mathrm{Fa}=\mathrm{NTU}(1-C_r)/2$	$\mathrm{Fa}=\mathrm{NTU}(1+C_r)/2$	$\mathrm{Fa}=\mathrm{NTU}/2$	$\mathrm{Fa}=\mathrm{NTU}\sqrt{1+C_r^2}/2$

The efficiency expressions for cross flow heat exchangers are more complex than Eq. (4), however, for several cross-flow heat exchangers, Eq. (4) can still be used with a high degree of accuracy by using a generalized fin analogy number [2,4]. It is also important to note that the parallel flow and counter-flow heat exchangers represent the low and high limits of efficiency for a given NTU and C_r, respectively.

Figure 1 is a plot of the heat exchanger efficiency as a function of the fin analogy number. The maximum efficiency (heat transfer) occurs for Fa=0, which, from Table 1, only happens for a balanced ($C_r=1$) counter-flow heat exchanger, or a balanced counter-flow heat exchanger has the efficiency of 100%. For a given Fa, the efficiency is obtained from Eq. (4) or Fig. 1 and the heat transfer can be determined from Eq. (3).

The analogy with fins provides additional insight into the concept of heat exchanger efficiency. For a constant area fin, the efficiency is given by

$$\eta = \frac{\tanh\left(\sqrt{\frac{h\bar{p}L^2}{kA_x}}\right)}{\left(\sqrt{\frac{h\bar{p}L^2}{kA_x}}\right)} \tag{5}$$

The heat transfer rate from a fin can be written as

$$q = \sqrt{kA_x h\bar{p}}\tanh\left(\frac{hA}{\sqrt{kA_x h\bar{p}}}\right)(T_b - T_\infty) \tag{6}$$

Rearranging Eqs. (3) and (4), the rate of heat transfer rate for a counter-flow heat exchanger becomes

$$q = \frac{2C_{\min}}{1-C_r}\tanh\left(\frac{UA}{\frac{2C_{\min}}{1-C_r}}\right)(\bar{T}-\bar{t}) \tag{7}$$

Although Eq. (5) indicates that increasing the fin length or the heat transfer coefficient leads to a reduction in the efficiency of a fin, the total amount of heat transfer actually increases with increasing these two parameters as seen from Eq. (6). In the limit, an infinitely long fin has an efficiency of zero, even though it still transfers a finite amount of heat. The same behavior can be seen for a heat exchanger. As the overall heat transfer coefficient or the area of the heat exchanger increases, the fin analogy number (Fa) increases, leading to a reduction in the heat exchanger efficiency. However, as can be seen from Eq. (7), the rate of heat transfer actually increases. Like a fin, an infinitely large heat exchanger has an efficiency of zero, even though it transfers a finite amount of heat.

Figure 2 is a plot of heat exchanger efficiency as a function of capacity ratio for a given NTU (=3). As can be seen, the efficiency of a counter-flow heat exchanger increases with capacity ratio, while the efficiency of shell and tube and parallel flow heat exchangers actually decreases with increasing capacity ratio.

The heat exchanger efficiency is based on the arithmetic mean temperature difference (AMTD) of the heat exchanger as the driving temperature potential and can be calculated from the knowledge of the inlet temperatures (the maximum temperature difference in the heat exchanger) and NTU and efficiency through

$$\bar{T}-\bar{t} = \frac{(T_1 - t_1)}{1+\eta\,\mathrm{NTU}\left(\frac{1+C_r}{2}\right)} \tag{8}$$

Substituting from Eq. (8) in Eq. (3) results in

$$q = \eta UA(\bar{T}-\bar{t}) = \frac{1}{\frac{1}{\eta\,\mathrm{NTU}}+\left(\frac{1+C_r}{2}\right)}C_{\min}(T_1 - t_1) \tag{9}$$

Note that the fraction on the right hand side of Eq. (9) is the effectiveness of the heat exchanger and thus establishes the relation between efficiency and effectiveness.

Using the concept of heat exchanger efficiency for analyzing heat exchanger rating and sizing problems is demonstrated by two examples [5] in the Appendix. As can be seen, both types of problems can be conveniently solved using the concept of heat exchanger efficiency without the need for charts or complicated performance equations. Furthermore, the heat exchanger effi-

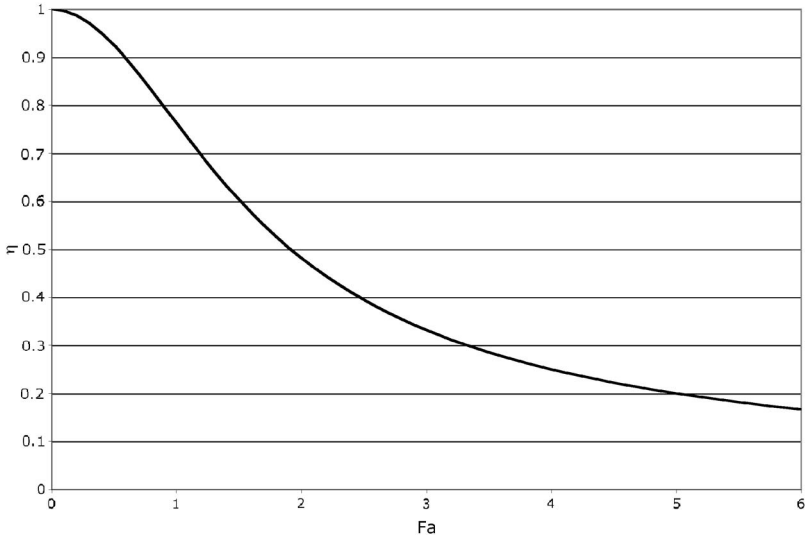

Fig. 1 Heat exchanger efficiency variation with capacity ratio

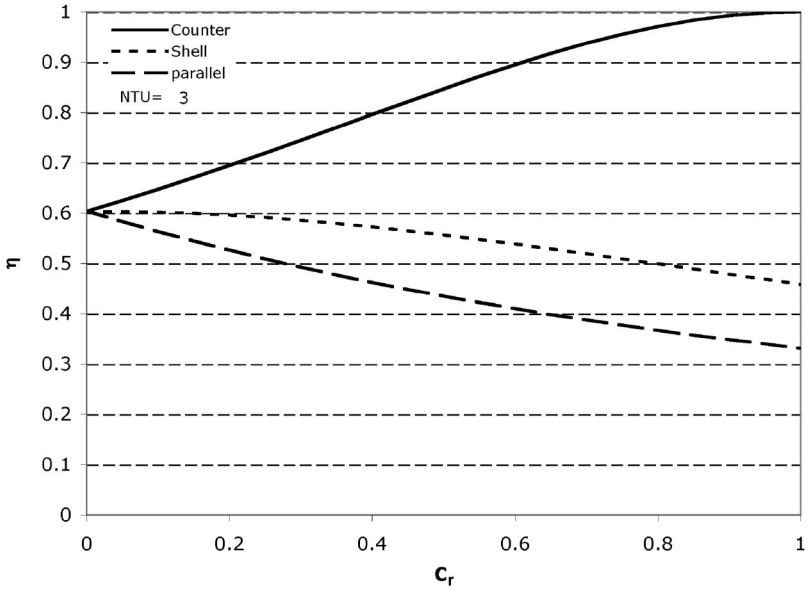

Fig. 2 Heat exchanger efficiency variation as with capacity ratio

ciency given by Eq. (4) is only a function of one nondimensional variable (Fa), whereas effectiveness (ε) depends on two parameters (C_r and NTU), and the LMTD correction factor (F) depends also on two parameters (P and R). The simple algebraic form of Eq. (4) and its dependence on one single nondimensional group simplify heat exchanger calculations and greatly facilitate comparison of different heat exchangers. The concept of thermal efficiency provides a new and more convenient approach for analyzing heat exchangers.

Like efficiency, the LMTD correction factor (F) and the heat exchanger effectiveness (ε) are also less than 1, but the efforts to relate them to the second law have not been successful. The challenge in defining a second-law-based efficiency for heat exchangers is defining an ideal heat transfer process in heat exchangers. An isentropic process is the ideal process for many components and is used to define isentropic efficiency. This obviously cannot be applied to a heat exchanger whose function is to transfer heat. Since entropy production will not be zero (notwithstanding the unrealistic case of an infinitely large heat exchanger), minimization of entropy has been considered in heat exchanger analysis.

The application of this method to heat exchangers was first proposed by McClintock [6]. Bejan [7] introduced a nondimensional parameter, the number of entropy generation units N_s, as a measure of heat exchanger irreversibility. N_s is the ratio of the total amount of entropy generated in the heat exchanger as a result of irreversibilities associated with heat transfer and fluid friction, and the maximum capacity rate. Aceves-Saborio et al. [8] extended the irreversibility minimization method by including a term to account for the exergy of the heat exchanger material.

These approaches have found limited application in heat exchanger design, partly due to the fact that the global optimum often leads to a heat exchanger with infinite area [8]. The efforts in linking the effectiveness of a heat exchanger to its rate of entropy production have also not been successful. The minimum irreversibility does not appear to correlate with the effectiveness of the heat exchanger, as pointed out by Shah and Skiepko [9]. They showed that the heat exchanger effectiveness can be maximum or minimum at the minimum irreversibility operating point, concluding that effectiveness is not a measure of heat exchanger reversibility [9]. The analysis presented below is to show that the efficiency defined above is based on the second law of thermodynamics. It will be shown that the minimum irreversibility is associated with the maximum efficiency for heat exchangers, clarifying how the second law can be extended to heat exchangers.

Consider a heat exchanger having an area A and an overall heat transfer coefficient of U, where the hot and cold fluids enter at temperatures T_1 and t_1 with capacities C_h and C_c, respectively. The heat exchanger efficiency is evaluated from Eq. (4). The average temperature difference in the heat exchanger is fixed and is determined from Eq. (8). As shown above, a balanced counter flow heat exchanger where the hot and cold fluid capacities are equal to the $C_{\min}$ of the actual heat exchanger, having the same UA and AMTD will transfer the maximum amount of heat. The inlet temperatures of the hot and cold fluids of the balanced counter-flow heat exchanger are not specified; thus, infinitely many exchangers will transfer the same maximum amount of heat. The rest of the paper is to show among all these balanced counter-flow heat exchangers, the one having the same temperature ratio (t_1/T_1) as the actual heat exchanger also generates the minimum amount of entropy.

Therefore, corresponding to an actual heat exchanger, there is an ideal balanced flow heat where the hot and cold fluid capacities are equal to the $C_{\min}$ of the actual heat exchanger. The ideal and actual heat exchangers have the same UA, the same AMTD, and the same inlet temperature ratio (t_1/T_1). The ideal heat exchanger transfers the maximum amount of heat, equal to the product of UA and AMTD, while generating the minimum amount of entropy. Note that from Eq. (8) the inlet and exit temperatures of the fluids in the ideal heat exchanger are different from those of the actual heat exchanger. The expressions for the determination of the ideal temperatures will be presented later. Based on the second law, the ideal heat exchanger is, therefore, the most efficient (transferring the maximum amount of heat) and least irreversible heat exchanger (generating the minimum amount of entropy). This ideal heat exchanger is the reference against which other heat exchangers can be compared and their efficiency assessed.

2 Analysis

Assuming heat transfer from the surroundings to be zero, and the specific heats to be constant, the nondimensional rate of entropy generation for a heat exchanger is given by [9]

$$\sigma = \sigma_T + \sigma_f = \frac{C_h}{C_{\min}} \ln \frac{T_2}{T_1} + \frac{C_c}{C_{\min}} \ln \frac{t_2}{t_1} - \frac{C_h}{C_{\min} c_{p,h}} \frac{R_h}{} \ln \frac{P_2}{P_1} - \frac{C_c}{C_{\min} c_{p,c}} \frac{R_c}{} \ln \frac{p_2}{p_1} \tag{10}$$

where

$$\sigma = \frac{\dot{S}_{\text{gen}}}{C_{\min}} \tag{11}$$

The first two terms can be considered as the amount of entropy produced due to temperature change, which is generally as a result of heat transfer (σ_T), and the last two terms are due to pressure change (σ_P), which is generally due to flow irreversibilities, including friction.

In defining an ideal heat transfer process based on the second law, only irreversibilities caused by heat transfer need to be considered. These account for most of the irreversibilities as the pressure drop across the heat exchanger is typically small, and for incompressible fluids, the entropy change is only a function of temperature. Mohamed [10] also showed that the entropy generation number due to pressure is too low compared with that due to temperature ($\sigma_P \ll \sigma_T$), so it can be neglected. The irreversibility due to heat transfer is given by

$$\sigma_T = \frac{C_h}{C_{\min}} \ln \frac{T_2}{T_1} + \frac{C_c}{C_{\min}} \ln \frac{t_2}{t_1} \tag{12}$$

Eliminating the exit temperatures

$$\sigma_T = \frac{C_h}{C_{\min}} \ln\left(1 - \frac{q}{C_h T_1}\right) + \frac{C_c}{C_{\min}} \ln\left(1 + \frac{q}{C_c t_1}\right) \tag{13}$$

Substituting for q from Eq. (8) results in

$$\sigma_T = \frac{1}{\frac{C_{\min}}{C_h}} \ln\left[1 - \frac{1}{\frac{1}{\text{NTU}\frac{C_{\min}}{C_h}\eta} + \frac{1}{2}\left(1 + \frac{C_h}{C_c}\right)} \frac{(T_1 - t_1)}{T_1}\right] + \frac{1}{\frac{C_{\min}}{C_c}} \ln\left[1 + \frac{1}{\frac{1}{\text{NTU}\frac{C_{\min}}{C_c}\eta} + \frac{1}{2}\left(1 + \frac{C_c}{C_h}\right)} \frac{(T_1 - t_1)}{t_1}\right] \tag{14}$$

from which the amount of entropy generated can be calculated. Either the cold or the hot fluid can have the minimum capacity. Assuming $C_c = C_{\min}$ results in

$$\sigma_T = \frac{1}{C_r} \ln\left[1 - C_r \frac{1}{\frac{1}{\text{NTU}\,\eta} + \frac{1 + C_r}{2}}\left(1 - \frac{t_1}{T_1}\right)\right] + \ln\left[1 + \frac{1}{\frac{1}{\text{NTU}\,\eta} + \frac{1 + C_r}{2}}\left(\frac{T_1}{t_1} - 1\right)\right] \tag{15}$$

and assuming $C_h = C_{\min}$, Eq. (14) becomes

$$\sigma_T = \ln\left[1 - \frac{1}{\frac{1}{\text{NTU}\,\eta} + \frac{1 + C_r}{2}}\left(1 - \frac{t_1}{T_1}\right)\right] + \frac{1}{C_r} \ln\left[1 + C_r \frac{1}{\frac{1}{\text{NTU}\,\eta} + \frac{1 + C_r}{2}}\left(\frac{T_1}{t_1} - 1\right)\right] \tag{16}$$

The product of NTU and η for four different heat exchangers can be obtained from Table 1 and Eq. (4) and is a function of NTU and capacity ratio. Therefore, the amount of entropy generated in the heat exchanger as given by Eqs. (15) and (16) is only a function of temperature ratio, NTU, and capacity ratio.

Figure 3 is a plot of entropy generated as a function of capacity ratio for different heat exchangers for both cases of the fluid with minimum capacity being the hot or the cold fluid. For a given NTU and inlet temperature ratio (0.7), the entropy generated is a decreasing function of capacity ratio for the three heat exchangers shown, assuming its lowest value for the balanced flow condition. For the conditions shown in Fig. 3(*a*) (NTU=3) at all capacity ratios, the counter-flow heat exchanger is the least irreversible heat exchanger, generating the least amount of entropy.

For the conditions shown in Fig. 3(*b*) (NTU=1.1) at all capacity ratios, the parallel flow heat exchanger generates the least amount of entropy. However, a parallel flow heat exchanger also has the lowest efficiency, transferring the least amount of heat compared to the others and hence the reason for lower generation of entropy. As can be seen in Fig. 3, the minimum entropy is generated for the balanced flow condition. For the balanced flow conditions, substituting $C_r = 1$ in Eqs. (15) and (16) and simplifying, results in

$$(\sigma_T)_{\min} = \ln\left[\frac{\left(1 + \frac{t_1}{T_1}\text{NTU}\,\eta\right)\left(1 + \frac{T_1}{t_1}\text{NTU}\,\eta\right)}{(1 + \text{NTU}\,\eta)^2}\right] \tag{17}$$

that is the minimum amount of entropy generated for any heat exchanger regardless of which fluid has the minimum capacity. The minimum entropy generated given by Eq. (17) is plotted in Fig. 4 as a function of the product of heat exchanger efficiency and the number of transfer units for several temperature ratios. As can be seen, the minimum entropy generated increases and reaches a maximum value and then decreases as the product ηNTU increases. This was first pointed out by Tribus and reported by Bejan [11] for a balanced counter-flow heat exchanger. This behavior is sometimes referred to as the entropy generation paradox and so far has only been reported for balanced counter-flow heat exchangers. A number of explanations [12,13] have been provided as to why such a behavior is observed for a counter-flow heat exchanger.

Equation (17) shows for all balanced flow heat exchangers, and not just counter-flow ones, that as the product ηNTU increases, the amount of entropy generated also increases to a maximum before decreasing. For all heat exchangers under the balanced flow condition, when NTU $\eta = 1$, the entropy generation reaches a maximum value of

$$(\sigma_T)_M = \ln\left[\frac{\left(1 + \frac{t_1}{T_1}\right)\left(1 + \frac{T_1}{t_1}\right)}{4}\right] \tag{18}$$

Since the efficiency of a balanced counter-flow heat exchanger is 1, maximum entropy generation for a counter-flow heat exchanger happens at NTU=1, which confirms the results of Bejan [11]. Substituting efficiency expressions of shell and tube and parallel flow heat exchangers in Eq. (17) shows that the maximum for a shell and tube heat exchanger occurs at NTU=1.2455, and for a parallel flow heat exchanger at NTU$\to\infty$.

Figure 5 shows the variation of the minimum entropy generated (Eq. (17)) normalized by its maximum (Eq. (18)) for three types of heat exchangers for a given value of the temperature ratio (0.1). For each value of NTU, efficiency is calculated from the expressions of Table 1, under the balanced flow condition. The general behavior seen in Fig. 5 is valid for all temperature ratios. The region near the point of maximum entropy is magnified to show the details of the behavior near this point. As can be seen, at a given NTU$\geq$1.2, a balanced counter-flow heat exchanger generates less entropy compared to the other heat exchangers, even though, having a higher efficiency, it transfers more heat. For small values of NTU, parallel flow or shell and tube heat exchang-

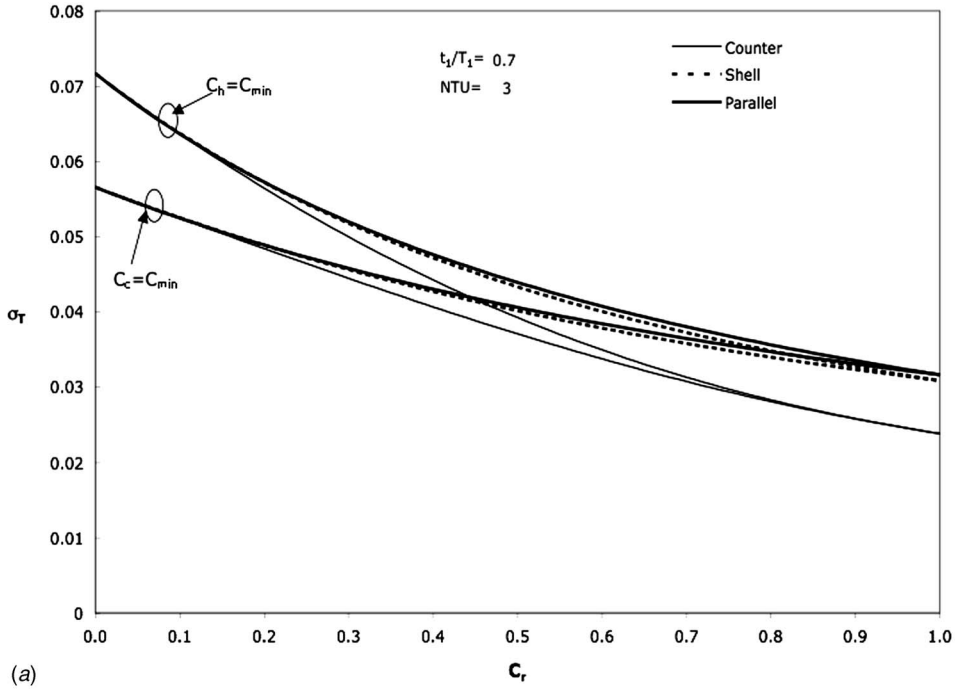

(*a*)

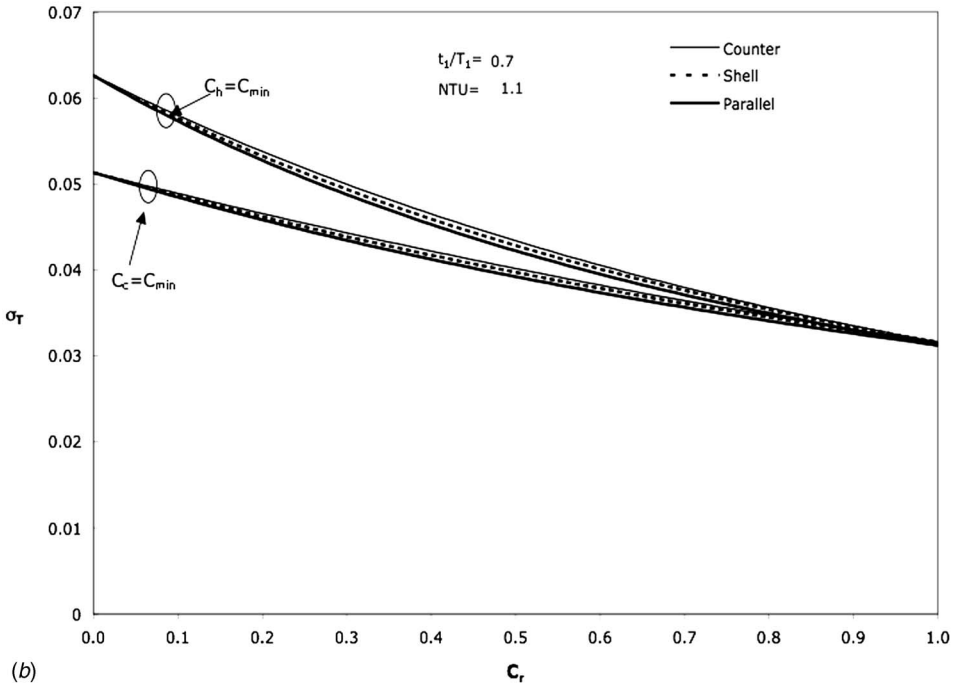

(*b*)

Fig. 3 Entropy generation with capacity ratio for different heat exchangers

ers generate less entropy than the counter-flow heat exchanger, due to their low efficiency (Fig. 2) and low heat transfer rates.

The minimum amount of entropy generated for a balanced counter-flow heat exchanger ($\eta=1$) is obtained from

$$(\sigma_T)_{\min} = \ln\left[\frac{\left(1+\frac{t_1}{T_1}\mathrm{NTU}\right)\left(1+\frac{T_1}{t_1}\mathrm{NTU}\right)}{(\mathrm{NTU}+1)^2}\right] \tag{19}$$

The point where the crossover, for example, for parallel flow exchanger, occurs is found by equating Eq. (17) evaluated for balanced counter-flow heat exchanger ($\eta=1$) to the same equation, evaluated for a balanced parallel flow heat exchanger ($\eta=\tanh \mathrm{NTU}/\mathrm{NTU}$)

$$\frac{\left(1+\frac{t_1}{T_1}\mathrm{NTU}\right)\left(1+\frac{T_1}{t_1}\mathrm{NTU}\right)}{(\mathrm{NTU}+1)^2} = \frac{\left(1+\frac{t_1}{T_1}\tanh \mathrm{NTU}\right)\left(1+\frac{T_1}{t_1}\tanh \mathrm{NTU}\right)}{(\tanh \mathrm{NTU}+1)^2} \tag{20}$$

Equation (20) simplifies to

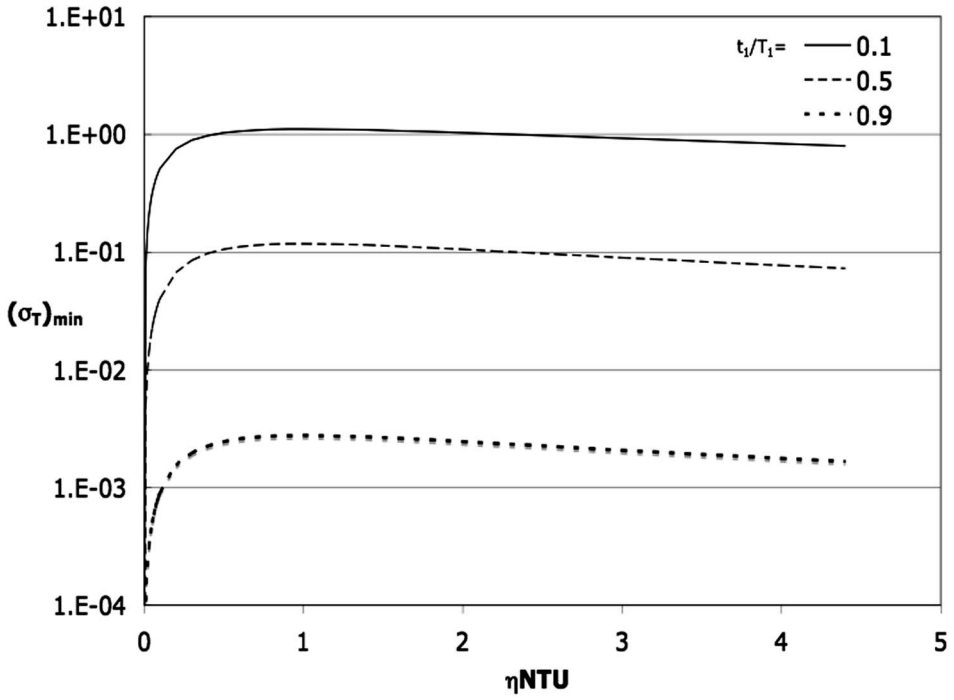

Fig. 4 Variation of entropy generation with ηNTU in balanced flow heat exchangers

$$\text{NTU} \tanh \text{NTU} = 1 \tag{21}$$

which results in the solution NTU=1.199679≅1.20. Note that at the crossover point, the parallel flow heat exchanger has an efficiency η=0.69%.

There is only one ideal heat exchanger corresponding to the specified heat exchanger under consideration. It is also helpful to further explore the idealized heat exchanger. As mentioned before, the ideal heat exchanger is a balanced counter-flow one, having the same *UA* as the actual heat exchanger where the hot and cold fluid capacities are equal to the C_{min} of the actual heat exchanger. The ideal and actual heat exchangers have the same AMTD, and the same temperature ratio (t_1/T_1). The ideal heat exchanger has an efficiency of 1 and transfers the maximum amount of heat given by

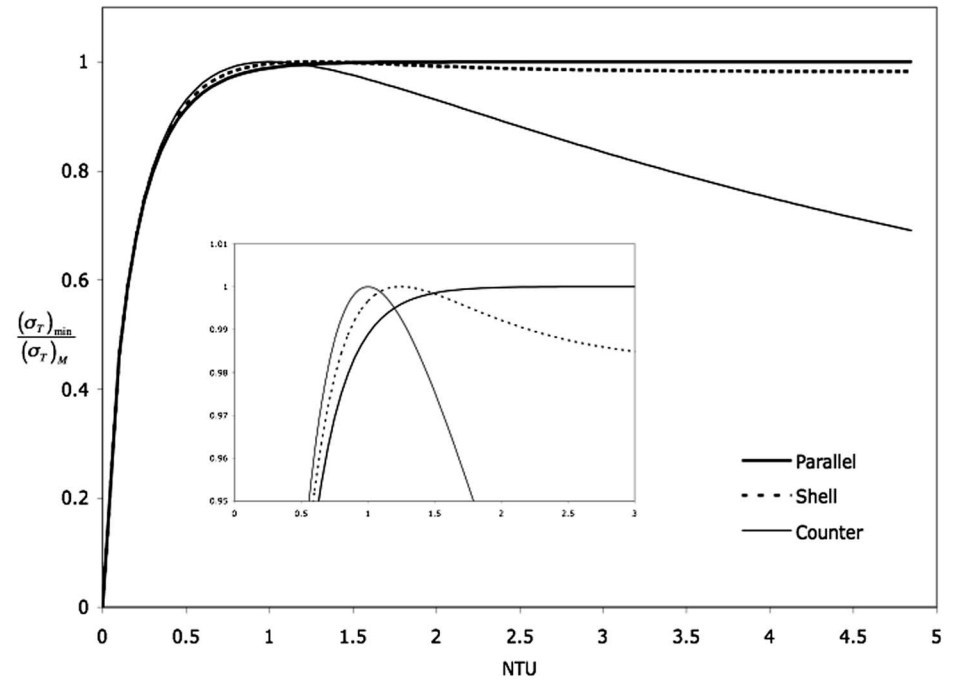

Fig. 5 Scaled entropy generation variation with NTU for different heat exchangers

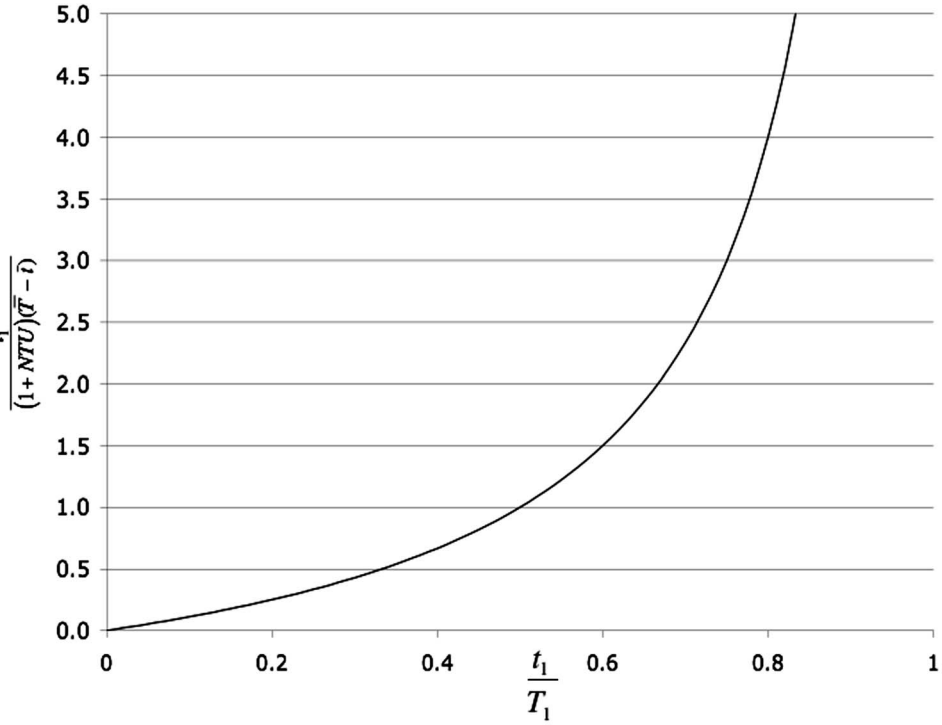

Fig. 6 Variation of the ideal temperatures as a function of the temperature ratio

$$q = UA(\bar{T} - \bar{t}) \tag{22}$$

and generates the minimum amount of entropy given by Eq. (19). The inlet and exit temperatures of the ideal heat exchanger (optimum values) are higher than those of the actual heat exchanger. Using Eqs. (8) and (9), it can be shown that they can be determined from

$$t_1^{o^*} = \frac{t_1^o}{(1 + \text{NTU})(\bar{T} - \bar{t})} = \frac{\frac{t_1}{T_1}}{1 - \frac{t_1}{T_1}} \tag{23}$$

$$t_2^{o^*} = \frac{t_2^o}{(1 + \text{NTU})(\bar{T} - \bar{t})} = t_1^{o^*} + \frac{\text{NTU}}{1 + \text{NTU}} \tag{24}$$

$$T_1^{o^*} = \frac{T_1^o}{(1 + \text{NTU})(\bar{T} - \bar{t})} = 1 + t_1^{o^*} \tag{25}$$

$$T_2^{o^*} = \frac{T_2^o}{(1 + \text{NTU})(\bar{T} - \bar{t})} = t_1^{o^*} + \frac{1}{1 + \text{NTU}} \tag{26}$$

The closer the inlet and exit temperatures of the actual heat exchanger are to their optimum values, the closer the heat exchanger is to its ideal performance. Equation (23) is plotted in Fig. 6, and represents the ideal nondimensional inlet temperature of the cold fluid. The temperature ratio for Examples 1 and 2 is $t_1/T_1 = 0.668$, where temperatures are in Kelvin. The inlet and exit temperatures of the ideal heat exchanger can be determined from Eqs. (23)–(26). For example, the optimum inlet temperature of the cold fluid is 40.7°C as compared to the actual temperature of 16°C.

The methodology described in this paper can also be used for optimization of heat exchangers, by defining an objective function and relaxing one or more of the specified parameters, like the heat exchanger type, U, A, inlet temperatures, etc., but is beyond the scope of the present work.

3 Conclusions

The heat exchanger efficiency is defined as the ratio of the actual heat transfer in a heat exchanger to the optimum heat transfer rate. For some of the commonly used heat exchangers, the efficiency expressions have the same simple algebraic function, similar to the efficiency of a constant area fin with an insulated tip and are a function of a single nondimensional parameter called a fin analogy (Fa) number. For a given heat exchanger and its operating condition, there exists an ideal heat exchanger, which transfers the maximum amount of heat and generates the minimum amount of entropy. The actual heat transfer from the heat exchanger is obtained by multiplying its efficiency and the optimum heat transfer rate, given by the product UA and the arithmetic mean temperature difference. The ideal heat exchanger also generates the minimum amount of entropy. The concept of heat exchanger efficiency provides a new and more convenient way for the design and analysis of heat exchangers and heat exchanger networks.

Nomenclature

A = heat exchanger surface area, m^2
A_x = fin cross section area, m^2
AMTD = arithmetic mean temperature difference; AMTD$=(\bar{T}-\bar{t})$
C_c = heat capacity rate of the cold fluid $C_c=(\dot{m}c_p)_c$
C_h = heat capacity rate of the hot fluid $C_h=(\dot{m}c_p)_h$
$C_{\min}$ = minimum heat capacity rate $=\min(C_c, C_h)$
$C_{\max}$ = maximum heat capacity rate $=\max(C_c, C_h)$
c_p = constant pressure specific heat
C_r = capacity ratio $C_r = C_{\min}/C_{\max}$
F = LMTD correction factor
Fa = fin analogy number
h = heat transfer coefficient
k = thermal conductivity

L = length
LMTD = log-mean temperature difference; LMTD=$((T_1-t_2)-(T_2-t_1))/\ln((T_1-t_2))/(T_2-t_1))$
NTU = number of transfer units NTU=$UA/C_{\min}$
P = pressure of hot fluid
p = pressure of cold fluid
P = $P=(t_2-t_1)/(T_1-t_1)$
$\bar{p}$ = circumference
q = rate of heat transfer
q_{opt} = optimum rate of heat transfer; $q_{\text{opt}}=UA(\bar{T}-\bar{t})$
R = $R=(T_1-T_2)/(t_2-t_1)$
$\dot{S}_{\text{gen}}$ = rate of entropy production
T = hot fluid temperature
t = cold fluid temperature
$\bar{T}$ = average temperature of the hot fluid $\bar{T}=(T_1+T_2)/2$
$\bar{t}$ = average temperature of the cold fluid $\bar{t}=(t_1+t_2)/2$
T^o = temperature of the hot fluid in the ideal heat exchanger
t^o = temperature of the cold fluid in the ideal heat exchanger
U = overall heat transfer coefficient, W/m^2 K
η = heat exchanger efficiency
ε = heat exchanger effectiveness $\varepsilon=q/C_{\min}(T_1-t_1)$
σ = nondimensional entropy generation rate $\sigma=\dot{S}_{\text{gen}}/C_{\min}$

Subscripts and Superscripts

1 = inlet
2 = outlet
* = nondimensional

Appendix

Example 1. Water at a rate of 10,000 kg/hr is used to cool oil from 160°C to 94°C on the shell side of a single shell and four-tube paths heat exchanger. Water having a specific heat of 4182 J/kg K enters the tubes at 16°C and exits at 84°C. If the overall heat transfer coefficient is 355 W/m^2 K, determine the heat exchanger area.

This example is based on problem 11.44 of Ref. [5] and an example of a sizing problem. Using the concept of heat exchanger efficiency, the solution is found as follows:

$$C_c=\frac{10{,}000}{3600}4182=11{,}617\ \text{W/K},$$

$$q=C_c(t_2-t_1)=11{,}617(84-16)=7.90\times10^5\ \text{W}$$

$$C_h=\frac{q}{T_1-T_2}=\frac{7.90\times10^5}{160-94}=11{,}970\ \text{W/K}\ ^\circ\text{C}$$

$$q=UA\,\eta(\bar{T}-\bar{t})=C_{\min}\text{NTU}\ \eta(\bar{T}-\bar{t})$$

$$\text{NTU}\ \eta=\frac{q}{C_{\min}(\bar{T}-\bar{t})}=\frac{7.90\times10^5}{11{,}617(77)}=0.8832$$

$$\eta=\frac{\tanh(\text{Fa})}{(\text{Fa})}$$

$$\eta=\frac{\tanh\left(\text{NTU}\dfrac{\sqrt{1+C_r^2}}{2}\right)}{\left(\text{NTU}\dfrac{\sqrt{1+C_r^2}}{2}\right)}$$

$$\text{NTU}\frac{\sqrt{1+C_r^2}}{2}=\tanh^{-1}\left(\eta\text{NTU}\frac{\sqrt{1+C_r^2}}{2}\right)$$

$$\text{NTU}=\frac{\tanh^{-1}\left(0.8832\dfrac{\sqrt{1+0.971^2}}{2}\right)}{\dfrac{\sqrt{1+0.971^2}}{2}}=1.030$$

$$\eta=\frac{0.8832}{1.030}=0.857$$

$$A=\frac{C_{\min}\text{NTU}}{U}=\frac{11{,}617\times1.030}{355}=33.71\ \text{m}^2$$

The area for the shell and tube heat exchanger calculated here matches the value given in the solutions manual for Ref. [5] by using the F correction factor.

Example 2. Water at a rate of 10,000 kg/hr and 16°C with specific heat of 4182 J/kg K is used to cool oil at 160°C in a shell and tube heat exchanger similar to Example 1, having an overall heat transfer coefficient of 355 W/m^2 K and an area of 33.71 m^2. If C_h=11,970 W/K, determine the rate of heat transfer.

This is the reverse problem, and an example of a heat exchanger rating problem, typically solved using the ε-NTU approach. Here the problem is solved using the concept of heat exchanger efficiency.

$$\text{Fa}=\text{NTU}\frac{\sqrt{1+C_r^2}}{2}=1.030\frac{\sqrt{1+0.971^2}}{2}=0.718$$

$$\eta=\frac{\tanh(\text{Fa})}{(\text{Fa})}=0.857$$

$$\bar{T}-\bar{t}=\frac{(T_1-t_1)}{1+\text{NTU}\ \eta\left(\dfrac{1+C_r}{2}\right)}=\frac{160-16}{1+1.030\times0.857\left(\dfrac{1+0.971}{2}\right)}$$

$$=77\ \text{K}$$

$$q=UA\,\eta(\bar{T}-\bar{t})=355\times33.71\times0.858\times77$$

$$=7.90\times10^5\ \text{W}$$

References

[1] Fakheri, A., 2003, "Arithmetic Mean Temperature Difference and the Concept of Heat Exchanger Efficiency," *Proceedings of the 2003 ASME Summer Heat Transfer Conference*, Las Vegas, Nevada, July 21–23, Paper No. HT2003-47360.

[2] Fakheri, A., 2003, "The Shell and Tube Heat Exchanger Efficiency and its Relation to Effectiveness," *Proceedings of the 2003 American Society of Mechanical Engineers (ASME) International Mechanical Engineering Congress and Exposition (IMECE)*, Washington, D.C., November 16–21.

[3] Fakheri, A., 2003, "An Alternative Approach for Determining Log Mean Temperature Difference Correction Factor and Number of Shells in Shell and Tube Heat Exchangers," J. Enhanced Heat Transfer, **10**(4), pp. 407–420.

[4] Fakheri, A., 2006, "Thermal Efficiency of the Cross Flow Heat Exchangers," *Proceedings of the 2006 American Society of Mechanical Engineers (ASME) International Mechanical Engineering Congress and Exposition (IMECE)*, Chicago, IL, November 5–10.

[5] Incropera, F. P., and DeWitt, D., 2002, *Fundamentals of Heat and Mass Transfer*, 4th ed., Wiley, New York.

[6] McClintock, F. A., 1951, "The Design of Heat Exchangers for Minimum Irreversibility," Presented at the ASME Annual Meeting, Paper No. 51-A-108.

[7] Bejan, A., 1977, "Concept of Irreversibility in Heat Exchanger Design: Counterflow Heat Exchangers for Gas-to-Gas Applications," ASME J. Heat Transfer, **99**(3), pp. 374–380.

[8] Aceves-Saborio, S., Ranasinghe, J., and Reistad, G. M., 1989, "Extension to

the Irreversibility Minimization Analysis Applied to Heat Exchangers," ASME J. Heat Transfer, **111**(1), pp. 29–36.
[9] Shah, R. K., and Skiepko, T., 2004, "Entropy Generation Extrema and Their Relationship With Heat Exchanger Effectiveness—Number of Transfer Unit Behavior for Complex Flow Arrangements," ASME J. Heat Transfer, **126**(6), pp. 994–1002.
[10] Mohamed, H. A., 2006, "Entropy Generation in Counter Flow Heat Exchangers," ASME J. Heat Transfer, **128**, pp. 87–92.
[11] Bejan, A., 1982, "Second-Law Analysis in Heat Transfer and Thermal Design," Adv. Heat Transfer, **15**, pp. 1–58.
[12] Sekulic, D. P., 1990, "The Second Law Quality of Energy Transformation in Heat Exchanger," ASME J. Heat Transfer, **112**, pp. 295–300.
[13] Ogiso, K., 2003, "Duality of Heat Exchanger Performance in Balanced Counter-Flow Systems," ASME J. Heat Transfer, **125**(3), pp. 530–532.

Experimental Study and Genetic-Algorithm-Based Correlation on Shell-Side Heat Transfer and Flow Performance of Three Different Types of Shell-and-Tube Heat Exchangers

Qiu-wang Wang
e-mail: wangqw@mail.xjtu.edu.cn

Gong-nan Xie

Bo-tao Peng

Min Zeng

State Key Laboratory of Multiphase Flow in Power Engineering,
School of Energy and Power Engineering,
Xi'an Jiaotong University,
Xi'an, 710049, China

The heat transfer and pressure drop of three types of shell-and-tube heat exchangers, one with conventional segmental baffles and the other two with continuous helical baffles, were experimentally measured with water flowing in the tube side and oil flowing in the shell side. The genetic algorithm has been used to determine the coefficients of correlations. It is shown that under the identical mass flow, a heat exchanger with continuous helical baffles offers higher heat transfer coefficients and pressure drop than that of a heat exchanger with segmental baffles, while the shell structure of the side-in-side-out model offers better performance than that of the middle-in-middle-out model. The predicted heat transfer rates and friction factors by means of the genetic algorithm provide a closer fit to experimental data than those determined by regression analysis. The predicted corrections of heat transfer and flow performance in the shell sides may be used in engineering applications and comprehensive study. It is recommended that the genetic algorithm can be used to handle more complicated problems and to obtain the optimal correlations. [DOI: 10.1115/1.2739611]

Keywords: heat transfer, pressure drop, shell-and-tube heat exchanger, experimental study, genetic algorithm, regression analysis, correlations

Introduction

Heat exchangers are important apparatuses for heat and mass exchange employed in the fields of refrigeration engineering, oil-refinery engineering, chemical engineering, environmental protection, electric power plants, and so on. Generally speaking, the fraction of heat exchanger investment to total investment is about 10% to 20% in oil-refineries, while 30% to 40% in chemical engineering factories. It is preferable to design and manufacture heat exchange apparatuses with high effectiveness, low energy consumption, and low cost. Shell-and-tube heat exchangers (STHXs) are widely used for evaporators and condensers. In STHX, performance of heat transfer may be improved in the shell side, where baffles are located. Segmental baffles (supporting tubes and changing fluid flow direction), are commonly used in traditional STHXs. Segmental baffles make shell-side fluid to flow in a tortuous, zigzag manner across the tube bundles, which enhance heat transfer rates due to flow normal to the tube banks. In aforementioned scenario, however, there exist many problems (Kral et al. [1], Peng [2], Reppich and Zagermann [3], Wang [4], Wang et al. [5], Xie et al. [6], Bell [7]): (1) high pressure drop occurs due to fluid impact normal to shell wall; (2) heat transfer rates decrease due to flow stagnate in connection region with baffles and shell wall; (3) mass velocity decreases due to bypass and leakage, since accuracy of manufacture and installation is not reached; and (4) operation time decreases due to librations from flow normal to tube banks in high mass velocity. When the traditional segmental baffles are used in STHXs, higher pump power is needed to satisfy higher pressure drop. Therefore, it is essential to modify the shape of common baffles.

In 1960s, the idea of STHXs with helical baffles was proposed (Bell [7], Li and Kottke [8], Naim and Bar-Cohen [9]). In STHX with helical baffles, baffles were arranged by approximate helicoids, which makes the flow in the shell side continuously helical, resulting in decrease of pressure drop and in enhanced heat transfer rates in the shell side. Many new productions of this type appeared in 1990s. Nowadays, these types of STHXs are used in many countries such as Russia and Japan.

From 1990s, few studies on STHXs with continuous helical baffles are reported in open literatures, while most of them are with non-continuous helical baffles. The absence of reliable performance data for STHXs with continuous helical baffles causes difficulty for designers and engineers. Thus in this study, an experimental system has been designed, fabricated, and investigated experimentally, and performances of heat transfer for STHXs with different baffles have been compared.

In recent years, application of genetic algorithms (GAs) to thermal engineering has received much attention for solving real-word problems (Sen and Yang [10]). For example, the fin-tube heat exchanger performance was predicted using GA (Pacheco-Vega et al. [11]). Plate-fin heat exchangers were optimized by means of GAs (Ozkol and Komurgoz [12], Xie and Wang [13], Mishra et al. [14]). A new design method was proposed to optimize a STHX from an economic point of view by GA (Selbas et al. [15]). Geometrical optimization of cross-wavy and cross-corrugated primary surface recuperators was studied via GAs (Liang et al. [16,17]). Heat transfer correlations of compact heat exchangers were obtained using GAs, to estimate their performance (Pacheco-Vega et

Contributed by the Heat Transfer Division of ASME for publication in the JOURNAL OF HEAT TRANSFER. Manuscript received July 8, 2006; final manuscript received December 3, 2006. Review conducted by Anthony M. Jacobi.

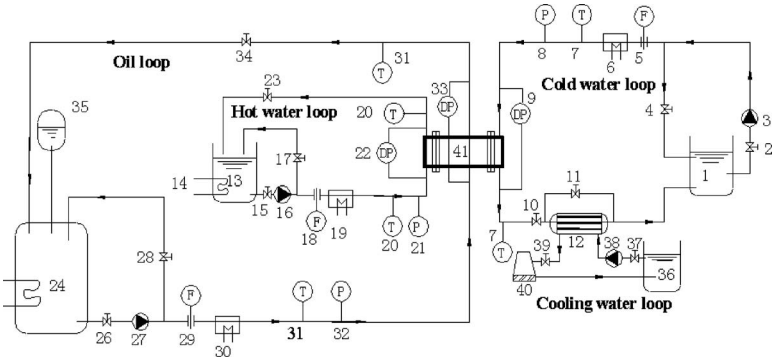

Fig. 1 Experimental loop. Cold-water loop: 1-water box; 2,10-valve; 4,11-electric value; 3-pump; 5-flowmeter; 6-heater; 7-thermo couples; 8-pressure transducer; 9-pressure drop transducer; 12-heat exchanger. Hot-water loop: 13-water box; 14-heater; 15,23-valve; 16-pump; 17-electric valve; 18-flowmeter; 19-heater; 20-thermo couples; 21-pressure transducer; 22-pressure drop transducer. Oil loop: 24-oil box; 25-heater; 26,34-valve; 27-pump; 28-electric valve; 29-flowmeter; 30-heater; 31-thermo couples; 32-pressure transducer; 33-pressure drop transducer; 35-expand box. Cooling water loop: 36-water box; 37,39-valve; 38-pump; 40-tower; 41-test heat exchanger.

al. [18], Pacheco-Vega et al. [19]), other applications in estimating of the radiative properties and the surface emissivities [20], and in modeling phonon-phonon normal and umklapp scattering processes [21] were presented. These reports suggest that the genetic algorithm has a strong ability search and optimize, which can successfully optimize and predict thermal problems. Therefore, the present study has employed the genetic algorithm to correlate and predict the heat transfer performance, to correlate the Nusselt number versus Reynolds number, and the flow resistance to correlate the friction factor versus Reynolds number, in the shell side for three different types of STHXs.

Experimental System

Experimental Loop. The experimental loop, shown in Fig. 1, was designed and fabricated at School of Energy and Power Engineering, Xi'an Jiaotong University. There are three sub-loops (an oil loop, a cold water loop, and a cooling water loop) for achieving the heat exchange of the experimental loop in the present study. In Fig. 1, 41 is the test heat exchanger. Oil-water (by oil loop and cold water loop) or water-water (by hot water loop and cold water loop) heat exchange is carried out in the experimental loop. The cooling water loop is used to cool the heated water of the cold water loop. A more detailed description of the experimental system and tested heat exchangers can be found in Ref. [2].

Oil loop: The oil loop includes the oil-refined loop and the experimental loop. In the oil-refined loop, the heated oil flows in an expanded box, elicited by a pump, and then flows into the heater after flow in the refiner. In the experimental loop, the heated oil is elicited by the pump, flows through the turbine flowmeter, flows downstream through the test section, and last flows into the heater. The loops were switched by a valve.

Cold water loop: Water flows through turbine flowmeter by a pump, flows through the test section of tube-side, and then flows into one side of the heat exchanger 12 in the cold water loop, and last flows into the water box.

Cooling water loop: Cooling water flows through the other side of heat exchanger 12 by the pump, flows into the cooler, and last flows into the water box.

In the experimental process, there are seven parameters to be measured: inlet and outlet temperature of the oil side (shell side), i.e., t_{o1}, t_{o2}; inlet and outlet temperature of water side (tube side), i.e., t_{w1}, t_{w2}; volume flow rate of both sides, i.e., v_o,v_w; and total pressure drop between the inlet and outlet of the oil side. The temperatures at the inlet and outlet of the oil side and water side were measured by the copper-constantan thermocouples. The accuracy of the thermocouple reading is estimated with 0.1°C. The volume flow rates of the oil side and water side were measured by turbine flowmeters, and the oil-side pressure drop was measured by a differential pressure transducer with an error less than 0.25%. All the digital data obtained from thermocouples, flowmeters, and transducer were collected into the computer, and then translated into real physical data by a data transition system. Finally, the corresponding experimental data are saved and averaged on the computer for data reduction.

In the experiments, once all the temperature data were stabilized within 0.1°C, the system was allowed to approach the steady state before any data were recorded and saved. The water flow rate was fixed at a specific value, through which the water-side Reynolds numbers were around 3000. Thus, *Gnielinski's* correlation can be validly used for calculation of water-side/tube-side heat transfer and friction. Experiments were conducted with the inlet oil temperature ranging between 50°C and 60°C, inlet water temperature ranging between 15°C and 30°C, and oil flow rate ranging between 0.5 and 4.5 kg/s. The uncertainty of the heat balance between the oil side and water side was within 8%, and a 60-set of data per half-minute were averaged and saved into the computer.

Three tested heat exchangers are shown in Fig. 2. Figure 2(*a*) is a heat exchanger with segmental baffles (hereafter, this type of heat exchanger is called as HX1), the other two are the heat exchangers with continuous helical baffles, as shown in Figs. 2(*b*) and 2(*c*). The only difference between these latter two helical heat exchangers is in the manner of inlet-outlet flow of the shell-side fluid. One is middle-in-middle-out (HX2, Fig. 2(*b*)) and the other one is side-in-side-out (HX3, Fig. 2(*c*)). The cores of HX2 and HX3 are the same (the layouts of tubes and baffles are identical), the only difference between the HX2 and HX3 is the locations of inlets and outlets of the shell-side flows. The locations of inlet and outlet of HX2 are on the middle of the shell side, which is normal to shell, while the positions of inlet and outlet of HX3 are on the side of shell side, which is tangential to the shell. It should be noted that for helical heat exchangers (HX2, HX3), there is a blocked center tube.

The heat exchangers are 1-2 type (one shell pass and two tube passes), with hot oil flowing in the shell side and cold water flowing in the tube side. The detailed values of the parameters for

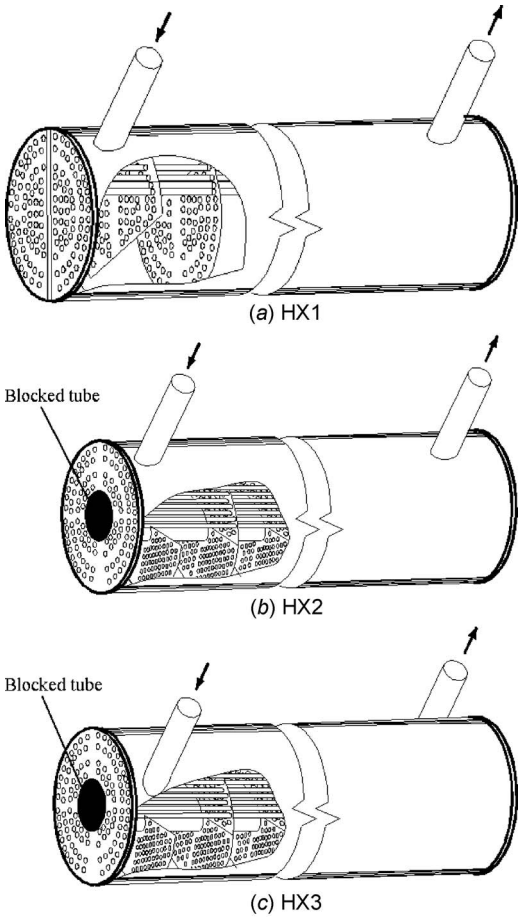

Fig. 2 Shell-and-tube heat exchangers

Table 1 Geometrical parameters of heat exchangers [2]

Parameters	Value
Inner diameter of shell, mm	207
Outer diameter of tube, mm	10
Inner diameter of tube, mm	8
Arrangement of tube	Triangle
Effective length of tube (l), mm	620
Number of tubes (helical)	158
Number of tubes (segmental)	176
Outer diameter of inlet tube in water side, mm	57
Inner diameter of inlet tube in water side, mm	50
Outer diameter of outlet tube in water side, mm	57
Inner diameter of outlet tube in water side, mm	50
Outer diameter of inlet tube in oil side, mm	57
Inner diameter of inlet tube in oil side, mm	50
Outer diameter of outlet tube in oil side, mm	57
Inner diameter of outlet tube in oil side, mm	50
Length of heat exchanger (L) mm	670

the three tested heat exchangers are shown in Tables 1 and 2. Experiments were performed for Reynolds number ranging from 300 to 7000 on the shell side. Heat transfer rates varied from 20 kW to 50 kW. It should be noted that the diameter of center tube in HX1 is zero because there is no center tube.

Data Reduction. The main purpose of the data reduction is to determine the shell-side heat transfer and friction characteristic, i.e., Nu and f, of the heat exchangers from the data, which recorded at steady state conditions during the each test run, and to find out corresponding power-law correlations of Nu versus Re, and f versus Re for each heat exchanger. The average values of the inlet and outlet temperatures of the oil side and water side were used to evaluate the physical properties of oil and water, respectively.

The oil-side/shell-side heat transfer rate can be given as

$$Q_o = m_o c_{p,o}(t_{o1} - t_{o2}) \tag{1}$$

where the oil mass flow rate m is obtained from the volume flow rate multiplying corresponding density, as is the water mass flow rate. The water-side heat transfer rate can be given as

$$Q_w = m_w c_{p,w}(t_{w1} - t_{w2}) \tag{2}$$

Thus, the total rate of heat transfer used in the calculation is the average of the oil side and water side as follows:

$$Q_{\text{ave}} = (Q_o + Q_w)/2 \tag{3}$$

and the heat transfer balance can be determined by

$$\varepsilon = 100\,\% \frac{|Q_o - Q_w|}{Q_{\text{ave}}} \tag{4}$$

The oil-side heat transfer coefficient h_o is determined from the overall heat transfer resistance relationship

$$\frac{1}{U} = \frac{1}{h_o} + R_o + \frac{d_o}{2k_{\text{wall}}} \ln \frac{d_o}{d_i} + \frac{d_o}{d_i}\frac{1}{h_w} + R_w \tag{5}$$

where d_o and d_i are outside and inside diameters of the tube, respectively. Because of the new test heat exchanger, the fouling resistances are neglected, that is, $R_o = R_w = 0$. The overall heat transfer coefficient U can be determined from

$$U = \frac{Q_{\text{ave}}}{A\Delta t_m} \tag{6}$$

where the heat transfer area A is based on the area outside tubes,

$$A = \pi d_o l N \tag{7}$$

where, l and N are the length of tube and the number of tubes, respectively. The logarithmic-mean temperature difference Δt_m is determined by

$$\Delta t_m = F\Delta t_c \tag{8}$$

where F is the correction factor and Δt_m is the counter-flow logarithmic-mean temperature difference. They can be determined

Table 2 Geometrical parameters for test sections [2]

Test section	Spiral pitch, mm	Number of baffles	Diameter of center tube, mm
HX with segmental baffles (HX1)	70	7	NA
HX with continuous helical baffles, middle-in-middle-out (HX2)	48	9	48
HX with continuous helical baffles, side-in-side-out (HX3)	48	9	48

by

$$\Delta t_c = \frac{(t_{o1} - t_{w2}) - (t_{o2} - t_{w1})}{\ln\left(\frac{t_{o1} - t_{w2}}{t_{o2} - t_{w1}}\right)} \tag{9}$$

$$F = \frac{\ln\left(\frac{1-P}{1-PR}\right)}{\ln\left(\frac{2 - P(1 + R - \sqrt{R^2+1})}{2 - P(1 + R + \sqrt{R^2+1})}\right)} \tag{10}$$

$$P = \frac{t_{w1} - t_{w2}}{t_{o1} - T_{w2}} \quad R = \frac{t_{o1} - t_{o2}}{t_{w1} - t_{w2}} \tag{11}$$

The water-side/tube-side heat transfer coefficient h_w is evaluated from the semi-empirical correlation of *Gnielinski* [22]:

$$h_w = \left(\frac{k_w}{d_i}\right)\frac{(f_w/8)(\mathrm{Re} - 1000)\mathrm{Pr}}{1 + 12.7\sqrt{f_w/2}(\mathrm{Pr}^{2/3} - 1)}\left[1 + \left(\frac{d_1}{l}\right)^{2/3}\right] \tag{12}$$

where the friction factor is given by

$$f_w = (1.82 \log_{10} \mathrm{Re} - 1.64)^{-2} \tag{13}$$

where the water-side $\mathrm{Re} = \rho u d_i / \mu$.

Thus, the oil-side heat transfer coefficient h_o can be calculated from Eq. (4), and then the Nusselt number Nu can be calculated by

$$\mathrm{Nu} = h_o \frac{d_o}{k_o} \tag{14}$$

For simplicity, the flow friction characteristic can be presented in terms of f-factors as follows

$$f = \frac{2\Delta P}{\rho u_{\max}^2}\frac{d_o}{L} \tag{15}$$

where L is the effective length of the heat exchanger, and $u_{\max}$ is the velocity at the minimum free flow area, and can be determined by

For HX1:

$$A = B d_s (1 - d_o/S) \tag{16}$$

For HX2 and HX3

$$A = (1 - B/d_s) B d_s (1 - d_o/S) \tag{17}$$

The uncertainty of measured temperature difference, flow rate, heat transfer rate, and heat transfer coefficient are less than 1.8%, 0.14%, 2.5%, and 3.7%, respectively. Typical uncertainty of the shell-side heat transfer coefficient is about 15.64 $\mathrm{W/m^2\,k}$. The maximum and minimum uncertainties for pressure drop are 155.9 Pa and 190 Pa, respectively.

Correlations for Friction Factor and Nusselt Number. The experimental data are often compressed into dimensionless correlations as follows:

$$\mathrm{Nu}\,\mathrm{Pr}^{-1/3} = \alpha\,\mathrm{Re}^{\beta} \quad f = \phi\,\mathrm{Re}^{\varphi} \tag{18}$$

So far, Eq. (18) has been used to correlate the average heat transfer rate and pressure drop (experimental data). Engineers use Eq. (18), which covers the ranges of the parameters for the same type of exchangers. The dimensional values for heat transfer coefficient and friction factor are used in practical design and/or operation. The coefficients α, β, ϕ, and φ in Eq. (18) can be determined by regression analysis or by importing into post-software such as ORIGIN, MATLAB, etc. It is possible that the traditional method, i.e., regression analysis, is not the best method to correlate the experimental data, and thereby the errors may not be minimum. Therefore, some other new methods have to be found for correlating the data.

The genetic algorithm was developed about two decades ago and is now widely used in various research areas, since it has a powerful ability for global search and optimization of complex systems. In this paper, the genetic algorithm has been used to search for the numerical values of constants in Eq. (18), for closer fitting to experimental data.

Genetic Algorithm

Simple Descriptions. The genetic algorithm is maintained by a population of parent individuals that represent the latent solutions of a real-world problem. Figure 3 shows the flowchart of the genetic algorithm. Each individual is assigned a fitness based on how well each individual fits in a given environment, evaluated by survival of the fitness. Fit individuals go through the process of survival selection, crossover, and mutation, creating a next generation, called child individuals. A new population is therefore formed by selection of good individuals from parent and child individuals. After some generations, the algorithm is converged to the best individual, which possibly represents the best solution of the given problem. More details about the description of the genetic algorithm can be found in many books (Goldberg [23]; Michalewicz [24]).

Variables Ranges. A binary string is adopted for encoding the variables of a given model. Two coefficients of correlations were assigned to vary between $[-1, 1]$. Considering the ability of computers to handle bit operations and engineering applications, the computational precision is set to four decimals (0.0001). Thus, a coefficient needs a 15-character binary, and an individual coefficient of a model needs a 30-character binary.

Fitness Function. The conventional genetic algorithm determines the global maximum value in search spaces; however, the objective of the present correlation and prediction is to make the deviation minimum between the predicted and the experimental results. Thus, when searching the coefficients α and β in Eq. (18), a fitness function should be given as follows:

$$\mathrm{Fit} = \frac{C_Q}{\sqrt{\frac{1}{M}\sum_{i=1}^{M}(Q^p - Q^e)^2}} \tag{19}$$

where C_Q is a constant and its value is assigned 5000; i.e., about 10% of maximum heat transfer rate [2]. M refers to the number of experimental data. Q^e and Q^p refer to experimental and predicted heat transfer rates, respectively. The flowchart of prediction is shown in Fig. 3. Note that global maximum fitness corresponds minimum deviation leading to the best predicted heat transfer rate. Calculation of heat transfer rate can be found in Ref. [2]. When searching the coefficients ϕ and φ in Eq. (18), another fitness function should be given as follows:

$$\mathrm{Fit} = \frac{C_f}{\sqrt{\frac{1}{M}\sum_{i=1}^{M}(f^p - f^e)^2}} \tag{20}$$

In this case, C_f is assigned 0.05, about 10% of maximum friction factor [2].

Genetic Operators and Parameters. In the present study, tournament selection, uniform crossover, and one-point mutation were selected. Niching and elitism were adopted (Carroll [25,26]; Michalewicz [27]). The size of the population and maximum evolution generation were set to 20 and 1000, respectively. The probability of crossover and mutation were set to 0.5 and 0.005, respectively. The selection of genetic parameters is a trial-and-error process, and with the variation of these parameters, results are not exactly identical but are very close to one another. On the other hand, in this study the selection of genetic parameters and operators is based on the previous recommendations [25,26].

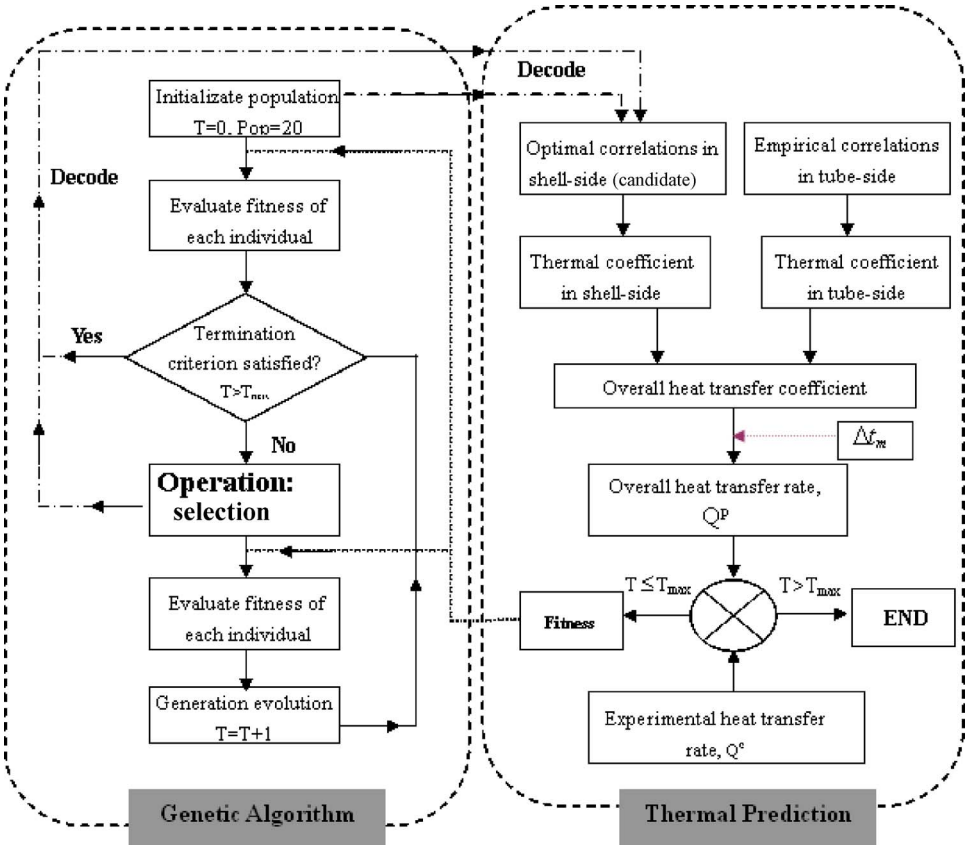

Fig. 3 Flow chart of genetic algorithm and thermal prediction

Results and Discussion

The Nusselt number versus Reynolds number in the shell side of the three heat exchangers is shown in Fig. 4. The points refer to experimental data, while the lines refer to approximate lines fitted by the genetic algorithm. For all three heat exchangers, it can be seen that the Nusselt number increases with the increase of the Reynolds number. Heat transfer coefficients of three heat exchangers versus mass flow rate are shown in Fig. 5. It can be found that, under identical mass flow rates, heat transfer coefficients of both HX2 and HX3 are higher than that of HX1. This difference increases with the increase in mass flow rate. The heat transfer coefficient of HX3 is slightly higher than that of HX2.

The friction factor number versus Reynolds number in the shell side of the three heat exchangers is shown in Fig. 6. Again, the black solid points refer to experimental data while the lines refer to approximate lines fitted by the genetic algorithm. For all three heat exchangers, it can be seen that the friction factor decrease with the increase of the Reynolds number. The total pressure drop versus the mass flow rate in the shell side of the three heat exchangers is shown in Fig. 7. It can be seen that, under identical mass flow rates, pressure drops of both HX2 and HX3 are higher than that of HX1. The difference is higher at higher mass flow rates. The pressure drop of HX2 is slightly higher than that of HX3.

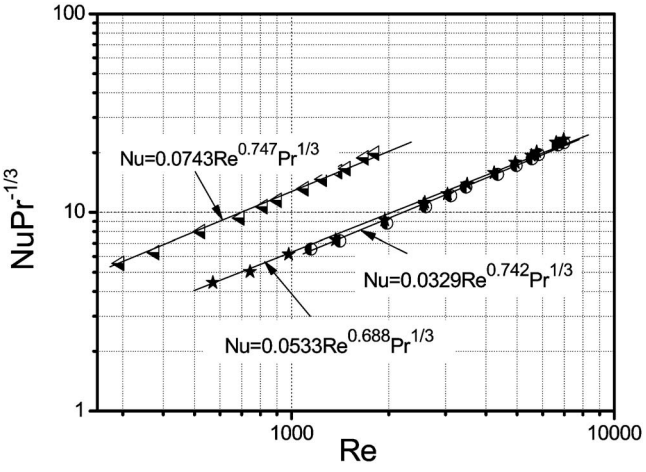

Fig. 4 Heat transfer performance for three heat exchangers

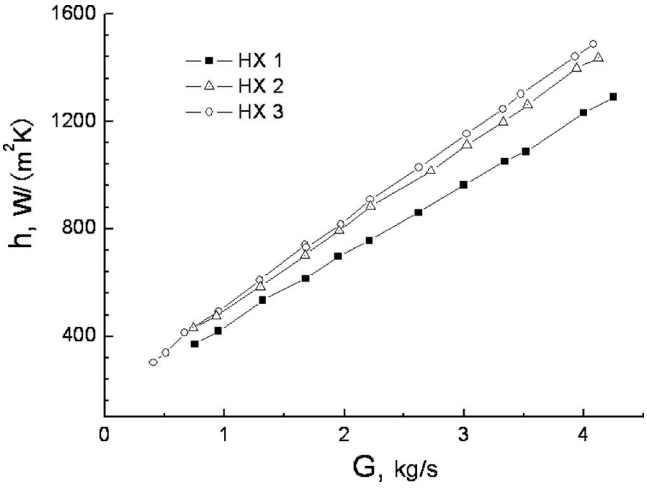

Fig. 5 Heat transfer coefficient versus flow rate

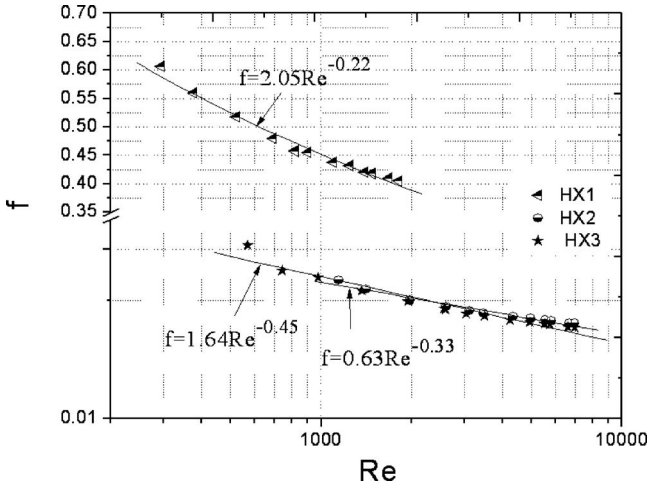

Fig. 6 Flow friction performance for three heat exchangers

The evolution process for the fitness is shown in Fig. 8. At the beginning of evolution process (less than about 20 generations), the differences between every individual are relatively large, which in turn leads to the individuals with low fitness being eliminated and individuals with higher fitness being saved. After certain generations (larger than about 100 generations), the variation of fitness for minimum deviation is small, finally approaching to a constant value. The predicted Nusselt number versus experimental Nusselt number of the three heat exchangers is shown in Fig. 9. In the figure, the middle straight line indicates that the predicted results agree perfectly with the experimental data. It can be observed that the predicted Nusselt numbers obtained by the genetic algorithm are quite close to the experimental data. All the deviations are less than 10% and the maximum deviation is 9.6%.

The predicted heat transfer rate versus experimental data of the three heat exchangers is shown in Fig. 10. In this figure, GA refers to the results obtained by genetic Algorithm, while RA refers to the results fitted by regression analysis [2]. From these figures, it can be seen that the predicted data (+) obtained by genetic algorithms are closer to experimental data than that by regression analysis (◦), because most of predicted results are much closer to the middle straight line, which represents the best agreements with the experimental data.

In order to compare the results obtained by genetic algorithm with that by regression analysis [2], two factors, i.e., R and σ, are defined as

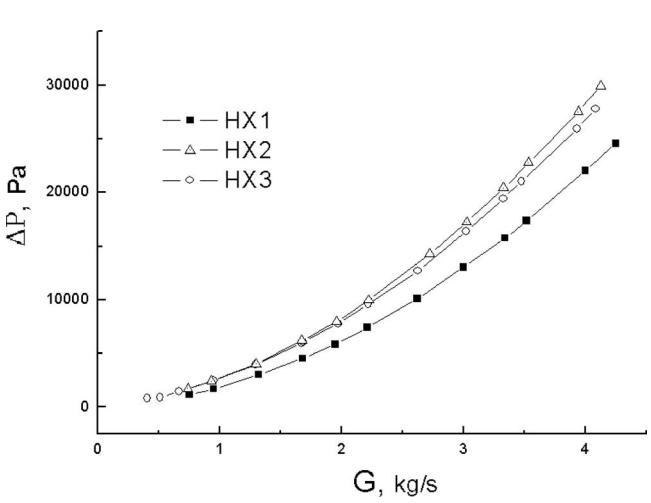

Fig. 7 Pressure drop versus flow rate

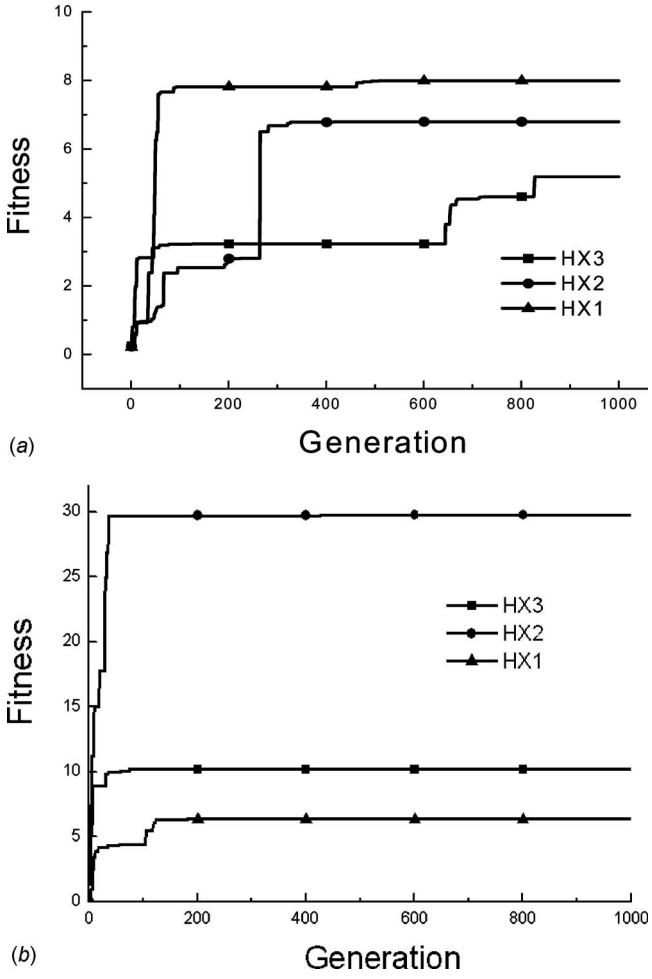

Fig. 8 Evolution process of maximizing fitness

$$R_{iQ} = \left(\frac{Q^p}{Q^e}\right)_i \quad \text{and} \quad R_{if} = \left(\frac{f^p}{f^e}\right)_i \tag{21}$$

$$R_Q = \frac{1}{M}\sum_{i=1}^{M} R_{iQ} \quad \text{and} \quad R_f = \frac{1}{M}\sum_{i=1}^{M}\left(\frac{f^p}{f^e}\right) \tag{22}$$

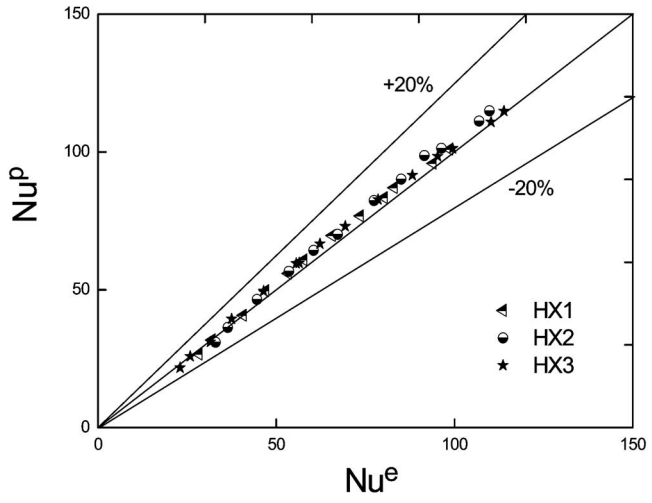

Fig. 9 Predicted Nusselt number versus experimental data

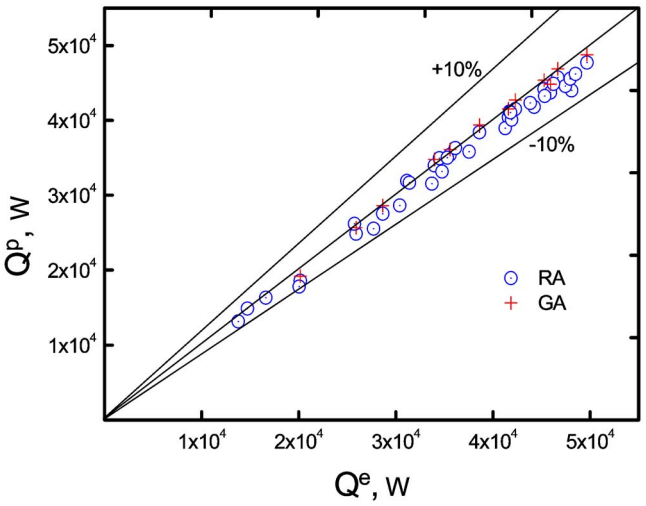

Fig. 10 Predicted heat transfer rates versus experimental data of three exchangers

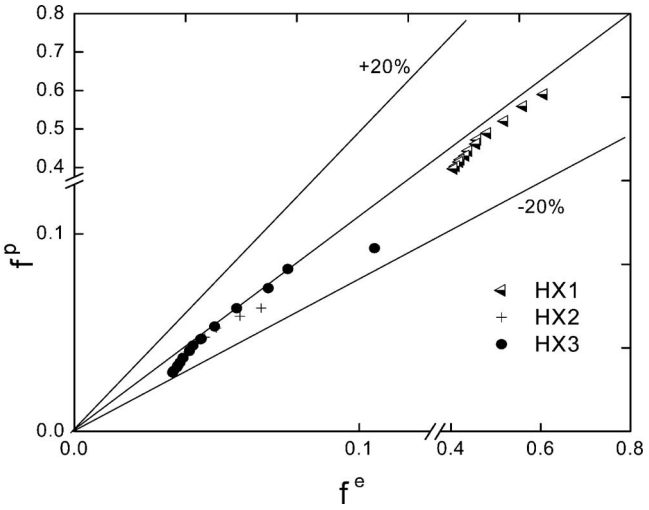

Fig. 11 Predicted friction factors versus experimental data of three exchangers

$$\sigma_Q = \sqrt{\sum_{i=1}^{M} \frac{(R_Q - R_{iQ})}{M}} \quad \text{and} \quad \sigma_f = \sqrt{\sum_{i=1}^{M} \frac{(R_f - R_{if})}{M}} \tag{23}$$

The two factors, i.e., R and σ, are important evaluation factors, which quantitatively reflect the order of agreement between the predicted results and the experimental results. Sen and Yang [10] stated that the R represented the average accuracy of the predicted results, while σ represented the scatter of the prediction. The values of R and σ for three heat exchangers are listed in Table 3, where the results obtained by GA and the ones by RA are compared. It can be seen that the values of R by GA are closer to unity than those by RA, and the σ by GA is smaller than that by RA. This shows that the predicted results by GA are much better than those by RA [2].

The predicted friction factor versus experimental friction factor of three heat exchangers is shown in Fig. 11. It can be observed that, the predicted friction factors obtained by GA are well close to the experimental data. Most of all deviations are less than 10%, and only three of the deviations are about 13% (the number of datapoints is 39).

The predicted coefficients of correlations, determined by regression analysis (RA) and by the genetic algorithm (GA), are listed in Table 4. Such correlations of heat transfer and flow performance in the shell sides may be used in engineering applications and comprehensive study; for example, engineers may borrow them to design STHXs with segmental or continuous helical baffles, or researchers may use them to optimize corresponding STHXs under a valid range of parameters.

The cross-sectional area in the shell side of HX2 or HX3 is smaller than that of HX1, because there is a blocked center tube. In this result, under identical mass flow rate conditions, higher fluid velocity occurs in the shell side of HX2 or HX3, in turn leading to higher consumption of pressure drop than that of HX1. On the other hand, in HX2 or HX3, there is no sluggish region and shell fluid does not flow normal to tube bundles. The fluid flows in a continuous helical manner with uniform velocity, covering and brushing the tubes, resulting in decrease of pressure drop and in enhancement of heat transfer rates in the shell side. The shell fluid flows from the side of the shell in HX3, improving the manner of helical flow, in turn leading to smaller pressure drop and higher heat transfer rate than that of HX2, in which the shell fluid flows through the middle of the shell side.

Table 3 Quantitative comparison of predicted results

		HX1	HX2	HX3
R_Q	Obtained by RA [2]	0.971386	0.93746	0.988464
	Obtained by GA	1.027565	1.045204	1.016262
σ_Q	Obtained by RA [2]	0.02184	0.01982	0.02452
	Obtained by GA	0.00512	0.00991	0.00868
R_f	Obtained by RA [2]	1.005584	0.997579	0.988199
	Obtained by GA	0.999171	0.999466	0.988733
σ_f	Obtained by RA [2]	0.01714	0.03832	0.08637
	Obtained by GA	0.01710	0.03566	0.07197

As shown above, the heat transfer rate and the friction factor by the genetic algorithm are closer to the corresponding real values. This indicates that the genetic algorithm can reflect the real performance better and it has advantages over RA, such as searching and predicting. It is recommended that engineers should use the genetic algorithm to fit and predict the experimental results, leading to further studies or engineering applications.

In engineering practice, the heat transfer rate, Q, is frequently desired. Application of a computational intelligent method to predict performance of thermal devices has received much attention. For example, in recent years, some researchers use artificial neural networks to predict the performance of heat exchangers [28,29], where the aim is to make the predicted results closer to real performance. Thus, the application of the genetic algorithm to more engineering real-world problems can show its superiority with searching, optimizing, and predicting, leading to further challenges.

Conclusions

In this paper the experimental system for testing the shell-side heat transfer and pressure drop performances of shell-and-tube heat exchangers is designed and built. Heat transfer and flow performance for three kinds of heat exchanger are investigated and compared. The genetic algorithm is also applied to correlate the heat transfer and pressure drop performances in the shell sides. The main conclusions are summarized as follows.

(1) Both the heat transfer coefficient and friction factor of the three heat exchangers increase with the increase of Reynolds number. Under identical mass flow rates in the shell side, heat transfer coefficients and pressure drops in STHXs with continuous helical baffles are higher than that of STHXs with segmental baffles. In addition, for heat exchangers with continuous helical baffles, the one with

Table 4 Predicted coefficients by RA and GA

Correlations	Coefficients	Regression Analysis [2]			Genetic Algorithm		
		HX1	HX2	HX3	HX1	HX2	HX3
$Nu=\alpha Re^{\beta} Pr^{1/3}$	α	0.106	0.0451	0.0598	0.0743	0.0329	0.0533
	β	0.717	0.699	0.669	0.747	0.742	0.688
$f=\phi Re^{\varphi}$	ϕ	2.02	1.07	0.53	2.05	0.63	1.64
	φ	−0.22	−0.40	−0.31	−0.22	−0.33	−0.45

"side-in-side-out" inlet-outlet flow manner has better comprehensive performance than that with "middle-in-middle-out" flow manner.

(2) The heat transfer rates and friction factors correlated by means of the genetic algorithm are quite close to the experimental data. It is beneficial to use the genetic algorithm to correlate and predict performances for complicated problems. The predicted correlations for heat transfer and flow performance in the shell sides may be used in engineering application and comprehensive study.

Acknowledgment

This work was supported by the NSFC Fund for Creative Research Groups (Grant No. 50521604) and National Defense Science and Technology Key Laboratory Foundations of China (Grant No. 51482100204JW0801). The authors also greatly appreciates Professor Hiroyuki Ozoe, a foreign expert at Xi'an Jiaotong University, for his efforts on the improvement of English writing in this article.

Nomenclature

A = area, m^2
B = pitch of baffles, m
C_f, C_Q = constant of fitness
c_p = specific heat at constant pressure, J/(kg K)
d_i = inside diameter of tube, m
d_o = outside diameter of tube, m
d_s = Diameter of shell, m
Fit = fitness
f^e = experimental friction factor
f^p = predicted friction factor by genetic algorithm (GA)
k = thermal conductivity, W/(m K)
m = mass flow rate, kg/s
h = heat transfer coefficient of STHX, $W/(m^2 K)$
l = length of tube, m
L = effective length of heat exchanger, m
M = number of experimental datapoints
N = number of tubes
Nu^e = experimental Nusselt number
Nu^p = predicted Nusselt number by GA
Pr = Prandtl number
Pop = size of population
Q = heat transfer rate, W
Q^e = experimental heat transfer rate, W
Q^p = predicted heat transfer rate, W
R = fouling resistance, $(m^2 K)/W$
R_f = predicted factor for friction factors
R_Q = predicted factor for heat transfer rates
Re = Reynolds number
S = distance between two centers of tube
T = evolution generation
U = total heat transfer coefficient, $W/(m^2 K)$
u_{max} = maximum velocity at minimum free flow area, m/s
v = volume fallow rate, m^3/s

Greek Symbols

α, β = constants of heat transfer correlation
ϕ, φ = constants of friction factor correlation
ρ = fluid density, kg/m^3
μ = dynamic viscosity, Pa s
ΔP = pressure drop in shell side, Pa
Δt_m = logarithmic-mean temperature difference, K

Subscripts

1 = Inlet
2 = Outlet
o = Oil side,
w = Water side
wall = tube wall

References

[1] Krai, D., Stehlik, P., Van der Ploeg, H. J., and Master, B. I., 1996, "Helical Baffles in Shell-and-Tube Heat Exchangers, Part I: Experimental Verification," Heat Transfer Eng., **17**, pp. 93–101.
[2] Peng, B. T., 2005, "Experimental Study of Heat Transfer and Pressure Drop for Shell-and-Tube Heat Exchangers With Continuous Helical Baffles," Master's thesis, Department of Energy and Power Engineering, Xi'an Jiaotong University (in Chinese).
[3] Reppich, M., and Zagermann, S., 1995, "A New Design Method For Segmentally Baffled Heat Exchangers," Comput. Chem. Eng., **19**, pp. 37–142.
[4] Wang, Q. W., 2004, "Current Status and Development of Shell-Side Heat Transfer Enhancement of Shell-and-Tube Heat Exchangers With Helical Baffles," Journal of Xi'an Jiaotong University, **38**, pp. 881–886 (in Chinese).
[5] Wang, Q. W., Luo, L. Q., Zeng, M., and Tao, W. Q., 2005, "Shell-Side Heat Transfer and Pressure Drop of Shell-and-Tube Heat Exchangers With Overlap Helical Baffles," Journal of Chemical Industry and Engineering (China), **56**, pp. 598–601 (in Chinese).
[6] Xie, G. N., Peng, B. T., Chen, Q. Y., Wang, Q. W., Luo, L. Q., Huang, Y. P., and Xiao, Z. J., 2006, "Experimental Study and Prediction of Pressure Drop and Heat Transfer in Shell-Side of Tube-and-Shell Heat Exchangers," Proc. Chin. Soc. Electr. Eng., **26**(21), pp. 104–108 (in Chinese).
[7] Bell, K. J., 2004, "Heat Exchanger Design for the Process Industries," ASME J. Heat Transfer, **126**(6), pp. 877–885.
[8] Li, H. D., and Kottke, V., 1998, "Effect of the Leakage on Pressure Drop and Local Heat Transfer in Shell-and Tube Heat Exchangers for Staggered Tube Arrangement," Int. J. Heat Mass Transfer, **41**, pp. 425–433.
[9] Naim, A., and Bar-Cohen, A., 1996, *A New Developments in Heat Exchangers*, Gordon and Breach Publishers, Amsterdam, pp. 467–499.
[10] Sen, M., and Yang, K. T., 2000, "Applications of Artificial Neural Networks and Genetic Algorithms in Thermal Engineering," in: *The CRC Handbook of Thermal Engineering*, F. Kreith, eds., CRC Press, Boca Raton, FL, pp. 620–661.
[11] Pacheco-Vega, A., Sen, M. Yang, K. T., and McClain, R. L., 1998, "Genetic Algorithms-Based Predictions of Fin-Tube Heat Exchanger Performance," *Proceedings of 11th International Heat Transfer Conference*, Kyongju, Korea, August 23–28.
[12] Ozkol, I., and Komurgoz, G., 2005, "Determination of the Optimum Geometry of the Heat Exchanger Body via a Genetic Algorithm," Numer. Heat Transfer, Part A, **48**, pp. 283–296.
[13] Xie, G. N., and Wang, Q. W., 2006, "Geometrical Optimization of Plate-Fin Heat Exchanger Using Genetic Algorithms," Proc. Chin. Soc. Electr. Eng., **26**(7), pp. 53–57 (in Chinese).
[14] Mishra, M., Das, P. K., and Sarangi, S., 2004, "Optimum Design of Crossflow Plate-Fin Heat Exchangers through Genetic Algorithm," International Journal of Heat Exchangers, **5**, pp. 379–401.
[15] Selbas, R., Kizilkan, O., and Reppich, M., 2006, "A New Design Approach for

Shell-and-Tube Heat Exchangers Using Genetic Algorithms From Economic Point of View," Chem. Eng. Process., **45**, pp. 268–275.
[16] Liang, H. X., Xie, G. N., Zeng, M., Wang, Q. W., and Feng, Z. P., 2005, "Application Genetic Algorithm to Optimization Recuperator in Micro-Turbine," *The 2nd International Symposium on Thermal Science and Engineering*, Beijing, China, October 23–25.
[17] Liang, H. X., Xie, G. N., Zeng, M., Wang, Q. W., and Feng, Z. P., 2006, "Genetic Algorithm Optimization for Primary Surfaces Recuperator of Microturbine," *Proceedings of GT2006, ASME Turbo Expo*, Barcelona, Spain, Paper No. GT 2006-90366, May 8–11, 2006.
[18] Pacheco-Vega, A., Sen, M., Yang, K. T., and McClain, R. L., 2001, "Correlations of Fin-Tube Heat Exchanger Performance Data Using Genetic Algorithms Simulated Annealing and Interval Methods," *Proceedings of ASME the Heat Transfer Division*, New York, November 11–16.
[19] Pacheco-Vega, A., Sen, M., and Yang, K. T., 2003, "Simultaneous Determination of In- and Over-Tube Heat Transfer Correlations in Heat Exchangers by Global Regression," Int. J. Heat Mass Transfer, **46**, pp. 1029–1040.
[20] Deiveegan, M., Balaji, C., and Venkateshan, S. P., 2006, "Comparison of Various Methods for Simultaneous Retrieval of Surface Emissivities and Gas Properties in Gray Participating Media," ASME J. Heat Transfer, **128**, pp. 829–837.
[21] Chen, Y. F., Li, D. Y., Lukes, J. R., and Majumdar, A, 2005, "Monte Carlo Simulation of Silicon Nanowire Thermal Conductivity," ASME J. Heat Transfer, **127**, pp. 1129–1137.
[22] Gnielinski, V., 1976, "New Equations for Heat and Mass Transfer in Turbulent Pipe and Channel Flows," Indian Chem. Eng., **16**, pp. 359–368.
[23] Goldberg, D. E., 1989, *Genetic Algorithms in Search, Optimization and Machine Learning*, Addison-Wesley Publishing Company Inc., Reading, MA.
[24] Michalewicz, Z., and Fogel, D. B., 2000, *How to Solve it: Modern Heuristics*, Springer, New York.
[25] Carroll, D. L., 1996, "Chemical Laser Modeling With Genetic Algorithms," AIAA J., **34**, pp. 338–346.
[26] Carroll, D. L., 1996, "Genetic Algorithms and Optimizing Chemical Oxygen-Iodine Lasers," Developments in Theoretical and Applied Mechanics, H. Wilson et al., eds., School of Engineering, The University of Alabama, Vol. XVIII, pp. 411–424.
[27] Michalewicz, Z., Deb, K., Schmidt, M., and Stidsen, T, 2000, "Test-Case Generator for Constrained Parameter Optimization Techniques," IEEE Trans. Evol. Comput., **4**, pp. 197–215.
[28] Pacheco-Vega, A., Diaz, G, Sen, M., Yang, K. T., and McClain, R. L., 2001, "Heat Rate Predictions in Humid Air-Water Heat Exchangers Using Correlations and Neural Networks," ASME J. Heat Transfer, **123**, pp. 348–354.
[29] Xie, G. N., Wang, Q. W., Zeng, M., and Luo, L. Q., 2007, "Heat Transfer Analysis for Shell-and-Tube Heat Exchangers With Experimental Data by Artificial Neural Networks Approach," Appl. Therm. Eng., **27**, pp. 1096–1104.

Journal of Heat Transfer

Technical Briefs

Performance Evaluation of a Compartmented Cooling Coil Using the Monte Carlo Simulation Approach

Uma Maheswaran
Department of Architecture,
National University of Singapore,
Singapore 117566

S. C. Sekhar
Department of Building,
National University of Singapore,
Singapore 117566

A compartmented cooling coil is a single undivided coil section located in an intermediate point between the upstream and downstream sections of the air handling unit. A thermally insulated metal barrier is provided for the separation of two different air streams that are conditioned through the coil. The coolant flow through the heat exchanger is such that both the air streams encounter each pass of the coolant feed. This paper aims to address the performance of a compartmented coil through the concept of fin efficiency. The compartmented coil geometry involves two distinct sets of air-side characteristics coupled with one set of coolant-side characteristics and it is practically difficult to obtain the values of fin efficiency through empirical measurements alone over a wide range of operating conditions. Hence, the conventional methods of evaluation resort to numerical models for predicting fin performance. The paper questions the validity of certain fundamental assumptions based on which conventional models have been formulated to obtain the local heat transfer coefficient values. A simplified numerical model is formulated and evaluated using a Monte Carlo simulation approach. Performance curves across all ranges of input values are presented and empirical results are used to validate these curves at intermediate values. Results show that air face velocity and surface temperature at a given point on the fin has significant impact on the heat transfer coefficient. It is also shown that for a given fin height of 9.5 mm*, the assumption of an average heat transfer coefficient as calculated from the LMTD method could vary significantly up to 10% from the predicted results.* [DOI: 10.1115/1.2740662]

Keywords: compartmented cooling coil, fin efficiency, Monte Carlo simulation, numerical model

Introduction

Performance of cooling and dehumidifying coils is the key factor underlying the design of a typical air handling unit. A number of performance evaluation criteria including fin efficiency [1], fin resistance number [2], enhancement factor [3], augmentation factor [4], energy index [5] and many others have been developed through past research works. However, it is seen that the concept of "fin efficiency" is the widely accepted performance index. Although past research efforts have formulated expressions for calculating dry and wet fin efficiencies, there is scope to refine the concept because of the underlying assumptions in such formulations by Gardner [1], McQuiston [6], Huang and Shah [7]. It has been shown that the deviations of the actual fin efficiency from the predicted values, when such violations are considered, ranges from 3% to 50% depending on the assumption violated [8] which becomes even more significant in a compartmented cooling coil [9]. This shows the need for a more comprehensive formulation for fin efficiency. Earlier research works have identified that a variable heat transfer coefficient could result in very high deviations in the range of 3–40% in the computed fin efficiency values [10]. Extensive studies have been made on the variability of heat transfer coefficient on the fin surface and studies including works of Mokheimer [10], Kundu and Das [11], Jambunathan et al. [12], Ma et al. [13], Barrow [14], and Brian and Wells [15] show that there is a significant variation in the overall fin performance when the assumption of a constant heat transfer coefficient is violated. However, the models proposed by individual research attempts adopt an assumed variation to the coefficient values across the fin surface. A linear variation in the heat transfer coefficient has been assumed in the years 1951, 1963 and 1970 (Ghai [16], Migai [17], Thomas and Hayes [18]). However, it is seen that between these years, a number of other variations including power law variations, temperature and other parameter dependent variations and others have been attempted. A power law variation with no variation was attempted in 1960 (Han and Lefkowitz [19]) and a refined model of the same was adopted by Unal [20] in 1985. There seems to be a wide controversy in the variation pattern of the heat transfer coefficient. However, certain parameters that affect the h-value have been established in this process. In 1951, Ghai proposed measurement of surface temperature on a small fin surface using thermocouples to obtain the variability of the heat transfer coefficient over the region. However, the usage of thermocouples makes the accuracy of the measurement questionable and the measurement was done on a scaled fin type. However, there have been no further attempts in the available literature that uses surface temperature measurement as a technique to evaluate heat transfer coefficient. This paper uses the method of surface temperature measurement on an actual compartmented coil at the 12 points shown in Fig. 1, in conjunction with the other parameters as identified from previous studies to obtain a model for the heat transfer coefficients. In addition, this is achieved separately across the fresh air and the recirculated air sides of a compartmented coil.

Contributed by the Heat Transfer Division of ASME for publication in the JOURNAL OF HEAT TRANSFER. Manuscript received May 17, 2005; final manuscript received October 25, 2006. Review conducted by Louis C. Burmeister.

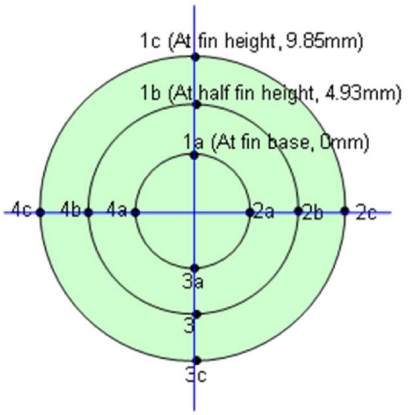

Fig. 1 Layout of the points of surface temperature measurement on the fin

Monte Carlo Simulation

Quantitative knowledge of random and systematic uncertainty represents a measure of the state of information available for a given set of experimental data or observable parameters and Monte Carlo simulation (MCS) method can be used to evaluate interdependent parameters involved in an experiment. Uncertainties that are detected by repeating measuring procedures under the same conditions are called random errors. The experimental data used for the presented simulation are obtained during steady state periods and this minimizes the random errors. On the other hand, the errors that are not revealed in this way are called systematic errors (constant bias). In order to remove systematic errors, the calibration of all the instruments was done to a predetermined accuracy level. The sensitivity of each of the input variables on the overall results was quantified using MCS and a stepwise addition or removal of variables during a model formulation was attempted. It is necessary that the formulation of any model is rigorous in methodology and one of the necessary criteria for evaluation of the rigor of the model is to ensure that the model was not formulated on assumptions based on the strictly given condition. MCS helped in nullifying this assumption as there is an inherent element of randomness in generating the results and hence a repetition of the simulation and use of an exhaustive range would validate the model obtained over all possible combinations. The simplicity of use and the rigor the tool provides in testing and formulating models renders it ideal to explain a complex physical phenomenon like heat and mass transfer in cooling coil. MCS has been used earlier to study the sensitivity and uncertainty of heat exchanger designs to physical properties estimation [21]. MCS has also been used to validate existing conceptual models on fin efficiency and a reasonable convergence of results with past research works was observed [8]. In the current study, MCS was used to generate random possible combinations across these input variables within the range of input variables as shown in Table 1.

Results and Discussion

MCS was used to obtain the curve profiles of dry and wet fin efficiencies for a range of air side convective heat transfer coefficient. The results shown in Fig. 2 clearly show that an increase in the heat transfer coefficient causes the fin efficiency to decrease. It is also shown that the effect varies with different fin heights and fin thicknesses. The curves shown are for a particular thickness of 0.6 mm which is close to that of the fin used in the experiments. It is seen that at lower fin heights of up to 8 mm, a variation of the heat transfer coefficient of almost three times has an insignificant variation in the range of only 0.03–3.71% on both the dry and wet fin efficiencies (Table 2). However, when the fin height increases to 24 mm which is quite common in high fins category, the variation has a steeper slope with a difference of up to 11.58% in the dry fins and 20.99% in the wet fins. Table 3 clearly shows that the average difference between the dry and wet fin efficiency is also varying across fin height and fin thicknesses apart from the inlet relative humidity and it is higher at smaller thickness values of around 0.2–0.4 mm. The maximum difference between the dry and wet fin efficiencies resulting from the analysis is 19% and the

Table 1 Input variables used for MCS

Input parameters	Values
Fin length perpendicular to direction of tubes, L_f	320 mm
Fin depth in direction of air flow, L_d	32.9 mm
Finned tube length, L_t	297 mm
Fin thickness, Y_f	0.7 mm
Fin thermal conductivity, k_f	221 W/m K
Length of the external collar, L_c	3.175 mm
Fin height, b	9.850 mm
Fin spacing (for 9 fins/in.)	3.175 mm
Tube outside diameter, D_o	16.85 mm
Total number of tubes in the coil, N_t	9 nos.
Number of holes in the plate fins, N_h	9 nos.
Number of fins in net finned tube length, N_{fT}	9 nos.
Flow Rate of Air, a	Fresh air: 349–688 cm h Recirculated air: 701–1129 cm h
Density of air, ρ	Fresh air: 1.164–1.170 kg/m^3 Recirculated air: 1.178–1.180 kg/m^3
Entering air dry bulb temperature, t_1	Fresh air: 28.6–30.2°C Recirculated air: 26.0–26.6°C
Leaving air dry bulb temperature, t_2	Fresh air: 22.9–25.0°C Recirculated air: 21.2–22.6°C
Coil surface temperature at air entry, t_{s1}	Fresh air: 10.33–19.05°C Recirculated air: 9.84–17.31°C
Coil surface temperature at air exit, t_{s2}	Fresh air: 10.33–19.05°C Recirculated air: 9.84–17.31°C
Coil base temperature at air entry, t_{s1}	Fresh air: 9.73–13.27°C Recirculated air: 9.27–13.25°C
Coil base temperature at air exit, t_{s2}	Fresh air: 9.73–13.27°C Recirculated air: 9.27–13.25°C
Air humid specific heat, c_p	1018 J/(kg K)

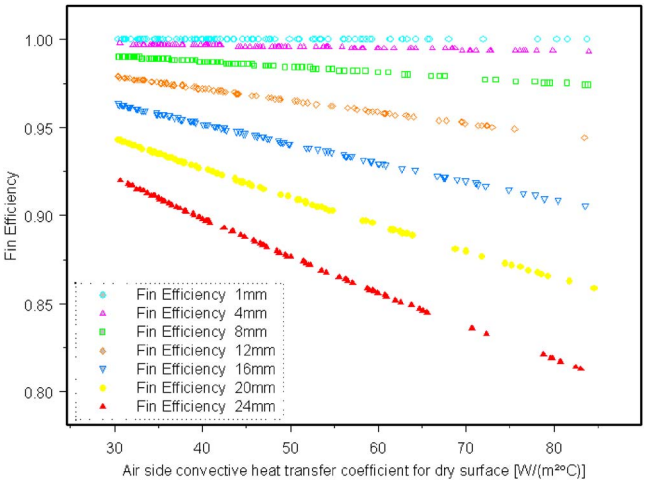

Fig. 2 Heat transfer coefficient versus dry fin efficiency for a fin thickness of 0.6 mm

Table 2 Maximum variation of wet fin efficiency with varying heat transfer coefficient

Fin thickness (mm)	Fin height (mm)						
	1	4	8	12	16	20	24
0.2	0.18%	2.75%	8.92%	18.21%	24.31%	28.10%	33.18%
0.3	0.12%	1.89%	7.05%	12.30%	18.93%	23.25%	27.03%
0.4	0.09%	1.35%	5.02%	10.20%	16.71%	20.96%	25.01%
0.5	0.08%	1.13%	3.94%	8.73%	13.17%	17.09%	20.54%
0.6	0.06%	0.97%	3.71%	7.23%	11.27%	15.82%	20.99%

Table 3 Average percentage variation between dry and wet fin efficiency

Fin thickness (mm)	Fin height (mm)						
	1	4	8	12	16	20	24
0.2	0.08%	1.22%	4.87%	7.87%	13.15%	15.19%	19.09%
0.3	0.05%	0.85%	3.14%	5.89%	10.35%	14.25%	16.78%
0.4	0.04%	0.63%	2.19%	5.02%	7.97%	11.36%	12.60%
0.5	0.03%	0.43%	2.00%	4.14%	6.83%	9.64%	11.61%
0.6	0.03%	0.41%	1.64%	3.89%	5.34%	8.88%	10.85%

value is far above the 12% as suggested by McQuiston [6]. An advanced sensitivity analysis was done on the data and it was found that the sensitivity of change to heat transfer coefficient was the highest (0.3% change for every 1% change in h-value) at the smallest thickness (0.2 mm) and the greatest fin height (24 mm) and the results showed consistent pattern as seen in Table 4.

Log mean temperature difference method (LMTD method) identifies the geometry of the coil, inlet air Dry Bulb Temperature (DBT), outlet air DBT, fin surface temperature at the entry and the exit as well as the sensible heat capacity as functions underlying the computation of h-value. Values of the heat transfer coefficient were computed from the values obtained from the random combinations of the input variables (Table 1) and the impact of every variable on the resulting heat transfer coefficient was studied separately. Results obtained from experiments were used to verify the predictions made. Figures 3–6 clearly show the nonlinear nature of the input variables on the heat transfer coefficient. The data was then subjected to a nonlinear regression model in order to obtain the local heat transfer coefficient values with refined input parameters namely the inlet air DBT, outlet air DBT, surface temperature at a given point and the air flow rate across the compartment. Fin base temperature is used to nondimensionalize the temperature values. On the fresh air side:

$$h = 0.0223a^{1.144}\left(\frac{t_1 - t_s}{t_b}\right)^{1.718}\left(\frac{t_2 - t_s}{t_b}\right)^{-1.359} \quad (1)$$

Table 4 Advanced sensitivity analysis for a fin thickness of 0.6 mm

Fin Height	Change of fin efficiency at every 1% change of f_{aD}	Significance
1	−0.000003	−0.0003%
4	−0.000046	−0.0046%
8	−0.000177	−0.0180%
12	−0.000378	−0.0393%
16	−0.000624	−0.0670%
20	−0.000892	−0.0993%
24	−0.001158	−0.1345%

f_{aD}=local heat transfer coefficient of a dry fin

On the recirculated air side:

$$h = 0.1466a^{0.849}\left(\frac{t_1 - t_s}{t_b}\right)^{1.657}\left(\frac{t_2 - t_s}{t_b}\right)^{-1.468} \quad (2)$$

where h=local heat transfer coefficient at a given point on the fin ($W/m^2 K$), a=face velocity across the compartment (m/s), t_1=inlet air DBT (K), t_2=outlet air DBT (K), t_s=fin surface temperature at the given point (K), and t_b=average fin base temperature (K).

Local values of the heat transfer coefficient were obtained (Table 5) at different points from the above formula separately for the fresh air side and the recirculated air side based on experimental conditions and the average was computed. This average was then compared with that obtained from the LMTD method and the error (Table 6) was found to be in the similar uncertainty range as seen from Table 2 for the given fin thickness of 0.6 mm and a fin height of 9.58 mm (±5%). The fin efficiency values at these different points are computed using the model and it was found that the values were very close to that at the base even when the heat transfer coefficient was doubled. This confirms the previous results obtained in Tables 2 and 3 as the height of the fin used in the

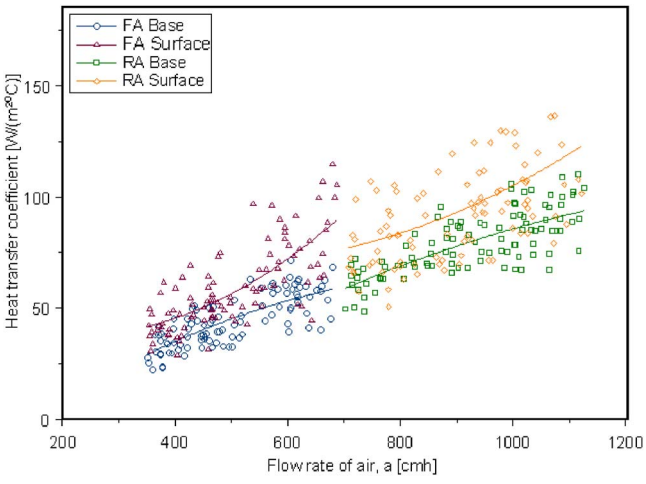

Fig. 3 Airflow rate versus heat transfer coefficient

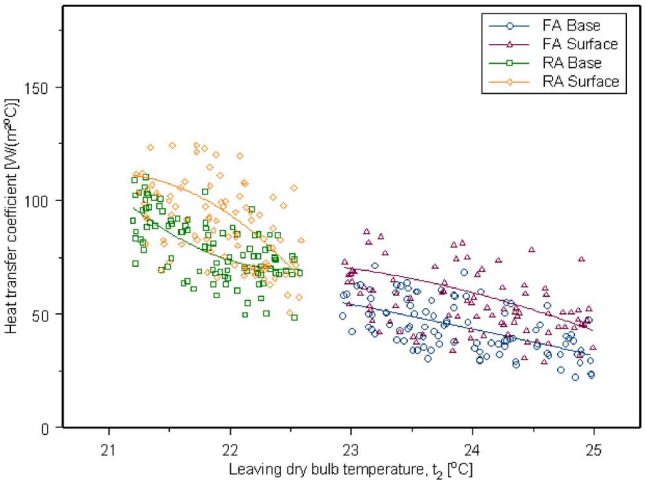

Fig. 4 Outlet dry bulb temperature versus heat transfer coefficient

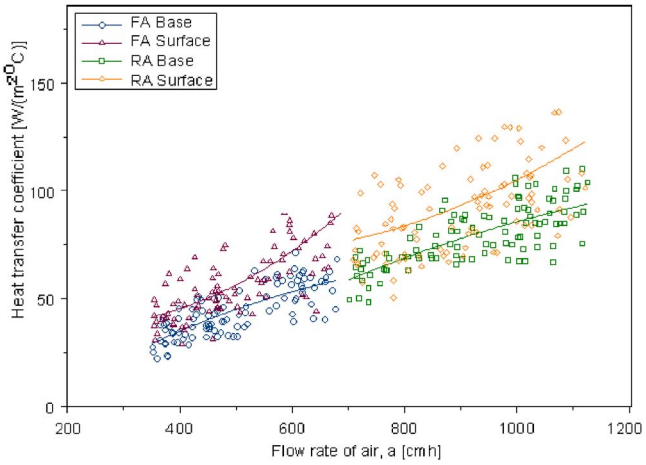

Fig. 5 Fin surface temperature at entry versus heat transfer coefficient

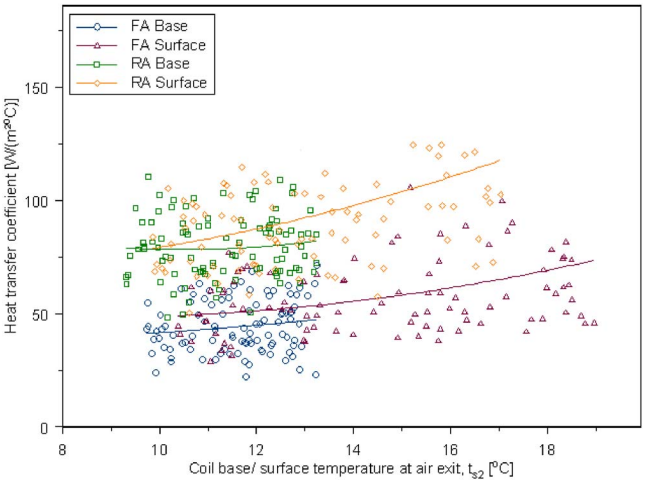

Fig. 6 Fin surface temperature at exit versus heat transfer coefficient

Table 5 Sample values of local heat transfer coefficient at different points on the fin surface

Points	h–fresh air (FE)	h–return air (RE)
1b	41.9063	89.360
1c	42.551	91.959
2b	39.743	76.922
2c	40.463	79.039
3b	40.695	83.626
3c	41.196	83.626
4b	42.383	89.360
4c	45.532	91.959

experiment was only 9.85 mm. For that particular height, it was seen that the variation in the heat transfer coefficient is likely to vary the fin efficiency by a maximum of 5% and it was also noticed that the difference between dry and the wet fin efficiency for this particular fin geometry is 2.4%, which is negligible when computed in terms of actual fin efficiency. This validates the results obtained from the model. However, it is to be noted that for high fins which are more widely used in the industry, the difference resulting from adopting bulk design parameters could be significant and this may lead to a nonoptimal design of the coil. It is also evident for the given fin that fresh air side on which the control on the entering conditions is less has a higher error band than the recirculated air side. Hence it is evident that dealing with the two air streams separately could be beneficial to the designers for optimizing the performance of each of these air streams. Results also clearly show that the level of uncertainty in the results obtained by LMTD method and the model increases with increase in the air flow rate (face velocity) (Table 6) and this clearly elucidates the fact that at higher face velocities, the use of bulk values to design may result in larger errors. Earlier works on the impact of face velocities on the heat transfer coefficient by Saboya and Sparrow [22] is reinforced by the results and the need to consider local variation of the h-value is established clearly from different perspectives.

Conclusion

This study clearly shows that heat transfer coefficient is one of the most important factors that affect the performance of a cooling and dehumidifying coil. The classical assumption of a constant heat transfer coefficient could lead to a totally under predicted design of the system especially under conditions where high fins with less thickness are used. A model has been formulated to obtain the local values of the heat transfer coefficient and the values are used in the Gardner's formulation to obtain the corresponding fin efficiency across the two compartments at various points. This method overcomes the inadequacy in the previous literature where only the mean values of both the heat transfer coefficient as well as the fin efficiency were obtained for design purposes. In the case of high fins, this method could be of great significance as the method shows clearly a deviation of more than 20% in the computed values of fin efficiency when the fin is about 24 mm high. Hence, it is evident that the use of the formulations discussed above to obtain the local values of the heat transfer coefficient and in turn the computed average could provide a better solution over the conventional method of using bulk values for the design of the compartmented coil.

Table 6 Error analysis for the output obtained from the model against experimental results on the fresh air side (end fin)

Input variables (FA end fin)		Experiment 1	2	3	4
a—air flow rate (cmh)		349	437	547	688
t_1—entering DBT of air (°C)		27.5	28.9	29.7	30.0
t_2—leaving DBT of air (°C)		21.4	22.7	23.5	24.4
t_s—surface temperature (°C)		Surface temperature at a given point on the fin surface			
t_b–fin base temperature		10.2	10.5	10.8	11.4
h-value	LMTD method	43.419	51.113	62.231	72.815
h-value	Proposed model	41.809	52.608	66.533	79.595
Error percentage	$[(\text{LMTD-model})/\text{LMTD}]^2 \times 100$	3.7%	−2.9%	−6.9%	−9.3%

Acknowledgment

The financial assistance of the National University of Singapore in the form of Research Grant No. RP 296-000-076-112 is gratefully acknowledged.

References

[1] Gardner, K. A., 1945, "Efficiency of Extended surfaces," Trans. ASME, **67**, pp. 621–631.

[2] Rich, D. G., 1966, "The Efficiency and Thermal Resistance of Annular and Rectangular Fins," *Proceedings of the 3rd International Heat Transfer Conference*, Chicago, Vol. 3, p. 281.

[3] Manzoor, M., 1984, *Heat Flow Through Extended Surface Heat Exchangers* Springer, Berlin.

[4] Stones, P. R., 1980, Ph.D. thesis, University of Leeds.

[5] Hassan, A., and Siren, K., 2003, "Performance Investigation of Plain and Finned Tube Evaporatively Cooled Heat Exchangers," Appl. Therm. Eng., **23**, pp. 325–340.

[6] McQuiston, F. C., 1975, "Fin Efficiency with Combined Heat and Mass Transfer," ASHRAE Trans., **81**(1), p. 350.

[7] Huang, L. J., and Shah, R. K., 1992, "Assessment of Calculation Methods for Efficiency of Straight Fins of Rectangular Profile," Int. J. Heat Fluid Flow, **13**, pp. 282–293.

[8] Uma Maheswaran, C., R., and Sekhar, S. C., 2006, "Evaluation of Concepts of Fin Efficiency Using Monte Carlo Simulation Method," Int. J. Heat Mass Transfer, **49**(9), pp. 1643–1646.

[9] Sekhar, S. C., Uma Maheswaran, C., R., Tham, K. W., and Cheong, K. W., 2004, "Development of Energy Efficient Single Coil Twin Fan Air-conditioning System with Zonal Ventilation Control," ASHRAE Trans., **110**, Part 2, pp. 204–217.

[10] Mokheimer, E. M. A., 2002, "Performance of annular fins with different profiles subject to variable heat transfer coefficient," Int. J. Heat Mass Transfer, **45**, pp. 3631–3642.

[11] Kundu, B., and Das, P. K., 2002, "Performance Analysis and Optimization of Straight Taper Fins with Variable Heat Transfer Coefficient," Int. J. Heat Mass Transfer, **45**, pp. 4739–4751.

[12] Jambunathan, K., Hartle, S., Frost, A., and Fontama, V. N., 1996, "Evaluating Convective Heat Transfer Coefficients Using Neural Networks," Int. J. Heat Mass Transfer, **39**(11), pp. 2329–2332.

[13] Ma, S. W., Bebhahani, A. I., and Tsuei, Y. G., 1991, "Two Dimensional Rectangular Fin with Variable Heat Transfer Coefficient," Int. J. Heat Mass Transfer, **34**, pp. 79.

[14] Barrow, H., 1986, "Theoretical Solution for the Temperature in a Straight Fin with Variable Surface Heat Transfer Coefficient," J. Heat Recovery Syst., **6**(6), pp. 465–468.

[15] Brian, V., and Wells, R. G., 1986, "Laminar Flow with an Axially Varying Heat Transfer Coefficient," Int. J. Heat Mass Transfer, **29**(12), pp. 1881–1889.

[16] Ghai, M. L., 1951, "Heat Transfer in Straight Fins," *Proceedings of the General Discussion of Heat Transfer*, Institute of Mechanical Engineers, London, p. 180.

[17] Migai, V. K., 1963, "Effect of Non-uniform Heat Transfer Over the Height of a Fin on its Efficiency," Inzh.-Fiz. Zh., **6**(3), p. 51.

[18] Thomas, D. G., and Hayes, P. H., 1970, "High Performance Heat Transfer Surfaces," Ind. Eng. Chem., **62**(2), p. 4.

[19] Han, L. S., and Lefkowitz, S. G., 1960, "Constant Cross Section Fin Efficiencies for Non-uniform Surface Heat Transfer Coefficients," ASME Paper 60-WA-41, American Society of Mechanical Engineers, New York.

[20] Unal, H. C., 1985, "Determination of the Temperature Distribution in an Extended Surface with a Non Uniform Heat Transfer Coefficient," Int. J. Heat Mass Transfer, **28**(12), p. 2279.

[21] Clarke, D. D., Vasquez, V. R., Whiting, W. B., Greiner, M., 2001, "Sensitivity and Uncertainty Analysis of Heat Exchanger Designs to Physical Properties Estimation," Soryushiron Kenkyu **21** pp. 993–1017.

[22] Saboya, F. E. M., and Sparrow, E. M., 1974, "Local and Average Heat Transfer Coefficients for One-Row Plate Fin and Tube Heat Exchanger Configurations," ASME J. Heat Transfer, **96**, p. 265.

Characteristics of the Hydrodynamic Coefficient for Flow of a Steam-Water Mixture in a Pebble Bed

Alexandr A. Avdeev[1]
All-Russia Nuclear-Power Machine Building Research and Development Institute (VNIIAM),
125171 Moscow, Russia
e-mail: aaa@vniiam.ru

Boris F. Balunov

Rostislav A. Rybin

Polzunov Scientific & Development Association on Research and Design of Power Equipment (NPO CKTI),
191167, St. Petersburg, Russia

Ruslan I. Soviev

Yuri B. Zudin

All-Russia Nuclear-Power Machine Building Research and Development Institute (VNIIAM),
125171 Moscow, Russia

*Pressure loss for flow of a steam-water mixture in a pebble bed is experimentally investigated (the first stage of the study was described in Avdeev, et al., 2003 [High Temp., **41**, pp. 371–383]). The measurements of the care performed within the wide range of regime parameters: pressures of* 0.9–15.6 MPa*, mass-flow rates of* 107–770 kg/(m^2 s) *and steam quality of 0–0.49. The experimental data for the pressure loss of single-phase air and water flows were used as reference data. The final results are represented in the form of the ratio of the pressure loss for the steam-water flow to that for the single-phase water flow at identical mass-flow rates.* [DOI: 10.1115/1.2712862]

Keywords: steam-water mixture, pebble bed, hydrodynamic coefficient

Introduction

Studies of pressure loss of single-phase flows due to the hydrodynamical drag in a fixed pebble bed have been carried out as early as the 1930s [1]. The most well-known relationship for calculating the hydrodynamic coefficient is the Ergun equation [2]

$$\xi = A/\mathrm{Re} + B \tag{1}$$

adequate in the entire variation range of Reynolds numbers [3]. To approximate available experimental data in the region $\mathrm{Re} > 100$, the dependences of the form [4]

$$\xi = C/\mathrm{Re}^n \tag{2}$$

are also applicable. In (2), $n \approx 0.2$, and the coefficients A, B, C depend on the porosity m of a granular layer.

The use of modern measurement techniques, in particular, laser Doppler anemometry [5] and the magnetic-resonance method [6] has implied the existence of non-single-dimensional features of flow in a pebble bed (longitudinal and transversal anisotropy of the velocity field and spatial-periodic flows between adjacent pebbles). In spite of these facts, the critical analysis performed in [7,8] has shown that simple equations (1) and (2) describe available experimental data related to the pressure loss in a pebble bed not worse than results of numerical simulations based on the two-dimensional approach.

A number of studies are devoted to the problem of the frictional pressure loss of two-phase flows in a liquefied bed [9]. At the same time, analogous experimental data for a fixed bed are virtually absent. In the present paper continuing our publication [10], we describe the results of the experimental investigation of the hydrodynamic coefficient for single-phase (air, water) and two-phase (steam-water mixture) flows in a pebble bed within a wide variation range of pressures, mass-flow rates, and mass steam quality.

The Experimental Setup

In our experiment, the motion of the working medium (turbine condensate) occurred along a closed contour at a pressure of 32 MPa and temperature of 550°C. The circulation was realized using a pump (with the maximum capacity of 25 m^3/h and the hydraulic head of 5 MPa), the pump capacity being controlled by the number of motor revolutions. The desired values of both the water temperature and flow steam quality at the input to the working section of the experimental setup were provided by preliminary activated 360-kW and 65-kW electric heaters. The sketch of the measurement section of the contour under consideration is shown in Fig. 1. The ranges of both the mass-flow rates and the steam qualities were significantly extended compared to the preceding study [10] (from 237 to 770 kg/(m^2 s) and from 0.24 to 0.48, respectively).

In the preceding study, lead shots of the average diameter $d = 2.033$ mm and consisting of 90% of lead and 10% of antimony were used in the pebble bed. By virtue of a possible strain of the shots when the temperature of the working medium approached the lead melting point, the pressure range under investigation was restricted by the value of 3.3 MPa. In the present study, we used polished pebbles made of stainless steel, which allowed us to carry out the experiments up to pressures of 15.6 MPa.

The mean pebble diameter ($d = 2.123$ mm) was determined as the mean value of diameters for 200 randomly chosen balls whose diameters were measured by a micrometer with the scale division of 0.005 mm. In Fig. 2, we present photographs of the pebbles for two indicated series of the experiment. As is clearly seen, the replacement of lead pebbles by stainless-steel ones (the present study) has allowed us to significantly improve the homogeneity of the pebble bed.

The pressures at different points of the contour were determined by manometers with the measurement ranges of 6 to 25 MPa. Electric differential pressure gauges with the measurement range of 10 to 400 kPa were employed as sensors of the pressure drop in both the working segment and flow-meter devices. The upper limit of the measurement ranges for these manometers was chosen in such a manner that the maximum relative error in the pressure-drop determination did not exceed ±1.5%. The error of temperature measurements by thermocouples was not worse than ±1 K.

Analysis of the Experimental Data

The mean porosity over the cross-sectional area (i.e., the volume fraction m of voids) in the pebble bed was determined by the volume-weight method and calculated using the relationship

[1]Corresponding author.

Contributed by the Heat Transfer Division of ASME for publication in the JOURNAL OF HEAT TRANSFER. Manuscript received November 10, 2005; final manuscript received July 25, 2006. Review conducted by Satish G. Kandlikar.

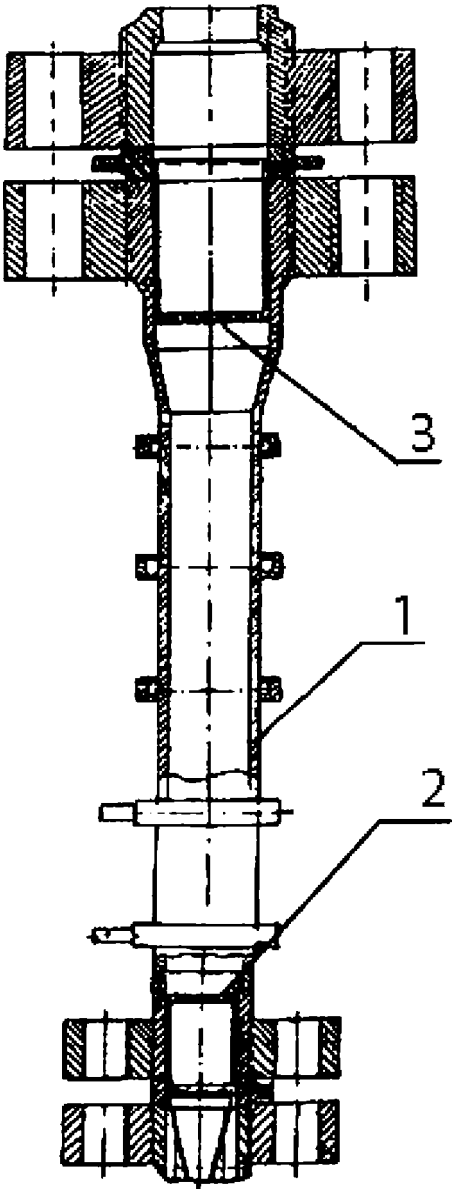

Fig. 1 Sketch of the measuring section: (1) working segment, (2) lower grid, and (3) upper grid

$$m = 1 - V/V_0 \tag{3}$$

where V_0 is the volume of the measuring vessel of the same diameter as the working section and V is the volume occupied by the pebbles. The measured value of the porosity was $m=0.392$. (in [10], $m=0.37$). Apparently, the difference in the measured porosity is explained by both the nonsphericity of lead pebbles and the spread of their size distribution. The coolant mass flow was determined on the basis of the measured pressure drop Δp at the measuring diaphragm of the flow area F and was calculated by the formula

$$G = \alpha F\sqrt{2\Delta p\rho}, \tag{4}$$

where α is the mass-flow coefficient and ρ is the density of fluid. The hydrodynamical-drag coefficient was calculated for the case of single-phase fluid flow of air and water in a pebble bed according to the relationship

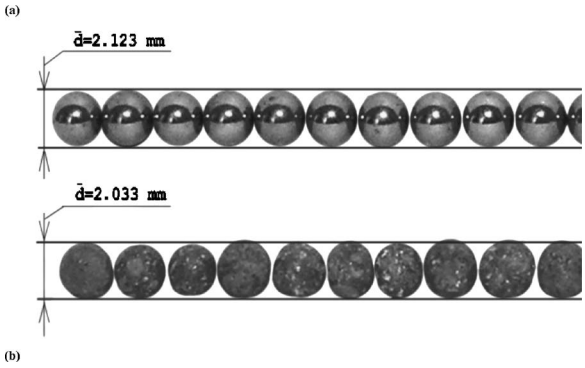

Fig. 2 Photographs of pebbles used in the pebble bed: (*a*) present study and (*b*) Avdeev et al. [10]

$$\xi = \frac{2\Delta p}{(\rho u^2)(H/\bar{d})} \tag{5}$$

For the single-phase medium, the Reynolds number was determined as

$$\mathrm{Re} = u\bar{d}/\nu \tag{6}$$

where ν is the kinematic viscosity. The mass-flow steam quality x at the input of the working segment was determined from the thermal balance by the measurement of the electric load and the thermal power of a preliminary activated heater with allowance for the heat transfer to the environment

$$x = \frac{1}{L}\left(\frac{N}{G} - c_p\Delta T\right) \tag{7}$$

To verify the validity of the thermal balance, each of the experimental series with the two-phase medium was preceded by experiments with water underheated to the saturation temperature. The heat loss from the electric-heater surface did not exceed 2% of the total electric power and was not taken into account in Eq. (7).

The Measurement Errors

The relative error in the determination of the volume $V_0 = (\pi d_0^2/4)H_0$ of the measuring vessel of diameter d_0 and height H_0, which was used to measure the porosity of the pebble bed, is

$$\frac{\delta V_0}{V_0} = 2\frac{\delta d_0}{d_0} + \frac{\delta H_0}{H_0} = 2\frac{0.1}{34} + \frac{0.5}{182} \approx 0.009$$

The relative error in the determination of the volume $V = \pi\bar{d}^3/6$ for a single ball of diameter $\bar{d}$ is

$$\frac{\delta V}{V} = 3\frac{\delta\bar{d}}{\bar{d}} = 3\frac{0.005}{2.123} \approx 0.007$$

From (3), it follows the formula for the absolute error of the porosity measurement:

$$\delta m = (1-m)\left(\frac{\delta V_0}{V_0} + \frac{\delta V}{V}\right) \approx 0.01$$

The relative maximum error of the porosity measurements is then $\delta m/m \approx 0.025$. In accordance with [4], the quantity C in Eq. (2) has the form of a power dependence: $C \sim m^{-(3\cdots4)}$. Therefore, the measurement error can result in a rather large inaccuracy of the determination of the quantity ξ, i.e., $\delta\xi/\xi = 4\,\delta m/m \approx 0.1$. It is worth noting that this calculated deviation corresponds to the systematic error. According to the results of an additional experiment, the relative error in the determination of the product αF was estimated to be 0.04. The relative error in the measurement of the pressure drop Δp was 0.015. With allowance for this fact, the

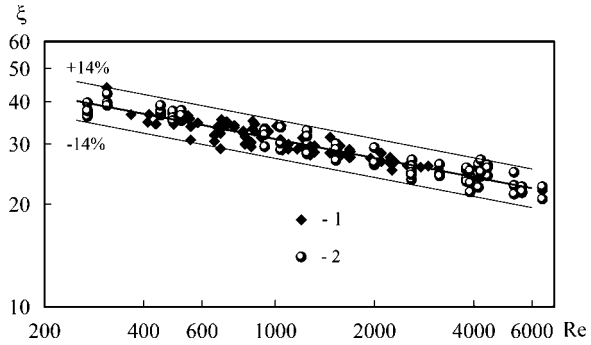

Fig. 3 Dependence of the hydrodynamic-drag coefficient on the Reynolds number for fluid flow in the pebble bed: (1) air and (2) water

maximum relative error in the mass-flow calculation according to formula (4) is

$$\frac{\delta G}{G} = \frac{\delta(\alpha F)}{\alpha F} + \frac{1}{2}\left(\frac{\delta \Delta p}{\Delta p} + \frac{\delta \rho}{\rho}\right) = 0.04 + \frac{1}{2}(0.015 + 0) \approx 0.05$$

It then follows from (6) that the maximum relative error in the determination of the Reynolds number is

$$\frac{\delta \mathrm{Re}}{\mathrm{Re}} = \frac{\delta u}{u} + \frac{\delta \bar{d}}{\bar{d}} + \frac{\delta \nu}{\nu} = 0.05 + \frac{0.005}{2.132} + 0 \approx 0.05$$

The maximum relative error in the determination of the hydrodynamic coefficient is

$$\frac{\delta \xi}{\xi} = \frac{\delta \Delta p}{\Delta p} + 2\frac{\delta u}{u} + \frac{\delta \rho}{\rho} + \frac{\delta H}{H} + \frac{\delta \bar{d}}{\bar{d}}$$

$$= 0.015 + 2 * 0.05 + 0 + \frac{0.5}{200} + \frac{0.005}{2.132}$$

$$\approx 0.12$$

Everywhere above, we calculated the maximum relative error in the determination of a certain quantity, which is rarely realized in practice. The calculation of the relative root-mean-square error (under the assumption on the absence of correlation dependence between the initial errors of the quantities entering into the calculation formula) yields considerably lesser values. In particular, the calculated root-mean-square error in the determination of the hydrodynamical-drag coefficient is

$$\sigma_\xi = \sqrt{\left(\frac{\delta \Delta p}{\Delta p}\right)^2 + 2\left(\frac{\delta j}{j}\right)^2 + \left(\frac{\delta \rho}{\rho}\right)^2 + \left(\frac{\delta H}{H}\right)^2 + \left(\frac{\delta \bar{d}}{\bar{d}}\right)^2} = 0.07$$

As is well known, in the use of the majority of measuring systems, the normal distribution law takes place for random errors. The confidence interval of these errors is determined from the condition that this interval contains 95% of all experimental points. In Fig. 3, the experimental data are presented in the coordinates $\xi = f(\mathrm{Re})$ for the case of single-phase fluid flows of air and water. Their statistical treatment leads to the following averaging dependence

$$\xi = \frac{112}{\mathrm{Re}^{0.186}} \tag{8}$$

In this case, 95% of the experimental points reside within the interval of ±14%, which coincides with the confidence interval of the standard error: $2\sigma_\xi = 0.14$. This is an argument in favor of the correct estimate of the error for the hydrodynamical-drag coefficient.

As was indicated above, the thermal-loss calculation yields $Q \leqslant 0.02N$. The relative errors in the determination of N and G are $\delta N/N = 0.03$, $\delta G/G = 0.05$, whereas the subcooling of fluid was measured with the absolute error $\delta \Delta T = 1$ K. For maximum studied values of x (practically, for $x \geqslant 0.3$), the first term in the right-hand side of (7) considerably exceeds the second term. Thus, in this case, we arrive at

$$\frac{\delta x}{x} \approx \frac{\delta N}{N} + \frac{\delta G}{G} = 0.08 \tag{9}$$

In the region of the steam qualities close to zero, the both terms in the right-hand side of (7) are approximately equal to each other: $N/G \approx c_p \Delta T$. Then, as $x \to 0$, we have

$$\delta x \approx \frac{c_p \Delta T}{L}\left(\frac{\delta N}{N} + \frac{\delta G}{G} + \frac{\delta(\Delta T)}{\Delta T}\right) \tag{10}$$

Thus, in the region of small x, the maximum absolute error in the determination of the steam quality increases with a decrease in the specific latent heat of evaporation (i.e., with increasing pressure), as well as with an increase in the subcooling of fluid at the heater input. The calculation based on formula (10) for the minimal studied steam qualities at a pressure $p = 14.6$–15.6 MPa yields $\delta x \approx 0.01$. For lower pressures, the error decreases and attains the value $\delta x \approx 0.005$ at $p = 2.0$–3.0 MPa. Therefore, for low steam qualities, the measurement error of the quantity x may be rather large, which should be taken into account in analysis of the experimental data obtained under these conditions.

Discussion of the Results

To reveal an effect of the steam quality, mass-flow rate, and pressure on the pressure loss of steam-water flow, the pressure loss was represented in the form of the ratio

$$\frac{\Delta p}{\Delta p_0} = f(x) \tag{11}$$

where Δp_0 is the pressure loss corresponding to the saturated-fluid flow at the same mass-flow rate (the quantity ξ_0 is calculated on the basis of Eq. (8)). For flow of a homogeneous two-phase mixture, we can write Eq. (11) in the form [11]

$$\frac{\Delta p}{\Delta p_0} = 1 + \left(\frac{\rho'}{\rho''} - 1\right)x \tag{12}$$

This implies the following approximate formula for the representation of the dependence (11)

$$\frac{\Delta p}{\Delta p_0} \approx 1 + \psi\left(\frac{\rho'}{\rho''} - 1\right)x \tag{13}$$

where ψ is the inhomogeneity factor. As it follows from the theoretical model of [9], two-phase flow in the pebble bed within the wide range of the steam quality is realized in the form of a homogeneous regime characterized by multiple bubble contacts with each other and with bed pebbles. This allows us to suppose that the inhomogeneity factor is independent of the steam quality and of the mass-flow rate and is the function of pressure only: $\psi \approx \psi(\rho'/\rho'')$. On the basis of the assumptions made above, the experimental points in Fig. 4 were approximated by the linear functions $\Delta p/\Delta p_0 = f(x)$.

To reveal effects of pressure, the experimental data obtained were divided in four groups: 2.0–3.0 MPa, 4.6–5.6 MPa, 8.4–10.4 MPa, and 14.6–15.6 MPa. As is seen from Fig. 4, the relative pressure loss increases with the growth of the mass steam quality and a decrease in pressure. The more thorough analysis of the experimental data shows that their spread (especially significant within the range 2.0–3.0 MPa) is explained in a great extent by the stratification over pressure within the corresponding interval. Therefore, we cannot consider the assumptions made above as final ones: in the actual situation, the function $\Delta p/\Delta p_0 = f(x)$ can

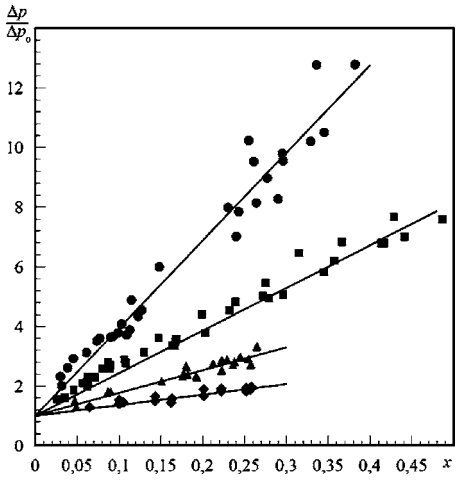

Fig. 4 Dependence of the relative pressure loss on steam quality for fluid flow of a steam-water mixture in the pebble bed; ●: p=2.0–3.0 Mpa; ■: p=4.6–5.6 Mpa; ▲: p =8.4–10.4 Mpa; ♦: p=14.6–15.6 MPa

have a nonlinear character (in particular, in the region $x>0.5$ not studied in the present paper) and also can be dependent on j. To obtain more reliable information on the pressure loss for two-pase flows in a pebble bed, we need to carry out further experimental investigations and theoretical calculations.

Building models of heat transfer in boiling and two-phase flow in porous media [9] and microchannels [12] requires knowledge of local pressure gradients in a steam water flow. To this end, the experimental data on pressure drops in a pebble bed for a broad range of parameters obtained in the present study can be particularly useful.

Conclusions

As an extension of the preceding study [10], the experimental investigation is performed of the hydrodynamic coefficient for steam-water flow in a pebble bed. Compared to the study [10], the variation range of regime parameters was considerably extended, and the significant improvement of the pebble-bed homogeneity was attained owing to the replacement of lead balls by calibrated steel balls. It is found that the relative pressure loss of two-phase flow in a fixed pebble bed is independent (with allowance for the spread of the experimental data) of the mass-flow rate. For each fixed pressure value, they can be approximated by linear functions of the mass-flow steam quality. The simple form of the experimental dependences obtained presents the basis for constructing a physical model for two-phase flows in pebble beds, which makes it possible to obtain urgent calculation results important for practice. Specifically, the data are applicable for modeling heat transfer in two-phase flow in porous media and microchannels.

Acknowledgment

This work was supported by the Russian Foundation of Basic Research (Grant No. 06-08-00323-a).

Nomenclature

c_p = specific heat capacity at constant pressure
$\bar{d}$ = mean ball diameter
G = mass flow
H = layer height between points of the pressure measurement in a pebble bed
j = mass-flow rate
L = specific (latent) heat of evaporation
m = pebble-bed porosity
N = electric power
Δp = pressure drop
Q = heat loss
Re = Reynolds number, $u\bar{d}/\nu$
ΔT = subcooling
u = flow velocity
V = volume
x = steam quality

Greek Symbols

ρ = mass density
ρ' = density of liquid
ρ'' = steam density
ν = kinematic viscosity
ξ = hydrodynamical-drag coefficient
ψ = inhomogeneity factor

References

[1] Damköhler, G., 1936, "Einflüsse der Strömung, Diffusion und des Wärmeüberganges auf die Leistung von Reaktionsöfen," Z. Elektrochem., **42**, pp. 846–863.
[2] Ergun, S., 1952, "Flow Through Packed Columns," Chem. Eng. Prog., **48**, pp. 89–94.
[3] Perry, R. H., and Green, D. W., 1997, *Chemical Engineers' Handbook*, 7th Ed., McGraw-Hill, New York.
[4] Schlünder, G.-J., 2002, *VDI-Wärmeatlas*, Springer-Verlag, Berlin.
[5] Haidegger, E., Vortmeyer, D. et al., 1989, "Simultane Lösung von Energie-, Stoff- und Impuls-gleichungen für wandgekühlte chemische Festbettreaktoren," Chem.-Ing.-Tech., **61**, pp. 647–650.
[6] Johns, M. L., Sederman, A. J. et al., 2000, "Local Transitions in Flow Phenomena Through Packed Beds Inentified by MRI," AIChE J., **46**, pp. 2151–2161.
[7] Giese, M., 1998, "Strömung in porösen Medien unter Berücksichtigung effektiver Viskositäten," Ph.D. thesis, Fachbereich Maschinenwesen, Technische Universität München, München.
[8] Winterberg, M., 2000, "*Modellierung des Wärme- und Stofftransports in durchströmten Festbetten mit homogenen Einphasenmodellen*," VDI Verlag, Düsseldorf.
[9] Dhir, V. K., 1994, "Boiling and Two-Phase Flow in Porous Media," Annu. Rev. Heat Transfer, **5**, pp. 303–350.
[10] Avdeev, A. A., Balunov, B. F. et al., 2003, "Hydrodynamical Drag for Two-Phase Flow Mixture in a Pebble Bed," High Temp., **41**, pp. 377–383.
[11] Wallis, G. B., 1969, *One Dimensional Two-Phase Flow*, McGraw Hill, New York.
[12] Koo, J.-M., Sungjun, I. et al., 2005, "Integrated Microchannel Cooling for Three-Dimensional Electronic Circuit Architectures," ASME J. Heat Transfer, **127**, pp. 49–58.

Developing Turbulent Forced Convection in Two-Dimensional Duct

Y. T. Chen[1]

J. H. Nie

Department of Mechanical Engineering,
University of Nevada,
Las Vegas, NV 89154

B. F. Armaly
Department of Mechanical and Aerospace Engineering,
University of Missouri-Rolla,
Rolla, MO 65401

H. T. Hsieh

R. F. Boehm

Department of Mechanical Engineering,
University of Nevada,
Las Vegas, NV 89154

Developing turbulent forced convection flow in a two-dimensional duct is simulated for Reynolds numbers ranging from 4560 to 12,000. Simultaneously developing velocity and temperature distributions are reported by treating the inlet flow as isothermal with uniform velocity profile. The walls are supplied with uniform heat flux. Distributions of the streamwise and the transverse velocity components exhibit a maximum near the walls, but not at the center of the duct, in the developing region of the flow. The friction coefficient and the Nusselt number do not reach the fully developed values monotonously, and a minimum in their distributions appears in the developing region. Some results are compared with the available data, and very favorable comparisons are obtained. [DOI: 10.1115/1.2740659]

Keywords: turbulent, heat transfer, forced convection, developing flow, duct

Introduction

The fundamental turbulent flow and heat transfer mechanism is of great importance from both scientific and engineering viewpoints because it occurs frequently and plays a predominant role in convective momentum, heat and mass transfer in many industrial applications, such as compact heat exchangers, gas turbine cooling systems, nuclear reactors, and numerous others. Turbulent forced channel flow, due to its geometric simplicity and fundamental nature to understand the transport mechanism, has been studied extensively from both experimental [1–3] and numerical [4–6] approaches. Wei and Willmarth [2] presented the velocity components for the Reynolds numbers of 3000–40,000 using laser Doppler anemometer. The measurements using hot-film anemometry were reported by Johansson and Alfredsson [3]. During the recent years, the performance of turbulence and heat transfer models in predicting the velocity and temperature fields of relevant industrial flows has become increasingly important. Recent advances in large-scale computers have made it possible to conduct the fundamental studies of turbulent flow numerically at moderate Reynolds numbers. Kim et al. [4] numerically solved the unsteady Navier-Stokes equations using direct numerical simulation (DNS) at Reynolds number of 3300. A number of statistical correlations which were complementary to the existing experimental data were reported. Moser et al. [5] simulated the fully developed channel flow for the friction Reynolds number of 180-590 using direct numerical simulation. Abe et al. [6] reported the effects of Reynolds number on various turbulent statistics for the friction Reynolds numbers of 180, 395, and 640.

These experimental/numerical results are restricted to the fluid mechanics case. Kim and Moin [7] studied the heat transfer (mass transport) in two-dimensional forced convection channel flow for different Prandtl (Schmidt) numbers. Kasagi et al. [8] revisited the problems by employing a constant time-averaged heat flux boundary condition on the walls for a mild Reynolds number of 4580. Recently, Debusschere and Rutland [9] investigated the transport of passive heat transfer in a plane channel and Couette flow for the Reynolds number of 3000.

However, most of the published results are limited to the fully developed turbulent channel flow and/or the Reynolds number is mild. To the best of the authors' knowledge, study of simultaneously developing turbulent convection flow in channel has not been reported in the published literature. This fact, together with the realization that in the practical applications the flow and heat transfer start with the developing region and the Reynolds number is high, motivated the present study.

Problem Statement and Simulation Procedures

Turbulent developing forced convection flow in a parallel channel is numerically simulated. The simulated geometry has a height (h) of 0.01 m. By exploiting the symmetry of the flow and temperature fields in the transverse direction, the computational domain was reduced to half of the actual height of the channel (δ =0.005 m). This assumption of symmetry is confirmed by computation with a whole domain. The length of the computational domain is 2 m, i.e., $x/\delta \leqslant 400$. This computational domain was used in order to obtain the asymptotic behavior for the fully developed regime. The origin of the coordinates system is located at the bottom edge and the inlet of the channel. The steady turbulent Navier–Stokes and energy equations are solved numerically together with the continuity equation using the finite volume method and four-equation low-Reynolds-number model [10,11]. The governing equations based on the approximation of eddy-viscosity for fluid and eddy-diffusivity for heat and the constants appearing in the governing equations can be found in Ref. [12]. They are not shown here due to space limitation. The physical properties are treated as constants and evaluated for air at the inlet temperature (T_0) of 20°C, that is, density (ρ) is 1.205 kg/m^3, molecular dynamic viscosity (μ) is 1.82×10^{-5} kg/(m s), specific heat (C_p) is 1005 J/(Kg°C), and thermal conductivity (λ) is 0.0258W/(m°C). Flow at the inlet section of the channel (x/δ =0) is considered to be isothermal (T_0=20°C), with a uniform streamwise velocity component (u) equal to the bulk velocity (u_0). The other velocity component, v, is set to be equal to zero at that inlet section. No slip boundary condition (zero velocities) is applied to the wall surface. Uniform heat flux (q_w=500 W/m^2) is applied at the walls. The kinetic energies (k and $\overline{t^2}$) at the wall are equal to zero. The dissipation rate for the fluid field (ε) is set to be $\varepsilon_w = 2\nu k_1/n_1^2$ and the dissipation rate for the thermal field (ε_t) is $\varepsilon_{t_w} = \alpha(\partial\sqrt{\overline{t^2}}/\partial n)^2$ at the solid walls, where k_1 is the kinetic energy and n_1 is the normal distance of the first node near the wall, respectively, and α is thermal diffusivity. Fully developed flow and thermal boundary conditions are imposed at the exit section of the computational domain (x/δ=400).

[1]Corresponding author.

Contributed by the Heat Transfer Division of ASME for publication in the JOURNAL OF HEAT TRANSFER. Manuscript received December 28, 2005; final manuscript received October 24, 2006. Review conducted by N. K. Anand.

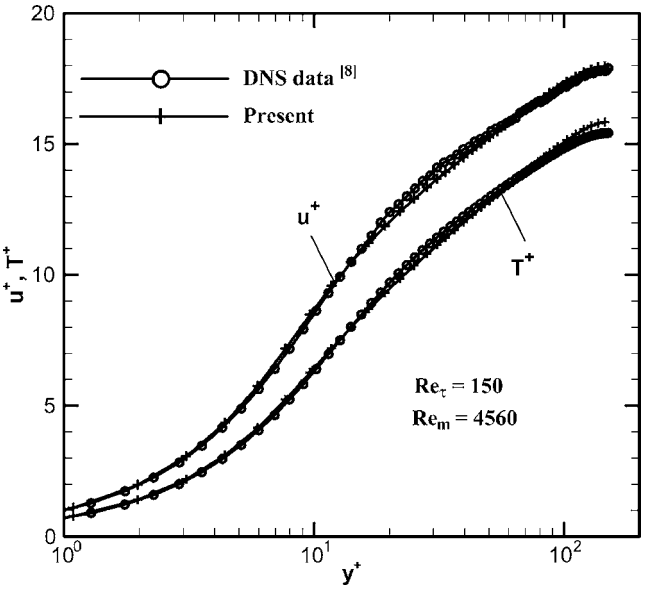

Fig. 1 Comparisons with the DNS data for the mean profiles

The governing equations are discretized using the staggered grid arrangement, and the resulting finite volume equations using SIMPLE algorithm are solved numerically by making use of a line-by-line method combined with ADI scheme [13]. Nonuniform grid system is employed in the simulations, and the grid is highly concentrated near the solid wall, in order to ensure the accuracy of the numerical simulations. Comparisons of the dimensionless mean velocity ($u^+=u/u_\tau$, where $u_\tau=\sqrt{\tau_w/\rho}$ and τ_w is wall shear stress) and temperature [$T^+=(T_w-T)/t_\tau$, where T_w is wall temperature and $t_\tau=q_w h/(\rho C_p u_\tau)$] profiles with the direct simulated data [8] are shown in Fig. 1. These profiles are taken at the streamwise location of $x/\delta=390$, where the flow and heat transfer have already become fully developed. The mean velocity and temperature profiles agree closely well with those DNS results. Results from several grid densities for a Reynolds number ($\mathrm{Re}_m=2\rho u_m \delta/\mu$) of 6000 were used in developing a grid independence solution for this study. The velocity and temperature values at a selected point in the flow domain are presented in Table 1 for different computational grids. A grid of $100(x)\times 41(y)$ is used during the present simulations and a denser grid of $120(x)\times 51(y)$ results in less than 1% difference in the predicted streamwise velocity component at the selected point. The convergence criterion required that the maximum relative mass residual based on the inlet mass be smaller than 3×10^{-6}. It usually takes about 45,000 iterations to meet this requirement. The other test case to validate the flow simulation code that is used in this study is the two-dimensional turbulent flow and heat transfer over backward-facing step [12]. Predicted velocity profiles at several streamwise locations are compared with the laser Doppler measurements [14] as shown in Fig. 2 with good agreement between the predicted

Table 1 Velocities and temperatures at $x=0.2$ m and $y=0.002$ m for different computational grids ($\mathrm{Re}_m=6000$)

Grid	Size ($x\times y$)	u (m/s)	v (m/s)	T (°C)
1	40×11	9.294	0.001381	22.26
2	60×21	9.429	0.002070	22.14
3	80×31	9.457	0.002196	22.10
4	100×41	9.465	0.002218	22.08
5	120×51	9.471	0.002231	22.07

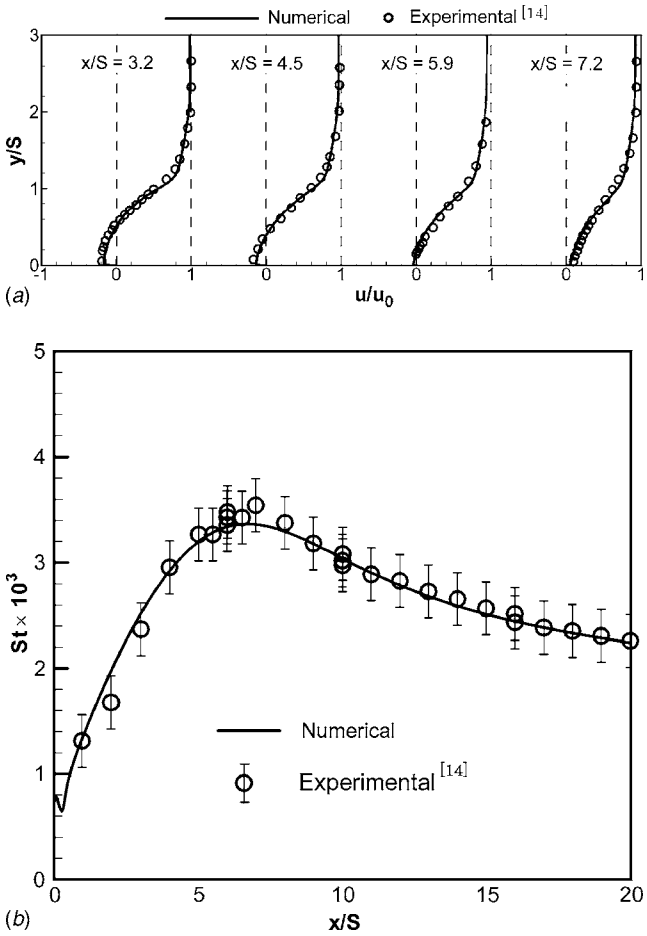

Fig. 2 Comparisons of the mean velocity profiles and the Stanton number for the separated convection flow

and measured data (S is step height). Comparison of the computed Stanton number [$\mathrm{St}=q_w/(\rho C_p u_c(T_w-T_0))$], where u_c is the centerline velocity) on the heated bottom wall is made with the available measured data [14] as shown in Fig. 2. Very close agreement is obtained for the Stanton number profile inside the recirculation region and near the reattachment region, which justifies the present convection flow simulation code and provides with confidence for the next simulations.

Results and Discussions

The simultaneously developing turbulent flow and heat transfer in a parallel channel is simulated for different Reynolds numbers of 4560, 6000, 7500, 9000, 10,500 and 12,000. The bulk Nusselt number [$\mathrm{Nu}_b=q_w h/\lambda(T_w-T_b)$, where T_b is bulk temperature] for the fully developed turbulent channel flow with a constant heat flux is shown in Fig. 3. The direct simulated result [8] and the experimental data [15] are also included in Fig. 3. The Nusselt number increases with the increase of Reynolds number. The Nusselt number obtained by the present simulation for $\mathrm{Re}_m=4560$ is 15.5, and it is in excellent agreement with the DNS data which is 15.4 [8].

Distributions of the mean streamwise velocity component (u) at different streamwise locations in the entrance region of the channel are shown in Fig. 4 for the Reynolds numbers of 4560 and 12,000. Similar results are also obtained for other Reynolds numbers but not presented in the manuscript due to space limitation. Velocity at the centerline of the channel increases from the uniform inlet velocity profile to the fully developed velocity profile. The nonparabolic pattern observed for the laminar flow in a cir-

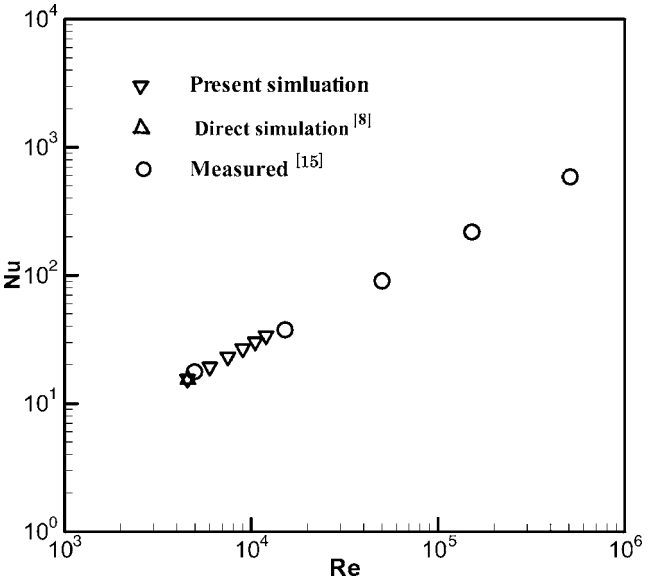

Fig. 3 Distribution of the Nusselt number for the fully developed turbulent channel flow

cular duct [16] is also seen for the turbulent flow in the parallel channel. In the entrance region, the maximum streamwise velocity component does not appear at the center of the channel, but near the solid wall ($y/\delta=0$). For the Reynolds numbers of 4560 and 12,000, at $x/\delta=1$, their peak values develop at $y/\delta\approx0.16$ and 0.11, respectively. The similar feature can also be seen at the section of $x/\delta=0.5$. Distributions of the streamwise velocity component in the entrance region are displayed in Fig. 5. The dashed line denotes the locations where the streamwise velocity component (u) is a maximum at the streamwise planes. Figure 5 also shows that in the entrance region the maximum of this velocity component does not appear at the center of the channel, but near the wall.

Distributions of the transverse velocity component (v) at several streamwise locations for the Reynolds numbers of 4560 and 12,000 are shown in Fig. 6. The dashed line denotes the locations where the transverse velocity component (v) is a maximum at the streamwise planes. This velocity component is zero at the wall ($y/\delta=0$) and the symmetry centerline ($y/\delta=1$). For $\mathrm{Re}_m=4560$ and 12,000 at $x/\delta=1$, their maximum values develop at $y/\delta\approx0.12$ and 0.09, respectively. Its magnitude decreases and its location moves toward the centerline as the x-planes increase in the streamwise direction. At the same x-planes, the magnitudes of the peak v-velocity component decrease as the Reynolds number increases. Distributions of the transverse velocity component in the entrance region are presented in Fig. 7. The locations where the transverse velocity component is a maximum in the transverse direction for the x-planes are shown in Fig. 7 with the dashed lines. Near the inlet section, the maximum v-velocity component develops to appear close to the wall ($y/\delta=0$). Its location moves toward the centerline of the channel as the location of the x-plane increases in the flow direction.

Distributions of the temperature difference based on the wall temperature ($\delta T=T_w-T$) at several streamwise planes are shown in Fig. 8 for the Reynolds numbers of 4560 and 12,000. At the same streamwise planes, the temperature difference deceases as the Reynolds number increases. One feature in the temperature distribution is that the temperature difference increases at first from the inlet section ($x/\delta=0$) to the streamwise section of $x/\delta=20$, then it decreases at the downstream x-planes (from $x/\delta=40$ to 100). The results show that profiles of the temperature difference at other downstream x-planes ($x/\delta>100$) are almost

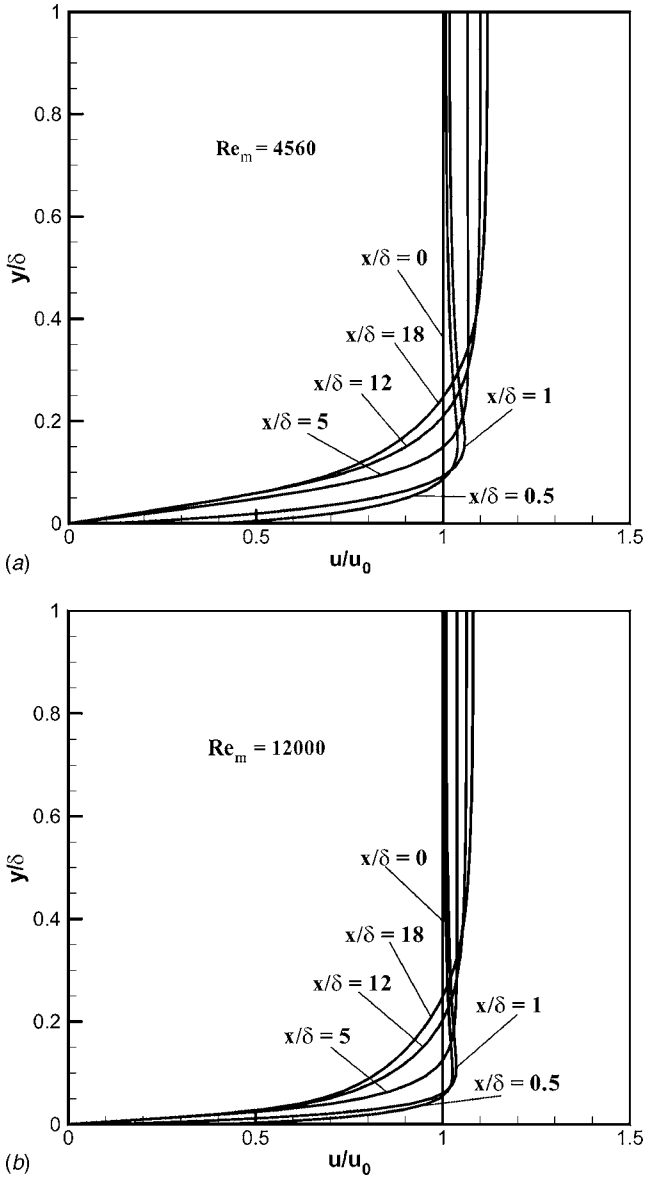

Fig. 4 Distributions of the streamwise velocity at several *x*-planes

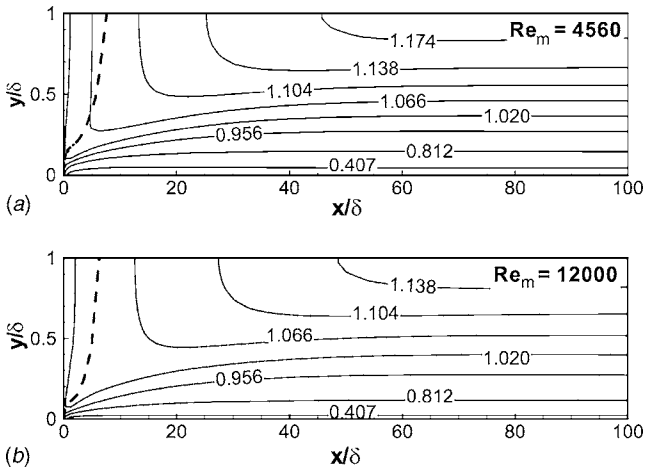

Fig. 5 Distributions of the streamwise velocity component (u)

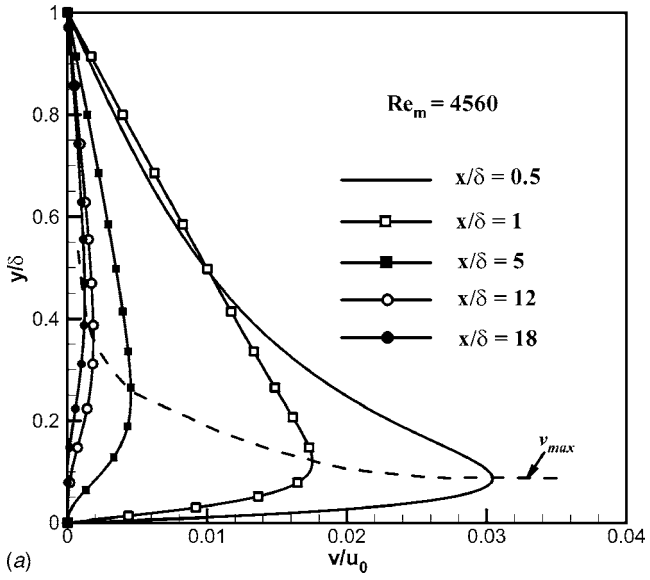

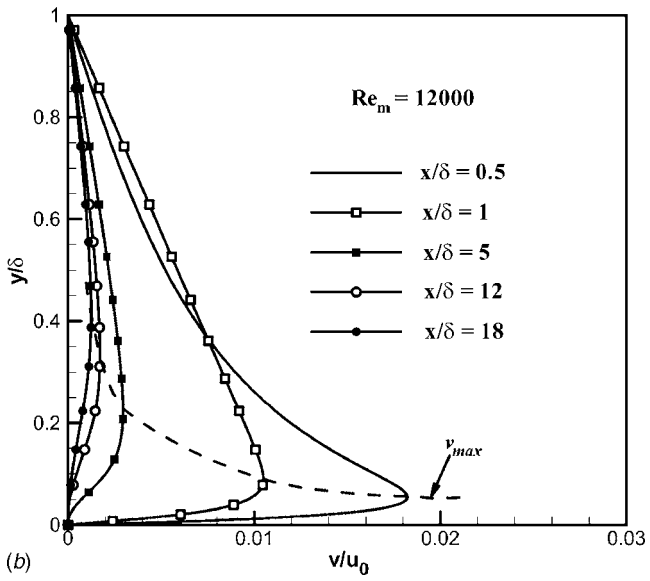

Fig. 6 Distributions of the transverse velocity component at several *x*-planes

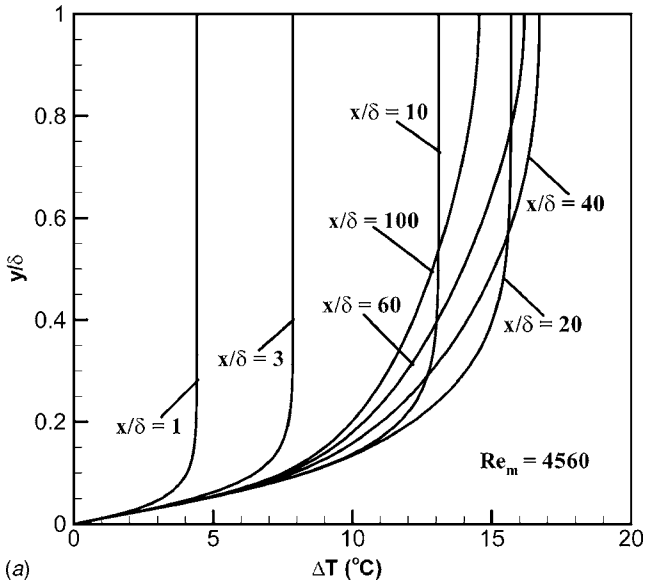

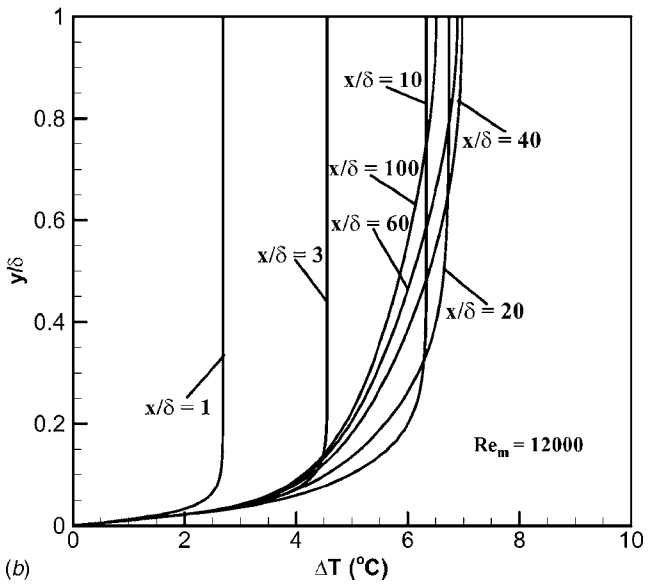

Fig. 8 Distributions of the temperature difference ($T_w - T$) at several *x*-planes

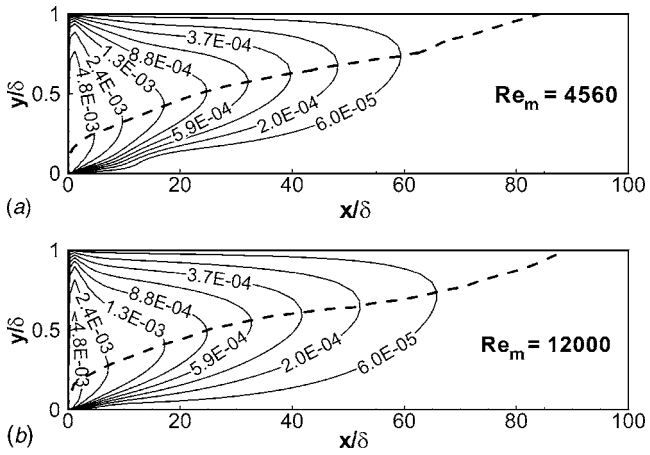

Fig. 7 Distributions of the transverse velocity component (v)

overlaid with the profile at ($x/\delta = 100$). The similar features are also observed for other studied Reynolds numbers.

The friction coefficient ($C_f = 2\tau_w/\rho u_0^2$) for different Reynolds numbers is presented in Fig. 9. The friction coefficient decreases with the increase of Reynolds number. The friction coefficient becomes smaller from the inlet section and reaches the fully-developed values ($x/\delta > 100$). One feature in its distributions is that decrease of the friction coefficient in the streamwise direction does not follow the monotonous way in the entrance region. A minimum value is observed near the inlet section, which can be seen more clearly for the Reynolds number of 4560. Distributions of the bulk Nusselt number for different Reynolds numbers are shown in Fig. 10. The magnitude of Nusselt number increases with the increase of Reynolds number. The Nusselt number becomes smaller in its magnitude from the inlet section and approaches the fully developed values ($x/\delta > 120$). Similarly, the Nusselt number in the streamwise direction does not decrease monotonously in the entrance region. A minimum value in the

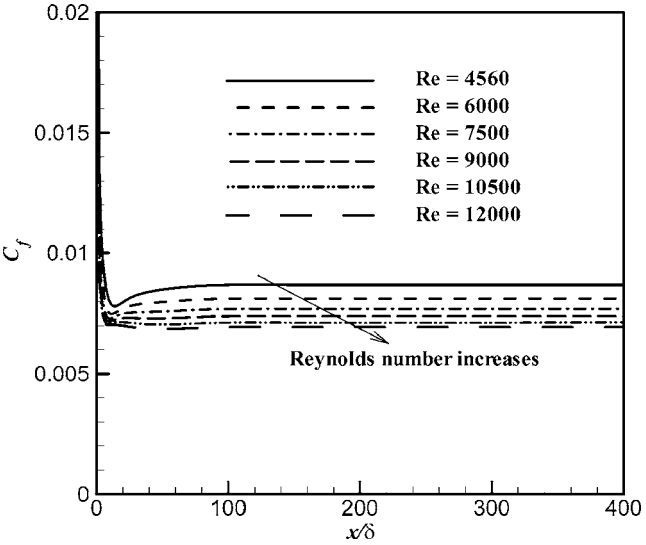

Fig. 9 Distributions of the friction coefficient (C_f)

streamwise distribution of the Nusselt number develops in the entrance region of turbulent convention channel flow for the studied Reynolds numbers

Conclusions

Convection in turbulent forced flow in a parallel channel, where the walls are heated with constant heat flux, is examined for the purpose of determining the flow and thermal behavior that simultaneously develops in the entrance region of this geometry. Nonparabolic patterns in the mean streamwise velocity component are observed for the studied Reynolds numbers. The peak streamwise velocity component develops to appear near the wall, but not at the centerline, in the entrance region. Such patterns are also seen in the distribution of temperature field. The friction coefficient decreases with the increase of Reynolds number. The Nusselt number increases with the increase of Reynolds number. It does not reach the fully developed value monotonously and a minimum develops in the developing region.

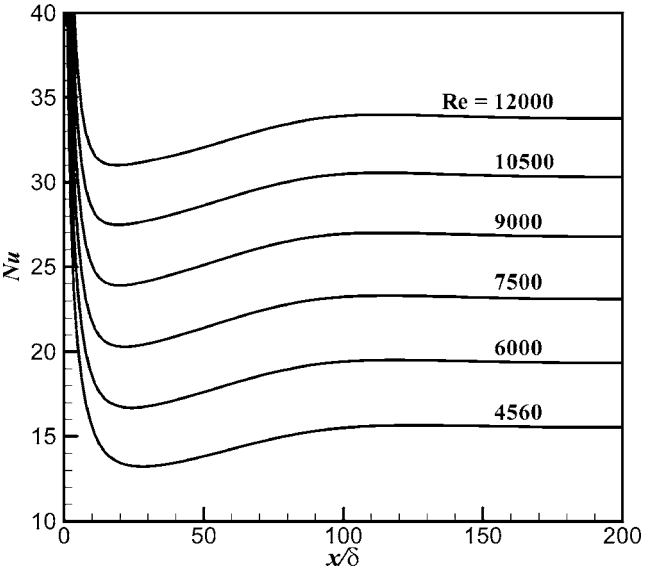

Fig. 10 Distributions of the bulk Nusselt number (Nu_b)

Acknowledgment

This work was in part supported by U.S. Army Research Laboratory under Grant No. DAAD 19-03-2-0007 and by U.S. Department of Energy under Grant Nos. DE-FG02-03ER46067 and RF-05-HFS-006. J.H.N. gratefully acknowledges H. Lan for useful discussions.

References

[1] Hussain, A. K. M. F, and Reynolds, W. C., 1975, "Measurements in Fully Developed Turbulent Channel Flow," ASME J. Fluids Eng., **97**(4), pp. 568–580.
[2] Wei, T., and Willmarth, W. W., 1989, "Reynolds-Number Effects on the Structure of a Turbulent Channel Flow," J. Fluid Mech., **204**, pp. 57–95.
[3] Johansson, A. V., and Alfredsson, P. H., 1982, "On the Structure of Turbulent Channel Flow," J. Fluid Mech., **122**, pp. 295–314.
[4] Kim, J., Moin, P., and Moser, R., 1987, "Turbulence Statistics in Fully Developed Turbulent Channel Flow at Low Reynolds Number," J. Fluid Mech., **177**, pp. 133–166.
[5] Moser, R. D., Kim, J., and Mansour, N. N., 1999, "Direct Numerical Simulation of a Fully Developed Turbulent Channel Flow Up to Re_τ=590," Phys. Fluids, **11**(4), pp. 943–945.
[6] Abe, H., Kawamura, H., and Matsuo, Y., 2000, "Direct Numerical Simulation of a Fully Developed Turbulent Channel Flow With Respect to the Reynolds Number Dependence," ASME J. Fluids Eng., **123**(2), pp. 382–393.
[7] Kim, J., and Moin, P., 1989, "Transport of Passive Scalars in a Turbulent Channel Flow," *Turbulent Shear Flow VI*, J.-C. Andre, J. Cousteix, F. Durst, B. E. Launder, F. W. Schmidt, and J. H. Whitelaw, eds., Springer, Berlin, pp. 85–96.
[8] Kasagi, N., Tomita, Y., and Kuroda, A., 1992, "Direct Numerical Simulation of Passive Scalar Field in a Turbulent Channel Flow," ASME J. Heat Transfer, **114**(3), pp. 598–606.
[9] Debusschere, B., and Rutland, C. J., 2004, "Turbulent Scalar Transport Mechanisms in Plane Channel and Couette Flows," Int. J. Heat Mass Transfer, **47**(8&9), pp. 1771–1781.
[10] Abe, K., Kondoh, T., and Nagano, Y., 1994, "A New Turbulence Model for Predicting Fluid Flow and Heat Transfer in Separating and Reattaching Flows—I. Flow Field Calculations," Int. J. Heat Mass Transfer, **37**(1), pp. 139–154.
[11] Abe, K., Kondoh, T., and Nagano, Y., 1995, "A New Turbulence Model for Predicting Fluid Flow and Heat Transfer in Separating and Reattaching Flows—II. Thermal Field Calculations," Int. J. Heat Mass Transfer, **38**(8), pp. 1467–1481.
[12] Chen, Y. T., Nie, J. H., Armaly, B. F., and Hsieh, H. T., 2006, "Turbulent Separated Convection Flow Adjacent to Backward-Facing Step—Effects of Step Height," Int. J. Heat Mass Transfer, **49**(19&20), pp. 3670–3680.
[13] Patankar, S. V., 1980, *Numerical Heat Transfer and Fluid Flow*, Hemisphere, New York.
[14] Vogel, J. C., and Eaton, J. K., 1985, "Combined Heat Transfer and Fluid Dynamic Measurements Downstream of a Backward-Facing Step," ASME J. Heat Transfer, **107**(4), pp. 922–929.
[15] Kays, W., and Crawford, M. E., 1980, *Convective Heat and Mass Transfer*, McGraw-Hill, New York.
[16] Yu, B., and Ozoe, H., 2001, "Non-Parabolic Flow Pattern at the Entrance Region in a Circular Tube With a Uniform Inlet Velocity," Numer. Heat Transfer, Part A, **39**(8), pp. 857–862.

Journal of Heat Transfer

Discussion

Discussion: "Heat Transfer and Wall Heat Flux Partitioning During Subcooled Flow Nucleate Boiling–A Review" (Warrier, G.R., and Dhir, V.K., 2006, Journal of Heat Transfer, 128, pp. 1243–1256)

Satish G. Kandlikar
Fellow Member ASME
Rochester Institute of Technology,
Rochester, NY
e-mail: sgkeme@rit.edu

In their paper [1], the authors state on p. 1245 that Boyd and Meng [2] in 1996 suggested an interpolation method for calculating the heat transfer characteristics in the partial boiling region, along with Eqs. (13)-(14). The authors of [1] further state that Kandlikar [3] in 1998 proposed a similar scheme and that the constants a, b, and m were assumed to be constant.

In this discussion, we would like to point out a few errors/omissions in the above referenced paper [1].

1. In their technical note, Boyd and Meng [2] refer to the paper by Kandlikar [4], published in 1990, for the Eqs. (13)-(14) referred to in [1]. Unfortunately, Boyd and Meng quoted the wrong reference for the Kandlikar work in which the original model and equations were reported. The 1990 paper by Kandlikar [4], erroneously referred by Boyd and Meng, presents a correlation in the saturated flow boiling region and makes no reference to subcooled flow boiling. The correct reference in Boyd and Meng's paper should have been Kandlikar [5], which was published in 1991.

2. In his 1991 paper, Kandlikar [5] presented Eqs. (21)-(29) with an accompanying Fig. 4 explaining the construction in the subcooled partial boiling region. Immediately following Eq. (26), a note appears regarding the exponent m, which matches the slope at the two ends. Kandlikar [5], however, contains typographical errors in Eqs. (25) and (26) for coefficients a and b.

3. Those typographical errors were later corrected by Kandlikar [3] in 1998.

4. Another error that appears in [1] is the incorrect year of publication of the paper by Boyd and Meng [2], cited as Ref. [12]; the correct year of publication is 1995, not 1996.

5. Discussion related to Fig. 6 appearing in [1] is correct, except that the 1998 paper by Kandlikar [3] referred therein simply corrects the typographical error and provides a more detailed comparison with the available experimental data.

6. Equation (21) appearing in Warrier and Dhir [1] is based on the paper by Kandlikar [3] as correctly reported by the authors of [1]. However, the equation itself is incorrectly reproduced. The correct form of the equation (appearing as Eq. 14 in Ref [3]) is as follows:

$$\dot{q} = [1058.0(\dot{m}h_{fg})^{-0.7} F_{\mathrm{Fl}} h_{\mathrm{LO}} \Delta T_{\mathrm{sat}}]^{1/0.3} \tag{1}$$

where $\dot{m}$ is the mass flux (kg/m^2 s). The negative sign in the exponent 0.7 is missing in Eq. (21) in [1], and the wall superheat ΔT_{sat} is incorrectly replaced by $(\Delta T_w + \Delta T_{\mathrm{sub}})$.

Subcooled Flow Boiling Model Description

For convenience, the correct form of the subcooled flow boiling model and coefficients are presented below.

Figure 1 shows a schematic representation of the subcooled flow boiling curve extending from the single-phase region at point C to the fully developed boiling at point E. In the single-phase region, to the left of C in Fig. 1, heat flux $\dot{q}$ is given by the following equation:

$$\dot{q} = h_{\mathrm{LO}}(\Delta T_{\mathrm{sat}} + \Delta T_{\mathrm{sub}}) \tag{2}$$

where h_{LO} is the single-phase heat transfer coefficient with all flow as liquid, the local wall superheat is $\Delta T_{\mathrm{sat}} (= T_w - T_{\mathrm{sat}})$ and the local liquid subcooling is $\Delta T_{\mathrm{sub}} (= T_{\mathrm{sat}} - T_f)$, the local saturation temperature is T_{sat}, the wall temperature is T_w and the liquid temperature is T_f.

In the fully developed boiling region, the heat transfer rate is related to the local wall superheat by the following equation:

$$\frac{\dot{q}}{\Delta T_{\mathrm{sat}}} = 1058.0 \mathrm{Bo}^{0.7} F_{\mathrm{Fl}} h_{\mathrm{LO}} \tag{3}$$

where Bo is the boiling number $(\dot{q}/(Gh_{fg}))$ G is the total mass flux (kg/m^2 s), and h_{fg} is the latent heat of vaporization (J/kg), and F_{Fl} is the fluid-dependent parameter in the Kandlikar correlation [3]. The value of F_{Fl} is 1 for water and all other fluids flowing in stainless steel tubes. For specific fluids in different tube materials, refer to [4] or other more recent publications.

The equation for the $\dot{q} - \Delta T_{\mathrm{sat}}$ plot in the partial boiling region, the main focus of the current discussion, is given by the following equation:

$$\dot{q} = a + b(T_w - T_{\mathrm{sat}})^m = a + b(\Delta T_{\mathrm{sat}})^m \tag{4}$$

The constants a, b, and m are functions of heat flux $\dot{q}$. The slope of the heat flux versus wall superheat in the partial boiling region is matched with the two limiting values, i.e., $m=1$ in the single-phase region at the beginning of the partial boiling region, identified by point C, and $m=1/0.3$ at the beginning of the fully developed boiling region identified by point E. Thus, the values of a and b are obtained in terms of the heat fluxes and wall superheats at C and E, and the value of m is obtained in terms of the heat fluxes at C, E and at the desired location, where heat flux is $\dot{q}$ and wall superheat is ΔT_{sat}.

Contributed by the Heat Transfer Division of ASME for publication in the JOURNAL OF HEAT TRANSFER. Manuscript received February 5, 2007; final manuscript received March 26, 2007. Review conducted by Yogesh Jaluria.

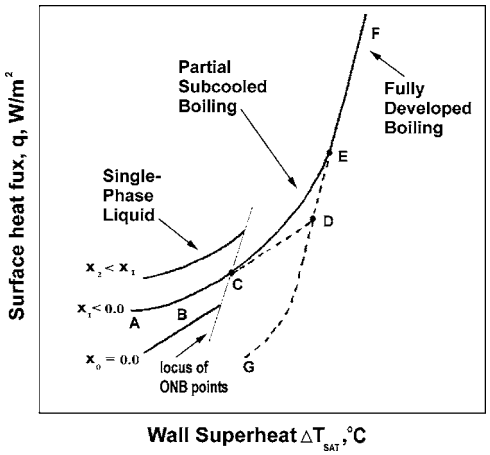

Fig. 1 A representative log-log plot of $\dot{q}$ versus ΔT_{sat} for describing the Kandlikar model in the partial boiling region, adapted from Kandlikar [5]

$$b = \frac{\dot{q}_E - \dot{q}_C}{(\Delta T_{sat,E})^m - (\Delta T_{sat,C})^m} \tag{5}$$

and

$$a = \dot{q}_C - b(\Delta T_{sat,C})^m \tag{6}$$

Note that there were typographical errors in Kandlikar [5] that erroneously omitted the exponent m in Eqs. (5) and (6).

The value of m depends on the heat flux, and is allowed to vary linearly from $m=1$ at C to $m=1/0.3$ at D. Thus,

$$m = n + p\dot{q} \tag{7}$$

and the values of n and p are obtained as follows:

$$p = (1/0.3 - 1)/(\dot{q}_E - \dot{q}_C) \tag{8}$$

and

$$n = 1 - p\dot{q}_C \tag{9}$$

Note that n and p are constants for a system (for a given geometry and operating conditions), whereas the values of m, a, and b depend of the local value of $\dot{q}$. Thus, the value of ΔT_{sat} can be obtained directly from a known value of $\dot{q}$, while an iterative scheme is needed to calculate $\dot{q}$ for a given value of ΔT_{sat} in this region.

Further details on calculating $\dot{q}_C$ and $\dot{q}_E$ are given in Kandlikar [3].

References

[1] Warrier, G. R., and Dhir, V. K., 2006, "Heat Transfer and Wall Heat Flux Partitioning During Subcooled Flow Nucleate Boiling–A Review," ASME J. Heat Transfer, **128**, pp. 1243–1256.

[2] Boyd, R. D., and Meng, X., 1995, "Boiling Curve Correlation for Subcooled Flow Boiling," Int. J. Heat Mass Transfer, **38**, pp. 758–760.

[3] Kandlikar, S. G., 1998, "Heat Transfer Characteristics in Partial Boiling, Fully Developed Boiling, and Significant Void Flow Regions of Subcooled Flow Boiling," ASME J. Heat Transfer, **120**, pp. 390–401.

[4] Kandlikar, S. G., 1990, "A General Correlation for Two-phase Flow Boiling Heat Transfer Inside Horizontal and Vertical Tubes," ASME J. Heat Transfer, **112**, pp. 219–228.

[5] Kandlikar, S. G., 1991, "Development of a Flow Boiling Map for Subcooled and Saturated Flow Boiling of Different Fluids Inside Circular Tubes," ASME J. Heat Transfer, **113**, pp. 190–200.

Discussion: "Second Law Analysis of Laminar Viscous Flow Through a Duct Subjected to Constant Wall Temperature" (Sahin, A. Z., 1998, ASME J. Heat Transfer, 120, pp. 76–83)

M. M. Awad
Faculty of Engineering and Applied Science,
Memorial University of Newfoundland,
St. John's, Newfoundland, A1B 3X5, Canada
e-mail: awad@engr.mun.ca

*In the paper Sahin, A. Z., 1998, "Second Law Analysis of Laminar Viscous Flow Through a Duct Subjected to Constant Wall Temperature" ASME J. Heat Transfer, **120**(1), pp. 76–83, there are many errors in equations, values, etc. The errors will be summarized below.* [DOI: 10.1115/1.2745836]

Based on the definition of the dimensionless temperature difference (τ)

$$\tau = \frac{T_w - T_o}{T_w} \tag{1}$$

For T_w=373 K (Table 1) and T_o=293 K (Tables 2*a*, and 3*a*), τ =0.214 > τ=0.0–0.2 (Table 1). Thus, the range of τ in Table 1 must be τ=0.0–0.25.

Based on Eqs. (8) and (9), then Eq. (10) must be

$$\psi = \left\{ \ln\left(\frac{1-\tau^{e-4St\lambda}}{1-\tau}\right) - \tau(1-e^{-4St\lambda}) + \frac{1}{8}\frac{f\tau Ec}{St}\ln\left(\frac{e^{4St\lambda}-\tau}{1-\tau}\right)\right\} \Big/ (1-e^{-4St\lambda}) \tag{2}$$

The major error in Eq. (10) leads to other many errors in the equations. First, Eq. (14) must be

$$\psi = \left\{ \ln\left(\frac{1-\tau^{e-4\Pi_1}}{1-\tau}\right) - \tau(1-e^{-4\Pi_1}) + 8\tau\Pi_2\ln\left(\frac{e^{4\Pi_1}-\tau}{1-\tau}\right)\right\} \Big/ (1-e^{-4\Pi_1}) \tag{3}$$

Second, Eq. (17) must be

$$\psi = \left\{ \ln\left(\frac{1-\tau^{e-4\Pi_1}}{1-\tau}\right) - \tau(1-e^{-4\Pi_1}) + 8\tau\Pi_2\left[\ln\left(\frac{e^{4\Pi_1}-\tau}{1-\tau}\right) + \left(\frac{bT_{\text{ref}}}{a}\right)\ln\left(\frac{e^{4\Pi_1}-\tau}{1-\tau}\right) - 4\left(\frac{bT_w}{a}\right)\Pi_1\right]\right\} \Big/ (1-e^{-4\Pi_1}) \tag{4}$$

Third, Eq. (20) must be

$$\psi = \left\{ \ln\left(\frac{1-\tau^{e-4\Pi_1}}{1-\tau}\right) - \tau(1-e^{-4\Pi_1}) + 32\Pi_2 \times \int_0^l \frac{\Pi_1}{l}\frac{T_w - T_o}{T_{\text{ref}}^n}T^{n-1}\exp\left[B\left(\frac{1}{T}-\frac{1}{T_{\text{ref}}}\right)\right]dx\right\} \Big/ (1-e^{-4\Pi_1}) \tag{5}$$

Finally, Eq. (22) must be

$$\psi' = \psi(1-e^{-4\Pi_1}) \tag{6}$$

These errors in the above equations lead to errors in values in both figures and tables. For example, values of dimensionless entropy generation (ψ) are incorrect and must be calculated again based on the correct form of Eqs. (14), (17), and (20), respectively. In addition, based on the correct form of Eq. (22), values of dimensionless entropy generation (ψ) must be greater than values of modified dimensionless entropy generation (ψ') at the same modified Stanton number (Π_1) (not as shown, $\psi < \psi'$ at the same Π_1, in Figs. 2 and 3, Tables 2*a* and 3*a*).

On p. 81 (second column), the total dimensionless entropy change using Eq. (14) becomes

$$\psi = 32(\tau\Pi_2)\Pi_1/(1-e^{-4\Pi_1}) \tag{7}$$

On pp. 81 and 82 (Tables 2*b*, 3*b*), values of T_o are in K, not in °C.

In addtion, Sahin [1] made a second law comparison for optimum shape of duct subjected to constant wall temperature and laminar flow. In this paper, the following error is found.

For laminar flow the thermal entry length may be expressed as [2,3]:

$$\left(\frac{x_{fd,t}}{D_H}\right)_{\text{lam}} \approx 0.05\,\text{Re}_{D_H}\,\text{Pr} \tag{8}$$

From Table 1, the hydraulic diameter (D_H) for circular duct geometry can be expressed as

$$D_H = \frac{2}{\sqrt{\pi}}\sqrt{A_c} \tag{9}$$

Combining Eqs. (8) and (9), we obtain

$$(x_{fd,t})_{\text{lam}} \approx \frac{0.1}{\sqrt{\pi}}\sqrt{A_c}\,\text{Re}_{D_H}\,\text{Pr} \tag{10}$$

From Table 2, $(A_c)_{\max}=6\times10^{-7}$ m^2 and Pr=7. From Figs. 1–7, $(\text{Re}_{D_H})_{\max}$=3000. Thus,

$$(x_{fd,t})_{\text{lam}} \approx \frac{0.1}{\sqrt{\pi}}\sqrt{6\times10^{-7}}(3000)(7) \approx 0.92\text{ m} \tag{11}$$

The above value is greater than the length of the duct: L =0.1 m (Table 2). This indicated that the flow is still in thermal entrance laminar region and does not reach fully developed laminar region. This error is repeated for other duct geometries such as square, triangle, etc. As a result, the assumption of the fluid is fully developed laminar as it enters the duct in all types of geometry is not acceptable.

References

[1] Sahin, A. Z., 1998, "A Second Law Comparison for Optimum Shape of Duct Subjected to Constant Wall Temperature and Laminar Flow," Heat Mass Transfer, **33**(5-6), pp. 425–430.
[2] Kays, W. M., Crawford, M. E., and Weigand, B., 2005, *Convective Heat and Mass Transfer*, McGraw Hill, New York.
[3] Incropera, F. P., and DeWitt, D. P., 2002, *Fundamentals of Heat and Mass Transfer*, John Wiley & Sons, Inc., New York.

Contributed by the Heat Transfer Division of ASME for publication in the JOURNAL OF HEAT TRANSFER. Manuscript received February 12, 2007; final manuscript received March 17, 2007. Review conducted by Anthony M. Jacobi.

Closure to "Discussion of 'Second Law Analysis of Laminar Viscous Flow Through a Duct Subjected to Constant Wall Temperature' " (2007, ASME J. Heat Transfer, 129, p. 1302)

Ahmet Z. Sahin
Department of Mechanical Engineering,
King Fahd University of Petroleum and Minerals,
Dhahran, 31261 Saudi Arabia
e-mail: azsahin@kfupm.edu.sa

I would like to thank M. M. Awad for the time he spent and appreciate his consideration in reading and carefully reviewing the paper, Sahin, A. Z., 1998, "Second Law Analysis of Laminar Viscous Flow Through a Duct Subjected to Constant Wall Temperature" ASME J. Heat Transfer, **120**(1), pp. 76–83.

Obviously, the term $(1-e^{-4Sr\lambda})$ in Eq. (10) was supposed to be $(1-e^{-4Sr\lambda})^{-1}$. Unfortunately, this error was propagated in the rest of the paper in Eqs. (14), (17), (20), (22) and in p. 81. Perhaps this is the only major concern about the paper.

As for the range of τ in Table 1, the choice was $0.0 \leq \tau \leq 0.2$ and it is not an error. The reason for this choice is to make sure that all the temperatures in the flow domain remain within the range of temperatures $293\ \mathrm{K} \leq T \leq 373\ \mathrm{K}$, within which the viscosity model parameters a, b, B, and n given in Table 1 are valid (especially for the case of glycerol).

The values of T_0 in Tables 2*b* and 3*b* are in K; however, (°C) in the labels are typing errors.

In the paper, Sahin, A. Z., 1998, "A Second Law Comparison for Optimum Shape of Duct Subjected to Constant Wall Temperature and Laminar Flow," Heat and Mass Transfer /Wärme-und Stoffübertragung, 33(5-6), pp. 425–430, the fluid was assumed to be fully developed laminar as it enters the duct in all types of geometry. Therefore, the comments made regarding the thermal entry length are not relevant.

Contributed by the Heat Transfer Division of ASME for publication in the JOURNAL OF HEAT TRANSFER. Manuscript received March 19, 2007; final manuscript received March 21, 2007. Review conducted by Yogesh Jaluria.

Discussion: "Performance and Optimization Analysis for Fins of Straight Taper with Simultaneous Heat and Mass Transfer" (Kundu, B., and Das, P. K., 2004, ASME J. Heat Transfer, 126, pp. 862–868)

Panagiotis Razelos
Department of Engineering Science and Physics,
College of Staten Island/CUNY,
2800 Victory Blvd.,
Staten Island, NY 10314

In this paper the authors employed a new rather unorthodox approach, and unusual parameterization entirely different from that existing in the literature, to obtain their results. In their abstract, the authors claim to have obtained the performance prediction, i.e., the efficiency and effectiveness, of wet fins, for tapered longitudinal, spines and radial fins. Their lengthy explanation for the obvious differences between wet and dry fins is unnecessary. They further assert to have derived a generalized criterion (what is the meaning of generalized?) for the optimization of the three types of fins they analyze. The authors describe the fins as tapered, shown in their Fig. 1, however the expressions of their profiles such as $y/y_b=f(X,\lambda)$ is missing. Also, their keywords refer to dehumidification and heat exchanger that are not used in the manuscript. Moreover, what is conspicuously missing in this paper is the exact description of the mathematical problem they solve. The authors abruptly start with a differential (Eq. (1)), without any boundary conditions, or any other comments such symmetry, etc. In fact this paper lacks the mathematical perspicuousness and rigor required in any such endeavor.

The following comments are addressed to specific sections of the manuscript.

Nomenclature

We begin with the authors' Nomenclature because it contains several errors, thus making the reading of this manuscript extremely difficult. The Nomenclature is a mirror of the symbols found in the text, which is used to explain their meanings to the reader who frequently needs to consult it.

(i) The authors assume the following linear temperature variation of the specific humidity:

$$\omega = b_1 + b_2 T \tag{1}$$

Considering the values of ω to be specified at the temperatures T_t and T_b, we obtain the following values for of the above constants:

$$b_2 = (\omega_t - \omega_b)/(T_t - T_b), \quad b_1 = \omega_b - b_2 \times T_b \tag{2}$$

The authors' expression for b_1 is incorrect and unless this is a typographical error, this mistake is propagated in their results, although the incautious reader may tempted to ask, are both temperatures, T_b and T_t, that are used in Eq. (2) of this Discussion specified?

(ii) I think $\mathrm{Bi}_t=h_t y_b/k$ should have been $\mathrm{Bi}_t=h_t y_t/k$, although h_t is never defined.

(iii) The authors assert "f, g to be functions defined by Eq. (18) and Eq. (19) respectively." However, Eq. (18) defines the dimensionless volume U, whereas $f(\mathrm{Bi},\psi)$ is defined by Eq. (19), and $g(\mathrm{Bi},\psi)$ by Eq. (20).

(iv) The symbol h_m, which appears in the last term on the left-side of the authors' Eq. (1), has never been defined. Also, the dimensions of q, the actual heat transfer rate, for longitudinal fins should be expressed in watts per meter.

(v) The correct definition of q_e is: "the heat transfer from the base of the fin, with the same heat transfer coefficient in its absence." The assumption for the ideal heat dissipation q_i is: "the entire fin is maintained at the base temperature."

(vi) Q is defined by Eq. (11) not Eq. (10), Q_e by Eq. (16) not Eq. (15), Q_i by Eq. (14) not Eq. (13), and U by Eq. (18) not Eq. (17).

(vii) The parameter Z_0 is recognized as the one which used by Gardner [1] to plot his efficiency graphs and is expressed as the product of the aspect number L/y_b and the $\sqrt{\mathrm{Bi}}$. The quotient L/y_b is always referred in the literature as aspect number, however, the authors' ψ is the reciprocal, but still defined as the aspect number. As shown in Refs. [2,3] the authors' parameters $Z_0^2=\mathrm{Bi}/\psi^2$ and Bi have physical significances.

(viii) Normally, the solutions should be able to handle any values of the parameter $0\leqslant\lambda\leqslant 1$, hence the parameters Z_1, Z_2, and α that, are divided by $(1-\lambda)$, cannot be used unless they are redefined.

(ix) The authors created a huge aggregate of dimensionless parameters, whereas only a few appearing in their results. The principal parameters that are used by the authors in their result are: Z_0, Bi, and λ; however, the temperature is independent of Bi.

Formulation of Mathematical Model

(i) In this section the authors make the following statements: *(1) at any point, the temperature over the fin cross section is assumed to be constant and (2) the transport processes can be rendered one-dimensional (1D) as is conventionally done for dry fins*. The authors should be reminded that, in mathematical analyses nothing is conventionally done, but it must be based on certain fundamental principles. In this case, there are certain conditions, known as simplified assumptions, described in Ref. [1], that must be met, in order to allow using the 1D conduction model. For example here, the restrictive condition for using the 1D approach is the small values of the Biot number (of the order of 0.01). As shown in Refs. [2,3], when one employs the 1D approach, the simplified assumptions, insulated tip and the length of arc idealization are valid. Thus the expression $\sqrt{1+(dy/dx)^2}$ can be eliminated, and the tip boundary condition should be modified accordingly.

(ii) There in no explanation as to why the authors introduce the radius r_i in Eq. (1), which for longitudinal fins and spines is zero, and in radial fins the coordinate x varies from 0 to r_i, instead of $r_i\leqslant x\leqslant r_t$, which is universally used. In this case an important new parameter is introduced namely the ratio parameter r_t/r_i. For example, what is the value of this parameter in the results plotted in the original Fig. 4?

(iii) Now, in any mathematical equation involving symbols with dimensions, like those in Eq. (1), one should always first check if it is dimensionally correct. For longitudinal fins, the dimensions of the left-side and the first right-side terms are kelvin per meter whereas the dimensions of the last term h_{fg} are watts per square meter, with similar contradictions appearing in the other cases. I believe the authors neglected to divide this term with the thermal conductivity k.

(iv) The authors assert that have employed the Chilton Colburn analogy and some algebraic manipulations to derive their Eq. (2). However, the temperature becomes now a function of $Y=y/y_b$ instead of $X=x/L$. This is indeed a very puzzling operation for mainly two reasons. First, according to the authors' earlier statement the temperature along this direction is constant. In the other hand, how could the profiles of the fins, which are $y/y_b=f(X)$, possibly influence the results?

Contributed by the Heat Transfer Division of ASME for publication in the JOURNAL OF HEAT TRANSFER. Manuscript received April 7, 2006; final manuscript received October 18, 2006. Review conducted by Anthony M. Jacobi.

Results and Discussion

At the beginning of this section the authors engage in a long and unnecessary explanation for the self-evident conceptions, of what is meant by dry fins and their performance. Then they present a few graphs, which in the abstract claim to be design curves, while they only refer to one specific case. I am indeed puzzled how these plots were contracted using those formidable equations ((4)–(20)), with all these dimensionless variables, which as was pointed out earlier, they contain several mistakes? What are exactly the differences between efficiencies and effectiveness with the authors' over-all counterparts? I believe that their results are incorrect despite the agreement with previous work shown in the original Fig. 2. Moreover, the variation of the effectiveness versus Z_0 in their Fig. 4 physically does not make sense. For example, when the value of $Z_0=0$ (absence of the fin), by definition, the effectiveness value is equal to 1 instead of the authors' 20. To help the authors revise their paper certain additional references are given here.

I regret to say, that due to space limitations of the journal I cannot describe the correct formulation of the problem that the authors should solve.

References

[1] Gardner, K. A., 1945, "Efficiency of Extended Surfaces," Trans. ASME, **67**, pp. 621–631.

[2] Razelos, P., 2002, "A Critical Review of Extended Surface Heat Transfer," Heat Transfer Eng., **24**(6), pp. 11–28.

[3] Razelos, P., 2005, "A New Approach of Extended Surface Heat Transfer," *Proceedings of IMECE2005*, Paper 83057, Orlando, FL.

Journal of Heat Transfer

Erratum

Erratum: "Natural Convection in a Partitioned Vertical Enclosure With a Uniform Heat Flux" [Journal of Heat Transfer, 2007, 129(6), contents on inside cover]

The paper entitled "Natural Convection in a Partitioned Vertical Enclosure Heated With a Uniform Heat Flux" should be placed under the category "*Natural and Mixed Convection*." It was put in the wrong category of "*Micro/Nanoscale Heat Transfer*" by mistake.

